



MOSCOW CENTER
FOR DIAGNOSTICS & TELEMEDICINE

ISSN 2712-8490 (Print)
ISSN 2712-8962 (Online)

DIGITAL DIAGNOSTICS

A peer-reviewed scientific medical journal

4 Volume 4 Issue



2023



ECO • VECTOR

<https://journals.eco-vector.com/DD>

УЧРЕДИТЕЛИ

- ГБУЗ «Научно-практический клинический центр диагностики и телемедицинских технологий ДЗМ»
- ООО «Эко-Вектор»

Свидетельство о регистрации СМИ ПИ
ПИ № ФС 77 - 79539 от 09.11.2020

ИЗДАТЕЛЬ

ООО «Эко-Вектор»
Адрес: 191186, Санкт-Петербург, Аптекарский
переулок, д. 3, литера А, помещение 1Н
E-mail: info@eco-vector.com
WEB: https://eco-vector.com

РЕКЛАМА

Отдел рекламы
Тел.: +7 (968) 545 78 20
E-mail: adv2@eco-vector.com

РЕДАКЦИЯ

Зав. редакцией
Елена Андреевна Филиппова
E-mail: ddjournal@eco-vector.com
Тел.: +7 (965) 012 70 72
Адрес: 125040, г. Москва,
ул. Расковой, д. 16/26, стр. 1

ПОДПИСКА

Подписка на печатную версию через интернет:
www.journals.eco-vector.com/
www.akc.ru
www.pressa-rr.ru

OPEN ACCESS

В электронном виде журнал распространяется
бесплатно —
в режиме немедленного открытого доступа

ИНДЕКСАЦИЯ

- SCOPUS
- РИНЦ
- Google Scholar
- Ulrich's International Periodicals Directory
- WorldCat

Оригинал-макет

подготовлен в издательстве «Эко-Вектор».
Литературный редактор: *А.А. Ридэль*
Корректор: *А.А. Ридэль*
Вёрстка: *Ф.А. Игнащенко*
Обложка: *Е.Д. Бугаенко*

Сдано в набор 06.12.2023. Подписано в печать 18.12.2023.
Формат 60 × 88%. Печать офсетная. Печ. л. 25,75.
Усл. печ. л. 23,9. Уч.-изд. л. 14,0. Тираж 5000 экз.
Цена свободная.

Отпечатано в ООО «Типография Фурсова»,
196105, Санкт-Петербург, ул. Благодатная, 69.
Тел.: +7 (812) 646-33-77

16+

© ООО «Эко-Вектор», 2023

ISSN 2712-8490 (Print)
ISSN 2712-8962 (Online)

Digital Diagnostics

Том 4 | Выпуск 4 | 2023

ЕЖЕКВАРТАЛЬНЫЙ РЕЦЕНЗИРУЕМЫЙ НАУЧНЫЙ
МЕДИЦИНСКИЙ ЖУРНАЛ

Главный редактор

Синицын Валентин Евгеньевич, д.м.н., профессор (Москва, Россия)
ORCID: 0000-0002-5649-2193

Заместитель главного редактора

Васильев Юрий Александрович, к.м.н., (Москва, Россия)
ORCID: 0000-0002-0208-5218

Научный редактор

Березовская Татьяна Павловна, д.м.н., профессор (Обнинск, Россия)
ORCID: 0000-0002-3549-4499

Ответственный секретарь

Виноградова Ирина Александровна, к.т.н. (Москва, Россия)
ORCID: 0000-0001-6465-4132

Редакционная коллегия

Berlin L., профессор (Иллинойс, США)

ORCID: 0000-0002-0717-0307

Беляев М.Г., к.ф.-м.н. (Москва, Россия)

ORCID: 0000-0001-9906-6453

Важенина Д.А., д.м.н., доцент (Москва, Россия)

ORCID: 0000-0002-6236-709X

Bisdas S., MBBS, MD, PhD (Лондон, Великобритания)

ORCID: 0000-0001-9930-5549

Гомболевский В.А., к.м.н. (Москва, Россия)

ORCID: 0000-0003-1816-1315

Доможирова А.С., д.м.н., доцент (Москва, Россия)

ORCID: 0000-0003-0806-3164

Frija G., профессор (Париж, Франция)

ORCID: 0000-0003-0415-0586

Guglielmi G., MD, профессор (Фоджа, Италия)

ORCID: 0000-0002-4325-8330

Holodny A., д.м.н. (Нью-Йорк, США)

ORCID: 0000-0002-1159-2705

Лебедев Г.С., д.т.н., профессор (Москва, Россия)

ORCID: 0000-0002-4289-2102

Li H., MD, профессор (Пекин, КНР)

ORCID: 0000-0002-9102-4176

Матвеев И.А., д.т.н. (Москва, Россия)

ORCID: 0000-0003-2005-9467

Маццелишвили С.Т., д.м.н., профессор (Москва, Россия)

ORCID: 0000-0002-5670-167X

Митков В.В., д.м.н., профессор (Санкт-Петербург, Россия)

ORCID: 0000-0003-1959-9618

Морозов С.П., д.м.н., профессор (Москва, Россия)

ORCID: 0000-0001-6545-6170

Neri E., д.м.н. (Пиза, Италия)

ORCID: 0000-0001-7950-4559

Омельяновский В.В., д.м.н., профессор (Москва, Россия)

ORCID: 0000-0003-1581-0703

Омельянская О.В., (Москва, Россия)

ORCID: 0000-0002-0245-4431

Oudkerk M., профессор (Гронинген, Нидерланды)

ORCID: 0000-0003-2800-4110

Ros P.R., MD, MPH, PhD, профессор (Нью-Йорк, США)

ORCID: 0000-0003-3974-0797

Rovira A., профессор (Барселона, Испания)

ORCID: 0000-0002-2132-6750

Решетников Р.В., к.ф.-м.н., (Москва, Россия)

ORCID: 0000-0002-9661-0254

Румянцев П.О., д.м.н. (Москва, Россия)

ORCID: 0000-0002-7721-634X

Храмов А.Е., докт.ф.-м.н, профессор (Санкт-Петербург, Россия)

ORCID: 0000-0003-2787-2530

Аншелес А.А., д.м.н. (Москва, Россия)

ORCID: 0000-0002-2675-3276

Арутюнов Г.П., д.м.н. (Москва, Россия)

ORCID: 0000-0002-6645-2515

Белевский А.С., д.м.н., профессор (Москва, Россия)

ORCID: 0000-0001-6050-724X

Васильева Е.Ю., д.м.н., профессор (Москва, Россия)

ORCID: 0000-0003-4111-0874

Гехт А.Б., д.м.н., профессор (Москва, Россия)

ORCID: 0000-0002-1170-6127

Кобякова О.С., д.м.н. (Москва, Россия)

ORCID: 0000-0001-9396-6063

Кремнева Е.И., к.м.н. (Москва, Россия)

ORCID: 0000-0003-3292-8789

Петриков С.С., д.м.н., профессор (Москва, Россия)

ORCID: 0000-0002-5166-3280

Проценко Д.Н., к.м.н. (Москва, Россия)

ORCID: 0000-0002-5166-3280

Хатьков И.Е., д.м.н., профессор (Москва, Россия)

ORCID: 0000-0002-4088-8118

Редакция не несет ответственности за содержание рекламных материалов. Точка зрения авторов может не совпадать с мнением редакции. К публикации принимаются только статьи, подготовленные в соответствии с правилами для авторов. Направляя статью в редакцию, авторы принимают условия договора публичной оферты. С правилами для авторов и договором публичной оферты можно ознакомиться на сайте: <https://journals.eco-vector.com/DD/>. Полное или частичное воспроизведение материалов, опубликованных в журнале, допускается только с письменного разрешения издателя — издательства «Эко-Вектор».

FOUNDERS

- Moscow Center for Diagnostics and Telemedicine
- Eco-Vector

PUBLISHER

Eco-Vector

Address: 3 liter A, 1H, Aptekarsky pereulok, 191186,

Saint Petersburg, Russian Federation

E-mail: info@eco-vector.com

WEB: <https://eco-vector.com>

ADVERTISE

Adv. department

Phone: +7 (968) 545 78 20

E-mail: adv2@eco-vector.com

EDITORIAL OFFICE

Executive editor

Elena A. Philippova

E-mail: ddjournal@eco-vector.com

Phone: +7 (965) 012 70 72

SUBSCRIPTION

For print version:

www.journals.eco-vector.com/

PUBLICATION ETHICS

Journal's ethic policies are based on:

- ICMJE
- COPE
- ORE
- CSE
- EASE

OPEN ACCESS

Immediate Open Access is mandatory for all published articles

INDEXATION

- SCOPUS
- Russian Science Citation Index
- Google Scholar
- Ulrich's International Periodicals Directory
- WorldCat

TYPESET

completed in Eco-Vector

Copyeditor: *A.A. Ridel*

Proofreader: *A.A. Ridel*

Layout editor: *Ph. Ignashchenko*

Cover: *E. Bugaenko*

ISSN 2712-8490 (Print)

ISSN 2712-8962 (Online)

Digital Diagnostics

Volume 4 | Issue 4 | 2023

QUARTERLY PEER-REVIEWED MEDICAL JOURNAL

EDITOR-IN-CHIEF

Valentin E. Sinitsyn, MD, Dr. Sci. (Med.), Professor (Moscow, Russia)

ORCID: 0000-0002-5649-2193

DEPUTY EDITOR-IN-CHIEF

Yuriy A. Vasilev, MD, Cand. Sci. (Med.) (Moscow, Russia)

ORCID: 0000-0002-0208-5218

SCIENTIFIC EDITOR

Tatiana P. Berezovskaya MD, Dr. Sci. (Med.), Professor (Obninsk, Russia)

ORCID: 0000-0002-3549-4499

RESPONSIBLE SECRETARY

Irina A. Vinogradova, Cand. Sci. (Tech.) (Moscow, Russia)

ORCID: 0000-0001-6465-4132

EDITORIAL BOARD

L. Bertin, Professor (Illinois, United States)

ORCID: 0000-0002-0717-0307

M.G. Belyaev, Cand. Sci. (Phys.-Math.), Assistant Professor (Moscow, Russia)

ORCID: 0000-0001-9906-6453

S. Bisdas, MBBS, MD, PhD (London, United Kingdom)

ORCID: 0000-0001-9930-5549

D.A. Vazhenina, MD, Dr. Sci. (Med.), Associate Professor (Moscow, Russia)

ORCID: 0000-0002-6236-709X

V.A. Gomboleviskiy, MD, Dr. Sci. (Med.) (Moscow, Russia)

ORCID: 0000-0003-1816-1315

A.S. Domozhirova, MD, Dr. Sci. (Med.), Associate Professor (Moscow, Russia)

ORCID: 0000-0003-0806-3164

G. Frija, Professor (Paris, France)

ORCID: 0000-0003-0415-0586

G. Guglielmi, MD, Professor (Foggia, Italy)

ORCID: 0000-0002-4325-8330

A. Holodny, MD (New York, United States)

ORCID: 0000-0002-1159-2705

H. Li, MD, Professor (Beijing, China)

G.S. Lebedev, Dr.Sci. (Tech.), Professor (Moscow, Russia)

ORCID: 0000-0002-4289-2102

L. Mannelli, MD (New York, United States)

ORCID: 0000-0002-9102-4176

I.A. Matveev, Dr. Sci. (Tech.) (Moscow, Russia)

ORCID: 0000-0003-2005-9467

S.T. Matskeplishvili, MD, Dr. Sci. (Med.), Professor (Moscow, Russia)

ORCID: 0000-0002-5670-167X

V.V. Mit'kov, MD, Dr. Sci. (Med.), Professor (Saint Petersburg, Russia)

ORCID: 0000-0003-1959-9618

S.P. Morozov, MD, Dr. Sci. (Med.), Professor (Moscow, Russia)

ORCID: 0000-0001-6545-6170

E. Neri, MD, Associate Professor (Pisa, Italy)

ORCID: 0000-0001-7950-4559

V.V. Omet'yanovskiy, MD, Dr. Sci. (Med.), Professor (Moscow, Russia)

ORCID: 0000-0003-1581-0703

D.V. Omelyanskaya, (Moscow, Russia)

ORCID: 0000-0002-0245-4431

M. Oudkerk, Professor (Groningen, Netherlands)

ORCID: 0000-0003-2800-4110

P.R. Ros, MD, MPH, PhD, Professor (New York, United States)

ORCID: 0000-0003-3974-0797

A. Rovira, Professor (Barcelona, Spain)

ORCID: 0000-0002-2132-6750

R.V. Reshetnikov, Cand. Sci. (Phys.-Math.) (Moscow, Russia)

ORCID: 0000-0002-9661-0254

P.O. Rumyantsev, MD, Dr. Sci. (Med.) (Moscow, Russia)

ORCID: 0000-0002-7721-634X

A.E. Khamov, Dr. Sci. (Phys.-Math.), Professor (Saint Petersburg, Russia)

ORCID: 0000-0003-2787-2530

A.A. Ansheles, MD, Dr. Sci. (Med.) (Moscow, Russia)

ORCID: 0000-0002-2675-3276

G.P. Arutyunov, MD, Dr. Sci. (Med.) (Moscow, Russia)

ORCID: 0000-0002-6645-2515

A.S. Belevskiy, MD, Dr. Sci. (Med.), Professor (Moscow, Russia)

ORCID: 0000-0001-6050-724X

E.Y. Vasilieva, MD, Dr. Sci. (Med.), Professor (Moscow, Russia)

ORCID: 0000-0003-4111-0874

A.B. Gekht, MD, Dr. Sci. (Med.), Professor (Moscow, Russia)

ORCID: 0000-0002-1170-6127

O.S. Kobayakova, MD, Dr. Sci. (Med.), Professor (Moscow, Russia)

ORCID: 0000-0003-0098-1403

E.I. Kremneva, MD, Cand. Sci. (Med.) (Moscow, Russia)

ORCID: 0000-0001-9396-6063

S.S. Petrikov, MD, Dr. Sci. (Med.), Professor (Moscow, Russia)

ORCID: 0000-0002-3292-8789

D.N. Protsenko, MD, Cand. Sci. (Med.) (Moscow, Russia)

ORCID: 0000-0002-5166-3280

I.E. Khatkov, MD, Dr. Sci. (Med.), Professor (Moscow, Russia)

ORCID: 0000-0002-4088-8118

16+

© Eco-Vector, 2023



The editors are not responsible for the content of advertising materials. The point of view of the authors may not coincide with the opinion of the editors. Only articles prepared in accordance with the guidelines are accepted for publication. By sending the article to the editor, the authors accept the terms of the public offer agreement. The guidelines for authors and the public offer agreement can be found on the website: <https://journals.eco-vector.com/DD/>. Full or partial reproduction of materials published in the journal is allowed only with the written permission of the publisher — the Eco-Vector publishing house.

СОДЕРЖАНИЕ

ОРИГИНАЛЬНЫЕ ИССЛЕДОВАНИЯ

Ю.А. Васильев, О.В. Омелянская, А.В. Владимирский, П.Б. Гележе, Р.В. Решетников, А.П. Гончар, И.А. Блохин, И.И. Абдуллин, И.Н. Кива

Сравнение мультипараметрического и бипараметрического протоколов магнитно-резонансной томографии для выявления рака предстательной железы рентгенологами с различным опытом 455

Д.Р. Ахмадуллина, Р.Н. Коновалов, Ю.А. Шпилюкова, Е.Ю. Федотова

Структурные изменения серого вещества при вариантах первичной прогрессирующей афазии 467

Ю.Ф. Шумская, Д.А. Ахмедзянова, М.Г. Мнацаканян, К.Ю. Колосова, О.В. Тащян, М.В. Юраж, Р.В. Решетников

Определение методом дельфийского консенсуса списка оцениваемых с помощью опросников параметров при наблюдении пациентов с воспалительными заболеваниями кишечника 481

Н.В. Денисова, М.А. Гурко, И.П. Колинко, А.А. Аншелес, В.Б. Сергиенко

Виртуальная платформа для имитационного компьютерного моделирования радионуклидной визуализации в ядерной кардиологии. Сравнение с клиническими данными 492

СИСТЕМАТИЧЕСКИЕ ОБЗОРЫ И МЕТААНАЛИЗЫ

М.О. Гуля, К.В. Завадовский

Скорость вымывания 99mTc-метокси-изобутил-изонитрила как маркер митохондриальной дисфункции миокарда: систематический обзор и метаанализ 509

А.В. Капишников, Е.Н. Суворцев

Магнитно-резонансная томография в дифференциальной диагностике первичных внеозгловых опухолей: обзор радиомических исследований 529

НАУЧНЫЕ ОБЗОРЫ

М.В. Рейнберг, К.Ю. Слащук, А.А. Трухин, К.И. Аврамова, М.С. Шеремета

Современный взгляд на основные аспекты подготовки пациентов с дифференцированным раком щитовидной железы к радиойодтерапии: научный обзор 543

Ю.А. Васильев, О.В. Омелянская, А.А. Насибуллина, Д.В. Леонов, Ю.В. Булгакова,

Д.А. Ахмедзянова, Ю.Ф. Шумская, Р.В. Решетников

Антропоморфные фантомы молочной железы для лучевой диагностики: научный обзор 569

ТЕХНИЧЕСКИЕ ОТЧЁТЫ

В.В. Зинченко, К.М. Арзамасов, А.В. Кремнева, Е.И. Владимирский, Ю.А. Васильев

Технологические дефекты программного обеспечения с искусственным интеллектом 593

КЛИНИЧЕСКИЕ СЛУЧАИ

Н.Г. Потешкина, Е.А. Ковалевская, В.Е. Синицын, Е.А. Мершина, Д.А. Филатова, Г.Б. Селиванова, Я.Р. Шашкина

Трудности диагностики миокардита: клинический случай 605

С.Ф. Агеева, Д.А. Филатова, Е.А. Мершина, В.Е. Синицын

Симптом «рисовых телец» при магнитно-резонансной томографии плечевого сустава у пациентки с ревматоидным артритом 616

Т.Б. Даутов, Б.Б. Калиев, Б.Т. Ерекеш

Некомпактный миокард и аневризма левого желудочка у 6-летнего ребёнка 625

Д.А. Ахмедзянова, О.К. Юцевич, Р.В. Решетников, О.В. Тащян, С.С. Пирогов, М.П. Мазурова,

Н.Н. Волченко, А.К. Камалов, Ю.Ф. Шумская, М.Г. Мнацаканян

Ограничения использования гистологического исследования биоптатов как «золотого стандарта» диагностики на примере аденокарциномы пищевода: описание случая 633

Т.С. Нефедова, Ю.Ф. Шумская, М.В. Юраж, А.С. Панферов, П.В. Сенчихин,

А.Е. Грабарник, И.О. Щекотуров, М.Г. Мнацаканян

Сложность дифференциальной диагностики карциноматоза и туберкулёза брюшины у молодой пациентки с асцитом: описание случая 643

CONTENTS

ORIGINAL STUDY ARTICLES

- Yuriy A. Vasilev, Olga V. Omelyanskaya, Anton V. Vladzimirskyy, Pavel B. Gelezhe, Roman V. Reshetnikov, Anna P. Gonchar, Ivan A. Blokhin, Iskander I. Abdullin, Irina N. Kieva*
Comparison of multiparametric and biparametric magnetic resonance imaging protocols for prostate cancer diagnosis by radiologists with different experience 455
- Diliara R. Akhmadullina, Rodion N. Konovalov, Yulia A. Shpilyukova, Ekaterina Yu. Fedotova*
Structural gray matter changes in primary progressive aphasia variants 467
- Yuliya F. Shumskaya, Dina A. Akhmedzyanova, Marina G. Mnatsakanyan, Ksenia Yu. Kolosova, Olga V. Tashchyan, Marta V. Yurazh, Roman V. Reshetnikov*
Delphi method to determine a list of questionnaire-assessed parameters in the follow-up of patients with inflammatory bowel disease 481
- Natalya V. Denisova, Mikhail A. Gurko, Inna P. Kolinko, Alexey A. Ansheles, Vladimir B. Sergienko*
Virtual platform for computer simulation of radionuclide imaging in nuclear cardiology: Comparison with clinical data 492

SYSTEMATICAL REVIEWS AND META-ANALYSES

- Marina O. Gulya, Konstantin V. Zavadovsky*
99mTc-MIBI washout rate as a marker of myocardial mitochondrial dysfunction: A systematic review and meta-analysis 509
- Aleksandr V. Kapishnikov, Evgeniy N. Surovcev*
Magnetic resonance imaging for the differential diagnosis of primary extra-axial brain tumors: a review of radiomic studies 529

REVIEWS

- Maria V. Reinberg, Konstantin Yu. Slashchuk, Alexey A. Trukhin, Karina I. Avramova, Marina S. Sheremeta*
Preparation for radioiodine therapy in patients with differentiated thyroid cancer: a modern perspective (a review) 543
- Yuriy A. Vasilev, Olga V. Omelyanskaya, Anastasia A. Nasibullina, Denis V. Leonov, Julia V. Bulgakova, Dina A. Akhmedzyanova, Yuliya F. Shumskaya, Roman V. Reshetnikov*
Anthropomorphic breast phantoms for radiology imaging: a review 569

TECHNICAL REPORTS

- Viktoria V. Zinchenko, Kirill M. Arzamasov, Elena I. Kremneva, Anton V. Vladzimirskyy, Yuriy A. Vasilev*
Technological defects in software based on artificial intelligence 593

CASE REPORTS

- Natalia G. Poteshkina, Elena A. Kovalevskaya, Valentin E. Sinitsyn, Elena A. Mershina, Daria A. Filatova, Galina B. Selivanova, Yavilika R. Shashkina*
Difficulties in myocarditis diagnosis: a case report 605
- Sofia F. Ageeva, Daria A. Filatova, Elena A. Mershina, Valentin E. Sinitsyn*
"Rice bodies" symptoms on magnetic resonance imaging of the shoulder in a patient with rheumatoid arthritis 616
- Tairkhan B. Dautov, Bauyrzhan B. Kaliyev, Bibissara T. Yerekesh*
Left ventricular noncompaction with ventricular aneurysm in a 6-year-old patient 625
- Dina A. Akhmedzyanova, Olga K. Yutsevich, Roman V. Reshetnikov, Olga V. Tashchyan, Sergey S. Piragov, Maria P. Mazurova, Nadezhda N. Volchenko, Aziz K. Kamalov, Yuliya F. Shumskaya, Marina G. Mnatsakanyan*
Tissue sampling and histopathological limitations in esophageal cancer 633
- Tamara S. Nefedova, Yuliya F. Shumskaya, Marta V. Yurazh, Alexandr S. Panferov, Pavel V. Senchikhin, Alexei E. Grabarnik, Igor O. Shchekoturov, Marina G. Mnatsakanyan*
Difficulty in the differential diagnosis of peritoneal carcinomatosis and tuberculosis in a young female patient with ascites: a case report 643

DOI: <https://doi.org/10.17816/DD322816>

Сравнение мультипараметрического и бипараметрического протоколов магнитно-резонансной томографии для выявления рака предстательной железы рентгенологами с различным опытом

Ю.А. Васильев¹, О.В. Омелянская¹, А.В. Владимирский¹, П.Б. Гележе^{1,2},
Р.В. Решетников¹, А.П. Гончар¹, И.А. Блохин¹, И.И. Абдуллин¹, И.Н. Киева³

¹ Научно-практический клинический центр диагностики и телемедицинских технологий, Москва, Российская Федерация;

² Акционерное общество «Европейский Медицинский Центр», Москва, Российская Федерация;

³ Детская городская клиническая больница № 9 имени Г.Н. Сперанского, Москва, Российская Федерация

АННОТАЦИЯ

Обоснование. Проведение магнитно-резонансной томографии позволяет выявить клинически значимый рак предстательной железы, диагностировать экстракапсулярную экстензию, стадировать онкологический процесс. Протокол сканирования, включающий только T2-взвешенные и диффузионно-взвешенные изображения, представляет собой жизнеспособную альтернативу мультипараметрической магнитно-резонансной томографии при условии сохранения высокой диагностической точности теста. В недавних исследованиях диагностическая точность бипараметрической и мультипараметрической магнитно-резонансной томографии в выявлении рака предстательной железы продемонстрировала незначительные различия.

Цель — сравнение диагностической точности бипараметрической и мультипараметрической магнитно-резонансной томографии для выявления клинически значимого рака предстательной железы по системе PI-RADS v2.1 с использованием мультифокальной биопсии под контролем магнитно-резонансной томографии в качестве золотого стандарта.

Материалы и методы. Данное исследование является ретроспективным. Мы изначально обработали записи историй болезни 126 пациентов. Критериями включения в исследование были наличие мультипараметрической магнитно-резонансной томографии по стандарту PI-RADS 2.1, клинической информации об уровнях свободного и связанного простатспецифического антигена крови, мультифокальной биопсии предстательной железы при соблюдении временного интервала между магнитно-резонансной томографией и биопсией не более 14 дней. Три исследователя (врачи-рентгенологи с опытом работы менее 2 лет, от 2 до 5 лет, более 5 лет соответственно) независимо друг от друга оценивали бипараметрическую магнитно-резонансную томографию предстательной железы на предмет наличия патологических очагов. Спустя 2 недели исследователи оценивали датасет мультипараметрической магнитно-резонансной томографии предстательной железы. Каждый выявленный очаг, начиная с категории PI-RADS 3, сопоставлялся с результатом мультифокальной фьюжн-биопсии. Результат биопсии представлялся в виде суммы значений по шкале Gleason, при этом к клинически значимым данным биопсии относилась сумма Gleason 7 и выше. Опухолевыми очагами по данным магнитно-резонансной томографии считались находки, соответствующие критериям PI-RADS 4 и 5.

Результаты. Наилучшие показатели чувствительности и специфичности выявления очагов на магнитно-резонансной томографии предстательной железы — 62,5 и 74,6% соответственно. Наивысшая достигнутая диагностическая точность составила 70,1%. Мультипараметрическая магнитно-резонансная томография обладает более высокими показателями специфичности выявления очагов предстательной железы при интерпретации рентгенологами с опытом работы менее 2 лет и более 5 лет.

Заключение. Как бипараметрическая, так и мультипараметрическая магнитно-резонансная томография предстательной железы продемонстрировала неоптимальные показатели диагностической точности. Имеется тенденция к улучшению чувствительности и специфичности метода с увеличением опыта работы рентгенолога. Бипараметрические протоколы сканирования предстательной железы имеют безусловное экономическое преимущество перед мультипараметрическими за счёт отсутствия расходов на контрастное вещество и расходные материалы и значительного снижения времени загрузки МР-сканера, однако их использование может привести к снижению диагностической точности метода.

Ключевые слова: магнитно-резонансная томография; МРТ; рак предстательной железы, PI-RADS.

Как цитировать:

Васильев Ю.А., Омелянская О.В., Владимирский А.В., Гележе П.Б., Решетников Р.В., Гончар А.П., Блохин И.А., Абдуллин И.И., Киева И.Н. Сравнение мультипараметрического и бипараметрического протоколов магнитно-резонансной томографии для выявления рака предстательной железы рентгенологами с различным опытом // Digital Diagnostics. 2023. Т. 4, № 4. С. 455–466. DOI: <https://doi.org/10.17816/DD322816>

Рукопись получена: 15.04.2023

Рукопись одобрена: 15.06.2023

Опубликована online: 05.09.2023

DOI: <https://doi.org/10.17816/DD322816>

Comparison of multiparametric and biparametric magnetic resonance imaging protocols for prostate cancer diagnosis by radiologists with different experience

Yuriy A. Vasilev¹, Olga V. Omelyanskaya¹, Anton V. Vladzimirskyy¹, Pavel B. Gelezhe^{1,2}, Roman V. Reshetnikov¹, Anna P. Gonchar¹, Ivan A. Blokhin¹, Iskander I. Abdullin¹, Irina N. Kieva³

¹ Moscow Center for Diagnostics and Telemedicine, Moscow, Russian Federation;

² Joint stock company "European Medical Center", Moscow, Russian Federation;

³ Speransky Children's Hospital, Moscow, Russian Federation

ABSTRACT

BACKGROUND: Magnetic resonance imaging can detect clinically significant prostate cancer and diagnose extracapsular extension and cancer stage. A scanning protocol that includes only T2-weighted and diffusion-weighted images represents a viable alternative to multiparametric magnetic resonance imaging provided that the high diagnostic accuracy of the test is maintained. In recent studies, biparametric and multiparametric magnetic resonance imaging demonstrated slight differences in the diagnostic accuracy in detecting prostate cancer.

AIM: To compare the diagnostic accuracy of biparametric and multiparametric magnetic resonance imaging for the detection of clinically significant prostate cancer using PI-RADS v2.1 with magnetic resonance imaging-guided multifocal biopsy as the gold standard.

MATERIALS AND METHODS: This retrospective study initially processed the medical records of 126 patients. The inclusion criteria were as follows: presence of PI-RADS 2.1 multiparametric magnetic resonance imaging, clinical information on free and bound prostate-specific antigen blood levels, a multifocal prostate biopsy performed, and a time interval between magnetic resonance imaging and biopsy of no more than 14 days. Three investigators (radiologists with <2, 2–5, and >5 years of experience) independently evaluated biparametric magnetic resonance imaging of the prostate for the presence of pathological foci. After 2 weeks, the researchers evaluated the multiparametric magnetic resonance imaging dataset of the prostate. Each lesion detected, starting from PI-RADS category 3, was compared with the result of a multifocal fusion biopsy. The biopsy result was presented as a sum of Gleason scores, and a Gleason score of ≥ 7 was considered clinically relevant. According to magnetic resonance imaging data, findings meeting PI-RADS criteria 4 and 5 were considered tumor foci.

RESULTS: The best values of sensitivity and specificity of foci detection on magnetic resonance imaging of the prostate gland were 62.5% and 74.6%, respectively. The highest diagnostic accuracy achieved was 70.1%. Magnetic resonance imaging had higher specificity rates for detecting prostatic foci when interpreted by radiologists with 2 years and >5 years of experience.

CONCLUSION: Both biparametric and multiparametric magnetic resonance imaging of the prostate demonstrated suboptimal diagnostic accuracy. The sensitivity and specificity of the method tended to improve with increasing experience of the radiologist. Biparametric protocols of prostate scanning have a definite economic advantage over multiparametric protocols because of the absence of contrast agents and consumables and a significant decrease in magnetic resonance scanner loading time; however, their use can lead to a decrease in the diagnostic accuracy of the method.

Keywords: magnetic resonance imaging; MRI; prostate cancer; PI-RADS.

To cite this article:

Vasilev YuA, Omelyanskaya OV, Vladzimirskyy AV, Gelezhe PB, Reshetnikov RV, Gonchar AP, Blokhin IA, Abdullin II, Kieva IN. Comparison of multiparametric and biparametric magnetic resonance imaging protocols for prostate cancer diagnosis by radiologists with different experience. *Digital Diagnostics*. 2023;4(4):455–466. DOI: <https://doi.org/10.17816/DD322816>

Received: 15.04.2023

Accepted: 15.06.2023

Published online: 05.09.2023

DOI: <https://doi.org/10.17816/DD322816>

比较具有不同经验的放射科医生检测前列腺癌的多参数和双参数磁共振成像协议

Yuriy A. Vasilev¹, Olga V. Omelyanskaya¹, Anton V. Vladzimirskyy¹, Pavel B. Gelezhe^{1,2}, Roman V. Reshetnikov¹, Anna P. Gonchar¹, Ivan A. Blokhin¹, Iskander I. Abdullin¹, Irina N. Kieva³

¹ Moscow Center for Diagnostics and Telemedicine, Moscow, Russian Federation;

² Joint stock company "European Medical Center", Moscow, Russian Federation;

³ Speransky Children's Hospital, Moscow, Russian Federation

简评

论证。磁共振成像（MRI）允许发现有临床意义的前列腺癌、诊断囊外扩展并对癌症发展进行分期。如果扫描协议仅包括T2加权和弥散加权图像，只要检查的诊断准确度保持较高水平，其就能很好地替代多参数磁共振成像。在最近的研究中，双参数（bpMRI）和多参数（mpMRI）磁共振成像在检测前列腺癌方面的诊断准确度差别不大。

该研究的目的是比较bpMRI和mpMRI在检测有临床意义的前列腺癌方面的诊断准确度。比较是根据PI-RADS v2.1系统进行的，以MRI引导下的多点活检为金标准。

材料和方法。本研究是一项回顾性研究。我们初步处理了126名患者的病史。纳入标准为：（1）符合PI-RADS 2.1标准的mpMRI；（2）血液中游离和结合前列腺特异性抗原水平的临床信息；（3）前列腺多点活检。磁共振成像与活检之间的时间间隔不超过14天。

研究由三名放射科医生进行。医生的工作经验分别为2年以下、2至5年和5年以上。这些医生（研究人员）独立评估前列腺bpMRI 是否存在病灶。2周后，研究人员（这些医生）对前列腺mpMRI 数据集进行了评估。从PI-RADS 3类别开始，将发现的每个病灶与多点融合活检结果进行了比较。活检结果显示为Gleason评分值的总和。Gleason评分7分或更高被认为是具有临床意义的活检结果。磁共振成像显示的肿瘤灶被认为是符合PI-RADS标准4和5的结果。

结果。前列腺磁共振成像检测病灶的最佳灵敏度和特异度分别为62.5%和74.6%。诊断准确率最高达到70.1%。由工作经验少于2年和多于5年的放射科医生进行mpMRI解读时，前列腺病灶检测的特异度更高。

结论。前列腺的bpMRI和mpMRI都显示出不理想的诊断准确度。随着放射科医生经验的增加，该方法的灵敏度和特异度有提高的趋势。与多参数协议相比，双参数前列腺扫描协议具有明显的经济优势。这种优势是不需要造影剂和消耗品的费用，并大大减少磁共振扫描仪的装载时间。不过，使用这种方法可能会降低诊断准确度。

关键词：磁共振成像；MRI；前列腺癌；PI-RADS。

引用本文：

Vasilev YuA, Omelyanskaya OV, Vladzimirskyy AV, Gelezhe PB, Reshetnikov RV, Gonchar AP, Blokhin IA, Abdullin II, Kieva IN. 比较具有不同经验的放射科医生检测前列腺癌的多参数和双参数磁共振成像协议. *Digital Diagnostics*. 2023;4(4):455-466. DOI: <https://doi.org/10.17816/DD322816>

收到: 15.04.2023

接受: 15.06.2023

发布日期: 05.09.2023

List of Abbreviations

DWI: diffusion-weighted imaging
 DCE: dynamic contrast enhancement
 MRI: magnetic resonance imaging
 bpMRI: biparametric magnetic resonance imaging

mpMRI: multiparametric magnetic resonance imaging
 T2WI: T2-weighted imaging
 SS-EPI: single-shot echo planar imaging
 TSE: turbo-spin echo

BACKGROUND

Multiparametric magnetic resonance imaging (mpMRI), which includes T2-weighted imaging (T2WI), diffusion-weighted imaging (DWI), and dynamic contrast enhancement (DCE) sequences, is critical in the clinical assessment of patients with high prostate-specific antigen (PSA) levels.

MRI can be used to diagnose clinically significant prostate cancer, detect extracapsular extension, and determine the disease stage. In 2019, the American College of Radiology and the European Association of Urology (European Symposium on Urogenital Radiology, ESUR) released the Prostate Imaging Reporting and Data System, version 2.1 (PI-RADS v2.1) for standardizing MRI data acquisition and image interpretation [1].

Since 2020, the American Urological Association and European Association of Urology have recommended the use of mpMRI for biopsy-naïve men who were suspected of prostate cancer [2, 3]. A clinical study by O. Rouvière et al. [3] showed that 27% of men with high PSA levels could avoid an unnecessary biopsy using mpMRI. Since most men undergo PSA testing at least once in their lifetime, these guidelines have resulted in a marked increase in demand for prostate MRI.

Assigning a PI-RADS assessment category relegates the use of DCE imaging to a minor role because it is only used for the differential diagnosis between PI-RADS 3 and 4 lesions in the peripheral zone. In addition, the use of DCE poses a risk of nephrogenic systemic fibrosis in patients with renal insufficiency. Therefore, interest in parametric MRI (bpMRI) is growing, which is an abbreviated prostate MRI protocol that excludes DCE imaging [4–6].

Owing to its high diagnostic accuracy, the bpMRI protocol, a combination of T2WI and DWI sequences, is emerging as a viable alternative to mpMRI [7]. Recent studies have shown minor differences in the diagnostic accuracy between bpMRI and mpMRI for detecting prostate cancer [6]. Efforts to create a bpMRI protocol have been successful in demonstrating intensity nonuniformity, resolution, and nonlinearity comparable to those of mpMRI [8].

The growing interest in bpMRI has encouraged the PI-RADS Steering Committee to issue a consensus statement calling for a higher-quality data before making evidence-based recommendations on bpMRI as an initial diagnostic work-up [9].

The aim of this study was to compare the diagnostic accuracy of bpMRI with that of mpMRI in detecting

clinically significant prostate cancer based on PI-RADS v2.1 using targeted MRI/transrectal ultrasound (TRUS) fusion-guided prostate biopsy (number of points) as the gold standard.

The objectives of this study were to identify the sensitivity and specificity of mpMRI in comparison with bpMRI in diagnosing clinically significant prostate cancer (PI-RADS ≥ 4). In addition, the study compared the sensitivity and specificity of mpMRI with those of bpMRI images assessed by radiologists with different levels of experience. Finally, the interobserver agreement between radiologists with different levels of experience in assessing mpMRI and bpMRI images was evaluated.

MATERIALS AND METHODS

Study Design

This was an observational, single-center, retrospective extrapolation study.

Eligibility Criteria

Inclusion criteria: availability of a PI-RADS 2.1 mpMRI scan, clinical laboratory values of blood-free and bound PSA levels, and targeted MRI/TRUS fusion biopsy. Biopsy must be performed within 14 days after MRI.

Noninclusion criteria: image artifacts on the prostate MRI scan or MR images not compliant with PI-RADS 2.1, absence of one or more clinical markers, and a time interval between mpMRI and biopsy of >14 days.

Exclusion criteria: significant mpMRI artifacts, which precluded an adequate assessment, and uninformative biopsies.

Following the above criteria, radiologists with <2 years or >5 years of experience excluded 19 patients from the sample, whereas those with 2–5 years of experience excluded 23 patients.

Study Site

Patients who underwent prostate MRI and TRUS fusion biopsy were recruited from the European Medical Center (a private medical institution).

Study Duration

The study analyzed electronic medical records from January 1, 2022, to June 1, 2022.

Medical Intervention

The medical records of 126 patients were analyzed. Prostate mpMRI was performed using a Siemens Magnetom Aera 1.5T 4G (Germany) with a body coil. The scanning protocol included the following set of pulse sequences (Table 1). After unloading and anonymization, several DCE images were removed from the mpMRI sequences, resulting in a dataset of bpMRI sequences. Three investigators (radiologists with <2 years of experience, 2–5 years of experience, and >5 years of experience) independently evaluated prostate bpMRI sequences for pathological lesions. The lesion was assigned a score from 1 to 5 (as instructed in PI-RADS v2.1, DWI was used for peripheral zone lesions, and T2WI for transition zone lesions); then, an overall prostate PI-RADS v2.1 score was determined. The reference method was prostate histopathology based on targeted MRI/TRUS fusion biopsy.

After 2 weeks, the investigators evaluated the prostate mpMRI dataset, which included a series of dynamic contrast enhancement images. MRI interpretation was conducted by investigators who were blinded to the biopsy results. According to PI-RADS 2.1 [1], early contrast enhancement allows for reliable differentiation between PI-RADS 3 and 4 lesions localized in the peripheral zone.

Primary Outcome

The prostate lesion identified by bpMRT or mpMRI should be consistent with the histopathological findings.

Outcome Reporting Method

The identified lesions were tabulated, specifying their zonal location based on the PI-RADS 2.1 sector map. The central zone and anterior fibromuscular stroma were excluded from the assessment.

Each identified lesion of PI-RADS ≥ 3 was compared with the findings of targeted MRI/TRUS fusion biopsy. MRI/TRUS

fusion biopsy overlays a prostate ultrasound on the saved prostate MR images (typically, axial T2WI). The biopsy sites were targeted and tracked on the obtained three-dimensional reconstruction of the prostate.

The biopsy findings were presented as the total Gleason score [10]. A total Gleason score of ≥ 7 is considered clinically significant. PI-RADS 4 and 5 MR images were consistent with malignant lesions.

Ethics Review

This study was approved by the Local Ethics Committee of the European Medical Center (Minutes of the Meeting No. 1 of April 24, 2023).

Statistical Analysis

For each dataset, the experts separately calculated the diagnostic power parameters, including the Youden index. Interobserver agreement between radiologists was estimated as percentages and Fleiss kappa.

Calculations were performed using R software version 4.1.3¹ using *irr*² and *dplyr* packages³.

RESULTS

Study Subjects (Participants)

Radiologists with <2 and >5 years of experience analyzed a total of 107 patient datasets, whereas radiologists with 2–5 years of experience analyzed 103 patient datasets.

Key Findings

The highest sensitivity and specificity of bpMRI for detecting pathological lesions in the prostate were 70.0% and 67.2%, respectively. The highest sensitivity and specificity of mpMRI for detecting pathological lesions in the prostate were 62.5% and 74.6%, respectively. No adverse events were reported.

Table 1. Prostate multiparametric magnetic resonance imaging protocol

Pulse sequence	Slice orientation	TE/TR, ms	FOV, mm	Pixel size, mm	Slice thickness/overlap, mm	Estimated scanning time, min
T2WI TSE	Sagittal	120/3800	250 × 250	1 × 1	3/0.3	2:26
T2WI TSE	Axial	110/3938	180 × 180	0.45 × 0.6	2.5/0	3:33
DWI SS-EPI	Axial	87/2425	160 × 160	1.25 × 1.32	3/0.3	6:50
T2WI TSE	Coronal	110/2500	160 × 160	0.38 × 0.42	2.5/0	4:50
DCE-T1WI, temporal resolution of 15 s	Axial	2.3/4.6	250 × 250	0.9 × 1	3/0	5:46
CE-T1WI	Axial	1.3/2.3	400 × 350	1.6 × 1.7	4/0	0:21

Notes. CE, contrast enhancement; DCE, dynamic contrast enhancement.

¹ R Project for Statistical Computing. Available at: <https://www.r-project.org/>.

² *irr*: Various coefficients of interrater reliability and agreement. Available at: <https://cran.r-project.org/web/packages/irr/index.html>.

³ *dplyr*: Grammar of data manipulation. Available at: <https://github.com/tidyverse/dplyr>.

The number of prostate lesions detected by radiologists with different levels of experience is presented in Table 2. The diagnostic accuracy of the radiologists is presented in Tables 3 and 4 for the bpMRI and mpMRI sequences, respectively. The interobserver agreement values are shown in Tables 5 (unit fractions) and 6 (Fleiss kappa).

DISCUSSION

Summary of the Key Findings

The main finding of our study is that the diagnostic power of prostate MRI is low. The maximum diagnostic accuracy for lesion detection was 70.1%, with a sensitivity of $\leq 62.5\%$ and specificity of $\leq 74.6\%$. Based on the obtained values, MRI cannot be considered a reliable method for early diagnosis because of its suboptimal sensitivity (Fig. 1).

This study also showed that mpMRI improved the diagnostic power of the method by increasing specificity. This is true when interpreted by radiologists with <2 (77.6% with mpMRI vs. 70.2% with bpMRI) and >5 years (74.6% with mpMRI vs. 67.2% with bpMRI) of experience.

Discussion of the Key Findings

The results obtained are consistent with those published in the scientific literature worldwide. J. Wallström et al. [6] reported that the mpMRI scan identified one additional case compared with the bpMRI (84 vs. 83 cases, respectively). In a retrospective study by C.K. Kuhl et al. [7], mpMRI

detected an additional 10 out of a total of 329 cancers. In a prospective study by J.P. Zawaideh et al. [11], bpMRI identified 116 cases, whereas mpMRI identified 117 cases. In meta-analyses, Z. Kang [12] and X.K. Niu [13] reported similar diagnostic accuracy of bpMRI and mpMRI in detecting prostate cancer.

Our findings are inconsistent with those of the classical PROMIS study [14], which demonstrated high sensitivity (93%) but low specificity (41%) of MRI. However, this study considered PI-RADS 3 lesions to be positive MRI results. The histological criteria for clinically significant prostate cancer differed because Gleason 3 + 4 lesions were excluded. The suboptimal diagnostic accuracy of MRI may be due to the abnormal distribution of normal cases and pathologies in our sample.

The main difference in mpMRI is the inclusion of DCE in the scanning protocol. This study demonstrates that DCE enhances the specificity of detecting prostate lesions by radiologists with <2 years and those with >5 years of experience (Tables 2 and 3; Fig. 2). However, radiologists with 2–5 years of background paradoxically experienced a decrease in specificity when evaluating the mpMRI datasets.

DCE imaging in prostate mpMRI has traditionally been limited by longer image acquisition times. This includes the time-consuming procedure of contrast administration, which involves preparing for the injection by catheterizing the patient. Longer analysis times for DCE images and

Table 2. Absolute and relative number of prostate lesions detected by radiologists with different levels of experience, *n* (%)

Level of experience, years	Protocol	True positive	True negative	False-positive	False negative
<2	bpMRI	19 (17.8)	47 (43.9)	20 (18.7)	21 (19.6)
	mpMRI	19 (17.8)	52 (48.6)	15 (14.0)	21 (19.6)
2–5	bpMRI	31 (29.8)	23 (22.1)	42 (40.4)	8 (7.7)
	mpMRI	32 (30.8)	19 (18.3)	46 (44.2)	7 (6.7)
≥ 5	bpMRI	28 (26.2)	45 (42.1)	22 (20.6)	12 (11.2)
	mpMRI	25 (23.4)	50 (46.7)	17 (15.9)	15 (14.0)

Notes. bpMRI/mpMRI, biparametric/multiparametric magnetic resonance imaging.

Table 3. Comparison of the PI-RADS 2.1 diagnostic criteria for prostate lesions using biparametric magnetic resonance imaging by radiologists with different levels of experience

Level of experience, years	Sensitivity	Specificity	Accuracy	Prognostic value		Youden index
				Positive	Negative	
<2	47.5 (31.5–63.9)	70.2 (57.7–80.7)	61.7 (51.8–70.9)	48.7 (36.8–60.8)	69.1 (61.6–75.8)	0.177
2–5	79.5 (63.5–90.7)	35.4 (23.9–48.2)	51.9 (41.9–61.8)	42.5 (36.7–48.4)	74.2 (58.8–85.3)	0.149
≥ 5	70.0 (53.5–83.4)	67.2 (54.6–78.2)	68.2 (58.5–76.9)	56.0 (46.1–65.5)	79.0 (69.4–86.1)	0.372

Notes. The values are presented as the median (Me) and 95% confidence interval (95% CI).

Table 4. Comparison of the PI-RADS 2.1 diagnostic criteria for prostate lesions using multiparametric magnetic resonance imaging by radiologists with different levels of experience

Level of experience, years	Sensitivity	Specificity	Accuracy	Prognostic value		Youden index
				Positive	Negative	
<2	47.5 (31.5–63.9)	77.6 (65.8–86.9)	66.4 (56.6–75.2)	37.4 (28.2–47.3)	55.9 (42.2–68.8)	0.251
2–5	82.1 (66.5–92.5)	28.2 (18.6–41.8)	49.0 (39.1–59.0)	41.0 (35.9–46.3)	73.1 (55.7–85.4)	0.113
≥5	62.5 (45.8–77.3)	74.6 (62.5–84.5)	70.1 (60.5–78.6)	59.5 (47.8–70.3)	76.9 (68.6–83.6)	0.371

Notes. The values are presented as the median (Me) and 95% confidence interval (95% CI).

Table 5. Interobserver agreement between radiologists (unit fractions)

Protocol Level of experience	bpMRI, <2 years	mpMRI, <2 years	bpMRI, >5 years	mpMRI, >5 years	bpMRI, 2–5 years	mpMRI, 2–5 years
bpMRI, <2 years	1	0.798	0.558	0.673	0.413	0.356
mpMRI, <2 years		1	0.654	0.817	0.356	0.298
bpMRI, >5 years			1	0.808	0.442	0.452
mpMRI, >5 years				1	0.413	0.357
bpMRI, 2–5 years					1	0.904
mpMRI, 2–5 years						1

Notes. bpMRI/mpMRI: biparametric/multiparametric magnetic resonance imaging.

Table 6. Interobserver Agreement Between Radiologists (Fleiss's kappa)

Protocol Level of experience	bpMRI, <2 years	mpMRI, <2 years	bpMRI, >5 years	mpMRI, >5 years	bpMRI, 2–5 years	mpMRI, 2–5 years
bpMRI, <2 years	1	0.669	0.318	0.482	0.195	0.136
mpMRI, <2 years		1	0.446	0.693	0.129	0.087
bpMRI, >5 years			1	0.699	0.206	0.229
mpMRI, >5 years				1	0.194	0.165
bpMRI, 2–5 years					1	0.846
mpMRI, 2–5 years						1

Notes. bpMRI/mpMRI, biparametric/multiparametric magnetic resonance imaging.

higher software requirements are also important factors. However, DCE helped increase the diagnostic accuracy (66.4% vs. 61.7% for a radiologist with <2 years of experience and 70.1% vs. 68.2% for a radiologist with >5 years of experience).

The use of bpMRI is also supported by concerns over the long-term safety of gadolinium-based contrast agents. Small amounts of gadolinium may be retained in the brain and other tissues. Although newer macrocyclic contrast agents have not been reported to cause adverse effects in clinical practice

for patients with normal renal function, MRI contrast agents should be used only when they provide significant diagnostic value [15], as demonstrated in this study.

As previously mentioned, DCE as part of mpMRI is used to distinguish between PI-RADS 3 and 4 lesions located in the peripheral zone of the prostate. Based on the Epstein criteria, a clinically insignificant cancer is defined as a Gleason score of ≤6, being organ-limited (TNM stage of <T3), and having a volume of <0.5 cm³, which must be confirmed histopathologically [16]. The same definition was used in

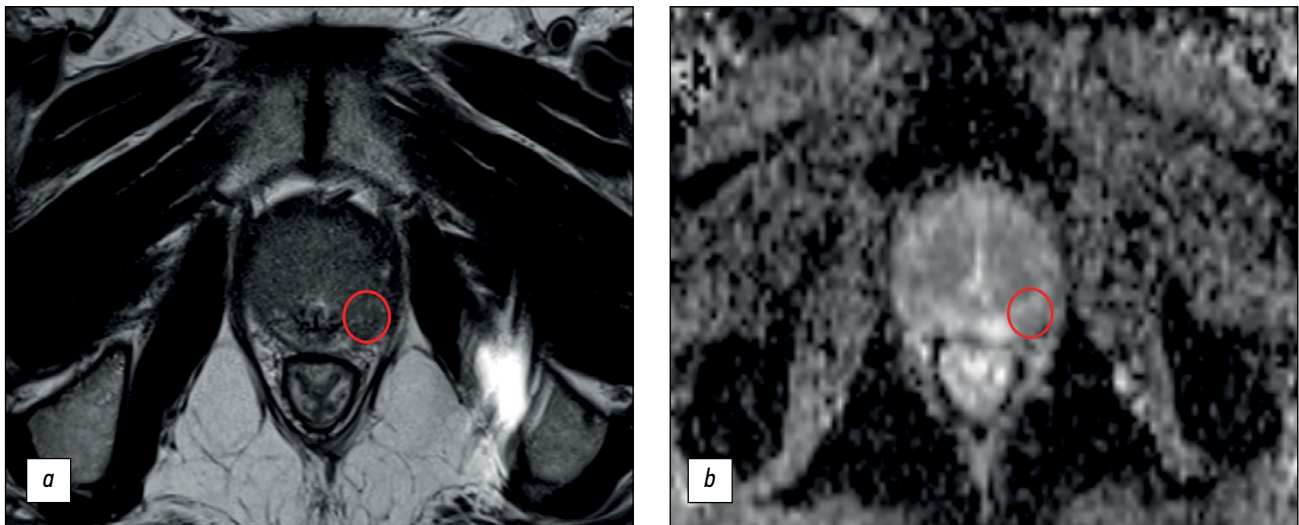


Fig. 1. An example of a false-positive result of parametric magnetic resonance imaging: (a) T2-weighted image in the axial plane: in the lateral posterior segment of the peripheral zone of the left lobe in the middle part of the prostate, a low-signal lesion consistent with the diffusion restriction zone is observed; (b) apparent diffusion coefficient map. This lesion was judged by the radiologist as PI-RADS 5. Fusion biopsy showed no signs of tumor growth in the prostate tissue.

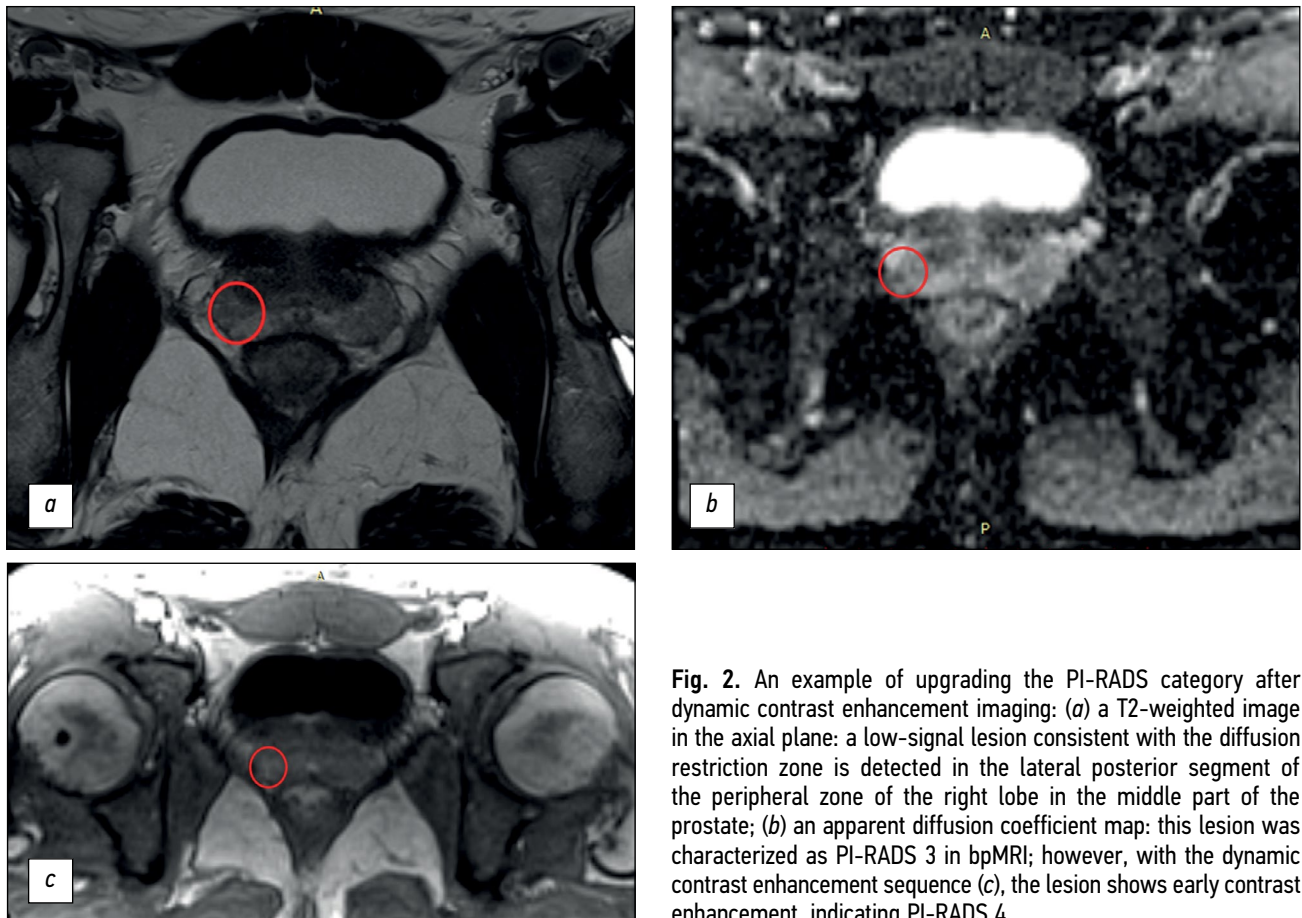


Fig. 2. An example of upgrading the PI-RADS category after dynamic contrast enhancement imaging: (a) a T2-weighted image in the axial plane: a low-signal lesion consistent with the diffusion restriction zone is detected in the lateral posterior segment of the peripheral zone of the right lobe in the middle part of the prostate; (b) an apparent diffusion coefficient map: this lesion was characterized as PI-RADS 3 in bpMRI; however, with the dynamic contrast enhancement sequence (c), the lesion shows early contrast enhancement, indicating PI-RADS 4.

PI-RADS v2.1 [1]. Identifying clinically insignificant tumors is crucial for active follow-up.

This study differs from those by the authors mentioned above [6, 7] in that it reports a decrease in the number of false-positive prostate tumors with DCE. As a result, this

method had a higher positive prognostic value. J.P. Zawaideh et al. [11] obtained similar results.

If a lesion of the PI-RADS ≥ 3 is detected, DCE will not alter the approach to scheduling a prostate biopsy. It is important to consider that transrectal biopsy is an invasive

procedure that carries the risk of infection and requires hospitalization [17].

Limitations

This study has significant limitations. The retrospective design of the study required the selection of patients who underwent fusion biopsy. Therefore, the distribution of normal cases and pathologies in our sample did not correlate with that of the general population. Sequential viewing of both bpMRI and mpMRI datasets by radiologists, even after the 2-week washout period, did not eliminate bias. The limited number of participating radiologists in the study prevented us from making a definitive conclusion about the consistency of their evaluations.

The interobserver agreement among experts with <2 and >5 years of work experience was moderate. However, the results were more consistent with the use of mpMRI. The literature presents varying data on the influence of radiologists' experience on the diagnostic quality of both protocols. For instance, E.D. *Campfi et al.* [18] found no significant effect, whereas M. Gatti *et al.* [19] demonstrated that radiologists with little experience evaluated bpMRI with less accuracy.

CONCLUSION

Regardless of the protocol used, prostate MRI demonstrated suboptimal diagnostic power. Although parametric prostate scanning protocols may have economic benefits over multiparametric ones because of the absence of costs for contrast agents and consumables and a significant reduction

in the loading time of the MR scanner, their use may lead to a decrease in the diagnostic accuracy of the method.

The observed trend of increased sensitivity and specificity of the method with a higher level of radiologist experience highlights the importance of training in the interpretation of prostate MRI based on PI-RADS.

A prospective study is necessary to confirm the role of bpMRI in the early diagnosis of prostate cancer.

ADDITIONAL INFORMATION

Funding source. This article was prepared by a group of authors as a part of the research and development effort titled "Scientific evidence for using radiomics-guided medical imaging to diagnose cancer", No. 123031400009-1", (USIS No. 123031500005-2) in accordance with the Order No. 1196 dated December 21, 2022 "On approval of state assignments funded by means of allocations from the budget of the city of Moscow to the state budgetary (autonomous) institutions subordinate to the Moscow Health Care Department, for 2023 and the planned period of 2024 and 2025" issued by the Moscow Health Care Department.

Competing interests. The authors declare that they have no competing interests.

Authors' contribution. All authors made a substantial contribution to the conception of the work, acquisition, analysis, interpretation of data for the work, drafting and revising the work, final approval of the version to be published and agree to be accountable for all aspects of the work. Yu.A. Vasilev, O.V. Omelyanskaya, A.V. Vladzimirskyy — research concept; P.B. Gelezhe, R.V. Reshetnikov — data analysis, text writing; A.P. Gonchar, I.A. Blokhin, I.I. Abdullin, I.N. Kieva — data analysis.

REFERENCES

1. Turkbey B, Rosenkrantz AB, Haider MA, et al. Prostate imaging reporting and data system version 2.1: 2019 Update of prostate imaging reporting and data system version 2. *Eur Urol.* 2019;76(3):340–351. doi: 10.1016/j.eururo.2019.02.0331
2. Bjurlin MA, Carroll PR, Eggener S, et al. Update of the standard operating procedure on the use of multiparametric magnetic resonance imaging for the diagnosis, staging and management of prostate cancer. *J Urol.* 2020;203(4):706–712. doi: 10.1097/JU.0000000000000617
3. Rouvière O, Puech P, Renard-Penna R, et al. Use of prostate systematic and targeted biopsy on the basis of multiparametric MRI in biopsy-naive patients (MRI-FIRST): A prospective, multicentre, paired diagnostic study. *Lancet Oncology.* 2019;20(1):100–109. doi: 10.1016/S1470-2045(18)30569-2
4. Boesen L, Thomsen FB, Nørgaard N, et al. A predictive model based on biparametric magnetic resonance imaging and clinical parameters for improved risk assessment and selection of biopsy-naive men for prostate biopsies. *Prostate Cancer Prostatic Dis.* 2019;22(4):609–616. doi: 10.1038/s41391-019-0149-y
5. Tamada T, Kido A, Yamamoto A, et al. Comparison of biparametric and multiparametric MRI for clinically significant prostate cancer detection with PI-RADS Version 2.1. *J Magnetic Resonance Imaging.* 2021;53(1):283–291. doi: 10.1002/jmri.27283
6. Wallström J, Geterud K, Kohestani K, et al. Bi- or multiparametric MRI in a sequential screening program for prostate cancer with PSA followed by MRI? Results from the Göteborg prostate cancer screening 2 trial. *Eur Radiol.* 2021;31(11):8692–8702. doi: 10.1007/s00330-021-07907-9
7. Kuhl CK, Bruhn R, Krämer N, et al. Abbreviated biparametric prostate MR imaging in men with elevated prostate-specific antigen. *Radiology.* 2017;285(2):493–505. doi: 10.1148/radiol.2017170129
8. Abuladze LR, Semenov DS, Panina OV, Vasil AA. Optimized protocol of biparametric magnetic resonance imaging for prostate. *Digital Diagnostics.* 2022;3(3):166–177. doi: 10.17816/DD108484
9. Schoots IG, Barentsz JO, Bittencourt LK, et al. PI-RADS committee position on MRI without contrast medium in biopsy-naive men with suspected prostate cancer: Narrative review. *Am J Roentgenol.* 2021;216(1):3–19. doi: 10.2214/AJR.20.24268
10. Gleason DF. Classification of prostatic carcinomas. *Cancer Chemother Rep.* 1966;50(3):125–128.
11. Zawaideh JP, Sala E, Shaïda N, et al. Diagnostic accuracy of biparametric versus multiparametric prostate MRI: Assessment of contrast benefit in clinical practice. *Eur Radiol.* 2020;30(7):4039–4049. doi: 10.1007/s00330-020-06782-0

12. Kang Z, Min X, Weinreb J, et al. Abbreviated biparametric versus standard multiparametric MRI for diagnosis of prostate cancer: A systematic review and meta-analysis. *Am J Roentgenol.* 2019;212(2):357–365. doi: 10.2214/AJR.18.20103
13. Niu XK, Chen XH, Chen ZF, et al. Diagnostic performance of biparametric MRI for detection of prostate cancer: A systematic review and meta-analysis. *Am J Roentgenol.* 2018;211(2):369–378. doi: 10.2214/AJR.17.18946
14. Ahmed HU, El-Shater Bosaily A, Brown LC, et al. Diagnostic accuracy of multi-parametric MRI and TRUS biopsy in prostate cancer (PROMIS): A paired validating confirmatory study. *Lancet.* 2017;389(10071):815–822. doi: 10.1016/S0140-6736(16)32401-1
15. McDonald RJ, Levine D, Weinreb J, et al. Gadolinium retention: A research roadmap from the 2018 NIH/ACR/RSNA workshop on gadolinium chelates. *Radiology.* 2018;289(2):517–534. doi: 10.1148/radiol.2018181151
16. Ploussard G, Epstein JI, Montironi R, et al. The contemporary concept of significant versus insignificant prostate cancer. *Eur Urol.* 2011;60(2):291–303. doi: 10.1016/j.eururo.2011.05.006
17. Loeb S, Vellekoop A, Ahmed HU, et al. Systematic review of complications of prostate biopsy. *Eur Urol.* 2013;64(6):876–892. doi: 10.1016/j.eururo.2013.05.049
18. Campli ED, Pizzi DA, Seccia B, et al. Diagnostic accuracy of biparametric vs multiparametric MRI in clinically significant prostate cancer: Comparison between readers with different experience. *Eur J Radiol.* 2018;(101):17–23. doi: 10.1016/j.ejrad.2018.01.028
19. Gatti M, Faletti R, Callaris G, et al. Prostate cancer detection with biparametric magnetic resonance imaging (bpMRI) by readers with different experience: Performance and comparison with multiparametric (mpMRI). *Abdominal Radiol (New York).* 2019;44(5):1883–1893. doi: 10.1007/s00261-019-01934-3

СПИСОК ЛИТЕРАТУРЫ

1. Turkbey B, Rosenkrantz A.B., Haider M.A., et al. Prostate imaging reporting and data system version 2.1: 2019 Update of prostate imaging reporting and data system version 2 // *Eur Urol.* 2019. Vol. 76, N 3. P. 340–351. doi: 10.1016/j.eururo.2019.02.033
2. Bjurlin M.A., Carroll P.R., Eggener S., et al. Update of the standard operating procedure on the use of multiparametric magnetic resonance imaging for the diagnosis, staging and management of prostate cancer // *J Urol.* 2020. Vol. 203, N 4. P. 706–712. doi: 10.1097/JU.0000000000000617
3. Rouvière O., Puech P., Renard-Penna R., et al. Use of prostate systematic and targeted biopsy on the basis of multiparametric MRI in biopsy-naïve patients (MRI-FIRST): A prospective, multicentre, paired diagnostic study // *Lancet Oncology.* 2019. Vol. 20, N 1. P. 100–109. doi: 10.1016/S1470-2045(18)30569-2
4. Boesen L., Thomsen F.B., Nørgaard N., et al. A predictive model based on biparametric magnetic resonance imaging and clinical parameters for improved risk assessment and selection of biopsy-naïve men for prostate biopsies // *Prostate Cancer Prostatic Dis.* 2019. Vol. 22, N 4. P. 609–616. doi: 10.1038/s41391-019-0149-y
5. Tamada T., Kido A., Yamamoto A., et al. Comparison of biparametric and multiparametric MRI for clinically significant prostate cancer detection with PI-RADS Version 2.1 // *J Magnetic Resonance Imaging.* 2021. Vol. 53, N 1. P. 283–291. doi: 10.1002/jmri.27283
6. Wallström J., Geterud K., Kohestani K., et al. Bi- or multiparametric MRI in a sequential screening program for prostate cancer with PSA followed by MRI? Results from the Göteborg prostate cancer screening 2 trial // *Eur Radiol.* 2021. Vol. 31, N 11. P. 8692–8702. doi: 10.1007/s00330-021-07907-9
7. Kuhl C.K., Bruhn R., Krämer N., et al. Abbreviated biparametric prostate MR imaging in men with elevated prostate-specific antigen // *Radiology.* 2017. Vol. 285, N 2. P. 493–505. doi: 10.1148/radiol.2017170129
8. Абуладзе Л.П., Семенов Д.С., Панина О.Ю., Васильев Ю.А. Оптимизированный протокол бипараметрической магнитно-резонансной томографии для диагностики рака предстательной железы // *Digital Diagnostics.* 2022. Т. 3, № 3. С. 166–177. doi: 10.17816/DD108484
9. Schoots I.G., Barentsz J.O., Bittencourt L.K., et al. PI-RADS committee position on MRI without contrast medium in biopsy-naïve men with suspected prostate cancer: Narrative review // *Am J Roentgenol.* 2021. Vol. 216, N 1. P. 3–19. doi: 10.2214/AJR.20.24268
10. Gleason D.F. Classification of prostatic carcinomas // *Cancer Chemother Rep.* 1966. Vol. 50, N 3. P. 125–128.
11. Zawaideh J.P., Sala E., Shaida N., et al. Diagnostic accuracy of biparametric versus multiparametric prostate MRI: Assessment of contrast benefit in clinical practice // *Eur Radiol.* 2020. Vol. 30, N 7. P. 4039–4049. doi: 10.1007/s00330-020-06782-0
12. Kang Z., Min X., Weinreb J., et al. Abbreviated biparametric versus standard multiparametric MRI for diagnosis of prostate cancer: A systematic review and meta-analysis // *Am J Roentgenol.* 2019. Vol. 212, N 2. P. 357–365. doi: 10.2214/AJR.18.20103
13. Niu X.K., Chen X.H., Chen Z.F., et al. Diagnostic performance of biparametric MRI for detection of prostate cancer: A systematic review and meta-analysis // *Am J Roentgenol.* 2018. Vol. 211, N 2. P. 369–378. doi: 10.2214/AJR.17.18946
14. Ahmed H.U., El-Shater Bosaily A., Brown L.C., et al. Diagnostic accuracy of multi-parametric MRI and TRUS biopsy in prostate cancer (PROMIS): A paired validating confirmatory study // *Lancet.* 2017. Vol. 389, N 10071. P. 815–822. doi: 10.1016/S0140-6736(16)32401-1
15. McDonald R.J., Levine D., Weinreb J., et al. Gadolinium retention: A research roadmap from the 2018 NIH/ACR/RSNA workshop on gadolinium chelates // *Radiology.* 2018. Vol. 289, N 2. P. 517–534. doi: 10.1148/radiol.2018181151
16. Ploussard G., Epstein J.I., Montironi R., et al. The contemporary concept of significant versus insignificant prostate cancer // *Eur Urol.* 2011. Vol. 60, N 2. P. 291–303. doi: 10.1016/j.eururo.2011.05.006
17. Loeb S., Vellekoop A., Ahmed H.U., et al. Systematic review of complications of prostate biopsy // *Eur Urol.* 2013. Vol. 64, N 6. P. 876–892. doi: 10.1016/j.eururo.2013.05.049
18. Campli E.D., Pizzi D.A., Seccia B., et al. Diagnostic accuracy of biparametric vs multiparametric MRI in clinically significant prostate cancer: Comparison between readers with different experience // *Eur J Radiol.* 2018. N 101. P. 17–23. doi: 10.1016/j.ejrad.2018.01.028
19. Gatti M., Faletti R., Callaris G., et al. Prostate cancer detection with biparametric magnetic resonance imaging (bpMRI) by readers with different experience: Performance and comparison with multiparametric (mpMRI) // *Abdominal Radiol (New York).* 2019. Vol. 44, N 5. P. 1883–1893. doi: 10.1007/s00261-019-01934-3

AUTHORS' INFO

*** Pavel B. Gelezhe;**

address: 24/1 Petrovka street, 127051 Moscow, Russia;
ORCID: 0000-0003-1072-2202;
eLibrary SPIN: 4841-3234;
e-mail: gelezhe.pavel@gmail.com

Yuriy A. Vasilev, MD, Cand. Sci. (Med);

ORCID: 0000-0002-0208-5218;
eLibrary SPIN: 4458-5608;
e-mail: npcmmr@zdrav.mos.ru

Olga V. Omelyanskaya;

ORCID: 0000-0002-0245-4431;
eLibrary SPIN: 8948-6152;
e-mail: o.omelyanskaya@npcmmr.ru

Anton V. Vladzimirskyy, MD, Dr. Sci. (Med), Professor;

ORCID: 0000-0002-2990-7736;
eLibrary SPIN: 3602-7120;
e-mail: npcmmr@zdrav.mos.ru

Roman V. Reshetnikov;

ORCID: 0000-0002-9661-0254;
eLibrary SPIN: 8592-0558;
e-mail: reshetnikov@fbb.msu.ru

Anna P. Gonchar;

ORCID: 0000-0001-5161-6540;
eLibrary SPIN: 3513-9531;
e-mail: a.gonchar@npcmmr.ru

Ivan A. Blokhin;

ORCID: 0000-0002-2681-9378;
eLibrary SPIN: 3306-1387;
e-mail: i.blokhin@npcmmr.ru

Iskander I. Abdullin;

ORCID: 0000-0003-1138-0822;
eLibrary SPIN: 6560-5219;
e-mail: iabdullin@emcmos.ru

Irina N. Kievа;

ORCID: 0000-0002-4060-5966;
eLibrary SPIN: 2279-9141;
e-mail: kievа.irina@gmail.com

ОБ АВТОРАХ

*** Гележе Павел Борисович;**

адрес: Россия, 127051, Москва, ул. Петровка, д. 24, стр. 1;
ORCID: 0000-0003-1072-2202;
eLibrary SPIN: 4841-3234;
e-mail: gelezhe.pavel@gmail.com

Васильев Юрий Александрович, канд. мед. наук;

ORCID: 0000-0002-0208-5218;
eLibrary SPIN: 4458-5608;
e-mail: npcmmr@zdrav.mos.ru

Омелянская Ольга Васильевна;

ORCID: 0000-0002-0245-4431;
eLibrary SPIN: 8948-6152;
e-mail: o.omelyanskaya@npcmmr.ru

Владзимирский Антон Вячеславович, д-р мед. наук, профессор;

ORCID: 0000-0002-2990-7736;
eLibrary SPIN: 3602-7120;
e-mail: npcmmr@zdrav.mos.ru

Решетников Роман Владимирович;

ORCID: 0000-0002-9661-0254;
eLibrary SPIN: 8592-0558;
e-mail: reshetnikov@fbb.msu.ru

Гончар Анна Павловна;

ORCID: 0000-0001-5161-6540;
eLibrary SPIN: 3513-9531;
e-mail: a.gonchar@npcmmr.ru

Блохин Иван Андреевич;

ORCID: 0000-0002-2681-9378;
eLibrary SPIN: 3306-1387;
e-mail: i.blokhin@npcmmr.ru

Абдуллин Искандер Ильфакович;

ORCID: 0000-0003-1138-0822;
eLibrary SPIN: 6560-5219;
e-mail: iabdullin@emcmos.ru

Киева Ирина Николаевна;

ORCID: 0000-0002-4060-5966;
eLibrary SPIN: 2279-9141;
e-mail: kievа.irina@gmail.com

* Corresponding author / Автор, ответственный за переписку

DOI: <https://doi.org/10.17816/DD567783>

Структурные изменения серого вещества при вариантах первичной прогрессирующей афазии

Д.Р. Ахмадуллина, Р.Н. Коновалов, Ю.А. Шпилюкова, Е.Ю. Федотова

Научный центр неврологии, Москва, Российская Федерация

АННОТАЦИЯ

Обоснование. Первичная прогрессирующая афазия — редкое нейродегенеративное заболевание, гетерогенность которого значительно усложняет его диагностику. Воксель-ориентированная морфометрия позволяет объективно оценить поражение серого вещества головного мозга и определить паттерны атрофии, характерные для каждого из вариантов заболевания, что может улучшить его диагностику, а также использоваться в изучении патогенеза.

Цель — выявить паттерны атрофии при каждом из вариантов первичной прогрессирующей афазии в сравнении с контрольной группой.

Материалы и методы. В основную группу были включены пациенты с диагнозом одного из вариантов первичной прогрессирующей афазии, установленных в соответствии с действующими диагностическими критериями. Группу контроля составили здоровые добровольцы без неврологических проявлений и структурных изменений головного мозга. Всем участникам проводилась магнитно-резонансная томография головного мозга с последующей постобработкой изображений и проведением воксель-ориентированной морфометрии со сравнением объема серого вещества между каждым из вариантов заболевания и контрольной группой. Исследование проводилось с поправкой на пол, возраст и интракраниальный объем участников.

Результаты. В исследование были включены 25 пациентов с аграмматическим, 11 — с семантическим и 9 — с логопеническим вариантами первичной прогрессирующей афазии, а также 20 здоровых добровольцев. Воксель-ориентированная морфометрия показала, что для каждого варианта характерен свой паттерн атрофии с преимущественным вовлечением лобной и островковой долей при аграмматическом, височной доли и гиппокампа — при семантическом и более диффузным лобно-височным паттерном — при логопеническом вариантах.

Заключение. В ходе исследования были выявлены паттерны атрофии головного мозга, характерные для каждого из вариантов первичной прогрессирующей афазии. В основном, полученные результаты соответствуют клиническим проявлениям заболевания. При этом отдельные находки (отсутствие атрофии задней перисильвиевой области, а также поражение моторной коры при логопеническом варианте; поражение орбитофронтальной коры и мозжечка при аграмматическом варианте; поражение премоторной коры, прецентральной и нижней лобной извилины при семантическом варианте) не соотносятся с привычным представлением о патогенезе первичной прогрессирующей афазии и требуют дальнейшего изучения.

Ключевые слова: первичная прогрессирующая афазия; воксель-ориентированная морфометрия; лобно-височная деменция; болезнь Альцгеймера.

Как цитировать:

Ахмадуллина Д.Р., Коновалов Р.Н., Шпилюкова Ю.А., Федотова Е.Ю. Структурные изменения серого вещества при вариантах первичной прогрессирующей афазии // Digital Diagnostics. 2023. Т. 4, № 4. С. 467–480. DOI: <https://doi.org/10.17816/DD567783>

DOI: <https://doi.org/10.17816/DD567783>

Structural gray matter changes in primary progressive aphasia variants

Diliara R. Akhmadullina, Rodion N. Konovalov, Yulia A. Shpilyukova, Ekaterina Yu. Fedotova

Research Center of Neurology, Moscow, Russian Federation

ABSTRACT

BACKGROUND: Primary progressive aphasia is a rare neurodegenerative disease with high clinical, genetic, and pathomorphological heterogeneity that greatly complicates its diagnosis. Voxel-based morphometry can be used to objectively assess structural gray matter changes and determine atrophy patterns in variants of primary progressive aphasia, which can improve the diagnosis and our understanding of its pathogenesis.

AIMS: This study aimed to evaluate the patterns of atrophy in each of the primary progressive aphasia variants in comparison with the control group.

MATERIALS AND METHODS: Patients diagnosed with one of the primary progressive aphasia variants, established in accordance with the current diagnostic criteria, were included in the main group. The control group consisted of healthy volunteers without any neurological symptoms or structural brain changes. All participants underwent brain magnetic resonance imaging. The obtained images were processed and used for voxel-based morphometry, which was performed by comparing the gray matter volume between each of the primary progressive aphasia variants and the control group. The study was adjusted for the sex, age, and intracranial volume of the participants.

RESULTS: The study enrolled 25 patients with nonfluent, 11 with semantic, and 9 with logopenic variants of primary progressive aphasia, as well as 20 healthy volunteers. Voxel-based morphometry showed a specific atrophy pattern in each of the variants of primary progressive aphasia, with predominant involvement of the frontal and insular lobes in nonfluent, temporal lobe and hippocampus in semantic, and a more diffuse frontotemporal pattern in logopenic variants.

CONCLUSIONS: The study revealed gray matter atrophy patterns specific to each variant of primary progressive aphasia. The obtained results mainly correspond to the clinical presentations of the disease. Moreover, some findings (e.g., absence of the posterior perisylvian atrophy and reduced motor cortex volume in the logopenic variant, atrophy of the orbitofrontal cortex and cerebellum in the nonfluent variant, and premotor cortex, precentral, and inferior frontal gyrus degeneration in the semantic variant) do not correlate with the usual understanding of primary progressive aphasia pathogenesis and require further study.

Keywords: primary progressive aphasia; voxel-based morphometry; frontotemporal dementia; Alzheimer's disease.

To cite this article:

Akhmadullina DR, Konovalov RN, Shpilyukova YuA, Fedotova EYu. Structural gray matter changes in primary progressive aphasia variants. *Digital Diagnostics*. 2023;4(4):467–480. DOI: <https://doi.org/10.17816/DD567783>

Received: 27.07.2023

Accepted: 22.08.2023

Published online: 14.09.2023

DOI: <https://doi.org/10.17816/DD567783>

原发性进行性失语症变体的灰质结构变化

Diliara R. Akhmadullina, Rodion N. Konovalov, Yulia A. Shpilyukova, Ekaterina Yu. Fedotova

Research Center of Neurology, Moscow, Russian Federation

简评

论证。原发性进行性失语症是一种罕见的神经退行性疾病。它的异质性使诊断变得非常复杂。基于体素的形态测量法可对大脑灰质病变进行客观评估，并确定每种疾病变异的萎缩模式特征。这可以改善诊断，也可被用于发病机制的研究。

该研究的目的是确定原发性进行性失语症各变体与对照组相比的萎缩模式。

材料与方法。被诊断为原发性进行性失语症变体之一的患者被纳入主研究组。诊断是根据现行诊断标准确定的。对照组由无神经系统表现和脑结构变化的健康志愿者组成。我们对所有参与者都进行了脑部磁共振成像，随后进行了图像后处理和基于体素的形态测量。对每种疾病变体与对照组的灰质体积进行了比较。研究人员考虑到参与者的性别、年龄和颅内容积。

结果。研究对象包括25名非流利型原发性进行性失语的患者、11名语义型原发性进行性失语的患者和9名logopenic型原发性进行性失语的患者，以及20名健康志愿者。基于体素的形态测量显示了，每种变体都有不同的萎缩模式。在非流利型原发性进行性失语症中，额叶和岛叶主要受累。在语义型原发性进行性失语症中，颞叶和海马主要受累。logopenic型原发性进行性失语症的特点是额颞叶模式更加弥漫。

结论。在研究过程中，我们发现了原发性进行性失语症各变体特有的脑萎缩模式。基本上，这些结果与疾病的临床表现相符。但是有些研究结果（logopenic型没有后外侧裂部位萎缩和有运动皮层病变；非流利型有眶额皮质和小脑病变；语义型有运动前皮层、中央前回和额下回病变）与原发性进行性失语症发病机制的通常观点不符，需要进一步研究。

关键词：原发性进行性失语症；基于体素的形态计量学；额颞叶痴呆；阿尔茨海默病。

引用本文：

Akhmadullina DR, Konovalov RN, Shpilyukova YuA, Fedotova EYu. 原发性进行性失语症变体的灰质结构变化. *Digital Diagnostics*. 2023;4(4):467–480. DOI: <https://doi.org/10.17816/DD567783>

收到: 27.07.2023

接受: 22.08.2023

发布日期: 14.09.2023

ABBREVIATIONS

AV-PPA: agrammatic variant of primary progressive aphasia
 FTD: frontotemporal dementia
 GM: gray matter
 IFG: inferior frontal gyrus
 ITG: inferior temporal gyrus
 LV-PPA: logopenic variant of primary progressive aphasia
 MNI: Montreal Neurological Institute
 mPFC: medial prefrontal cortex

MRI: magnetic resonance imaging
 MTG: middle temporal gyrus
 OFC: orbitofrontal cortex
 PPA: primary progressive aphasia
 SMA: supplementary motor area
 STG: superior temporal gyrus
 SV-PPA: semantic variant of primary progressive aphasia
 VBM: voxel-based morphometry

BACKGROUND

Primary progressive aphasia (PPA) is a neurodegenerative disease characterized by early, constantly progressive speech disorders in the absence of other cognitive, motor, and/or behavioral disorders. PPA refers to early-onset dementias (<65 years) and, despite its low incidence, presents a relevant socioeconomic problem. Three clinical variants of PPA are distinguished based on clinical presentation: agrammatic (AV-PPA), semantic (SV-PPA), and logopenic (LV-PPA) variants. AV- and SV-PPA are usually a sign of frontotemporal dementia (FTD), whereas LV-PPA indicates atypical Alzheimer's disease. However, this distinction is not definitive because any PPA variant may demonstrate different pathomorphological and genetic variants, which results in diverse clinical presentations of the disease and complicates its diagnosis.

Apart from a neurological examination, neuroimaging is the only approved method for the differential diagnosis of PPA variants. A previous study helped identify specific involvement areas for each PPA variant, which was included in the 2011 diagnostic criteria [1]:

- AV-PPA is mainly characterized by atrophy of posterior frontal areas—inferior frontal gyrus (IFG), premotor cortex, and supplementary motor area (SMA) — and of the insula, prevailing on the left side.
- In SV-PPA, atrophy of the anterior–inferior sections of the left temporal lobe is typical.
- In LV-PPA, posterior perisylvian areas and/or the parietal lobe of the left hemisphere are commonly involved.

A later meta-analysis verified the presence of a specific pattern of neural degeneration in each PPA variant; however, the involvement appeared to be more extensive, including medial areas of the temporal lobes in SV-PPA; precentral gyrus, superior gyrus (STG), and middle temporal gyrus (MTG) in AV-PPA; and posterior cingulate cortex in LV-PPA [2]. However, the number of studies on gray matter (GM) involvement in PPA remains limited. To illustrate, the

meta-analysis mentioned above included only 20 papers, with the data of 317 patients (of which 169, 90, and 58 had SV-PPA, AV-PPA, and LV-PPA, respectively). In addition, many studies included were conducted using outdated diagnostic criteria, which makes the relevance of the results questionable, particularly for AV-PPA and LV-PPA. In recent years, larger studies have suggested that GM involvement in PPA is probably more extensive than previously thought; however, the atrophy patterns identified often differ [3, 4]. In addition, the clinical signs of PPA variants may vary in different populations because of language differences, which in turn may result in differences in the underlying GM degeneration [5]. The only paper evaluating structural changes of the brain in PPA in the Russian population included patients with AV-PPA exclusively, and no studies have focused on SV-PPA and LV-PPA when this paper was being written [6].

Meanwhile, neuroimaging methods are increasingly used for the diagnosis, evaluation, and follow-up of patients with PPA. For instance, machine learning based on the data of structural magnetic resonance imaging (MRI) may be used for the differential diagnosis of PPA variants and FTD and for the more extensive differential diagnosis of neurodegenerative dementias. Moreover, neuroimaging may be used to evaluate the therapeutic effect of novel treatment modalities [3, 7, 8]. All of the above emphasizes the relevance of such studies.

AIM

This study aimed to characterize the atrophy patterns in each of the PPA variants in the Russian population and compare the data obtained with those of previous studies.

METHODS

Study design

This was an experimental, single-center, cross-sectional study.

Eligibility

Subjects were enrolled in the study on the basis of their compliance with the inclusion/non-inclusion criteria.

Inclusion criteria for the experimental group (PPA group): age >18 years and diagnosis of one of the PPA variants based on the current diagnostic criteria [1].

Inclusion criteria for the control group: age >18 years and absence of neurological symptoms.

Noninclusion criteria: MRI contraindications and structural focal changes in the brain.

Site

The study was conducted at the Research Center of Neurology (Moscow).

Study duration

The subjects were recruited from 2022 to 2023.

Medical intervention

Addenbrooke's Cognitive Examination Revised was used to evaluate cognitive functions in the PPA group. Emotional and behavioral disorders were evaluated using a neuropsychiatric questionnaire. Disease severity was assessed using the FTD severity scale.

Brain MRI in the 3D-T1 MPR sequence using Magnetom Verio or Magnetom Prisma at a field magnitude of 3 Tesla was performed for all study subjects.

The MR images obtained were used for voxel-based morphometry (VBM).

SPM12 software (Institute of Neurology, UK) based on Matlab R2019b (MathWorks Inc., Natick, MA, USA) was used for postprocessing and statistical analysis. Postprocessing involved the following:

- Normalizing the images to the same MNI stereotaxic space (3D system of coordinates of the human brain by the Montreal Neurological Institute)
- Segmentation into GM, white matter, and cerebrospinal fluid using the DARTEL algorithm
- Further smoothing of the images was obtained with an isotropic Gaussian kernel with full width at a half height of 8 mm.

VBM results were assessed for every PPA variant versus the control group. The two-sample *t*-test with voxel-wise comparison was used for the study groups. Exclusive analysis of GM was possible using a GM mask generated specifically for each group. The age and sex of the participants were used as covariates. The study was performed with adjustment for intracranial volume, which was measured as the sum of GM, white matter, and cerebrospinal fluid volumes. Clusters with a minimum volume of 100 voxels were included in the analysis. The cutoff for the inclusion of individual voxels into clusters was set at a level of $P < 0.05$ with an adjustment for the expected percentage of false rejections.

The bspmview software was used for VBM result visualization, presentation of the statistical data, and coordinate localization [9].

Ethical evaluation

This study was approved by the Ethics Committee of the Research Center of Neurology (Protocol No. 11-7/22 dated December 21, 2022).

Statistical analysis

IBM SPSS Statistics version 26.0 (IBM Corp., Armonk, NY, USA) was used for statistical analysis. Differences in nominal and ordinal variables were analyzed using Fisher's exact test, and differences in quantitative variables were analyzed using the Kruskal–Wallis test with Bonferroni correction.

RESULTS

Study subjects

The study included 45 patients with PPA variants and 30 control subjects. Of the 45 patients, 25, 11, and 9 had AV-PPA, SV-PPA, and LV-PPA, respectively. The key characteristics of the study groups are summarized in Table 1. The median ages were 64, 67, and 65 years for the AV-PPA, SV-PPA, and LV-PPA groups, respectively. Female patients prevailed in the AV-PPA and SV-PPA groups, whereas male patients prevailed in the LV-PPA group. The disease duration ranged from 6 to 108 months, with the longest duration in the AV-PPA group. The disease severity ranged from very mild to severe, and mild to moderate symptoms were the most

Table 1. Clinical characteristics of the study groups

Index	AV-PPA (n=25)	SV-PPA (n=11)	LV-PPA (n=9)	Control group (n=30)
Sex, M/F (%)	9/16 (36%; 64%)	5/6 (45%; 55%)	6/3 (67%; 33%)	10/20 (33%; 67%)
Age, years	64 [57; 67]*	67 [63,5; 68,5]†	65 [56; 67]	56 [51; 59]*,†
Disease duration, months	48 [36; 60]	36 [16; 48]	36 [23; 48]	–
ACE-R, total score/100	68 [36; 80]	38 [26; 50]	53 [37; 75]	–
Neuropsychiatric questionnaire, score/144	8 [1; 14]*	18 [11,5; 20,5]*	15 [4; 33,5]	–

Notes: The data are described as Me [Q1; Q3]; ACE-R, Addenbrooke's Cognitive Examination Revised; M, male; F, female; *, †: the difference between groups is statistically significant ($P < 0.05$).

common. Despite the shorter disease duration, the most severe cognitive, emotional, and behavioral disorders were observed in SV-PPA.

Despite the described differences, no statistically significant differences in sex, age, disease duration, and severity of cognitive disorders were observed among the PPA variants.

No difference in the distribution by sex was observed against the control group; however, the control group was statistically significantly younger than the AV-PPA and SV-PPA groups.

Key findings

VBM identified areas of atrophy in each PPA variant compared with the control group (Fig. 1). Atrophy in all cases was asymmetric, prevailing in the left hemisphere.

AV-PPA group: The atrophic “core” was localized in the left IFG and precentral gyrus (Table 2). Significant changes were also observed in the SMA, premotor cortex, orbitofrontal cortex (OFC), and insular cortex of both hemispheres. The temporal lobe was mainly involved in the MTG and inferior temporal gyrus (ITG), continuing into the area of the temporoparietal junction and inferior parietal lobule. In addition, atrophic involvement of subcortical structures was observed, namely, the left caudate nucleus, thalamus, putamen, and cerebellum.

SV-PPA group: Atrophy was predominantly localized in the left temporal lobe, including its pole, inferior–lateral and medial regions, and left hippocampus and insula (Table 3).

Individual lesions were observed in the left frontal lobe, including the OFC, medial prefrontal cortex (mPFC), premotor cortex, precentral gyrus, and IFG. Overall, the changes were more localized than in AV-PPA and were limited to the frontal, temporal, and insular cortices, except for an atrophic lesion in the left caudate nucleus. Similar but less extensive atrophic areas were identified in the right hemisphere.

LV-PPA group: The most pronounced loss of the GM volume was also localized in the left temporal lobe but was mostly involved in the posterior parts of MTG and ITG and, to a lesser extent, the temporal pole. In addition, it continued into the parahippocampal gyrus, hippocampus, and amygdala (Table 4). Atrophy was the most pronounced in the precentral gyrus, anterior cingulate cortex, OFC, and mPFC. Apart from the frontal and temporal lobes, atrophy in this PPA variant involved the insular lobes, left parietal and occipital lobes, cerebellum, and left caudate nucleus.

DISCUSSION

Key findings summary

The study revealed GM areas with the involvement typical of each PPA variant. The identified atrophy patterns were largely consistent with literature data, although certain specifics were discovered.

Key findings discussion

In AV-PPA, the GM was expectedly seen in the IFG, precentral gyrus, premotor cortex, SMA, and anterior

Table 2. Areas of the loss of the gray matter volume in the group with agrammatic variant of primary progressive aphasia vs. control group

Brain area	Volume, voxels	MNI peak coordinates x, y, z
Precentral gyrus, inferior frontal gyrus, supplementary motor area, insula, superior and middle frontal gyri, orbitofrontal cortex, cingulate cortex, lower parietal lobule, angular and supramarginal gyri, lateral areas of the temporal lobe, putamen, caudate nucleus, S	37,644	-40, 4, 34 -42, -2, 42 -57, -4, 4 39, 18, 26
Opercular and triangular parts of the IFG, D	2,264	38, 6, 27 36, 4, 40 -16, -16, 22
Caudate nucleus; thalamus, D	1,065	-14, -12, 10 -10, 10, 16
OFC, D	180	24, 38, -9
Cerebellar crus I, D	101	18, -72, -36
Precuneus, S	105	-10, -57, 27
Postcentral gyrus, D	314	33, -34, 38 36, -26, 39
Insula, D	191	34, 20, 10
Precentral gyrus, D	257	52, -6, 45 57, -6, 33

Note: D, on the right; S, on the left.

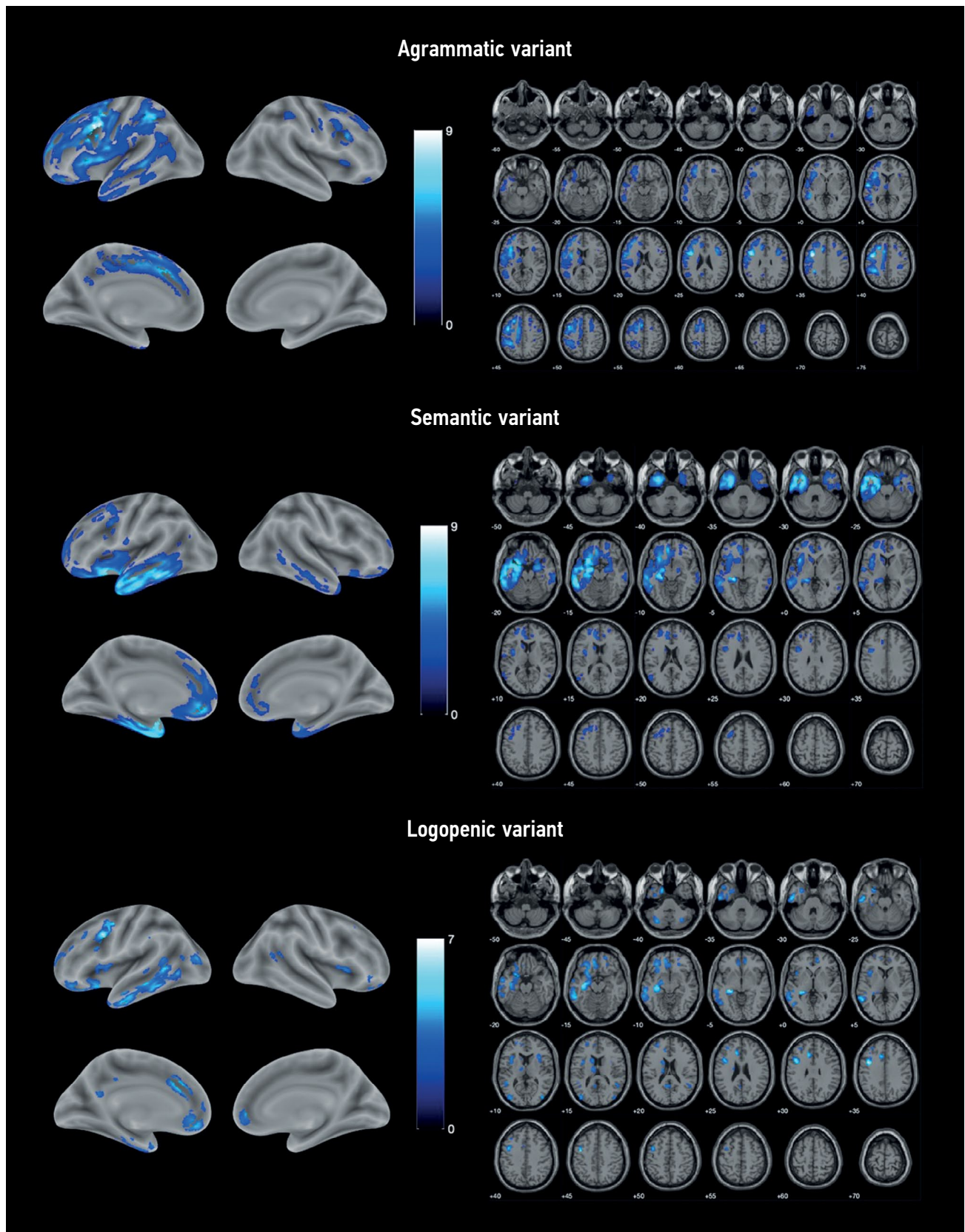


Fig. 1. Localization of the areas of the loss of the gray matter volume in variants of primary progressive aphasia vs. control group. The color coding is for the T-value.

Table 3. Areas of the loss of the gray matter volume in the group with semantic variant of primary progressive aphasia versus control group

Brain area	Volume, voxels	MNI peak coordinates x, y, z
Hippocampus; lateral and medial areas of the temporal lobe; temporal pole; insula; anterior cingulate cortex; OFC; caudate nucleus, S; OFC, D	36,682	-24, -30, -4 -52, -46, -15 -56, -39, -16 24, -6, -21
Hippocampus, temporal lobe pole, ITG, OFC, D	6,563	39, 10, -33 24, 9, -21
Middle regions of STG, S	344	-57, -6, 4 -28, 10, 54
Premotor cortex, middle parts of the precentral gyrus, opercular part of IFG, S	1,809	-40, 3, 32 -24, 6, 38
Posterior regions of MTG, S	253	-51, -68, 16 -44, -57, 15
mPFC, S	125	-9, 22, 48
Posterior regions of the MTG and ITG, D	104	56, -62, 9 58, -54, -3

Note: D, on the right; S, on the left.

Table 4. Areas of the loss of the gray matter volume in the group with logopenic variant of primary progressive aphasia versus control group

Brain area	Volume, voxels	MNI peak coordinates x, y, z
Precentral gyrus, S	1,304	-40, 6, 34 -42, 0, 45 -36, 3, 52 -26, -30, -3
Hippocampus, amygdala, ITG, MTG, OFC, S	8,136	-36, -16, -15 -27, -24, -9
Anterior cingulate cortex, S	501	-12, 26, 27 -10, 44, -14
Anterior cingulate cortex, S; mPFC, S and D	1,130	14, 45, -2 -9, 38, -6
Cerebellar crus II, S	325	-32, -70, -39 -38, -60, -42
Middle occipital gyrus, S	328	-40, 82, 14
Caudate nucleus, S	325	-14, -10, 20 -14, 16, 8
Insula and IFG, S	537	-38, 4, 15
Temporal lobe pole, S	218	-45, -15, -36
Posterior regions of MTG, D	166	46, -48, 15 -30, 51, 21
Rostrolateral prefrontal cortex, S	389	-21, 56, 10 -33, 42, 24
OFC, D	110	20, 52, -14
Cerebellar crus I, D	145	32, -66, -39
Caudate nucleus, S	201	-14, 6, 18
Precuneus, S	170	-8, -54, 18
Insula, D	211	33, 18, 12 34, 9, 14

Note: D, on the right; S, on the left.

insula, i.e., the areas in which atrophy has been repeatedly described in AV-PPA and correlates closely with speech disorders specific for this PPA variant [10]. For instance, the loss of the GM volume in the IFG correlated with the general severity of aphasia and agrammatisms; in the left insula, with the severity of speech fluency disorders; and atrophy of SMA and premotor cortex was associated with speech apraxia, articulation rate, and nonverbal oral apraxia [11–14]. Moreover, the degeneration of the precentral gyrus may be associated with concomitant AV-PPA through motor neuronal disease, which was found in 16% of patients with AV-PPA in our sample.

Apart from the frontal lobes, atrophy also spreads to the lateral regions of the left temporal lobe. Although its involvement is considered less “classic” in AV-PPA, it is present in most studies of structural changes in this variant. This might be indicative of progressive neurodegeneration over time and account for difficulties in understanding individual words and naming [2, 15, 16].

Bilateral OFC atrophy is of particular interest because it is extremely rare in AV-PPA and is more often associated with emotional and behavioral disorders. Mild-to-moderate behavioral disorders were observed in most patients in our sample, which could account for this finding. In addition, OFC atrophy was previously described in patients with PPA associated with *GRN* mutation, albeit only in nonclassifiable PPA cases, the clinical presentation of which does not match any of the variants [17]. *GRN* mutations were verified in two patients with AV-PPV from our sample; however, their clinical presentation was standard for this variant; therefore, the identified atrophy was not attributable to the genetic features of the group. This finding requires further studies in a larger sample in our region.

Atrophy in AV-PPV was observed in subcortical structures, such as the left thalamus, putamen, and caudate nucleus. Recently, more studies have reported thalamic atrophy in FTD variants, particularly in genetic disease forms; however, such changes are more typical of the behavioral variant of FTD than of AV-PPA, in which thalamic atrophy is more localized and is not observed in all cases [2, 16–19]. Atrophy of the putamen and caudate nucleus was previously described in single papers but not in larger studies [4, 10, 13]. Overall, despite the evidence of the role of the thalamus and basal ganglia in speech articulation and phonology because of their connections with frontal and parietal regions, there is no conclusive opinion on how their degeneration affects speech disorders in PPA [20].

Another outstanding finding in AV-PPA is that the cerebellum is reduced in size. Cerebellar atrophy in FTD was first described in the disease secondary to a *C9ORF72* mutation; however, a more typical finding of this case was bilateral, relatively symmetric atrophy, which, apart from the cerebellum, also usually spreads to parietal and occipital areas, and we did not observe this in our study. Another possible explanation is the role of the cerebellum

in speech functions. Previously, lobule VII of the cerebellar hemispheres (atrophy of which we identified in our study) is involved in feedback control in oral speech, and its significance is greater in the gradual disorganization of the speech regions of the brain [20].

The atrophy pattern identified in the SV-PPA group is largely consistent with literature data. The most significant reduction in the GM volume was observed in the temporal poles of both hemispheres, predominantly on the left side. The left temporal pole is a semantic hub from which verbal semantic information is stored, processed, and extracted. Its atrophy is the key sign of SV-PPA, and anomia and difficulty understanding individual words in this variant are associated with it [21]. Asymmetric atrophy of the hippocampus and medial and inferior regions of the temporal lobes identified in our study is another major sign of SV-PPA, which has been reported repeatedly. Notably, unlike Alzheimer’s disease, SV-PPA is characterized by atrophy of the anterior regions of the hippocampi, which also correlates with semantic deficit severity in patients [22]. The involvement of the inferior regions of the temporal lobes in SV-PPA, particularly the fusiform gyrus, correlates with emotional and behavioral disorders and prosopagnosia, whereas the involvement of the lateral regions of STG and MTG is associated with the severity of anomia, difficulty understanding individual words, and dyslexia severity [21, 23]. The loss in the volume of the anterior cingulate cortex, mPFC, OFC, insula, and caudate nucleus is typical of more advanced stages of SV-PPA and is associated with a gradual spread of the process from the left temporal pole to closely related areas [24, 25]. The involvement of these regions is associated with social activity disorders; however, only a few papers have focused on this subject [26]. Atrophy of the left IFGs, premotor cortex, and precentral gyrus, which we identified, is less common in SV-PPA. Such changes may cause gradual development of the clinical presentation consistent with the disease and occurrence of motor speech disorders [16].

The GM volume loss observed in LV-PPA was more diffuse, with multiple small degenerative lesions. The most prominent areas of atrophy in our sample were located in the left temporal and frontal lobes. The loss of MTG and ITG volume is often reported in LV-PPA and is associated with specific speech disorders in this variant (e.g., anomia and difficulties in repeating long phrases and sentences), which results from the dysfunction of short-term phonological memory [27]. Asymmetric atrophy of the hippocampus and amygdala is also characteristic of LV-PPA and most likely develops because of underlying Alzheimer’s degeneration. The spread of atrophy to more posterior regions with the involvement of the parietal and occipital lobes and the cerebellum may be explained by the same process.

The loss of the volume of the left temporal pole, the same as that of the IFG, insular lobes, and lateral prefrontal cortex, was also reported in LV-PPA, generally, at more advanced stages. It appears to reflect the involvement of other speech

areas and correlate with the onset of symptoms more typical of other PPA variants, such as difficulty understanding individual words [16].

Atrophy of the precentral gyrus, OFC, and medial regions of the frontal lobe is less common even in the advanced stages of LV-PPA. As mentioned above, OFC involvement may be associated with emotional and behavioral disorders. The loss of the cingulate cortex volume, in turn, has been repeatedly described in Alzheimer's disease and may correlate with the development of nonlinguistic cognitive deficits. Severe degeneration of the precentral gyrus is of the greatest interest; despite earlier reports of such changes, they are usually not one of the most significant areas of atrophy and are observed only in the long-term follow-up [3]. None of the patients from the LV-PPA group had any clinical signs of motor cortex involvement at the time of the examination; therefore, atrophy of this area is most probably secondary, not contributing significantly to disease pathogenesis.

Contrary to our expectations, no degenerations of the inferior parietal lobule, supramarginal and angular gyri, and posterior regions of STG were observed in the LV-PPA group, although it is considered the most pathognomonic for this variant and is included in the diagnostic criteria. This fact and the more diffuse focal nature of atrophy identified in our study in LV-PPA may be accounted for by the relatively small sample size and its pathomorphological heterogeneity. Although Alzheimer-type degeneration prevails in LV-PPA and is observed in 85%–100% of cases [28, 29], it was only present in one-third of our sample. Previously, atrophy patterns in PPA may vary depending on the underlying pathomorphological process, which may have affected the results of this study [30]. Our results demonstrate that the atrophy of the posterior perisylvian regions is not key for the development of the clinical presentations of LV-PPA and indirectly emphasizes a greater contribution of MTG to disease pathogenesis.

Study limitations

This study has several limitations. As mentioned earlier, the sample sizes of the LV-PPA and SV-PPA groups were

small. The genetic and pathomorphological heterogeneities of the study groups may be considered a relative limitation. Although it improves the representation of the PPA patient population, it may affect the VBM results because every genetic and pathomorphological variant could have its specific patterns. In addition, we did not perform a correlation analysis as part of the study, comparing the identified atrophy with clinical manifestations, which prevents us from making an unambiguous conclusion on the clinical significance of the changes detected and on the role of the newly identified areas of atrophy on PPA pathogenesis. These limitations should be considered when planning further research on the subject.

CONCLUSION

This study identified patterns of GM atrophy characteristic of each PPA variant using the VBM. The results are consistent with current knowledge of the functional anatomy of speech functions and social behavior. Our findings are partly consistent with those of previous studies conducted in other countries. However, several distinctive features were identified, which require further validation in larger samples.

ADDITIONAL INFORMATION

Funding source. This research was funded by Russian Science Foundation, grant number 23-25-00483.

Competing interests. The authors declare that they have no competing interests.

Authors' contribution. All authors made a substantial contribution to the conception of the work, acquisition, analysis, interpretation of data for the work, drafting and revising the work, final approval of the version to be published and agree to be accountable for all aspects of the work. D.R. Akhmadullina participated in clinical and neuroimaging data collection, data analysis and interpretation and original draft preparation; R.N. Konovalov conceptualized and supervised the study, performed data analysis and interpretation, reviewed and edited the manuscript; Yu.A. Shpilyukova collected clinical data, reviewed and edited the manuscript; E.Yu. Fedotova planned research design, supervised the study, reviewed and edited the manuscript.

REFERENCES

- Gorno-Tempini ML, Hillis AE, Weintraub S, et al. Classification of primary progressive aphasia and its variants. *Neurology*. 2011; 76(11):1006–1014. doi: 10.1212/WNL.0b013e31821103e6
- Bisenius S, Neumann J, Schroeter ML. Validating new diagnostic imaging criteria for primary progressive aphasia via anatomical likelihood estimation meta-analyses. *European Journal of Neurology*. 2016;23(4):704–712. doi: 10.1111/ene.12902
- Lombardi J, Mayer B, Semler E, et al. Quantifying progression in primary progressive aphasia with structural neuroimaging. *Alzheimer's & Dementia*. 2021;17(10):1595–1609. doi: 10.1002/alz.12323
- Chapman CA, Polyakova M, Mueller K, et al. Structural correlates of language processing in primary progressive aphasia. *Brain Communications*. 2023;5(2). doi: 10.1093/braincomms/fcad076
- Canu E, Agosta F, Battistella G, et al. Speech production differences in English and Italian speakers with nonfluent variant PPA. *Neurology*. 2020;94(10):e1062–e1072. doi: 10.1212/WNL.0000000000008879
- Akhmadullina D, Konovalov R, Shpilyukova Y, et al. Brain atrophy patterns in patients with frontotemporal dementia: voxel-based morphometry. *Bulletin of Russian State Medical University*. 2020;(6):84–89. doi: 10.24075/brsmu.2020.075

7. Lampe L, Huppertz HJ, Anderl-Straub S, et al. Multiclass prediction of different dementia syndromes based on multi-centric volumetric MRI imaging. *NeuroImage: Clinical*. 2023;37:103320. doi: 10.1016/j.nicl.2023.103320
8. Staffaroni AM, Ljubenkov PA, Kornak J, et al. Longitudinal multimodal imaging and clinical endpoints for frontotemporal dementia clinical trials. *Brain*. 2019;142(2):443–459. doi: 10.1093/brain/awy319
9. zenodo.org [Internet]. spunt/bspmview: BSPMVIEW v.20161108 (Version 20161108). Zenodo. [cited 26 July 2023]. Available from: <https://zenodo.org/badge/latestdoi/21612/spunt/bspmview> doi: 10.5281/zenodo.168074
10. Gorno-Tempini ML, Dronkers NF, Rankin KP, et al. Cognition and anatomy in three variants of primary progressive aphasia. *Annals of Neurology*. 2004;55(3):335–346. doi: 10.1002/ana.10825
11. Tetzloff KA, Utianski RL, Duffy JR, et al. Quantitative analysis of agrammatism in agrammatic primary progressive aphasia and dominant apraxia of speech. *Journal of Speech, Language, and Hearing Research*. 2018;61(9):2337–2346. doi: 10.1044/2018_JSLHR-L-17-0474
12. Whitwell JL, Duffy JR, Strand EA, et al. Distinct regional anatomic and functional correlates of neurodegenerative apraxia of speech and aphasia: An MRI and FDG-PET study. *Brain and Language*. 2013;125(3):245–252. doi: 10.1016/j.bandl.2013.02.005
13. Mandelli ML, Vitali P, Santos M, et al. Two insular regions are differentially involved in behavioral variant FTD and nonfluent/agrammatic variant PPA. *Cortex*. 2016;74:149–157. doi: 10.1016/j.cortex.2015.10.012
14. Cordella C, Quimby M, Touroutoglou A, et al. Quantification of motor speech impairment and its anatomic basis in primary progressive aphasia. *Neurology*. 2019;92(17):e1992–e2004. doi: 10.1212/WNL.0000000000007367
15. Breining BL, Faria AV, Tippett DC, et al. Association of Regional Atrophy With Naming Decline in Primary Progressive Aphasia. *Neurology*. 2023;100(6):e582–e594. doi: 10.1212/WNL.00000000000201491
16. Rogalski E, Cobia D, Harrison TM, et al. Progression of language decline and cortical atrophy in subtypes of primary progressive aphasia. *Neurology*. 2011;76(21):1804–1810. doi: 10.1212/WNL.0b013e31821ccd3c
17. Samra K, MacDougall AM, Bouzigues A, et al. Genetic forms of primary progressive aphasia within the GENetic Frontotemporal dementia Initiative (GENFI) cohort: comparison with sporadic primary progressive aphasia. *Brain Communications*. 2023;5(2). doi: 10.1093/braincomms/fcad036
18. Rohrer JD, Nicholas JM, Cash DM, et al. Presymptomatic cognitive and neuroanatomical changes in genetic frontotemporal dementia in the Genetic Frontotemporal dementia Initiative (GENFI) study: a cross-sectional analysis. *The Lancet Neurology*. 2015;14(3):253–262. doi: 10.1016/S1474-4422(14)70324-2
19. McKenna MC, Li Hi Shing S, Murad A, et al. Focal thalamus pathology in frontotemporal dementia: Phenotype-associated thalamic profiles. *Journal of the Neurological Sciences*. 2022;436:120221. doi:10.1016/j.jns.2022.120221
20. Ziegler W, Ackermann H. Subcortical Contributions to Motor Speech: Phylogenetic, Developmental, Clinical. *Trends in Neurosciences*. 2017;40(8):458–468. doi: 10.1016/j.tins.2017.06.005
21. Migliaccio R, Boutet C, Valabregue R, et al. The Brain Network of Naming: A Lesson from Primary Progressive Aphasia. *PLOS ONE*. 2016;11(2):e0148707. doi: 10.1371/journal.pone.0148707
22. Wisse LEM, Ungrady MB, Ittyerah R, et al. Cross-sectional and longitudinal medial temporal lobe subregional atrophy patterns in semantic variant primary progressive aphasia. *Neurobiology of Aging*. 2021;98:231–241. doi: 10.1016/j.neurobiolaging.2020.11.012
23. Fittipaldi S, Ibanez A, Baez S, et al. More than words: Social cognition across variants of primary progressive aphasia. *Neuroscience & Biobehavioral Reviews*. 2019;100:263–284. doi: 10.1016/j.neubiorev.2019.02.020
24. Brown JA, Deng J, Neuhaus J, et al. Patient-Tailored, Connectivity-Based Forecasts of Spreading Brain Atrophy. *Neuron*. 2019;104(5):856–868.e5. doi: 10.1016/j.neuron.2019.08.037
25. Collins JA, Montal V, Hochberg D, et al. Focal temporal pole atrophy and network degeneration in semantic variant primary progressive aphasia. *Brain*. 2017;140(2):457–471. doi: 10.1093/brain/aww313
26. Kumfor F, Landin-Romero R, Devenney E, et al. On the right side? A longitudinal study of left- versus right-lateralized semantic dementia. *Brain*. 2016;139(3):986–998. doi: 10.1093/brain/awv387
27. Henry ML, Wilson SM, Babiak MC, et al. Phonological Processing in Primary Progressive Aphasia. *Journal of Cognitive Neuroscience*. 2016;28(2):210–222. doi: 10.1162/jocn_a_00901
28. Montembeault M, Brambati SM, Gorno-Tempini ML, Migliaccio R. Clinical, Anatomical, and Pathological Features in the Three Variants of Primary Progressive Aphasia: A Review. *Frontiers in Neurology*. 2018;9. doi: 10.3389/fneur.2018.00692
29. Bergeron D, Gorno-Tempini ML, Rabinovici GD, et al. Prevalence of amyloid- β pathology in distinct variants of primary progressive aphasia. *Annals of Neurology*. 2018;84(5):729–740. doi: 10.1002/ana.25333
30. Preiß D, Billette OV, Schneider A, et al. The atrophy pattern in Alzheimer-related PPA is more widespread than that of the frontotemporal lobar degeneration associated variants. *NeuroImage: Clinical*. 2019;24:101994. doi: 10.1016/j.nicl.2019.101994

СПИСОК ЛИТЕРАТУРЫ

1. Gorno-Tempini M.L., Hillis A.E., Weintraub S., et al. Classification of primary progressive aphasia and its variants // *Neurology*. 2011. Vol. 76, N 11. P. 1006–1014. doi: 10.1212/WNL.0b013e31821103e6
2. Bisenius S., Neumann J., Schroeter M.L. Validating new diagnostic imaging criteria for primary progressive aphasia via anatomical likelihood estimation meta-analyses // *European Journal of Neurology*. 2016. Vol. 23, N 4. P. 704–712. doi: 10.1111/ene.12902
3. Lombardi J., Mayer B., Semler E., et al. Quantifying progression in primary progressive aphasia with structural neuroimaging // *Alzheimer's & Dementia*. 2021. Vol. 17, N 10. P. 1595–1609. doi: 10.1002/alz.12323

4. Chapman C.A., Polyakova M., Mueller K., et al. Structural correlates of language processing in primary progressive aphasia // *Brain Communications*. 2023. Vol. 5, N 2. doi: 10.1093/braincomms/fcad076
5. Canu E., Agosta F., Battistella G., et al. Speech production differences in English and Italian speakers with nonfluent variant PPA // *Neurology*. 2020. Vol. 94, N 10. P. e1062–e1072. doi: 10.1212/WNL.0000000000008879
6. Akhmadullina D., Kononov R., Shpilyukova Y., et al. Brain atrophy patterns in patients with frontotemporal dementia: voxel-based morphometry // *Bulletin of Russian State Medical University*. 2020. N 6. P. 84–89. doi: 10.24075/brsmu.2020.075
7. Lampe L., Huppertz H.J., Anderl-Straub S., et al. Multiclass prediction of different dementia syndromes based on multi-centric volumetric MRI imaging // *NeuroImage: Clinical*. 2023. Vol. 37. P. 103320. doi: 10.1016/j.nicl.2023.103320
8. Staffaroni A.M., Ljubenkov P.A., Kornak J., et al. Longitudinal multimodal imaging and clinical endpoints for frontotemporal dementia clinical trials // *Brain*. 2019. Vol. 142, N 2. P. 443–459. doi: 10.1093/brain/awy319
9. zenodo.org [Internet]. spunt/bspmview: BSPMVIEW v.20161108 (Version 20161108). Zenodo. [дата обращения: 26.07.2023]. Доступ по ссылке: <https://zenodo.org/badge/latestdoi/21612/spunt/bspmview> doi: 10.5281/zenodo.168074
10. Gorno-Tempini M.L., Dronkers N.F., Rankin K.P., et al. Cognition and anatomy in three variants of primary progressive aphasia // *Annals of Neurology*. 2004. Vol. 55, N 3. P. 335–346. doi: 10.1002/ana.10825
11. Tetzloff K.A., Utianski R.L., Duffy J.R., et al. Quantitative analysis of agrammatism in agrammatic primary progressive aphasia and dominant apraxia of speech // *Journal of Speech, Language, and Hearing Research*. 2018. Vol. 61, N 9. P. 2337–2346. doi: 10.1044/2018_JSLHR-L-17-0474
12. Whitwell J.L., Duffy J.R., Strand E.A., et al. Distinct regional anatomic and functional correlates of neurodegenerative apraxia of speech and aphasia: An MRI and FDG-PET study // *Brain and Language*. 2013. Vol. 125, N 3. P. 245–252. doi: 10.1016/j.bandl.2013.02.005
13. Mandelli M.L., Vitali P., Santos M., et al. Two insular regions are differentially involved in behavioral variant FTD and nonfluent/agrammatic variant PPA // *Cortex*. 2016. Vol. 74. P. 149–157. doi: 10.1016/j.cortex.2015.10.012
14. Cordella C., Quimby M., Touroutoglou A., et al. Quantification of motor speech impairment and its anatomic basis in primary progressive aphasia // *Neurology*. 2019. Vol. 92, N 17. P. e1992–e2004. doi: 10.1212/WNL.0000000000007367
15. Breining B.L., Faria A.V., Tippett D.C., et al. Association of Regional Atrophy With Naming Decline in Primary Progressive Aphasia // *Neurology*. 2023. Vol. 100, N 6. P. e582–e594. doi: 10.1212/WNL.00000000000201491
16. Rogalski E., Cobia D., Harrison T.M., et al. Progression of language decline and cortical atrophy in subtypes of primary progressive aphasia // *Neurology*. 2011. Vol. 76, N 21. P. 1804–1810. doi: 10.1212/WNL.0b013e31821ccd3c
17. Samra K., MacDougall A.M., Bouzigues A., et al. Genetic forms of primary progressive aphasia within the GENetic Frontotemporal dementia Initiative (GENFI) cohort: comparison with sporadic primary progressive aphasia // *Brain Communications*. 2023. Vol. 5, N 2. doi: 10.1093/braincomms/fcad036
18. Rohrer J.D., Nicholas J.M., Cash D.M., et al. Presymptomatic cognitive and neuroanatomical changes in genetic frontotemporal dementia in the Genetic Frontotemporal dementia Initiative (GENFI) study: a cross-sectional analysis // *The Lancet Neurology*. 2015. Vol. 14, N 3. P. 253–262. doi: 10.1016/S1474-4422(14)70324-2
19. McKenna M.C., Li Hi Shing S., Murad A., et al. Focal thalamus pathology in frontotemporal dementia: Phenotype-associated thalamic profiles // *Journal of the Neurological Sciences*. 2022. Vol. 436. P. 120221. doi:10.1016/j.jns.2022.120221
20. Ziegler W., Ackermann H. Subcortical Contributions to Motor Speech: Phylogenetic, Developmental, Clinical // *Trends in Neurosciences*. 2017. Vol. 40, N 8. P. 458–468. doi: 10.1016/j.tins.2017.06.005
21. Migliaccio R., Boutet C., Valabregue R., et al. The Brain Network of Naming: A Lesson from Primary Progressive Aphasia // *PLOS ONE*. 2016. Vol. 11, N 2. P. e0148707. doi: 10.1371/journal.pone.0148707
22. Wisse L.E.M., Ungrady M.B., Ittyerah R., et al. Cross-sectional and longitudinal medial temporal lobe subregional atrophy patterns in semantic variant primary progressive aphasia // *Neurobiology of Aging*. 2021. Vol. 98. P. 231–241. doi: 10.1016/j.neurobiolaging.2020.11.012
23. Fittipaldi S., Ibanez A., Baez S., et al. More than words: Social cognition across variants of primary progressive aphasia // *Neuroscience & Biobehavioral Reviews*. 2019. Vol. 100. P. 263–284. doi: 10.1016/j.neubiorev.2019.02.020
24. Brown J.A., Deng J., Neuhaus J., et al. Patient-Tailored, Connectivity-Based Forecasts of Spreading Brain Atrophy // *Neuron*. 2019. Vol. 104, N 5. P. 856–868.e5. doi: 10.1016/j.neuron.2019.08.037
25. Collins J.A., Montal V., Hochberg D., et al. Focal temporal pole atrophy and network degeneration in semantic variant primary progressive aphasia // *Brain*. 2017. Vol. 140, N 2. P. 457–471. doi: 10.1093/brain/aww313
26. Kumfor F., Landin-Romero R., Devenney E., et al. On the right side? A longitudinal study of left- versus right-lateralized semantic dementia // *Brain*. 2016. Vol. 139, N 3. P. 986–998. doi: 10.1093/brain/aww387
27. Henry M.L., Wilson S.M., Babiak M.C., et al. Phonological Processing in Primary Progressive Aphasia // *Journal of Cognitive Neuroscience*. 2016. Vol. 28, N 2. P. 210–222. doi: 10.1162/jocn_a_00901
28. Montembeault M., Brambati S.M., Gorno-Tempini M.L., Migliaccio R. Clinical, Anatomical, and Pathological Features in the Three Variants of Primary Progressive Aphasia: A Review // *Frontiers in Neurology*. 2018. Vol. 9. doi: 10.3389/fneur.2018.00692
29. Bergeron D., Gorno-Tempini M.L., Rabinovici G.D., et al. Prevalence of amyloid- β pathology in distinct variants of primary progressive aphasia // *Annals of Neurology*. 2018. Vol. 84, N 5. P. 729–740. doi: 10.1002/ana.25333
30. Preiß D., Billette O.V., Schneider A., et al. The atrophy pattern in Alzheimer-related PPA is more widespread than that of the frontotemporal lobar degeneration associated variants // *NeuroImage: Clinical*. 2019. Vol. 24. P. 101994. doi: 10.1016/j.nicl.2019.101994

AUTHORS' INFO

*** Diliara R. Akhmadullina**, MD;
address: 80 Volokolamskoje shosse, 125367,
Moscow, Russian Federation;
ORCID: 0000-0001-6491-2891;
eLibrary SPIN: 5721-8567;
e-mail: akhmadullinadr1@gmail.com

Rodion N. Konovalov, MD, Cand. Sci. (Med.);
ORCID: 0000-0001-5539-245X;
eLibrary SPIN: 2515-7673;
e-mail: krn_74@mail.ru

Yulia A. Shpilyukova, MD, Cand. Sci. (Med.);
ORCID: 0000-0001-7214-583X;
eLibrary SPIN: 7502-8984;
e-mail: jshpilyukova@gmail.com

Ekaterina Yu. Fedotova, MD, Dr. Sci. (Med.);
ORCID: 0000-0001-8070-7644;
eLibrary SPIN: 3466-2212;
e-mail: ekfedotova@gmail.com

ОБ АВТОРАХ

*** Ахмадуллина Диляра Робертовна**;
адрес: Россия, 125367, Москва,
Волоколамское шоссе, д. 80;
ORCID: 0000-0001-6491-2891;
eLibrary SPIN: 5721-8567;
e-mail: akhmadullinadr1@gmail.com

Коновалов Родион Николаевич, канд. мед. наук;
ORCID: 0000-0001-5539-245X;
eLibrary SPIN: 2515-7673;
e-mail: krn_74@mail.ru

Шпилюкова Юлия Александровна, канд. мед. наук;
ORCID: 0000-0001-7214-583X;
eLibrary SPIN: 7502-8984;
e-mail: jshpilyukova@gmail.com

Федотова Екатерина Юрьевна, д-р мед. наук;
ORCID: 0000-0001-8070-7644;
eLibrary SPIN: 3466-2212;
e-mail: ekfedotova@gmail.com

* Corresponding author / Автор, ответственный за переписку

DOI: <https://doi.org/10.17816/DD545997>

Определение методом дельфийского консенсуса списка оцениваемых с помощью опросников параметров при наблюдении пациентов с воспалительными заболеваниями кишечника

Ю.Ф. Шумская¹, Д.А. Ахмедзянова¹, М.Г. Мнацаканян², К.Ю. Колосова², О.В. Тащян², М.В. Юраж², Р.В. Решетников¹

¹ Научно-практический клинический центр диагностики и телемедицинских технологий, Москва, Российская Федерация;

² Первый Московский государственный медицинский университет имени И.М. Сеченова, Москва, Российская Федерация

АННОТАЦИЯ

Обоснование. Пациенты с воспалительными заболеваниями кишечника часто нуждаются в пожизненном наблюдении врача. Перспективным направлением таких услуг здравоохранения является телемедицинское наблюдение, часто основывающееся на оценке медицинским работником результатов удалённого анкетирования пациентов.

Цель. Используя дельфийский метод, определить список оцениваемых с помощью анкетирования параметров для последующего применения в наблюдении и лечении пациентов с воспалительными заболеваниями кишечника.

Материалы и методы. Экспертную группу участников исследования составили врачи-гастроэнтерологи с различным опытом работы. Для сбора информации была создана электронная форма опроса, при заполнении которой обязательно указывался стаж участника. Исследование состояло из трёх этапов. На первом этапе респонденты отвечали на открытый вопрос о том, какие параметры, оцениваемые с помощью опросников, необходимо мониторировать у пациентов с воспалительными заболеваниями кишечника. На втором этапе участники отвечали на тот же вопрос, выбирая пункты из предложенных, без ограничений по количеству. Третьим этапом исследования выполнен анализ полученных ответов. Первичной конечной точкой считалось достижение по каждому параметру консенсуса более чем 75% респондентов.

Результаты. В исследовании приняли участие 15 человек, из них 13,3% — мужчины. Из всех респондентов, 46% работают в амбулаторно-поликлинических организациях, 54% — в стационаре. Возрастной диапазон составил от 25 до 53 лет, при этом 53% участников имели стаж от 1 до 4 лет, 47% — от 17 до 29 лет. По результатам первого этапа ни один из параметров не достиг уровня согласия 75%. После второго этапа респонденты достигли согласия по 72% параметров. Связи между возрастом, полом, стажем респондентов, а также местом их работы и ответами как на первом, так и на втором этапах обнаружено не было.

Заключение. В итоговый список параметров, рекомендуемых для оценки во время лечения и наблюдения пациентов с ВЗК, вошли: боль в животе; частота дефекации и качество стула; наличие патологических примесей в кале; температура тела; боли в суставах/мышцах; качество сна; эмоциональное состояние: тревожность, настроение; трудоспособность для работающих/возможность посещать занятия для обучающихся; энергичность, количество сил; фиксированность на заболевании; общая оценка пациентом качества своей жизни; приверженность лечению.

Ключевые слова: дельфийский метод; качество жизни; оценка трудоспособности; приверженность к приёму лекарственных препаратов; воспалительные заболевания кишечника.

Как цитировать:

Шумская Ю.Ф., Ахмедзянова Д.А., Мнацаканян М.Г., Колосова К.Ю., Тащян О.В., Юраж М.В., Решетников Р.В. Определение методом дельфийского консенсуса списка оцениваемых с помощью опросников параметров при наблюдении пациентов с воспалительными заболеваниями кишечника // Digital Diagnostics. 2023. Т. 4, № 4. С. 481–491. DOI: <https://doi.org/10.17816/DD545997>

doi: <https://doi.org/10.17816/DD545997>

Delphi method to determine a list of questionnaire-assessed parameters in the follow-up of patients with inflammatory bowel disease

Yuliya F. Shumskaya¹, Dina A. Akhmedzyanova¹, Marina G. Mnatsakanyan², Ksenia Yu. Kolosova², Olga V. Tashchyan², Marta V. Yurazh², Roman V. Reshetnikov¹

¹ Research and Practical Clinical Center for Diagnostics and Telemedicine Technologies, Moscow, Russian Federation;

² The First Sechenov Moscow State Medical University, Moscow, Russian Federation

ABSTRACT

BACKGROUND: Patients with inflammatory bowel disease often require lifelong follow-up by a clinician. Telemedicine monitoring is a promising area of such healthcare services, often based on the evaluation of patients' remote questionnaire results by a medical practitioner.

AIM: To define, using the Delphi method, a list of questionnaire-assessed parameters for monitoring and treating patients with IBD.

MATERIALS AND METHODS: The study was conducted in three stages. An electronic survey form was created to collect information, ensuring that the respondent's experience was included when completing the survey. In the first stage, respondents answered an open-ended question about what parameters assessed by questionnaires should be monitored in patients with IBD. In the second stage, participants answered the same question but selected any number of items from a list. In the third stage, the responses were analyzed. The primary endpoint was a consensus on each parameter, defined as >75% respondent agreement.

RESULTS: The study had 15 participants, 13.3% of whom were male. Of all respondents, 46% worked in an outpatient setting, whereas 54% worked in an inpatient setting. Their ages ranged from 25 to 53 years, with 53% of the participants having 1–4 years of experience and 47% having 17–29 years of experience. None of the parameters reached a 75% agreement level based on the results of the first stage. In the second stage, respondents reached a consensus on 72% of the parameters. No relationship was found between respondents' age, sex, years of experience, or job settings and responses in the first and second stages.

CONCLUSIONS: The final list of parameters recommended for evaluation during the monitoring and treatment of patients with IBD included abdominal pain, frequency of defecation and stool quality, presence of pathological stool impurities, body temperature, joint/muscle pain, sleep quality, anxiety, depression, work capacity for employed/ability to attend lessons for students, energy and quantity of vigor, fixation on the disease, patients' general evaluation of their quality of life, and treatment adherence.

Keywords: Delphi method; quality of life; disability evaluation; medication adherence; inflammatory bowel diseases.

To cite this article:

Shumskaya YuF, Akhmedzyanova DA, Mnatsakanyan MG, Kolosova KYu, Tashchyan OV, Yurazh MV, Reshetnikov RV. Delphi method to determine a list of questionnaire-assessed parameters in the follow-up of patients with inflammatory bowel disease. *Digital Diagnostics*. 2023;4(4):481–491. DOI: <https://doi.org/10.17816/DD545997>

Received: 11.07.2023

Accepted: 31.08.2023

Published online: 14.09.2023

doi: <https://doi.org/10.17816/DD545997>

在对炎症性肠病患者进行随访时采用德尔菲法确定一份通过问卷评估的参数清单

Yuliya F. Shumskaya¹, Dina A. Akhmedzyanova¹, Marina G. Mnatsakanyan²,
Ksenia Yu. Kolosova², Olga V. Tashchyan², Marta V. Yurazh², Roman V. Reshetnikov¹

¹ Research and Practical Clinical Center for Diagnostics and Telemedicine Technologies, Moscow, Russian Federation;

² The First Sechenov Moscow State Medical University, Moscow, Russian Federation

简评

论证。炎症性肠病患者通常需要医生的终生随访。远程随访是提供此类医疗服务的一个很有前途的途径。远程随访通常基于医疗服务提供者对远程患者问卷调查结果的评估。

该研究的目的是采用德尔菲法，确定一份通过问卷评估的参数清单，以便日后应用于炎症性肠病患者的随访和治疗。

材料和方法。参与研究的专家组由具有不同工作经验的消化内科医生组成。我们制作了一份电子调查表来收集信息。在填写问卷时，必须注明参与者的工作年限。研究分为三个阶段。在第一阶段，受访者回答了一个开放式问题，即应该对炎症性肠病患者的哪些参数进行评估。在第二阶段，受访者回答了同样的问题。但在这一阶段，他们从建议的项目中选择项目，项目数量不限。研究的第三阶段是对回答进行分析。每个参数的主要终点是75%以上的受访者达成共识。

结果。15人参与了研究，其中13.3%为男性。在所有受访者中，46%在门诊机构工作，54%在医院工作。年龄范围为25岁至53岁之间。同时，53%的参与者拥有1至4年的工作经验，47%的参与者拥有17至29年的工作经验。在第一阶段结束时，没有一个参数达到75%的同意程度。第二阶段结束后，受访者对72%的参数达成了一致意见。在第一阶段和第二阶段，受访者的年龄、性别、工作年限和工作地点与答复之间都未发现相关性。

结论。炎症性肠病患者治疗和随访期间的最终评估参数清单包括：腹痛；排便次数和粪便质量；粪便中是否有病理性杂质；体温；关节/肌肉疼痛；睡眠质量；情绪状态：焦虑、情绪；工作的人的工作能力/学习的人的上课能力；精力、体力；对疾病的固执；患者对其生活质量的总体评价；坚持治疗的情况。

关键词：德尔菲法；生活质量；工作能力评估；坚持用药的情况；炎症性肠病。

引用本文：

Shumskaya YuF, Akhmedzyanova DA, Mnatsakanyan MG, Kolosova KYu, Tashchyan OV, Yurazh MV, Reshetnikov RV. 在对炎症性肠病患者进行随访时采用德尔菲法确定一份通过问卷评估的参数清单. *Digital Diagnostics*. 2023;4(4):481–491. DOI: <https://doi.org/10.17816/DD545997>

收到: 11.07.2023

接受: 31.08.2023

发布日期: 14.09.2023

BACKGROUND

Inflammatory bowel diseases (IBDs), particularly ulcerative colitis and Crohn's disease, are major public health concerns because of their severity, comorbidities, and high treatment costs. IBDs frequently affect not only health but also quality of life, deteriorating patients' physical and mental well-being and limiting their social capabilities [1]. The incidence of IBD is steadily increasing both globally [2] and in Russia [3], with 55.4% of patients with ulcerative colitis and 48.5% of patients with Crohn's disease were 21 to 40 years old [4]. Because of the recurring nature of IBD, most patients require lifelong monitoring; however, no unified protocol has been established for the outpatient management of these patients during remission.

Telemedicine is a promising approach to the outpatient management of patients with IBD. Patients under remote follow-up have a significantly better quality of life and seek medical attention less frequently than patients receiving standard treatment [5]. However, with remote follow-up, the question of what must be assessed arises.

The assessment of critical laboratory parameters such as C-reactive protein and fecal calprotectin is undeniably important. However, in addition to IBD activity parameters, other factors are crucial for quality of life, such as psychological status, which are not assessed in routine practice.

Questionnaires are a convenient and relevant method for assessing a patient's condition. They provide the clinician with the necessary information, such as the clinical activity of IBD or compliance, without requiring high costs or time commitments. Most studies have assessed disease activity and associated quality of life; however, other studies have less frequently assessed the overall quality of life, depression severity, adherence to drug therapy, and patient satisfaction with medical care [5]. Moreover, few studies have assessed visceral sensitivity [6] and the effect of the disease on work productivity [7, 8] and sexual activity [9] in patients with IBD. In addition, researchers did not explain why they chose specific endpoints. As a result, the lack of consensus on the parameters assessed by questionnaires prevents their standardized use managing patients with IBD.

PURPOSE

This study aimed to use the Delphi method to assess the expert opinions of gastroenterologists to determine a list of questionnaire-assessed parameters in the follow-up of patients with IBD.

MATERIALS AND METHODS

Between May and June 2023, gastroenterologists treating IBD were invited to participate in a survey to achieve a consensus on the inclusion/exclusion of various parameters in patient assessment during treatment and follow-up.

The Delphi method was used to obtain a collective opinion with reasonable level of validity and reliability and explore areas outside existing knowledge [10]. Before the study commenced, a literature review on the use of questionnaires in the assessment of patients with IBD was performed. Following the literature review, the areas assessed by Russian and foreign authors were determined (Table 1).

Participants were chosen at random by convenience sampling. No consensus on the sample size for studies using the Delphi method, guidelines, or a clear definition of a "small" or "large" sample was reached [11, 12]. In this study, the sample size was determined according to R.B. Akins et al., who demonstrated that the results of the Delphi method in a group of experts in the studied area are stable with 15–23 participants [13].

The study included three stages. Information was collected using an electronic survey form using Yandex Forms.

Stage I

To participate in the survey, all participants had to specify their work experience as a gastroenterologist. In stage I, all participants answered the following open-ended questions:

"What aspects of life and health, in your opinion, should be assessed in a patient with inflammatory bowel disease, both during treatment of an attack and during follow-up in remission?"

Respondents could proceed to the next stage of the survey after filling out the answer field. Stage I answers were stratified into four:

- Clinical activity assessment
- Psychological status assessment
- Quality of life assessment
- Others

Stage II

In stage II, the participants had to select items from the list. The question was as follows:

"Select the items from the list below that you believe are crucial to assess in a patient with inflammatory bowel disease, both during treatment of an attack and during follow-up in remission."

The possible answers presented in Table 1 were derived from a literature review using PubMed. Original studies and systematic reviews that assessed the efficacy of treatment in patients with IBD were analyzed, and the endpoints of these studies were identified. No restrictions were set on the number of the selected items.

Upon completion of stage II, the survey participants were invited to optionally supplement their answers to stage I question (without showing respondents the text of their previous answers).

Stage III

In stage III, the responses were analyzed. The primary endpoint was the consensus on the inclusion of patient assessment parameters in the final list. The consensus on a

Table 1. Response options for multiple-choice questions in the second stage of the survey

Area	Proposed parameter
Clinical activity of the disease	Abdominal pain
	Defecation frequency and stool form
	Pathological admixtures in the feces
	Body temperature
Psychological status	Joint/muscle pain
	Emotional state: anxiety
	Emotional state: mood
	Sleep quality
Quality of life	Body image perception (negative/positive)
	Patient global assessment of quality of life
	Quality of communication
	Quality of sexual life
Others	Ability to work/study
	Anxious attitude toward the disease
	Visceral sensitivity
	Energy level
	Patient satisfaction with medical care

specific parameter was reached when >75% of respondents choose the parameter [14].

The software and language R 4.2.0 were used for data analysis. The Shapiro–Wilk test was employed to check the normality of the distribution. Variables with normal distribution are presented as mean \pm standard deviation. Variables with non-normal distribution are presented as median and interquartile range. The correlation between variables was assessed by calculating Spearman's or Pearson's rank correlation coefficient, depending on the type of distribution.

After the study, the respondents were interviewed, using the following questions:

- Which was easier to answer: an open-ended question or a multiple-choice question?
- Why do you think some items did not receive enough votes? (This question included items that received <75% of the votes)

RESULTS

The study included 15 respondents, 13.3% of whom were men. The mean age of the participants was 36.6 ± 9.9 years, ranging from 25 to 53 years. Outpatient physicians accounted for 46% of all respondents, whereas hospital physicians accounted for 54%. None of the respondents withdrew from the study. The distribution of participants according to work experience is presented in Fig. 1.

According to the results of stage I, in which study participants must answer an open-ended question, no obvious overlaps were found in the answers because of the free format. After categorizing the answers, none of the categories attained the level of agreement (Fig. 2).

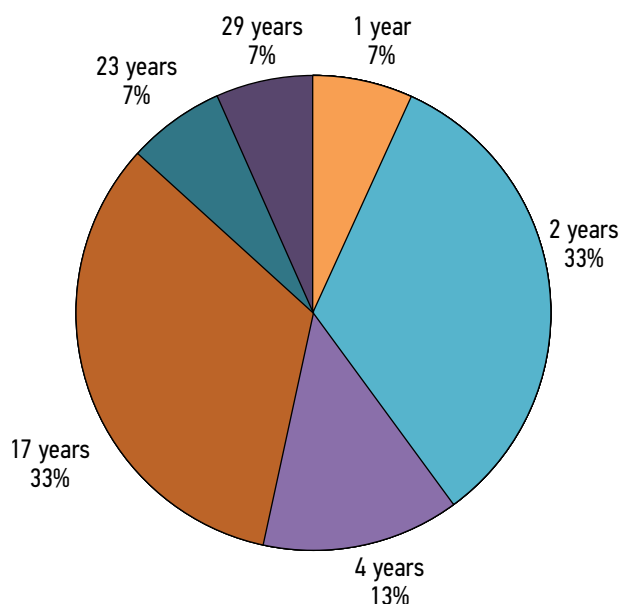


Fig. 1. Distribution of the study participants according to their work experience as gastroenterologists.

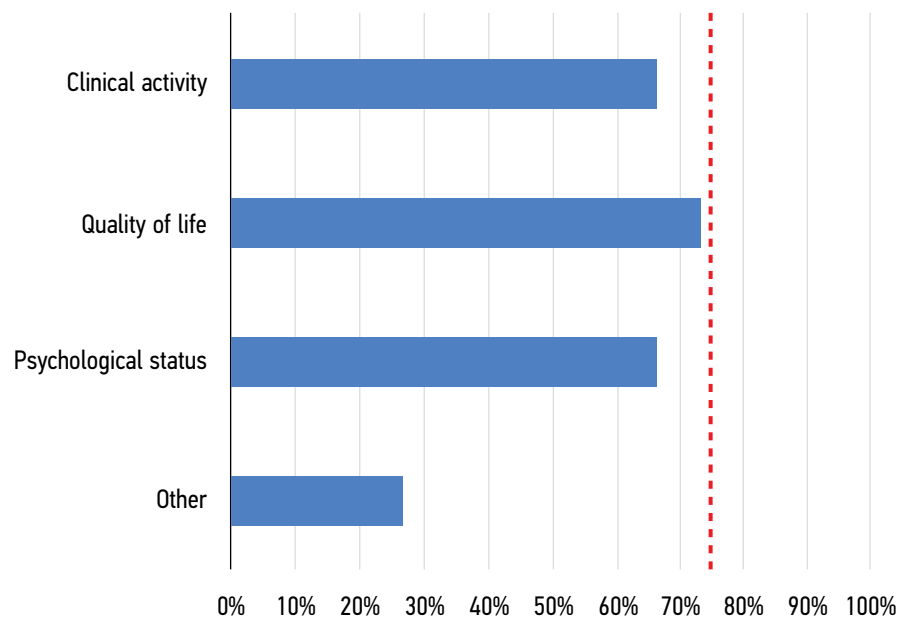


Fig. 2. Study results (first stage). The red dotted line indicates 75% of the respondents.

Based on the results of stage I, the “compliance” parameter was added to the possible answers in stage II (in addition to the items listed in Table 1). The results of stage II differed from those of stage I for each respondent: the number of questionnaire-assessed parameters (median number of parameters, 4 [3; 5.5] and 16 [13.5; 17] for stages I and II, respectively) increased.

In the correlation analysis, no link was found between the age, sex, work experience, and place of work (outpatient clinic/hospital) of respondents and their answers during stages I and II.

Participants were interviewed after receiving the results of stage II. Compared with answering a multiple-choice question, answering an open-ended question was more challenging for 100% of the respondents. In total, 27% of the participants responded when asked why some items did not receive enough votes. Each of them emphasized that the quality of sexual life and communication in patients with IBD is frequently influenced by factors other than the disease. According to the respondents, body image perception is unrelated to the disease and does not warrant assessment by a gastroenterologist. Respondents also did not believe that satisfaction with medical care was a parameter that clinicians should monitor in all patients with IBD. Regarding visceral sensitivity, respondents agreed on the importance of assessing this parameter in some patients whose symptoms cannot be explained solely by the clinical course of IBD and who may benefit from the addition of a functional component.

DISCUSSION

The study generated a final list of parameters recommended for assessment during the treatment and follow-up of patients with IBD, which included the following:

- Abdominal pain
- Defecation frequency and stool form
- Pathological admixtures in the feces
- Body temperature
- Joint/muscle pain
- Sleep quality
- Emotional state: anxiety
- Emotional state: mood
- Ability to work/study
- Energy level
- Anxious attitude toward the disease
- Patient global assessment of quality of life
- Compliance

This list was compiled after a two-stage survey of gastroenterologists. Two approaches were used to collect information in this study: an open-ended question and a multiple-choice question. In the first scenario, no consensus could be reached on any of the categories; however, in the second scenario, respondents agreed on 72% of the parameters. This could be due to the simplicity of stage II: during the interview, respondents stated that answering a multiple-choice question was easier and more convenient for them.

Furthermore, no correlation was found between the characteristics of the survey participants, such as sex, age, work experience, and place of work (outpatient clinic or hospital), and their answers during stages I and II.

Our findings support the use of the Delphi method, which offers equal opportunities to survey participants and allows for the concealment of expertise and skill level to prevent the authority pressure that is unavoidable in face-to-face discussions. In this study, clinicians with minimal experience had the same perceptions of follow-up strategies as their more experienced colleagues. There may be other scenarios

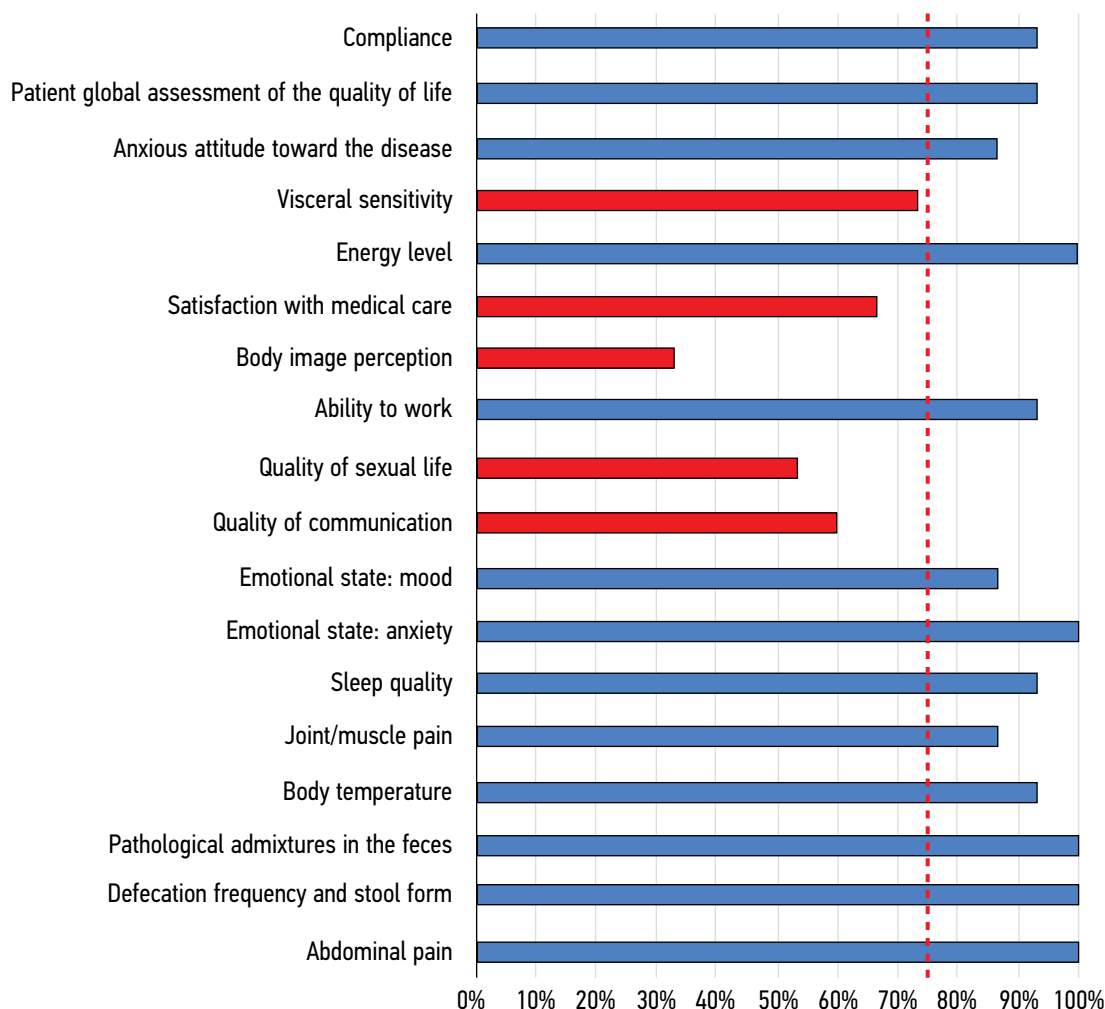


Fig. 3. Study results (second stage). The red columns indicate parameters that received <75% of the responses.

in which the consensus is not as strong; in such cases, a fresh look at the topic under discussion by young specialists may lead to a more objective decision.

According to foreign literature, health-related quality of life, disability/ability to work, and disease activity are the key questionnaire-assessed parameters in patients with IBD [15]. In this study, these areas were also included in the final list. The first five parameters selected by the participants (abdominal pain, defecation frequency and stool form, pathological admixtures in feces, body temperature, and joint/muscle pain) are related to assessing the clinical activity of IBD. The ability to work/study and patient global assessment of quality of life were also selected by >90% of the respondents.

Furthermore, the final list included parameters that assessed the emotional state, such as sleep quality, anxiety, and mood. Given the high incidence of anxiety and depression symptoms in patients with IBD [16], assessing these parameters will surely provide valuable information to researchers and clinicians.

Assessing energy levels in patients with IBD is also critical, given the subjective and complex nature of asthenic

syndrome in these patients [17]. We believe that this parameter must be used by clinicians and researchers, depending on the clinical setting or study endpoints.

Compliance assessment in patients with IBD is also important, given the often lifelong drug therapy, including immunosuppressants. Because compliance is one of the treatment goals [18], its assessment is critical for clinicians and researchers.

In a systematic review, Pang et al. used disease-related quality of life, inflammation activity, and remission rate as primary endpoints. Secondary endpoints included overall quality of life, depression, compliance, and satisfaction with medical care [5]. However, the researchers did not explain why these specific parameters were selected as outcomes. Our study presents a consensus list of questionnaire-assessed parameters in the follow-up of patients with IBD.

Advantages and limitations

Clinicians from various backgrounds were invited to participate in the study, which has advantages and disadvantages. Analysis of a large proportion of young participants brings a fresh viewpoint; however, these

participants have limited practical experience. Participation of both outpatient and inpatient care workers allows for a wider range of perspectives.

Further studies

A larger-scale survey with more gastroenterologists from various Russian regions appears to be a logical and necessary extension of this study. Professionals discussing scientific challenges together allow us to address current issues and propose new solutions [19]. Guidelines detailing a pool of questionnaires in areas determined by consensus will be developed as part of the practical implementation of the study findings.

ADDITIONAL INFORMATION

Funding source. This article was prepared by the authors as a part of the research and development effort titled "Scientific evidence for using telemedicine-based models and methods

for organization and delivery of medical care" (Russian United scientific information system No. 123031400008-4) in accordance with the order of the Moscow Healthcare Department No. 1196 dated December 21, 2022 "On approval of state assignments funded by means of allocations from the budget of the city of Moscow to the state budgetary (autonomous) institutions subordinate to the Moscow Healthcare Department, for 2023 and the planned period of 2024 and 2025".

Competing interests. The authors declare that they have no competing interests.

Authors' contribution. All authors made a substantial contribution to the conception of the work, acquisition, analysis, interpretation of data for the work, drafting and revising the work, final approval of the version to be published and agree to be accountable for all aspects of the work. Yu.F. Shumskaya, D.A. Akhmedzynova, K.Yu. Kolosova, M.V. Yurazh — writing the original draft; Yu.F. Shumskaya, O.V. Tashchyan — data curation, investigation; M.G. Mnatsakanyan, R.V. Reshetnikov, Yu.F. Shumskaya — conceptualization, study design; Yu.F. Shumskaya, R.V. Reshetnikov — data curation.

REFERENCES

- Romberg-Camps MJL, Bol Y, Dagnelie PC, et al. Fatigue and health-related quality of life in inflammatory bowel disease. *Inflammatory Bowel Diseases*. 2010;16(12):2137–2147. doi: 10.1002/ibd.21285
- Windsor JW, Kaplan GG. Evolving Epidemiology of IBD. *Current Gastroenterology Reports*. 2019;21(8). doi: 10.1007/s11894-019-0705-6
- Khalif IL, Shapina MV. Inflammatory bowel disease treatment in Eastern Europe. *Current Opinion in Gastroenterology*. 2017;33(4):230–233. doi: 10.1097/mog.0000000000000370
- Belousova EA, Shelygin YuA, Achkasov SI, et al. Clinical and Demographic Features and Treatment Approaches for Inflammatory Bowel Diseases (Crohn's Disease, Ulcerative Colitis) in the Russia. The Primery Results of the Analysis of the National Register. *Koloproktologia*. 2023;22(1):65–82. (In Russ) doi: 10.33878/2073-7556-2023-22-1-65-82
- Pang L, Liu H, Liu Zh, et al. Role of Telemedicine in Inflammatory Bowel Disease: Systematic Review and Meta-analysis of Randomized Controlled Trials. *Journal of Medical Internet Research*. 2022;24(3):e28978. doi: 10.2196/28978
- Trieschmann K, Chang L, Park S, et al. The visceral sensitivity index: A novel tool for measuring GI-symptom-specific anxiety in inflammatory bowel disease. *Neurogastroenterology & Motility*. 2022;34(9). doi: 10.1111/nmo.14384
- Jackson BD, Con D, Gorelik A, et al. Examination of the relationship between disease activity and patient-reported outcome measures in an inflammatory bowel disease cohort. *Internal Medicine Journal*. 2018;48(10):1234–1241. doi: 10.1111/imj.13937
- Thomas PWA, Broeder N, Derikx M, et al. Impact of Biological Therapies and Tofacitinib on Real-world Work Impairment in Inflammatory Bowel Disease Patients: A Prospective Study. *Inflammatory Bowel Diseases*. 2022;28(12):1813–1820. doi: 10.1093/ibd/izac002
- Chen B, Zhou B, Song G, et al. Inflammatory bowel disease is associated with worse sexual function: a systematic review and meta-analysis. *Translational Andrology and Urology*. 2022;11(7):959–973. doi: 10.21037/tau-22-190
- Murphy MK, Black NA, Lamping DL, et al. Consensus development methods, and their use in clinical guideline development. *Health Technology Assessment*. 1998;2(3):I–IV. doi: 10.3310/hta2030
- Williams PL, Webb C. The Delphi technique: a methodological discussion. *Journal of Advanced Nursing*. 1994;19(1):180–186. doi: 10.1111/j.1365-2648.1994.tb01066.x
- Wilhelm W. Alchemy of the Oracle: the Delphi technique. *The Delta Pi Epsilon Journal*. 2001;43:6–26.
- Akins RB, Tolson H, Cole BR. Stability of response characteristics of a Delphi panel: application of bootstrap data expansion. *BMC Medical Research Methodology*. 2005;5(1). doi: 10.1186/1471-2288-5-37
- Diamond IR, Grant RC, Feldman BM, et al. Defining consensus: A systematic review recommends methodologic criteria for reporting of Delphi studies. *Journal of Clinical Epidemiology*. 2014;67(4):401–409. doi: 10.1016/j.jclinepi.2013.12.002
- Andel EM, Koopmann BDM, Crouwel F, et al. Systematic Review of Development and Content Validity of Patient-reported Outcome Measures in Inflammatory Bowel Disease: Do We Measure What We Measure? *Journal of Crohn's and Colitis*. 2020;14(9):1299–1315. doi: 10.1093/ecco-jcc/jjaa057
- Barberio B, Zamani M, Black CJ, et al. Prevalence of symptoms of anxiety and depression in patients with inflammatory bowel disease: a systematic review and meta-analysis. *The Lancet Gastroenterology & Hepatology*. 2021;6(5):359–370. doi: 10.1016/s2468-1253(21)00014-5
- Halpin SJ, Ford AC. Prevalence of Symptoms Meeting Criteria for Irritable Bowel Syndrome in Inflammatory Bowel Disease: Systematic Review and Meta-Analysis. *American Journal of Gastroenterology*. 2012;107(10):1474–1482. doi: 10.1038/ajg.2012.260

18. Yu N, Basnayake C, Connell W, et al. Interventions to Improve Adherence to Preventive Care in Inflammatory Bowel Disease: A Systematic Review. *Inflammatory Bowel Diseases*. 2022;28(8):1177–1188. doi: 10.1093/ibd/izab247

19. Vinogradova IA, Nizovtsova LA, Omelyanskaya OV. Innovative strategic session in the scientific activity of the Center for Diagnostics and Telemedicine. *Digital Diagnostics*. 2023;3(4):414–420. (In Russ) doi: 10.17816/DD111833

СПИСОК ЛИТЕРАТУРЫ

- Romberg-Camps M.J.L., Bol Y., Dagnelie P.C., et al. Fatigue and health-related quality of life in inflammatory bowel disease // *Inflammatory Bowel Diseases*. 2010. Vol. 16, N 12. P. 2137–2147. doi: 10.1002/ibd.21285
- Windsor J.W., Kaplan G.G. Evolving Epidemiology of IBD // *Current Gastroenterology Reports*. 2019. Vol. 21, N 8. doi: 10.1007/s11894-019-0705-6
- Khalif I.L., Shapina M.V. Inflammatory bowel disease treatment in Eastern Europe // *Current Opinion in Gastroenterology*. 2017. Vol. 33, N 4. P. 230–233. doi: 10.1097/mog.0000000000000370
- Белоусова Е.А., Шельгин Ю.А., Ачкасов С.И., и др. Клинико-демографические характеристики и лечебные подходы у пациентов с воспалительными заболеваниями кишечника (болезнь Крона, язвенный колит) в РФ. Первые результаты анализа национального Регистра // *Колопроктология*. 2023. Т. 22, № 1. С. 65–82. doi: 10.33878/2073-7556-2023-22-1-65-82
- Pang L., Liu H., Liu Zh., et al. Role of Telemedicine in Inflammatory Bowel Disease: Systematic Review and Meta-analysis of Randomized Controlled Trials // *Journal of Medical Internet Research*. 2022. Vol. 24, N 3. P. e28978. doi: 10.2196/28978
- Trieschmann K., Chang L., Park S., et al. The visceral sensitivity index: A novel tool for measuring GI-symptom-specific anxiety in inflammatory bowel disease // *Neurogastroenterology & Motility*. 2022. Vol. 34, N 9. doi: 10.1111/nmo.14384
- Jackson B.D., Con D., Gorelik A., et al. Examination of the relationship between disease activity and patient-reported outcome measures in an inflammatory bowel disease cohort // *Internal Medicine Journal*. 2018. Vol. 48, N 10. P. 1234–1241. doi: 10.1111/imj.13937
- Thomas P.W.A., Broeder N., Derikx M., et al. Impact of Biological Therapies and Tofacitinib on Real-world Work Impairment in Inflammatory Bowel Disease Patients: A Prospective Study // *Inflammatory Bowel Diseases*. 2022. Vol. 28, N 12. P. 1813–1820. doi: 10.1093/ibd/izac002
- Chen B., Zhou B., Song G., et al. Inflammatory bowel disease is associated with worse sexual function: a systematic review and meta-analysis // *Translational Andrology and Urology*. 2022. Vol. 11, N 7. P. 959–973. doi: 10.21037/tau-22-190
- Murphy M.K., Black N.A., Lamping D.L., et al. Consensus development methods, and their use in clinical guideline

- development // *Health Technol Assess*. 1998. Vol. 2, N 3. P. I–IV. doi: 10.3310/hta2030
- Williams P.L., Webb C. The Delphi technique: a methodological discussion // *Journal of Advanced Nursing*. 1994. Vol. 19, N 1. P. 180–186. doi: 10.1111/j.1365-2648.1994.tb01066.x
- Wilhelm W. Alchemy of the Oracle: the Delphi technique // *The Delta Pi Epsilon Journal*. 2001. Vol. 43. P. 6–26.
- Akins R.B., Tolson H., Cole B.R. Stability of response characteristics of a Delphi panel: application of bootstrap data expansion // *BMC Medical Research Methodology*. 2005. Vol. 5, N 1. doi: 10.1186/1471-2288-5-37
- Diamond I.R., Grant R.C., Feldman B.M., et al. Defining consensus: A systematic review recommends methodologic criteria for reporting of Delphi studies // *Journal of Clinical Epidemiology*. 2014. Vol. 67, N 4. P. 401–409. doi: 10.1016/j.jclinepi.2013.12.002
- Andel E.M., Koopmann B.D.M., Crouwel F., et al. Systematic Review of Development and Content Validity of Patient-reported Outcome Measures in Inflammatory Bowel Disease: Do We Measure What We Measure? // *Journal of Crohn's and Colitis*. 2020. Vol. 14, N 9. P. 1299–1315. doi: 10.1093/ecco-jcc/jjaa057
- Barberio B., Zamani M., Black C.J., et al. Prevalence of symptoms of anxiety and depression in patients with inflammatory bowel disease: a systematic review and meta-analysis // *The Lancet Gastroenterology & Hepatology*. 2021. Vol. 6, N 5. P. 359–370. doi: 10.1016/s2468-1253(21)00014-5
- Halpin S.J., Ford A.C. Prevalence of Symptoms Meeting Criteria for Irritable Bowel Syndrome in Inflammatory Bowel Disease: Systematic Review and Meta-Analysis // *American Journal of Gastroenterology*. 2012. Vol. 107, N 10. P. 1474–1482. doi: 10.1038/ajg.2012.260
- Yu N., Basnayake C., Connell W., et al. Interventions to Improve Adherence to Preventive Care in Inflammatory Bowel Disease: A Systematic Review // *Inflammatory Bowel Diseases*. 2022. Vol. 28, N 8. P. 1177–1188. doi: 10.1093/ibd/izab247
- Виноградова И.А., Низовцова Л.А., Омелянская О.В. Инновационная стратегическая сессия в научной деятельности Центра диагностики и телемедицины // *Digital Diagnostics*. 2023. Т. 3. № 4. С. 414–420. doi: 10.17816/DD111833

AUTHORS' INFO

* Yuliya F. Shumskaya;
address: 24/1 Petrovka street, 127051, Moscow, Russia;
ORCID: 0000-0002-8521-4045;
eLibrary SPIN: 3164-5518;
e-mail: shumskayayf@zdrav.mos.ru

ОБ АВТОРАХ

* Шумская Юлия Федоровна;
адрес: Россия, 127051, Москва, ул. Петровка, д.24, стр. 1;
ORCID: 0000-0002-8521-4045;
eLibrary SPIN: 3164-5518;
e-mail: shumskayayf@zdrav.mos.ru

* Corresponding author / Автор, ответственный за переписку

Dina A. Akhmedzyanova;

ORCID: 0000-0001-7705-9754;

eLibrary SPIN: 6983-5991;

e-mail: AkhmedzyanovaDA@zdrav.mos.ru

Marina G. Mnatsakanyan, MD, Dr. Sci. (Med.), Professor;

ORCID: 0000-0001-9337-7453;

eLibrary SPIN: 2015-1822;

e-mail: mnatsakanyan_m_g@staff.sechenov.ru

Ksenia Yu. Kolosova, MD, Cand. Sci. (Med.);

ORCID: 0000-0001-7641-2755;

e-mail: kolosova_k_yu@staff.sechenov.ru

Olga V. Tashchyan, MD, Cand. Sci. (Med.);

ORCID: 0000-0001-6759-6820;

e-mail: olgatash1@rambler.ru

Marta V. Yurazh, MD;

ORCID: 0000-0002-4459-7481;

eLibrary SPIN: 4872-7130;

e-mail: yurazh_m_v@staff.sechenov.ru

Roman V. Reshetnikov, Cand. Sci. (Phys.-Math.);

ORCID: 0000-0002-9661-0254;

eLibrary SPIN: 8592-0558;

e-mail: reshetnikov@fbb.msu.ru

Ахмедзянова Дина Альфредовна;

ORCID: 0000-0001-7705-9754;

eLibrary SPIN: 6983-5991;

e-mail: AkhmedzyanovaDA@zdrav.mos.ru

Мнацакян Марина Генриковна, д-р мед. наук, профессор;

ORCID: 0000-0001-9337-7453;

eLibrary SPIN: 2015-1822;

e-mail: mnatsakanyan_m_g@staff.sechenov.ru

Колосова Ксения Юрьевна, канд. мед. наук;

ORCID: 0000-0001-7641-2755;

e-mail: kolosova_k_yu@staff.sechenov.ru

Ташян Ольга Валерьевна, канд. мед. наук;

ORCID: 0000-0001-6759-6820;

e-mail: olgatash1@rambler.ru

Юраж Марта Валериевна;

ORCID: 0000-0002-4459-7481;

eLibrary SPIN: 4872-7130;

e-mail: yurazh_m_v@staff.sechenov.ru

Решетников Роман Владимирович, канд. физ.-мат. наук;

ORCID: 0000-0002-9661-0254;

eLibrary SPIN: 8592-0558;

e-mail: reshetnikov@fbb.msu.ru

DOI: <https://doi.org/10.17816/DD595696>

Виртуальная платформа для имитационного компьютерного моделирования радионуклидной визуализации в ядерной кардиологии. Сравнение с клиническими данными

Н.В. Денисова^{1,2}, М.А. Гурко^{1,2}, И.П. Колинко^{1,2}, А.А. Аншелес³, В.Б. Сергиенко³¹ Новосибирский государственный университет, Новосибирск, Российская Федерация;² Институт теоретической и прикладной механики имени С.А. Христиановича, Новосибирск, Российская Федерация;³ Национальный медицинский исследовательский центр кардиологии имени академика Е.И. Чазова, Москва, Российская Федерация

АННОТАЦИЯ

Обоснование. В области радионуклидной визуализации клинические исследования на людях *in vivo* ограничены из-за лучевой нагрузки и этических норм, поэтому всё возрастающее значение приобретают методы математического моделирования и имитационных компьютерных испытаний *in silico*, основанные на цифровых моделях. В англоязычной литературе этот подход получил название «Virtual clinical trials».

Цель — развитие программных средств для имитационного моделирования радионуклидной визуализации перфузии миокарда методом однофотонной эмиссионной компьютерной томографии, совмещённой с компьютерной томографией, с использованием радиофармацевтического препарата ^{99m}Tc-МИБИ, а также проведение исследований, направленных на повышение точности однофотонной эмиссионной компьютерной томографии.

Материалы и методы. Разработан программный комплекс «Виртуальная платформа для имитационных испытаний метода однофотонной эмиссионной компьютерной томографии, совмещённой с компьютерной томографией, в ядерной кардиологии» с использованием цифровых моделей пациента, сканера и оценки состояния миокарда с помощью цифровых изображений левого желудочка в виде «полярной карты». Выполнена верификация программного комплекса путём сравнения с клиническими данными, полученными в Национальном медицинском исследовательском центре кардиологии имени академика Е.И. Чазова (Москва). Проведены имитационные компьютерные испытания, в которых исследовалась точность оценки состояния миокарда в зависимости от подхода к нормализации полярной карты и учёта корректирующих факторов в алгоритме реконструкции.

Результаты. Результаты имитационных испытаний показали, что оценка перфузии миокарда левого желудочка существенно зависит от метода нормализации полярной карты и учёта корректирующих факторов в алгоритме реконструкции. Наиболее точные оценки были получены при расчёте коэффициента нормализации по усреднённому значению активности в нормальной зоне миокарда. Показано, что распространённый подход к нормализации по пикселю с максимальной интенсивностью может приводить к ошибкам. Результаты «виртуальных» испытаний полностью соответствовали клиническим наблюдениям.

Заключение. Переход от относительных нормализованных значений накопления активности в миокарде к абсолютным количественным оценкам может снять существующие ограничения и неопределённости и является главным условием повышения диагностической точности метода однофотонной эмиссионной компьютерной томографии, совмещённой с компьютерной томографией, в ядерной кардиологии.

Ключевые слова: однофотонная эмиссионная компьютерная томография, совмещённая с компьютерной томографией; ядерная кардиология; математический фантом; математическое моделирование.

Как цитировать:

Денисова Н.В., Гурко М.А., Колинко И.П., Аншелес А.А., Сергиенко В.Б. Виртуальная платформа для имитационного компьютерного моделирования радионуклидной визуализации в ядерной кардиологии. Сравнение с клиническими данными // Digital Diagnostics. 2023. Т. 4, № 4. С. 492–508. DOI: <https://doi.org/10.17816/DD595696>

DOI: <https://doi.org/10.17816/DD595696>

Virtual platform for computer simulation of radionuclide imaging in nuclear cardiology: Comparison with clinical data

Natalya V. Denisova^{1,2}, Mikhail A. Gurko^{1,2}, Inna P. Kolinko^{1,2}, Alexey A. Ansheles³, Vladimir B. Sergienko³

¹ Novosibirsk State University, Novosibirsk, Russian Federation;

² Khristianovich Institute of Theoretical and Applied Mechanics, Novosibirsk, Russian Federation;

³ National Medical Research Centre of Cardiology Named After Academician E.I. Chazov, Moscow, Russian Federation

ABSTRACT

BACKGROUND: In radionuclide imaging, in vivo human clinical studies are limited because of radiation exposure and ethical concerns; therefore, mathematical modeling and in silico computer simulations based on digital models are becoming increasingly important. In the English-language literature, this approach is called “virtual clinical trials.”

AIMS: This study aimed to develop software tools for the simulation of radionuclide visualization of myocardial perfusion by single-photon emission computed tomography combined with computed tomography using ^{99m}Tc-MIBI as the radiopharmaceutical and perform studies aimed at improving the accuracy of single-photon emission computed tomography.

MATERIALS AND METHODS: A software package “Virtual platform for simulations of single-photon emission computed tomography combined with computed tomography method in nuclear cardiology” was developed using digital patient models, a scanner, and assessment of the state of the myocardium using digital images of the left ventricle in the form of a “polar map.” Verification of the software package was performed by comparison with clinical data obtained at the National Medical Research Center of Cardiology Named After Academician E.I. Chazov (Moscow). Simulation computer tests were performed, in which the accuracy of assessing the state of the myocardium was assessed, depending on the approach to normalizing the polar map and corrective factors in the reconstruction algorithm.

RESULTS: The results of the simulation tests revealed that the assessment of left ventricular myocardial perfusion significantly depended on the method of normalizing the polar map and considered corrective factors in the reconstruction algorithm. The most accurate estimates were obtained by calculating the normalization coefficient from the average value of activity in the normal zone of the myocardium. The common approach to pixel normalization with maximum intensity can lead to errors. The results of the virtual trials were fully consistent with clinical observations.

CONCLUSIONS: The transition from relative normalized values of activity in the myocardium to absolute quantitative estimates may eliminate existing limitations and uncertainties and is the main condition for improving the diagnostic accuracy of single-photon emission computed tomography combined with computed tomography in nuclear cardiology.

Keywords: single-photon emission computed tomography combined with computed tomography; nuclear cardiology; mathematical phantom; mathematical simulation.

To cite this article:

Denisova NV, Gurko MA, Kolinko IP, Ansheles AA, Sergienko VB. Virtual platform for computer simulation of radionuclide imaging in nuclear cardiology: Comparison with clinical data. *Digital Diagnostics*. 2023;4(4):492–508. DOI: <https://doi.org/10.17816/DD595696>

Received: 22.09.2023

Accepted: 31.10.2023

Published online: 16.11.2023

DOI: <https://doi.org/10.17816/DD595696>

核心脏病学放射性核素成像模拟计算机建模虚拟平台。与临床数据比较

Natalya V. Denisova^{1,2}, Mikhail A. Gurko^{1,2}, Inna P. Kolinko^{1,2}, Alexey A. Ansheles³, Vladimir B. Sergienko³

¹ Novosibirsk State University, Novosibirsk, Russian Federation;

² Khristianovich Institute of Theoretical and Applied Mechanics, Novosibirsk, Russian Federation;

³ National Medical Research Centre of Cardiology Named After Academician E.I. Chazov, Moscow, Russian Federation

简评

论证。在放射性核素成像领域，人体临床试验（in vivo）因辐射负荷和伦理规范而受到限制。因此，数学建模方法和模拟计算机试验（in silico）方法越来越重要。这些方法以数值模型为基础。在英文文献中，这种方法被称为“Virtual clinical trials”（虚拟临床试验）。

该研究的目的是利用放射性药物^{99m}Tc-MIBI，开发单光子发射计算机断层扫描及计算机断层扫描对心肌灌注进行放射性核素成像模拟建模的软件工具；开展旨在提高单光子发射计算机断层扫描准确度的研究。

材料与方法。我们开发了“核心脏病学单光子发射计算机断层扫描及计算机断层扫描方法模拟测试虚拟平台”综合软件。开发综合软件的时候，我们使用了患者、扫描仪的数字模型和心肌评估，心肌评估是使用“极坐标靶心图”形式的左心室数字图像进行的。通过与临床数据对比，对软件系统进行了验证。临床数据是在以E. I. CHAZOV院士命名的国家心脏病学医学研究中心（NATIONAL MEDICAL RESEARCH CENTRE OF CARDIOLOGY NAMED AFTER ACADEMICIAN E. I. CHAZOV，莫斯科）获得的。我们还进行了模拟计算机测试，在测试期间研究了心肌评估的准确度，这取决于极坐标靶心图归一化的方法和重建算法中校正因子的考虑。

结果。模拟测试结果表明了，左心室心肌灌注的评估很大程度上取决于极坐标靶心图归一化的方法和重建算法中校正因子的考虑。使用心肌正常区域活动的平均值计算归一化因子时，估算结果最为准确。结果表明了，用强度最大的像素进行归一化的常见方法会导致误差。“虚拟”测试的结果与临床观察完全一致。

结论。从心肌活性累积的相对归一化值过渡到绝对定量估计值，可以消除现有的局限性和不确定性，是提高核心脏病学中单光子发射计算机断层扫描及计算机断层扫描方法诊断准确度的主要条件。

关键词：单光子发射计算机断层扫描及计算机断层扫描；核心脏病学；数学模型；数学建模。

引用本文：

Denisova NV, Gurko MA, Kolinko IP, Ansheles AA, Sergienko VB. 核心脏病学放射性核素成像模拟计算机建模虚拟平台。与临床数据比较。 *Digital Diagnostics*. 2023;4(4):492–508. DOI: <https://doi.org/10.17816/DD595696>

收到: 22.09.2023

接受: 31.10.2023

发布日期: 16.11.2023

BACKGROUND

Single-photon emission computed tomography with computed tomography (SPECT/CT) is a modern diagnostic technique in nuclear medicine. It is widely accepted as the clinical standard for examining patients with cardiovascular diseases [1]. SPECT/CT imaging can detect myocardial perfusion defects (impaired blood supply) that precede irreversible fatal damage. An intravenous radiopharmaceutical is administered during the examination, which is distributed in the myocardium proportional to blood flow and reflects myocardial perfusion. Radiopharmaceuticals accumulate only in healthy myocardial cells and hence serve as a marker of normal function.

SPECT imaging assesses heterogeneous radiopharmaceutical uptake in left ventricular (LV) cardiomyocytes. Slices and “polar maps” are used to visualize the LV. A polar map is a graphical digital representation of the entire surface of the LV myocardium in a single planar image that enables measurement of normal perfusion areas and the extent and severity of damage. Three commercial software packages were developed to display the LV as a polar map:

- 4D-MSPECT (University of Michigan Medical Center, Michigan, USA) [2];
- Emory Cardiac Toolbox (ECTb; Emory University, Atlanta, USA) [3];
- Quantitative Perfusion SPECT (QPS) (Cedars-Sinai Medical Center, Los Angeles, USA) [4].

All three packages are currently standardized and widely used in clinical SPECT systems. However, these packages provide different quantitative assessments of the myocardium [5]. According to an editorial by Germano [6], the final results of different software packages are generally comparable; however, significant differences were found between the packages in the quantitative assessment of myocardial perfusion.

How precise the estimates are and how closely they match the actual distribution of radiopharmaceuticals in the myocardium remains unclear. Studies that compare the polar maps of the reconstructed image of the LV myocardium to a reference polar map of a myocardial phantom with a known radiopharmaceutical distribution are required to assess the accuracy of SPECT imaging in nuclear cardiology. Such studies are performed in clinical settings using calibration phantoms (in vitro). However, owing to the high cost and radiation exposure of researchers, performing dozens or hundreds of such studies is challenging. Furthermore, studies with calibration phantoms do not capture the entire range of clinical cases. A viable alternative is computer simulation (in silico) using digital anthropomorphic phantoms to represent patients with various body types and lesions of various sizes and locations. Computer simulation encompasses all sequential stages of SPECT/CT imaging, from radiopharmaceutical distribution in the patient’s organs to semiquantitative perfusion assessment using a polar map.

This approach, called virtual clinical trials, has been actively evolving in high-tech nuclear medical centers worldwide over the last two decades [7]. Such research has only recently become available in Russia [8, 9].

AIM

This study aimed to develop a virtual platform for simulation testing of SPECT/CT in nuclear cardiology that will use digital models of the patient, scanner, and myocardial assessment based on digital representations of the left ventricle in the form of a polar map. For the first time, computer simulation experiments included the analysis of the relationship between semiquantitative LV myocardial perfusion assessment and the polar map standardization approach and correction factors in the reconstruction algorithm.

MATERIALS AND METHODS

We developed a virtual platform for simulation testing of SPECT/CT in nuclear cardiology using digital models of the patient, scanner, and myocardial assessment based on digital representations of the left ventricle in the form of a polar map. The software package has a modular structure and includes four modules that simulate all sequential stages of the examination, from radiopharmaceutical (technetium-99m methoxy isobutyl isonitrite, ^{99m}Tc -MIBI) distribution in the patient’s organs to LV myocardial perfusion assessment using polar maps:

- Virtual patient program;
- Virtual scanner program;
- Image reconstruction algorithms program;
- Polar map program.

Virtual Patient program

An anthropomorphic mathematical phantom (mathematical model of torso, MMT) developed at the Institute of Theoretical and Applied Mechanics (Novosibirsk) was used [9, 10]. Each organ of the MMT phantom was generated using analytical geometry equations describing appropriate three-dimensional (3D) shapes (planes, cones, cylinders, paraboloids, ellipsoids, etc.). These shapes were overlaid, intersected, and truncated using logical Boolean operators to generate complex geometric compositions that describe the outlines of organs close to the Atlas images [11]. The phantom is represented as $64 \times 64 \times 64$ or $128 \times 128 \times 128$ digital arrays.

MMT is a voxel phantom based on analytical geometry equations that describe surfaces (boundaries) dividing structures with different morphological characteristics. It is possible to generate phantoms with different anatomical structures and in different positions by modifying the parameters of the geometric shapes. This study used an anatomical model of a typical male patient in a position with

his arms up. The model includes the torso, chest bones, lungs, heart, spleen, stomach, and kidneys. The large intestine represents the intestines. Diagnostic nuclear medicine rarely requires detailed imaging of fine anatomical structures. The MMT does not consider heartbeat and respiratory excursion. This model generally corresponds to modern SPECT/CT systems in the phase mode, with cardiac and respiratory motions removed. The model is presented in Fig. 1.

The distribution of radiopharmaceuticals in various organs, rather than the anatomical structure of the patient, plays a critical role in nuclear medicine simulation studies. The virtual patient program generates a 3D map of radiopharmaceutical uptake (“activity map”) in the MMT phantom using clinical data on the distribution of ^{99m}Tc-MIBI. As an example, Fig. 2 shows clinically reconstructed SPECT images of a real patient, with activity values in several organs

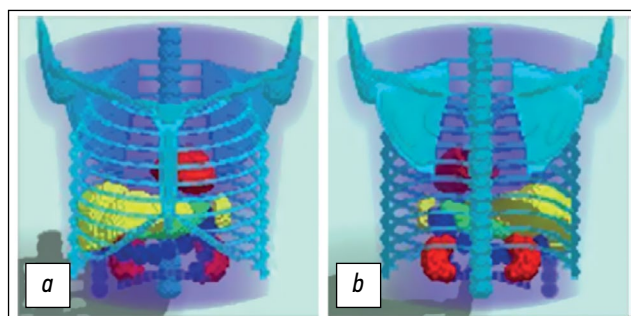


Fig. 1. 3D mathematical model of the torso simulating the anatomical structure of a typical male patient in the position with arms up: *a*: anterior view; *b*: posterior view. Model in a discrete representation, 128 × 128 × 128.

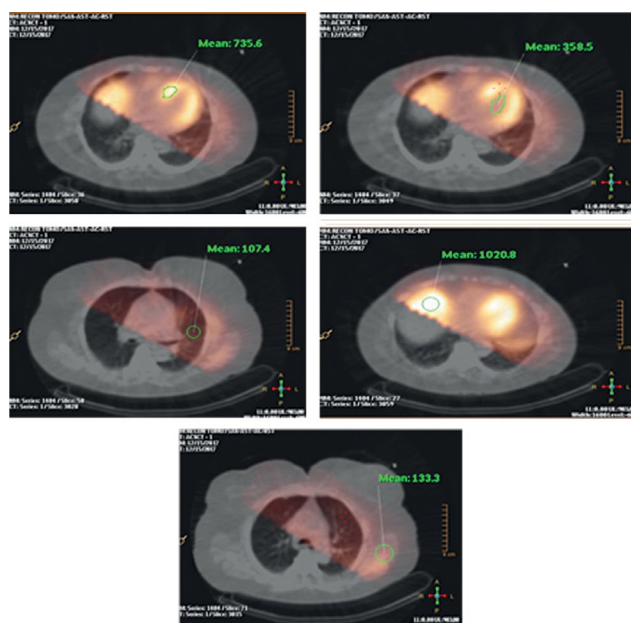


Fig. 2. Clinical data. Relative ^{99m}Tc-MIBI uptake (pulse/voxel) in chest organs. The images were obtained using single-photon emission computed tomography with computed tomography (Philips BrightView XCT) at the El Chazov National Medical Research Center of Cardiology.

Table 1. Relative ^{99m}Tc-MIBI uptake in phantom organs in the mathematical model of the torso

Organ	Relative ^{99m} Tc-MIBI uptake, pulse/voxel
Soft tissues	130
Lungs	100
Liver	900
Heart	750
Large intestine	1000
Gallbladder	2500

in pulse/voxel units. Data were collected using SPECT/CT imaging (Philips BrightView XCT, Philips, Netherlands) at the El Chazov National Medical Research Center of Cardiology. These values may differ among patients. The present study used the values shown in Table 1 when creating an activity map for the MMT phantom. A homogeneous distribution of activity within each organ was specified, except for modeling LV myocardial ischemic injury.

Figure 3 shows the activity map for the phantom. The image is cropped in accordance with the gamma camera dimensions. The lungs, kidneys, spleen, and stomach are not shown because the concentration of radiopharmaceutical is nearly the same as that in soft tissues. LV, liver, gallbladder, and intestinal loops are clearly visualized. The heart model is represented by the LV because the right ventricle is practically invisible on SPECT images because of its thin walls.

In clinical tests, CT findings are used to account for the attenuation of gamma radiation in biological tissues of various densities, and an individual 3D attenuation map is generated. An attenuation map for the MMT phantom was generated in this study, which included the main differences by substance density. Three media of different densities were studied: lungs (air), soft tissues (water), and skeletal bones. Table 2 presents the attenuation coefficients for 140 keV gamma radiation used in this study [12].

Thus, the virtual patient program generates three phantoms: anthropomorphic anatomical MMT phantom, activity map, and attenuation map.

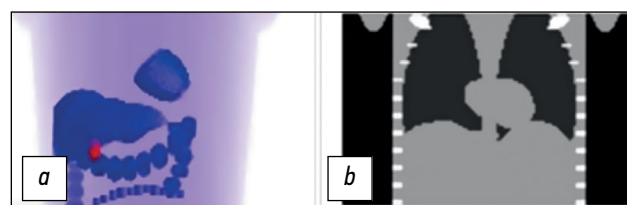


Fig. 3. *a*: Radiopharmaceutical uptake map: 3D distribution of relative ^{99m}Tc-MIBI concentrations calculated based on a mathematical model of the torso. Map in a discrete representation, 128 × 128 × 100; *b*: attenuation map generated based on a mathematical model of the torso. Map in a discrete representation, 128 × 128 × 100. The central longitudinal cross-section is presented.

Table 2. Attenuation coefficients for 140 keV gamma radiation (technetium)

Organ (medium)	Attenuation coefficients for 140 keV gamma radiation, 1/cm
Soft tissues (water)	0.15
Lungs (air)	0.04
Bones	0.28

Virtual Scanner program

The virtual scanner program modeled SPECT/CT imaging in a “virtual patient.” Raw projection data were calculated using the Monte Carlo procedure. From a mathematical standpoint, this stage solves a direct problem: gamma radiation transmission from a specified spatial source through substances of different densities. There are two main approaches to solving such problems.

The first is based on solving transfer equations that describe gamma radiation transmission in a substance and on geometric approximations when calculating gamma ray transmission through a collimator detector system. However, this approach requires additional shadowing procedures to account for Poisson data.

The second is a statistical approach based on the Monte Carlo procedure. This approach employs a random (pseudorandom) number generator in various statistical modeling methods for distributions characterizing physical processes such as the Poisson distribution (radioactive decay, mean free path), Klein–Nishina–Tamm distribution (angular distribution of scattered photons), and Gaussian distribution (different fluctuations of the detecting system). The modeling of the raw data collection included several stages:

1. Gamma ray emission by a source;
2. Radiation transmission through a substance;
3. Detector response formation.

At the stage of modeling gamma ray emission by a source, coordinates, directions, energy, and other variable gamma ray characteristics are generated based on specified distributions. For modeling the ^{99m}Tc -MIBI source, the distribution of particle emission directions was considered to be uniform over the entire solid angle, and the energy distribution was specified by a delta function of 140.5 keV. The activity map defines the distribution of the gamma ray emission coordinates.

Modeling radiation transmission through a substance is time-consuming. Thus, properly selecting models for describing physical processes and accurately implementing them algorithmically is critical. We used our own software, which implements several validated algorithms for modeling both the transmission of gamma rays and their interactions with a substance.

The NIST XCOM database was used as an interaction cross-sectional database for gamma ray interactions with substances [13]. Three main types of interaction were

considered during gamma ray transmission through a substance: the photoelectric effect, Compton scattering, and coherent scattering. The scattering angle indicators for Compton and coherent scattering were modeled using the algorithms provided in the Livermore low-energy electromagnetic models of the Geant4 modeling package (Geant4 Collaboration) [14]. A combination of algorithms was used for gamma ray transmission modeling. If the volume in which the gamma ray is located at a time moment is inhomogeneous (defined voxel-wise or parametrically), the peak cross-section method is used to generate the mean free path (Woodcock tracking) [15]. If the volume is homogeneous, the mean free path is generated according to the law of exponential attenuation. These methods determine the mean free path, which is then compared to the particle path length before leaving or entering another volume, which is calculated via algorithms for determining the ray intersection with geometric shapes.

In this study, the gamma ray transmission was calculated through a low-energy high-resolution collimator. The method for calculating projection data was verified by comparing it with clinical findings. Figure 4 shows an example of raw data generated using the Monte Carlo procedure: left anterior oblique (a), frontal (b), right anterior oblique (c), and left lateral (d) projections. The projections were obtained considering the ^{99m}Tc -MIBI uptake map and virtual patient attenuation map (Fig. 3). Similar clinical projections obtained using SPECT/CT imaging (Philips BrightView XCT) at the El Chazov National Medical Research Center of Cardiology are shown for comparison. The LV myocardium images in these projections are in good agreement.

Image Reconstruction Algorithms program

For image reconstruction, modern commercial SPECT/CT systems use algorithms based on maximum likelihood expectation maximization (MLEM) [16] and its accelerated version, ordered subset expectation maximization (OSEM):

$$\tilde{f}_j^{n+1} = \frac{\tilde{f}_j^n}{\sum_i a_{ij}} \sum_i \frac{g_i a_{ij}}{\sum_k a_{ik} \tilde{f}_k^n} \quad (1)$$

where:

- \tilde{f}_j^{n+1} and \tilde{f}_j^n are activity (pulse/voxel) in the j^{th} voxel during iteration steps $(n + 1)$ and n , respectively;
- g_i is the number of recorded pulses in the i^{th} pixel of the detector;
- a_{ij} is a system matrix that describes the probability that a photon emitted in the j^{th} voxel of the uptake map will be recorded in the i^{th} pixel of the detector.

A homogeneous distribution is used during the first step.

We used our own image reconstruction algorithms software to calculate the system matrix, which considers the physical effects associated with gamma radiation transmission through biological tissues and a collimator–detector system. The accuracy of the system matrix calculation determines

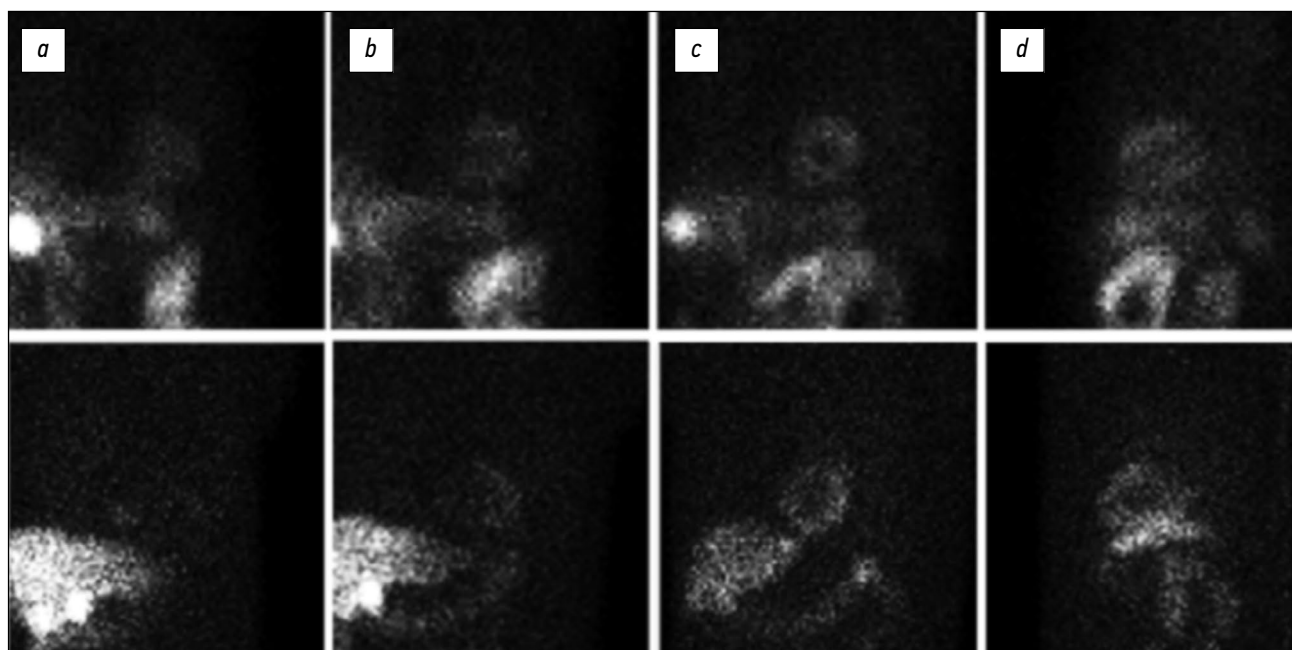


Fig. 4. Comparison of projections obtained in a clinical setting during examination (top) and those calculated according to the Monte Carlo procedure (bottom) using a 3D activity map of a virtual patient: *a*: left anterior oblique projection; *b*: frontal projection; *c*: right anterior oblique projection; *d*: left lateral projection. Clinical data were obtained using single-photon emission computed tomography (Philips BrightView XCT) at the El Chazov National Medical Research Center of Cardiology.

the quality of the reconstructed images. The system matrix elements are presented as follows:

$$a_{ij} = P_{jk}^{att} \times P_{ki}^{col-det} \quad (2)$$

where:

- P_{jk}^{att} estimates the likelihood that a photon emitted in the j^{th} voxel of the activity map will pass through the virtual patient's biological tissues and hit the k^{th} pixel of the collimator surface. That is, this variable describes the gamma flux attenuation due to scattering in biological tissues. Attenuation correction (AC) is used to describe this effect.
- $P_{ki}^{col-det}$ estimates the likelihood that a photon will pass through the collimator and be recorded as a pulse in the k^{th} pixel of the detector. That is, this variable describes the effect of passing through the collimator and detector crystal while accounting for the point spread function. Resolution recovery (RR) is used to describe this effect.

Figure 5 shows a fragment of the ^{99m}Tc -MIBI uptake map of the MMT phantom and its reconstruction using the OSEM algorithm based on the data obtained in the virtual scanner

program (Fig. 4). A similar clinical image obtained at the El Chazov National Medical Research Center of Cardiology using the Astonish algorithm during myocardial perfusion imaging in a real patient is shown for comparison.

Polar Map program

Because existing commercial polar map packages are closed source software and cannot be modified, several researchers use their own software [17–20]. One of the first polar map generation programs was created at the Catholic University of Leuven (Belgium) for computer simulation studies [17]; it was later used by Turco et al. [20].

A research group from Kanazawa University, Japan, proposed an alternative to the three standard packages [18]. The authors discovered that the diagnostic results of the same patient differed when different software packages (4D-MSPECT, ECTb, and QPS) were used; thus, they created their own open source software to standardize the research. In Russia, polar maps were developed by Kotina et al. in St. Petersburg [19].

An example of a clinical image obtained at the El Chazov National Medical Research Center of Cardiology using the



Fig. 5. ^{99m}Tc -MIBI distribution in chest organs: *a*: phantom; *b*: reconstruction; *c*: clinical case. The clinical case was obtained using single-photon emission computed tomography at the El Chazov National Medical Research Center of Cardiology.

QPS package is shown in Fig. 6. The first column (on the left) presents images in slice mode after a stress test; the second column presents the same images at rest. In the tomographic slice mode, data were displayed in three cross-sections: along the vertical long axis, horizontal long axis, and short axis. The third column presents polar maps in percentage mode (from top to bottom: stress map, rest map, and map of differences). The third column shows 3D LV images.

In this study, a method for generating a polar map that is similar to the commercial QPS software was devised. The LV image is manually segmented, the main axis is determined, and the image is rotated. The epicardial and endocardial surfaces specified in the phantom were used to eliminate delineation errors. The LV is moved to a separate file and divided into layers along the long axis (Fig. 7). Subsequently,

data on cumulative activity (pulse/voxel) in each layer are collected. The distribution of cumulative activity proportional to the degree of myocardial perfusion was recorded sequentially in each layer as circular profiles. The data collection process can be divided into two nested cycles. In the first cycle, there is a descent through the layers from the top of the LV (basal part) to the bottom (apical part). In the second cycle, data on cumulative activity in each sector of the cross-section are collected. The mean value was calculated based on the thickness of the myocardium and in each sector of the slice. According to Turco et al. [20], this method of calculating cumulative activity provides better accuracy than using the uptake value based on the maximum value in the myocardium. The number of sectors into which each slice is divided is calculated automatically based on the

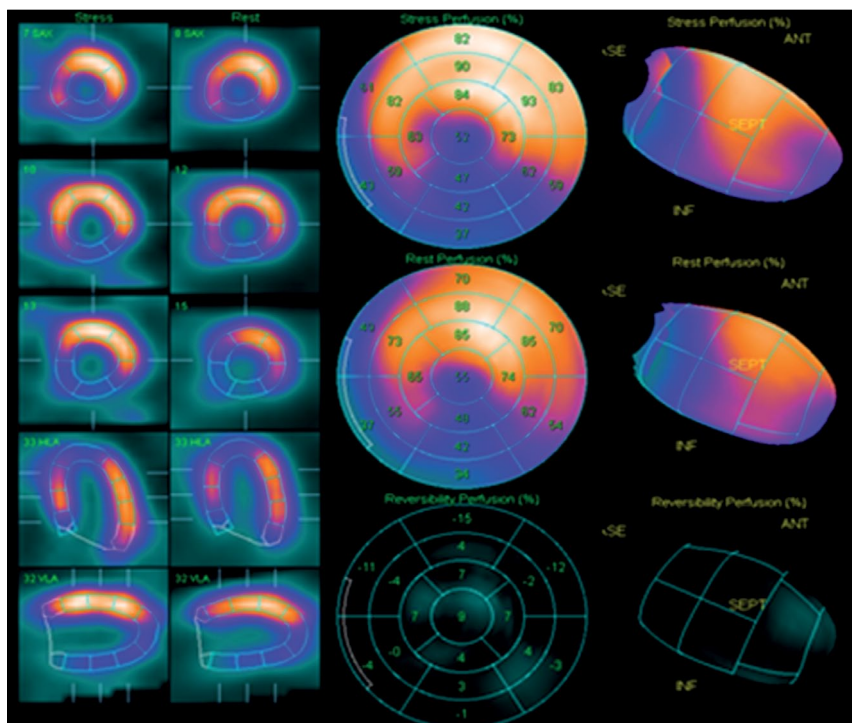


Fig. 6. Graphical representation of clinical myocardial perfusion assessment using single-photon emission computed tomography. Images were obtained using the QPS software during examination at the El Chazov National Medical Research Center of Cardiology.

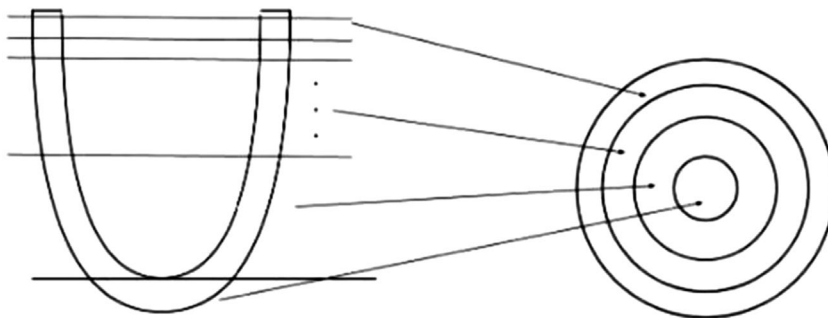


Fig. 7. Left ventricle model cross-section along the vertical long axis (left) is divided into layers of short axis (SAX), and the cumulative activity values in each cross-section are projected onto the polar diagram as concentric rings, with the basal part of the left ventricle corresponding to the outer ring and the apical part corresponding to the inner ring (arrows show where each layer is projected onto the polar map).

shape and size of the LV. As shown in Fig. 7, the cumulative activity values in each cross-section are projected onto the polar diagram as concentric rings, with the basal part of the LV corresponding to the outer ring and the apical part corresponding to the inner ring.

“VIRTUAL” studies

Methodology of computer simulation

Computer simulation included all sequential stages of myocardial perfusion assessment using SPECT/CT imaging with ^{99m}Tc -MIBI, from radiopharmaceutical distribution in the patient's organs to perfusion assessment using a polar map. First, the virtual patient program calculated the radiopharmaceutical distribution using the MMT anatomical model. Imaging in a virtual patient was modeled using the virtual scanner program and the Monte Carlo procedure. The data collection parameters were close to clinical parameters and were determined according to the European Association of Nuclear Medicine (EANM) protocol [21]. The gamma camera had a 180° arc from the left posterior oblique projection to the right anterior oblique projection. Data recording was simulated in a step-by-step mode with a circular orbit. The number of projections ($n = 32$) and exposure time per projection (15 s) corresponded to the standard clinical protocol for Philips BrightView XCT. Approximately 100,000 pulses (counts) were recorded in each projection because of simulation using the Monte Carlo procedure. The total number of recorded pulses during raw data collection was 4,000,000. The image was reconstructed using the conventional OSEM algorithm (eight subsets, two iterations) based on the calculated projection data. Using a polar map software, the 3D LV image was then displayed as slices and a polar map, and a semiquantitative myocardial perfusion assessment was performed. The accuracy of SPECT imaging was assessed by comparing the polar map of the reconstructed image of the LV myocardium with a reference polar map of a phantom, i.e., a virtual patient with a known, specified radiopharmaceutical distribution.

Problems of interest

Computer simulation studies analyzed the accuracy of myocardial perfusion assessment depending on the polar map standardization approach and correction factors in the reconstruction algorithm.

Relationship between myocardial perfusion assessment and the polar map standardization approach

The homogeneity of radiopharmaceutical distribution was assessed based on reconstructed LV image mapping as a standard 17-segment polar map. Clinical studies have assessed the following parameters of LV myocardial perfusion: summed rest score (SRS), summed stress score (SSS), and summed difference score. In mathematical modeling, the radiopharmaceutical distribution was supposed to correspond to the rest mode. In this study, the

total SRS and local relative perfusion in percentage mode (normalization) were calculated using the three approaches described in the literature:

A. S_{\max} score

This approach is the most common and used to generate polar maps with the 4D-MSPEC [2], ECTb [3], and QPS [4] software. The pixel with the highest activity is selected on the polar map and assigned a value of 100%. The remaining pixels are assigned a percentage value based on their proportion to the maximum value. The mean uptake values (in percentage) for each sector are then calculated, as well as their sum (S_{\max}), which is an analog of the SRS parameter.

B. S_{90} score

To minimize the impact of false hot spots, the Cedar-Sinai AutoQUANT QPS/QGS v.7.2 user manual recommends normalizing polar maps so that the 90th percentile equals 100%. The mean uptake values (in percentage) for each sector are then calculated, as well as their sum (S_{90}).

C. S_{norm} score

In a recent publication, Garcia et al. [22] have presented recommendations from the authors of the commercial software 4D-MSPEC [2], ECTb [3], and QPS [4] (2007) for polar map standardization. The authors recommend using “the perfusion intensity in the most normal area within the LV,” rather than the maximum intensity value, as 100%. All pixel values greater than or equal to the normal intensity are considered as 100%; the rest are calculated by proportion. The mean uptake values for each sector are then calculated, as well as their sum (S_{norm}). Okuda et al. [18] have proposed standardization based on the mean intensity in the normal area of the myocardium. In this case, a normal area is defined as a cluster of pixels with intensity in the 80th (± 10) percentile for the entire data sample.

For all three approaches, the mean radiopharmaceutical uptake was calculated in percentage mode for each sector of the polar map. Perfusion was assessed using the threshold values shown in Table 3, which serve as the default template. Based on the calculated percentages of uptake, each sector is assigned a score from 0 to 4, and these scores are added together. As a result, total scores (analog of the SRS parameter) are obtained.

Relationship between myocardial perfusion assessment and correction factors in the reconstruction algorithm

In Russia and worldwide, there are various operational SPECT systems that do not have CT support. Computer simulation studies included a comparative analysis of myocardial perfusion assessment with and without attenuation correction in the reconstruction algorithm. When reconstructing images with AC, the value P_{jk}^{att} in formula (2) was calculated individually for each nonzero activity voxel, taking the attenuation map into account. In computer simulation without attenuation correction (non-AC), $P_{jk}^{\text{att}} = 1$. For the reconstructed images of the LV myocardium, AC and non-AC polar maps were generated.

Table 3. Left ventricular myocardial perfusion assessment

Lesion severity	Score	Segment perfusion (relative to the maximum)
Normal value	0	≥70%
Mild perfusion defect	1	50–69%
Moderate perfusion defect	2	30–49%
Severe perfusion defect	3	10–29%
No perfusion	4	<10%

According to the EANM manual [21], integrating the effect of “blurring” of a point source image (RR) in the reconstruction algorithm requires rigorous phantom tests. In this study, computer simulation studies included a comparative analysis of polar maps generated in reconstruction modes with and without image blurring (RR and non-RR, respectively).

RESULTS

Study subjects

Computer simulation studies included two virtual patients: one with a healthy heart and the other with an ischemic injury in the anterolateral zone of the LV myocardium. Based on the MMT model, the virtual patient program specified the matching ^{99m}Tc -MIBI uptake maps or activity maps for these patients.

In the first case, an MMT phantom with a homogeneous distribution of ^{99m}Tc -MIBI activity in the LV myocardium was used as a virtual patient. The reference polar map for this phantom is shown in Fig. 8. It is homogeneous and independent of the standardization approach. In each sector, the relative radiopharmaceutical uptake corresponded to 100%, and the reference SRS perfusion score (S^{ref}) was 0.

In the second case, a virtual patient with an ischemic injury of the left ventricle (LV) myocardium was studied. The ^{99m}Tc -MIBI uptake map of the MMT mathematical phantom included a defect in the anterolateral zone of LV with decreased radiopharmaceutical uptake. Reference polar maps generated based on the described standardization approaches (A, B, and C) (Fig. 12). Reference SRS perfusion scores for these maps differed slightly:

$$S_{\max}^{ref} = 6; S_{90}^{ref} = 5; S_{norm}^{ref} = 6.$$

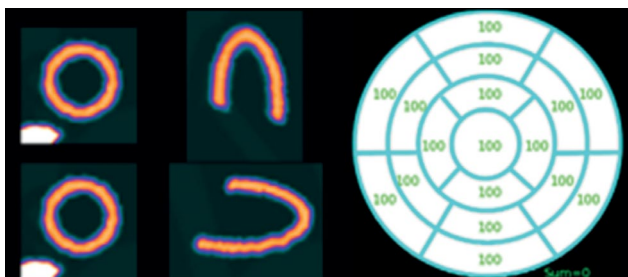


Fig. 8. Reference polar map of left ventricular myocardial perfusion in a virtual patient with a healthy myocardium (normal value). Summed rest score (SRS): $S_{\max}^{ref} = S_{90}^{ref} = S_{norm}^{ref} = 0$.

The general scheme of the computer tests was as follows. After simulation imaging in virtual patients, image reconstruction was performed using the OSEM technique with or without correction factors. On the reconstructed images, LV segmentation was performed, and three types of polar maps standardized in accordance with approaches A, B, and C were generated.

Key study findings

Case 1: a virtual patient with a healthy left ventricular myocardium

The reference polar map for this case is shown in Fig. 8; the reference SRS (S^{ref}) = 0. Figure 9 shows the polar maps generated using reconstruction with attenuation correction and resolution recovery (AC/RR). The polar maps were standardized according to approaches A, B, and C. The activity distribution no longer appears heterogeneous because of reconstruction errors. In all three maps, a visible decrease in activity was noted in the apical region. This occurrence, known as a false apical defect, is frequently observed on clinical images. SRS perfusion scores calculated using various standardization approaches were as follows: $S_{\max} = 10$, $S_{90} = 1$, and $S_{norm} = 3$. S_{90} and S_{norm} scores are within the normal range, whereas S_{\max} is overestimated and provides an incorrect perfusion assessment. Overestimation of S_{\max} corresponds to clinical practice. The software used in SPECT systems uses polar map normalization by the pixel with maximum intensity. According to Ansheles [1], “one of the problems with images is that, for unknown reasons, the total scores (SSS, SRS) can be significantly overestimated.”

Figure 10 shows polar maps generated by image reconstruction using the OSEM algorithm without attenuation correction but with resolution recovery (non-AC/RR). The images show an artifact in the form of decreased activity at the bottom of the polar map. This artifact is typical of non-AC clinical images. Notably, the false apical defect disappeared, which is common in non-AC images in clinical practice. The total SRS perfusion scores were as follows: $S_{\max} = 17$, $S_{90} = 9$, and $S_{norm} = 4$. It is significantly higher than the reference value ($S^{ref} = 0$). Non-AC images require a different template obtained in the same mode.

Figure 11 shows the polar maps generated by image reconstruction using the OSEM algorithm with attenuation correction but without resolution recovery (AC/non-RR). The total SRS perfusion scores were as follows: $S_{\max} = 9$, $S_{90} = 3$,

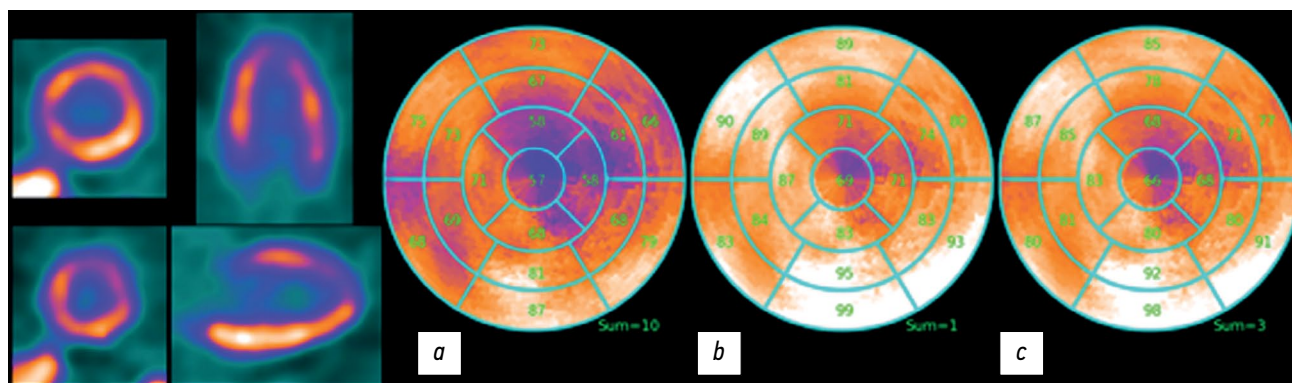


Fig. 9. AC/RR. Polar map of the reconstructed image of left ventricular myocardial perfusion. Reconstruction was performed with attenuation correction (AC) and resolution recovery (RR). Summed rest score (SRS) for three methods of polar map calculation: *a* — $S_{max}=10$; *b* — $S_{90}=1$; *c* — $S_{norm}=3$.

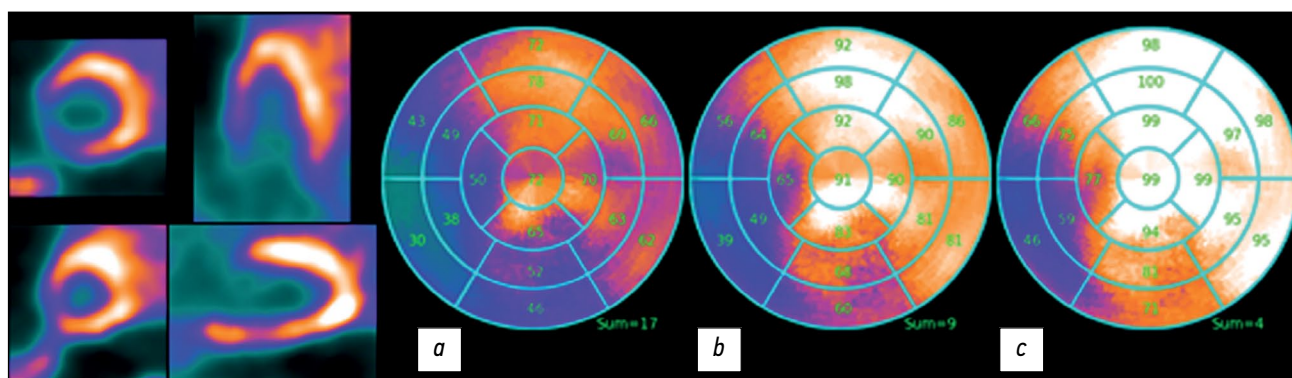


Fig. 10. Non-AC/RR. Polar map of the reconstructed left ventricle. The reconstruction was performed without attenuation correction (non-AC) but with resolution recovery (RR). Summed rest score (SRS): *a* — $S_{max}=17$; *b* — $S_{90}=9$; *c* — $S_{norm}=4$.

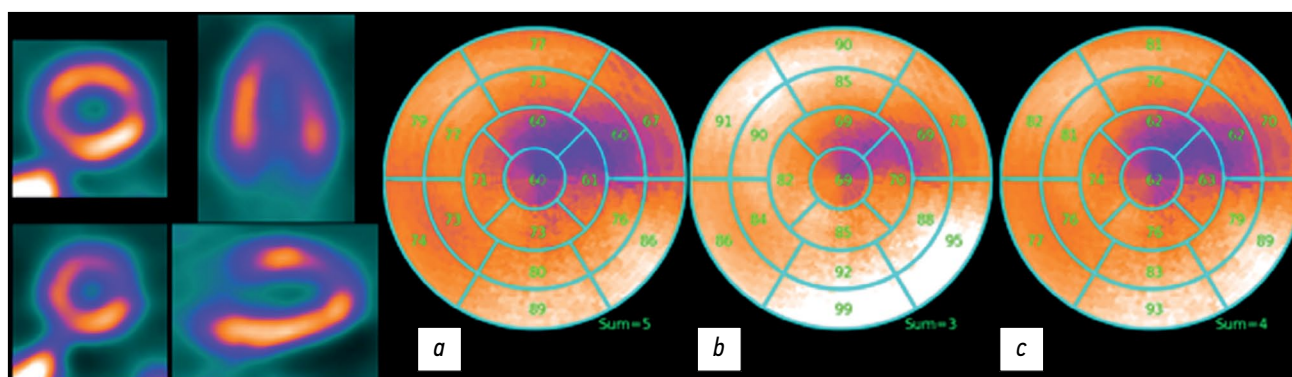


Fig. 11. AC/non-RR. Polar map of the reconstructed image of left ventricular myocardial perfusion. Reconstruction was performed with attenuation correction (AC) but without resolution recovery (non-RR). Estimated summed rest score (SRS): *a* — $S_{max}=9$; *b* — $S_{90}=3$; *c* — $S_{norm}=4$.

$S_{norm} = 4$. The AC/RR images in Fig. 9 and the AC/non-RR images in Fig. 11 look similar; however, the SRS scores in the AC/RR mode are more accurate.

Case 2: a virtual patient with an ischemic injury in the LV myocardium

The reference polar map for case 2 is shown in Fig. 12; the reference SRS scores for the three polar map standardization approaches differ slightly and amount to $S_{max}^{ref} = 6$; $S_{90}^{ref} = 5$; $S_{norm}^{ref} = 6$. Polar maps generated for AC/

RR reconstructed images of a virtual patient with an ischemic injury are shown in Fig. 13. SRS: $S_{max} = 12$, $S_{90} = 6$, and $S_{norm} = 6$.

The reconstructed defect in Fig. 13 corresponds to the images on the reference polar map in Fig. 12 for all three polar map standardization approaches on AC/RR images. However, an artifact from the right ventricle appeared, which mirrored the true defect.

Figure 14 reveals the polar maps generated by image reconstruction in the non-AC/RR mode. The defect is smaller

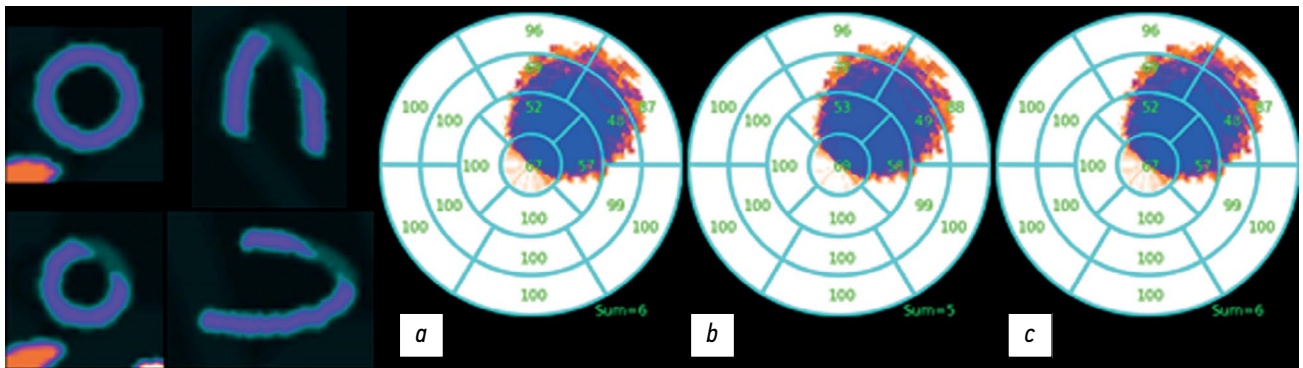


Fig. 12. Reference polar maps of left ventricular myocardial perfusion with ischemic injury. Summed rest score (SRS): *a* — $S_{\max}=6$; *b* — $S_{90}=5$; *c* — $S_{\text{norm}}=6$.

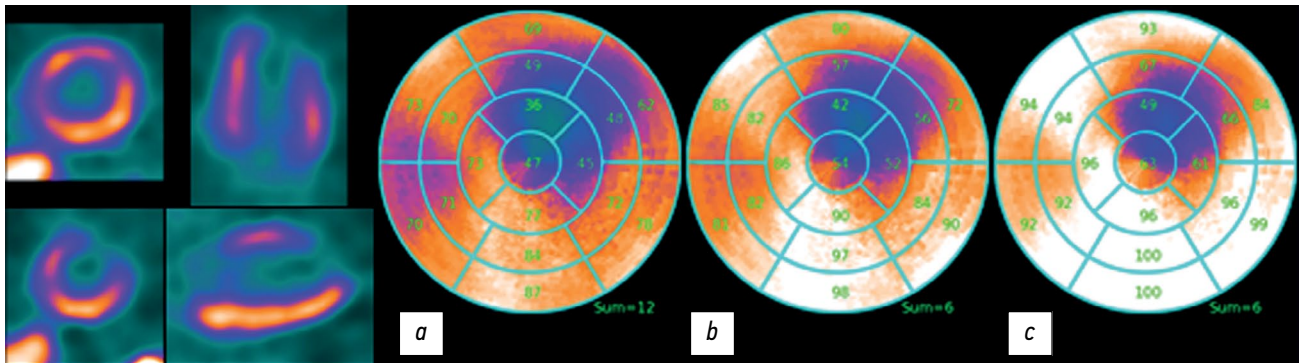


Fig. 13. AC/RR. Polar maps of the reconstructed image of left ventricular myocardial perfusion. Reconstruction was performed with attenuation correction (AC) and resolution recovery (RR). Estimated summed rest score (SRS): *a* — $S_{\max}=12$; *b* — $S_{90}=6$; *c* — $S_{\text{norm}}=6$.

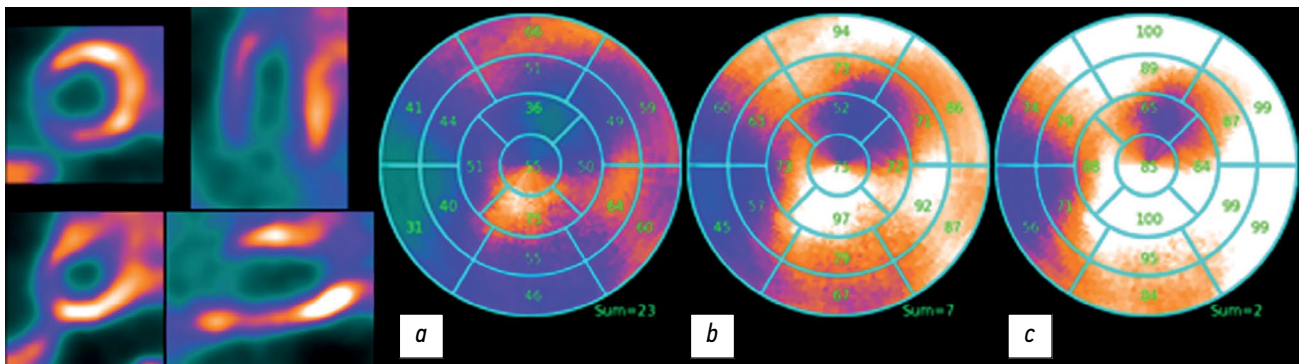


Fig. 14. Non-AC/RR. Polar map of the reconstructed image of left ventricular myocardial perfusion. The reconstruction was performed without attenuation correction (non-AC) but with resolution recovery (RR). Estimated summed rest score (SRS): *a* — $S_{\max}=23$; *b* — $S_{90}=7$; *c* — $S_{\text{norm}}=2$.

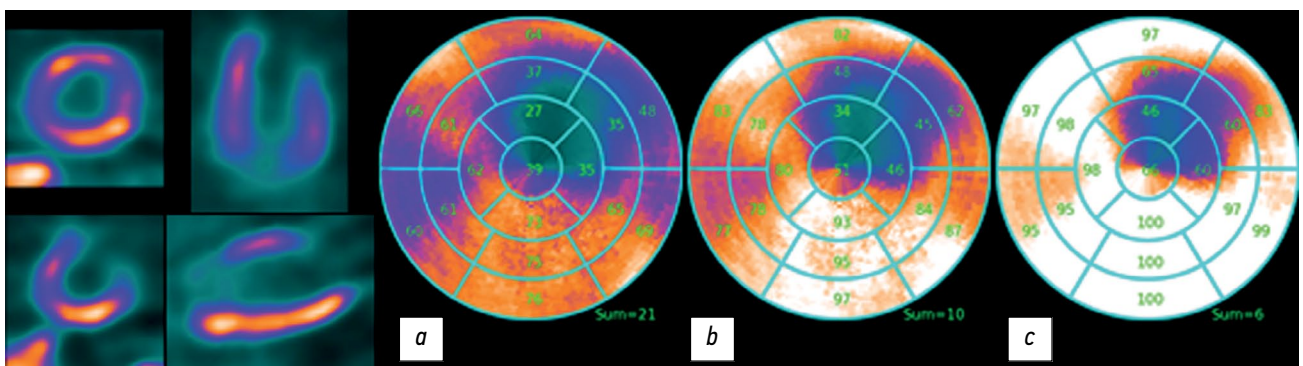


Fig. 15. AC/non-RR. Polar map of the reconstructed left ventricle. Reconstruction was performed with attenuation correction (AC) but without resolution recovery (non-RR). Estimated summed rest score (SRS): *a* — $S_{\max}=21$; *b* — $S_{90}=10$; *c* — $S_{\text{norm}}=6$.

than the reference polar map in Fig. 12. A false defect was observed in the lower right part, whereas the apical defect was absent.

Figure 15 shows polar maps generated by image reconstruction in AC/non-RR mode: with attenuation correction but without resolution recovery. The defect boundaries roughly correspond to those in the AC/RR mode. The total SRS scores for various map generation approaches were as follows: $S_{max} = 21$, $S_{g0} = 10$, and $S_{norm} = 6$.

DISCUSSION

Summary of the key study findings

The findings of the virtual tests were completely consistent with the clinical data. The polar maps of the reconstructed LV images of virtual patients showed the same errors (artifacts) as in the clinical images of real patients. These findings confirm that the virtual platform for the simulation testing of SPECT/CT in nuclear cardiology is appropriate for addressing nuclear cardiology problems. AC/RR mode reconstruction and polar map standardization by the mean activity in the normal area of the myocardium yielded perfusion and ischemic focus assessment results closest to the exact values.

Discussion of the key study findings

LV myocardial perfusion imaging by SPECT/CT is an outcome of solving the inverse ill-posed problem of image reconstruction based on Poisson data. Because the theory of solving ill-posed stochastic problems is a relatively young branch of mathematics, complex current reconstruction algorithms “cannot work miracles” [21], and the resulting solutions are prone to errors (artifacts). The same artifacts seen in clinical images were observed in mathematical modeling similar to clinical conditions.

In image reconstruction using the OSEM algorithm in AC mode, a false apical defect is observed on all polar maps. According to Ansheles [1], this artifact occurs in ~50% of clinical cases after reconstruction in AC mode and is rarely considered a significant defect. In practice, distinguishing between a false apical defect and minor focal lesion in the apical region can be challenging. In our simulation studies of a virtual patient with an ischemic injury of the myocardium, the lesion partially overlapped the area of the false apical defect (Fig. 13), leading to overestimation of defect severity.

In non-AC images (Figs. 13 and 14), an artifact in the form of decreased activity was noted in the bottom of the polar map. The false apical defect was absent. This is common for clinical polar maps generated in the non-AC mode. A visual comparison of polar maps derived from a mathematical simulation of a case with an ischemic injury of the LV myocardium reveals that the lesion size closest to the reference size is observed in AC/RR mode. In image reconstruction in the non-AC/RR mode, the lesion is significantly smaller, which corresponds to the clinical findings. According to Ansheles [23], the SRS scores and area

of transient ischemia are significantly greater in AC mode than in non-AC mode.

The simulation approach has the benefit of comparing semiquantitative assessments for each sector of polar maps, as well as the total SRS parameters of the reconstructed image, to a template (polar map of the phantom). A comparison analysis revealed that the lower LV wall exhibited falsely increased activity, which could be influenced by liver activity (an effect not obvious to the doctor and is caused by the scattering of gamma rays emitted by the liver and scattered on the lower LV wall). Some of these scattered photons enter the detector exactly in the image of the left ventricle, which may cause an error.

In this situation, standardization by the maximum pixel results in hypoperfusion and increased total SRS score compared with the reference polar map. Polar map standardization using the maximum pixel resulted in overestimation of SRS in all cases. The best results were obtained when standardization using the mean activity in the normal area was used. This is consistent with the novel recommendations by the authors of standard commercial polar map packages [22].

Furthermore, artifacts caused by limitations in the reconstruction algorithms are present in images of healthy subjects. Thus, modern SPECT/CT systems use relative values based on a polar map of the reconstructed LV and relative values in comparison to reference databases, allowing identification of perfusion defects. The findings of these studies indicate that one should rely on comparative relative values rather than relative values based on a polar map of the reconstructed LV. However, this approach has a significant limitation: all conditions for obtaining clinical images should be similar to those for creating a reference database.

CONCLUSION

Our findings demonstrate that computer simulation can help clinicians better understand the limitations, uncertainties, and errors in myocardial perfusion assessment. The transition from relative standardized values of activity accumulation in the myocardium to absolute quantitative assessments can eliminate existing limitations and uncertainties and is the primary condition for improving the diagnostic accuracy of SPECT/CT imaging in nuclear cardiology.

ADDITIONAL INFORMATION

Funding source. This study was not supported by any external sources of funding.

Competing interests. The authors declare that they have no competing interests.

Authors' contribution. All authors made a substantial contribution to the conception of the work, acquisition, analysis, interpretation of data for the work, drafting and revising the work, final approval of the version

to be published and agree to be accountable for all aspects of the work. N.V. Denisova — development of the concept and planning of scientific work, drafting the manuscript, final approval of the published version of the manuscript, development of the “Virtual Patient” and “Reconstruction Algorithms” programs; M.A. Gurko — development

of the “Virtual Tomograph” program, participation in writing and editing the manuscript; I.P. Kolinko — development of the “Polar map” program; A.A. Ansheles, V.B. Sergienko — clinical data, analysis of scientific papers, critical revision with the introduction of valuable intellectual content.

REFERENCES

1. Ansheles AA, Sergienko VB. *Yadernaya Kardiologiya*. Sergienko VB, editor. Moscow: FGBU «NMITs kardiologii» Minzdrava Rossii; 2021. (In Russ).
2. Ficaro E, Lee B, Kritzman J, Corbett J. Corridor4DM: The Michigan method for quantitative nuclear cardiology. *Journal of Nuclear Cardiology*. 2007;14(4):455–465. doi: 10.1016/j.nuclcard.2007.06.006
3. Garcia E, Faber T, Cooke C, et al. The increasing role of quantification in clinical nuclear cardiology: The Emory approach. *Journal of Nuclear Cardiology*. 2007;14(4):420–432. doi: 10.1016/j.nuclcard.2007.06.009
4. Germano G, Kavanagh P, Slomka P, et al. Quantitation in gated perfusion SPECT imaging: The Cedars-Sinai approach. *Journal of Nuclear Cardiology*. 2007;14(4):433–454. doi: 10.1016/j.nuclcard.2007.06.008
5. Wolak A. Quantitative myocardial-perfusion SPECT: Comparison of three state-of-the-art software packages. *Journal of Nuclear Cardiology*. 2008;15(1):27–34. doi: 10.1016/j.nuclcard.2007.09.020
6. Germano G. Quantitative measurements of myocardial perfusion and function from SPECT (and PET) studies depend on the method used to perform those measurements. *Journal of Nuclear Cardiology*. 2018;25(3):925–928. doi: 10.1007/s12350-016-0757-z
7. Abadi E, Segars WP, Tsui BMW, et al. Virtual clinical trials in medical imaging: a review. *Journal of Medical Imaging*. 2020;7(4):1. doi: 10.1117/1.JMI.7.4.042805
8. Denisova NV, Ansheles AA. A study of false apical defects in myocardial perfusion imaging with SPECT/CT. *Biomedical Physics & Engineering Express*. 2018;4(6):065018. doi: 10.1088/2057-1976/aae414
9. Denisova N, Ondar M, Kertesz H, Beyer T. Development of anthropomorphic mathematical phantoms for simulations of clinical cases in diagnostic nuclear medicine. *Computer Methods in Biomechanics and Biomedical Engineering: Imaging & Visualization*. 2023;11(3):433–441. doi: 10.1080/21681163.2022.2074308
10. Denisova NV. Computational Phantoms for Medical Radiology. *Medical Radiology and Radiation Safety*. 2022;67(6):51–61. doi: 10.33266/1024-6177-2022-67-6-51-61
11. Sinel'nikov RD, Sinel'nikov AY, Sinel'nikov YaR. *Atlas Anatomii Cheloveka. 2nd Volume*. Moscow: Novaya volna; 2022. (In Russ).
12. Patton JA, Turkington TG. SPECT/CT Physical Principles and Attenuation Correction. *Journal of Nuclear Medicine Technology*. 2008;36(1):1–10. doi: 10.2967/jnmt.107.046839
13. Seltzer S. XCOM-Photon Cross Sections Database [Internet]. Gaithersburg (MD): NIST Standard Reference Database 8. [cited 2023 Oct 10]. Available from: <https://www.nist.gov/pml/xcom-photon-cross-sections-database> doi: 10.18434/T48G6X
14. Ivanchenko VN, Incerti S, Allison J, et al. Geant4 electromagnetic physics: improving simulation performance and accuracy. In: Caruge D, Calvin C, Diop CM, Malvagi F, Trama JC, editors. *SNA + MC 2013 — Joint International Conference on Supercomputing in Nuclear Applications + Monte Carlo*. doi: 10.1051/snmc/201403101
15. Behlouli A, Visvikis D, Bert J. Improved Woodcock tracking on Monte Carlo simulations for medical applications. *Physics in Medicine & Biology*. 2018;63(22):225005. doi: 10.1088/1361-6560/aae937
16. Shepp LA, Vardi Y. Maximum Likelihood Reconstruction for Emission Tomography. *IEEE Transactions on Medical Imaging*. 1982;1(2):113–122. doi: 10.1109/TMI.1982.4307558
17. Nuyts J, Mortelmans L, Suetens P, Oosterlinck A, de Rou M. Model-based quantification of myocardial perfusion images from SPECT. *Journal of nuclear medicine*. 1989;30(12):1992–2001.
18. Okuda K, Nakajima K, Hosoya T, et al. Quantification of myocardial perfusion SPECT using freeware package (cardioBull). *Annals of Nuclear Medicine*. 2011;25(8):571–579. doi: 10.1007/s12149-011-0504-0
19. Ploskikh V, Kotina E. Challenges of gated myocardial perfusion SPECT processing. *Cybernetics and Physics*. 2021;10(3):171–177. doi: 10.35470/2226-4116-2021-10-3-171-177
20. Turco A, Nuyts J, Gheysens O, et al. Lesion quantification and detection in myocardial 18F-FDG PET using edge-preserving priors and anatomical information from CT and MRI: a simulation study. *EJNMMI Physics*. 2016;3(1):9. doi: 10.1186/s40658-016-0145-4
21. Verberne HJ, Acampa W, Anagnostopoulos C, et al. EANM procedural guidelines for radionuclide myocardial perfusion imaging with SPECT and SPECT/CT: 2015 revision. *European Journal of Nuclear Medicine and Molecular Imaging*. 2015;42(12):1929–1940. doi: 10.1007/s00259-015-3139-x
22. Garcia EV, Slomka P, Moody JB, Germano G, Ficaro EP. Quantitative Clinical Nuclear Cardiology, Part 1: Established Applications. *Journal of Nuclear Medicine*. 2019;60(11):1507–1516. doi: 10.2967/jnumed.119.229799
23. Ansheles AA. Specific features of interpretation of myocardial perfusion single-photon emission computed tomography with computed tomographic absorption correction. *Journal of Radiology and Nuclear Medicine (Vestnik rentgenologii i radiologii)*. 2014;(2):5–20. (In Russ). doi: 10.20862/0042-4676-2014-0-2-5-20

СПИСОК ЛИТЕРАТУРЫ

1. Аншелес А.А., Сергиенко В.Б. Ядерная Кардиология / под ред. В.Б. Сергиенко. Москва : Издательство ФГБУ «НМИЦ кардиологии» Минздрава России, 2021.
2. Ficaro E, Lee B, Kritzman J, Corbett J. Corridor4DM: The Michigan method for quantitative nuclear cardiology // *Journal of Nuclear Cardiology*. 2007. Vol. 14, N 4. P. 455–465. doi: 10.1016/j.nuclcard.2007.06.006

3. Garcia E., Faber T., Cooke C., et al. The increasing role of quantification in clinical nuclear cardiology: The Emory approach // *Journal of Nuclear Cardiology*. 2007. Vol. 14, N 4. P. 420–432. doi: 10.1016/j.nuclcard.2007.06.009
4. Germano G., Kavanagh P., Slomka P., et al. Quantitation in gated perfusion SPECT imaging: The Cedars-Sinai approach // *Journal of Nuclear Cardiology*. 2007. Vol. 14, N 4. P. 433–454. doi: 10.1016/j.nuclcard.2007.06.008
5. Wolak A. Quantitative myocardial-perfusion SPECT: Comparison of three state-of-the-art software packages // *Journal of Nuclear Cardiology*. 2008. Vol. 15, N 1. P. 27–34. doi: 10.1016/j.nuclcard.2007.09.020
6. Germano G. Quantitative measurements of myocardial perfusion and function from SPECT (and PET) studies depend on the method used to perform those measurements // *Journal of Nuclear Cardiology*. 2018. Vol. 25, N 3. P. 925–928. doi: 10.1007/s12350-016-0757-z
7. Abadi E., Segars W.P., Tsui B.M.W., et al. Virtual clinical trials in medical imaging: a review // *Journal of Medical Imaging*. 2020. Vol. 7, N 4. P. 1. doi: 10.1117/1.JMI.7.4.042805
8. Denisova N.V., Ansheles A.A. A study of false apical defects in myocardial perfusion imaging with SPECT/CT // *Biomedical Physics & Engineering Express*. 2018. Vol. 4, N 6. P. 065018. doi: 10.1088/2057-1976/aae414
9. Denisova N., Ondar M., Kertesz H., Beyer T. Development of anthropomorphic mathematical phantoms for simulations of clinical cases in diagnostic nuclear medicine // *Computer Methods in Biomechanics and Biomedical Engineering: Imaging & Visualization*. 2023. Vol. 11, N 3. P. 433–441. doi: 10.1080/21681163.2022.2074308
10. Denisova N.V. Computational Phantoms for Medical Radiology // *Medical Radiology and Radiation Safety*. 2022. Vol. 67, N 6. P. 51–61. doi: 10.33266/1024-6177-2022-67-6-51-61
11. Синельников Р.Д., Синельников А.Я., Синельников Я.Р. Атлас Анатомии Человека. Том второй. Москва : Новая волна, 2022.
12. Patton J.A., Turkington T.G. SPECT/CT Physical Principles and Attenuation Correction. *Journal of Nuclear Medicine Technology*. 2008. Vol. 36, N 1. P. 1–10. doi: 10.2967/jnmt.107.046839
13. Seltzer S. XCOM-Photon Cross Sections Database [Internet]. Gaithersburg (MD) : NIST Standard Reference Database 8. [дата обращения: 15.10.2023]. Доступ по ссылке: <https://www.nist.gov/pml/xcom-photon-cross-sections-database> doi: 10.18434/T48G6X
14. Ivanchenko V.N., Incerti S., Allison J., et al. Geant4 electromagnetic physics: improving simulation performance and accuracy. In: Caruge D., Calvin C., Diop C.M., Malvagi F., Trama J.C., editors. *SNA + MC 2013 — Joint International Conference on Supercomputing in Nuclear Applications + Monte Carlo*. EDP Sciences; 2014:03101. doi:10.1051/snmc/201403101
15. Behloul A., Visvikis D., Bert J. Improved Woodcock tracking on Monte Carlo simulations for medical applications // *Physics in Medicine & Biology*. 2018. Vol. 63, N 22. P. 225005. doi: 10.1088/1361-6560/aae937
16. Shepp L.A., Vardi Y. Maximum Likelihood Reconstruction for Emission Tomography // *IEEE Transactions on Medical Imaging*. 1982. Vol. 1, N 2. P. 113–122. doi: 10.1109/TMI.1982.4307558
17. Nuyts J., Mortelmans L., Suetens P., Oosterlinck A., de Rou M. Model-based quantification of myocardial perfusion images from SPECT // *Journal of nuclear medicine*. 1989. Vol. 30, N 12. P. 1992–2001.
18. Okuda K., Nakajima K., Hosoya T., et al. Quantification of myocardial perfusion SPECT using freeware package (cardioBull) // *Annals of Nuclear Medicine*. 2011. Vol. 25, N 8. P. 571–579. doi: 10.1007/s12149-011-0504-0
19. Ploskikh V., Kotina E. Challenges of gated myocardial perfusion SPECT processing // *Cybernetics and Physics*. 2021. Vol. 10, N 3. P. 171–177. doi: 10.35470/2226-4116-2021-10-3-171-177
20. Turco A., Nuyts J., Gheysens O., et al. Lesion quantification and detection in myocardial 18F-FDG PET using edge-preserving priors and anatomical information from CT and MRI: a simulation study // *EJNMMI Physics*. 2016. Vol. 3, N 1. P. 9. doi: 10.1186/s40658-016-0145-4
21. Verberne H.J., Acampa W., Anagnostopoulos C., et al. EANM procedural guidelines for radionuclide myocardial perfusion imaging with SPECT and SPECT/CT: 2015 revision // *European Journal of Nuclear Medicine and Molecular Imaging*. 2015. Vol. 42, N 12. P. 1929–1940. doi: 10.1007/s00259-015-3139-x
22. Garcia E.V., Slomka P., Moody J.B., Germano G., Ficaro E.P. Quantitative Clinical Nuclear Cardiology, Part 1: Established Applications // *Journal of Nuclear Medicine*. 2019. Vol. 60, N 11. P. 1507–1516. doi: 10.2967/jnumed.119.229799
23. Аншелес А.А. Особенности интерпретации перфузионной однофотонной эмиссионной компьютерной томографии миокарда с компьютерно-томографической коррекцией поглощения // *Вестник Рентгенологии и Радиологии*. 2014. № 2. С. 5–20. doi: 10.20862/0042-4676-2014-0-2-5-20

AUTHORS' INFO

* **Natalya V. Denisova**, Dr. Sci. (Phys.-Math.),
Professor;
address: 7-47 Zolotodolinskaya Str., 630090, Novosibirsk,
Russian Federation;
ORCID: 0000-0001-9374-1753;
eLibrary SPIN: 4928-8185;
e-mail: NVDenisova2011@mail.ru

Mikhail A. Gurko;
ORCID: 0000-0002-6154-172X;
eLibrary SPIN: 3214-5765;
e-mail: m.gurko@g.nsu.ru

ОБ АВТОРАХ

* **Денисова Наталья Васильевна**, д-р физ.-мат. наук,
профессор;
адрес: Российская Федерация, г. Новосибирск, 630090,
ул. Золотолинская, д. 7-47;
ORCID: 0000-0001-9374-1753;
eLibrary SPIN: 4928-8185;
e-mail: NVDenisova2011@mail.ru

Гурко Михаил Адамович;
ORCID: 0000-0002-6154-172X;
eLibrary SPIN: 3214-5765;
e-mail: m.gurko@g.nsu.ru

* Corresponding author / Автор, ответственный за переписку

Inna P. Kolinko;

ORCID: 0009-0001-6779-1535;
eLibrary SPIN: 1625-6043;
e-mail: kiina131313@gmail.com

Alexey A. Ansheles, MD, Dr. Sci. (Med.), Assistant Professor;

ORCID: 0000-0002-2675-3276;
eLibrary SPIN: 7781-6310;
e-mail: aansheles@gmail.com

Vladimir B. Sergienko, MD, Dr. Sci. (Med.), Professor;

ORCID: 0000-0002-0487-6902;
eLibrary SPIN: 4918-3443;
e-mail: aansheles@gmail.com

Колинко Инна Павловна;

ORCID: 0009-0001-6779-1535;
eLibrary SPIN: 1625-6043;
e-mail: kiina131313@gmail.com

Аншелес Алексей Аркадьевич, д-р мед. наук, доцент;

ORCID: 0000-0002-2675-3276;
eLibrary SPIN: 7781-6310;
e-mail: aansheles@gmail.com

Сергиенко Владимир Борисович, д-р мед. наук, профессор;

ORCID: 0000-0002-0487-6902;
eLibrary SPIN: 4918-3443;
e-mail: aansheles@gmail.com

DOI: <https://doi.org/10.17816/DD568668>

Скорость вымывания ^{99m}Tc -метокси-изобутил-изонитрила как маркёр митохондриальной дисфункции миокарда: систематический обзор и метаанализ

М.О. Гуля, К.В. Завадовский

Научно-исследовательский институт кардиологии, Томский национальный исследовательский медицинский центр, Томск, Российская Федерация

АННОТАЦИЯ

Обоснование. В обзоре изложены особенности фармакокинетики перфузионного радиофармпрепарата ^{99m}Tc -MIBI, которые позволяют оценить митохондриальную дисфункцию миокарда, а также показаны основные клинические точки приложения феномена ускоренного вымывания данного индикатора.

Цель. Систематизация данных фундаментальных (экспериментальных) и клинических исследований в области изучения и оценки митохондриальной дисфункции по результатам перфузионной сцинтиграфии миокарда; проведение метаанализа клинических исследований в данной области.

Материалы и методы. Поиск проводился в базах данных Pubmed, Scopus, Google Scholar и eLibrary до середины 2023. Были использованы ключевые слова, их комбинации и англоязычные аналоги: митохондриальная дисфункция, ^{99m}Tc -МИБИ, ^{99m}Tc -Тетрофосмин, перфузионная сцинтиграфия миокарда, обратное перераспределение, вымывание, скорость вымывания. При выполнении метаанализа для расчёта средней оценки разницы была использована модель случайных эффектов.

Результаты. Для систематического анализа было отобрано 40 статей: 13 — экспериментальные, 24 — оригинальные клинические работы, 2 — клинические случаи, 1 обзор. Для выполнения метаанализа было отобрано 6 исследований по дизайну «случай–контроль». Общее число пациентов, составивших основу систематического обзора, — 551; число пациентов, составивших основу метаанализа — 196. Анализ литературы показал, что выраженность феномена обратного перераспределения и скорость вымывания ^{99m}Tc -MIBI взаимосвязаны с микроструктурой митохондрий и миокарда, сократимостью и гемодинамикой левого желудочка, уровнем натрийуретических пептидов, толерантностью к физическим нагрузкам, тяжестью коронарного атеросклероза, окислительным метаболизмом миокарда, уровнем риска сердечно-сосудистых событий. Метаанализ показал, что скорость вымывания статистически значимо повышена у лиц с патологией сердца, по отношению к контролю (средняя оценка разницы 9,5771 (95% доверительный интервал: от 6,6001 до 12,5540; $z=6,3053$; $p < 0,0001$).

Заключение. Оценка функции митохондрий по данным оценки вымывания ^{99m}Tc -MIBI может предоставить дополнительные сведения о функциональном состоянии сердечной мышцы.

Ключевые слова: митохондриальная дисфункция; ^{99m}Tc -МИБИ; ^{99m}Tc -Тетрофосмин; перфузионная сцинтиграфия миокарда; обратное перераспределение; скорость вымывания; кардиомиопатии; хроническая сердечная недостаточность; ишемическая болезнь сердца

Как цитировать:

Гуля М.О., Завадовский К.В. Скорость вымывания ^{99m}Tc -метокси-изобутил-изонитрила как маркёр митохондриальной дисфункции миокарда: систематический обзор и метаанализ // Digital Diagnostics. 2023. Т. 4, № 4. С. 509–528. DOI: <https://doi.org/10.17816/DD568668>

DOI: <https://doi.org/10.17816/DD568668>

99mTc-MIBI washout rate as a marker of myocardial mitochondrial dysfunction: A systematic review and meta-analysis

Marina O. Gulya, Konstantin V. Zavadovsky

Cardiology Research Institute, Tomsk National Research Medical Center, Tomsk, Russian Federation

ABSTRACT

BACKGROUND: This review outlines the features of the pharmacokinetics of the perfusion radiopharmaceutical 99mTc-MIBI, which allows the assessment of myocardial mitochondrial dysfunction, and shows the main clinical applications of the phenomenon of increased 99mTc-MIBI washout rate.

AIM: To systematize the data of fundamental (experimental) and clinical studies evaluating and estimating mitochondrial dysfunction according to myocardial perfusion scintigraphy data and perform meta-analysis of clinical studies in this field.

MATERIALS AND METHODS: PubMed, Scopus, Google Scholar, and eLibrary databases were searched until mid-2023. The following keywords, their combinations, and Russian-language counterparts were used: mitochondrial dysfunction, 99mTc-MIBI, 99mTc-Tetrofosmin, myocardial perfusion scintigraphy, reverse redistribution, washout, and washout rate. In the meta-analysis, a random-effects model was used to calculate the mean difference estimate.

RESULTS: Forty articles were selected for systematic analysis: 13 were experimental, 24 were original clinical papers, 2 were clinical cases, and 1 was a review. Six studies using a case-control design were selected for the meta-analyses. The total number of patients in the systematic review and meta-analysis were 551 and 196, respectively. In the analysis of the literature, the severity of the reverse redistribution phenomenon and 99mTc-MIBI washout rate correlated with mitochondrial and myocardial microstructure, left ventricular contractility and hemodynamics, natriuretic peptide levels, exercise tolerance, coronary atherosclerosis severity, myocardial oxidative metabolism, and risk of cardiovascular events. The meta-analysis showed that the washout rate was statistically significantly accelerated in individuals with cardiac pathologies, relative to controls (mean difference score, 9.5771 [95%]; confidence interval, 6.6001–12.5540; $z=6.3053$, $p < 0.0001$).

CONCLUSION: The assessment of mitochondrial function by 99mTc-MIBI washout evaluation may provide additional insights into the functional status of cardiac muscles.

Keywords: mitochondrial dysfunction; 99mTc-MIBI; 99mTc-Tetrofosmin; myocardial perfusion scintigraphy; reverse redistribution; washout rate; cardiomyopathies; congestive heart failure; ischemic heart disease

To cite this article:

Gulya MO, Zavadovsky KV. 99mTc-MIBI washout rate as a marker of myocardial mitochondrial dysfunction: A systematic review and meta-analysis. *Digital Diagnostics*. 2023;4(4):509–528. DOI: <https://doi.org/10.17816/DD568668>

Received: 22.08.2023

Accepted: 11.09.2023

Published online: 10.10.2023

DOI: <https://doi.org/10.17816/DD568668>

99m锝-甲氧基异丁基异腓 (99mTc-MIBI) 洗脱率作为心肌线粒体功能障碍的标志物；系统综述和荟萃分析

Marina O. Gulya, Konstantin V. Zavadovsky

Cardiology Research Institute, Tomsk National Research Medical Center, Tomsk, Russian Federation

简评

论证。本综述概述了灌注放射性药物99mTc-MIBI的药代动力学特征。这些特征可被用于评估心肌线粒体功能障碍。综述还说明了该指标加速洗脱现象的临床应用要点。

该研究的目的是系统整理关于通过心肌灌注闪烁成像研究和评估线粒体功能障碍领域的基础（实验）和临床研究数据；对该领域的临床研究进行荟萃分析。

材料与方法。检索是在Pubmed、Scopus、Google Scholar和eLibrary数据库中进行的，检索期截至2023年年中。使用的关键词及其组合和英文对应词包括：线粒体功能障碍、99mTc-MIBI、99m锝-替曲膦、心肌灌注闪烁成像、反向再分布、洗脱、洗脱率。在进行荟萃分析时，采用了随机效应模型来计算平均差异估计值。

结果。我们一共选中了40篇文章，以进行系统分析：其中13篇为实验性文章，24篇为临床医学论文，2篇为临床病例，1篇为综述。我们一共选中了6项研究，以进行病例对照模型的荟萃分析。系统综述中的患者总人数为551人；荟萃分析中的患者人数为196人。文献分析显示了，反向再分布现象的严重程度和99mTc-MIBI洗脱率与线粒体和心肌微结构、左室收缩力和血流动力、利尿钠肽水平、运动耐量、冠状动脉粥样硬化严重程度、心肌氧化代谢和心血管事件风险水平相关。荟萃分析表明了，与对照组相比，心脏病变受试者的洗脱率在统计学上显著较高。平均差异估计值为9.5771（95%置信区间：6.6001至12.5540； $z=6.3053$ ； $p<0.0001$ ）。

结论。通过99mTc-MIBI洗脱评估对线粒体功能进行评估，可为了解心肌功能状态提供更多信息。

关键词：线粒体功能障碍；99mTc-MIBI；99m锝-替曲膦；心肌灌注闪烁成像；反向再分布；洗脱率；心肌病；慢性心力衰竭；缺血性心脏病。

引用本文：

Gulya MO, Zavadovsky KV. 99m锝-甲氧基异丁基异腓 (99mTc-MIBI) 洗脱率作为心肌线粒体功能障碍的标志物；系统综述和荟萃分析. *Digital Diagnostics*. 2023;4(4):509–528. DOI: <https://doi.org/10.17816/DD568668>

收到: 22.08.2023

接受: 11.09.2023

发布日期: 10.10.2023

Abbreviations

¹²³I-BMIPP: iodine-123 labeled β-methyl iodophenyl pentadecanoic acid

¹²³I-MIBG: ¹²³I-metaiodobenzylguanidine

^{99m}Tc-MIBI: iodine-123-labeled metaiodobenzylguanidine

ACS: acute coronary syndrome

AMI: acute myocardial infarction

CAD: coronary artery disease

CHF: chronic heart failure

DCM: dilated cardiomyopathy

HCM: hypertrophic cardiomyopathy

LV: left ventricular

MD: mitochondrial dysfunction

MPS: myocardial perfusion scintigraphy

RR: reverse redistribution

SPECT: single-photon emission computed tomography

WR: washout rate

BACKGROUND

Cardiovascular diseases are the leading cause of morbidity and mortality [1]. Among cardiovascular diseases, acute and chronic coronary syndromes and chronic heart failure (CHF) are the leading causes of disability.

The pathophysiology of coronary artery disease (CAD) is influenced by coronary atherosclerosis, progressive lumen narrowing, and myocardial ischemia.

The pathogenesis of CHF is more complex and is largely determined by etiology. The most common manifestation of CHF is reduced left ventricular (LV) contractility. The pathogenesis of both diseases is influenced by mitochondrial function. Mitochondria are vital organelles that control cell energy metabolism and overall homeostasis. A steady energy supply is required to maintain the contractile activity of the human heart. Myocardial mitochondria perform the most difficult task of producing approximately 30 kg of adenosine triphosphate per day to keep the heart pumping [2]. To meet this requirement, the following aspects are necessary:

- Continuous supply of the substrate to the mitochondria is ensured.
- Mitochondria have sufficient oxidative capacity.
- The cell has an effective system for transporting adenosine triphosphate from the mitochondria to the consumption sites [3].

The transmembrane potential is one of the main parameters representing mitochondrial function [4]. Under normal conditions, mitochondria have the largest negative charge (in absolute value) of all intracellular organelles and serve as a destination for charged lyophilic molecules entering the cell via the sarcolemma. Retention of these substances in the cell is proportional to the transmembrane potential of mitochondria. Consequently, a reduction in the transmembrane potential decreases the accumulation of these substances. Various diagnostic agents (mainly dyes) are available for assessing mitochondrial function *in vitro*. However, few diagnostic agents are used for assessing mitochondria *in vivo*.

The search for new tools for assessing mitochondrial function appears to be a pressing issue in modern

cardiology and X-ray diagnosis. The monovalent lipophilic cation technetium-99m methoxy isobutyl isonitrile (also known as technetium (99mTc) sestamibi, or 99mTc-MIBI) is a widely used diagnostic agent for myocardial perfusion imaging. Unlike other *in vivo* diagnostic agents, this drug accumulates in cardiomyocyte mitochondria based on their membrane potential [5]. A decrease in mitochondrial function in cardiomyocytes results in a decrease in mitochondrial internal matrix potential, followed by an increase in radiopharmaceutical clearance. Thus, accelerated 99mTc-MIBI washout suggests mitochondrial functional abnormalities. In addition to 99mTc-MIBI, technetium tetrofosmin (99mTc-TF) can be used.

The mechanism of accumulation of various diagnostic agents in the myocardium is schematically depicted in Figure 1.

Moreover, no reviews exist in the Russian-language literature on the use of myocardial perfusion scintigraphy (MPS) with 99mTc-MIBI to identify and characterize mitochondrial dysfunction (MD, damage).

PURPOSE

To systematize experimental and clinical findings in the examination and assessment of MD according to MPS and conduct a meta-analysis of clinical studies on this topic.

LITERATURE SEARCH METHODS

The review was performed according to the Preferred Reporting Items for Systematic Reviews and Meta-Analyses protocol [6]. To analyze available data on MD in cardiovascular diseases, a systematic literature search was performed in PubMed, Scopus, Google Scholar, and eLibrary databases using the following keywords, their combinations, and English-language analogs: mitochondrial dysfunction, 99mTc-MIBI, 99mTc-TF, myocardial perfusion scintigraphy, reverse redistribution, and washout rate (WR).

The search was performed from the database inception until the middle of 2023 and included all studies published

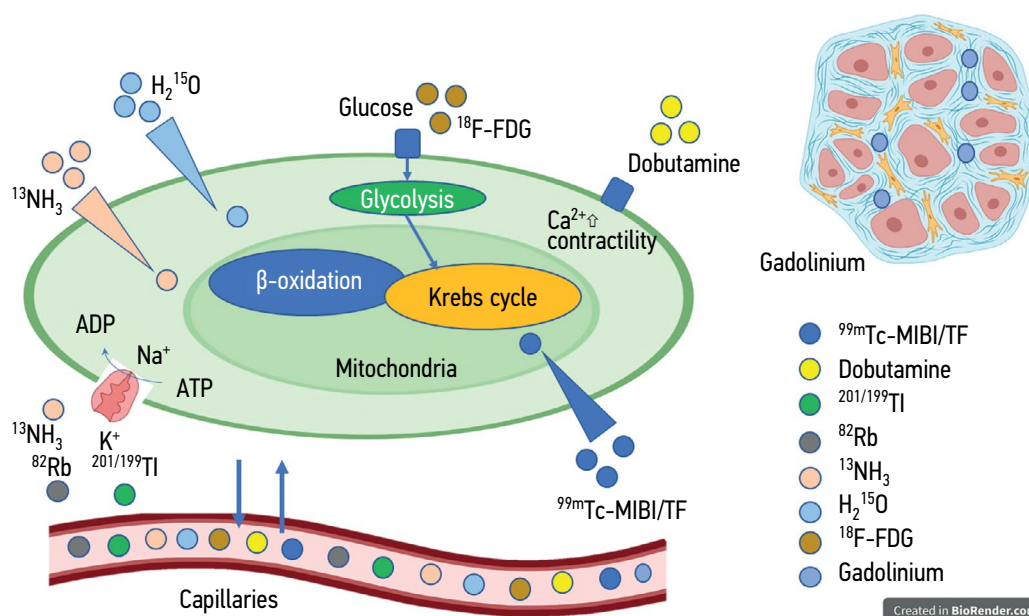


Fig. 1. Schematic depiction of the mechanism of the accumulation of various diagnostic agents in the cell and intercellular space. $^{201/199}\text{Tl}$: thallium-201 or thallium-199; its uptake is determined by membrane integrity and normal functioning of the Na^+/K^+ pump. ^{82}Rb : rubidium-82; its uptake is also determined by the Na^+/K^+ pump. $^{99\text{m}}\text{Tc-MIBI/TF}$ -based tracers: lipophilic cations that freely pass through the mitochondrial membrane and are retained because of the transmembrane potential. Dobutamine stimulates β_1 and β_2 adrenergic receptors, increasing the intracellular calcium concentration and inotropic function of the heart. $^{18}\text{F-FDG}$: fluorodeoxyglucose accumulates in the cell via the glucose transporter protein. $^{13}\text{NH}_3$: ammonium is accumulated via passive diffusion and active transport of the Na^+/K^+ pump. H_2^{15}O : oxygen-15 labeled water readily diffuses into the cell, forming an equilibrium between the extracellular and intracellular pools. Gadolinium is an extracellular diagnostic agent that is retained in the intercellular space.

up to that date. Further analysis included studies in which MPS with $^{99\text{m}}\text{Tc-MIBI}$ or $^{99\text{m}}\text{Tc-TF}$ was used to assess MD in various cardiovascular diseases. The following articles were excluded: articles in which MD was mentioned in the references, articles in languages other than English and Russian, and articles examining the washout of $^{99\text{m}}\text{Tc-MIBI}$ (or $^{99\text{m}}\text{Tc-TF}$) in cancer and other disorders not associated with cardiovascular diseases. In total, 40 articles were selected based on these criteria. These included 13 experimental studies, 24 original clinical studies, 2 clinical cases, and 1 review. A meta-analysis was performed for case-control studies using Jamovi v. 2.4.2 (The Jamovi Project, Australia) and the expansion module MAJOR v. 1.2.1. During the meta-analysis, a random-effects model was used to calculate the mean difference.

EXPERIMENTAL STUDIES

The $^{99\text{m}}\text{Tc-MIBI}$ is used for noninvasive imaging of myocardial perfusion. This radiopharmaceutical is currently the most widely used diagnostic agent for MPS in Russia and worldwide [7, 8]. A tracer enters the cell via the cardiomyocyte sarcolemma and accumulates in negatively charged mitochondria in proportion to the transmembrane gradient [9]. In an experimental study on a culture of chicken heart cells, electron microscopy and electron microprobe

analysis revealed that approximately 90% of the drug binds to the mitochondria as an energy-dependent free cationic complex [10].

In an experimental study in which cardiomyocyte cell cultures were exposed to various mitochondrial and plasma membrane potential inhibitors, the drug primarily accumulated in mitochondria and did not accumulate in the cytoplasm, owing to the significantly higher electrical potential of the mitochondrial membrane [9]. Further retention of the tracer depends on the membrane potential, as demonstrated in an experiment using an artificial respiratory chain uncoupler carbonyl cyanide *m*-chlorophenyl hydrazone, which causes a rapid decrease in $^{99\text{m}}\text{Tc-MIBI}$ concentration.

In an *in vitro* experiment on the subcellular fraction of mitochondria, P. Crane et al. revealed that increasing the concentration of calcium ions causes faster $^{99\text{m}}\text{Tc-MIBI}$ washout from the mitochondria [11]. In ischemia models with ischemic cardiomyocytes overloaded with calcium ions, $^{99\text{m}}\text{Tc-MIBI}$ washout is a marker of mitochondrial damage. In an ischemia-reperfusion model on isolated rat hearts, K. Fukushima et al. [12] demonstrated that $^{99\text{m}}\text{Tc-MIBI}$ washout increases during mild ischemia and is more pronounced during severe ischemia.

Thus, accelerated $^{99\text{m}}\text{Tc-MIBI}$ washout from the myocardium is associated with impaired mitochondrial function and cardiomyocyte damage.

IN VIVO ASSESSMENT OF MD USING MYOCARDIAL PERFUSION SCINTIGRAPHY

For the in vivo detection of MD, early and delayed planar or tomographic perfusion imaging is used. Early imaging is performed for 30 min [13] to 1 h [14] after a radiopharmaceutical injection; delayed imaging is performed for 3–4 h [15]. Typically, imaging is performed at rest. The radiopharmaceutical dose is 370–470 MBq, which is similar to the dose used for conventional MPS [16]. The MD visual pattern is a defect in tracer uptake that occurs (or intensifies) during delayed perfusion single-photon emission computed tomography (SPECT) of the myocardium: the so-called reverse redistribution (RR) of a radiopharmaceutical occurs. Thus, a generally accepted technique is used to determine the size of the perfusion defect.

The second parameter of MD assessment is the heart-to-mediastinum ratio (HM). It is determined using the average number of pulses in the area of interest (heart and mediastinum, respectively) according to the anterior planar scintigraphy images.

Moreover, the global clearance or WR of ^{99m}Tc -MIBI was calculated as the ratio of radiotracer uptake in the heart area on early and delayed planar scintigraphy images. Some authors have used the number of pulses in the heart area minus the number of pulses in the mediastinum [14]. Furthermore, some authors consider the half-life of ^{99m}Tc (6.04 h) into account when determining WR. A few studies have examined the ^{99m}Tc -MIBI WR by LV regions [18].

The normal values for people aged 50 ± 13 years are as follows:

- WR: $11\% \pm 5\%$
- Early HM: 3.5 ± 0.3
- Delayed HM: 3.1 ± 0.3 [14, 19]

The pathological pattern was accelerated ^{99m}Tc -MIBI washout from the myocardium, similar to the study with ^{123}I -metaiodobenzylguanidine (^{123}I -MIBG, a marker of cardiac sympathetic activity). The main clinical studies of mitochondrial damage based on MPS with ^{99m}Tc -MIBI are presented in Table 1.

MD ASSESSMENT IN CAD

Acute coronary syndrome (ACS)

RR and accelerated washout of ^{99m}Tc -MIBI are observed in patients with ACS. Y. Takeishi et al. [20] quantified the regional patterns of ^{99m}Tc -MIBI distribution in patients with ACS 7 days after successful primary angioplasty. In symptom-related artery areas, 68% of patients had accelerated washout of the radiopharmaceutical, whereas the remaining had stable perfusion defects. Coronary angiography 1 month after ACS revealed patency of the symptom-related artery in accelerated washout areas in 100% of cases. The pathological mobility of the myocardial

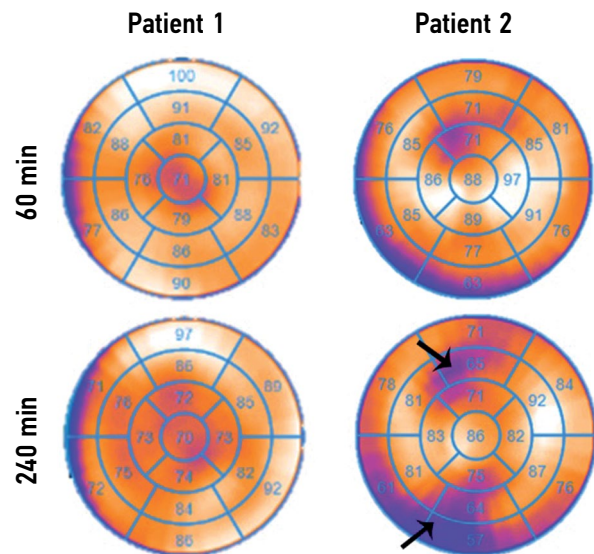


Fig. 2. An example of the absence and presence of ^{99m}Tc -MIBI reverse redistribution. Patient 1: female, 56 years old, CAD (grade II stable angina) secondary to nonobstructive coronary atherosclerosis; CHF, NYHA class II; LV ejection fraction, 64%; end-systolic volume, 42 mL; end-diastolic volume, 117 mL. Delayed imaging (240 min) revealed no perfusion defects. Patient 2: male, 58 years old; CAD (grade II stable angina); anterior descending artery stenosis, 75%; right coronary artery stenosis, 70%; CHF, NYHA class II; LV ejection fraction, 65%; end-systolic volume, 39 mL; end-diastolic volume, 112 mL. Delayed imaging (240 min) revealed perfusion defects (arrows) that were not detected during early imaging (60 min). Images were obtained at the Research Institute of Cardiology, Tomsk National Research Medical Center.

wall was less pronounced than that in patients with stable defects (-2.6 ± 0.4 and -3.4 ± 0.6 , respectively; $P < 0.01$). The authors concluded that accelerated washout is a marker of postischemic myocardial stunning and, a predictor of myocardial contractility restoration within a month following reperfusion.

S. Fujiwara et al. [21] sought to detect viable myocardium in patients with ACS by identifying RR areas and accelerating regional washout of ^{99m}Tc -MIBI. We assessed the functional characteristics of myocardial segments with ^{99m}Tc -MIBI RR in 30 patients after percutaneous coronary intervention for acute myocardial infarction (AMI). The findings of myocardial perfusion SPECT were compared with those of low-dose dobutamine stress echocardiography: $5\text{--}10 \text{ mg}/(\text{kg} \times \text{min})$.

In this sample of 250 myocardial segments, 41% were in the infarct-related artery zone, with only 22% demonstrating accelerated radiopharmaceutical washout. Accelerated washout was significantly more common in segments in the infarct-related artery zone. According to stress echocardiography findings, practically all RR segments (96%) and only 70% of non-RR segments had impaired contractility at rest. Dobutamine infusion improved contractility in 83%

Table 1. Main clinical studies of mitochondrial damage based on myocardial perfusion scintigraphy using 99mTc-MIBI

1	2	3	4	5	6	7	8
Authors	Underlying condition	Number of patients	LV ejection fraction (%)	Time of early and delayed imaging	Washout rate calculation formula	Washout rate (%)	Main conclusion
S. Fujiwara et al., 2001 [21]	ACS	30	Acute phase: patients with RR: 55 ± 7 patients without RR: 54 ± 9 After 1 month: patients with RR: 59 ± 8 patients without RR: 58 ± 12	Early: 60 minutes; Delayed: 3 h	Adjustment for the count in the mediastinum: no Adjustment for T1/2 of 99mTc: yes	Normal segments: 15; Ischemic segments without RR: 18; Ischemic segments with RR: 30	RR suggests reversible functional disorders associated with dobutamine-induced contractile reserve preservation. Early and delayed imaging with 99mTc-MIBI provides useful information on the residual viability of dysfunctional myocardium in patients with AMI
A. Masuda et al., 2016 [13]	ACS	19	56.5 ± 9.5	Early: 30 min; Delayed: 3 h	Differences in perfusion defect scores were assessed	No data are available	In patients with ACS, myocardial segments with accelerated 99mTc-MIBI washout showed a decrease in oxidative metabolism. 99mTc-MIBI washout can be associated with MD
Y. Chen et al., 2022 [23]	ACS	1	63	A series of 7 images from injection to the 7th minute post-injection	No data are available	Up to 31	Serial changes in 99mTc-MIBI WR during dynamic myocardial perfusion SPECT may help assess MD and severity of myocardial ischemia in ACS
T. Kato et al., 2022 [24]	ACS	165	54.5 ± 8.6	Early: 60 minutes; Delayed: 4 h	Differences in TPD were assessed	No data are available	Accelerated 99mTc-MIBI washout can predict exercise tolerance in patients with ACS
B. Du et al., 2014 [18]	Stable CAD	CAD: 8 Control: 10	-	Early: 90 minutes; Delayed: 4 h	Adjustment for the count in the mediastinum: no Adjustment for T1/2 of 99mTc: no	Three-vessel CAD: 21.1 ± 4.6 Control: 9.5 ± 4.9 P < 0.001	In patients with impaired mitochondrial function due to three-vessel CAD, the global and regional 99mTc-MIBI WRs were consistently higher than those in healthy volunteers. Global 99mTc-MIBI WR is a sensitive parameter for severity stratification in patients with advanced coronary atherosclerosis
M.O.M. Othman et al., 2021 [15]	Stable CAD	100	No data are available	Early: 60–90 min; Delayed: 4 h	Adjustment for the count in the mediastinum: no Adjustment for T1/2 of 99mTc: yes	Low-risk group: 7.9 Intermediate-risk group: 15.1 High-risk group: 19.3	The global 99mTc-MIBI WR positively correlated with the risk stratification in patients with stable CAD. It can be used as an additional parameter for risk assessment

Table 1. Continued

1	2	3	4	5	6	7	8
Authors	Underlying condition	Number of patients	LV ejection fraction (%)	Time of early and delayed imaging	Washout rate calculation formula	Washout rate (%)	Main conclusion
S. Kumita et al., 2002 [33]	Nonischemic CHF	CHF: 28 Control: 8	CHF: 43.2 ± 15.7 Control: 67.0 ± 11.8	Early: 30 min; Delayed: 3 h	Adjustment for the count in the mediastinum: yes Adjustment for T1/2 of 99mTc: no	CHF: 39.6 ± 5.2 Control: 31.2 ± 5.5 P < 0.01	Myocardial 99mTc-MIBI WR is considered a new marker for the diagnosis of myocardial injury in patients with CHF
T. Sugijura et al., 2006 [34]	Dilated cardiomyopathy	DCM: 17 Control: 10	DCM: 37.4 ± 11.1 Control: 61.3 ± 9.4	Early: 60 minutes; Delayed: 3 h	Adjustment for the count in the mediastinum: yes Adjustment for T1/2 of 99mTc: no	DCM: 31.2 ± 6.3 Control: 25.2 ± 4.7 P < 0.05	Scintigraphy using 99mTc-MIBI is a valuable tool for assessing the severity of congestive heart failure
S. Matsuo et al., 2007 [35]	Nonischemic CHF	CHF: 61 Control: 7	CHF: 48 ± 15 Control: 73 ± 7	Early: 30 min; Delayed: 3 h	Adjustment for the count in the mediastinum: no Adjustment for T1/2 of 99mTc: yes	CHF: 28.2 ± 5 Control: 22.9 ± 4.1 P < 0.01	99mTc-MIBI WR is a new diagnostic marker of myocardial injury that provides prognostic information for patients with heart failure
M.K. Shiroodi et al., 2010 [38]	DCM	DCM: 17 Control: 6	DCM: 28.8 ± 11.3 Control: 65.5 ± 5.26	Early: 30 min; Delayed: 3.5 h	Adjustment for the count in the mediastinum: no Adjustment for T1/2 of 99mTc: yes	DCM: 29.13 ± 6.68 Control: 14.17 ± 3.31 P = 0.001	The 99mTc-MIBI WR correlates with the functional parameters of the heart during MPS in patients with DCM. Scintigraphy with 99mTc-MIBI is a valuable molecular imaging tool for the diagnosis and severity assessment of myocardial injury or dysfunction in DCM
E.V. Migunova et al., 2020 [47]	Patients after heart transplantation (DCM)	2	Patient 1: 60 Patient 2: 61	Early: 60 minutes; Delayed: 4 h	Adjustment for the count in the mediastinum: no Adjustment for T1/2 of 99mTc: yes	Patient 1: 23.78–57.50; Patient 2: < 23.0	The washout rate can be a predictor of myocardial injury, which is important for follow-up in patients after heart transplantation
D. Hayashi et al., 2013 [14]	DCM	20	34 ± 9	Early: 60 minutes; Delayed: 4 h	Adjustment for the count in the mediastinum: yes Adjustment for T1/2 of 99mTc: yes	24.4 ± 8.4	In patients with DCM, accelerated 99mTc-MIBI washout can be a predictor of MD and myocardial contractile reserve impairment during a dobutamine stress test

Table 1. Ending

1	2	3	4	5	6	7	8
Authors	Underlying condition	Number of patients	LV ejection fraction (%)	Time of early and delayed imaging	Washout rate calculation formula	Washout rate (%)	Main conclusion
M. Yamanaka et al., 2021 [36]	Nonischemic CHF	25	49.4 ± 15.5	Early: 45 minutes; Delayed: 4 h	Visual analysis of segments during early and delayed imaging (quantitative assessment of the WR was not performed)	No data are available	In nonischemic CHF, MD is manifested at early stages by the washout of 99mTc-MIBI; fibrotic changes in the myocardium are detected at later stages using time-delayed contrast-enhanced cardiac MRI
M. Sun et al., 2008 [41]	HCM	HCM: 15 Control: 12	HCM: 54.47 ± 10.14 Control: 60.17 ± 4.0	Early: 10 min; Second early: 90 minutes; Delayed: 4 h	Adjustment for the count in the mediastinum: no Adjustment for T1/2 of 99mTc: no	HCM: 42.66 ± 3.30 Control: 31.27 ± 4.04 P < 0.01	The 99mTc-MIBI WR in the HCM group was significantly higher than that in the control group. 99mTc-MIBI WR correlates with hypertrophic LV wall thickness
S. Isobe et al., 2010 [42]	HCM	24	74.5 ± 5.6	Early: 40 min; Delayed: 4 h	Adjustment for the count in the mediastinum: yes Adjustment for T1/2 of 99mTc: yes	23.8 ± 4.8	Accelerated 99mTc-MIBI washout in HCM suggests myocardial degradation. The 99mTc-MIBI WR can be a valuable tool for the early detection of myocardial injury in HCM patients
M. Ikawa et al., 2006 [19]	Primary mitochondrial DNA mutation	5	44.4 ± 10.9	Early: 60 minutes; Delayed: 4 h	Adjustment for the count in the mediastinum: no Adjustment for T1/2 of 99mTc: no	21.2 ± 6.18	In mitochondrial cardiomyopathy, the combination of increased uptake of 123I-BMIPP with decreased uptake and accelerated 99mTc-MIBI washout may be a valuable tool for assessing the severity of MD and can be used for the differential diagnosis of mitochondrial cardiomyopathy.
M. Sarai et al., 2013 [43]	Cardiac sarcoidosis	11	Before therapy: 57 ± 19 After therapy: 58 ± 21 (NS)	Early: 60 minutes; Delayed: 4 h	Adjustment for the count in the mediastinum: no Adjustment for T1/2 of 99mTc: no	Before therapy: 25 ± 5 After therapy: 17 ± 5 P < 0.0001	The 99mTc-MIBI WR can be used to assess heart function in patients with sarcoidosis during steroid therapy. When assessing disease activity in mild myocardial injury during steroid therapy, quantitative assessment of 99mTc-MIBI WR is more useful than semiquantitative assessment (in points)

Note: ACS, acute coronary syndrome; AMI, acute myocardial infarction; CAD, coronary artery disease; CHF, chronic heart failure; DCM, dilated cardiomyopathy; DNA, deoxyribonucleic acid; HCM, hypertrophic cardiomyopathy; MD, mitochondrial dysfunction; MPS, myocardial perfusion scintigraphy; NS, not significant; RR, reverse redistribution; T1/2, half-life; TPD, total perfusion deficit.

of initially dysfunctional RR segments and 54% of non-RR segments. These findings suggest that accelerated 99mTc-MIBI washout is linked to the reversibility of functional myocardial contractility disorders. Early and delayed myocardial perfusion SPECT with 99mTc-MIBI can provide clinically valuable information on cardiomyocyte viability following AMI.

Accelerated 99mTc-MIBI washout was also observed in patients with vasospastic angina [22]. S. Ono et al. performed early and delayed myocardial perfusion SPECT with 99mTc-MIBI at rest in 39 patients with vasospastic angina confirmed by the ergometrine (ergonovine) test. Decreased uptake was found in 32 cases (82%), either on delayed images or on both early and delayed images. Furthermore, 23 (72%) of all ergometrine-induced vasospastic areas showed decreased uptake on delayed images. The tracer WR in the reduced accumulation area was significantly higher than that in the normal area, indicating a decline in the mitochondrial membrane's ability to retain MIBI. According to the authors, delayed SPECT with 99mTc-MIBI at rest is a viable tool for the diagnosis of coronary vasospastic angina.

In 2022, Y. Chen et al. [23] published a clinical case in which an accelerated 99mTc-MIBI washout (up to 31%) was observed in the anterior descending artery, with a spasm detected via invasive angiography. Unlike other studies, washout in this study was assessed by dynamic SPECT (using a gamma camera with cadmium-zinc-telluride detectors) from the radiopharmaceutical injection to the seventh minute. Myocardial flow reserve in the anterior descending artery was reduced to 1.26.

T. Kato et al. [24] performed total perfusion deficit (TPD) analysis in 165 patients with ACS and found an association between 99mTc-MIBI RR and cardiopulmonary exercise test parameters. Ergospirometry revealed that patients with a TPD difference of ≥ 4 had a significantly lower anaerobic threshold than those without RR. Furthermore, the difference in TPD between early and delayed images, as well as the presence of diabetes mellitus, were independent predictors of exercise tolerance recovery during a 3-month follow-up.

A. Masuda et al. compared accelerated 99mTc-MIBI washout with the findings of echocardiography and positron emission tomography (PET) with 11C-acetate in 19 patients with ACS (unstable angina, AMI with and without ST elevation). PET with 11C-acetate enables noninvasive assessment of myocardial oxidative metabolism [25] and myocardial blood flow [26, 27]. The clearance of 11C-acetate is linked to Krebs cycle activity in mitochondria, where acetate is converted to acetyl-CoA and metabolized by acetyl-CoA synthetase-2 [28]. As a result, oxidative metabolism as measured by PET with 11C-acetate could be linked to mitochondrial function. Segments with accelerated 99mTc-MIBI washout were associated with decreased oxidative metabolism in the myocardium and impaired regional contractility. The authors concluded that accelerated 99mTc-MIBI washout

is associated with MD and may serve as a predictor of myocardial contractility restoration in patients with ACS.

Stable CAD

The presence of balanced ischemia, which implies an underestimation of the severity of the decrease in myocardial perfusion during visual analysis of scintigraphy data, makes identifying patients with stable CAD with multivessel CAD by MPS challenging [29, 30]. This issue could be resolved with quantitative blood flow assessment [31], determination of transient ischemic dilatation and/or stunning, or 99mTc-MIBI WR evaluation.

B. Du et al. investigated the 99mTc-MIBI WR in healthy individuals and patients with three-vessel CAD and the relationship with the clinician-administered dissociative states scale, using invasive coronary angiography data, to determine the potential use of this parameter in stratifying CAD severity [18]. The 99mTc-MIBI WR was significantly higher in patients with three-vessel CAD than in the control group ($21.1\% \pm 4.6\%$ and $9.5\% \pm 4.9\%$, respectively, $P < 0.001$). A positive correlation was found between the radiopharmaceutical WR and the severity index of coronary artery obstructive lesions ($r^2 = 0.73$, $P = 0.006$). Furthermore, the results of regional 99mTc-MIBI washout across vascular territories are presented in this study. The authors proposed incorporating delayed imaging into the protocol of routine perfusion scintigraphy with 99mTc-MIBI at rest and using WR as an additional indicator of balanced ischemia in three-vessel CAD when suspiciously normal perfusion does not match the clinical presentation.

M.O.M. Othman et al. [15] discovered that the global 99mTc-MIBI WR positively correlated with the risk of cardiovascular events as measured by the Framingham risk score and the Duke treadmill score ($r = 0.4$ and $r = 0.6$, respectively), as well as the risk as measured by MPS ($r = 0.7$). Moreover, WR negatively correlated with LV ejection fraction ($r = -0.4$). The authors concluded that the global 99mTc-MIBI WR can be used to stratify patients with stable CAD into high (annual mortality $> 3\%$) and low (annual mortality $< 1\%$) risk groups [32].

Nonischemic CHF

The majority of studies assessing MD by MPS were performed in patients with nonischemic CHF. In these studies, 99mTc-MIBI RR was assessed in isolated groups of patients with dilated and hypertrophic cardiomyopathies, as well as in mixed groups of patients with hypertrophic, hypertensive, valvular, and toxic cardiomyopathy, cardiac sarcoidosis, and Takotsubo cardiomyopathy.

S. Kumita et al. performed one of the first studies on the use of 99mTc-MIBI WR as a marker of myocardial injury in patients with CHF [33]. The following was observed in 25 patients with nonischemic cardiomyopathy compared with the control group:

- A significantly higher 99mTc-MIBI WR ($39.6\% \pm 5.2\%$ and $31.2\% \pm 5.5\%$, $P < 0.01$).

- A significant inverse correlation of WR with LV ejection fraction ($r = -0.61$) and peak ejection rate ($r = -0.47$).
- A positive correlation with end-systolic ($r = 0.45$) and end-diastolic ($r = 0.48$) LV volumes.

The authors concluded that this approach can be used to evaluate LV damage and contractile dysfunction.

T. Sugiura et al. [34] investigated the association of ^{99m}Tc -MIBI WR with brain natriuretic peptide (BNP) levels and the findings of myocardial scintigraphy with ^{123}I -MIBG in patients with dilated cardiomyopathy (DCM).

The ^{99m}Tc -MIBI WR was significantly higher in the DCM group than in the control group. In the DCM group, WR significantly correlated with the following:

- BNP level ($r = 0.72$, $P < 0.0001$): positive correlation
- Indexed values of end-diastolic ($r = 0.556$, $P < 0.01$) and end-systolic ($r = 0.567$; $P < 0.01$) volumes: positive correlation
- LV ejection fraction ($r = -0.545$, $P < 0.01$): negative correlation

Furthermore, this study found a correlation ($r = 0.603$, $P < 0.01$) between the WRs of ^{99m}Tc -MIBI and ^{123}I -MIBG.

Given that the ^{99m}Tc -MIBI WR correlates with well-known predictors of the CHF course (BNP level and cardiac scintigraphy with ^{123}I -MIBG), the authors suggest that ^{99m}Tc -MIBI WRs can also be used for the prognosis and risk stratification of patients with CHF. This is especially relevant because ^{99m}Tc -MIBI is considerably cheaper, more readily available, and more widely used radiopharmaceutical than ^{123}I -MIBG, which requires radioactive iodine to be produced in a cyclotron.

S. Matsuo et al. studied 61 patients and found an increase in the ^{99m}Tc -MIBI WR in the nonischemic cardiomyopathy group compared with the control group; however, no abnormalities were found in the heart-to-mediastinum ratio [35]. Furthermore, a correlation was found between ^{99m}Tc -MIBI WR and the following:

- BNP level ($r = 0.31$)
- End-systolic ($r = 0.39$) and end-diastolic ($r = 0.49$) volumes
- LV ejection fraction ($r = 0.52$)
- Peak LV filling velocity ($r = 0.44$)

According to the Kaplan–Meier analysis, WR $>28\%$ was a predictor of CHF progression. M. Yamanaka et al. [36] performed early (45 min) and delayed (4 h) MPS with ^{99m}Tc -MIBI at rest and contrast-enhanced cardiac magnetic resonance imaging in patients with clinical signs of nonischemic cardiomyopathy. Myocardial segments with normal radiopharmaceutical uptake during early imaging and perfusion defects detected during delayed imaging were significantly more frequently associated with delayed contrast enhancement on magnetic resonance imaging. This suggests impaired mitochondrial function in areas with even minor fibrotic changes, as seen in the early stages of cardiomyopathy. The authors advocate delayed scintigraphy for the early detection of myocardial injury in

cardiomyopathies because it is straightforward and easy to perform and does not involve the additional administration of radiopharmaceuticals.

K. Takehana et al. [37] studied 20 patients with DCM (LV end-systolic volume, 177 ± 78 mL; LV ejection fraction, $28.2\% \pm 12.4\%$). Three subgroups of myocardial segments were identified according to early (after 1 h) and delayed (after 3 h) MPS: with accelerated, normal, and delayed washout. Systolic thickening and systolic motion of the LV wall were significantly decreased in the accelerated washout group compared with the other two groups, where no significant differences were observed. A strong negative correlation was found between LV ejection fraction and the number of segments with accelerated washout ($r = -0.65$, $P < 0.01$) and global ^{99m}Tc -MIBI WR. Because ^{99m}Tc -MIBI WR is linked to mitochondrial membrane dysfunction, accelerated washout of radiopharmaceuticals may suggest that MD plays a major role in the pathogenesis of DCM.

M.K. Shiroodi et al. [38] reported similar findings when they investigated the relationship between the WR of radiopharmaceuticals, NYHA functional class of CHF, and LV functional parameters according to myocardial perfusion SPECT synchronized with the echocardiogram. A significant ($P < 0.05$) correlation was found between ^{99m}Tc -MIBI WR and the following:

- End-diastolic ($r^2 = 0.216$) and end-systolic ($r^2 = 0.23$) volumes: positive correlation
- LV wall kinesis ($r^2 = 0.54$): positive correlation
- LV ejection fraction ($r^2 = 0.679$): negative correlation

The authors concluded that this method is essential in determining the degree of myocardial injury, particularly in patients with idiopathic DCM, because the ^{99m}Tc -MIBI WR increased significantly as the functional class of CHF increased.

D. Hayashi et al. performed an intriguing study in terms of the methodology used [14]. They performed ^{99m}Tc -MIBI WR assessment, dobutamine stress echocardiography, and endomyocardial biopsy with quantitative analysis of mitochondrial RNA (mRNA) expression and mitochondrial microstructure analysis by electron microscopy in 20 patients with DCM. These patients showed a significant correlation of the ^{99m}Tc -MIBI WR with changes in the rate of increase in LV pressure with increasing dobutamine doses and severity of mitochondrial damage, in accordance with the severity of crista degeneration ($r = 0.88$; $P = 0.048$) and the presence of glycogen-positive zones ($r = 0.90$; $P = 0.044$) according to electron microscopy. Patients with accelerated ^{99m}Tc -MIBI washout ($>24.3\%$) had higher rates of LV pressure increase than those with ^{99m}Tc -MIBI WR below the predefined threshold value. The mRNA level for mitochondrial electron transport enzymes was significantly reduced in the subgroup of patients with accelerated ^{99m}Tc -MIBI washout. To our knowledge, this is the first study to show a link between accelerated ^{99m}Tc -MIBI washout and decreased mRNA expression and impaired mitochondrial microstructure in patients with DCM.

Hypertrophic cardiomyopathy (HCM)

The characteristics of ^{99m}Tc -MIBI WR have been studied in patients with HCM [39–42]. This pathology is characterized by primary damage to the cardiomyocyte mitochondria caused by genetic factors.

M. Sun et al. [41] examined 15 patients with HCM and discovered that the ^{99m}Tc -MIBI WR was significantly higher in this group than in the control group. The authors also discovered a link between WR and maximum LV wall thickness in the HCM group. Accelerated ^{99m}Tc -MIBI washout in the HCM group may be due to mitochondrial DNA mutations.

S. Isobe et al. [42] identified two subgroups of patients with HCM: those with accelerated ($\geq 22.5\%$) and normal ($< 22.5\%$) washout of ^{99m}Tc -MIBI. The authors also performed direct pressure measurements in both ventricles and echocardiography with atrial electrical stimulation. The ^{99m}Tc -MIBI WR showed a significant positive correlation with peak and basal LV pressure ($r = 0.63$, $P < 0.005$; $r = 0.67$, $P < 0.0005$, respectively) and BNP level ($r = 0.57$, $P < 0.005$). A negative correlation was found between the WR and the rate of increase in LV pressure ($r = -0.63$, $P < 0.005$). The LV wall thickness and the ratio of the transmitral flow velocity to the mitral annular velocity were significantly higher in the group with accelerated ^{99m}Tc -MIBI washout than in the group without it. For the first time, this study showed a link between stress-induced changes in central hemodynamics and ^{99m}Tc -MIBI washout parameters in patients with HCM. The authors underlined the potential use of this method for noninvasive assessment of the severity of hemodynamic abnormalities and prognosis in these patients.

Cardiac sarcoidosis

M. Sarai et al. demonstrated that the ^{99m}Tc -MIBI WR can be used for the functional assessment of the heart in cardiac sarcoidosis during steroid therapy [43]. Specifically, quantitative ^{99m}Tc -MIBI WR assessment (based on the difference in the number of pulses between early and delayed imaging) was superior to visual assessment of regional washout in predicting the restoration of LV diastolic function in sarcoidosis. Thus, visual analysis revealed no significant differences in the size of the perfusion defect before and after 6 months of therapy, whereas quantitative analysis revealed a significant decrease in the WR of radiopharmaceuticals after therapy ($25\% \pm 5\%$ vs. $17\% \pm 5\%$, respectively, $P < 0.0001$). The authors discovered a link between changes in WR and LV diastolic function restoration during long-term steroid therapy.

In 2022, M. Suzuki et al. [44] described more pronounced changes in the size of perfusion defects during delayed imaging with ^{99m}Tc -MIBI in patients with sarcoidosis compared with patients without it ($3.0 [-1.0 \text{ to } 5.0]$ vs. $0.0 [-0.5 \text{ to } 1.0]$, $P = 0.010$). Furthermore, according to early and delayed PET findings, patients with sarcoidosis had a more pronounced decrease in ^{18}F -fluorodeoxyglucose uptake

than patients without sarcoidosis. These findings show that metabolic disorders reduce the ability of the myocardium to retain the tracer.

Systemic mitochondrial heart disease

A few studies have reported accelerated ^{99m}Tc -MIBI washout in patients with mitochondrial encephalomyopathy, with a simultaneous increase in 123I-phenyl-methyl-pentadecanoic acid (123I-BMIPP, an analog of free fatty acids) uptake, indicating an imbalance in the energy state of cardiomyocytes [45], including genetic damage to mitochondrial DNA [46].

M. Ikawa et al. [19] used cardiac scintigraphy with ^{99m}Tc -MIBI and 123I-BMIPP to assess damage to the mitochondrial respiratory chain in patients with a primary mitochondrial DNA mutation. The authors present the findings for five patients. Pronounced involvement of the heart muscle in the pathological process was associated with significantly decreased ^{99m}Tc -MIBI uptake and accelerated washout, in combination with increased 123I-BMIPP (perfusion–metabolism mismatch). The authors explain the first phenomenon by impaired mitochondrial transmembrane potential and the second by high blood triglyceride levels. As a result, detecting a perfusion–metabolism mismatch can be used to determine the severity of mitochondrial respiratory chain disruption. An important aspect of this study was the increased 123I-BMIPP uptake in the myocardium in contrast to hypertrophic and congestive heart failure, which can be used to differentiate primary mitochondrial DNA mutation from other types of cardiomyopathies.

Heart transplantation

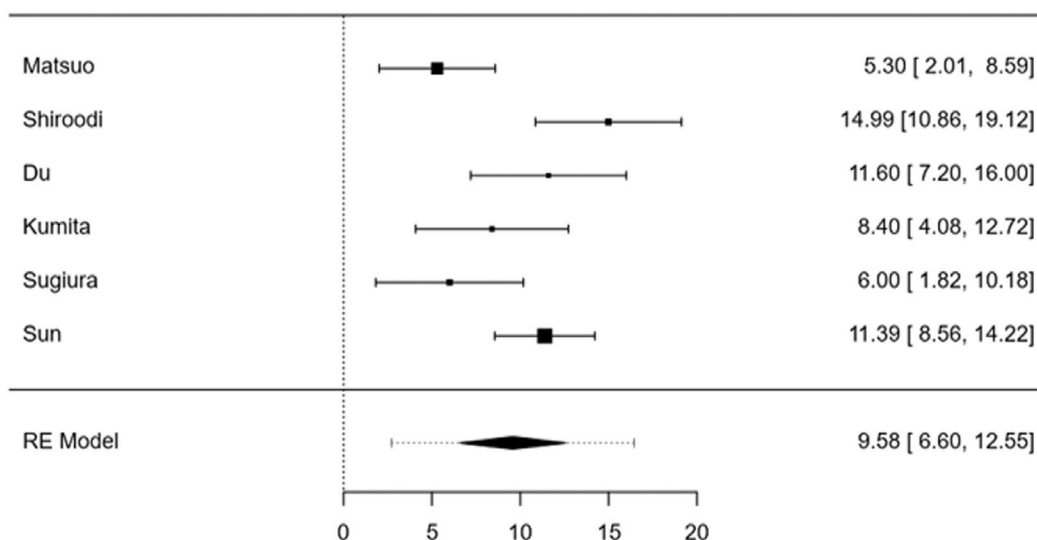
E.V. Migunova et al. [47] discovered that accelerated tracer washout in patients who had undergone heart transplantation is associated with histochemical signs of mild acute rejection, such as localized perivascular and interstitial mononuclear cell infiltrates. The authors concluded that calculating the radiopharmaceutical WR allows the identification of segments with impaired mitochondrial function, which can aid clinicians in the differential diagnosis of a transplanted heart rejection crisis with CAD.

META-ANALYSIS FINDINGS

The hypothesis that WR in the pathology group was significantly higher than that in the control group was tested during the meta-analysis. Six case–control studies were selected for the meta-analysis [18, 33, 34, 38, 41, 46]. The results are presented in Fig. 3.

PERSPECTIVES AND LIMITATIONS OF THE PROPOSED METHOD

The ^{99m}Tc -MIBI washout assessment method is applicable to areas of cardiology not covered in this review. For example, it appears promising to assess MD in patients



Random-Effects Model (k=6)						
	Estimate	se	Z	p	CI Lower Bound	CI Upper Bound
Intercept	9,58	1,52	6,31	<0,001	6,600	12,554

Note. Tau² Estimator: Restricted Maximum-Likelihood

Heterogeneity Statistics								
Tau	Tau ²	I ²	H ²	R ²	df	Q	p	
3,158	9,9697 (SE=8,7429)	73,13%	3.721	.	5,000	18,575	0,002	

Fig. 3. Meta-analysis findings (k=6 studies). The mean differences ranged from 5.3000 to 14.9900; most estimates were positive (100%). The mean difference based on the random-effects model was 9.5771 (95% confidence interval: 6.6001–12.5540); the mean result was significantly different from zero (z = 6.3053; P < 0.0001).

with preserved CHF (HFpEF) and reduced LV ejection fraction and assess cardiotoxicity when using doxorubicin-based drugs.

An experimental study on isolated rat hearts revealed that adding doxorubicin to the perfusion mixture decreased ^{99m}Tc-MIBI uptake, and increasing the doxorubicin concentration caused a dose-dependent progressive decrease in radiopharmaceutical uptake. Furthermore, the ability of the myocardium to retain ^{99m}Tc-MIBI was compromised after 5 min of doxorubicin infusion, and not only was the administered dose lost, but the tracer that had previously entered the heart was washed out to the baseline level [48]. In continuation of the experiment, in vivo studies were performed 14 days after the intraperitoneal injection of doxorubicin in rats. It was found that increasing the doxorubicin dose resulted in a significant decrease in ^{99m}Tc-MIBI uptake (from 2.3% ± 0.3% to 0.9% ± 0.2% of the injected dose/g when using doxorubicin at a dose of 10 mg/kg, P < 0.05). Doxorubicin 10 mg/kg induced a threefold increase in the number of visibly damaged mitochondria per field of view.

In Russia, patients with HFpEF account for 53% of the CHF population, whereas in Europe and the United States, they account for 51%–63%. The phenotypic diversity of HFpEF is associated with several risk factors that activate one or more pathophysiological mechanisms, including MD. The identification of patients with HFpEF and accelerated ^{99m}Tc-MIBI washout may contribute to better risk stratification in this cohort [49]. Furthermore, the proposed method can be used to assess the efficacy of potential CHF therapies and predict the efficacy of cardiac resynchronization therapy and the use of cardioverter defibrillators.

Despite the fundamental and clinical findings presented in the review, studies of ^{99m}Tc-MIBI WR are limited. The analyzed literature contained no systematic reviews or meta-analyses. Furthermore, no randomized studies have used ^{99m}Tc-MIBI washout to guide treatment. This is most likely due to factors affecting washout parameters, such as patient age, sex, and underlying pathology. The data collection protocol and methods for determining ^{99m}Tc-MIBI WR are not standardized. The threshold values for normal

and pathological clearance of this radiopharmaceutical have not been determined. This primarily applies to normal clearance values (Table 1), which are highly variable. The formulas used to calculate the WR vary: some studies apply an adjustment to the half-life of ^{99m}Tc and/or consider the scintillation count in the mediastinum, whereas others do not. Most studies used small patient samples. Only one study found a link between radiological findings that characterize MD and organelle microscopy data [14].

CONCLUSION

The reverse redistribution of ^{99m}Tc -MIBI and its accelerated washout represent a universal nonspecific scintigraphy pattern of myocardial injury caused by MD. According to the literature review, the most extensive evidence base for the use of this method has been accumulated for nonischemic CHF.

In vivo studies have demonstrated a link between the accelerated ^{99m}Tc -MIBI washout and the following:

- Findings of mitochondrial microscopy and myocardial histological examination
- LV contractility and hemodynamics
- Natriuretic peptide levels
- Exercise tolerance
- Severity of coronary atherosclerosis

REFERENCES

1. Vaduganathan M, Mensah GA, Turco JV, et al. The Global Burden of Cardiovascular Diseases and Risk. *Journal of the American College of Cardiology*. 2022;80(25):2361–2371. doi: 10.1016/j.jacc.2022.11.005
2. Murray AJ, Edwards LM, Clarke K. Mitochondria and heart failure. *Current Opinion in Clinical Nutrition and Metabolic Care*. 2007;10(6):704–711. doi: 10.1097/MCO.0b013e3282f0e3be. Erratum in: *Current Opinion in Clinical Nutrition and Metabolic Care*. 2011;14(1):111.
3. Ventura-Clapier R, Garnier A, Veksler V. Energy metabolism in heart failure. *The Journal of Physiology*. 2004;555(1):1–13. doi: 10.1113/jphysiol.2003.055095
4. Dedkova EN, Blatter LA. Measuring mitochondrial function in intact cardiac myocytes. *Journal of Molecular and Cellular Cardiology*. 2012;52(1):48–61. doi: 10.1016/j.yjmcc.2011.08.030
5. Schuster A, Morton G, Chiribiri A, et al. Imaging in the management of ischemic cardiomyopathy: special focus on magnetic resonance. *Journal of the American College of Cardiology*. 2012;59(4):359–370. doi: 10.1016/j.jacc.2011.08.076
6. Liberati A, Altman DG, Tetzlaff J, et al. The PRISMA statement for reporting systematic reviews and meta-analyses of studies that evaluate healthcare interventions: explanation and elaboration. *BMJ*. 2009;339(1):b2700. doi: 10.1136/bmj.b2700
7. Boschi A, Uccelli L, Marvelli L, et al. Technetium- 99m Radiopharmaceuticals for Ideal Myocardial Perfusion Imaging: Lost and Found Opportunities. *Molecules*. 2022;27(4):1188. doi: 10.3390/molecules27041188
8. Zavadovsky KV, Vesnina ZhV, Anashbaev ZhZh, et al. Current status of nuclear cardiology in the Russian Federation. *Russian Journal of Cardiology*. 2022;27(12):105–114. (In Russ). doi: 10.15829/1560-4071-2022-5134
9. Piwnica-Worms D, Kronauge JF, Chiu ML. Enhancement by tetraphenylborate of technetium- 99m -MIBI uptake kinetics and accumulation in cultured chick myocardial cells. *Journal of nuclear medicine*. 1991;32(10):1992–1999.
10. Backus M, Piwnica-Worms D, Hockett D, et al. Microprobe analysis of Tc-MIBI in heart cells: calculation of mitochondrial membrane potential. *American Journal of Physiology-Cell Physiology*. 1993;265(1):C178–C187. doi: 10.1152/ajpcell.1993.265.1.C178
11. Crane P, Laliberté R, Heminway S, et al. Effect of mitochondrial viability and metabolism on technetium- 99m -sestamibi myocardial retention. *European Journal of Nuclear Medicine*. 1993;Vol. 20(1):20–25. doi: 10.1007/BF02261241
12. Fukushima K, Momose M, Kondo C, et al. Myocardial kinetics of (201)Thallium, (99m Tc)-tetrofosmin, and (99m Tc)-sestamibi in an acute ischemia-reperfusion model using isolated rat heart. *Annals of Nuclear Medicine*. 2007;21(5):267–273. doi: 10.1007/s12149-007-0019-x
13. Masuda A, Yoshinaga K, Naya M, et al. Accelerated (99m Tc)-sestamibi clearance associated with mitochondrial dysfunction and regional left ventricular dysfunction in reperfused myocardium in patients with acute coronary syndrome. *EJNMMI Research*. 2016;6(1):41. doi: 10.1186/s13550-016-0196-5
14. Hayashi D, Ohshima S, Isobe S, et al. Increased (99m Tc)-sestamibi washout reflects impaired myocardial contractile and relaxation reserve during dobutamine stress due to mitochondrial dysfunction

ADDITIONAL INFORMATION

Funding source. This study was not supported by any external sources of funding.

Competing interests. The authors declare that they have no competing interests.

Authors' contribution. All authors made a substantial contribution to the conception of the work, acquisition, analysis, interpretation of data for the work, drafting and revising the work, final approval of the version to be published and agree to be accountable for all aspects of the work. M.O. Gulya — selection and analysis of publications, writing the manuscript, preparing tables and illustrations; K.V. Zavadovsky — concept and design of the article, writing the text of the manuscript.

- in dilated cardiomyopathy patients. *Journal of the American College of Cardiology*. 2013;61(19):2007–2017. doi: 10.1016/j.jacc.2013.01.074
15. Othman MOM, Moustafa HM, El-Ghany MMA, et al. The value of myocardial MIBI washout rate in risk stratification of coronary artery disease. *Egyptian Journal of Radiology and Nuclear Medicine*. 2021;52(1). doi: 10.1186/s43055-020-00382-0
16. Henzlova MJ, Duvall WL, Einstein AJ, et al. ASNC imaging guidelines for SPECT nuclear cardiology procedures: Stress, protocols, and tracers. *Journal of Nuclear Cardiology*. 2016;23(3):606–639. doi: 10.1007/s12350-015-0387-x. Erratum in: *Journal of Nuclear Cardiology*. 2016;23(3):640–642.
17. Dorbala S, Ananthasubramaniam K, Armstrong IS, et al. Single Photon Emission Computed Tomography (SPECT) Myocardial Perfusion Imaging Guidelines: Instrumentation, Acquisition, Processing, and Interpretation. *Journal of Nuclear Cardiology*. 2018;25(5):1784–1846. doi: 10.1007/s12350-018-1283-y
18. Du B, Li N, Li X, et al. Myocardial washout rate of resting ^{99m}Tc-Sestamibi (MIBI) uptake to differentiate between normal perfusion and severe three-vessel coronary artery disease documented with invasive coronary angiography. *Annals of Nuclear Medicine*. 2014;28(3):285–292. doi: 10.1007/s12149-013-0803-8
19. Ikawa M, Kawai Y, Arakawa K, et al. Evaluation of respiratory chain failure in mitochondrial cardiomyopathy by assessments of ^{99m}Tc-MIBI washout and 123I-BMIPP/^{99m}Tc-MIBI mismatch. *Mitochondrion*. 2007;7(1-2):164–170. doi: 10.1016/j.mito.2006.11.008
20. Takeishi Y, Sukekawa H, Fujiwara S, et al. Reverse redistribution of technetium-99m-sestamibi following direct PTCA in acute myocardial infarction. *Journal of nuclear medicine*. 1996;37(8):1289–1294.
21. Fujiwara S, Takeishi Y, Hirono O, et al. Reverse redistribution of ^{99m}Tc-sestamibi after direct percutaneous transluminal coronary angioplasty in acute myocardial infarction: relationship with wall motion and functional response to dobutamine stimulation. *Nuclear Medicine Communications*. 2001;22(11):1223–1230. doi: 10.1097/00006231-200111000-00009
22. Ono S, Yamaguchi H, Takayama S, et al. [Rest delayed images on ^{99m}Tc-MIBI myocardial SPECT as a noninvasive screen for the diagnosis of vasospastic angina pectoris]. *Kaku Igaku*. 2002;39(2):117–124. (In Japanese).
23. Chen Y, Pang ZK, Wang J, et al. Serial Changes of ^{99m}Tc-Sestamibi Washout Due to Coronary Spasm Captured by Dynamic Myocardial Perfusion Imaging With Cardiac Dedicated CZT-SPECT: a Case Report. *Circulation: Cardiovascular Imaging*. 2022;15(3). doi: 10.1161/CIRCIMAGING.121.013687
24. Kato T, Noda T, Tanaka S, et al. Impact of accelerated washout of Technetium-99m-sestamibi on exercise tolerance in patients with acute coronary syndrome: single-center experience. *Heart and Vessels*. 2022;37(9):1506–1515. doi: 10.1007/s00380-022-02058-3
25. Bengel FM, Permanetter B, Ungerer M, et al. Non-invasive estimation of myocardial efficiency using positron emission tomography and carbon-11 acetate--comparison between the normal and failing human heart. *European Journal of Nuclear Medicine and Molecular Imaging*. 2000;27(3):319–326. doi: 10.1007/s0025900500040
26. Hoff J, Burchert W, Börner AR, et al. [1-(11)C]Acetate as a quantitative perfusion tracer in myocardial PET. *Journal of nuclear medicine*. 2001;42(8):1174–1182.
27. Zavadovsky KV, Mochula AV, Maltseva AN, et al. The current status of CZT SPECT myocardial blood flow and reserve assessment: Tips and tricks. *Journal of Nuclear Cardiology*. 2022;29(6):3137–3151. doi: 10.1007/s12350-021-02620-y
28. Wu IC, Ohsawa I, Fuku N, et al. Metabolic analysis of ¹³C-labeled pyruvate for noninvasive assessment of mitochondrial function. *Annals of the New York Academy of Sciences*. 2010;1201(1):111–120. doi: 10.1111/j.1749-6632.2010.05636.x
29. Zavadovsky KV, Mishkina AI, Mochula AV, et al. The method for correction of motion artefacts to improve myocardial perfusion imaging. *Russian Electronic Journal of Radiology*. 2017;7(2):56–64. (In Russ). doi: 10.21569/2222-7415-2017-7-2-56-64
30. Zavadovsky KV, Mochula AV, Vrublevsky AV, et al. Role of stress in dynamic single-photon emission computed tomography with myocardial perfusion reserve determination in assessing the severity of coronary artery stenosis. *Russian Journal of Cardiology*. 2019;24(12):40–46. (In Russ). doi: 10.15829/1560-4071-2019-12-40-46
31. Zavadovsky KV, Mochula AV, Maltseva AN, et al. The diagnostic value of SPECT CZT quantitative myocardial blood flow in high-risk patients. *Journal of Nuclear Cardiology*. 2022;29(3):1051–1063. doi: 10.1007/s12350-020-02395-8
32. Knuuti J, Wijns W, Saraste A, et al. ESC Scientific Document Group. 2019 ESC Guidelines for the diagnosis and management of chronic coronary syndromes. *European Heart Journal*. 2020;41(3):407–477. doi: 10.1093/eurheartj/ehz425. Erratum in: *European Heart Journal*. 2020;41(44):4242.
33. Kumita S, Seino Y, Cho K, et al. Assessment of myocardial washout of Tc-^{99m}-sestamibi in patients with chronic heart failure: comparison with normal control. *Annals of Nuclear Medicine*. 2002;16(4):237–242. doi: 10.1007/BF03000101
34. Sugiura T, Takase H, Toriyama T, et al. Usefulness of Tc-^{99m} methoxyisobutylisonitrile scintigraphy for evaluating congestive heart failure. *Journal of Nuclear Cardiology*. 2006;13(1):64–68. doi: 10.1016/j.nuclcard.2005.10.003
35. Matsuo S, Nakae I, Tsutamoto T, et al. A novel clinical indicator using Tc-^{99m} sestamibi for evaluating cardiac mitochondrial function in patients with cardiomyopathies. *Journal of Nuclear Cardiology*. 2007;14(2):215–220. doi: 10.1016/j.nuclcard.2006.10.022
36. Yamanaka M, Takao S, Otsuka H, et al. The Utility of a Combination of ^{99m}Tc-MIBI Washout Imaging and Cardiac Magnetic Resonance Imaging in the Evaluation of Cardiomyopathy. *Annals of Nuclear Cardiology*. 2021;7(1):8–16. doi: 10.17996/anc.21-00124
37. Takehana K, Maeba H, Ueyama T, et al. Direct correlation between regional systolic function and regional washout rate of ^{99m}Tc-sestamibi in patients with idiopathic dilated cardiomyopathy. *Nuclear Medicine Communications*. 2011;32(12):1174–1178. doi: 10.1097/MNM.0b013e32834b60be
38. Shiroodi MK, Shafiei B, Baharfard N, et al. ^{99m}Tc-MIBI washout as a complementary factor in the evaluation of idiopathic dilated cardiomyopathy (IDCM) using myocardial perfusion imaging. *The International Journal of Cardiovascular Imaging*. 2012;28(1):211–217. doi: 10.1007/s10554-010-9770-5
39. Morishita S, Kondo Y, Nomura M, et al. Impaired retention of technetium-^{99m} tetrofosmin in hypertrophic cardiomyopathy. *The American Journal of Cardiology*. 2001;87(6):743–747. doi: 10.1016/s0002-9149(00)01494-6
40. Thet-Thet-Lwin, Takeda T, Wu J, et al. Enhanced washout of ^{99m}Tc-tetrofosmin in hypertrophic cardiomyopathy: quantitative comparisons with regional 123I-BMIPP uptake and wall thickness determined by MRI. *European Journal of*

Nuclear Medicine and Molecular Imaging. 2003;30(7):966–973. doi: 10.1007/s00259-003-1163-8

41. Sun M, Li Y, Li N, et al. Preliminary clinical investigation of ^{99m}Tc-methoxyisobutylisonitrile washout rate in hypertrophic cardiomyopathy. *Nuclear Medicine Communications*. 2008;29(8):686–689. doi: 10.1097/MNM.0b013e3283009f36

42. Isobe S, Ohshima S, Unno K, et al. Relation of ^{99m}Tc-sestamibi washout with myocardial properties in patients with hypertrophic cardiomyopathy. *Journal of Nuclear Cardiology*. 2010;17(6):1082–1090. doi: 10.1007/s12350-010-9266-7

43. Sarai M, Motoyama S, Kato Y, et al. (^{99m}Tc)-MIBI Washout Rate to Evaluate the Effects of Steroid Therapy in Cardiac Sarcoidosis. *Asia Oceania journal of nuclear medicine & biology*. 2013;1(2):4–9.

44. Suzuki M, Izawa Y, Fujita H, et al. Efficacy of myocardial washout of ^{99m}Tc-MIBI/Tetrofosmin for the evaluation of inflammation in patients with cardiac sarcoidosis: comparison with ¹⁸F-fluorodeoxyglucose positron emission tomography findings. *Annals of Nuclear Medicine*. 2022;36(6):544–552. doi: 10.1007/s12149-022-01735-7

45. Zavadovsky KV, Gulya MO, Lishmanov YB, Lebedev DI. Perfusion and metabolic scintigraphy with (¹²³I)-BMIPP in prognosis

of cardiac resynchronization therapy in patients with dilated cardiomyopathy. *Annals of Nuclear Medicine*. 2016;30(5):325–333. doi: 10.1007/s12149-016-1064-0

46. Matsuo S, Nakajima K, Kinuya S, et al. Cardiac scintigraphic findings of mitochondrial myopathy, encephalopathy, lactic acidosis and stroke-like episodes: A case report. *Experimental and clinical cardiology*. 2008;13(2):93–95.

47. Migunova EV, Nefedova GA, Kudryashova NE, et al. Evaluation of mitochondrial dysfunction of a transplanted heart with radionuclide method (clinical observations). *Russian Electronic Journal of Radiology*. 2020;10(3):156–164. (In Russ). doi: 10.21569/2222-7415-2020-10-3-156-164

48. Safee ZM, Baark F, Waters ECT, et al. Detection of anthracycline-induced cardiotoxicity using perfusion-corrected ^{99m}Tc sestamibi SPECT. *Scientific Reports*. 2019;9(1):216. doi: 10.1038/s41598-018-36721-5

49. Mochula AV, Kop'eva KV, Maltseva AN, et al. Coronary flow reserve in patients with heart failure with preserved ejection fraction. *Russian Journal of Cardiology*. 2022;27(2):44–52. (In Russ). doi: 10.15829/1560-4071-2022-4743

СПИСОК ЛИТЕРАТУРЫ

1. Vaduganathan M., Mensah G.A., Turco J.V., et al. The Global Burden of Cardiovascular Diseases and Risk // *Journal of the American College of Cardiology*. 2022. Vol. 80, N 25. P. 2361–2371. doi: 10.1016/j.jacc.2022.11.005

2. Murray A.J., Edwards L.M., Clarke K. Mitochondria and heart failure // *Current Opinion in Clinical Nutrition and Metabolic Care*. 2007. Vol. 10, N 6. P. 704–711. doi: 10.1097/MCO.0b013e3282f0ecbe. Erratum in: *Current Opinion in Clinical Nutrition and Metabolic Care*. 2011. Vol. 14, N 1. P. 111.

3. Ventura-Clapier R., Garnier A., Veksler V. Energy metabolism in heart failure // *The Journal of Physiology*. 2004. Vol. 555, N 1. P. 1–13. doi: 10.1113/jphysiol.2003.055095

4. Dedkova E.N., Blatter L.A. Measuring mitochondrial function in intact cardiac myocytes // *Journal of Molecular and Cellular Cardiology*. 2012. Vol. 52, N 1. P. 48–61. doi: 10.1016/j.yjmcc.2011.08.030

5. Schuster A., Morton G., Chiribiri A., et al. Imaging in the management of ischemic cardiomyopathy: special focus on magnetic resonance // *Journal of the American College of Cardiology*. 2012. Vol. 59, N 4. P. 359–370. doi: 10.1016/j.jacc.2011.08.076

6. Liberati A., Altman D.G., Tetzlaff J., et al. The PRISMA statement for reporting systematic reviews and meta-analyses of studies that evaluate healthcare interventions: explanation and elaboration // *BMJ*. 2009. Vol. 339, N 1. P. b2700. doi: 10.1136/bmj.b2700

7. Boschi A., Uccelli L., Marvelli L., et al. Technetium-^{99m} Radiopharmaceuticals for Ideal Myocardial Perfusion Imaging: Lost and Found Opportunities // *Molecules*. 2022. Vol. 27, N 4. P. 1188. doi: 10.3390/molecules27041188

8. Завадовский К.В., Веснина Ж.В., Анашбаев Ж.Ж., и др. Современное состояние ядерной кардиологии в Российской Федерации // *Российский кардиологический журнал*. 2022. Т. 27, № 12. С. 105–114. doi: 10.15829/1560-4071-2022-5134

9. Piwnica-Worms D., Kronauge J.F., Chiu M.L. Enhancement by tetraphenylborate of technetium-^{99m}-MIBI uptake kinetics and accumulation in cultured chick myocardial cells // *Journal of nuclear medicine*. 1991. Vol. 32, N 10. P. 1992–1999.

10. Backus M., Piwnica-Worms D., Hockett D., et al. Microprobe analysis of Tc-MIBI in heart cells: calculation of mitochondrial membrane potential // *American Journal of Physiology-Cell Physiology*. 1993. Vol. 265, N 1. P. C178–C187. doi: 10.1152/ajpcell.1993.265.1.C178

11. Crane P., Laliberté R., Heminway S., et al. Effect of mitochondrial viability and metabolism on technetium-^{99m}-sestamibi myocardial retention // *European Journal of Nuclear Medicine*. 1993. Vol. 20, N 1. P. 20–25. doi: 10.1007/BF02261241

12. Fukushima K., Momose M., Kondo C., et al. Myocardial kinetics of (²⁰¹)Thallium, (^{99m})Tc-tetrofosmin, and (^{99m})Tc-sestamibi in an acute ischemia-reperfusion model using isolated rat heart // *Annals of Nuclear Medicine*. 2007. Vol. 21, N 5. P. 267–273. doi: 10.1007/s12149-007-0019-x

13. Masuda A., Yoshinaga K., Naya M., et al. Accelerated (^{99m})Tc-sestamibi clearance associated with mitochondrial dysfunction and regional left ventricular dysfunction in reperfused myocardium in patients with acute coronary syndrome. *EJNMMI Research*. 2016. Vol. 6, N 1. P. 41. doi: 10.1186/s13550-016-0196-5

14. Hayashi D., Ohshima S., Isobe S., et al. Increased (^{99m})Tc-sestamibi washout reflects impaired myocardial contractile and relaxation reserve during dobutamine stress due to mitochondrial dysfunction in dilated cardiomyopathy patients // *Journal of the American College of Cardiology*. 2013. Vol. 61, N 19. P. 2007–2017. doi: 10.1016/j.jacc.2013.01.074

15. Othman M.O.M., Moustafa H.M., El-Ghany M.M.A., et al. The value of myocardial MIBI washout rate in risk stratification of coronary artery disease. *Egyptian Journal of Radiology and Nuclear Medicine*. 2021. Vol. 52, N 1. doi: 10.1186/s43055-020-00382-0

16. Henzlova M.J., Duvall W.L., Einstein A.J., et al. ASNC imaging guidelines for SPECT nuclear cardiology procedures: Stress, protocols, and tracers // *Journal of Nuclear Cardiology*. 2016. Vol. 23, N 3. P. 606–639. doi: 10.1007/s12350-015-0387-x. Erratum in: *Journal of Nuclear Cardiology*. 2016. Vol. 23, N 3. P. 640–642.

17. Dorbala S., Ananthasubramaniam K., Armstrong I.S., et al. Single Photon Emission Computed Tomography (SPECT) Myocardial

- Perfusion Imaging Guidelines: Instrumentation, Acquisition, Processing, and Interpretation // *Journal of Nuclear Cardiology*. 2018. Vol. 25, N 5. P. 1784–1846. doi: 10.1007/s12350-018-1283-y
18. Du B., Li N., Li X., et al. Myocardial washout rate of resting ^{99m}Tc -Sestamibi (MIBI) uptake to differentiate between normal perfusion and severe three-vessel coronary artery disease documented with invasive coronary angiography // *Annals of Nuclear Medicine*. 2014. Vol. 28, N 3. P. 285–292. doi: 10.1007/s12149-013-0803-8
19. Ikawa M., Kawai Y., Arakawa K., et al. Evaluation of respiratory chain failure in mitochondrial cardiomyopathy by assessments of ^{99m}Tc -MIBI washout and ^{123}I -BMIPP/ ^{99m}Tc -MIBI mismatch // *Mitochondrion*. 2007. Vol. 7, N 1–2. P. 164–170. doi: 10.1016/j.mito.2006.11.008
20. Takeishi Y., Sukekawa H., Fujiwara S., et al. Reverse redistribution of technetium- 99m -sestamibi following direct PTCA in acute myocardial infarction // *Journal of nuclear medicine*. 1996. Vol. 37, N 8. P. 1289–1294.
21. Fujiwara S., Takeishi Y., Hirono O., et al. Reverse redistribution of ^{99m}Tc -sestamibi after direct percutaneous transluminal coronary angioplasty in acute myocardial infarction: relationship with wall motion and functional response to dobutamine stimulation // *Nuclear Medicine Communications*. 2001. Vol. 22, N 11. P. 1223–1230. doi: 10.1097/00006231-200111000-00009
22. Ono S., Yamaguchi H., Takayama S., et al. [Rest delayed images on ^{99m}Tc -MIBI myocardial SPECT as a noninvasive screen for the diagnosis of vasospastic angina pectoris] // *Kaku Igaku*. 2002. Vol. 39, N 2. P. 117–124. (In Japanese).
23. Chen Y., Pang Z.K., Wang J., et al. Serial Changes of ^{99m}Tc -Sestamibi Washout Due to Coronary Spasm Captured by Dynamic Myocardial Perfusion Imaging With Cardiac Dedicated CZT-SPECT: a Case Report // *Circulation: Cardiovascular Imaging*. 2022. Vol. 15, N 3. doi: 10.1161/CIRCIMAGING.121.013687
24. Kato T., Noda T., Tanaka S., et al. Impact of accelerated washout of Technetium- 99m -sestamibi on exercise tolerance in patients with acute coronary syndrome: single-center experience // *Heart and Vessels*. 2022. Vol. 37, N 9. P. 1506–1515. doi: 10.1007/s00380-022-02058-3
25. Bengel F.M., Permanetter B., Ungerer M., et al. Non-invasive estimation of myocardial efficiency using positron emission tomography and carbon-11 acetate—comparison between the normal and failing human heart // *European Journal of Nuclear Medicine and Molecular Imaging*. 2000. Vol. 27, N 3. P. 319–326. doi: 10.1007/s002590050040
26. Hoff J., Burchert W., Börner A.R., et al. [^{11}C]Acetate as a quantitative perfusion tracer in myocardial PET // *Journal of nuclear medicine*. 2001. Vol. 42, N 8. P. 1174–1182.
27. Zavadovsky K.V., Mochula A.V., Maltseva A.N., et al. The current status of CZT SPECT myocardial blood flow and reserve assessment: Tips and tricks // *Journal of Nuclear Cardiology*. 2022. Vol. 29, N 6. P. 3137–3151. doi: 10.1007/s12350-021-02620-y
28. Wu I.C., Ohsawa I., Fuku N., et al. Metabolic analysis of ^{13}C -labeled pyruvate for noninvasive assessment of mitochondrial function // *Annals of the New York Academy of Sciences*. 2010. Vol. 1201, N 1. P. 111–120. doi: 10.1111/j.1749-6632.2010.05636.x
29. Завадовский К.В., Мишкина А.И., Мочула А.В., и др. Методика устранения артефактов движения сердца при выполнении перфузионной сцинтиграфии миокарда // *Российский электронный журнал лучевой диагностики*. 2017. Т. 7, № 2. С. 56–64. doi: 10.21569/2222-7415-2017-7-2-56-64
30. Завадовский К.В., Мочула А.В., Врублевский А.В., и др. Роль нагрузочной динамической однофотонной эмиссионной компьютерной томографии с определением резерва миокардиального кровотока в оценке значимости стенозов коронарных артерий // *Российский кардиологический журнал*. 2019. Т. 24, № 12. С. 40–46. doi: 10.15829/1560-4071-2019-12-40-46
31. Zavadovsky K.V., Mochula A.V., Maltseva A.N., et al. The diagnostic value of SPECT CZT quantitative myocardial blood flow in high-risk patients // *Journal of Nuclear Cardiology*. 2022. Vol. 29, N 3. P. 1051–1063. doi: 10.1007/s12350-020-02395-8
32. Knuuti J., Wijns W., Saraste A., et al. ESC Scientific Document Group. 2019 ESC Guidelines for the diagnosis and management of chronic coronary syndromes // *European Heart Journal*. 2020. Vol. 41, N 3. P. 407–477. doi: 10.1093/eurheartj/ehz425. Erratum in: *European Heart Journal*. 2020. Vol. 41, N 44. P. 4242.
33. Kumita S., Seino Y., Cho K., et al. Assessment of myocardial washout of ^{99m}Tc -sestamibi in patients with chronic heart failure: comparison with normal control // *Annals of Nuclear Medicine*. 2002. Vol. 16, N 4. P. 237–242. doi: 10.1007/BF03000101
34. Sugiura T., Takase H., Toriyama T., et al. Usefulness of ^{99m}Tc -methoxyisobutylisonitrile scintigraphy for evaluating congestive heart failure // *Journal of Nuclear Cardiology*. 2006. Vol. 13, N 1. P. 64–68. doi: 10.1016/j.nuclcard.2005.10.003
35. Matsuo S., Nakae I., Tsutamoto T., et al. A novel clinical indicator using ^{99m}Tc -sestamibi for evaluating cardiac mitochondrial function in patients with cardiomyopathies // *Journal of Nuclear Cardiology*. 2007. Vol. 14, N 2. P. 215–220. doi: 10.1016/j.nuclcard.2006.10.022
36. Yamanaka M., Takao S., Otsuka H., et al. The Utility of a Combination of ^{99m}Tc -MIBI Washout Imaging and Cardiac Magnetic Resonance Imaging in the Evaluation of Cardiomyopathy // *Annals of Nuclear Cardiology*. 2021. Vol. 7, N 1. P. 8–16. doi: 10.17996/anc.21-00124
37. Takehana K., Maeba H., Ueyama T., et al. Direct correlation between regional systolic function and regional washout rate of ^{99m}Tc -sestamibi in patients with idiopathic dilated cardiomyopathy // *Nuclear Medicine Communications*. 2011. Vol. 32, N 12. P. 1174–1178. doi: 10.1097/MNM.0b013e32834b60be
38. Shiroodi M.K., Shafiei B., Baharfard N., et al. ^{99m}Tc -MIBI washout as a complementary factor in the evaluation of idiopathic dilated cardiomyopathy (IDCM) using myocardial perfusion imaging // *The International Journal of Cardiovascular Imaging*. 2012. Vol. 28, N 1. P. 211–217. doi: 10.1007/s10554-010-9770-5
39. Morishita S., Kondo Y., Nomura M., et al. Impaired retention of technetium- 99m tetrofosmin in hypertrophic cardiomyopathy // *The American Journal of Cardiology*. 2001. Vol. 87, N 6. P. 743–747. doi: 10.1016/s0002-9149(00)01494-6
40. Thet-Thet-Lwin, Takeda T., Wu J., et al. Enhanced washout of ^{99m}Tc -tetrofosmin in hypertrophic cardiomyopathy: quantitative comparisons with regional ^{123}I -BMIPP uptake and wall thickness determined by MRI // *European Journal of Nuclear Medicine and Molecular Imaging*. 2003. Vol. 30, N 7. P. 966–973. doi: 10.1007/s00259-003-1163-8
41. Sun M., Li Y., Li N., et al. Preliminary clinical investigation of ^{99m}Tc -methoxyisobutylisonitrile washout rate in hypertrophic cardiomyopathy // *Nuclear Medicine Communications*. 2008. Vol. 29, N 8. P. 686–689. doi: 10.1097/MNM.0b013e3283009f36
42. Isobe S., Ohshima S., Unno K., et al. Relation of ^{99m}Tc -sestamibi washout with myocardial properties in patients with hypertrophic cardiomyopathy // *Journal of Nuclear Cardiology*. 2010. Vol. 17, N 6. P. 1082–1090. doi: 10.1007/s12350-010-9266-7

- 43.** Sarai M., Motoyama S., Kato Y., et al. (99m)Tc-MIBI Washout Rate to Evaluate the Effects of Steroid Therapy in Cardiac Sarcoidosis // *Asia Oceania journal of nuclear medicine & biology*. 2013. Vol. 1, N 2. P. 4–9.
- 44.** Suzuki M., Izawa Y., Fujita H., et al. Efficacy of myocardial washout of 99mTc-MIBI/Tetrofosmin for the evaluation of inflammation in patients with cardiac sarcoidosis: comparison with 18F-fluorodeoxyglucose positron emission tomography findings // *Annals of Nuclear Medicine*. 2022. Vol. 36, N 6. P. 544–552. doi: 10.1007/s12149-022-01735-7
- 45.** Zavadovsky K.V., Gulya M.O., Lishmanov Y.B., Lebedev D.I. Perfusion and metabolic scintigraphy with (123)I-BMIPP in prognosis of cardiac resynchronization therapy in patients with dilated cardiomyopathy // *Annals of Nuclear Medicine*. 2016. Vol. 30, N 5. P. 325–333. doi: 10.1007/s12149-016-1064-0
- 46.** Matsuo S., Nakajima K., Kinuya S., et al. Cardiac scintigraphic findings of mitochondrial myopathy, encephalopathy, lactic acidosis and stroke-like episodes: A case report // *Experimental and clinical cardiology*. 2008. Vol. 13, N 2. P. 93–95.
- 47.** Мигунова Е.В., Нефедова Г.А., Кудряшова Н.Е., и др. Оценка митохондриальной дисфункции пересаженного сердца радионуклидным методом (два клинических наблюдения) // *Russian Electronic Journal of Radiology*. 2020. Т. 10, № 3. С. 156–164. doi: 10.21569/2222-7415-2020-10-3-156-164
- 48.** Safee Z.M., Baark F., Waters E.C.T., et al. Detection of anthracycline-induced cardiotoxicity using perfusion-corrected 99mTc sestamibi SPECT // *Scientific Reports*. 2019. Vol. 9, N 1. P. 216. doi: 10.1038/s41598-018-36721-5
- 49.** Мочула А.В., Копьева К.В., Мальцева А.Н., и др. Резерв коронарного кровотока у пациентов с хронической сердечной недостаточностью с сохраненной фракцией выброса левого желудочка // *Российский кардиологический журнал*. 2022. Т. 27, № 2. С. 44–52. doi: 10.15829/1560-4071-2022-4743

AUTHORS' INFO

* **Konstantin V. Zavadovsky**, MD, Dr. Sci. (Med.);
address: Russia, 634012, Tomsk, Kievskaya Str 111A;
ORCID: 0000-0002-1513-8614;
eLibrary SPIN: 5081-3495;
e-mail: konstzav@gmail.com

Marina O. Gulya, MD, Cand. Sci. (Med.);
ORCID: 0000-0001-5689-9754;
eLibrary SPIN: 3064-3773;
e-mail: mgulyatomsk@mail.ru

ОБ АВТОРАХ

* **Завадовский Константин Валерьевич**, д-р мед. наук;
адрес: Россия, 634012, г. Томск, ул. Киевская 111А;
ORCID: 0000-0002-1513-8614;
eLibrary SPIN: 5081-3495;
e-mail: konstzav@gmail.com

Гуля Марина Олеговна, канд. мед. наук;
ORCID: 0000-0001-5689-9754;
eLibrary SPIN: 3064-3773;
e-mail: mgulyatomsk@mail.ru

* Corresponding author / Автор, ответственный за переписку

DOI: <https://doi.org/10.17816/DD569149>

Магнитно-резонансная томография в дифференциальной диагностике первичных внеозговых опухолей: обзор радиомических исследований

А.В. Капишников¹, Е.Н. Суровцев^{1,2}

¹ Самарский государственный медицинский университет, Самара, Российская Федерация;

² Лечебно-диагностический центр Международного института биологических систем имени Сергея Березина, Тольятти, Российская Федерация

АННОТАЦИЯ

Обоснование. Анализ данных магнитно-резонансной томографии является основным методом для предоперационной дифференциальной диагностики первичных внеозговых опухолей. Однако точное их разграничение только на основе визуальной оценки этих данных может быть затруднительно.

Радиомика — это количественный подход к анализу данных медицинских изображений, позволяющий выявить взаимосвязь данных визуализации с фенотипическими и генотипическими особенностями опухолей.

Ранее в ряде аналитических публикаций проводилось обобщение результатов исследований, посвящённых дифференциальной диагностике первичных внеозговых опухолей на основе принципов радиомики. Быстрое накопление новых клинических примеров и увеличение количества исследований по данной проблеме обуславливают необходимость их дальнейшего анализа и систематизации, что и послужило основанием для выполнения настоящей работы.

Цель — систематизировать существующие данные о возможностях радиомики для дифференциальной диагностики первичных внеозговых опухолей.

Материалы и методы. Проведены поиск и анализ публикаций на русском и английском языках за последние пять лет. Поиск осуществлялся в системах PubMed/Medline, Google Scholar и eLibrary. В окончательный анализ включено 19 публикаций, касающихся дифференциальной диагностики первичных внеозговых опухолей, в которых были приведены радиомические признаки, использованные для дифференциальной диагностики новообразований.

Результаты. Во всех исследованиях было показано наличие взаимосвязи между радиомическими параметрами (текстурными и гистограммными) и типом опухоли. Эффективность дифференциальной диагностики опухолей радиомическими моделями превосходила эффективность классификации новообразований рентгенологами.

Наиболее часто использовались следующие алгоритмы для создания математических моделей классификации опухолей на основе радиомических параметров: метод опорных векторов, логистическая регрессия, случайный лес. Методы опорных векторов и логистической регрессии продемонстрировали лучшие и более стабильные результаты.

Заключение. Использование концепции радиомики показывает многообещающие результаты в дифференциальной диагностике первичных внеозговых опухолей. Дальнейшее развитие этого направления требует стандартизации как методов сегментации, так и набора признаков, а также эффективного метода математического моделирования.

Ключевые слова: первичные внеозговые опухоли; магнитно-резонансная томография; менингиомы; радиомика; информационные технологии.

Как цитировать:

Капишников А.В., Суровцев Е.Н. Магнитно-резонансная томография в дифференциальной диагностике первичных внеозговых опухолей: обзор радиомических исследований // Digital Diagnostics. 2023. Т. 4, № 4. С. 529–542. DOI: <https://doi.org/10.17816/DD569149>

DOI: <https://doi.org/10.17816/DD569149>

Magnetic resonance imaging for the differential diagnosis of primary extra-axial brain tumors: a review of radiomic studies

Aleksandr V. Kapishnikov¹, Evgeniy N. Surovcev^{1,2}

¹ Samara State Medical University, Samara, Russian Federation;

² Dr. Sergey Berezin Medical Institute (MIBS), Togliatti, Russian Federation

ABSTRACT

BACKGROUND: The analysis of magnetic resonance imaging data is considered the main method for the preoperative differential diagnosis of primary extra-axial tumors. However, the exact distinction of different primary extra-axial tumors based only on visual rating can be challenging. Radiomics is a quantitative method of analyzing medical image data, which allows us to understand and observe the connection between visual data and phenotypic and genotypic features of tumors. Earlier, several publications presented generalized results of research aimed at the differential diagnosis of primary extra-axial tumors based on the principles of radiomics. Fast accumulation of new clinical cases and increasing of the amounts of research on these cases demonstrate the need for their further analysis and systematization, which has led to this review.

AIM: To conduct a systematic analysis of existing data on radiomics potential for the differential diagnosis of primary extra-axial tumors.

MATERIALS AND METHODS: The search for publications over the past 5 years in Russian and English was conducted in PubMed/Medline, Google Scholar, and eLibrary databases. The final analysis included 19 papers on the differential diagnosis of extra-axial tumors. The included publications provided radiomic features used for the differential diagnosis of neoplasms.

RESULTS: All studies demonstrated the existence of a connection between radiomic parameters (textural and histogram) and tumor type. The effectiveness of tumor differential diagnostics with radiomic models exceeded the neoplasm classification made by radiologists. The most frequently used algorithms for creating mathematical models of tumor classification based on radiomic parameters were the reference vector method, logistic regression, and random forest.

CONCLUSION: The use of the radiomic concept shows promising results in the differential diagnosis of primary extra-axial tumors. Further development in this area demands the standardization of both the segmentation method and the set of features and an effective method of mathematics modeling.

Keywords: primary extra-axial brain tumors; magnetic resonance imaging; meningiomas; radiomics; information technology.

To cite this article:

Kapishnikov AV, Surovcev EN. Magnetic resonance imaging for the differential diagnosis of primary extra-axial brain tumors: a review of radiomic studies. *Digital Diagnostics*. 2023;4(4):529–542. DOI: <https://doi.org/10.17816/DD569149>

Submitted: 07.09.2023

Accepted: 19.10.2023

Published online: 16.11.2023

DOI: <https://doi.org/10.17816/DD569149>

磁共振成像在原发性脑外肿瘤鉴别诊断中的应用：放射组学研究综述

Aleksandr V. Kapishnikov¹, Evgeniy N. Surovcev^{1,2}¹ Samara State Medical University, Samara, Russian Federation;² Dr. Sergey Berezin Medical Institute (MIBS), Togliatti, Russian Federation

简评

论证。磁共振成像数据分析是术前原发性脑外肿瘤鉴别诊断的主要方法。然而，仅凭对这些数据的目测评估很难准确区分不同的原发性脑外肿瘤。

放射组学是一种分析医学影像数据的定量方法。其允许确定成像数据与肿瘤表型和基因型特征之间的关系。

此前，一些分析性出版物总结了根据放射组学原理对原发性脑外肿瘤进行鉴别诊断的研究结果。随着新临床病例的迅速积累和相关研究的不断增加，有必要对其进行进一步分析和系统化。这就是本研究的基础。

该研究的目的是系统整理有关放射组学在原发性脑外肿瘤鉴别诊断方面潜力的现有数据。

材料与方法。我们搜索并分析了过去五年中用俄语和英语发表的出版物。搜索是在PubMed/Medline、Google Scholar和eLibrary数据库中进行。最终分析包括19篇关于原发性脑外肿瘤鉴别诊断的出版物。这些出版物包括用于肿瘤鉴别诊断的放射组学特征。

结果。所有研究都表明了，放射组学参数（纹理的和直方图的）与肿瘤类型之间存在相关性。通过放射组学模型对肿瘤进行鉴别诊断的效率优于放射科医生对肿瘤进行分类的效率。为了创建肿瘤分类的模型，我们最常使用了以下算法：支持向量法、逻辑回归法和随机森林法。支持向量法和逻辑回归法显示出更好、更稳定的结果。

结论。放射组学概念在原发性脑外肿瘤鉴别诊断中的应用显示出良好效果。这一方向的进一步发展需要分割方法和特征集的标准化，以及有效的数学建模方法。

关键词：原发性脑外肿瘤；磁共振成像；脑膜瘤；放射组学；信息技术。

引用本文：

Kapishnikov AV, Surovcev EN. 磁共振成像在原发性脑外肿瘤鉴别诊断中的应用：放射组学研究综述. *Digital Diagnostics*. 2023;4(4):529–542. DOI: <https://doi.org/10.17816/DD569149>

收到: 07.09.2023

接受: 19.10.2023

发布日期: 16.11.2023

BACKGROUND

Preoperative differential diagnosis of primary extra-axial brain tumors (PEABTs) is based on the analysis of magnetic resonance imaging (MRI) semiotics, which most commonly includes a standard set of weighted images (WI), such as T2-WI, T1-WI, FLAIR, diffusion-weighted imaging (DWI), and contrast-enhanced T1-WI (T1-CE) [1–3].

PEABTs include both benign and malignant neoplasms of the meninges (meningiomas and mesenchymal tumors) and cranial nerves (neurinomas) [4].

The MRI semiotics of PEABTs have been studied in detail and described in established guidelines; however, atypical MRI patterns can complicate the differential diagnosis of tumors based on visual assessment alone [5,6]. Incorrect tumor type determination can result in incorrect treatment [1,2,7,8]. The most common difficulties are differentiating meningiomas of various grades, distinguishing solitary fibrous tumors from meningiomas, and localizing PEABTs in cerebellopontine angles [9–12].

Radiomics is a quantitative approach to medical image analysis and aims to identify the relationship between the digital characteristics of a diagnostic image and phenotypic and genotypic characteristics of a tumor [13].

Radiomics involves extracting quantitative features from images to provide an objective description of an imaging phenotype and determine the relationship between radiomic and genetic, molecular, and clinical features of tumors [14]. To extract quantitative parameters from images, morphometric, histogram, and texture analysis of segmented areas of interest is performed. Histogram and texture features reflect structural features not detectable visually [15]. In radiomics studies, various mathematical modeling and deep learning methods are used. The resulting differential diagnostic and

prognostic models should be validated using an independent sample. Radiomics may be a powerful tool in clinical decision-making [16]. Figure 1 shows the steps of radiomic analysis.

Some analytical publications have summarized previous studies on radiomics-based differential diagnosis of PEABTs [13, 17]. The rapid accumulation of new clinical cases and increase in the number of studies related to this problem require further analysis and systematization, and thus, is the basis of the present study.

MATERIALS AND METHODS

A systematic review for the last 5 years was conducted according to PRISMA (Preferred Reporting Items for Systematic Reviews and Meta-Analyses Protocols, 2009).

PubMed/MEDLINE, Google Scholar, and eLibrary databases were searched for scientific articles from the last 5 years using the following keywords: MRI, meningioma, neuroma, schwannoma, solitary fibrous tumor, radiomics, texture, MPT, менингиома, невринома, шваннома, солитарная фиброзная опухоль, радиомика, текстура.

Articles with abstracts unrelated to the differential diagnosis of PEABTs were excluded, as well as those without a description in text of radiomic features in the differential diagnosis of tumors.

Finally, 19 publications were included in the review. Figure 2 shows the design of the current study.

Estimated parameters

As part of the systematic review, the following parameters were assessed in the selection of publications:

- Diagnostic task
- Number of patients

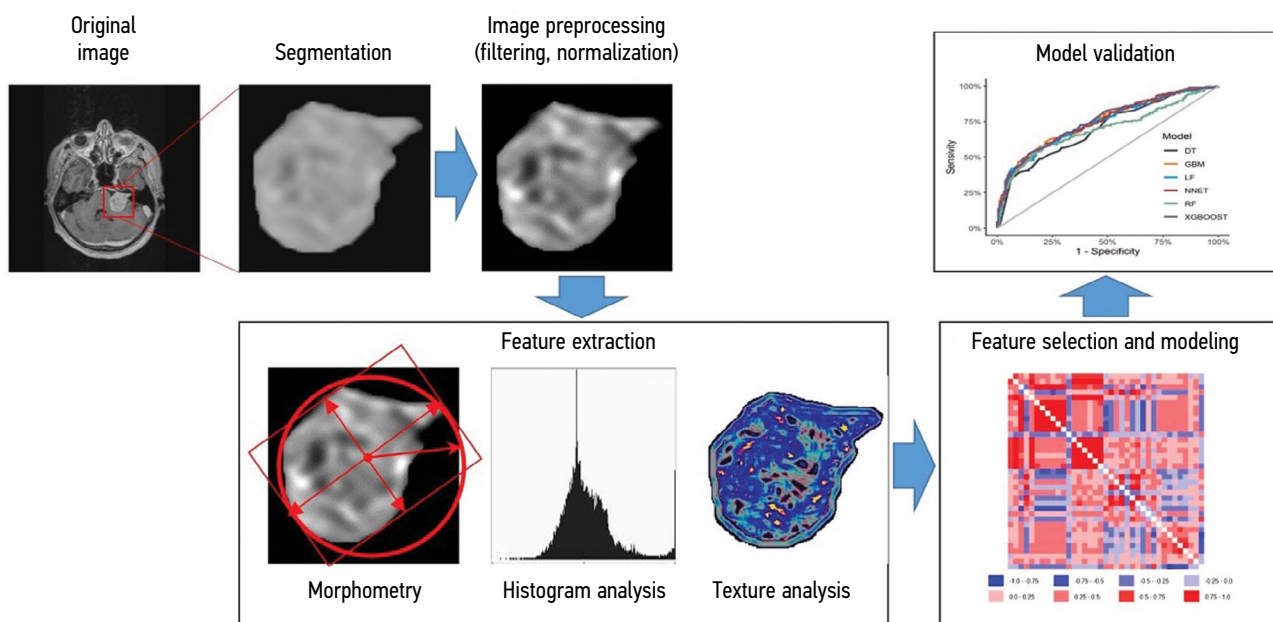


Fig. 1. Radiomic analysis stages.

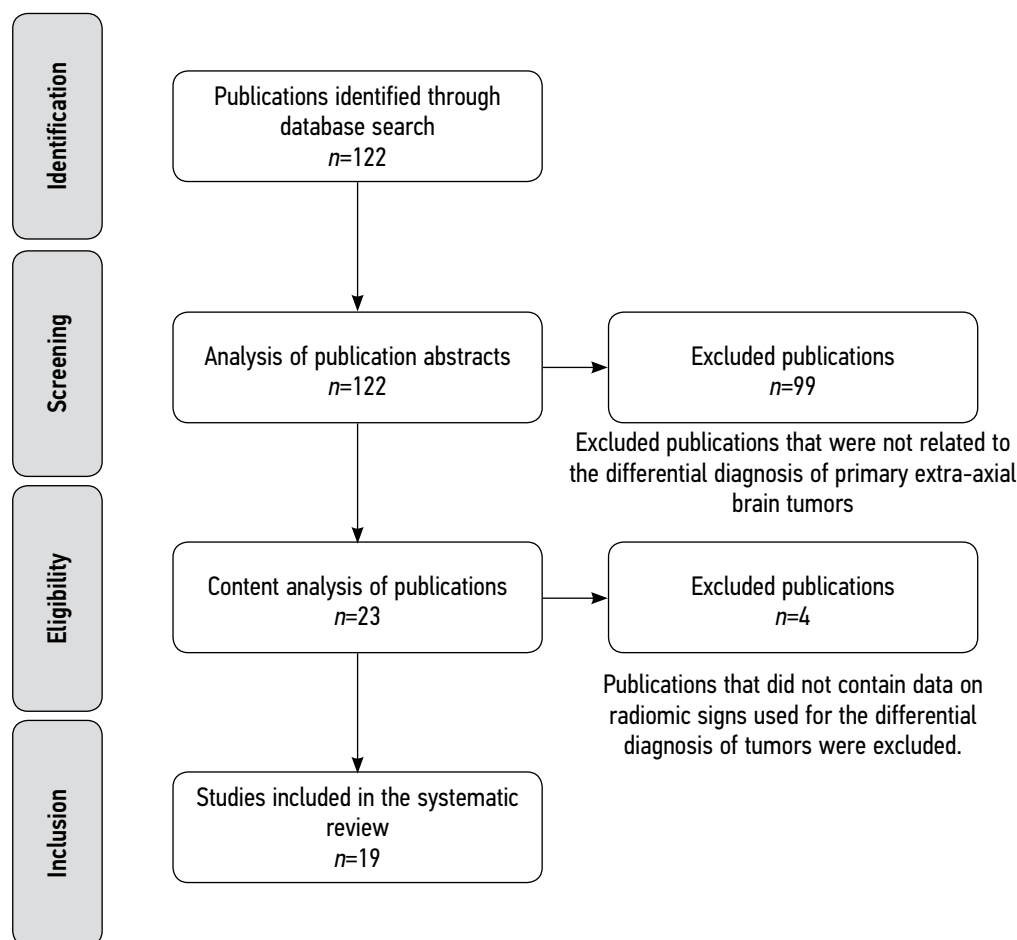


Fig. 2. Research design.

- Method of tumor segmentation
- WI types
- Significant differential diagnostic features
- Mathematical models used
- Validating the mathematical models used to classify tumors

This review included data from original clinical trials.

RESULTS

Several studies have investigated the effectiveness of radiomic features of MRI images in the differential diagnosis of PEABTs. In total, 121 studies published in the last 5 years were found in PubMed/MEDLINE and Google Scholar for the search query “meningioma or neuroma or schwannoma or solitary fibrous tumor) + (texture or radiomic) + MRI.” For queries with different combinations of the words “MRI, meningioma, neuroma, schwannoma, solitary fibrous tumor, radiomics, and texture,” only one publication was found in eLibrary. After analyzing the publications, 19 articles in English and Russian were included in the review.

Table 1 shows the characteristics of the selected articles according to research design.

DISCUSSION

Differential diagnosis

Twelve studies were found to have investigated the differential diagnosis of benign and malignant meningiomas. The differential diagnosis of meningiomas and solitary fibrous tumors was evaluated in four studies, and the differentiation between meningioma and hemangioma/craniopharyngioma/neurinoma was examined in one study.

Most studies have discussed a “binary” classification between two types of PEABTs [18,19,22-32,34,35]. Given the similar semiotics of all PEABTs, models capable of performing multiclass rather than binary classification between two prespecified tumor types have an advantage for clinical use. However, only four studies have distinguished between three or more types of PEABTs [20,21,33,36].

Comparison of the effectiveness of tumor classification by visual assessment and models based on mri semiotics or radiomic parameters

Two studies have compared the effectiveness of tumor classification between radiologists and radiomics models [20,30]. In these studies, the tumor type was determined by a radiologist based on the MRI image, without mathematical

Table 1. Diagnostic tasks of radiomic analysis for the differential diagnosis of primary extra-axial brain tumors

1	2	3	4	5	6	7	8
Authors	Types of tumors	Number of patients	Segmentation	The most informative signs	Method of modeling	Validation (number; %)	Diagnostic information content
Y.W. Park et al. 2019 [18]	Mb/Mm	136	SA	T1-CE (Histo, GLCM, GLRLM) ADC (Histo, GLCM, GLRLM)	RF, SVM	58; 42.6%	The best model (SVM): AUC 0.86; Acc 89.7%; Sn 75%; Sp 93.5% Other models: AUC 0.74–0.85
<i>K.R. Laukamp et al. 2019 [19]</i>							
Y. Lu et al. 2019 [20]	Gr 1/2/3	152	Man	ADC (Histo, GLCM, GLRLM, AU, Wav)	DT	46; 30.2%	Radiomics model: Acc, 79.51% Model (semiotics + clinical data): Acc, 62.96% Classification by radiologists: Acc, 61%–62%
C. Chen et al. 2019 [21]	Gr 1/2/3	150	Man	Shape T1-CE (GLCM, GLRLM, GLSZM)	LDA, SVM	30; 20%	The best model (LDA): Acc, 75.6% Other models: 57.6%–73.3%
Y. Zhu et al. 2019 [22]	Mb/Mm	181	Man	Shape T1-CE (GLCM, GLRLM, GLSZM)	SVM	82; 45.3%	The best model: AUC, 0.811; Sn, 76.9%; Sp, 89.8%
O. Morin et al. 2019 [23]	Mb/Mm	303	NA	Shape T1-CE (Histo, Wav GLCM, GLRLM, GLSZM)	RF	85; 28.1%	Semiotics model: AUC, 0.68; Acc, 62% Radiomics model: AUC, 0.71; Acc, 65%
X. Li et al. 2019 [24]	Mb/Mm	90	Man	Shape T2-WI, T1-WI и T1-CE (Histo)	LR	28; 31.1%	Models of individual weight types: AUC, 0.781–0.821
C. Ke et al. 2020 [25]	Mb/Mm	263	Man	T2-WI (GLCM, GLRLM, GLSZM) T1-WI (GLCM) T1-CE (GLRLM, GLSZM)	SVM	79; 30%	Models of individual weight types: AUC, 0.67–0.75; Acc, 68%–75%; Sn, 42%–74%; Sp, 67%–82% Models of weight combination: AUC, 0.83; Acc, 80%; Sn, 84%; Sp, 78%
J. Hu et al. 2020 [26]	Mb/Mm	316	SA	Shape T2-WI и T1-WI (Wav) T1-CE (Histo, GLSZM, Wav) ADC (Histo, GLCM, Wav) SWI (GLCM, Wav)	RF	NP	Model (semiotics + clinical data): AUC, 0.7 Model (T2-WI + T1-WI + T1-CE): AUC, 0.78; Acc, 74%; Sn, 65.5%; Sp, 77.7% Model (T2-WI + T1-WI + T1-CE + ADC + SWI): AUC, 0.81; Acc, 78%; Sn, 66.7%; Sp, 83%
Y.W. Park et al. 2019 [18]	Mb/Mm	136	SA	T1-CE (Histo, GLCM, GLRLM) ADC (Histo, GLCM, GLRLM)	RF, SVM	58; 42.6%	The best model (SVM): AUC, 0.86; Acc, 89.7%; Sn, 75%; Sp, 93.5% Other models: AUC, 0.74–0.85
K.R. Laukamp et al. 2019 [19]	Mb/Mm	71	SA	Shape FLAIR (GLCM) ADC (GLSZM)	LR	NP	Models of weight types: AUC, 0.72–0.8 Models of weight combination: AUC, 0.91; Sn, 79%; Sp, 89%
H. Chu et al. 2021 [27]	Mb/Mm	98	SA	Shape T1-CE (Histo, GLCM, GLRLM, GLSZM)	LR	30; 30.6%	Radiomics model: AUC, 0.948; Acc, 92.9%; Sn, 91.7%; Sp, 100%
Y. Han et al. 2021 [28]	Mb/Mm	131	NA	Shape T1 FLAIR (Histo, GLRLM, GLSZM)	LR, RF, SVM, KNN, DT, and XGB	27; 20.6%	Model T1 FLAIR: AUC, 0.956; Sn, 87%; Sp, 92% Models of weight combination: AUC, 0.922; Sn, 87%; Sp, 93%

1	2	3	4	5	6	7	8
J. Zhang et al. 2022 [29]	Gr 1/2	242	Man	T2-WI (GLRLM, Wav) T1-CE (GLSZM, Wav)	LR	73; 30.2%	Models of individual weight types: AUC, 0.67–0.717; Acc, 61.1%–69.4%; Sn, 60.7%–75%; Sp, 61.4%–65.9% Models of weight combination: AUC, 0.734; Acc, 72.2%; Sn, 67.9%; Sp, 75%
<i>Differential diagnosis of meningiomas and solitary fibrous tumors</i>							
X. Li et al. 2019 [30]	Mb/SFT	67	Man	FLAIR, DWI и T1-CE (GLRLM)	SVM	20; 29.9%	Model T1-CE: AUC, 0.90; Acc, 87.5% Classification by radiologists: AUC, up to 0.7; Acc, up to 77.3% Models of individual weight types: AUC, 0.772–0.864; Acc, 69.5%–81.4%; Sn, 60%–73.3%; Sp, 79.3%–89.7% Models of weight combination: AUC, 0.939; Acc, 83.1; Sn, 90%; Sp, 75.9% Models of individual weight types: AUC, 0.75–0.85; Acc, 69.9%–72.6%; Sn, 68.5%–98%; Sp, 13.6%–87.5% Models of weight combination: AUC, 0.9; Acc, 82.2%; Sn, 79.6%; Sp, 87.5% Model (clinical data + semiotics): AUC, 0.79; Acc, 76.7%; Sn, 79.6%; Sp, 70.8% Model (clinical data + semiotics): AUC, 0.766; Acc, 65.9%; Sn, 67.4%; Sp, 64.3%
J. Dong et al. 2020 [31]	Mb/SFT	192	Man	T2-WI (GLCM, GLRLM, GLSZM) T1-WI (Histo, GLCM, GLSZM) T1-CE (Histo, GLCM, GLRLM)	LR	59; 30.7%	
Y. Fan et al. 2022 [32]	Mb/SFT	220	NA	Semiotics T2-WI (Histo, GLCM, GLRLM, GLRLM) T1-CE (GLRLM)	SVM, LR	73; 33.2%	
J. Wei et al. 2022 [33]	Gr 1–3/ SFT	292	Man	T2-WI (Histo, GLCM, GLRLM, GLSZM, NGTDM, Wav) T1-WI (GLCM, Wav, GLRLM) T1-CE (GLCM, Wav, GLSZM)	LR, DT, RF, and SVM	88; 30.1%	Models of individual weight types: AUC, 0.731–0.818; Acc, 64.8%–71.6%; Sn, 63%–89.1%; Sp, 52.4%–66.7% Models of weight combination: AUC, 0.902; Acc, 81.8%; Sn, 89.1%; Sp, 73.8%
Z. Tian et al. 2020 [34]	M/C	127	Man	<i>Differential diagnosis of meningiomas from other PEABTs</i> Semiotics T2-WI (Histo) T1-CE (Histo, GLCM)	LR	NP	Model AUC T1-CE: 0.776
C. Wang et al. 2022 [35]	M/H	96	Man	Shape T2-WI, T1-CE и ADC (Histo, Wav) T1-WI (Histo, GLSZM, GLRLM, Wav) DWI (GLCM, Wav)	KNN, LR, RF, SVM, XGB, and DT	19; 20%	Classification by radiologists: AUC, 0.545–0.756 Semiotics model: AUC, 0.805 The best model (ADC, SVM): AUC, 0.95 Other radiomics models: AUC, 0.73–0.94
Yevgeniy N. Surovisev et al. 2023 [36]	Mb/Mm/H	66	A	T2-WI (GLCM, GLRLM, Wav) T1-WI (GLCM Wav) FLAIR (Wav) ADC (GLCM, GLRLM) T1-CE (Histo)	LDA	27; 40.9%	Semiotics model: AUC, 0.78; Sn, 50%–83.3%; Sp, 75%–81% Radiomics model: AUC, 0.86; Sn, 83.3%–100%; Sp, 91.7%–100%

Note. Abbreviations:
Tumors: Mb, benign meningiomas (grade 1); Mm, malignant meningiomas (grades 2 and 3); M, meningiomas without grade; N, neurinomas; C, craniopharyngiomas; H, hemangiomas; SFT, solitary fibrous tumors; Gr, grade
Segmentation: Man, manual; SA, semiautomatic; A, automatic
Features: ADC, apparent diffusion coefficient; SWI, susceptibility weighted imaging; Histo, histogram; GLCM, gray level co-occurrence matrix; GLRLM, gray level run length matrix; GLSZM, gray level size zone matrix; NGTDM, gray-tone difference matrix; AU, autoregressive model; Wav, wavelet
Mathematical modeling methods: LR, logistic regression; NB, naive Bayes classifier; SVM, support vector machine; TC, text categorization; KNN, K-nearest neighbors method; DT, decision tree; RF, random forest; LDA, linear discriminant analysis; XGB, extreme gradient boost; MLP, multilayer perceptron
Test information parameters: Acc, accuracy; Sn, sensitivity; Sp, specificity; AUC, area under the curve
Other: NP, not performed; NA, not available

modeling based on visual features. The use of radiomics models was advantageous, with an accuracy of 10%–17%.

Five studies have compared the accuracy of tumor classification between models based on MRI semiotics and radiomics features [20,23,32,33,36]. In these studies, the visual semiotic features were systematized and stratified. Based on these features, mathematical models may be developed.

The use of mathematical semiotic models for tumor classification may be more advantageous over the radiologist's opinion because a radiologist's differential diagnosis is largely based on experience and subjective. Moreover, systematizing and integrating the evaluation of MRI semiotic features increases their information value.

Differentiating tumors using models based on radiomic parameters was significantly superior to classifying tumors by radiologists, and their information value was higher than that of semiotic models.

The most valuable studies are those that compare the information value of radiomics models with the results of visual assessment of MRI semiotics. Furthermore, the ability to automate image analysis for computer decision support systems remains an advantage of the radiomics approach.

Patient sample size and model validation

Most studies have included relatively small numbers of patients:

- <100 patients: 6 publications [19,24,27,30,35,36],
- 100–200 patients: 7 publications [18,20–22,28,31,34],
- 200–300 patients: 4 publications [25,29,32,33],
- >300 patients: 2 publications [23,26].

Larger samples are typical for differential diagnosis studies of meningiomas. The small sample size may be because of the unequal prevalence of the different types of PEABTs. Most PEABTs (> 80%) are benign meningiomas, and other tumors are rare [4], making it challenging to select a large patient population.

Validation was completed in 84.2% of the trials. In most studies, the validated group comprised approximately one-third of the total enrolled patients. Note that the clinical significance of differential diagnostic models is reduced by the lack of testing of model performance on the validation set.

Tumor segmentation

Segmenting the tumor is the first and fundamental step in radiomics analysis [14]. To avoid distortion of radiomic features and ensure reproducibility of results, the segmentation technique should accurately distinguish neoplastic tissue from brain matter and peripheral edema.

Most PEABTs are characterized by a marked increase in MRI signal intensity on T1-WI after contrast administration, whereas the isointense and hypointense MRI signals of adjacent structures are preserved [9]. This feature is the basis for the sharp difference in brightness between the

contrasted tumor and adjacent structures and accuracy of tumor margin visualization. Most studies included in the review (63.2%) have performed segmentation specifically on contrast-enhanced T1-WI [18,21–28,30,33,36].

The segmentation method affects the final simulation result. The automatic and semiautomatic methods have a higher reproducibility than the manual methods in the determination of tumor boundaries [37]. In the presented studies, less preferred manual segmentation was most common [18–20,22,23,27–29,31–33]. Only five studies have used automated or semiautomated methods [18,19,26,27,36].

Significant radiomic features

A feature of radiomics studies is the presence of a sufficiently large initial set of parameters, and the most informative parameters are selected to solve the problem. Histogram and texture parameters of tumors are the most informative radiomic features for the differential diagnosis of PEABTs.

The power of radiomics models for the differential diagnosis of PEABTs is increased by expanding the set of radiomic parameters to include different WI types. Seven studies have compared models based on the radiomic parameters of one WI type with models that included the features of different WI types [19,25,28,29,31–33]. In six of these studies, the advantage of the latter was demonstrated based on a comparison of the information values of the tests [19,25,29,31–33]. One study has revealed the poor results of weight combination models [28].

In comparing the two combined models, Hu et al. [26] have shown that a model containing an extended spectrum of weights (T2-WI, T1-WI, T1-CE, apparent diffusion coefficient [ADC] map, susceptibility weighted imaging [SWI]) was slightly superior to a model based on T2-WI, T1-WI, and T1-CE.

The advantage of models using several types of weights is their ability to reflect different aspects of the tumor. For example, T2-WI and T1-WI reflect the degree of hydration (amount of fluid) in the tumor, T1-CE reflects the permeability of the blood–brain barrier, DWI and ADC reflect the cellularity of the tumor, and SWI is sensitive to hemorrhage and fossilization. Therefore, integrating the parameters within the model allows a more complete representation of the morphological characteristics and better results.

The shape parameter values were limited. The information value of these parameters was evaluated in ten studies [21–23,26–28,31–33,35]. Shape parameters were informative in studies that have performed modeling based on one WI type [21–23,27,28,35]. Three studies [31–33] have shown that shape parameters are uninformative when constructing models that include multiple WI types. In a study by Hu et al. [26], shape parameters were informative and were included in the modeling; however, their proportion was not large compared with that of histogram and texture parameters (the model included 17 histogram and texture parameters and 3 morphometric parameters).

Mathematical modeling methods

In the presented studies, various mathematical modeling methods were used to create models. The most common algorithms were as follows:

- Support vector machine (SVM): 9 studies [18,21,22,25,28,30,32,33,35],
- Logistic regression (LR): 10 studies [19,24,27–29,31–35],
- Random forest (RF): 6 studies [18,23,26,28,33,35].

Three studies [18,28,33] have analyzed the results of tumor classification using models based on these methods and showed conflicting results. In a study by Park et al. [18] (RF and SVM) and in another by Wei et al. [33] (LR, RF, SVM), the methods showed a comparable level of information value. However, in a study by Han et al. [28], the results varied significantly according to the modeling technique (one of the information value parameters of the test, area under the curve (AUC), varied from 0.628 to 0.922), whereas the SVM showed more stable results.

Among all modeling methods, the best information value parameters were demonstrated by LR [27] and SVM [35], wherein the AUC was 0.95.

CONCLUSION

The use of radiomics approach shows promising results in the differential diagnosis of PEABTs. Additionally, clinical practice implementation requires greater methodological rigor in the conduct of radiomics studies, including mandatory

validation, standardization of segmentation methods, determination of the required feature set, and more informed choice of mathematical modeling methods. The use of histograms and texture parameters of different WI types for further revealing the potential of radiomics in the differential detection of PEABTs appears favorable.

Prospective studies using automated segmentation methods and an expanded set of WI types and the development of radiomics models that allow multiclass differential diagnosis of PEABTs may lay the foundation for creating powerful tools for digital clinical decision support systems and can ensure optimal patient treatment selection.

ADDITIONAL INFORMATION

Funding source. This study was not supported by any external sources of funding.

Competing interests. The authors declare that they have no competing interests.

Authors' contribution. All authors made a substantial contribution to the conception of the work, acquisition, analysis, interpretation of data for the work, drafting and revising the work, final approval of the version to be published and agree to be accountable for all aspects of the work. The major contributions were distributed as follows: A.V. Kapishnikov — the concept of the study, approval of the final version; E.N. Surovcev — concept and design of the work, manuscript text writing and editing, collection and processing of materials, data analysis.

REFERENCES

1. Goldbrunner R, Stavrinou P, Jenkinson MD, et al. EANO guideline on the diagnosis and management of meningiomas. *Neuro-Oncology*. 2021;23(11):1821–1834. doi: 10.1093/neuonc/noab150
2. Goldbrunner R, Weller M, Regis J, et al. EANO guideline on the diagnosis and treatment of vestibular schwannoma. *Neuro-Oncology*. 2020;22(1):31–45. doi: 10.1093/neuonc/noz153
3. Shin DW, Kim JH, Chong S, et al. Intracranial solitary fibrous tumor/hemangiopericytoma: tumor reclassification and assessment of treatment outcome via the 2016 WHO classification. *Journal of Neuro-Oncology*. 2021;154:171–178. doi: 10.1007/s11060-021-03733-7
4. Louis DN, Perry A, Wesseling P, et al. The 2021 WHO Classification of Tumors of the Central Nervous System: a summary. *Neuro-Oncology*. 2021;23(8):1231–1251. doi: 10.1093/neuonc/noab106
5. Fountain DM, Young AMH, Santarius T. Malignant meningiomas. *Handbook of Clinical Neurology*. 2020;170:245–250. doi: 10.1016/B978-0-12-822198-3.00044-6
6. Laviv Y, Thomas A, Kasper EM. Hypervascular Lesions of the Cerebellopontine Angle: The Relevance of Angiography as a Diagnostic and Therapeutic Tool and the Role of Stereotactic Radiosurgery in Management. A Comprehensive Review. *World Neurosurgery*. 2017;100:100–117. doi: 10.1016/j.wneu.2016.12.091
7. Konar S, Jayan M, Shukla D, et al. The risks factor of recurrence after skull base hemangiopericytoma management: A retrospective case series and review of literature. *Clinical Neurology and Neurosurgery*. 2021;208:106866. doi: 10.1016/j.clineuro.2021.106866
8. Kinslow CJ, Bruce SS, Rae AI, et al. Solitary-fibrous tumor/hemangiopericytoma of the central nervous system: a population-based study. *Journal of Neuro-Oncology*. 2018;138(1):173–182. doi: 10.1007/s11060-018-2787-7
9. Osborn AG, Salzman KL, Jhaveri MD. *Diagnostic Imaging. Brain*. Moscow: Izdatel'stvo Panfilova; 2018. (In Russ).
10. Cohen-Inbar O. Nervous System Hemangiopericytoma. *Canadian Journal of Neurological Sciences*. 2020;47(1):18–29. doi: 10.1017/cjn.2019.311
11. Zakhari N, Torres C, Castillo M, et al. Uncommon Cranial Meningioma: Key Imaging Features on Conventional and Advanced Imaging. *Clinical Neuroradiology*. 2017;27(2):135–144. doi: 10.1007/s00062-017-0583-y
12. Hale AT, Wang L, Strother MK, et al. Differentiating meningioma grade by imaging features on magnetic resonance imaging. *Journal of Clinical Neuroscience*. 2018;48:71–75. doi: 10.1016/j.jocn.2017.11.013
13. Ugga L, Spadarella G, Pinto L, et al. Meningioma Radiomics: At the Nexus of Imaging, Pathology and Biomolecular Characterization. *Cancers (Basel)*. 2022;14(11):2605. doi: 10.3390/cancers14112605

14. Aerts HJ. The Potential of Radiomic-Based Phenotyping in Precision Medicine: A Review. *JAMA Oncology*. 2016;2(12):1636–1642. doi: 10.1001/jamaoncol.2016.2631
15. Gillies RJ, Kinahan PE, Hricak H. Radiomics: Images Are More than Pictures, They Are Data. *Radiology*. 2016;278(2):563–577. doi: 10.1148/radiol.2015151169
16. Liu Z, Wang S, Dong D, et al. The Applications of Radiomics in Precision Diagnosis and Treatment of Oncology: Opportunities and Challenges. *Theranostics*. 2019;9(5):1303–1322. doi: 10.7150/thno.30309
17. Kapishnikov AV, Surovcev EN, Udalov YuD. Magnetic Resonance Imaging of Primary Extra-Axial Intracranial Tumors: Diagnostic Problems and Prospects of Radiomics. *Medical Radiology and Radiation Safety*. 2022;67(4):49–56. (In Russ). doi: 10.33266/1024–6177–2022–67–4–49–56
18. Park YW, Oh J, You SC, et al. Radiomics and machine learning may accurately predict the grade and histological subtype in meningiomas using conventional and diffusion tensor imaging. *European Radiology*. 2019;29(8):4068–4076. doi: 10.1007/s00330–018–5830–3
19. Laukamp KR, Shakirin G, Baeßler B, et al. Accuracy of Radiomics–Based Feature Analysis on Multiparametric Magnetic Resonance Images for Noninvasive Meningioma Grading. *World Neurosurgery*. 2019;132:e366–e390. doi: 10.1016/j.wneu.2019.08.148
20. Lu Y, Liu L, Luan S, et al. The diagnostic value of texture analysis in predicting WHO grades of meningiomas based on ADC maps: an attempt using decision tree and decision forest. *European Radiology*. 2019;29(3):1318–1328. doi: 10.1007/s00330–018–5632–7
21. Chen C, Guo X, Wang J, et al. The Diagnostic Value of Radiomics–Based Machine Learning in Predicting the Grade of Meningiomas Using Conventional Magnetic Resonance Imaging: A Preliminary Study. *Frontiers in Oncology*. 2019;9:1338. doi: 10.3389/fonc.2019.01338
22. Zhu Y, Man C, Gong L, et al. A deep learning radiomics model for preoperative grading in meningioma. *European Journal of Radiology*. 2019;116:128–134. doi: 10.1016/j.ejrad.2019.04.022
23. Morin O, Chen WC, Nassiri F, et al, Vasudevan HN, et al. Integrated models incorporating radiologic and radiomic features predict meningioma grade, local failure, and overall survival. *Neuro–Oncology Advances*. 2019;1(1):z11. doi: 10.1093/neoajnl/vdz011
24. Li X, Miao Y, Han L, et al. Meningioma grading using conventional MRI histogram analysis based on 3D tumor measurement. *European Journal of Radiology*. 2019;110:45–53. doi: 10.1016/j.ejrad.2018.11.016
25. Ke C, Chen H, Lv X, et al. Differentiation Between Benign and Nonbenign Meningiomas by Using Texture Analysis From Multiparametric MRI. *Journal of Magnetic Resonance Imaging*. 2020;51(6):1810–1820. doi: 10.1002/jmri.26976
26. Hu J, Zhao Y, Li M, et al. Machine learning–based radiomics analysis in predicting the meningioma grade using multiparametric MRI. *European Journal of Radiology*. 2020;131. doi: 10.1016/j.ejrad.2020.109251
27. Chu H, Lin X, He J, et al. Value of MRI Radiomics Based on Enhanced T1WI Images in Prediction of Meningiomas Grade. *Academic Radiology*. 2021;28(5):687–693. doi: 10.1016/j.acra.2020.03.034
28. Han Y, Wang T, Wu P, et al. Meningiomas: Preoperative predictive histopathological grading based on radiomics of MRI. *Magnetic Resonance Imaging*. 2021;77:36–43. doi: 10.1016/j.mri.2020.11.009
29. Zhang J, Zhang G, Cao Y, et al. A Magnetic Resonance Imaging–Based Radiomic Model for the Noninvasive Preoperative Differentiation Between Transitional and Atypical Meningiomas. *Frontiers in Oncology*. 2022;12:811767. doi: 10.3389/fonc.2022.811767
30. Li X, Lu Y, Xiong J, et al. Presurgical differentiation between malignant haemangiopericytoma and angiomatous meningioma by a radiomics approach based on texture analysis. *Journal of Neuroradiology*. 2019;46(5):281–287. doi: 10.1016/j.neurad.2019.05.013
31. Dong J, Yu M, Miao Y, et al. Differential Diagnosis of Solitary Fibrous Tumor/Hemangiopericytoma and Angiomatous Meningioma Using Three–Dimensional Magnetic Resonance Imaging Texture Feature Model. *BioMed Research International*. 2020;2020. doi: 10.1155/2020/5042356
32. Fan Y, Liu P, Li Y, et al. Non–Invasive Preoperative Imaging Differential Diagnosis of Intracranial Hemangiopericytoma and Angiomatous Meningioma: A Novel Developed and Validated Multiparametric MRI–Based Clin–Radiomic Model. *Frontiers in Oncology*. 2022;11:792521. doi: 10.3389/fonc.2021.792521
33. Wei J, Li L, Han Y, et al. Accurate Preoperative Distinction of Intracranial Hemangiopericytoma From Meningioma Using a Multihabitat and Multisequence–Based Radiomics Diagnostic Technique. *Frontiers in Oncology*. 2020;10:534. doi: 10.3389/fonc.2020.00534
34. Tian Z, Chen C, Zhang Y, et al. Radiomic Analysis of Craniopharyngioma and Meningioma in the Sellar/Parasellar Area with MR Images Features and Texture Features: A Feasible Study. *Contrast Media & Molecular Imaging*. 2020;2020. doi: 10.1155/2020/4837156
35. Wang C, You L, Zhang X, et al. A radiomics–based study for differentiating parasellar cavernous hemangiomas from meningiomas. *Scientific Reports*. 2022;12. doi: 10.1038/s41598–022–19770–9
36. Surovcev EN, Kapishnikov AV, Kolsanov AV. Comparative evaluation of the possibilities of radiomic analysis of magnetic resonance imaging in the differential diagnostics of primary extra-axial intracranial tumors. *Research and Practical Medicine Journal*. 2023;10(2):50–61. (In Russ). doi: 10.17709/2410–1893–2023–10–2–5
37. Parmar C, Rios Velazquez E, Leijenaar R, et al. Robust Radiomics feature quantification using semiautomatic volumetric segmentation. *PLoS One*. 2014;9(7):e102107. doi: 10.1371/journal.pone.0102107

СПИСОК ЛИТЕРАТУРЫ

1. Goldbrunner R., Stavrinou P., Jenkinson M.D., et al. EANO guideline on the diagnosis and management of meningiomas // *Neuro–Oncology*. 2021. Vol. 23, N 11. P. 1821–1834. doi: 10.1093/neoajnl/noab150
2. Goldbrunner R., Weller M., Regis J., et al. EANO guideline on the diagnosis and treatment of vestibular schwannoma // *Neuro–Oncology*. 2020. Vol. 22, N 1. P. 31–45. doi: 10.1093/neoajnl/noz153
3. Shin D.W., Kim J.H., Chong S., et al. Intracranial solitary fibrous tumor/hemangiopericytoma: tumor reclassification and assessment of treatment outcome via the 2016 WHO classification // *Journal*

- of Neuro-Oncology. 2021. Vol. 154. P. 171–178. doi: 10.1007/s11060-021-03733-7
4. Louis D.N., Perry A., Wesseling P., et al. The 2021 WHO Classification of Tumors of the Central Nervous System: a summary // *Neuro-Oncology*. 2021. Vol. 23, N 8. P. 1231–1251. doi: 10.1093/neuonc/noab106
5. Fountain D.M., Young A.M.H., Santarius T. Malignant meningiomas // *Handbook of Clinical Neurology*. 2020. Vol. 170. P. 245–250. doi: 10.1016/B978-0-12-822198-3.00044-6
6. Laviv Y., Thomas A., Kasper E.M. Hypervascular Lesions of the Cerebellopontine Angle: The Relevance of Angiography as a Diagnostic and Therapeutic Tool and the Role of Stereotactic Radiosurgery in Management. A Comprehensive Review // *World Neurosurgery*. 2017. Vol. 100. P. 100–117. doi: 10.1016/j.wneu.2016.12.091
7. Konar S., Jayan M., Shukla D., et al. The risks factor of recurrence after skull base hemangiopericytoma management: A retrospective case series and review of literature // *Clinical Neurology and Neurosurgery*. 2021. Vol. 208. P. 106866. doi: 10.1016/j.clineuro.2021.106866
8. Kinslow C.J., Bruce S.S., Rae A.I., et al. Solitary-fibrous tumor/hemangiopericytoma of the central nervous system: a population-based study // *Journal of Neuro-Oncology*. 2018. Vol. 138, N 1. P. 173–182. doi: 10.1007/s11060-018-2787-7
9. Осборн А.Г., Зальцман К.Л., Завери М.Д. Лучевая диагностика. Головной мозг / пер. Д.И. Волобуева. Москва : Издательство Панфилова, 2018.
10. Cohen-Inbar O. Nervous System Hemangiopericytoma // *Canadian Journal of Neurological Sciences*. 2020. Vol. 47, N 1. P. 18–29. doi: 10.1017/cjn.2019.311
11. Zakhari N., Torres C., Castillo M., et al. Uncommon Cranial Meningioma: Key Imaging Features on Conventional and Advanced Imaging // *Clinical Neuroradiology*. 2017. Vol. 27, N 2. P. 135–144. doi: 10.1007/s00062-017-0583-y
12. Hale A.T., Wang L., Strother M.K., et al. Differentiating meningioma grade by imaging features on magnetic resonance imaging // *Journal of Clinical Neuroscience*. 2018. Vol. 48. P. 71–75. doi: 10.1016/j.jocn.2017.11.013
13. Ugga L., Spadarella G., Pinto L., et al. Meningioma Radiomics: At the Nexus of Imaging, Pathology and Biomolecular Characterization // *Cancers (Basel)*. 2022. Vol. 14, N 11. P. 2605. doi: 10.3390/cancers14112605
14. Aerts H.J. The Potential of Radiomic-Based Phenotyping in Precision Medicine: A Review // *JAMA Oncology*. 2016. Vol. 2, N 12. P. 1636–1642. doi: 10.1001/jamaoncol.2016.2631
15. Gillies R.J., Kinahan P.E., Hricak H. Radiomics: Images Are More than Pictures, They Are Data // *Radiology*. 2016. Vol. 278, N 2. P. 563–577. doi: 10.1148/radiol.2015151169
16. Liu Z., Wang S., Dong D., et al. The Applications of Radiomics in Precision Diagnosis and Treatment of Oncology: Opportunities and Challenges // *Theranostics*. 2019. Vol. 9, N 5. P. 1303–1322. doi: 10.7150/thno.30309
17. Капишников А.В., Суровцев Е.Н., Удалов Ю.Д. Магнитно-резонансная томография первичных внеозговых опухолей: проблемы диагностики и перспективы радиомики // *Медицинская радиология и радиационная безопасность*. 2022. Т. 67. № 4. С. 49–56. doi: 10.33266/1024-6177-2022-67-4-49-56
18. Park Y.W., Oh J., You S.C., et al. Radiomics and machine learning may accurately predict the grade and histological subtype in meningiomas using conventional and diffusion tensor imaging. *European Radiology*. 2019. Vol. 29, N 8. P. 4068–4076. doi: 10.1007/s00330-018-5830-3
19. Laukamp K.R., Shakirin G., Baeßler B., et al. Accuracy of Radiomics-Based Feature Analysis on Multiparametric Magnetic Resonance Images for Noninvasive Meningioma Grading // *World Neurosurgery*. 2019;132:e366–e390. doi: 10.1016/j.wneu.2019.08.148.
20. Lu Y., Liu L., Luan S., et al. The diagnostic value of texture analysis in predicting WHO grades of meningiomas based on ADC maps: an attempt using decision tree and decision forest // *European Radiology*. 2019. Vol. 29, N 3. P. 1318–1328. doi: 10.1007/s00330-018-5632-7
21. Chen C., Guo X., Wang J., et al. The Diagnostic Value of Radiomics-Based Machine Learning in Predicting the Grade of Meningiomas Using Conventional Magnetic Resonance Imaging: A Preliminary Study // *Frontiers in Oncology*. 2019. Vol. 9. P. 1338. doi: 10.3389/fonc.2019.01338
22. Zhu Y., Man C., Gong L., et al. A deep learning radiomics model for preoperative grading in meningioma // *European Journal of Radiology*. 2019. Vol. 116. P. 128–134. doi: 10.1016/j.ejrad.2019.04.022
23. Morin O., Chen W.C., Nassiri F., et al, Vasudevan HN, et al. Integrated models incorporating radiologic and radiomic features predict meningioma grade, local failure, and overall survival // *Neuro-Oncology Advances*. 2019. Vol. 1, N 1. P. z11. doi: 10.1093/oaajnl/vdz011
24. Li X., Miao Y., Han L., et al. Meningioma grading using conventional MRI histogram analysis based on 3D tumor measurement // *European Journal of Radiology*. 2019. Vol. 110. P. 45–53. doi: 10.1016/j.ejrad.2018.11.016
25. Ke C., Chen H., Lv X., et al. Differentiation Between Benign and Nonbenign Meningiomas by Using Texture Analysis From Multiparametric MRI // *Journal of Magnetic Resonance Imaging*. 2020. Vol. 51, N 6. P. 1810–1820. doi: 10.1002/jmri.26976
26. Hu J., Zhao Y., Li M., et al. Machine learning-based radiomics analysis in predicting the meningioma grade using multiparametric MRI // *European Journal of Radiology*. 2020. Vol. 131. doi: 10.1016/j.ejrad.2020.109251
27. Chu H., Lin X., He J., et al. Value of MRI Radiomics Based on Enhanced T1WI Images in Prediction of Meningiomas Grade // *Academic Radiology*. 2021. Vol. 28, N 5. P. 687–693. doi: 10.1016/j.acra.2020.03.034
28. Han Y., Wang T., Wu P., et al. Meningiomas: Preoperative predictive histopathological grading based on radiomics of MRI // *Magnetic Resonance Imaging*. 2021. Vol. 77. P. 36–43. doi: 10.1016/j.mri.2020.11.009
29. Zhang J., Zhang G., Cao Y., et al. A Magnetic Resonance Imaging-Based Radiomic Model for the Noninvasive Preoperative Differentiation Between Transitional and Atypical Meningiomas // *Frontiers in Oncology*. 2022. Vol. 12. P. 811767. doi: 10.3389/fonc.2022.811767

- 30.** Li X., Lu Y., Xiong J., et al. Presurgical differentiation between malignant haemangiopericytoma and angiomatous meningioma by a radiomics approach based on texture analysis // *Journal of Neuroradiology*. 2019. Vol. 46, N 5. P. 281–287. doi: 10.1016/j.neurad.2019.05.013
- 31.** Dong J., Yu M., Miao Y., et al. Differential Diagnosis of Solitary Fibrous Tumor/Hemangiopericytoma and Angiomatous Meningioma Using Three-Dimensional Magnetic Resonance Imaging Texture Feature Model // *BioMed Research International*. 2020. Vol. 2020. doi: 10.1155/2020/5042356
- 32.** Fan Y., Liu P., Li Y., et al. Non-Invasive Preoperative Imaging Differential Diagnosis of Intracranial Hemangiopericytoma and Angiomatous Meningioma: A Novel Developed and Validated Multiparametric MRI-Based Clini-Radiomic Model // *Frontiers in Oncology*. 2022. Vol. 11. P. 792521. doi: 10.3389/fonc.2021.792521
- 33.** Wei J., Li L., Han Y., et al. Accurate Preoperative Distinction of Intracranial Hemangiopericytoma From Meningioma Using a Multihabitat and Multisequence-Based Radiomics Diagnostic Technique // *Frontiers in Oncology*. 2020. Vol. 10. P. 534. doi: 10.3389/fonc.2020.00534
- 34.** Tian Z., Chen C., Zhang Y., et al. Radiomic Analysis of Craniopharyngioma and Meningioma in the Sellar/Parasellar Area with MR Images Features and Texture Features: A Feasible Study // *Contrast Media & Molecular Imaging*. 2020. Vol. 2020. doi: 10.1155/2020/4837156
- 35.** Wang C., You L., Zhang X., et al. A radiomics-based study for differentiating parasellar cavernous hemangiomas from meningiomas // *Scientific Reports*. 2022. Vol. 12. doi: 10.1038/s41598-022-19770-9
- 36.** Суровцев Е.Н., Капишников А.В., Колсанов А.В. Возможности радиомического анализа магнитно-резонансных томограмм в дифференциальной диагностике первичных внеозговых опухолей // *Исследования и практика в медицине*. 2023. Т. 10, № 2. С. 50–61. doi: 10.17709/2410-1893-2023-10-2-5
- 37.** Parmar C., Rios Velazquez E., Leijenaar R., et al. Robust Radiomics feature quantification using semiautomatic volumetric segmentation // *PLoS One*. 2014. Vol. 9, N 7. P. e102107. doi: 10.1371/journal.pone.0102107

AUTHORS' INFO

* **Evgeniy N. Surovcev**, MD;

address: 3 Leninsky Avenue, Togliatti, 445051, Russian Federation;

ORCID: 0000-0002-8236-833X;

eLibrary SPIN: 5252-5661;

e-mail: evgeniisurovcev@mail.ru

Aleksandr V. Kapishnikov, MD, Dr. Sci. (Med.), Professor;

ORCID: 0000-0002-6858-372X;

eLibrary SPIN: 6213-7455;

e-mail: a.v.kapishnikov@samsmu.ru

ОБ АВТОРАХ

* **Суровцев Евгений Николаевич**;

адрес: Российская Федерация, 445051, г. Тольятти, Ленинский проспект, д. 3;

ORCID: 0000-0002-8236-833X;

eLibrary SPIN: 5252-5661;

e-mail: evgeniisurovcev@mail.ru

Капишников Александр Викторович, д-р мед. наук, профессор;

ORCID: 0000-0002-6858-372X;

eLibrary SPIN: 6213-7455;

e-mail: a.v.kapishnikov@samsmu.ru

* Corresponding author / Автор, ответственный за переписку

DOI: <https://doi.org/10.17816/DD532728>

Современный взгляд на основные аспекты подготовки пациентов с дифференцированным раком щитовидной железы к радиойодтерапии: научный обзор

М.В. Рейнберг, К.Ю. Слащук, А.А. Трухин, К.И. Аврамова, М.С. Шеремета

Национальный медицинский исследовательский центр эндокринологии, Москва, Российская Федерация

АННОТАЦИЯ

Рак щитовидной железы — наиболее распространённая опухоль эндокринной системы, составляющая 1–3% всех злокачественных новообразований (по состоянию на 2021 год). В 90% случаев выявляют дифференцированные формы — папиллярный и фолликулярный варианты — обладающие относительно благоприятным прогнозом.

Комбинация хирургического лечения и последующей супрессивной гормональной терапии, радиойодтерапии, обеспечивают благоприятный прогноз у пациентов с высокодифференцированным раком щитовидной железы. Тем не менее сохраняется вероятность недостаточного ответа на радиойодтерапию, что может быть ассоциировано со многими факторами, включая этап подготовки к её проведению. На сегодняшний день сохраняется актуальным вопрос о выборе оптимального метода подготовки пациента к терапии радиоактивным йодом.

В публикации представлен обзор научной литературы, посвящённой аспектам подготовки пациента с высокодифференцированным раком щитовидной железы к проведению терапии радиоактивным йодом. Освещены и обобщены принципы подготовки пациентов на основании рекомендаций ведущих экспертных сообществ и публикаций по данной теме, приняты во внимание нежелательные явления, ассоциированные с радиойодтерапией, качество жизни пациентов, эффективность и отдалённые результаты лечения.

Основная цель обзора — составить целостное представление о методах подготовки пациента с высокодифференцированным раком щитовидной железы к проведению радиойодтерапии, осветить существующие проблемы и перспективные направления исследований с целью модернизации лечения в сторону персонализированной терапии.

Был проведен поиск научных статей и обзоров, опубликованных до конца января 2023 года, в базах данных National Library of Medicine, The Cochrane Library и Google Scholar по следующим ключевым словам: подготовка к радиойодтерапии, тиреотропин альфа, отмена тиреоидных гормонов, побочные эффекты, йод-ограниченная диета, сиалоаденит, первичный гипотиреоз, качество жизни, тиреоидэктомия, дифференцированный рак щитовидной железы, эффективность радиойодтерапии — в их различных комбинациях. Использовались рекомендации по высокодифференцированному раку щитовидной железы следующих научных сообществ: Российские клинические рекомендации по высокодифференцированному раку щитовидной железы, American Thyroid Association, European Thyroid Association, The National Comprehensive Cancer Network, European Association of Nuclear Medicine, British Thyroid Association, European Society for Medical Oncology. Критериями исключения были статьи, не доступные в полном объёме, не на английском или русском языках, систематические обзоры на аналогичную тему. Всего было отобрано и проанализировано 124 источника, выделены общие тенденции современного подхода к подготовке пациентов к терапии радиоактивным йодом и актуальные проблемы, освещены концепции оптимизации подготовки к радиойодтерапии в рамках персонализации терапии, сформированы результаты и выводы.

Ключевые слова: дифференцированный рак щитовидной железы; терапия радиоактивным йодом; йод-ограниченная диета; тиреотропин альфа; методы подготовки; нежелательные явления.

Как цитировать:

Рейнберг М.В., Слащук К.Ю., Трухин А.А., Аврамова К.И., Шеремета М.С. Современный взгляд на основные аспекты подготовки пациентов с дифференцированным раком щитовидной железы к радиойодтерапии: научный обзор // Digital Diagnostics. 2023. Т. 4, № 4. С. 543–568.

DOI: <https://doi.org/10.17816/DD532728>

DOI: <https://doi.org/10.17816/DD532728>

Preparation for radioiodine therapy in patients with differentiated thyroid cancer: a modern perspective (a review)

Maria V. Reinberg, Konstantin Yu. Slashchuk, Alexey A. Trukhin, Karina I. Avramova, Marina S. Sheremeta

Endocrinology Research Centre, Moscow, Russian Federation

ABSTRACT

Thyroid cancer is the most prevalent tumor of the endocrine system, accounting for 1%–3% of all malignant neoplasms as of 2021. Differentiated forms, papillary and follicular, with a relatively favorable prognosis, are detected in 90% of cases. The combination of surgical treatment, subsequent suppressive hormonal therapy, and radioiodine therapy provides a favorable prognosis in patients with differentiated thyroid cancer. However, an insufficient response to radioiodine therapy may be possible, which may be associated with multiple factors, including the preparation step for radioiodine therapy. To date, the question of choosing the optimal method of patient preparation remains relevant. This paper presents a review of the scientific literature on the preparation of patients with differentiated thyroid cancer for radioiodine therapy. The principles of preparation are based on the recommendations of leading expert societies, and publications related to this topic are highlighted and summarized, including the adverse events associated with radioiodine therapy, quality of life, efficacy, and long-term results of treatment. The main purpose of this review was to provide a comprehensive insight into the methods of preparing a patient with differentiated thyroid cancer for radioiodine therapy, highlight existing problems and promising areas of research, and modernize treatment toward personalized therapy. Scientific articles and reviews from the National Library of Medicine, Cochrane Library, and Google Scholar databases, published up to the end of January 2023, were searched by the keywords listed below in their various combinations. Recommendations from the following scientific communities were used: Russian Clinical Guidelines for Differentiated Thyroid Cancer, American Thyroid Association, European Thyroid Association, National Comprehensive Cancer Network, European Association of Nuclear Medicine, British Thyroid Association, and European Society for Medical Oncology. Articles not available in full, not in English or Russian, or systematic reviews of a similar topic, were excluded. In total, 124 sources were selected and analyzed, general tendencies of modern approaches to preparation for radioiodine therapy and actual problems were highlighted, concepts of optimization of preparation for radioiodine therapy within the framework of personalized therapy were covered, and results and conclusions were presented.

Keywords: differentiated thyroid cancer; radioiodine therapy; low-iodine diet; thyrotropin alpha; methods of preparation; side effects

To cite this article:

Reinberg MV, Slashchuk KYu, Trukhin AA, Avramova KI, Sheremeta MS. Preparation for radioiodine therapy in patients with differentiated thyroid cancer: a modern perspective (a review). *Digital Diagnostics*. 2023;4(4):543–568. DOI: <https://doi.org/10.17816/DD532728>

Received: 08.07.2023

Accepted: 05.09.2023

Published online: 10.10.2023

DOI: <https://doi.org/10.17816/DD532728>

目前对分化型甲状腺癌患者放射性碘治疗准备工作主要方面的看法：文献综述

Maria V. Reinberg, Konstantin Yu. Slashchuk, Alexey A. Trukhin, Karina I. Avramova, Marina S. Sheremeta

Endocrinology Research Centre, Moscow, Russian Federation

简评

甲状腺癌是内分泌系统中最常见的肿瘤。它占有恶性肿瘤的1%–3%（截至2021年）。在90%的病例中，可发现分化型甲状腺癌（乳头状癌和滤泡状癌）。它们的预后相对较好。

对于高分化甲状腺癌患者来说，手术治疗和随后的激素抑制治疗、放射性碘治疗相结合的预后良好。不过，放射性碘治疗仍有可能出现反应不充分的情况。这可能与许多因素有关，包括准备阶段。迄今为止，如何选择最佳的放射性碘治疗准备方法仍是一个重要问题。

该出版物对有关高分化甲状腺癌患者接受放射性碘治疗的准备问题的科学文献进行了综述。根据主要专家团体的建议和有关该主题的出版物，我们对患者准备工作的原则进行了介绍和总结。文章还考虑了（1）与放射性碘治疗相关的不良反应；（2）患者的生活质量；（3）疗效；（4）治疗的长期结果。

这篇综述的主要目的是提供一个全面的视角，介绍为高分化甲状腺癌患者接受放射性碘治疗做准备的方法，强调现有的问题和有前途的研究方向，以便使治疗现代化，实现个性化治疗。

在National Library of Medicine、The Cochrane Library和Google Scholar数据库中检索了截至2023年1月底发表的科学文章和综述。检索时使用了以下关键词：为放射性碘治疗做准备、促甲状腺素 α 、停用甲状腺激素、副作用、禁碘饮食、涎腺炎、原发性甲状腺功能减退症、生活质量、甲状腺切除术、分化型甲状腺癌、放射性碘治疗的疗效。采用了以下科学界关于高分化甲状腺癌的建议：俄罗斯高分化甲状腺癌临床指南、美国甲状腺协会、欧洲甲状腺协会、American Thyroid Association、European Thyroid Association、The National Comprehensive Cancer Network、European Association of Nuclear Medicine、British Thyroid Association、European Society for Medical Oncology。排除标准为：未提供全文的文章；非英语或俄语文章；类似主题的系统综述。共选择并分析了124个资料来源。本文强调现代放射性碘治疗患者准备工作的总体趋势和当前存在的问题，指出在治疗个性化框架内优化放射性碘治疗准备的概念，最后得出结论。

关键词：分化型甲状腺癌；放射性碘治疗；禁碘饮食；促甲状腺素 α ；准备方法；不良反应。

引用本文：

Reinberg MV, Slashchuk KYu, Trukhin AA, Avramova KI, Sheremeta MS. 目前对分化型甲状腺癌患者放射性碘治疗准备工作主要方面的看法：文献综述. *Digital Diagnostics*. 2023;4(4):543–568. DOI: <https://doi.org/10.17816/DD532728>

收到: 08.07.2023

接受: 05.09.2023

发布日期: 10.10.2023

INTRODUCTION

Thyroid cancer (TG) has five histological types:

- Papillary (80%–85%)
- Follicular (10%–15%)
- Medullary (5%)
- High grade (1%)
- Anaplastic (0.1%–0.2%)

The first two types are low-grade cancers with relatively good outcomes. The global incidence rate of malignant neoplasms is between 1% and 3% of all new diagnoses.

Among thyroid nodules, up to 5% of cases (according to some data, up to 20%) are cancerous [1], whereas the average annual growth rate in incidence is 3%. Since 2011, the incidence has increased by 36%, whereas the mortality rate has remained low [2]. This is mainly due to improvements in diagnostic methods, including the increased availability and quality of ultrasonography.

Despite a good response to surgical treatment and radioiodine therapy (RIT), 20% of patients may experience a relapse of the disease, and in this case, an unfavorable prognosis is observed in 8% of cases [1]. In Russia in 2021, 996 patients per 100,000 population died from thyroid cancer. From 2011 to 2021, a statistically significant increase was found in the “crude” incidence of malignant thyroid neoplasms in children aged <15 years (40%) [2].

Patients with highly differentiated thyroid carcinoma (HDTC), including those at high risk of recurrence, have a generally favorable overall survival profile, and approximately 90%–95% were responders to radioactive iodine therapy [3]. The prognosis is somewhat worse in patients with distant metastases, incomplete response after the first course of radiotherapy, and advanced disease. According to various sources, the 10- and 5-year overall survival rates of such patients are approximately 30% and 55%, respectively [3, 4]. The tumor-specific survival rate is approximately 30%–65% [5]. A. Hassan et al. [6] reported 5-year disease-free survival rates of 52% in intermediate-risk patients and 17% in high-risk patients. Currently, no consensus has been established on the reasons for the incomplete response to RIT and thyroid cancer progression, which may be due to various factors, including the methodology and principles of preparing the patient for RIT. Finding the reasons for an incomplete response to therapy and developing methods to improve the quality of life and treatment approaches remain urgent problems.

RIT refers to a radical method of treatment for HDTC and is part of combination therapy in patients with predominantly intermediate and high risks of disease relapse (according to the criteria of scientific communities [7–11]). The goal of radionuclide therapy is the ablation of residual thyroid tissue after thyroidectomy and the removal of tumor tissue and metastases that can accumulate iodine-131 (I-131).

The effectiveness of RIT depends on various factors, including the histological type of the tumor, size of the

primary tumor and/or metastases, presence of locoregional and/or distant metastases, patient’s age at the time of diagnosis, hormonal status of the thyroid gland at the time of HDTC detection, and RIT strategy. One of the important criteria is compliance with the conditions of preparation for RIT to optimize the uptake of I-131 by thyrocytes of residual tissues or thyroid cancer cells. Adequate thyroid-stimulating hormone (TSH) and low-iodine levels in the body are believed to be necessary for the adequate uptake of radiopharmaceuticals by tumor cells. These conditions are achieved through thyroid hormone withdrawal, injection of recombinant human thyrotropin alpha (rhTSH), and adherence to a low-iodine diet before RIT. However, no consensus has been reached on the timing and intensity of compliance with these recommendations regarding their effects on the long-term outcomes of therapy. In world practice (Table 1), the accepted standard for preparing for RIT includes the following steps:

- Discontinuation of levothyroxine sodium (LT4) for 3–6 weeks or
 - Replacing LT4 with liothyronine (LT3) for 2 weeks followed by a 2-week withdrawal
 - Use of rhTSH in patients at low and intermediate risk of relapse/progression
- Low-iodine diet for 1–4 weeks (with achievement of iodine concentration in single and/or daily urine <50–100 µg/L).

Taking into account current trends, the contribution of each point of preparation for RIT must separately consider the patient’s quality of life, development of side effects, and effectiveness of RIT.

THYROID HORMONE WITHDRAWAL

As the first method of preparation for RIT, the LT4 regimen was discontinued 6 weeks before the initiation of RIT; however, this regimen led to severe hypothyroidism and related side effects. Subsequently, various variations were used to improve the quality of life without compromising the effectiveness of RIT. A. Golger et al. and T. Davids et al. concluded the sufficient adequacy of a 3-week withdrawal of LT4 in most patients [14, 15]. Alternatively, the option of replacing LT4 with LT3 for 2 weeks and then withdrawing LT3 for the same period can be used. However, according to some studies, this method does not provide additional benefits regarding the quality of life of patients [16, 17] and can sometimes potentiate the side effects of LT3 [18]. The limited availability of triiodothyronine preparations on the Russian market and the above factors may make this preparation option less convenient for patients.

Despite the proposed methods, 4 weeks of LT4 withdrawal or 2 weeks of LT3 withdrawal are sufficient for the development of clinically significant hypothyroidism, accompanied by associated side effects that significantly reduce the quality of life of patients. In addition, patients

Table 1. Comparative characteristics of requirements and methods for radioiodine therapy in various scientific communities

Recommendations	Preparation strategy	Low-iodine diet	rhTSH	TSH before RIT	Iodine concentration
Russian clinical guidelines [7]	Discontinuation of LT4 for 4 weeks or rhTSH (2 injections)	2 weeks	Unspecified	>30 mIU/L	Unspecified
European Association of Nuclear Medicine [8]	Discontinuation of LT4 in 3–4 weeks or LT4/LT3/rhTSH (2 injections)	1–2 weeks	In low- or intermediate-risk patients or off-label in patients with distant metastases	>30 mIU/L	Adequate: <100 µg/L Optimal: <50 µg/L
American Thyroid Association [9]	Discontinuation of LT4 in 3–4 weeks or LT4/LT3/rhTSH (2 injections)	1–2 weeks	In low- or intermediate-risk patients	>30 mIU/L	Adequate: <100 µg/L Optimal: <50 µg/L
European Thyroid Association [10]	Discontinuation of LT4 in 3–4 weeks or LT4/LT3/rhTSH (2 injections), preferably rhTSH	A diet may be prescribed; however, its benefits have not been clearly proven. It is recommended to discontinue iodine-containing medications	Not recommended in patients with distant metastases	>>30 mIU/L	Adequate: <100 µg/L Optimal: <50 µg/L
European Society for Medical Oncology [11]	Discontinuation of LT4 in 4–5 weeks or rhTSH (2 injections)	Unspecified	Unspecified	>30 mIU/L	Unspecified
British Thyroid Association [12]	Discontinuation of LT4 in 4 weeks or LT4/LT3/rhTSH (2 injections)	1–2 weeks	Not recommended in patients with distant metastases and massive tumor spread beyond the thyroid capsule	>30 mIU/L	Unspecified
The National Comprehensive Cancer Network [13]	Discontinuation of LT4 in 4–6 weeks or rhTSH (2 injections)	10–14 days	Unapproved in patients with distant metastases	>30 mIU/L	< 100 µg/day

on suppressive therapy may tolerate symptoms of hypothyroidism less. Signs of hypothyroidism affecting the quality of life were reported to progress 2 weeks after cessation of suppressive therapy in most patients [19]. When analyzing the questionnaires, a deterioration in the quality of life was also noted 2 weeks after cessation of LT4 intake [20].

The issue of reducing the withdrawal time of LT4 to 2–3 weeks is being actively discussed. It can be effective in achieving the target TSH level and long-term treatment results.

Liel et al. analyzed 13 patients and reported that a TSH concentration >30 mIU/L was achieved in all patients an average of 17 days after LT4 cessation, and an exponential increase in TSH was observed [21].

R. Luna et al. studied TSH levels in 34 patients on days 4, 14, 21, and 28 after LT4 cessation, with an average of 20, 46, 75, and 112 mIU/L, respectively, corresponding to a linear increase in TSH levels. Thus, after 2 weeks, 75% of the patients achieved a TSH level >30 mIU/L, and 100% of the patients achieved this TSH level after 3 weeks of withdrawal [19].

According to A. Piccardo et al., the response to LT in the group with LT4 withdrawal in 2 weeks ($n = 85$) and 4 weeks ($n = 137$) did not differ, which was 82% over a 3–4-year follow-up period. However, the TSH level before RIT did not influence the incomplete therapeutic response [22]. Other authors have come to similar conclusions [23, 24].

Alternatively, P.W. Rosario et al. proposed a regimen with a reduction in the LT4 dose to 0.8 mg/(kg × day) 6–8 weeks before RIT, which was associated with the leveling of hypothyroidism that occurs during withdrawal, and this also made it possible to avoid the use of expensive rhTSH. Therefore, in 24 patients on the classic protocol, 71% noted a health deterioration, whereas in 27 patients on the reduced protocol, only 23% had symptoms of hypothyroidism. Laboratory parameters were also better in the second group. An increase in creatinine was noted in 63% of cases with the classic protocol compared with 30% with the reduced regimen, whereas 60% of patients noticed a difference in the various preparation methods, and 100% would prefer the reduced protocol if TSH stimulation was again necessary. The effectiveness rates of RIT were 75% and 79%, in the reduced and classic protocols, respectively [25].

This protocol has not received much attention from clinicians in other countries because the study was limited by a small sample size and previous RIT. However, this method can be considered in the preparation of low- and intermediate-risk groups for diagnostic procedures and RIT, and this issue requires further research.

Optimizing the preparation of patients for RIT is a current area of research. The above papers suggest that the duration of LT4 withdrawal can be reduced to 2–3 weeks without a decrease in the effectiveness of RIT. This may lead to a decrease in the risk of clinically significant hypothyroidism

and an improvement in the quality of life of patients because signs of hypothyroidism in most patients start to progress 2 weeks after the cessation of LT4 treatment.

IS TSH CONCENTRATION >30 MIU/L AN OUTDATED DOGMA?

Controversy exists regarding the optimal TSH concentration before RIT in residual thyroid tissue. The efficiency of I-131 uptake by the tumor and residual thyroid tissue was assumed to depend on the level of expression of the sodium-iodine symporter (SIS), which in turn depends on the TSH concentration [26, 27]. D.Yu. Semenova et al. [28] showed that the average expression of SIS on the membrane of thyroid gland cells does not exceed 4.5%, and the maximum reaches 10%, whereas in normal thyroid tissue, the expression level was 30%–50%. More than 60% of patients with relapsed HDTC had an SIS expression level of <1%. Low SIS expression has been theorized to be an independent prognostic factor for the risk of relapse and disease severity; however, further research on this topic is required.

In 1977, C.J. Edmonds et al. first concluded that adequate uptake of I-131 by the tumor was impossible with TSH <30 mIU/L, and since then, this cutoff point has been used as an indicator of adequate patient readiness for RIT, also serving as a standard in most subsequent studies. Notably, in this study, not all patients achieved adequate I-131 uptake at the “target” TSH values, the sample size was small, and patients with distant metastases of thyroid cancer were also included, which could have a greater effect on the radiopharmaceutical uptake than the TSH concentration. Finally, these studies were not subjected to statistical analysis; thus, the conclusions were not considered unambiguous [26].

In 2021, J. Xiao et al. reported that a group of patients with a TSH concentration of 30–70 mIU/L showed better treatment outcomes than a group of patients with a concentration of ≤30 mIU/L at the time of RIT. Moreover, the effectiveness of RIT in the group with a TSH concentration of >70 mIU/L did not differ from that in the group with a TSH concentration of 30–70 mIU/L [29]. However, patients at high risk of disease relapse were excluded from the statistical analysis, and they comprised the majority of patients in the group with TSH <30 mIU/L and could respond worse to therapy because of the stage of thyroid cancer. Therefore, it is impossible to statistically reliably state that RIT is less effective based on TSH levels. Interestingly, 76% of patients achieved a TSH level of ~70 mIU/L by the end of week 4 of LT4 withdrawal, whereas 46% had a TSH concentration of >100 mIU/L. The authors concluded that due to the lack of additional benefit from achieving TSH concentrations >70 mIU/L (probably due to the presence of a certain threshold for rhTSH expression in the tumor cell), the timing of thyroid hormone withdrawal can be reduced.

T. Zhao et al. also reported the need to achieve TSH concentration >30 mIU/L in patients at low and intermediate

risk; however, the study has its limitations: retrospective analysis, variability in I-131 activity (1.1–5.5 GBq), small sample size of patients with TSH <30 mIU/L, and short follow-up period [30].

In contrast to the above studies, an alternative opinion states achieving TSH concentration >30 mIU/L is unnecessary.

Z. Hasbek et al. observed 34 patients with an average median TSH concentration of 19.5 ± 6.0 mIU/L and 227 patients with TSH >30 mIU/L and noted that the lack of RIT effect was observed in one patient from the first group and 11 from the second group, which was not statistically significant. In non-responders, a significant increase in thyroglobulin levels and the presence of locoregional and distant metastases were observed. The authors concluded that TSH concentration is not the only and absolute factor for a successful response to RIT, whereas the patient's age at diagnosis (>45 years), presence of metastases, thyroglobulin concentration, and residual thyroid tissue volume should be considered possible criteria for the low efficiency of RIT [31]. A research group from Germany came to similar conclusions; the TSH level at the time of ablation did not affect the percentage of successful ablation, disease-free survival, or tumor-specific mortality (Figure 1) [32].

In a retrospective analysis of 1873 patients without evidence of distant metastasis who underwent RIT, no statistically significant effect of TSH concentration was found on the effectiveness of RIT, disease-free survival, or HDTC-associated mortality. RIT was effective in 230 of 275 patients with TSH <30 mIU/L and 1359 of 1598 patients with TSH >30 mIU/L. At the time of ablation, incomplete response to RIT depended on the following factors:

- I-131 activity
- Histological characteristics
- Patient's sex
- T-stage
- Presence of metastases in the regional lymph nodes
- Thyroglobulin concentration

The absence of metastases, low thyroglobulin concentration, smaller tumor size, high I-131 activity, and female sex were identified as independent factors for

successful RIT. The authors also note that TSH levels are stimulated more slowly in patients:

- With metastatic disease
- At an older age
- Female [32, 33]

In the absence of increased TSH concentrations to generally accepted target values (>30 mIU/L) in this group of patients after 3 weeks, further prolongation of thyroid hormone withdrawal was inappropriate. N. Ju et al. came to similar conclusions (Figure 2) [34].

Slow TSH stimulation is probably associated with the influence of estrogens on the level of mRNA expression of the TSH beta-subunit, leading to its suppression in hyperestrogenism [35]. However, this mechanism of regulation of TSH concentration, as well as the theory about the influence of the estrogen status of the body on the incidence and progression of HDTC, are not fully understood and require further research [36–38].

Therefore, some factors can significantly influence the success of RIT in HDTC. They require attention and an individual approach, and with them, the dominant role of the “target” TSH concentration >30 mIU/L may be exaggerated. The study of RIT in a setting of TSH concentration <30 mIU/L will change views on modern aspects of preparation for RIT toward its greater safety with equivalent effectiveness.

RECOMMENDED HUMAN THYROTROPIN ALPHA

In 1987, rhTSH was obtained from the human TSH cell culture FRTL-5 of Chinese hamster ovaries. In 1998 and 2001, rhTSH was approved in the USA and Europe, respectively, as a preparation for diagnostic examinations with radioactive iodine. rhTSH was later approved as an alternative to thyroid hormone withdrawal when preparing patients for RIT:

- In Europe: since 2005
- In the USA: since 2007
- In Russia: since 2018

Numerous studies have shown rhTSH comparable to thyroid hormone withdrawal as a preparation for

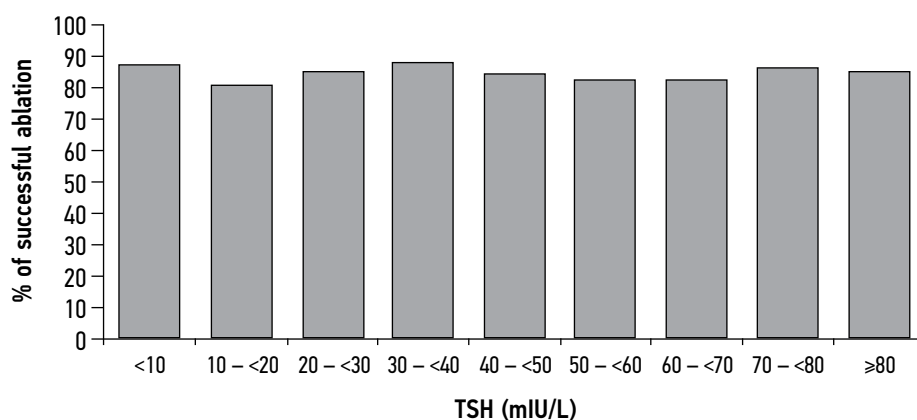


Fig. 1. Percentage of patients with successful ablation relative to thyroid-stimulating hormone levels at the time of therapy I-131

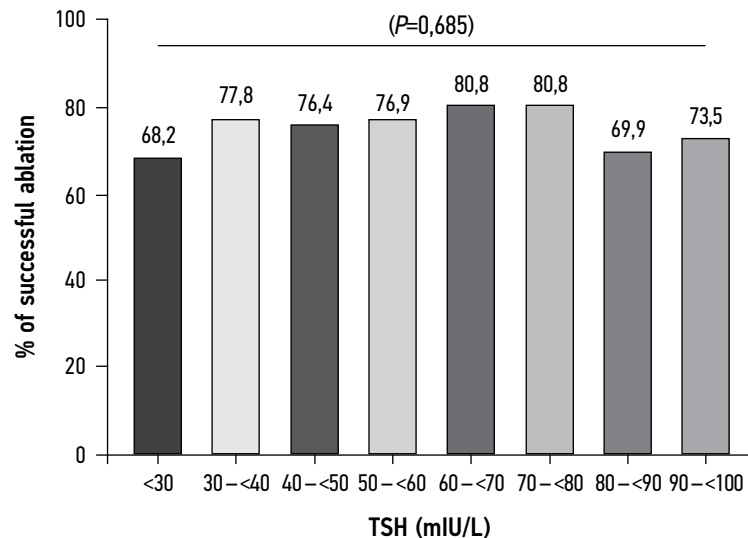


Fig. 2. Percentage of patients with successful ablation of residual thyroid tissue with I-131 relative to thyroid-stimulating hormone levels. In 8 subgroups, no statistical significance was observed.

postoperative RIT [39–43]. However, the issue regarding the possibility of using rhTSH as part of RIT in patients at high risk of recurrent thyroid cancer and in the treatment of distant metastases remains open. Previously, several cases of ineffectiveness of RIT in high-risk patients when prepared with rhTSH have been documented, whereas repeated courses of RIT in a setting of thyroid hormone withdrawal were successful [44–46].

One of the proposed mechanisms is related to the different actions of the recombinant hormone and the endogenous hormone because of the greater sialylation of the molecule, different degrees of glycosylation of the TSH receptor, and polyclonality of tumors, which can develop with increasing number of RIT courses [46].

Currently, the question of whether the dose- and time-dependent effects of TSH (in other words, the area under the curve) on radiopharmaceutical uptake and treatment outcome is more significant than the “cutoff point” of 30 mIU/L. A. Vrachimis et al. suggested that this may be one of the limiting factors in the use of rhTSH [32].

Despite this fact, recent data indicate the same effectiveness of the use of rhTSH in patients not only at low and intermediate risk but also at high risk. In a retrospective study, J. Hugo et al. analyzed 586 patients (321 prepared by stopping LT4 treatment and 265 prepared using rhTSH), including intermediate risk and high-risk groups, and showed that long-term clinical outcomes with a median 9-year follow-up were not different. Moreover, in the short term (median, 2.5 years), the withdrawal group showed a statistically higher likelihood of incomplete response to primary RIT than the rhTSH group (47% vs. 39%, $p = 0.03$), with a higher rate of requiring repeat therapy, surgical intervention, or an RIT course (37% vs. 29%, $p = 0.05$). Economically, the use of rhTSH can shorten the period of active follow-up for patients with signs of persistent and/or recurrent disease [41] and

reduce the economic budgetary costs [47–51], including a 70% probability of achieving economic benefits with a 30% reduction in the rhTSH cost [52].

Other researchers obtained similar results of at least equal effectiveness of rhTSH in the intermediate risk and high-risk groups [53–59].

In its HDTC guidelines, the American Thyroid Association does not recommend the use of the drug in patients at high risk of relapse [9]. Guidelines of the European Association of Nuclear Medicine allow the use of the drug off-label in patients with distant metastases [8].

The use of rhTSH is associated with fewer side effects. There remains some caution regarding the use of the drug in patients with metastases to the central nervous system because a strong TSH stimulation may lead to their growth/increase and severe clinical symptoms [60].

In a study of 88 patients prepared for RIT through thyroid hormone withdrawal and rhTSH (51 and 37, respectively), the 10-year survival rates were 62% and 73%, respectively. Therefore, the use of rhTSH was not associated with worse treatment outcomes or prognosis [61].

Table 2 summarizes the main advantages and disadvantages of using rhTSH and the target group of patients for its use.

Despite the controversy regarding the use of rhTSH in the high-risk group, a potential benefit may be a greater increase in TSH levels in a shorter period. Patients with metastases have a lower expression of SIS, which may require a higher TSH concentration for I-131 uptake by tumor cells. In addition, long-term preparation by thyroid hormone withdrawal can negatively affect cancer prognosis and lead to progression [62–64].

I.I. Dedov et al. [65] showed that 70% of patients had a TSH concentration >100 mIU/L after the second rhTSH injection; however, no studies are currently conducted on the

Table 2. Advantages and disadvantages of using recombinant human thyrotropin alpha and its preferred indications

Advantages	Disadvantages	Target group
Leveling the hypothyroidism phase is an opportunity to reduce the side effects on some risk organs Better quality of life compared with patients on withdrawal before and after RIT The preparation period for RIT/diagnostic studies is shorter Less risk of salivary gland damage Reducing the radiological load on the body as a whole (because of the absence of changes in GFR) and the risk of bone marrow damage Shorter possible hospitalization periods	Cost Higher incidence of damage to lacrimal gland ducts Lack of sufficient data on use in patients with distant metastases	Older age Chronic diseases of target organs that have a risk of exacerbation in the case of decompensated hypothyroidism (chronic heart failure, coronary heart disease of class II and higher, history of heart attacks/stroke, COPD, hepatitis, rheumatoid arthritis, diabetes mellitus, chronic kidney disease, mental illness, chronic pancreatitis, immunodeficiencies, etc.) Patients with a single/transplanted kidney Patients with carbohydrate metabolism disorders and obesity Patients with infections/diseases of the oral cavity, a history of sialadenitis, and stones in the ducts of the salivary glands Poorly controlled hypertension Non-alcoholic fatty liver disease and liver diseases in the stage of decompensation

optimal TSH level in the high-risk group and its contribution to treatment effectiveness.

Separately, the advantages of rhTSH over LT4 discontinuation must be considered in terms of the effect on organs at risk, which will be discussed further.

SIDE EFFECTS WHEN USING DIFFERENT PREPARATION PROTOCOLS AND WAYS TO SOLVE THEM

When preparing for RIT, patients who are undergoing thyroid hormone withdrawal have severe iatrogenic hypothyroidism, accompanied by a decrease in the quality of life and side effects affecting target organs. Such effects are mediated by the presence of TSH receptors not only in thyroid tissues but also on the membranes of adipocytes, fibroblasts, osteoclasts, leukocytes, monocytes, myocardiocytes, endothelial cells, and vascular smooth muscle cells, including the afferent glomerular arteriole [66].

In the cardiovascular system, the following are noted:

- Decreased ejection fraction
- Left ventricular diastolic dysfunction at rest
- Increase in total peripheral vascular resistance
- Endothelial dysfunction

All these factors may contribute to a decrease in the control of arterial hypertension in patients with essential hypertension [67]. Because of a decrease in the filtration function of the kidneys, the clearance of adrenaline, norepinephrine, and cortisol slows down [68]. Two studies have reported increased homocysteine levels [69, 70]. Such changes may contribute to the development and progression of the cardiorenal continuum. In patients who underwent thyroidectomy and were taking anticoagulants, an inverse correlation was found between TSH and INR levels during LT4 discontinuation, which may require additional monitoring of blood coagulation parameters to timely correct therapy.

Negative effects on the liver have been repeatedly reported; in patients with thyroid hormone withdrawal, increased activities of alanine aminotransferase and aspartate aminotransferase were reported [71, 72], whereas the use of rhTSH was not accompanied by impaired liver function [71]. Lipid metabolism is disturbed by an imbalance of high-density lipoproteins [67, 73]. This is because the lack of thyroid hormones leads to a decrease in the expression of receptors for high-density lipoproteins [74] and an increase in their concentration and an increase in total plasma cholesterol [73]. A definite connection has been established between thyroid dysfunction and affective disorders [75]. Moreover, disease control worsened as the intensity of hypothyroidism increased, which could be associated with reduced blood circulation in the brain and a diffuse [76] and/or regional [77] decrease in glucose clearance. The potentiation of the symptoms of depression, which most often accompanies hypothyroidism, is possible because of the insufficient ability of brain cells to receive adequate amounts of oxygen and glucose from the blood [78].

The causes of carbohydrate metabolism disorders may be increased evacuation capacity of the stomach and decreased transport of glucose by the liver, which leads to disturbances in both postprandial and fasting glycemia [79].

Evidence shows the influence of thyroid hormones on the modulation of the immune response [80], which in the case of hypothyroidism can lead to an increase in infectious morbidity. Particular attention has been paid to the suppression of renal functions, as proven in many studies [71, 81-87], including those that occur during LT4 discontinuation but not when using rhTSH. A study reported decreased renal perfusion on Doppler ultrasonography with rhTSH use. However, it was performed on a small sample of patients on day 5 after injection of the drug [66].

Cases of hyponatremia have been described following a low-iodine diet [88-91], with the following risk factors:

- Older age
- Treatment with thiazide diuretics
- Long duration of the low-iodine diet
- Long-term hypothyroidism
- Multiple metastases, which can contribute to the development of the syndrome of inappropriate antidiuretic hormone secretion, leading to its excessive increase [93, 94]

A common cause of hyponatremia was self-limitation of table salt by patients because of the low awareness of the principles of a low-iodine diet.

In a study by Horie et al., hyperkalemia developed in 5% of patients, correlating with age (over 60 years) and taking angiotensin-converting enzyme inhibitors, which could potentially also be associated with compromised renal function during long-term discontinuation of LT4 [93].

Interestingly, the choice of preparation method for RIT may also influence the frequency and intensity of side effects after exposure to I-131. Therefore, organs expressing SIS can accumulate I-131, which in some cases can lead to damage.

According to the clinical experience of our center, as well as worldwide publications, 20%–30% of the negative effects are related to the salivary glands [94–97]. Patients may experience taste changes, infections, facial nerve involvement, stomatitis, and candidiasis. The typical first symptom is obstructive swelling of the gland, resulting from the narrowing of the duct lumen associated with the inflammatory process. To prevent sialadenitis, many methods have been used, including the use of cholinomimetics, sialogogs, cytoprotectors (amifostine), and salivary gland massage. However, the efficacy was poor [97–100]. Moreover, the use of sialogogs on the first day after RIT leads to an increase in the radiation dose by approximately 28% in the salivary glands; therefore, the use of lemon/sucking sweets/other sialogogs on the first day after therapy is not recommended [99, 102]. If untreated, only 54% of patients were free of chronic sialadenitis after 6 years of follow-up [100], highlighting the need to find new methods to prevent sialadenitis.

In a study by A. Trukhin et al., rhTSH use was associated with a higher incidence of radiotracer accumulation in the lacrimal ducts than the 4-week discontinuation of LT4 [102]. According to other authors, the use of rhTSH reduced the number of cases of acute sialadenitis after RIT by approximately 20% [103], which may account for only 6.7% over the next year [104].

Secondary leukemia after ablation is one of the side effects of RIT that has not been widely recognized, but which deserves special attention. In a previous study, 148,215 patients were analyzed; the risk of developing acute and chronic myeloid leukemia in the first 3 years was higher and statistically significant in patients who underwent primary RIT for differentiated thyroid cancer compared with those who underwent surgical treatment only. Although the risk of acute myeloid leukemia rapidly declines to baseline levels

by 3 years after RIT, the risk of chronic myeloid leukemia remains high for 10 years [105].

Another controversial finding is the increased number of stable chromosomal aberrations in patients after the administration of a low dose of I-131, which persisted longer in patients on LT4 discontinuation than in those on rhTSH [106]. The clinical interpretation of the results requires longer follow-up and a detailed search for cause-and-effect relationships.

Therefore, when preparing for RIT and monitoring patients, a clinician should probably be more cautious about patients with the following:

- Hypertension
- Immunodeficiency
- Moderate/severe dysfunction of the liver and/or kidneys
- Disturbances in electrolyte and/or carbohydrate metabolism
- Affective disorders
- Other previously described conditions

One of the methods to prevent and reduce the severity of side effects in susceptible organs associated with hypothyroidism is the preferential use of rhTSH in patients at risk of hypothyroidism complications and educating them on the basic principles of adhering to a low-iodine diet and regimen during RIT.

LOW-IODINE DIET

Based on the data collected to date, the degree of iodine uptake by tumor and normal thyroid cells is believed to be determined by the following:

- Volume of the residual thyroid tissue
- Adequate TSH stimulation
- SIS expression
- Median iodine concentration at the time of therapy [107]

Early studies have shown that iodine uptake by residual thyroid tissue increases 2–3-fold in patients following a low-iodine diet [108, 109], which may affect the effectiveness of RIT. Most scientific communities adhere to the following criteria when preparing a patient for RIT: optimal level of urine iodine excretion (UIE) <50 µg/L [8–10] and adequate level <100 µg/L [8]. However, no clear criteria have been established for the duration and intensity of adherence to a low-iodine diet.

To answer the question of whether a low-iodine diet is needed, several studies were conducted, including one by J. Tala et al., which caused a certain dissonance in the scientific community. The authors did not find a relationship between the urine iodine level and RIT effectiveness and suggested no differences between groups of patients with urine iodine levels of >100 µg/L and <100 µg/L. However, the study was conducted in a moderately deficient region (Siena, Italy), the sample of patients with high iodine content in the body was

not sufficient, and the I-131 dose varied, which could greatly contribute to the clinical outcomes of RIT than moderate iodine deficiency [110].

The question of the optimal level of iodine in the body, after which the patient's preparation for RIT is considered adequate, remains ambiguous.

M. Lee et al. did not find the difference in the effectiveness of RIT in the moderate and mild iodine deficiency groups [111]. A.E. Tobey et al. showed no significant difference in the RIT effectiveness between groups with iodine levels 50/100/150 mg/day; however, the risk of disease progression was higher in groups with urinary iodine levels >200 mg/day. To our knowledge, this is the first study to evaluate the relationship between pre-RIT iodine status and long-term clinical outcomes with a median follow-up of 3.7 years [112]. Other authors came to similar conclusions [45, 107, 113]. However, in a study by L.F. Morris et al., the success of RIT did not differ between groups with and without a low-iodine diet [114].

The diet duration is the next urgent issue. The most common recommended period is 1–2 weeks; however, approaches and protocols for a low-iodine diet vary from country to country. The timing and intensity of the diet could not be specified because of differences in the iodine supply of regions. A 2-week diet with restriction of iodine-containing foods can affect the quality of life, social functioning, and risk of hyponatremia. However, in regions with excess iodine intake, 2 weeks may be preferable to achieve adequate pre-ablation iodine levels in the body [107, 115–117]. An important point is to properly educate patients about the basic aspects of a low-iodine diet. In studies with minimal patient education by dietitians/nutritionists or dietary nurses, with the distribution of handouts, in some patients provided with a 3–7-day menu, better results were seen in the percentage reduction of iodine levels compared with baseline [112, 117–119].

In studies conducted in regions with moderate iodine deficiency or adequate iodine intake, optimal levels were achieved after a week of a low-iodine diet [118, 120] and after 4 days in studies by M.J. Pluijmen et al. and B.L. Dekker et al. [113, 121]. Some studies conducted in regions with high iodine intake have also shown the effectiveness of a weekly low-iodine diet [111, 112, 118, 119].

A limitation of many studies, other than the study by A.E. Tobey et al. [112], was that they have been conducted in the low- and intermediate-risk groups. This does not allow a full assessment of short- and long-term outcomes in the high-risk group. In studies conducted in countries with moderate iodine deficiency (e.g., Italy), with a median urinary iodine level of 95 µg/L in patients discontinuing LT4, values ranged from 25 to 1890 µg/L, which may affect the effectiveness of treatment in some cases. In this study, patients were not assigned to a low-iodine diet because of regional iodine deficiency status, and the high-risk group was excluded from the analysis.

Studying the patient's iodine status before RIT is one of the methods for personalizing treatment. In each case, including those at high risk of disease relapse/progression, special attention should be paid to achieving an optimal iodine pool before RIT because each factor in the preparation process, including iodine status, can affect treatment success. The main studies on this topic are highlighted in Table 3.

When considering adherence to a nearly stringent low-iodine diet protocol, no clear evidence was found to support a restrictive diet in either the degree of iodine reduction or the effectiveness of RIT. A more stringent protocol may be more associated with iodine reduction, lower quality of life, and psychological discomfort of patients. Therefore, the choice of a specific preparation protocol will depend on the ability of a particular site to inform/educate patients, presence of comorbid pathology, and initial iodine status of the region.

The 2020 Russian Clinical Guidelines recommend a 2-week low-iodine diet. Considering the iodine status of the region and world data, the diet duration can be reduced to 4–7 days.

CONCLUSION

To date, no consensus has been made regarding the indications for adjuvant RIT in patients with low and intermediate risk of recurrence, who represent the majority of patients with HDTC. The use of RIT carries a potential risk of complications; thus, the clinical benefit in each specific case must be assessed. This can only be done with the help of dynamic stratification of the risk of recurrence of thyroid cancer. The studies presented in the literature over the 80-year history of the method show the heterogeneity of options for the preparation and treatment of HDTC, which form the modern view of RIT.

In the low-/intermediate-risk group, performing RIT in an euthyroid state with a TSH level of <30 mIU/L may neutralize the risks associated with hypothyroidism and its complications. To date, limited but methodologically sound studies have demonstrated that achieving a pre-ablation TSH level >30 mIU/L is not necessary, as well as the efficacy of 2 weeks of LT4 discontinuation (compared with 4 weeks) to induce hypothyroid status. More studies are needed to extrapolate the results to a high-risk group. Theoretically, higher TSH levels may be required to stimulate SIS and improve the quality of therapy. The preferred drug for use in this patient population would be rhTSH; however, studies of the influence of its pharmacokinetic characteristics on the efficacy of RIT are required. In addition, its availability is currently limited by its high cost, which justifies the need to reduce the cost of its production technology in the Russian Federation and consider its availability to needy patient groups.

To increase the effectiveness of RIT, one of the steps in a personalized treatment approach may be to measure the iodine concentration in a single urine sample before RIT

Table 3. Comparative characteristics of a low-iodine diet and its effectiveness in countries with different iodine levels

1	2	3	4	5	6	7
Study	Patient sample (details)	Characteristics of the LID	Education	Method for assessing the iodine concentration/efficacy of RIT	Results (effects on RIT outcomes, % reduction in the iodine pool in the body)	Study limitations
<i>Brazil: moderate-high iodine intake</i>						
R.P. Padovani et al. 2015 [122]	n = 125*	LID 15 days, n1 = 79; LID 30 days, n2 = 46	+	24-UJE	n1: M = 99 mg/L (60% reduction) n2: M = 80 mg/L (70% reduction)	*Most patients were excluded because of difficulty in complying with the protocol (initial, n = 306)
<i>Korea: excess iodine intake</i>						
S.U. Sohn et al. 2013 [107]	n = 295 (single activity I-131 - 1100 MBq)	LID 2 weeks	+++	UJE in a single urine sample adjusted for Cr	Successful ablation: 74.9% (221/295); in the group with UJE <66 µg/g (I/Cr ratio), the results were better than those in the group with UJE >66 µg/g: 81% versus 67%, p = 0.03; significantly lower results in the group with UJE >250 µg/g (p <0.05)	Retrospective analysis; patients with distant and cervical metastases were excluded, which could affect the statistics of RIT outcomes, without considering antithyroglobulin antibodies
IDKS Yoo et al. 2012 [115]	n = 161: n1(SLID) = 90; n2(MLID) = 71	SLID/MLID 2 weeks	++	UJE was not measured	Successful RIT: SLID, 75.8%; MLID, 80.3% (p = 0.48)	Patients with distant metastases were excluded. No information is available regarding patients receiving thyrotropin alpha
H.K. Kim et al. 2011 [118]	n = 19 (on LT4 discontinuation)	SLID 2 weeks	+++	UJE in a single urine sample, adjusted for Cr daily, 14 days	I/Cr ratio 0→7 day: ↓ from 576 to 26 µg/g 0→14 day: ↓ up to 19.6 µg/g By day 3: 95% I/Cr <150 µg/g By day 6: 95% I/Cr <66 µg/g	A single sample of urine was used to assess iodine excretion. The study results are not suitable for interpretation in iodine-deficient regions; the effectiveness of ablation has not been assessed
C.Y. Lim et al. 2015 [117]	n = 101 n1(SLID) = 47; n2(MLID)=54	SLID/MLID 4 weeks	++	24-UJE, adjusted for Cr, weeks 2 and 4	No statistical differences were found between n1 and n2. I/Cr ratio: Week 2: 28.6 µg/g Week 4: 35.0 µg/g. % I-131 uptake at weeks 2 and 4 did not differ between the groups	Short- and long-term outcomes of radioiodine therapy have not been assessed
M. Lee et al. 2014 [111]	n = 195	LID 2 weeks	+++	24-UJE at the end of weeks 1 and 2	Week 1 - M = 12.8 µg/L, 87.2% UJE <50 µg/L Week 2 - M = 13.4 µg/L, 92.3% UJE <50 µg/L Successful ablation: 82.4%; no differences were found between the moderate and mild iodine deficiency groups	Various therapeutic activities (3700-7400 MBq) Exclusion of the high-risk group

Table 3. Continued

1	2	3	4	5	6	7
Study	Patient sample (details)	Characteristics of the LID	Education	Method for assessing the iodine concentration/efficacy of RIT	Results (effects on RIT outcomes, % reduction in the iodine pool in the body)	Study limitations
<i>Italy: moderately deficient region</i>						
J. Tala et al., 2010 [110]	n = 201 (n1 = 25, discontinuation of LT4 for 4 weeks; n2 = 76 on rhTSH)	Absent	-	UIE in a single urine sample	Successful ablation in 84.6% (UIE M=104 µg/L, from 25 to 1890 µg/L). No statistical differences were found between the groups with complete (M = 104 µg/L) and incomplete (M = 104 µg/L, 25 to 851 µg/L) responses. No difference was found in the response to therapy between the groups with UIE <100 µg/L and >100 µg/L (p = 0.98)	Retrospective analysis, small sample of patients with high iodine concentrations in urine, various levels of I-131 activity at the time of ablation (1100–5550 MBq), and no control group and high relapse group
<i>Netherlands: adequate iodine intake</i>						
M.J. Pluijmen et al., 2003 [113]	n = 120: n(LID) = 59 n (RD) = 61	LID 4 days	+++	24-UIE: n (RD) = in 9 patients n (LID) = in 60 patients	n (LID): UIE avg. = 27 µg/day n (RD) UIE avg. = 159 µg/day I uptake in the thyroid region was higher in the LID group (5.1 ± 3.8 vs. 3.1 ± 2.5%, p < 0.001). Efficacy was higher in the LID than in the RD group (71% and 45%, respectively)	Retrospective analysis Patients with metastases were excluded
B.L. Dekker et al., 2022 [123]	n = 65	-	+++	24-UIE on days 4 and 7	Day 4: 24-UIE <50 µg in 72.1%, UIE avg. 36.1 g; Day 7: 24-UIE <50 µg in 82.0% (p = 0.18), UIE avg. 36.5 µg	These studies may not be applicable to countries with high iodine intake. Initial urinary iodine levels were not assessed
<i>USA: moderate-to-high iodine intake</i>						
L.F. Morris et al., 2001 [116]	n = 94: n (LID) = 44 n (RD) = 50	LID 10–14 days RD: limit preparations with iodine, iodized salt, and seafood	++	UIE in a single urine sample (in seven patients on LID and in seven on RD)	Successful ablation in 68.2% (LID) versus 62% (RD), p = 0.53. In patients with metastases: 80.0% and 66.7. n (LID): ↓ I by 69.4% (UIE avg. 567.7 µg/L → 173.9 µg/L); n (RD): ↓ by 23.6% (UIE avg. 444.0 µg/L → 498.9 µg/L)	Various therapeutic activities (3700–7400 MBq) Small sample of patients for urine iodine screening The ablation criteria excluded the level of thyroglobulin or antibodies to thyroglobulin
A.E. Tobey et al., 2018 [114]	n = 70 n1(rhTSH) = 16 n2 (discontinuation of LT4) = 54	LID 2 weeks	+++	24-UIE	21% had disease progression, and the risk was higher in patients with UIE >200 µg/day. Between groups with UIE 50, 100, 150 µg/day, no difference was found	Retrospective study and small sample I-131 activity from 1.1 to 11.1 GBq at RIT; Observation period of 3.7 years

Table 3. Ending

1	2	3	4	5	6	7
Study	Patient sample (details)	Characteristics of the LID	Education	Method for assessing the iodine concentration/efficacy of RIT	Results (effects on RIT outcomes, % reduction in the iodine pool in the body)	Study limitations
J.T. Park et al., 2004 [125]	n = 36	n1 = 15: 2 weeks of LT4 + 2 weeks of LID; n2 = 21: 2 weeks LID without LT4	+	UIE in a single urine sample at weeks 1 and 2, adjusted for Cr	I/Cr ratio: n1: M (week 1) = 76.91 µg/g (21% UI <50; 71% <100 µg/g); n2: M (week 1) = 26.16 µg/g (78% <50 µg/g), p < 0.001 The UI after 2 weeks of LID did not differ between groups 1 and 2 (p < 0.15)	Short- and long-term outcomes of RIT were not assessed
<i>Japan: excess iodine intake</i>						
S. Ito et al. 2018 [118]	n = 45 (single activity I-131 1100 MBq)	LID 2 weeks (SLID n = 12; LID n = 25)	+++	UIE in a single urine sample adjusted for Cr	UIE (I/Cr): M before and after diet: 286 µg/g (range, 40–7100 µg/g) and 74 µg/g (range, 16–876 µg/g), respectively. Successful ablation in 56% of the entire sample	Small sample; the effectiveness of RIT was assessed based on the results of scintigraphy without considering thyroglobulin and antibodies to thyroglobulin Patients with M1 were excluded. Complex interpretation for regions with moderate or adequate iodine intake
C. Tomoda et al. 2005 [121]	n = 252: n 1(MLID) = 220 n 2(LID) = 15 n 3(SLID) = 17	MLID = 1 week LID = 1 week SLID = 2 weeks	+	UIE in a single urine sample adjusted for Cr	n3(SLID): M I/Cr = 130 µg/g (range 23–218 µg/g) n1(UYND): M I/Cr 125 µg/g (range 13–986 µg/g), (p < 0. 01) I/Cr <100 µg/g – in 26% (n1) and 70% (n3)	Short- and long-term outcomes of radioiodine therapy have not been assessed. Iodine content was assessed in a single urine sample (not the “gold standard”)
<i>Malaysia: moderate iodine deficiency</i>						
W.F. Sohaimi et al. 2019 [122]	N = 104 (LT4 discontinuation)	SLID/MLID = 1 week	+	UIE in a single urine sample	Day 0→7: UIE <100 µg/L in 89.1% (SLID) and 91.8% (MLID) MLID: UIE avg. 89.24 µg/L → 56.85 µg/L (↓ by 36.3%) SLID: UIE avg. — 107.8 µg/L → 63.82 µg/L (↓ by 40.8%)	Short- and long-term outcomes of radioiodine therapy have not been assessed

Note:

- “-”: lack of any education
- “+”: printed instructions
- “++”: printed and oral instructions
- “+++”: printed, oral instructions, and training by healthcare personnel
- 24-UIE: daily urinary iodine excretion;
- Cr: creatinine
- I: iodine
- LID: low-iodine diet
- LT4: levothyroxine
- M: median
- MLID: moderate low-iodine diet
- RD: regular diet
- RIT: radioiodine therapy (first postoperative radioiodine therapy)
- SLID: strict low-iodine diet
- UI avg: average iodine levels in urine
- UIE: urinary iodine excretion.

to assess the patient's compliance with a low-iodine diet and predict the effectiveness of treatment. The procedure can be simplified by measuring the iodine concentration in saliva, as proposed by B.L. Dekker et al. [126]; although the information value is equivalent to the "gold standard" (iodine in 24-h urine sample), this method still needs to be validated and has certain limitations. An important contribution to the determination of patient management strategy can be made by determining the level of SIS expression as part of a standard pathological examination to predict the response to RIT, which may also influence the therapeutic activity of I-131.

The wide range of therapeutic activities of I-131 is one of the significant limiting factors in RIT preparation studies, affecting the final assessment of complex efficacy, which should be considered when carefully studying the issue addressed in the publication. The development of more precise and personalized approaches to RIT is based on an understanding of the many complex mechanisms, including individual patient characteristics, tumor biology, and other factors that underlie the efficacy and safety of this treatment. Careful selection of patients who will benefit from this intervention is necessary to minimize adverse events. The issue of the validity of prescribing RIT requires special attention and further study.

To summarize modern ideas and trends in the preparation for RIT, the following aspects are promising:

- Educate patients about the disease, RIT preparation, posttreatment regimen, and follow-up to improve quality of life.
- Reduce the period of a low-iodine diet to 4–7 days, eliminate significant dietary restrictions, or expand the dietary regime during the period of a low-iodine diet, depending on the iodine status of the region, and lower

the "threshold" of optimal iodine level before ablation to 100–150 µg/L,

- Consider the possibility of performing RIT with a TSH level <30 mIU/L in some groups of patients (low/intermediate risk of relapse) by reducing the RIT withdrawal period from 4 to 2 weeks.
- Expand the indications for the use of rhTSH to include patients at high risk of relapse and those with significant comorbidities.

ADDITIONAL INFORMATION

Funding source. This work was conducted within the fund of the State Assignment "Study of pharmacosafety of theranostic radiopharmaceuticals using hybrid molecular imaging in the diagnosis and treatment of endocrine and oncological diseases in children and adults". Registration number 123021000041-6.

Competing interests. The authors declare that they have no competing interests.

Authors' contribution. All authors made a substantial contribution to the conception of the work, acquisition, analysis, interpretation of data for the work, drafting and revising the work, final approval of the version to be published and agree to be accountable for all aspects of the work. M.V. Reinberg — contribution to the concept of the paper, design of the review, collection and processing of materials, analysis of the obtained data and writing the text; K.Yu. Slashchuk — assistance in collection and processing of materials, data analysis, making substantial revisions to the manuscript to improve the scientific value of the article; approval of the final version of the manuscript; A.A. Trukhin — text editing, data analysis, adding valuable comments to improve the scientific value of the article; K.I. Avramova — assistance in collection and processing of materials, text editing; M.S. Sheremeta — adding valuable comments, approval of the final version of the manuscript.

REFERENCES

1. Vanushko VE, Tsurkan AYu. Treatment of differentiated thyroid cancer: cureunt statement of the problem. *Clinical and experimental thyroidology*. 2010;6(2):24–33. (In Russ). doi: 10.14341/ket20106224-33
2. Kaprin AD, Starinskii VV, Shakhzadova AO, editors. *Zlokachestvennyye novoobrazovaniya v Rossii v 2021 godu (zabolevaemost' i smertnost')*. Moscow: MNI OI im. P.A. Gertsena –of NMRRC of the Ministry of Health of Russia; 2022. (In Russ).
3. Durante C, Haddy N, Baudin E, et al. Long-term outcome of 444 patients with distant metastases from papillary and follicular thyroid carcinoma: benefits and limits of radioiodine therapy. *The Journal of Clinical Endocrinology & Metabolism*. 2006;91(8):2892–2899. doi: 10.1210/jc.2005-2838
4. Cancer Stat Facts: Thyroid Cancer [Internet]. *National Cancer Institute: Surveillance, Epidemiology, and End Results Program*. [cited 2023 Sep 1]. Available from: <https://seer.cancer.gov/statfacts/html/thyro.html>
5. Braverman LE, Cooper DS, Kopp P. *Werner & Ingbar's The Thyroid: A Fundamental and Clinical Text. 11th ed.* Philadelphia, PA: Wolters Kluwer; 2021.
6. Hassan A, Razi M, Riaz S, et al. Survival Analysis of Papillary Thyroid Carcinoma in Relation to Stage and Recurrence Risk: A 20-Year Experience in Pakistan. *Clinical Nuclear Medicine*. 2016;41(8):606–613. doi: 10.1097/RLU.0000000000001237
7. *Well-differentiated thyroid cancer. Clinical guidelines*. ID 329. Approved by the Scientific and Practical Council of the Ministry of Health of the Russian Federation. 2020. Available from: https://cr.minzdrav.gov.ru/recomend/329_1 (In Russ)
8. Avram AM, Giovanella L, Greenspan B, et al. SNMMI Procedure Standard/EANM Practice Guideline for Nuclear Medicine Evaluation and Therapy of Differentiated Thyroid Cancer: Abbreviated Version. *Journal of Nuclear Medicine*. 2022;63(6):15N–35N.
9. Haugen BR, Alexander EK, Bible KC, et al. 2015 American Thyroid Association Management Guidelines for Adult Patients with Thyroid Nodules and Differentiated Thyroid Cancer: The American Thyroid Association Guidelines Task Force on Thyroid Nodules and Differentiated Thyroid Cancer. *Thyroid*. 2016;26(1):1–133. doi: 10.1089/thy.2015.0020
10. Pacini F, Fuhrer D, Elisei R, et al. 2022 ETA Consensus Statement: What are the indications for post-surgical radioiodine therapy in

- differentiated thyroid cancer? *European Thyroid Journal*. 2022;11(1). doi: 10.1530/etj-21-0046
11. Filetti S, Durante C, Hartl D, et al. Thyroid cancer: ESMO Clinical Practice Guidelines for diagnosis, treatment and follow-up. *Annals of Oncology*. 2019;30(12):1856–1883. doi: 10.1093/annonc/mdz400
12. Perros P, Boelaert K, Colley S, et al. Guidelines for the management of thyroid cancer. *Clinical Endocrinology*. 2014;81 Suppl. 1:1–122. doi: 10.1111/cen.12515
13. Haddad RI, Bischoff L, Ball D, et al. Thyroid Carcinoma, Version 2.2022, NCCN Clinical Practice Guidelines in Oncology. *Journal of the National Comprehensive Cancer Network*. 2022;20(8):925–951. doi: 10.6004/jnccn.2022.0040
14. Golger A, Fridman TR, Eski S, et al. Three-week thyroxine withdrawal thyroglobulin stimulation screening test to detect low-risk residual/recurrent well-differentiated thyroid carcinoma. *Journal of Endocrinological Investigation*. 2003;26(10):1023–1031. doi: 10.1007/bf03348202
15. Davids T, Witterick IJ, Eski S, et al. Three-Week Thyroxine Withdrawal: A Thyroid-Specific Quality of Life Study. *The Laryngoscope*. 2006;116(2):250–253. doi: 10.1097/01.mlg.0000192172.61889.43
16. Lee J, Yun MJ, Nam KH, et al. Quality of life and effectiveness comparisons of thyroxine withdrawal, triiodothyronine withdrawal, and recombinant thyroid-stimulating hormone administration for low-dose radioiodine remnant ablation of differentiated thyroid carcinoma. *Thyroid*. 2010;20:173–179. doi: 10.1089/thy.2009.0187
17. Leboeuf R, Perron P, Carpentier AC, Verreault J, Langlois MF. L-T3 preparation for whole-body scintigraphy: a randomized-controlled trial. *Clinical Endocrinology*. 2007;67(6):839–844. doi: 10.1111/j.1365-2265.2007.02972.x
18. Rajamanickam S, Chaukar D, Siddiq S, Basu S, D'Cruz A. Quality of life comparison in thyroxine hormone withdrawal versus triiodothyronine supplementation prior to radioiodine ablation in differentiated thyroid carcinoma: a prospective cohort study in the Indian population. *European Archives of Oto-Rhino-Laryngology*. 2021;279(4). doi: 10.1007/s00405-021-06948-6
19. Luna R, Penín M, Seoane I, et al. ¿Es necesario suspender durante 4 semanas el tratamiento con tiroxina antes de la realización de un rastreo-ablación? *Endocrinología y Nutrición*. 2012;59(4):227–231. (In Spanish). doi: 10.1016/j.endonu.2012.02.004
20. Dow KH, Ferrell BR, Anello C. Quality-of-life changes in patients with thyroid cancer after withdrawal of thyroid hormone therapy. *Thyroid*. 1997;7(4):613–619. doi: 10.1089/thy.1997.7.613
21. Liel Y. Preparation for radioactive iodine administration in differentiated thyroid cancer patients. *Clinical Endocrinology*. 2002;57(4):523–527. doi: 10.1046/j.1365-2265.2002.01631.x
22. Piccardo A, Puntoni M, Ferrarazzo G, et al. Could short thyroid hormone withdrawal be an effective strategy for radioiodine remnant ablation in differentiated thyroid cancer patients? *European Journal of Nuclear Medicine and Molecular Imaging*. 2018;45(7):1218–1223. doi: 10.1007/s00259-018-3955-x
23. Santos PA, Flamini ME, Mourato FA, et al. Is a four-week hormone suspension necessary for thyroid remnant ablation in low and intermediate risk patients? A pilot study with quality-of-life assessment. *Brazilian Journal of Radiation Sciences*. 2022;10(4):1–16. doi:10.15392/2319-0612.2022.2047
24. Cooper DS, Doherty GM, Haugen BR, et al. Revised American thyroid association management guidelines for patients with thyroid nodules and differentiated thyroid cancer. *Thyroid*. 2009;19(11):1167–1214. doi: 10.1089/thy.2009.0110
25. Rosário PW, Vasconcelos FP, Cardoso LD, et al. Managing thyroid cancer without thyroxine withdrawal. *Arquivos Brasileiros de Endocrinologia & Metabologia*. 2006;50(1):91–96. doi: 10.1590/s0004-27302006000100013
26. Edmonds CJ, Hayes S, Kermode JC, Thompson BD. Measurement of serum TSH and thyroid hormones in the management of treatment of thyroid carcinoma with radioiodine. *The British Journal of Radiology*. 1977;50(599):799–807. doi: 10.1259/0007-1285-50-599-799
27. Giovannella L, Piccardo A. A “new/old method” for TSH stimulation: could a third way to prepare DTC patients for 131I remnant ablation possibly exist? *European Journal of Nuclear Medicine and Molecular Imaging*. 2015;43(2):221–223. doi:10.1007/s00259-015-3245-9
28. Semenov DYu, Boriskova ME, Farafonova UV, et al. Prognostic value of Sodium-Iodide Symporter (NIS) in differentiated thyroid cancer. *Clinical and experimental thyroidology*. 2015;11(1):50. (In Russ). doi: 10.14341/ket2015150-58
29. Xiao J, Yun C, Cao J, et al. A pre-ablative thyroid-stimulating hormone with 30–70 mIU/L achieves better response to initial radioiodine remnant ablation in differentiated thyroid carcinoma patients. *Scientific Reports*. 2021;11(1). doi: 10.1038/s41598-020-80015-8
30. Zhao T, Liang J, Guo Z, Li T, Lin Y. In Patients with Low- to Intermediate-Risk Thyroid Cancer, a Preablative Thyrotropin Level of 30 μ U/mL Is Not Adequate to Achieve Better Response to 131I Therapy. *Clinical Nuclear Medicine*. 2016;41(6):454–458. doi:10.1097/rlu.0000000000001167
31. Hasbek Z, Turgut B. Is Very High Thyroid Stimulating Hormone Level Required in Differentiated Thyroid Cancer for Ablation Success? *Molecular Imaging and Radionuclide Therapy*. 2016;25(2):79–84. doi: 10.4274/mirt.88598
32. Vrachimis A, Riemann B, Mäder U, Reiners C, Verbarg FA. Endogenous TSH levels at the time of 131I ablation do not influence ablation success, recurrence-free survival or differentiated thyroid cancer-related mortality. *European Journal of Nuclear Medicine and Molecular Imaging*. 2016;43(2):224–231. doi: 10.1007/s00259-015-3223-2
33. Montesano T, Durante C, Attard M, et al. Age influences TSH serum levels after withdrawal of l-thyroxine or rhTSH stimulation in patients affected by differentiated thyroid cancer. *Biomedicine & Pharmacotherapy*. 2007;61(8):468–471. doi: 10.1016/j.biopha.2007.04.001
34. Ju N, Hou L, Song H, et al. TSH \geq 30 mIU/L may not be necessary for successful 131I remnant ablation in patients with differentiated thyroid cancer. *European Thyroid Journal*. 2023;12(4). doi: 10.1530/ETJ-22-0219
35. Ren B, Zhu Y. A New Perspective on Thyroid Hormones: Crosstalk with Reproductive Hormones in Females. *International Journal of Molecular Sciences*. 2022;23(5):2708. doi: 10.3390/ijms23052708
36. Rubio GA, Catanuto P, Glassberg MK, Lew JI, Elliot SJ. Estrogen receptor subtype expression and regulation is altered in papillary thyroid cancer after menopause. *Surgery*. 2018;163(1):143–149. doi: 10.1016/j.surg.2017.04.031
37. Derwahl M, Nicula D. Estrogen and its role in thyroid cancer. *Endocrine-Related Cancer*. 2014;21(5):T273–T283. doi: 10.1530/erc-14-0053
38. Rajoria S, Suriano R, Shanmugam A, et al. Metastatic phenotype is regulated by estrogen in thyroid cells. *Thyroid*. 2010;20(1):33–41. doi: 10.1089/thy.2009.0296

39. Tala H, Robbins R, Fagin JA, Larson SM, Tuttle RM. Five-year survival is similar thyroid cancer patients with metastases prepared for radioactive iodine therapy with either thyroid hormone withdrawal or recombinant human TSH. *The Journal of Clinical Endocrinology & Metabolism*. 2011;96(7):2105–2111. doi: 10.1210/jc.2011-0305
40. Rosario PW, Mourão GF, Calsolari MR. Recombinant human TSH versus thyroid hormone withdrawal in adjuvant therapy with radioactive iodine of patients with papillary thyroid carcinoma and clinically apparent lymph node metastases not limited to the central compartment (cN1b). *Archives of Endocrinology and Metabolism*. 2017;61(2):167–172. doi:10.1590/2359-3997000000247
41. Hugo J, Robenshtok E, Grewal R, Larson S, Tuttle RM. Recombinant human thyroid stimulating hormone-assisted radioactive iodine remnant ablation in thyroid cancer patients at intermediate to high risk of recurrence. *Thyroid*. 2012;22(10):1007–1015. doi: 10.1089/thy.2012.0183
42. Robenshtok E, Tuttle RM. Role of Recombinant Human Thyrotropin (rhTSH) in the Treatment of Well-Differentiated Thyroid Cancer. *Indian Journal of Surgical Oncology*. 2012;3(3):182–189. doi: 10.1007/s13193-011-0115-1
43. Higuchi CRS, Fernanda P, Jurnior PA, et al. Clinical Outcomes After Radioiodine Therapy, According to the Method of Preparation by Recombinant TSH vs. Endogenous Hypothyroidism, in Thyroid Cancer Patients at Intermediate-High Risk of Recurrence. *Frontiers in Nuclear Medicine*. 2021;1. doi: 10.3389/fnume.2021.785768
44. Lawhn-Heath C, Flavell RR, Chuang EY, Liu C. Failure of iodine uptake in microscopic pulmonary metastases after recombinant human thyroid-stimulating hormone stimulation. *World Journal of Nuclear Medicine*. 2020;19(1):61–64. doi: 10.4103/wjnm.WJNM_29_19
45. Lee H, Paeng JC, Choi H, et al. Effect of TSH stimulation protocols on adequacy of low-iodine diet for radioiodine administration. *PLoS One*. 2021;16(9):e0256727. doi: 10.1371/journal.pone.0256727
46. Driedger AA, Kotowycz N. Two Cases of Thyroid Carcinoma That Were Not Stimulated by Recombinant Human Thyrotropin. *The Journal of Clinical Endocrinology & Metabolism*. 2004;89(2):585–590. doi: 10.1210/jc.2003-031650
47. Mernagh P, Campbell S, Dietlein M, et al. Cost-effectiveness of using recombinant human TSH prior to radioiodine ablation for thyroid cancer, compared with treating patients in a hypothyroid state: The German perspective. *European Journal of Endocrinology*. 2006;155(3):405–414. doi: 10.1530/eje.1.02223
48. Mernagh P, Suebwongpat A, Silverberg J, Weston A. Cost-effectiveness of using recombinant human thyroid-stimulating hormone before radioiodine ablation for thyroid cancer: The Canadian perspective. *Value in Health*. 2010;13(3):180–187. doi: 10.1111/j.1524-4733.2009.00650.x
49. Borget I, Bonastre J, Catargi B, et al. Quality of life and cost-effectiveness assessment of radioiodine ablation strategies in patients with thyroid cancer: results from the randomized phase III ESTIMABL trial. *Journal of Clinical Oncology*. 2015;33(26):2885–2892. doi: 10.1200/JCO.2015.61.6722
50. Nijhuis TF, van Weperen W, de Klerk JMH. Costs associated with the withdrawal of thyroid hormone suppression therapy during the follow-up treatment of well-differentiated thyroid cancer. *Tijdschrift voor nucleaire geneeskunde*. 1999;21:98–100.
51. Vallejo JA, Muros MA. Cost-effectiveness of using recombinant human thyroid-stimulating hormone before radioiodine ablation for thyroid cancer treatment in Spanish hospitals. *Revista Española de Medicina Nuclear e Imagen Molecular (English Edition)*. 2017;36(6):362–370. doi: 10.1016/j.remnie.2017.09.001
52. Luster M, Felbinger R, Dietlein M, Reiners C. Thyroid hormone withdrawal in patients with differentiated thyroid carcinoma: a one hundred thirty-patient pilot survey on consequences of hypothyroidism and a pharmacoeconomic comparison to recombinant thyrotropin administration. *Thyroid*. 2005;15(10):1147–1155. doi: 10.1089/thy.2005.15.1147
53. Rosario PW, Xavier AC, Calsolari MR. Recombinant human thyrotropin in thyroid remnant ablation with 131I in high-risk patients. *Thyroid*. 2010;20(11):1247–1252. doi: 10.1089/thy.2010.0114
54. Iizuka Y, Katagiri T, Ogura K, Inoue M, et al. Comparison of thyroid hormone withdrawal and recombinant human thyroid-stimulating hormone administration for adjuvant therapy in patients with intermediate- to high-risk differentiated thyroid cancer. *Annals of Nuclear Medicine*. 2020;34(10):736–741. doi: 10.1007/s12149-020-01497-0
55. Robbins RJ, Driedger A, Magner J; The U.S. and Canadian Thyrogen Compassionate Use Program Investigator Group. Recombinant human thyrotropin-assisted radioiodine therapy for patients with metastatic thyroid cancer who could not elevate endogenous thyrotropin or be withdrawn from thyroxine. *Thyroid*. 2006;16(11):1121–1130. doi: 10.1089/thy.2006.16.1121
56. Tu J, Wang S, Huo Z, et al. Recombinant human thyrotropin-aided versus thyroid hormone withdrawal-aided radioiodine treatment for differentiated thyroid cancer after total thyroidectomy: a meta-analysis. *Radiotherapy and Oncology*. 2014;110(1):25–30. doi: 10.1016/j.radonc.2013.12.018
57. Ma C, Xie J, Liu W, et al. Recombinant human thyrotropin (rhTSH) aided radioiodine treatment for residual or metastatic differentiated thyroid cancer. *Cochrane Database of Systematic Reviews*. 2010. doi: 10.1002/14651858.CD008302
58. Wolfson RM, Rachinsky I, Morrison D, et al. Recombinant Human Thyroid Stimulating Hormone versus Thyroid Hormone Withdrawal for Radioactive Iodine Treatment of Differentiated Thyroid Cancer with Nodal Metastatic Disease. *Journal of Oncology*. 2016;1–6. doi: 10.1155/2016/6496750
59. Klubo-Gwiedzinska J, Burman KD, Van Nostrand D, et al. Treatment of metastatic thyroid cancer: relative efficacy and side effect profile of preparation by thyroid hormone withdrawal versus recombinant human thyrotropin. *Thyroid*. 2012;22(3):310–317. doi: 10.1089/thy.2011.0235
60. Wolfenbittel BH, Coppes MH, Bongaerts AH, Glaudemans AW, Links TP. Unexpected symptoms after rhTSH administration due to occult thyroid carcinoma metastasis. *The Netherlands journal of medicine*. 2013;71(5):253–256.
61. Tsai HC, Ho KC, Chen SH, et al. Feasibility of Recombinant Human TSH as a Preparation for Radioiodine Therapy in Patients with Distant Metastases from Papillary Thyroid Cancer: Comparison of Long-Term Survival Outcomes with Thyroid Hormone Withdrawal. *Diagnostics*. 2022;12(1):221 doi: 10.3390/diagnostics12010221
62. Goldberg LD, Ditchek NT. Thyroid carcinoma with spinal cord compression. *JAMA: The Journal of the American Medical Association*. 1981;245(9):953–954. doi: 10.1001/jama.1981.03310340043025
63. Hoelting T, Tezelman S, Siperstein AE, Duh QY, Clark OH. Biphasic effects of thyrotropin on invasion and growth of papillary and follicular thyroid cancer in vitro. *Thyroid*. 1995;5(1):35–40. doi: 10.1089/thy.1995.5.35

- 64.** Pietz L, Michałek K, Waśko R, et al. Wpływ stymulacji endogenego TSH na wzrost resztkowej objętości tarczycy u chorych po całkowitej tyreoidektomii z powodu raka zróżnicowanego tarczycy. *Endokrynologia Polska*. 2008;59:119–122. (In Polish)
- 65.** Dedov II, Romyantsev PO, Nizhegorodova KS, et al. Recombinant human thyrotropin in radioiodine diagnostics and radioiodine ablation of patients with well-differentiated thyroid cancer: the first experience in Russia. *Endocrine Surgery*. 2018;12(3):128–139. (In Russ). doi: 10.14341/serg9806
- 66.** Saracyn M, Lubas A, Bober B, et al. Recombinant human thyrotropin worsens renal cortical perfusion and renal function in patients after total thyroidectomy due to differentiated thyroid cancer. *Thyroid*. 2020;30(5):653–660. doi: 10.1089/thy.2019.0372
- 67.** Chaker L, Razvi S, Bensenor IM, et al. Hypothyroidism. *Nature Reviews Disease Primers*. 2022;8(1). doi: 10.1038/s41572-022-00357-7
- 68.** Ortiga-Carvalho TM, Sidhaye AR, Wondisford FE. Thyroid hormone receptors and resistance to thyroid hormone disorders. *Nature Reviews Endocrinology*. 2014;10(10):582–591. doi: 10.1038/nrendo.2014.143
- 69.** Lien EA, Nedrebo BG, Varhaug JE, et al. Plasma total homocysteine levels during short-term iatrogenic hypothyroidism. *Journal of Clinical Endocrinology and Metabolism*. 2000;85(3):1049–1053. doi: 10.1210/jcem.85.3.6439
- 70.** Bicikova M, Hampl R, Hill M, et al. Steroids, sex hormone-binding globulin, homocysteine, selected hormones and markers of lipid and carbohydrate metabolism in patients with severe hypothyroidism and their changes following thyroid hormone supplementation. *Clinical Chemistry and Laboratory Medicine*. 2003;41(3):284–292. doi: 10.1515/CCLM.2003.045
- 71.** Lee SJ, Lee HY, Lee WW, Kim SE. The effect of recombinant human thyroid stimulating hormone on sustaining liver and renal function in thyroid cancer patients during radioactive iodine therapy. *Nuclear Medicine Communications*. 2014;35(7):727–732. doi: 10.1097/MNM.000000000000118
- 72.** Targher G, Montagnana M, Salvagno G, et al. Association between serum TSH, free T4 and serum liver enzyme activities in a large cohort of unselected outpatients. *Clinical Endocrinology*. 2008;68(3):481–484. doi: 10.1111/j.1365-2265.2007.03068.x
- 73.** Pearce EN, Wilson PW, Yang Q, Vasani RS, Braverman LE. Thyroid function and lipid subparticle sizes in patients with short-term hypothyroidism and a population-based cohort. *The Journal of Clinical Endocrinology & Metabolism*. 2008;93(3):888–894. doi: 10.1210/jc.2007-1987
- 74.** Ness GC, Lopez D, Chambers CM, et al. Effects of L-triiodothyronine and the thyromimetic L-94901 on serum lipoprotein levels and hepatic low-density lipoprotein receptor, 3-hydroxy-3-methylglutaryl coenzyme A reductase, and apo A-I gene expression. *Biochemical Pharmacology*. 1998;56(1):121–129. doi: 10.1016/S0006-2952(98)00119-1
- 75.** Pattaravimonporn N, Chaikijurajai T, Chamroonrat W, Sriphrapradang C. Myxedema Psychosis after Levothyroxine Withdrawal in Radioactive Iodine Treatment of Differentiated Thyroid Cancer: A Case Report. *Case Reports in Oncology*. 2021;14(3):1596–1600. doi: 10.1159/000520128
- 76.** Nagamachi S, Jinnouchi S, Nishii R, et al. Cerebral blood flow abnormalities induced by transient hypothyroidism after thyroidectomy – analysis by tc-99m-HMPAO and SPM96. *Annals of Nuclear Medicine*. 2004;18(6):469–477. doi: 10.1007/BF02984562
- 77.** Constant EL, De Volder AG, Ivanoiu A, et al. Cerebral blood flow and glucose metabolism in hypothyroidism: a positron emission tomography study. *Journal of Clinical Endocrinology and Metabolism*. 2001;86(8):3864–3870. doi: 10.1210/jcem.86.8.7749
- 78.** Duntas LH, Biondi B. Short-term hypothyroidism after Levothyroxine-withdrawal in patients with differentiated thyroid cancer: clinical and quality of life consequences. *European Journal of Endocrinology*. 2007;156(1):13–19. doi: 10.1530/eje.1.02310
- 79.** Kao PF, Lin JD, Chiu CT, et al. Gastric emptying function changes in patients with thyroid cancer after withdrawal of thyroid hormone therapy. *Journal of Gastroenterology and Hepatology*. 2004;19(6):655–660. doi: 10.1111/j.1440-1746.2003.03326.x
- 80.** Botella-Carretero JI, Prados A, Manzano L, et al. The effects of thyroid hormones on circulating markers of cell-mediated immune response, as studied in patients with differentiated thyroid carcinoma before and during thyroxine withdrawal. *European Journal of Endocrinology*. 2005;153(2):223–230. doi: 10.1530/eje.1.01951
- 81.** Duranton F, Lacoste A, Faurous P, et al. Exogenous thyrotropin improves renal function in euthyroid patients, while serum creatinine levels are increased in hypothyroidism. *Clinical Kidney Journal*. 2013;6(5):478–483. doi: 10.1093/cjk/sft092
- 82.** Coura-Filho GB, Willegaignon J, Buchpiguel CA, Sapienza MT. Effects of thyroid hormone withdrawal and recombinant human thyrotropin on glomerular filtration rate during radioiodine therapy for well-differentiated thyroid cancer. *Thyroid*. 2015;25(12):1291–1296. doi: 10.1089/thy.2015.0173
- 83.** An YS, Lee J, Kim HK, Lee SJ, Yoon JK. Effect of withdrawal of thyroid hormones versus administration of recombinant human thyroid-stimulating hormone on renal function in thyroid cancer patients. *Scientific Reports*. 2023;13(1). doi: 10.1038/s41598-023-27455-0
- 84.** Den Hollander JG, Wulkan RW, Mantel MJ, Berghout A. Correlation between severity of thyroid dysfunction and renal function. *Clinical Endocrinology*. 2005;62(4):423–427. doi: 10.1111/j.1365-2265.2005.02236.x
- 85.** Cho YY, Kim SK, Jung JH, et al. Long-term outcomes of renal function after radioactive iodine therapy for thyroid cancer according to preparation method: thyroid hormone withdrawal vs. recombinant human thyrotropin. *Endocrine*. 2019;64(2):293–298. doi: 10.1007/s12020-018-1807-x
- 86.** Kreisman SH, Hennessey JV. Consistent Reversible Elevations of Serum Creatinine Levels in Severe Hypothyroidism. *Archives of Internal Medicine*. 1999;159(1):79–82. doi: 10.1001/archinte.159.1.79
- 87.** Mariani LH, Berns JS. The Renal Manifestations of Thyroid Disease. *Journal of the American Society of Nephrology*. 2012;23(1):22–26. doi: 10.1681/ASN.2010070766
- 88.** Kim SK, Yun GY, Kim KH, et al. Severe hyponatremia following radioactive iodine therapy in patients with differentiated thyroid cancer. *Thyroid*. 2014;24(4):773–777. doi: 10.1089/thy.2013.0110
- 89.** Nozu T, Yoshida Y, Ohira M, Okumura T. Severe hyponatremia in association with I (131) therapy in a patient with metastatic thyroid cancer. *Internal Medicine*. 2011;50(19):2169–2174. doi: 10.2169/internalmedicine.50.5740
- 90.** Shakir MK, Krook LS, Schraml FV, Clyde PW. Symptomatic hyponatremia in association with a low-iodine diet and levothyroxine withdrawal prior to I131 in patients with metastatic thyroid carcinoma. *Thyroid*. 2008;18(7):787–792. doi: 10.1089/thy.2008.0050
- 91.** Al Nozha OM, Vautour L, How J. Life-threatening hyponatremia following a low-iodine diet: a case report and review of all reported cases. *Endocrine Practice*. 2011;17(5):e113–e117. doi: 10.4158/EP11045.CR

92. Lee JE, Kim SK, Han KH, et al. Risk factors for developing hyponatremia in thyroid cancer patients undergoing radioactive iodine therapy. *PLoS One*. 2014;9(8):e106840. doi: 10.1371/journal.pone.0106840
93. Horie I, Ando T, Imaizumi M, Usa T, Kawakami A. Hyperkalemia develops in some thyroidectomized patients undergoing thyroid hormone withdrawal in preparation for radioactive iodine ablation for thyroid carcinoma. *Endocrine Practice*. 2015;21(5):488–494. doi: 10.4158/EP14532.OR
94. Hyer S, Kong A, Pratt B, Harmer C. Salivary gland toxicity after radioiodine therapy for thyroid cancer. *Clinical Oncology*. 2007;19(1):83–86. doi: 10.1016/j.clon.2006.11.005
95. Riachy R, Ghazal N, Haidar MB, Elamine A, Nasrallah MP. Early Sialadenitis After Radioactive Iodine Therapy for Differentiated Thyroid Cancer: Prevalence and Predictors. *International Journal of Endocrinology*. 2020;2020:1–7. doi: 10.1155/2020/8649794
96. Adramerinas M, Andreadis D, Vahtsevanos K, Pouloupoulos A, Pazaitou-Panayiotou K. Sialadenitis as a complication of radioiodine therapy in patients with thyroid cancer: where do we stand? *Hormones*. 2021;20(4):669–678. doi: 10.1007/s42000-021-00304-3
97. Silberstein E. Prevention of radiation sialadenitis and glossitis after radioiodine-131 therapy of thyroid cancer. *Journal of Nuclear Medicine*. 2007;48 Suppl. 2.
98. Ma C, Xie J, Jiang Z, Wang G, Zuo S. Does amifostine have radioprotective effects on salivary glands in high-dose radioactive iodine-treated differentiated thyroid cancer. *European Journal of Nuclear Medicine and Molecular Imaging*. 2010;37(9):1778–1785. doi: 10.1007/s00259-009-1368-6
99. Nakada K, Ishibashi T, Takei T. Does lemon candy decrease salivary gland damage after radioiodine therapy for thyroid cancer? *Journal of nuclear medicine*. 2005;46(2):261–266.
100. Le Roux MK, Graillon N, Guyot L. Salivary side effects after radioiodine treatment for differentiated papillary thyroid carcinoma: Long-term study. *Head & Neck*. 2020;42(11):3133–3140. doi: 10.1002/hed.26359
101. Jentzen W, Balschuweit D, Schmitz J, et al. The influence of saliva flow stimulation on the absorbed radiation dose to the salivary glands during radioiodine therapy of thyroid cancer using (124)I PET/CT imaging. *European Journal of Nuclear Medicine and Molecular Imaging*. 2010;37(12):2298–2306. doi: 10.1007/s00259-010-1532-z
102. Trukhin AA, Yartsev VD, Sheremeta MS, et al. Nasolacrimal Duct Obstruction Secondary to Radioactive Iodine-131 Therapy for Differentiated Thyroid Cancer. The Bulletin of the Scientific Centre for Expert Evaluation of Medicinal Products. *Regulatory Research and Medicine Evaluation*. 2022;12(4):415–424. doi: 10.30895/1991-2919-2022-12-4-415-424
103. Iakovou I, Goulis DG, Tsinaslanidou Z, et al. Effect of recombinant human thyroid-stimulating hormone or levothyroxine withdrawal on salivary gland dysfunction after radioactive iodine administration for thyroid remnant ablation. *Head & Neck*. 2016;38 Suppl. 1:E227–230. doi: 10.1002/hed.23974
104. Rosario PW, Calsolari MR. Salivary and lacrimal gland dysfunction after remnant ablation with radioactive iodine in patients with differentiated thyroid carcinoma prepared with recombinant human thyrotropin. *Thyroid*. 2013;23(5):617–619. doi: 10.1089/thy.2012.0050
105. Molenaar RJ, Sidana S, Radivoyevitch T, et al. Risk of Hematologic Malignancies After Radioiodine Treatment of Well-Differentiated Thyroid Cancer. *Journal of Clinical Oncology*. 2018;36(18):1831–1839. doi: 10.1200/JCO.2017.75.0232
106. Signore A, Campagna G, Marinaccio J, et al. Analysis of Short-Term and Stable DNA Damage in Patients with Differentiated Thyroid Cancer Treated with 131I in Hypothyroidism or with Recombinant Human Thyroid-Stimulating Hormone for Remnant Ablation. *Journal of Nuclear Medicine*. 2022;63(10):1515–1522. doi: 10.2967/jnumed.121.263442
107. Sohn SY, Choi JY, Jang HW, et al. Association between excessive urinary iodine excretion and failure of radioactive iodine thyroid ablation in patients with papillary thyroid cancer. *Thyroid*. 2013;23(6):741–747. doi: 10.1089/thy.2012.0136
108. Lakshmanan M, Schaffer A, Robbins J, Reynolds J, Norton J. A simplified low iodine diet in I-131 scanning and therapy of thyroid cancer. *Clinical Nuclear Medicine*. 1988;13(12):866–868. doi: 10.1097/00003072-198812000-00003
109. Maxon HR, Thomas SR, Boehringer A, et al. Low iodine diet in I-131 ablation of thyroid remnants. *Clinical Nuclear Medicine*. 1983;8(3):123–126. doi: 10.1097/00003072-198303000-00006
110. Tala Jury HP, Castagna MG, Fioravanti C, et al. Lack of association between urinary iodine excretion and successful thyroid ablation in thyroid cancer patients. *Journal of Clinical Endocrinology and Metabolism*. 2010;95(1):230–237. doi: 10.1210/jc.2009-1624
111. Lee M, Lee YK, Jeon TJ, et al. Low iodine diet for one week is sufficient for adequate preparation of high dose radioactive iodine ablation therapy of differentiated thyroid cancer patients in iodine-rich areas. *Thyroid*. 2014;24(8):1289–1296. doi: 10.1089/thy.2013.0695
112. Tobey AE, Hongxiu L, Auh S, et al. Urine iodine excretion exceeding 250 ug/24h is associated with higher likelihood of progression in intermediate and high-risk thyroid cancer patients treated with radioactive iodine [abstract]. *Thyroid*. 2018;28 Suppl. 1:A40–A41
113. Pluijmen MJ, Eustatia-Rutten C, Goslings BM, et al. Effects of low-iodide diet on postsurgical radioiodide ablation therapy in patients with differentiated thyroid carcinoma. *Clinical Endocrinology*. 2003;58(4):428–435. doi: 10.1046/j.1365-2265.2003.01735.x
114. Morris LF, Wilder MS, Waxman AD, Braunstein GD. Reevaluation of the impact of a stringent low-iodine diet on ablation rates in radioiodine treatment of thyroid carcinoma. *Thyroid*. 2001;11(8):749–755. doi: 10.1089/10507250152484583
115. Yoo IDKS, Kim SH, Seo YY, et al. The success rate of initial (131) i ablation in differentiated thyroid cancer: comparison between less strict and very strict low iodine diets. *Nuclear Medicine and Molecular Imaging*. 2012;46(1):34–40. doi: 10.1007/s13139-011-0111-y
116. Ito S, Iwano S, Kato K, Naganawa S. Predictive factors for the outcomes of initial I-131 low-dose ablation therapy to Japanese patients with differentiated thyroid cancer. journal article. *Annals of Nuclear Medicine*. 2018;32(6):418–424. doi: 10.1007/s12149-018-1261-0
117. Lim CY, Kim JY, Yoon MJ, et al. Effect of a low iodine diet vs. restricted iodine diet on postsurgical preparation for radioiodine ablation therapy in thyroid carcinoma patients. *Yonsei Medical Journal*. 2015;56(4):1021–1027. doi: 10.3349/ymj.2015.56.4.1021
118. Kim HK, Lee SY, Lee JI, et al. Daily urine iodine excretion while consuming a low-iodine diet in preparation for radioactive iodine therapy in a high iodine intake area. *Clinical Endocrinology*. 2011;75(6):851–856. doi: 10.1111/j.1365-2265.2011.04157.x
119. Tomoda C, Urano T, Takamura Y, et al. Reevaluation of stringent low iodine diet in outpatient preparation for radioiodine examination and therapy. *Endocrine Journal*. 2005;52(2):237–240. doi: 10.1507/endocrj.52.237

- 120.** Sohaimi WF, Abdul Manap M, Kasilingam L, et al. Randomised controlled trial of one-week strict low-iodine diet versus one-week non-specified low iodine diet in differentiated thyroid carcinoma. *Iranian Journal of Nuclear Medicine*. 2019;27(2):99–105.
- 121.** Dekker BL, Links MH, Muller Kobold AC, et al. Low-iodine Diet of 4 Days Is Sufficient Preparation for ¹³¹I Therapy in Differentiated Thyroid Cancer Patients. *The Journal of Clinical Endocrinology & Metabolism*. 2022;107(2):e604–e611. doi: 10.1210/clinem/dgab691
- 122.** Padovani RP, Maciel RM, Kasamatsu TS, et al. Assessment of the Effect of Two Distinct Restricted Iodine Diet Durations on Urinary Iodine Levels (Collected over 24 h or as a Single-Spot Urinary Sample) and Na (+)/I (-) Symporter Expression. *European Thyroid Journal*. 2015;4(2):99–105. doi: 10.1159/000433426
- 123.** Park JT, Hennessey JV. Two-week low iodine diet is necessary for adequate outpatient preparation for radioiodine rTSH scanning in patients taking levothyroxine. *Thyroid*. 2004;14(1):57–63. doi: 10.1089/105072504322783858
- 124.** Dekker BL, Touw DJ, van der Horst-Schrivers ANA, et al. Use of Salivary Iodine Concentrations to Estimate the Iodine Status of Adults in Clinical Practice. *The Journal of Nutrition*. 2021;151(12):3671–3677. doi: 10.1093/jn/nxab303

СПИСОК ЛИТЕРАТУРЫ

- 1.** Ванушко В.Э., Цуркан А.Ю. Лечение дифференцированного рака щитовидной железы: состояние проблемы // Клиническая экспериментальная тиреоидология. 2010. Т. 6, № 2. С. 24–33. doi: 10.14341/ket20106224-33
- 2.** Злокачественные новообразования в России в 2021 году (заболеваемость и смертность) / под ред. А.Д. Каприна, В.В. Старинского, А.О. Шахзадовой. Москва : МНИОИ им. П.А. Герцена — филиал ФГБУ «НМИЦ радиологии» Минздрава России, 2022.
- 3.** Durante C., Haddy N., Baudin E., et al. Long-term outcome of 444 patients with distant metastases from papillary and follicular thyroid carcinoma: benefits and limits of radioiodine therapy // *The Journal of Clinical Endocrinology & Metabolism*. 2006. Vol. 91, N 8. P. 2892–2899. doi: 10.1210/jc.2005-2838
- 4.** Cancer Stat Facts: Thyroid Cancer [Internet]. National Cancer Institute: Surveillance, Epidemiology, and End Results Program. [дата обращения: 01.09.2023]. Доступ по ссылке: <https://seer.cancer.gov/statfacts/html/thyro.html>
- 5.** Braverman L.E., Cooper D.S., Kopp P. Werner & Ingbar's The Thyroid: A Fundamental and Clinical Text. 11th ed. // Philadelphia, PA : Wolters Kluwer, 2021.
- 6.** Hassan A., Razi M., Riaz S., et al. Survival Analysis of Papillary Thyroid Carcinoma in Relation to Stage and Recurrence Risk: A 20-Year Experience in Pakistan // *Clinical Nuclear Medicine*. 2016. Vol. 41, N 8. P. 606–613. doi: 10.1097/RLU.0000000000001237
- 7.** Клинические рекомендации — Дифференцированный рак щитовидной железы. ID 329. Одобрено Научно-практическим Советом Минздрава РФ. 2020. Режим доступа: https://cr.minzdrav.gov.ru/recomend/329_1 Дата обращения: 1.09.2023
- 8.** Avram A.M., Giovanella L., Greenspan B., et al. SNMMI Procedure Standard/EANM Practice Guideline for Nuclear Medicine Evaluation and Therapy of Differentiated Thyroid Cancer: Abbreviated Version // *Journal of Nuclear Medicine*. 2022. Vol. 63, N 6. P. 15N–35N.
- 9.** Haugen B.R., Alexander E.K., Bible K.C., et al. 2015 American Thyroid Association Management Guidelines for Adult Patients with Thyroid Nodules and Differentiated Thyroid Cancer: The American Thyroid Association Guidelines Task Force on Thyroid Nodules and Differentiated Thyroid Cancer // *Thyroid*. 2016. Vol. 26, N 1. P. 1–133. doi: 10.1089/thy.2015.0020
- 10.** Pacini F., Fuhrer D., Elisei R., et al. 2022 ETA Consensus Statement: What are the indications for post-surgical radioiodine therapy in differentiated thyroid cancer? // *European Thyroid Journal*. 2022. Vol. 11, N 1. doi: 10.1530/etj-21-0046
- 11.** Filetti S., Durante C., Hartl D., et al. Thyroid cancer: ESMO Clinical Practice Guidelines for diagnosis, treatment and follow-up // *Annals of Oncology*. 2019. Vol. 30, N 12. P. 1856–1883. doi: 10.1093/annonc/mdz400
- 12.** Perros P., Boelaert K., Colley S., et al. Guidelines for the management of thyroid cancer // *Clinical Endocrinology*. 2014. Vol. 81, Suppl. 1. P. 1–122. doi: 10.1111/cen.12515
- 13.** Haddad R.I., Bischoff L., Ball D., et al. Thyroid Carcinoma, Version 2.2022, NCCN Clinical Practice Guidelines in Oncology // *Journal of the National Comprehensive Cancer Network*. 2022. Vol. 20, N 8. P. 925–951. doi: 10.6004/jnccn.2022.0040
- 14.** Golger A., Fridman T.R., Eski S., et al. Three-week thyroxine withdrawal thyroglobulin stimulation screening test to detect low-risk residual/recurrent well-differentiated thyroid carcinoma // *Journal of Endocrinological Investigation*. 2003. Vol. 26, N 10. P. 1023–1031. doi: 10.1007/bf03348202
- 15.** Davids T., Witterick I.J., Eski S., et al. Three-Week Thyroxine Withdrawal: A Thyroid-Specific Quality of Life Study // *The Laryngoscope*. 2006. Vol. 116, N 2. P. 250–253. doi: 10.1097/01.mlg.0000192172.61889.43
- 16.** Lee J., Yun M.J., Nam K.H., et al. Quality of life and effectiveness comparisons of thyroxine withdrawal, triiodothyronine withdrawal, and recombinant thyroid-stimulating hormone administration for low-dose radioiodine remnant ablation of differentiated thyroid carcinoma // *Thyroid*. 2010. Vol. 20. P. 173–179. doi: 10.1089/thy.2009.0187
- 17.** Leboeuf R., Perron P., Carpentier A.C., Verreault J., Langlois M.F. L-T3 preparation for whole-body scintigraphy: a randomized-controlled trial // *Clinical Endocrinology*. 2007. Vol. 67, N 6. P. 839–844. doi: 10.1111/j.1365-2265.2007.02972.x
- 18.** Rajamanickam S., Chaukar D., Siddiq S., Basu S., D'Cruz A. Quality of life comparison in thyroxine hormone withdrawal versus triiodothyronine supplementation prior to radioiodine ablation in differentiated thyroid carcinoma: a prospective cohort study in the Indian population // *European Archives of Oto-Rhino-Laryngology*. 2021. Vol. 279, N 4. doi: 10.1007/s00405-021-06948-6
- 19.** Luna R., Penín M., Seoane I., et al. ¿Es necesario suspender durante 4 semanas el tratamiento con tiroxina antes de la realización de un rastreo-ablación? // *Endocrinología y Nutrición*. 2012. Vol. 59, N 4. P. 227–231. (In Spanish) doi: 10.1016/j.endonu.2012.02.004
- 20.** Dow K.H., Ferrell B.R., Anello C. Quality-of-life changes in patients with thyroid cancer after withdrawal of thyroid hormone therapy // *Thyroid*. 1997. Vol. 7, N 4. P. 613–619. doi: 10.1089/thy.1997.7.613

21. Liel Y. Preparation for radioactive iodine administration in differentiated thyroid cancer patients // *Clinical Endocrinology*. 2002. Vol. 57, N 4. P. 523–527. doi: 10.1046/j.1365-2265.2002.01631.x
22. Piccardo A., Puntoni M., Ferrarazzo G., et al. Could short thyroid hormone withdrawal be an effective strategy for radioiodine remnant ablation in differentiated thyroid cancer patients? // *European Journal of Nuclear Medicine and Molecular Imaging*. 2018. Vol. 45, N 7. P. 1218–1223. doi: 10.1007/s00259-018-3955-x
23. Santos P.A., Flamini M.E., Mourato F.A., et al. Is a four-week hormone suspension necessary for thyroid remnant ablation in low and intermediate risk patients? A pilot study with quality-of-life assessment // *Brazilian Journal of Radiation Sciences*. 2022. Vol. 10, N 4. P. 1–16. doi:10.15392/2319-0612.2022.2047
24. Cooper D.S., Doherty G.M., Haugen B.R., et al. Revised American thyroid association management guidelines for patients with thyroid nodules and differentiated thyroid cancer // *Thyroid*. 2009. Vol. 19, N 11. P. 1167–1214. doi: 10.1089/thy.2009.0110
25. Rosário P.W., Vasconcelos F.P., Cardoso L.D., et al. Managing thyroid cancer without thyroxine withdrawal // *Arquivos Brasileiros de Endocrinologia & Metabologia*. 2006. Vol. 50, N 1. P. 91–96. doi: 10.1590/s0004-27302006000100013
26. Edmonds C.J., Hayes S., Kermode J.C., Thompson B.D. Measurement of serum TSH and thyroid hormones in the management of treatment of thyroid carcinoma with radioiodine // *The British Journal of Radiology*. 1977. Vol. 50, N 599. P. 799–807. doi: 10.1259/0007-1285-50-599-799
27. Giovanella L., Piccardo A. A “new/old method” for TSH stimulation: could a third way to prepare DTC patients for 131I remnant ablation possibly exist? // *European Journal of Nuclear Medicine and Molecular Imaging*. 2015. Vol. 43, N 2. P. 221–223. doi:10.1007/s00259-015-3245-9
28. Семенов Д.Ю., Борискова М.Е., Фарафонова У.В., и др. Прогностическое значение экспрессии натрий-йодного симпортера для высокодифференцированного рака щитовидной железы // *Клиническая и экспериментальная тиреоидология*. 2015. Т. 11, № 1. С. 50. doi: 10.14341/ket2015150-58
29. Xiao J., Yun C., Cao J., et al. A pre-ablative thyroid-stimulating hormone with 30–70 mIU/L achieves better response to initial radioiodine remnant ablation in differentiated thyroid carcinoma patients // *Scientific Reports*. 2021. Vol. 11, N 1. doi: 10.1038/s41598-020-80015-8
30. Zhao T., Liang J., Guo Z., Li T., Lin Y. In Patients with Low- to Intermediate-Risk Thyroid Cancer, a Preablative Thyrotropin Level of 30 μ IU/mL Is Not Adequate to Achieve Better Response to 131I Therapy // *Clinical Nuclear Medicine*. 2016. Vol. 41, N 6. P. 454–458. doi:10.1097/rlu.0000000000001167
31. Hasbek Z., Turgut B. Is Very High Thyroid Stimulating Hormone Level Required in Differentiated Thyroid Cancer for Ablation Success? // *Molecular Imaging and Radionuclide Therapy*. 2016. Vol. 25, N 2. P. 79–84. doi: 10.4274/mirt.88598
32. Vrachimis A., Riemann B., Mäder U., Reiners C., Verburg F.A. Endogenous TSH levels at the time of 131I ablation do not influence ablation success, recurrence-free survival or differentiated thyroid cancer-related mortality // *European Journal of Nuclear Medicine and Molecular Imaging*. 2016. Vol. 43, N 2. P. 224–231. doi:10.1007/s00259-015-3223-2
33. Montesano T., Durante C., Attard M., et al. Age influences TSH serum levels after withdrawal of l-thyroxine or rhTSH stimulation in patients affected by differentiated thyroid cancer // *Biomedicine & Pharmacotherapy*. 2007. Vol. 61, N 8. P. 468–471. doi: 10.1016/j.biopha.2007.04.001
34. Ju N., Hou L., Song H., et al. TSH \geq 30 mIU/L may not be necessary for successful 131I remnant ablation in patients with differentiated thyroid cancer // *European Thyroid Journal*. 2023. Vol. 12, N 4. doi: 10.1530/ETJ-22-0219
35. Ren B., Zhu Y. A New Perspective on Thyroid Hormones: Crosstalk with Reproductive Hormones in Females // *International Journal of Molecular Sciences*. 2022. Vol. 23, N 5. P. 2708. doi: 10.3390/ijms23052708
36. Rubio G.A., Catanuto P., Glassberg M.K., Lew J.I., Elliot S.J. Estrogen receptor subtype expression and regulation is altered in papillary thyroid cancer after menopause // *Surgery*. 2018. Vol. 163, N 1. P. 143–149. doi: 10.1016/j.surg.2017.04.031
37. Derwahl M., Nicula D. Estrogen and its role in thyroid cancer // *Endocrine-Related Cancer*. 2014. Vol. 21, N 5. P. T273–T283. doi: 10.1530/erc-14-0053
38. Rajoria S., Suriano R., Shanmugam A., et al. Metastatic phenotype is regulated by estrogen in thyroid cells // *Thyroid*. 2010. Vol. 20, N 1. P. 33–41. doi: 10.1089/thy.2009.0296
39. Tala H., Robbins R., Fagin J.A., Larson S.M., Tuttle R.M. Five-year survival is similar thyroid cancer patients with metastases prepared for radioactive iodine therapy with either thyroid hormone withdrawal or recombinant human TSH // *The Journal of Clinical Endocrinology & Metabolism*. 2011. Vol. 96, N 7. P. 2105–2111. doi: 10.1210/jc.2011-0305
40. Rosario P.W., Mourão G.F., Calsolari M.R. Recombinant human TSH versus thyroid hormone withdrawal in adjuvant therapy with radioactive iodine of patients with papillary thyroid carcinoma and clinically apparent lymph node metastases not limited to the central compartment (cN1b) // *Archives of Endocrinology and Metabolism*. 2017. Vol. 61, N 2. P. 167–172. doi:10.1590/2359-3997000000247
41. Hugo J., Robenshtok E., Grewal R., Larson S., Tuttle R.M. Recombinant human thyroid stimulating hormone-assisted radioactive iodine remnant ablation in thyroid cancer patients at intermediate to high risk of recurrence // *Thyroid*. 2012. Vol. 22, N 10. P. 1007–1015. doi: 10.1089/thy.2012.0183
42. Robenshtok E., Tuttle R.M. Role of Recombinant Human Thyrotropin (rhTSH) in the Treatment of Well-Differentiated Thyroid Cancer // *Indian Journal of Surgical Oncology*. 2012. Vol. 3, N 3. P. 182–189. doi: 10.1007/s13193-011-0115-1
43. Higuchi C.R.S., Fernanda P., Jurnior P.A., et al. Clinical Outcomes After Radioiodine Therapy, According to the Method of Preparation by Recombinant TSH vs. Endogenous Hypothyroidism, in Thyroid Cancer Patients at Intermediate–High Risk of Recurrence // *Frontiers in Nuclear Medicine*. 2021. Vol. 1. doi: 10.3389/fnume.2021.785768
44. Lawhn-Heath C., Flavell R.R., Chuang E.Y., Liu C. Failure of iodine uptake in microscopic pulmonary metastases after recombinant human thyroid-stimulating hormone stimulation // *World Journal of Nuclear Medicine*. 2020. Vol. 19, N 1. P. 61–64. doi: 10.4103/wjnm.WJNM_29_19
45. Lee H., Paeng J.C., Choi H., et al. Effect of TSH stimulation protocols on adequacy of low-iodine diet for radioiodine administration // *PLoS One*. 2021. Vol. 16, N 9. P. e0256727. doi: 10.1371/journal.pone.0256727
46. Driedger A.A., Kotowycz N. Two Cases of Thyroid Carcinoma That Were Not Stimulated by Recombinant Human Thyrotropin // *The*

- Journal of Clinical Endocrinology & Metabolism. 2004. Vol. 89, N 2. P. 585–590. doi: 10.1210/jc.2003-031650
- 47.** Mernagh P., Campbell S., Dietlein M., et al. Cost-effectiveness of using recombinant human TSH prior to radioiodine ablation for thyroid cancer, compared with treating patients in a hypothyroid state: The German perspective // *European Journal of Endocrinology*. 2006. Vol. 155, N 3. P. 405–414. doi: 10.1530/eje.1.02223
- 48.** Mernagh P., Suebwongpat A., Silverberg J., Weston A. Cost-effectiveness of using recombinant human thyroid-stimulating hormone before radioiodine ablation for thyroid cancer: The Canadian perspective // *Value in Health*. 2010. Vol. 13, N 3. P. 180–187. doi: 10.1111/j.1524-4733.2009.00650.x
- 49.** Borget I., Bonastre J., Catargi B., et al. Quality of life and cost-effectiveness assessment of radioiodine ablation strategies in patients with thyroid cancer: results from the randomized phase III ESTIMABL trial // *Journal of Clinical Oncology*. 2015. Vol. 33, N 26. P. 2885–2892. doi: 10.1200/JCO.2015.61.6722
- 50.** Nijhuis T.F., van Weperen W., de Klerk J.M.H. Costs associated with the withdrawal of thyroid hormone suppression therapy during the follow-up treatment of well-differentiated thyroid cancer // *Tijdschrift voor nucleaire geneeskunde*. 1999. Vol. 21. P. 98–100.
- 51.** Vallejo J.A., Muros M.A. Cost-effectiveness of using recombinant human thyroid-stimulating hormone before radioiodine ablation for thyroid cancer treatment in Spanish hospitals // *Revista Española de Medicina Nuclear e Imagen Molecular (English Edition)*. 2017. Vol. 36, N 6. P. 362–370. doi: 10.1016/j.remnie.2017.09.001
- 52.** Luster M., Felbinger R., Dietlein M., Reiners C. Thyroid hormone withdrawal in patients with differentiated thyroid carcinoma: a one hundred thirty-patient pilot survey on consequences of hypothyroidism and a pharmacoeconomic comparison to recombinant thyrotropin administration // *Thyroid*. 2005. Vol. 15, N 10. P. 1147–1155. doi: 10.1089/thy.2005.15.1147
- 53.** Rosario P.W., Xavier A.C., Calsolari M.R. Recombinant human thyrotropin in thyroid remnant ablation with ¹³¹I in high-risk patients // *Thyroid*. 2010. Vol. 20, N 11. P. 1247–1252. doi: 10.1089/thy.2010.0114
- 54.** Iizuka Y., Katagiri T., Ogura K., Inoue M., et al. Comparison of thyroid hormone withdrawal and recombinant human thyroid-stimulating hormone administration for adjuvant therapy in patients with intermediate- to high-risk differentiated thyroid cancer // *Annals of Nuclear Medicine*. 2020. Vol. 34, N 10. P. 736–741. doi: 10.1007/s12149-020-01497-0
- 55.** Robbins R.J., Driedger A., Magner J.; The U.S. and Canadian Thyrogen Compassionate Use Program Investigator Group. Recombinant human thyrotropin-assisted radioiodine therapy for patients with metastatic thyroid cancer who could not elevate endogenous thyrotropin or be withdrawn from thyroxine // *Thyroid*. 2006. Vol. 16, N 11. P. 1121–1130. doi: 10.1089/thy.2006.16.1121
- 56.** Tu J., Wang S., Huo Z., et al. Recombinant human thyrotropin-aided versus thyroid hormone withdrawal-aided radioiodine treatment for differentiated thyroid cancer after total thyroidectomy: a meta-analysis // *Radiotherapy and Oncology*. 2014. Vol. 110, N 1. P. 25–30. doi: 10.1016/j.radonc.2013.12.018
- 57.** Ma C., Xie J., Liu W., et al. Recombinant human thyrotropin (rhTSH) aided radioiodine treatment for residual or metastatic differentiated thyroid cancer // *Cochrane Database of Systematic Reviews*. 2010. doi: 10.1002/14651858.CD008302
- 58.** Wolfson R.M., Rachinsky I., Morrison D., et al. Recombinant Human Thyroid Stimulating Hormone versus Thyroid Hormone Withdrawal for Radioactive Iodine Treatment of Differentiated Thyroid Cancer with Nodal Metastatic Disease // *Journal of Oncology*. 2016. P. 1–6. doi: 10.1155/2016/6496750
- 59.** Klubo-Gwiezdzinska J., Burman K.D., Van Nostrand D., et al. Treatment of metastatic thyroid cancer: relative efficacy and side effect profile of preparation by thyroid hormone withdrawal versus recombinant human thyrotropin // *Thyroid*. 2012. Vol. 22, N 3. P. 310–317. doi: 10.1089/thy.2011.0235
- 60.** Wolffenbuttel B.H., Coppes M.H., Bongaerts A.H., Glaudemans A.W., Links T.P. Unexpected symptoms after rhTSH administration due to occult thyroid carcinoma metastasis // *The Netherlands journal of medicine*. 2013. Vol. 71, N 5. P. 253–256.
- 61.** Tsai H.C., Ho K.C., Chen S.H., et al. Feasibility of Recombinant Human TSH as a Preparation for Radioiodine Therapy in Patients with Distant Metastases from Papillary Thyroid Cancer: Comparison of Long-Term Survival Outcomes with Thyroid Hormone Withdrawal // *Diagnostics*. 2022. Vol. 12, N 1. P. 221. doi: 10.3390/diagnostics12010221
- 62.** Goldberg L.D., Ditchek N.T. Thyroid carcinoma with spinal cord compression // *JAMA: The Journal of the American Medical Association*. 1981. Vol. 245, N 9. P. 953–954. doi: 10.1001/jama.1981.03310340043025
- 63.** Hoelting T., Tezelman S., Siperstein A.E., Duh Q.Y., Clark O.H. Biphasic effects of thyrotropin on invasion and growth of papillary and follicular thyroid cancer in vitro // *Thyroid*. 1995. Vol. 5, N 1. P. 35–40. doi: 10.1089/thy.1995.5.35
- 64.** Pietz L., Michalek K., Waško R., et al. Wpływ stymulacji endogenego TSH na wzrost resztkowej objętości tarczycy u chorych po całkowitej tyreoidektomii z powodu raka zróżnicowanego tarczycy // *Endokrynologia Polska*. 2008. Vol. 59. P. 119–122. (In Polish).
- 65.** Дедов И.И., Румянцев П.О., Нижегородова К.С., и др. Первый отечественный опыт применения рекомбинантного человеческого тиреотропного гормона при подготовке больных высокодифференцированным раком щитовидной железы к радиойоддиагностике и радиойодаблации // *Эндокринная хирургия*. 2018. Т. 12, № 3. С. 128–139. doi: 10.14341/serg9806
- 66.** Saracyn M., Lubas A., Bober B., et al. Recombinant human thyrotropin worsens renal cortical perfusion and renal function in patients after total thyroidectomy due to differentiated thyroid cancer // *Thyroid*. 2020. Vol. 30, N 5. P. 653–660. doi: 10.1089/thy.2019.0372
- 67.** Chaker L., Razvi S., Bensenor I.M., et al. Hypothyroidism // *Nature Reviews Disease Primers*. 2022. Vol. 8, N 1. doi: 10.1038/s41572-022-00357-7
- 68.** Ortega-Carvalho T.M., Sidhaye A.R., Wondisford F.E. Thyroid hormone receptors and resistance to thyroid hormone disorders // *Nature Reviews Endocrinology*. 2014. Vol. 10, N 10. P. 582–591. doi: 10.1038/nrendo.2014.143
- 69.** Lien E.A., Nedrebo B.G., Varhaug J.E., et al. Plasma total homocysteine levels during short-term iatrogenic hypothyroidism // *Journal of Clinical Endocrinology and Metabolism*. 2000. Vol. 85, N 3. P. 1049–1053. doi: 10.1210/jcem.85.3.6439
- 70.** Bicikova M., Hampl R., Hill M., et al. Steroids, sex hormone-binding globulin, homocysteine, selected hormones and markers of lipid and carbohydrate metabolism in patients with severe hypothyroidism and their changes following thyroid hormone supplementation // *Clinical Chemistry and Laboratory Medicine*. 2003. Vol. 41, N 3. P. 284–292. doi: 10.1515/CCLM.2003.045

- 71.** Lee S.J., Lee H.Y., Lee W.W., Kim S.E. The effect of recombinant human thyroid stimulating hormone on sustaining liver and renal function in thyroid cancer patients during radioactive iodine therapy // *Nuclear Medicine Communications*. 2014. Vol. 35, N 7. P. 727–732. doi: 10.1097/MNM.000000000000118
- 72.** Targher G., Montagnana M., Salvagno G., et al. Association between serum TSH, free T4 and serum liver enzyme activities in a large cohort of unselected outpatients // *Clinical Endocrinology*. 2008. Vol. 68, N 3. P. 481–484. doi: 10.1111/j.1365-2265.2007.03068.x
- 73.** Pearce E.N., Wilson P.W., Yang Q., Vasani R.S., Braverman L.E. Thyroid function and lipid subparticle sizes in patients with short-term hypothyroidism and a population-based cohort // *The Journal of Clinical Endocrinology & Metabolism*. 2008. Vol. 93, N 3. P. 888–894. doi: 10.1210/jc.2007-1987
- 74.** Ness G.C., Lopez D., Chambers C.M., et al. Effects of L-triiodothyronine and the thyromimetic L-94901 on serum lipoprotein levels and hepatic low-density lipoprotein receptor, 3-hydroxy-3-methylglutaryl coenzyme A reductase, and apo A-I gene expression // *Biochemical Pharmacology*. 1998. Vol. 56, N 1. P. 121–129. doi: 10.1016/S0006-2952(98)00119-1
- 75.** Pattaravimonporn N., Chaikijurajai T., Chamroonrat W., Sriphrapradang C. Myxedema Psychosis after Levothyroxine Withdrawal in Radioactive Iodine Treatment of Differentiated Thyroid Cancer: A Case Report // *Case Reports in Oncology*. 2021. Vol. 14, N 3. P. 1596–1600. doi: 10.1159/000520128
- 76.** Nagamachi S., Jinnouchi S., Nishii R., et al. Cerebral blood flow abnormalities induced by transient hypothyroidism after thyroidectomy — analysis by tc-99m-HMPAO and SPM96 // *Annals of Nuclear Medicine*. 2004. Vol. 18, N 6. P. 469–477. doi: 10.1007/BF02984562
- 77.** Constant E.L., De Volder A.G., Ivanoiu A., et al. Cerebral blood flow and glucose metabolism in hypothyroidism: a positron emission tomography study // *Journal of Clinical Endocrinology and Metabolism*. 2001. Vol. 86, N 8. P. 3864–3870. doi: 10.1210/jcem.86.8.7749
- 78.** Duntas L.H., Biondi B. Short-term hypothyroidism after Levothyroxine-withdrawal in patients with differentiated thyroid cancer: clinical and quality of life consequences // *European Journal of Endocrinology*. 2007. Vol. 156, N 1. P. 13–19. doi: 10.1530/eje.1.02310
- 79.** Kao P.F., Lin J.D., Chiu C.T., et al. Gastric emptying function changes in patients with thyroid cancer after withdrawal of thyroid hormone therapy // *Journal of Gastroenterology and Hepatology*. 2004. Vol. 19, N 6. P. 655–660. doi: 10.1111/j.1440-1746.2003.03326.x
- 80.** Botella-Carretero J.I., Prados A., Manzano L., et al. The effects of thyroid hormones on circulating markers of cell-mediated immune response, as studied in patients with differentiated thyroid carcinoma before and during thyroxine withdrawal // *European Journal of Endocrinology*. 2005. Vol. 153, N 2. P. 223–230. doi: 10.1530/eje.1.01951
- 81.** Duranton F., Lacoste A., Faurous P., et al. Exogenous thyrotropin improves renal function in euthyroid patients, while serum creatinine levels are increased in hypothyroidism // *Clinical Kidney Journal*. 2013. Vol. 6, N 5. P. 478–483. doi: 10.1093/ckj/sft092
- 82.** Coura-Filho G.B., Willegaignon J., Buchpiguel C.A., Sapienza M.T. Effects of thyroid hormone withdrawal and recombinant human thyrotropin on glomerular filtration rate during radioiodine therapy for well-differentiated thyroid cancer // *Thyroid*. 2015. Vol. 25, N 12. P. 1291–1296. doi: 10.1089/thy.2015.0173
- 83.** An Y.S., Lee J., Kim H.K., Lee S.J., Yoon J.K. Effect of withdrawal of thyroid hormones versus administration of recombinant human thyroid-stimulating hormone on renal function in thyroid cancer patients // *Scientific Reports*. 2023. Vol. 13, N 1. doi: 10.1038/s41598-023-27455-0
- 84.** Den Hollander J.G., Wulkan R.W., Mantel M.J., Berghout A. Correlation between severity of thyroid dysfunction and renal function // *Clinical Endocrinology*. 2005. Vol. 62, N 4. P. 423–427. doi: 10.1111/j.1365-2265.2005.02236.x
- 85.** Cho Y.Y., Kim S.K., Jung J.H., et al. Long-term outcomes of renal function after radioactive iodine therapy for thyroid cancer according to preparation method: thyroid hormone withdrawal vs. recombinant human thyrotropin // *Endocrine*. 2019. Vol. 64, N 2. P. 293–298. doi: 10.1007/s12020-018-1807-x
- 86.** Kreisman S.H., Hennessey J.V. Consistent Reversible Elevations of Serum Creatinine Levels in Severe Hypothyroidism // *Archives of Internal Medicine*. 1999. Vol. 159, N 1. P. 79–82. doi: 10.1001/archinte.159.1.79
- 87.** Mariani L.H., Berns J.S. The Renal Manifestations of Thyroid Disease // *Journal of the American Society of Nephrology*. 2012. Vol. 23, N 1. P. 22–26. doi: 10.1681/ASN.2010070766
- 88.** Kim S.K., Yun G.Y., Kim K.H. et al. Severe hyponatremia following radioactive iodine therapy in patients with differentiated thyroid cancer // *Thyroid*. 2014. Vol. 24, N 4. P. 773–777. doi: 10.1089/thy.2013.0110
- 89.** Nozu T., Yoshida Y., Ohira M., Okumura T. Severe hyponatremia in association with I (131) therapy in a patient with metastatic thyroid cancer // *Internal Medicine*. 2011. Vol. 50, N 19. P. 2169–2174. doi: 10.2169/internalmedicine.50.5740
- 90.** Shakir M.K., Krook L.S., Schraml F.V., Clyde P.W. Symptomatic hyponatremia in association with a low-iodine diet and levothyroxine withdrawal prior to I131 in patients with metastatic thyroid carcinoma // *Thyroid*. 2008. Vol. 18, N 7. P. 787–792. doi: 10.1089/thy.2008.0050
- 91.** Al Nozha O.M., Vautour L., How J. Life-threatening hyponatremia following a low-iodine diet: a case report and review of all reported cases // *Endocrine Practice*. 2011. Vol. 17, N 5. P. e113–e117. doi: 10.4158/EP11045.CR
- 92.** Lee J.E., Kim S.K., Han K.H., et al. Risk factors for developing hyponatremia in thyroid cancer patients undergoing radioactive iodine therapy // *PLoS One*. 2014. Vol. 9, N 8. P. e106840. doi: 10.1371/journal.pone.0106840
- 93.** Horie I., Ando T., Imaizumi M., Usa T., Kawakami A. Hyperkalemia develops in some thyroidectomized patients undergoing thyroid hormone withdrawal in preparation for radioactive iodine ablation for thyroid carcinoma // *Endocrine Practice*. 2015. Vol. 21, N 5. P. 488–494. doi: 10.4158/EP14532.OR
- 94.** Hyer S., Kong A., Pratt B., Harmer C. Salivary gland toxicity after radioiodine therapy for thyroid cancer // *Clinical Oncology*. 2007. Vol. 19, N 1. P. 83–86. doi: 10.1016/j.clon.2006.11.005
- 95.** Riachy R., Ghazal N., Haidar M.B., Elamine A., Nasrallah M.P. Early Sialadenitis After Radioactive Iodine Therapy for Differentiated Thyroid Cancer: Prevalence and Predictors // *International Journal of Endocrinology*. 2020. Vol. 2020. P. 1–7. doi: 10.1155/2020/8649794
- 96.** Adramerinas M., Andreadis D., Vahtsevanos K., Pouloupoulos A., Pazaitou-Panayioutou K. Sialadenitis as a complication of radioiodine therapy in patients with thyroid cancer: where do we stand? // *Hormones*. 2021. Vol. 20, N 4. P. 669–678. doi: 10.1007/s42000-021-00304-3
- 97.** Silberstein E. Prevention of radiation sialadenitis and glossitis after radioiodine-131 therapy of thyroid cancer // *Journal of Nuclear Medicine*. 2007. Vol. 48, Suppl. 2.

- 98.** Ma C., Xie J., Jiang Z., Wang G., Zuo S. Does amifostine have radioprotective effects on salivary glands in high-dose radioactive iodine-treated differentiated thyroid cancer // *European Journal of Nuclear Medicine and Molecular Imaging*. 2010. Vol. 37, N 9. P. 1778–1785. doi: 10.1007/s00259-009-1368-6
- 99.** Nakada K., Ishibashi T., Takei T. Does lemon candy decrease salivary gland damage after radioiodine therapy for thyroid cancer? // *Journal of nuclear medicine*. 2005. Vol. 46, N 2. P. 261–266.
- 100.** Le Roux M.K., Graillon N., Guyot L. Salivary side effects after radioiodine treatment for differentiated papillary thyroid carcinoma: Long-term study // *Head & Neck*. 2020. Vol. 42, N 11. P. 3133–3140. doi: 10.1002/hed.26359
- 101.** Jentzen W., Balschuweit D., Schmitz J., et al. The influence of saliva flow stimulation on the absorbed radiation dose to the salivary glands during radioiodine therapy of thyroid cancer using (124) I PET/CT imaging // *European Journal of Nuclear Medicine and Molecular Imaging*. 2010. Vol. 37, N 12. P. 2298–2306. doi: 10.1007/s00259-010-1532-z
- 102.** Трухин А.А., Ярцев В.Д., Шеремета М.С., и др. Вторичная облитерация слезоотводящих путей при проведении радиойодтерапии 131I дифференцированного рака щитовидной железы // *Регуляторные исследования и экспертиза лекарственных средств*. 2022. Т. 12, № 4. С. 415–424. doi: 10.30895/1991-2919-2022-12-4-415-424
- 103.** Iakovou I., Goulis D.G., Tsinaslanidou Z., et al. Effect of recombinant human thyroid-stimulating hormone or levothyroxine withdrawal on salivary gland dysfunction after radioactive iodine administration for thyroid remnant ablation // *Head & Neck*. 2016. Vol. 38, Suppl. 1. P. E227–230. doi: 10.1002/hed.23974
- 104.** Rosario P.W., Calsolari M.R. Salivary and lacrimal gland dysfunction after remnant ablation with radioactive iodine in patients with differentiated thyroid carcinoma prepared with recombinant human thyrotropin // *Thyroid*. 2013. Vol. 23, N 5. P. 617–619. doi: 10.1089/thy.2012.0050
- 105.** Molenaar R.J., Sidana S., Radivoyevitch T., et al. Risk of Hematologic Malignancies After Radioiodine Treatment of Well-Differentiated Thyroid Cancer // *Journal of Clinical Oncology*. 2018. Vol. 36, N 18. P. 1831–1839. doi: 10.1200/JCO.2017.75.0232
- 106.** Signore A., Campagna G., Marinaccio J., et al. Analysis of Short-Term and Stable DNA Damage in Patients with Differentiated Thyroid Cancer Treated with 131I in Hypothyroidism or with Recombinant Human Thyroid-Stimulating Hormone for Remnant Ablation // *Journal of Nuclear Medicine*. 2022. Vol. 63, N 10. P. 1515–1522. doi: 10.2967/jnumed.121.263442
- 107.** Sohn S.Y., Choi J.Y., Jang H.W., et al. Association between excessive urinary iodine excretion and failure of radioactive iodine thyroid ablation in patients with papillary thyroid cancer // *Thyroid*. 2013. Vol. 23, N 6. P. 741–747. doi: 10.1089/thy.2012.0136
- 108.** Lakshmanan M., Schaffer A., Robbins J., Reynolds J., Norton J. A simplified low iodine diet in I-131 scanning and therapy of thyroid cancer // *Clinical Nuclear Medicine*. 1988. Vol. 13, N 12. P. 866–868. doi: 10.1097/00003072-198812000-00003
- 109.** Maxon H.R., Thomas S.R., Boehringer A., et al. Low iodine diet in I-131 ablation of thyroid remnants // *Clinical Nuclear Medicine*. 1983. Vol. 8, N 3. P. 123–126. doi: 10.1097/00003072-198303000-00006
- 110.** Tala Jury H.P., Castagna M.G., Fioravanti C., et al. Lack of association between urinary iodine excretion and successful thyroid ablation in thyroid cancer patients // *Journal of Clinical Endocrinology and Metabolism*. 2010. Vol. 95, N 1. P. 230–237. doi: 10.1210/jc.2009-1624
- 111.** Lee M., Lee Y.K., Jeon T.J., et al. Low iodine diet for one week is sufficient for adequate preparation of high dose radioactive iodine ablation therapy of differentiated thyroid cancer patients in iodine-rich areas // *Thyroid*. 2014. Vol. 24, N 8. P. 1289–1296. doi: 10.1089/thy.2013.0695
- 112.** Tobey A.E., Hongxiu L., Auh S., et al. Urine iodine excretion exceeding 250 ug/24h is associated with higher likelihood of progression in intermediate and high-risk thyroid cancer patients treated with radioactive iodine [abstract] // *Thyroid*. 2018. Vol. 28, Suppl. 1. P. A40–A41
- 113.** Pluijmen M.J., Eustatia-Rutten C., Goslings B.M., et al. Effects of low-iodide diet on postsurgical radioiodide ablation therapy in patients with differentiated thyroid carcinoma // *Clinical Endocrinology*. 2003. Vol. 58, N 4. P. 428–435. doi: 10.1046/j.1365-2265.2003.01735.x
- 114.** Morris L.F., Wilder M.S., Waxman A.D., Braunstein G.D. Reevaluation of the impact of a stringent low-iodine diet on ablation rates in radioiodine treatment of thyroid carcinoma // *Thyroid*. 2001. Vol. 11, N 8. P. 749–755. doi: 10.1089/10507250152484583
- 115.** Yoo I.D.K.S., Kim S.H., Seo Y.Y., et al. The success rate of initial (131) i ablation in differentiated thyroid cancer: comparison between less strict and very strict low iodine diets // *Nuclear Medicine and Molecular Imaging*. 2012. Vol. 46, N 1. P. 34–40. doi: 10.1007/s13139-011-0111-y
- 116.** Ito S., Iwano S., Kato K., Naganawa S. Predictive factors for the outcomes of initial I-131 low-dose ablation therapy to Japanese patients with differentiated thyroid cancer. journal article // *Annals of Nuclear Medicine*. 2018. Vol. 32, N 6. P. 418–424. doi: 10.1007/s12149-018-1261-0
- 117.** Lim C.Y., Kim J.Y., Yoon M.J., et al. Effect of a low iodine diet vs. restricted iodine diet on postsurgical preparation for radioiodine ablation therapy in thyroid carcinoma patients // *Yonsei Medical Journal*. 2015. Vol. 56, N 4. P. 1021–1027. doi: 10.3349/ymj.2015.56.4.1021
- 118.** Kim H.K., Lee S.Y., Lee J.I., et al. Daily urine iodine excretion while consuming a low-iodine diet in preparation for radioactive iodine therapy in a high iodine intake area // *Clinical Endocrinology*. 2011. Vol. 75, N 6. P. 851–856. doi: 10.1111/j.1365-2265.2011.04157.x
- 119.** Tomoda C., Uruno T., Takamura Y., et al. Reevaluation of stringent low iodine diet in outpatient preparation for radioiodine examination and therapy // *Endocrine Journal*. 2005. Vol. 52, N 2. P. 237–240. doi: 10.1507/endocrj.52.237
- 120.** Sohaimi W.F., Abdul Manap M., Kasilingam L., et al. Randomised controlled trial of one-week strict low-iodine diet versus one-week non-specified low iodine diet in differentiated thyroid carcinoma // *Iranian Journal of Nuclear Medicine*. 2019. Vol. 27, N 2. P. 99–105.
- 121.** Dekker B.L., Links M.H., Muller Kobold A.C., et al. Low-iodine Diet of 4 Days Is Sufficient Preparation for 131I Therapy in Differentiated Thyroid Cancer Patients // *The Journal of Clinical Endocrinology & Metabolism*. 2022. Vol. 107, N 2. P. e604–e611. doi: 10.1210/clinem/dgab691
- 122.** Padovani R.P., Maciel R.M., Kasamatsu T.S., et al. Assessment of the Effect of Two Distinct Restricted Iodine

Diet Durations on Urinary Iodine Levels (Collected over 24 h or as a Single-Spot Urinary Sample) and Na (+)/I (-) Symporter Expression // *European Thyroid Journal*. 2015. Vol. 4, N 2. P. 99–105. doi: 10.1159/000433426

123. Park J.T., Hennessey J.V. Two-week low iodine diet is necessary for adequate outpatient preparation for radioiodine rhTSH

scanning in patients taking levothyroxine // *Thyroid*. 2004. Vol. 14, N 1. P. 57–63. doi: 10.1089/105072504322783858

124. Dekker B.L., Touw D.J., van der Horst-Schrivers A.N.A., et al. Use of Salivary Iodine Concentrations to Estimate the Iodine Status of Adults in Clinical Practice // *The Journal of Nutrition*. 2021. Vol. 151, N 12. P. 3671–3677. doi: 10.1093/jn/nxab303

AUTHORS' INFO

* **Maria V. Reinberg**, MD;

address: 11 Dm. Ulyanova street, 115478, Moscow, Russia;

ORCID: 0009-0002-1632-2197;

e-mail: mrezerford12@gmail.com

Konstantin Yu. Slashchuk, MD, Cand. Sci. (Med.);

ORCID: 0000-0002-3220-2438;

eLibrary SPIN: 3079-8033;

e-mail: slashuk911@gmail.com

Alexey A. Trukhin, Cand. Sci. (Engin.);

ORCID: 0000-0001-5592-4727;

eLibrary SPIN: 4398-9536;

e-mail: Alexey.trukhin12@gmail.com

Karina I. Avramova, MD;

ORCID: 0009-0008-4970-8911;

eLibrary SPIN: 4330-0263;

e-mail: dravramovak@gmail.com

Marina S. Sheremeta, MD, Cand. Sci. (Med.);

ORCID: 0000-0003-3785-0335;

eLibrary SPIN: 7845-2194;

e-mail: marina888@yandex.ru

ОБ АВТОРАХ

* **Рейнберг Мария Валентиновна**;

адрес: Россия, Москва, 115478, ул. Дм. Ульянова, д.11;

ORCID: 0009-0002-1632-2197;

e-mail: mrezerford12@gmail.com

Слащук Константин Юрьевич, канд. мед. наук;

ORCID: 0000-0002-3220-2438;

eLibrary SPIN: 3079-8033;

e-mail: slashuk911@gmail.com

Трухин Алексей Андреевич, канд. техн. наук,

ORCID: 0000-0001-5592-4727;

eLibrary SPIN: 4398-9536;

e-mail: Alexey.trukhin12@gmail.com

Аврамова Карина Игоревна;

ORCID: 0009-0008-4970-8911;

eLibrary SPIN: 4330-0263;

e-mail: dravramovak@gmail.com

Шеремета Марина Сергеевна, канд. мед. наук;

ORCID: 0000-0003-3785-0335;

eLibrary SPIN: 7845-2194;

e-mail: marina888@yandex.ru

* Corresponding author / Автор, ответственный за переписку

DOI: <https://doi.org/10.17816/DD623341>

Антропоморфные фантомы молочной железы для лучевой диагностики: научный обзор

Ю.А. Васильев, О.В. Омелянская, А.А. Насибуллина, Д.В. Леонов, Ю.В. Булгакова, Д.А. Ахмедзянова, Ю.Ф. Шумская, Р.В. Решетников

Научно-практический клинический центр диагностики и телемедицинских технологий, Москва, Российская Федерация

АННОТАЦИЯ

Фантомы молочной железы применяются для разработки, валидации и усовершенствования методов лучевой диагностики. В визуализации молочной железы антропоморфные модели используются для валидации, оценки и оптимизации новых методов диагностики заболеваний молочной железы, а также для контроля качества диагностических систем, совершенствования клинических протоколов и алгоритмов реконструкции изображений. Ключевым требованием к фантомам для решения этих задач является реалистичная имитация органа.

В обзоре описаны существующие на настоящий момент варианты фантомов молочной железы для лучевой диагностики и процесса их создания.

Поиск литературы, соответствующей теме обзора, производился в базах данных PubMed, eLibrary, а также в поисковой системе Google Scholar. Всего в обзор включено 72 статьи и 13 тезисов материалов конференций.

Все виды фантомов молочной железы можно разделить на два вида: вычислительные и физические. Вычислительные, в свою очередь, подразделяются на группы в зависимости от типа первичных данных: на основе математических моделей, из образцов тканей, с использованием изображений медицинской визуализации молочной железы пациента. Физические фантомы классифицируются в зависимости от способа изготовления: литья, 3D-печати или послойного формирования с использованием контрастных веществ. Основными преимуществами вычислительных фантомов являются универсальность, эффективность, точность и безопасность, а также возможность генерировать большие объёмы виртуальных данных. Физические фантомы позволяют получать наиболее реалистичные диагностические изображения без участия пациентов и проводить неограниченное число лучевых исследований.

Ключевые слова: молочная железа; 3D-печать; фантомы; фантомы для лучевой диагностики; лучевая диагностика; научный обзор.

Как цитировать:

Васильев Ю.А., Омелянская О.В., Насибуллина А.А., Леонов Д.В., Булгакова Ю.В., Ахмедзянова Д.А., Шумская Ю.Ф., Решетников Р.В. Антропоморфные фантомы молочной железы для лучевой диагностики: научный обзор // Digital Diagnostics. 2023. Т. 4, № 4. С. 569–592. DOI: <https://doi.org/10.17816/DD623341>

DOI: <https://doi.org/10.17816/DD623341>

Anthropomorphic breast phantoms for radiology imaging: a review

Yuriy A. Vasilev, Olga V. Omelyanskaya, Anastasia A. Nasibullina, Denis V. Leonov, Julia V. Bulgakova, Dina A. Akhmedzyanova, Yuliya F. Shumskaya, Roman V. Reshetnikov

Research and Practical Clinical Center for Diagnostics and Telemedicine Technologies, Moscow, Russian Federation

ABSTRACT

Phantoms are used to validate diagnostic imaging methods or improve the skills of medical professionals. For instance, they allow conducting an unlimited number of imaging studies during medical training, assessing image quality, optimizing radiation dose, and testing novel techniques and equipment. Researchers in breast imaging use anthropomorphic models to validate, assess, and optimize new methods for diagnosing breast diseases. Such models also facilitate control over the quality of diagnostic systems, help optimize clinical protocols, and improve image reconstruction algorithms. Realistic simulation of the breast tissue is essential to address the challenges of advancing X-ray mammary gland studies. The review aimed to describe phantoms currently available for diagnostic imaging and the way they were fabricated. In this literature review, PubMed, eLIBRARY, and Google Scholar databases were screened for relevant articles. Thus, 72 articles and 13 conference papers were included. The study two major types of breast phantoms: computational and physical. Specifically, computational phantoms are classified into subgroups depending on the data they use. These include mathematical models, tissue samples, and medical images of the breast. The classification of the physical phantoms is based on their manufacturing process: casting silicone-like substances, 3D printing with resins and plastics, or printing on paper using X-ray contrast ink. Computational phantoms are generally advantageous with respect to versatility, efficiency, precision, and safety and allow the generation of large amounts of virtual data. Physical phantoms provide the most realistic diagnostic images without the need for a patient and allow performing an unlimited number of radiological studies.

Keywords: breast, 3D printing, phantoms, imaging phantoms, diagnostic radiology, literature review.

To cite this article:

Vasilev YuA, Omelyanskaya OV, Nasibullina AA, Leonov DV, Bulgakova JV, Akhmedzyanova DA, Shumskaya YuF, Reshetnikov RV. Anthropomorphic breast phantoms for radiology imaging: a review. *Digital Diagnostics*. 2023;4(4):569–592. DOI: <https://doi.org/10.17816/DD623341>

Received: 14.11.2023

Accepted: 27.11.2023

Published online: 06.12.2023

DOI: <https://doi.org/10.17816/DD623341>

用于放射诊断的仿真乳房模型：科学综述

Yuriy A. Vasilev, Olga V. Omelyanskaya, Anastasia A. Nasibullina, Denis V. Leonov,
Julia V. Bulgakova, Dina A. Akhmedzyanova, Yuliya F. Shumskaya, Roman V. Reshetnikov

Research and Practical Clinical Center for Diagnostics and Telemedicine Technologies, Moscow, Russian Federation

简评

乳房模型被用于放射诊断方法的开发、验证和改进。在乳腺成像中，仿真模型被用于验证、评估和优化诊断乳腺疾病的新方法。仿真模型还被用于诊断系统的质量控制、临床协议和图像重建算法的改进。为了解决这些问题，对仿真模型的关键要求是它作为逼真的器官模拟器。

本综述旨在介绍目前可用于放射诊断的乳腺模型变体，并描述其制作过程。

我们在PubMed、eLIBRARY和Google Scholar数据库中搜索了与本综述主题有关的文献。共有72篇文章和13份会议纪要被纳入该综述。

所有类型的乳房模型可分为两类：计算模型和物理模型。计算模型又根据原始数据的类型分为几组：基于数学模型、来自组织样本、使用患者乳房的医学成像图像。物理模型则根据制作方法分为几组：铸造、3D打印或使用造影剂的逐层制作。计算模型的主要优势在于多功能性、高效性、准确性和安全性，以及生成大量虚拟数据的能力。物理模型可提供最逼真的诊断图像，无需患者参与，并对其可进行无限量的放射检查。

关键词： 乳腺；3D打印；模型；用于放射诊断的模型；放射诊断；文献综述。

引用本文：

Vasilev YuA, Omelyanskaya OV, Nasibullina AA, Leonov DV, Bulgakova JV, Akhmedzyanova DA, Shumskaya YuF, Reshetnikov RV. 用于放射诊断的仿真乳房模型：科学综述. *Digital Diagnostics*. 2023;4(4):569–592. DOI: <https://doi.org/10.17816/DD623341>

收到: 14.11.2023

接受: 27.11.2023

发布日期: 06.12.2023

INTRODUCTION

Human phantoms are a key solution to many problematic aspects of medical imaging modalities such as ultrasonography [1], magnetic resonance imaging (MRI) [2], and computed tomography (CT) [3]. Breast phantoms (BPs) are important in the evaluation of X-ray imaging systems. They serve as a surrogate for the human body in cases where it is impractical or necessary to expose the patient to radiation. BPs are created for X-ray diagnostics to develop, optimize, and provide quality control for existing and developing imaging systems, such as full-field digital mammography (MMG), digital tomosynthesis, and CT.

Anthropomorphic BPs for X-ray diagnostics are both computational (mathematical) and physical breast models. Mathematical models describe organ structures using formulas and calculations. One of the limitations of this approach is its inability to cover the full range of anatomical variations in the breast structure and ensure its anatomical and radiological reliability. To overcome these limitations, anthropomorphic phantoms with natural distribution of different tissues were created based on segmented breast CT datasets, which guarantees a high degree of realism. Attempts to create such anthropomorphic computational phantoms have been made since the 1960s [4]. However, reliable anthropomorphic physical phantoms have only recently emerged with the advent of three-dimensional (3D)-printing technologies. The main methods for creating physical anthropomorphic MF models include casting, 3D printing, and paper-based approaches. Among these, 3D-printing technologies offer an excellent opportunity to create realistic models using materials with radiographic properties similar to those of breast tissue.

With the wider clinical use of modern quasi-3D and 3D imaging systems such as tomosynthesis and CT, physical phantoms with realistic patient anatomy are greatly needed to fully represent and evaluate the 3D behavior of such systems. In addition, considering the active and successful implementation of artificial intelligence (AI) systems in MMG analysis [5], phantoms will standardize radiographic examinations and help improve AI algorithms.

Search Methodology

PubMed and eLibrary were searched for related articles. The search terms used were selected to best reflect keywords and subject headings. PubMed search was performed using the following queries: “anthropomorphic AND breast* AND (phantom* OR phantoms, imaging [mh] OR (phantoms AND imaging) OR model*) AND (diagnostic X-ray OR radiography OR mammography OR tomography).” The eLibrary search was performed using “phantom” and “breast” keywords. Google Scholar was also used for conference proceedings search.

RESULTS

The search identified 335 papers; however, 263 papers did not meet the review criteria. The review included 72 papers and 13 conference abstracts.

Breast Anatomy

Accurate modeling of the breast using radiographic imaging requires detailed knowledge of its anatomical and radiological characteristics. The mammary gland, or the breast, is a modified cutaneous sweat gland consisting of tubuloalveolar glandular tissue, connective tissue, and other elements such as fat tissue, blood and lymphatic vessels, and nerve fibers. Most of the volume is occupied by glandular and fat tissues. Each breast is located on the fascia covering the pectoralis major muscle at the level of the III–VI ribs between the anterior axillary and parasternal lines of the corresponding side. The mammary gland is also surrounded by the anterior and posterior layers of the superficial fascia of the breast, which together form a capsule for the gland. The superficial fascia attaches to the clavicle and forms the suspensory ligament. Fibrocollagenous septa (Cooper’s ligaments) extend from the posterior layer deep into the mammary gland and from the anterior layer to the skin.

The breast comprises 15–20 lobules, which are arranged radially around the nipple and surrounded by loose connective and fatty tissue. Each lobule has its milk duct. In the subareolar region, the milk ducts widen to form lactiferous sinuses (ampullae). In these sinuses, the ducts of several lobules merge into larger ones, which exit independently into the nipple, forming separate holes on its surface. The diameter of the ducts up to the ampulla is approximately 1 mm, whereas the diameter of the main ducts varies from 2 to 4.5 mm. The total length of the ducts varies from 2 to 4.5 cm. A lobule with a diameter of 1–2 mm comprises ducts and alveoli that end in a common terminal duct. This structure is called the “terminal lobular duct unit.”

No clearly defined reference has been established for the radiographic appearance of the breast because the ratio of glandular to fatty tissue varies among women. Therefore, several classifications of mammographic density types have been developed, including Wolfe, BI-RADS, and Tabar. These classifications are shown in Table 1. BP modeling is aimed at certain categories according to the classification chosen by the researchers.

BI-RADS is the most widely used classification for describing radiographic breast density in clinical practice. The types of breast tissue structures are shown in Figure 1.

Mathematical models and diagnostic images of patients can be used to model the anatomical structures of the breast. Based on these data, three main approaches were used to create physical anthropomorphic phantoms:

- Casting methods

Table 1. Classifications of breast structure types

Type	Characteristics
<i>Wolfe</i>	
N1	The breast consists mainly of fat (N = normal); a low risk of breast cancer
P1	This pattern includes fat and linear densities (enlarged ducts) occupying no more than 25% of the breast; a low risk of breast cancer
P2	Linear densities (from enlarged ducts) occupying >25% of the breast. They are prominently in the upper outer quadrant but may be distributed throughout the breast (P = prominent ducts); a high risk of breast cancer
Dy	Dense breast (Dy = dysplasia); highest risk of breast cancer
Qdy	Quasi-dysplasia: this group consists of young women whose dense breasts have a somewhat spongy texture because of fatty infiltration
<i>BI-RADS</i>	
a	Almost entirely fat (<25% glandular density)
b	Scattered fibroglandular densities (25%–50% glandular density)
c	Heterogeneously dense (51%–75% glandular density)
d	Extremely dense (>75% glandular density)
<i>Tabar</i>	
I	Balanced proportion of all components of breast tissue with a slight predominance of fibrous tissue
II	Predominance of fat tissue (fat breast)
III	Predominance of fat tissue with retroareolar residual fibrous tissue
IV	Predominantly nodular density
V	Predominantly fibrous tissue (dense breast)

- Separate printing of various structures and assembling them into a complete phantom
- Printing the entire model

Computational 3D anthropomorphic models of the mammary glands

Anthropomorphic computational breast models provide anatomically reliable volumetric distribution of the radiographic absorption coefficients of different breast tissue types. Three types of approaches are available to such modeling:

1) Mathematical modeling

Phantoms based on mathematical models are designed to match certain physical or statistical properties of a human organ, such as radiographic density or statistical distribution patterns [6]. Several research groups have developed reliable model-based virtual BPs for use in projection and tomographic imaging [7–10]. An algorithm for generating this type of phantom is shown in Figure 2.

2) Tissue-based approach

These phantoms reproduce the fine-scale structure of breast tissue observed in abnormal specimens or super-resolution microtomography [11,12].

3) Approach based on the processing of patient tomograms

Such models are generated using two-dimensional (MMG) or three-dimensional (CT or MRI) images [13,14].

Mathematical breast models

This type of model is based on the modeling of the structural elements of the breast using mathematical methods. Such models comprehensively represent the shape of the organ, ductal system, Cooper’s ligaments, pectoralis major muscle, blood vessels, skin, DDFM pattern, and breast abnormalities. To generate a 3D anatomically realistic model of the breast, K. Bliznakova et al. [15] and P.R. Bakic et al. [16–18] used a combination of constructive solid geometry methods and voxel techniques.

Breast model from the University of Pennsylvania

In 2002, a research group from the University of Pennsylvania developed the first anthropomorphic computational BPs based on the modeling of two ellipsoidal regions of large-scale tissue elements: predominantly fat tissue and predominantly fibroglandular tissue [16,17]. These areas are mathematically modeled using realistically distributed medium-scale phantom elements, which include the membranes, lobules, and simulated milk ducts. The duct network model is generated using a branching matrix that describes the dichotomization of tree structures [18]. The reliability of the milk duct model was evaluated by comparison with ductography data. A compression model was also developed, which reliably represents breast deformation in the University of Pennsylvania model in 2D MMG and breast tomosynthesis. Further development of this phantom consisted of adding fine structures and

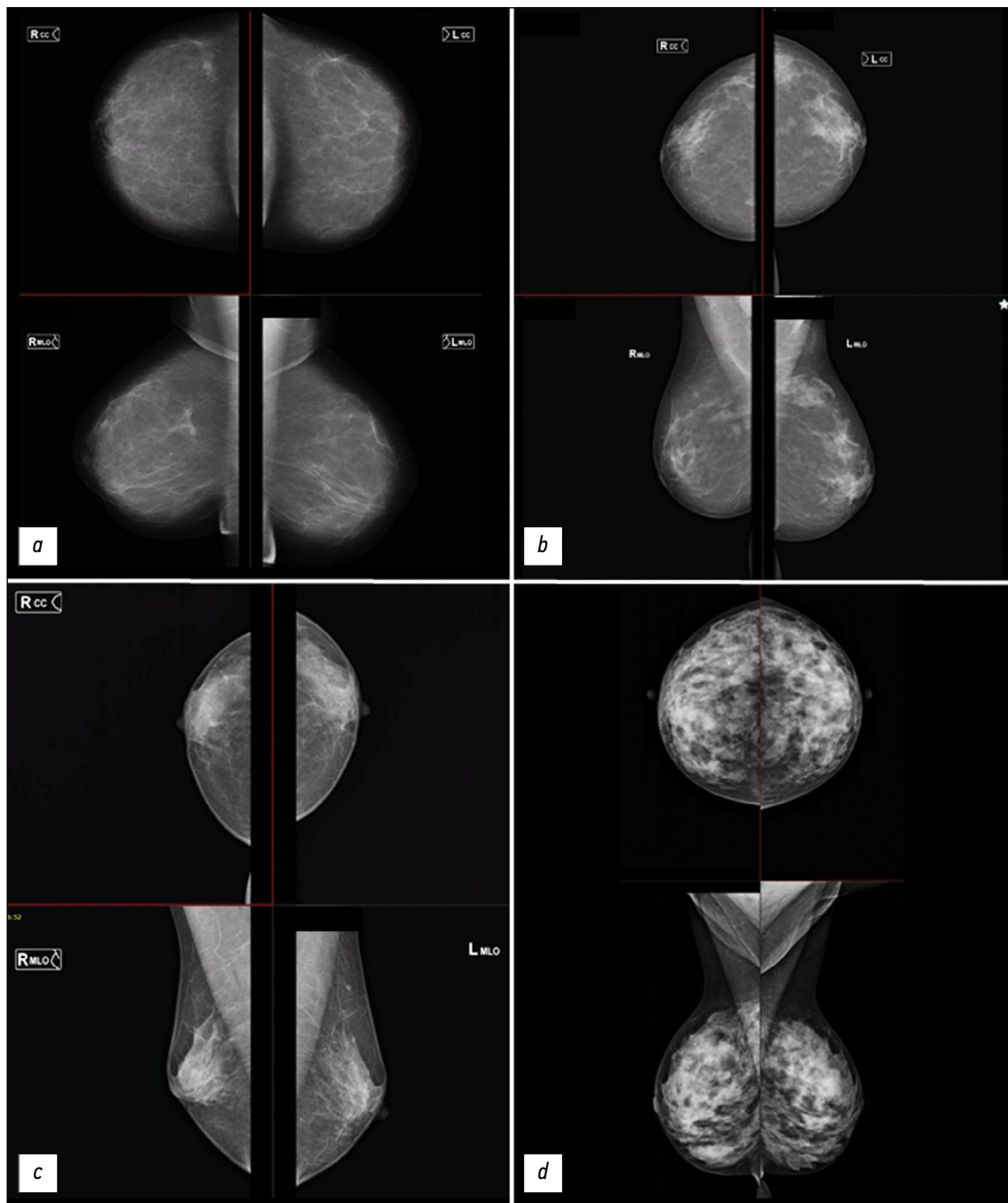


Fig. 1. Types of breast density according to the BI-RADS classification. For each image, the upper part is the craniocaudal projection, and the lower part is the mediolateral projection.

implementing an algorithm to rapidly generate high-resolution anthropomorphic phantoms with voxel sizes ranging from 25 to 1,000 μm^3 [19]. The result was an improved version of this digital phantom [12].

The proposed algorithms are based on the simplified assumption that each phantom voxel contains one tissue type. This simplification leads to the appearance of artifacts in the projection images near the boundaries between the areas of different materials, particularly at the skin-air interface. Several methods have been proposed to overcome these limitations. One of them is to model smaller voxels.

However, reducing the voxel size increases the phantom generation time and the workstation requirements to simulate the phantom. Another method considers the partial volume of various tissues in a voxel [20,21]. The linear radiographic attenuation coefficient at each voxel was calculated by combining attenuation coefficients proportional to the subvolume voxels occupied by different tissues.

Breast model by the University of Patras

A research group from the University of Patras developed an anthropomorphic model of the breast, which represents

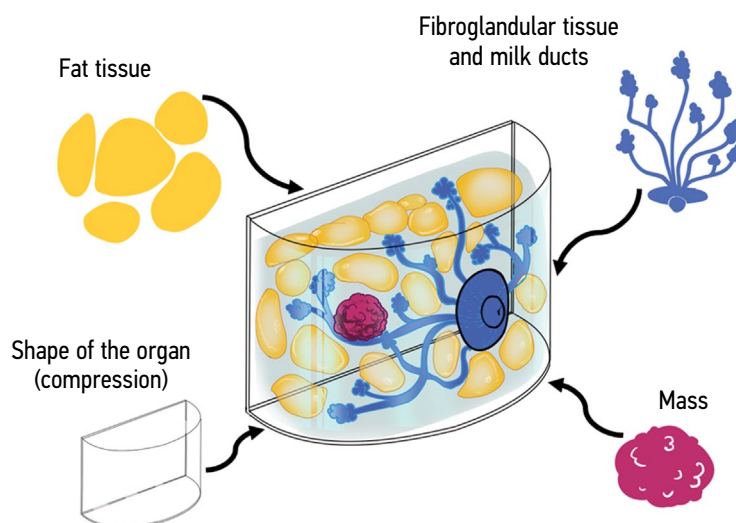


Fig. 2. An algorithm for generating a computational breast phantom.

a complex combination of anatomical shape, duct system, Cooper's ligaments, radiological tissue texture, and nodes [15]. The 3D texture simulates the presence of fatty, fibrous, and connective tissues and other tissue types that are not explicitly modeled. To obtain a realistic 3D MMG texture, a texturing algorithm based on random walk is used [10]. Cooper's ligaments are modeled as a set of thin ellipsoidal shells that appear at randomly selected points in the model. Fatty compartments are modeled by the volume of Cooper's ligaments. The pectoralis muscle is approximated as a conical object, and the nodes are modeled as round, ovoid, elongated, or irregular objects.

BPs by the United States Food and Drug Administration

Based on the above models, a research team from the United States Food and Drug Administration generated an improved, open-source, multimodal mathematical BP to be used by the scientific community [21]. Mammary glands are generated based on analytical formulas followed by voxel sampling. In this case, each voxel had an arbitrary size and consisted of one tissue type. A nipple and a 1-mm thick layer of skin are added to the front of the surface, and a layer of muscles supporting the breast is added to the back. In the inner surface, glandular sections are determined based on Voronoi segmentation. For each segmented gland compartment, a tree of ducts is grown using a random branching algorithm starting from the nipple. In the terminal branches of each "tree" of ducts, terminal lobular ducts are added. Initially, the internal part of the phantom was set as purely glandular tissue. To create subcutaneous and perilobular fat layers and some fat structures, random fat lobules should be inserted within the glandular areas. Each fat lobule is surrounded by a ligamentous structure [22]. At the final stage of phantom generation, additional structures such as blood vessels, pectoral muscles, and ligaments should be introduced.

OPTIMAM breast model

In parallel with the United States Food and Drug Administration, P. Elangovan et al. [9] presented a new method for generating quasirealistic voxel phantoms to simulate the compressed breast used in MMG and tomosynthesis. Anthropomorphic breast models were generated using a biomimetic technique with their features and structures extracted from the image planes of real breast images obtained using tomosynthesis. They are used to synthesize the 3D structure of the breast. The modeling process starts with the creation of a high-resolution blank breast model surrounded by a layer of skin. This template is populated with voxels corresponding to different tissues based on the structures extracted from the tomosynthesis images. The overall 3D shape is obtained from the tomosynthesis data using image thresholding. Then, a 1.5-mm thick layer of "skin" is added to the skin surfaces of the breast contour. Internal voxels are labeled as fat or glandular tissue.

A database of randomly selected fragments of glandular tissue was created to produce a 3D matrix of glandular tissue, which was placed in the fat tissue of the breast. The blood vessels and Cooper's ligaments are modeled as an extended 3D skeleton of the linear structures that are present in the patient's tomosynthesis images: 3–4 mm in diameter for the blood vessel network and 1–2 mm in diameter for the Cooper's ligament network.

Computational Breast Models Based on Medical Data

Several authors have attempted to create a more realistic tissue distribution in a breast model [20,23,24]. Three voxel-based breast models were generated using high-resolution segmented CT data of three compressed breasts (in three older women) [25]. These segmented breast models allowed a more realistic representation of glandular tissue and Monte Carlo calculations of the average radiation dose to

the breast during MMG and the simulation of various imaging techniques.

The development of a special breast CT system has advanced the creation of computational anthropomorphic BPs. This phantom was first developed in 2009 by CM Li et al. [14]. The key step was to develop a technique of processing breast CT scans and differentiating the breast tissue. The resulting simulated MMG image of the phantom was similar to a reliable MMG image of the breast tissue. This technique had some limitations because it did not allow for the reliable classification of small structures (Cooper's ligaments) that require higher resolution. To solve this problem, the authors proposed to express these structures mathematically and subsequently include them in the calculated breast volume.

Even though the technique by Li et al. guarantees a high degree of realism, it represents only one breast model and does not cover wide anatomical variations. To solve this problem, Hsu et al. [26,27] developed a computational technique to generate numerous anthropomorphic BPs [14]. This technique is based on morphing (a visual effect that sees one shape or object transform into another in a seamless transition) and deformation (significant distortion of shapes during digital image processing) and demonstrates the ability to create anthropomorphic BPs that are perceived as realistic by radiologists.

To enhance the development of CT-based breast models, accurate anatomical characterization of the breast using CT is required. Huang et al. [28] proposed and described in detail the anatomical features of the breast, including its shape, diameter, and length, proportion of glandular tissues in three areas of the breast, depending on the patient's age, and bra cup size. The study used the largest set of CT images of breasts available at that time (219 pieces). In addition, a research group at Duke University used them to create 224 virtual BPs [29,30]. We also developed an application to simulate different states of breast compression, allowing the use of phantoms for multimodal imaging.

Sarno et al. developed 88 computational BPs with realistic glandular tissue distribution to evaluate breast dose distribution and imaging data. These models contribute to the creation of an improved phantom that allows for a more accurate calculation of the average radiation dose to the gland during radiographic examinations [31] and optimizes tomosynthesis using virtual clinical trials.

Therefore, the main advantage of computational phantoms is their ability to generate potentially large amounts of data [21]; however, these phantoms are virtual, not physical. The quality of *in silico* studies depends not only on the characteristics of the virtual phantom but also on the accuracy of the simulated imaging system in representing the physical imaging modality. For example, with breast tomosynthesis or CT, virtual phantom scanning often requires detailed knowledge of the geometry of the diagnostic system and reconstruction algorithm, which is the property of the manufacturing company.

Physical anthropomorphic BPs

At the time of this review, 3D-printing technology was the most popular approach for creating physical models of breast cancer. 3D-printing technologies allow choosing printing methods and materials that resemble human tissue in density, composition, and radiographic properties. In the breast, such tissues include fat, glands, tumors, and skin.

The process of creating an anthropomorphic physical BP consists of two steps:

- 1) Creating a computational model of the breast using one of the methods discussed above

- 2) Using a computational model to produce a physical BP

Considerable efforts are being made to develop new materials because existing materials do not always have the required radiographic properties [32–34]. K. Bliznakova et al. conducted a comprehensive review of the materials used in the production of anthropomorphic models [35], and some of the main materials used to create BPs are presented in Table 2.

BPs made using casting technology

A CIRS BR3D phantom (CIRS Inc., Norfolk, USA) for MMG is produced in the form of D-shaped plates, which are connected into a single structure to form a one-piece phantom. Each plate consists of two tissue materials that simulate fat and glandular tissues in a 50:50 ratio (m/m). Two tissue-equivalent plastics are mixed to form a heterogeneous structure. Typically, several plates are produced, which can be rearranged in different orders and easily obtain different, but limited in number, variations of the underlying tissue. One of the plates contains a set of microcalcifications, fibrous tissue, and neoplasms. The phantom is used to evaluate image quality, breast tomosynthesis, and CT. The resulting images of structures on an MMG image have unclear boundaries but do not look as realistic as the patient's images. Small structures such as Cooper's ligament cannot be produced using this technology and therefore will not appear on radiographic images. In a recent study by Sage et al., the BR3D [43]-textured background was found to have high contrast and resulted in high-contrast artifacts throughout the phantom. In addition, tomosynthesis images clearly show the contours of the ring-shaped structures used to place inserts, and this phenomenon affects the results of measurements and image analysis.

An anthropomorphic BP for both X-ray and MRI was developed by Freed et al. [44] by mixing egg whites with melted refined lard and placing the resulting mixture in a breast-shaped jar. This phantom is a useful tool for quantifying image quality in 2D and 3D radiographic techniques. However, it does not allow the modeling of anatomical structures because the phantom represents them much larger than they are in the patient's body. In addition, no technique has been established for creating phantoms with sufficient glandular tissue content.

Table 2. Main materials used to produce breast phantoms for mammography.

Human tissue	Material	Density, g/cm ³
Fat tissue	Ultrahigh-molecular-weight polyethylene [36]	0.94
	Acrylonitrile butadiene styrene [32]	1.02
	PE-12 [37]	N/A
	Formlabs Clear Resin [38]	1.18
	QuickWater [33]	1.02
	Paraffin [32]	0.93
Glandular tissue	Polyvinyl alcohol (PVAL gel) [39]	1.19
	Water [40]	1.00
	Nylon [32]	1.11
	Flex polymer [32]	1.14
	TangoBlackPlus [33]	1.11
	VeroClear [33]	1.18
	VeroWhitePlus, TangoPlus	N/A
	Poly lactin alloyed with copper and water [41]	N/A
	Polyvinyl alcohol [42]	N/A
Formlabs gray resin [32]	1.175	
Tumor tissue	Polyethylene terephthalate [42]	N/A

Ruvio et al. [45] used bread molds to create multimodal BPs for radiography, MRI, and ultrasonography imaging. The manufacturing process included five stages using three breast molds: external (replicating the breast shape), skin, and internal fibroglandular. The external shape of the breast mold follows the shape of the human breast in the supine position according to MRI data collected from patients. The main material used in the production of the skin element is a polyvinyl alcohol cryogel. The fatty structure is represented by a mixture of water and beeswax, and the fibroglandular, tumor, and muscle components are represented by agar containing a mixture of liquid (water, glycerin, and benzalkonium chloride) and dry (agar, SiC, and Al₂O₃) components. The current limitation is related to the impossibility of compressing the phantom because the fat-simulating material is not susceptible and not elastic. In addition, this phantom can be stored for only 1 week because it is susceptible to bacterial damage and drying out. This results in insufficient contrast between the tumor and fibroglandular tissue. Despite the complexity of producing tissues simulating important imaging parameters across the three modalities, the study demonstrated high similarity between the reference and measured properties. This type of phantom is intended for use in multimodal cross-calibration and training when there are no living patients or cadaveric material.

BPs with integrated spherical elements

This is a special case of the approach discussed in the next subsection. Spherical elements of various sizes, made of tissue-equivalent material [46–48], are immersed into

the homogeneous underlying tissue. These phantoms are widely used to assess image quality and radiation dose measurements in MMG and optimize scanning procedures in new MMG techniques such as dual-energy MMG, dual-energy contrast-enhanced MMG, tomosynthesis, and CT. A research group from the Department of Radiology of the Catholic University of Leuven developed a BP consisting of two main parts: an acrylic semicylindrical container simulating a compressed breast shape with a thickness of 58 mm and equal volumes of acrylic spheres of six different diameters [49]. Alternatively, the space between the spheres can be filled with water, a material with radiographic properties similar to those of real breast tissue. This study used an MMG system with tomosynthesis capability. Although the image pattern obtained with these phantoms differs from the actual image of the breast, they are very simple to produce and allow for easy acquisition of different views of the underlying tissue. This physical phantom has air bubbles at the top because filling the phantom completely with water is difficult. This phantom can be improved using a computational model to optimize the phantom-filling options [50–52].

K. Bliznakova et al. [53–55] have described similar approaches with semicylindrical containers printed using photopolymer resin or nylon to be filled with spheres of photopolymer resin and paraffin or animal lard as fillers. One of the versions of this approach is a small BP with a half-cylindrical shape made of Formlabs white resin. This physical phantom contains 27 Formlabs gray resin spheres with a radius of 6–13 mm, with the addition of animal fat. The phantom was used to evaluate phase-contrast imaging of the

breast [54] and develop a synthetic observer model for the quality control of tomosynthesis systems [56].

Assembling BPs from separately printed elements

This approach requires the availability of digital models of the main breast tissues, including skin, glandular, and fat tissues, as well as various neoplasms and microcalcifications. These individual digital models are based on either mathematical calculations using special computer programs [15,57] or segmentation of medical images of patients [24]. Each simulated breast tissue was saved in a separate file and then prepared for 3D printing. An example of this approach is the phantom developed by NT Dukov et al., with stereolithography used to print the external shape, network of milk ducts and neoplasms, and FDM printing using ABS filaments for fat compartments [37,53]. The selection of these printed materials is based on extensive experimental research [32,34]. The phantom is filled with water. To simulate microcalcifications, the authors used eggshells crushed into fine powder. In this case, the breast was not visualized. Further research is required to create new 3D printing materials that can simulate the radiographic properties of all types of breast tissue.

In 2016, a new version of the phantom was created with spherical insert elements [6]. Models of manually segmented breast fat compartments derived from CT images of a mastectomy specimen [22] were printed on a stereolithography 3D printer using Formlabs clear resin. Then, they were placed in a semicylindrical 48-mm-thick container filled with water, and an MMG image was obtained using a Siemens Mammomat (Siemens Healthineers, Germany). As a result, the experimental images were better than the original model; however, they were very different from the MMG images taken from the patients.

Further improvements to the compartment phantom are aimed at better similarity with patient data. This can be achieved using a less dense printing material to increase the contrast of the compartments, using smaller compartments by reducing their scale, and refining the method of segmenting the compartments. Recently, a research group from the University of Vienna developed another version of a spherical phantom consisting of VeroClear spheres with paraffin oil as a filler [58].

Printing a one-piece BP

Single media printing

The UPenn physical BP [59] is based on the mathematical model of the breast developed by the University of Pennsylvania as described above [16-18]. This technology involves the initial segmentation of digital phantom voxels into two components: fibroglandular and fat tissues. The first one was produced using a PolyJet Eden500V printer (Stratasys, USA) using tissue-equivalent material with 50% glandular tissue content (FC-720 photopolymer). Printing is performed in layers to maintain access to empty spaces,

which are then filled with fat tissue equivalent. Slices are printed at 60- μ m voxel resolution. The plates are then joined together to create the final anthropomorphic phantom. The initial experimental evaluation of MMG and tomosynthesis images of this physical phantom shows its potential for use in both qualitative and quantitative evaluations of the performance of 2D and 3D breast radiography systems. MMG images obtained using this phantom are visually similar to clinical images. Some limitations of this technology are related to the unclear boundaries of the structures, presence of residual air bubbles that are visible on radiographs, long manufacturing time, and high production costs.

Mainprize et al. [40,60] used a similar approach to create a two-component full-size physical BP. A voxel-based digital phantom [61] is divided into four plates to accommodate different inserts at different heights. In each plate, the fibroglandular component is removed, leaving only the fatty component. The resulting fat layer was printed using a selective laser sintering printer with a 100- μ m resolution from polyamide-12. The phantom showed high similarity with data on the excess entropy parameter obtained on clinical full-fledged digital MMG.

CT and MRI scans of the breasts of individual patients are used as the basis for generating a two-chamber anthropomorphic BP proposed by Prionas et al. [62]. The glandular part consists of water, and the fatty part is made of polyethylene. 3D images are initially obtained using a special CT scan of the breast, noise is then removed, and tissue is segmented into fatty and glandular parts. The production process differs from that described above. Phantoms are produced using a numerically controlled water jet machine. A stack of breast segments was made from a 1.59-mm-thick ultrahigh-molecular-weight polyethylene sheet using a water jet machine, with the centerline of the tool path determined along the edges of the tissue structure. An outer container is molded around the thermoplastic BP, and its thickness approximately corresponds to the thickness of the skin. A container with a stack of breast segments is filled with water so that the air spaces in the phantom, which represent a glandular tissue compartment, are filled with water.

Large areas of glandular tissue in this phantom closely correspond to the original patient images. The advantage of the model is its modular design, which allows the implementation of additional objects into any glandular tissue compartment. The main limitations are related to both the technology and material used: the thickness of the polyethylene mass and the gaps between the produced breast segments resulted in the phantom being 2.6 cm longer than the patient's original breast. The characteristics of the material limit the use of the phantom in radiographic techniques where breast compression is not performed. Other minor problems are related to the presence of air bubbles in the glandular tissue, which can be removed using more complex degassing techniques during phantom assembly. Another minor concern is the waterjet cutting process, which

can also result in a reduction in the outer fat contour and an expansion of the glandular tissue contour.

2D MMG images of the patient are a key source of information in the technique of printing physical anthropomorphic BPs, as proposed and implemented by two research groups [63,64] in 2018 and 2019. A Badal et al. [63] developed an easily reproducible technique for producing anthropomorphic breast cancer models based on 2D MMG images. To produce breast objects, an Objet260 Connex3 inkjet printer (Stratasys, USA) with VeroMagenta and VeroCyan printing materials was used. The choice of this printing technology is well justified by extensive experimental data using three printers with different technologies: stereolithography, FDM modeling, and inkjet printing [65].

The key element of this approach is the mammorelocator script in the Python programming language, which calculates the thickness of the printed materials depending on the gray level of each pixel in the image and the differences in X-ray absorption between breast tissue and 3D-printing materials. Each pixel of the image is converted by the script into a column of the appropriate height.

The model was printed in 10 h, and it weighed 750 g. Currently, it is validated to correctly reproduce the radiographic properties of the breast during MMG. A study of the similarity between the original and phantom MMG showed that the anatomical features were reproduced with good accuracy. The main limitation is related to the resolution of the resulting phantom. Although the patient's initial MMG resolution is 100 μm , the 3D printer was unable to accurately reproduce the details of clinical MMG <300 μm . The authors propose using this technology to create collections of representative patient models that can be used to assess the effect of anatomical variability of the breast on the reliability of the diagnostic system.

In the study by Schophoven et al. [64], an MMG image of the breast compressed to 32 mm was used. A key challenge was to determine the pixel intensities of raw images for different thicknesses of the printed material (polypropylene) for a diverse range of clinical images. This is achieved by scanning printed plates of various thicknesses (up to 40 mm) using an MMG system. The corresponding attenuation at the pixel position of the clinical image was modeled by the height difference of the printing material, resulting in a relief-like structure on the phantom.

The phantom printing time was approximately 11 h using 791 g of RGD450 material and 31 g of auxiliary material. The described approach makes it possible to create anthropomorphic phantoms that realistically simulate the anatomy and density characteristics of the breast tissue. These phantoms can be used to solve various problems of quality control and system optimization, as well as for educational and scientific purposes. The main current limitations are related to the slightly reduced resolution of fine details compared with the original clinical image. This is due to the selected printer and material combination (PolyJet printer

combined with polypropylene print material), which limits the size of the output structures to approximately 200 μm . The structures are located on the top of the phantoms; therefore, they are placed higher above the detector than the structures in the patient's breast. This can lead to increased sharpness in MMG images of denser breast tissue because of geometric magnification.

Microcalcification accumulations in this phantom were simulated using a 3D-printed base plate with a diameter of 4 mm with movable inserts and crushed eggshells [38]. The base and inserts were printed using an Objet30 Pro PolyJet 3D printer and VeroClear RGD810 material (Stratasys, USA). The base plate contained three round cavities with a diameter of 60 mm, into which rings numbered "1" to "3" were placed separately. The first ring, the "lesion ring," contains three round 10-mm cavities with corresponding covers, into which the simulated microcalcifications are placed. The other two rings are modeled as solid and do not contain any structures. All three rings have the same dimensions, which ensures their interchangeability and ability to change the position of the lesions relative to the anthropomorphic phantom. Different accumulations of microcalcifications were modeled using different amounts and sizes of eggshells.

The advantage of this approach is the modular design to integrate additional plates and rings easily and cost-effectively with different damage depending on the purpose. Phantoms made using this technology are intended for use in 2D MMG. For 3D breast imaging, physical phantoms must simulate the spatial distribution of different breast tissues in three dimensions. This can be achieved using one of the approaches discussed below.

In 2018, Okkalidis et al. [66] proposed a new technique for simultaneous printing of BPs directly from patient CT data using FDM modeling technology by changing the filling density of a homogeneous template. This template is used to accurately simulate the internal structure of the modeled 3D object. The thickest parts of the object are printed at a maximum fill density of 100%, whereas softer, lighter fabrics are printed at a lower density. This allows different types of tissue to be realistically created, considering radiological features. The method is based on reading Hounsfield units from each voxel and using these data to adjust the extrusion speed of the polylactic acid filament to obtain the required amount of extruded filament. This method was used to print an anthropomorphic BP directly using CT data [67]. The first evaluation of the phantom on a conventional CT scanner showed visual similarities between the original CT images of the patient and the phantom, which motivated the team to develop a special phantom for CT and create a future experimental setup for precision CT dosimetry. The main limitations are the long printing time (several days) and visibility of the printed pattern because of the FDM modeling technology used in the study.

Printing using two or more materials

To create ideal anthropomorphic MF phantoms, the use of different printed materials is optimal. A major step toward the realization of this goal was made in 2015 by N. Kiarashi et al. [68]. They managed to produce an anthropomorphic phantom of a compressed breast by 3D printing using two materials in parallel [26,69]. Two anthropomorphic breast models were printed using an Objet500 Connex 3D printer. The first phantom, called Doublet, was printed using two materials simultaneously, simulating glandular and fat tissues. TangoGray and VeroWhite materials were used to print the fibroglandular component. A mixture of butter and lard in a 1:1 ratio, beeswax, resin, and olive oil were studied as filler materials approaching the radiographic density of fat tissue. The resin method was repeated several times using different filling techniques, which always resulted in the presence of some unwanted air bubbles.

Physical phantoms provide a realistic radiographic view of breast anatomy in 2D and 3D images. The description of MMG physical phantoms corresponds to real human MMGs [70,71]. The disadvantages of phantoms are related to the limited dynamic range and contrast caused by the lack of suitable printing materials. This problem can be solved with the advent of new materials. Despite its limitations, the Doublet phantom has a key advantage: it has an all-in-one design, where the phantom (whole or partial) can be fabricated in one run.

AH Rossman et al. [72] reported the further development of the above-described approach to printing anthropomorphic breast models to simulate the patient's anatomy to evaluate the effectiveness of clinical MMG and digital breast tomosynthesis. They created a modular phantom with an anthropomorphic region to improve the detection of lesions and calcifications and a homogeneous region to evaluate standard quality control parameters. VeroPureWhite and a special tungsten-doped Jf flexible resin were used for fibroglandular tissue printing, and TangoPlus material and a third-party Jf flexible resin without an alloy component were used for low-density adipose tissue imaging. The design allows the addition of masses, iodized inclusions, and calcifications. One of the current limitations of this phantom is its inability to achieve BI-RADS breast radiographic density <36%. The image sensitivity depends on the radiological density: the higher the density, the lower the sensitivity of the MMG. Efforts are currently focused on achieving lower densities.

In 2019, a group from Naples [73] for the first time used an FDM 3D printer to produce physical phantoms of both uncompressed and compressed breast tissue, simulating the shape and the anatomical and radiological properties of real breast tissue. Digital phantoms based on breast CT data, and three printing materials were used to produce a physical anthropomorphic BP. Polyvinyl acetate was used to print the skin, and ABS plastic and nylon were used to print fat and glandular tissues, respectively. The skin was

printed separately because computational BPs are made of three materials, and the available Ultimaker 3 FDM printer (Ultimaker, Netherlands) prints objects from a maximum of two materials. Models have 100% filling density to minimize air gaps. The internal area of the breast can be presented in the form of either printed 10-mm-thick sections or a single block of two-component material. In addition, the authors developed an area in the printed slices to accommodate TLD chips for dosimetry purposes and special holes to accommodate printed lesions [73,74].

Paper on anthropomorphic breast models

A budget-friendly way to create BPs is to use office printing paper and a regular inkjet printer [75]. Some radiopaque agents, such as potassium iodide, titanium oxide, and radiocontrast, can be used as paint additives. Parchment paper has also been tested and found to have a radiographic density similar to that of fat tissue. A physical phantom was produced using a digital model presented by Graff et al. [21] in the form of sections by inkjet printing using parchment paper and radiopaque ink containing 33% or 25% iohexol (v/v). The advantage of this approach to anthropomorphic phantom production is their low cost because they are produced using commercially available inkjet printers, inexpensive ink enhancement components, and some inexpensive additional materials. The inkjet printer used in this study was a commercially available Epson Workforce 630 desktop inkjet printer (Epson, Japan). Reusable cartridges were used instead of the original manufacturer cartridges. Because the printer has multiple color cartridges, additional "tissues" can be printed in different colors. For example, to print leather, determine the appropriate concentration of iodine ink and place it in a separate cartridge. Various colors can then be applied to the skin and glandular tissue of the image and printed accordingly.

In summary, 3D printing technology is a well-studied technique for producing anthropomorphic BPs for use in radiography [68,72]. As its main advantage, 3D printing allows the design and printing of complex structures. However, several features of the 3D-printing process limit its versatility and feasibility [41,76,77]. Although 3D printing can create products from various plastics and silicones, not all of them are amenable to the temperatures required for 3D printing. In addition, 3D printers have small printing chambers, which limits the size of the resulting features. From a practical point of view, 3D printing is an expensive and slow process and therefore impractical for high-volume production. This slowness is attributed to the time required to create anthropomorphic phantoms using 3D printing, which depends on the complexity of the design (the desired number of organic tissues and elements that must be included in the phantom structure and the desired size). In addition, postprocessing of the 3D-printed phantoms is often needed to remove the support material from the structure and smoothen the surface to achieve the desired finish. This

may include water-abrasive treatment, exposure to chemical compounds, and air-heat drying. However, these options may damage the phantoms or introduce unwanted particles into the phantoms, which could affect radiography results.

An alternative approach to creating physical phantoms is to build the model layer by layer. Each layer is a planar section. With this approach, the complexity of creating a phantom is reduced to processing 2D layers. This approach was first introduced by Theodorakou et al. [78]. In this study, each phantom layer consisted of a substrate and a contrast material (dye) applied to the substrate using a standard inkjet printer. Since then, several research groups have improved this concept and reported successful implementations [79,80]. The process of layer-by-layer generation of a phantom allows the detailed formation of radiographic density properties by adding dyes to a 2D layer; however, it has some inherent limitations. These limitations are mainly due to the dependence on the use of contrast materials (dyes). In addition to the difficulties associated with optimizing dye chemistry, the contrast material is often in a liquid state, whereas the substrate is in a solid state. Applying a liquid contrast material to a solid substrate often results in the dye bleeding into or spreading across the substrate, making it difficult to control the positioning of the contrast material. In addition, this approach usually requires multilayer application of dyes onto a single substrate, which leads to multistage drying, which negatively affects production time. Finally, inkjet printer components often cannot withstand repeated ink injections. Inkjet printers use small nozzles to deliver ink. Some contrast materials, such as iodine-based compounds, which are widely used in radiography, often lead to nozzle clogging, requiring extensive maintenance to correct process failures.

Overview of commercial phantoms

BP for MMG and tomosynthesis developed by Erler Zimmer and marketed by GTSimulators

The creation of this commercial phantom consists of two stages. Initially, a calculation model of the breast is created using the C.G. Graff method [21]. The breast surface is formed by creating a shell in the form of a quadratic hemisphere, on which a layer of skin and a nipple are applied. The shape of the shell is determined using two parameters: those that determine the total breast volume and those that correct the surface curvature. Using the Voronoi segmentation technique, the interior of the shell is randomly divided into fat and glandular components, with each glandular component containing a network of ducts with terminal lobular units. The volume is then filled with additional elements of the breast, such as Cooper's ligaments, pectoral muscles, and blood vessels. In addition, a malignant neoplasm was modeled [81], which was subsequently introduced into the model.

To create a compressed breast, its volume was converted into a four-dimensional matrix, and each element of this matrix was given elastic properties determined by voxels

of the glandular or fat tissue located in the center of the element. The matrix was then formed using linear elastic finite-element modeling, and the breast was compressed in the craniocaudal direction to a thickness of 30 mm. However, no restrictions are set for creating a phantom with any breast thickness. Because the phantom model is based on analytical formulas, the compression thickness and voxel size are arbitrary. In this study, the breast model was discretized with an isotropic voxel size of 70 μm , which corresponds to the thickness of parchment paper. Depending on the size of the detector elements, undesirable effects caused by image sampling may occur at a given voxel size.

The second step is to create a physical phantom using inkjet printing. The printer used was a commercially available desktop inkjet printer (Epson Workforce 630). The print resolution was set to 363 dpi to provide a dot size of 70 μm and match the voxel size of the digital phantom (70 μm). In this procedure, special ink was applied to paper serving as background tissue to create density characteristics similar to glandular tissue. The ink was synthesized by mixing conventional pigment inks (InkThrift, Vermont PhotoInkjet, East Topsham Village, VT) with 350 mg/mL iohexol (Omnipaque, GE Healthcare, USA). One solution contains 67% ink and 33% iohexol, and the other contains 75% ink and 25% iohexol. To align the sheets, a specialized hole punch was created to make holes above the fiducial markers, and the sheets were then slid onto racks attached to a specialized backing plate to ensure that the sheets remained stationary once placed. Once the printed sheets were stacked on the base plate, a large, specialized compression paddle with post holes was placed on top of the stack to secure the sheets and ensure even compression.

To demonstrate the capabilities of the phantom, 3D lesions measuring approximately 5 mm and clusters containing microcalcifications were included in the phantom after the entire stack of sheets was manufactured. The 3D lesion was first introduced virtually and then placed into the physical phantom by reprinting the selected slices to which it extended and replacing them with nonlesional sheets at the appropriate locations. Microcalcifications were modeled by crushing eggshells and placing them at locations of varying gland densities on a physical BP. The number of elements in one cluster varied from 11 to >30. The diameter of the clusters ranged from 3.5 to 8 mm.

The materials used are similar to fat and glandular tissues in terms of radiographic density, and the production process is accurate and reproducible and can be used for both 2D and 3D imaging of the breast. In addition, this phantom is not limited to a single breast model, and any virtual model, once voxelized, can be printed using this unique approach.

This phantom has passed the validation process [75] and was used to study the capabilities of convolutional neural networks in the differential diagnosis of benign and malignant calcifications with conventional and dual-energy full-format digital MMG [84].

BR3D Breast Imaging Phantom

This phantom is described above in the section “Breast phantoms manufactured using casting technology” and is presented in Figure 3.

The model has been validated and used in many studies:

- Model-based optimization of digital breast tomosynthesis images for iterative reconstruction [83]. A new image reconstruction algorithm for digital breast tomosynthesis implemented using a total variation regularizer was tested on a Model 20 BR3D phantom. The results obtained confirm the ability of this algorithm to accurately image microcalcifications and breast formations.
- Evaluation of GPU acceleration of a model-based iterative method for digital breast tomosynthesis [84]. This study shows that parallel processing implemented on three different GPU boards allows for rapid iterative reconstruction of images obtained using digital breast tomosynthesis.

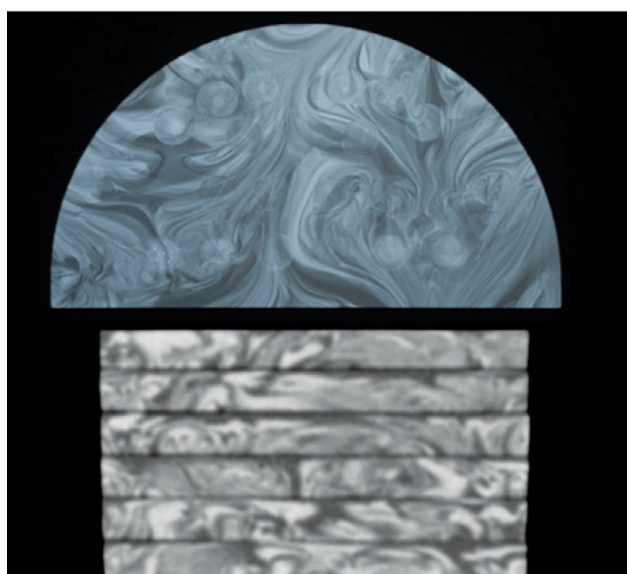


Fig. 3. BR3D Breast Imaging Phantom [82].

- Evaluation of a generative adversarial network for image quality improvement and radiation dose reduction in digital breast tomosynthesis [85]. An improvement in image quality was demonstrated during digital breast tomosynthesis under low radiation dose conditions when preprocessing the reconstruction using conditional generative adversarial networks [cGAN (pix2pix)].

Other BPs

Commercial BPs are available; however, data on their use in scientific research are unavailable. They include the following:

- Model 011A by CIRS is a tissue-equivalent anthropomorphic phantom designed to test the performance of all types of MMG systems. Models of calcifications, ducts, and neoplasms were built into the phantom as test objects. The sizes of the test objects vary, which allows testing the system at different levels of complexity. The resin material simulates the photon attenuation coefficients of various breast tissues. The average elemental composition of the simulated tissue was based on the individual elemental composition of fat and glandular tissues. This phantom has been used in some studies aimed at improving the accuracy of diagnostic methods [86–88]. The phantom is shown in Figure 4.
- BT-A01 by True Phantom Solutions (Canada) is a life-size image of a female torso, carefully crafted to reflect typical anatomical features. It is used for MMG, CT, and MRI. The target audience is healthcare professionals and students.
- Complex Breast Phantom SynAtomy 160,650 by SynDaver (USA) is an anthropomorphic breast phantom intended for training students and medical personnel. Modalities include ultrasonography, elastography, and MMG.

CONCLUSION

This study provides a brief historical overview of the development and use of anthropomorphic breast models for radiography. Different approaches to creating such phantoms have both advantages and limitations. Depending on the specific medical imaging task, one or the other approach may be preferred. Although computational anthropomorphic phantoms offer anatomical fidelity and relative ease of modeling, the creation of physical anthropomorphic models is challenging. Available technologies are costly and labor intensive, and the range of materials used is limited. Although much work has been done in this area, searching for new materials with X-ray absorption coefficients that correspond to different types of breast tissue is necessary. In addition, low-cost production technologies are also needed. This will improve and accelerate the production of anthropomorphic BPs for radiography.

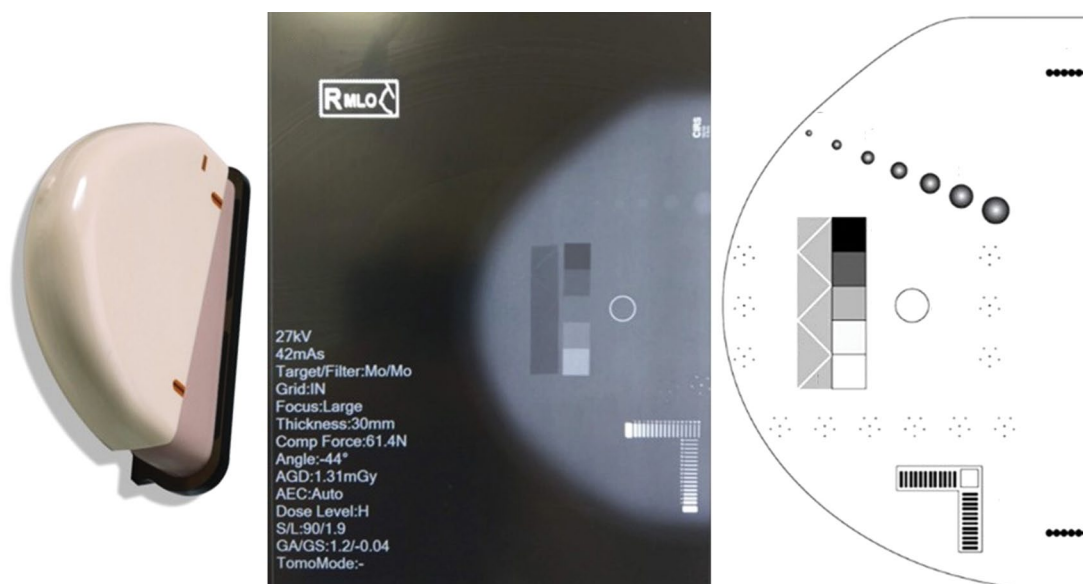


Fig. 4. 011A by CIRS.

ADDITIONAL INFORMATION

Funding source. This article was prepared by a group of authors as a part of the research and development effort titled “Scientific rationale for development and use of tissue-equivalent materials to design test objects for radiology” (USIS No.: № 123092000013-3) in accordance with the Order No. 1196 dated December 21, 2022 “On approval of state assignments funded by means of allocations from the budget of the city of Moscow to the state budgetary (autonomous) institutions subordinate to the Moscow Health Care Department, for 2023 and the planned period of 2024 and 2025” issued by the Moscow Health Care Department.

Competing interests. The authors declare that they have no competing interests.

REFERENCES

- Leonov D, Venidiktova D, Costa-Júnior JFS, et al. Development of an anatomical breast phantom from polyvinyl chloride plastisol with lesions of various shape, elasticity and echogenicity for teaching ultrasound examination. *International Journal of Computer Assisted Radiology and Surgery*. 2023. doi: 10.1007/s11548-023-02911-4
- Nuzov NB, Bhusal B, Henry KR, et al. True location of deep brain stimulation electrodes differs from what is seen on postoperative magnetic resonance images: An anthropomorphic phantom study. *Annual International Conference of the IEEE Engineering in Medicine and Biology Society. IEEE Engineering in Medicine and Biology Society*. 2022:1863–1866. doi: 10.1109/EMBC48229.2022.9871619
- Cannella R, Shahait M, Furlan AA, et al. Efficacy of single-source rapid kV-switching dual-energy CT for characterization of non-uric acid renal stones: a prospective ex vivo study using anthropomorphic phantom. *Abdominal Radiology*. 2020;45(4):1092–1099. doi: 10.1007/s00261-019-02164-3
- Kramer R, Zankl M, Williams G, Drexler G, et al. *The calculation of dose from external photon exposures using reference human phantoms and Monte Carlo methods*. 1982.
- Vasilev YA, Tyrov IA, Vladzmyrskyy AV, et al. Double-reading mammograms using artificial intelligence technologies: A new model of mass preventive examination organization. *Digital Diagnostics*. 2023;4(2):93–104. doi: 10.17816/DD321423
- Cockmartin L, Bosmans H, Marshall NW. Comparative power law analysis of structured breast phantom and patient images in digital mammography and breast tomosynthesis. *Medical physics*. 2013;40(8):081920. doi: 10.1118/1.4816309
- Ma AKW, Gunn S, Darambara DG. Introducing DeBRa: a detailed breast model for radiological studies. *Physics in medicine and biology*. 2009;54(14):4533–4545. doi: 10.1088/0031-9155/54/14/010
- Chen B, Shorey J, Saunders RS, et al. An Anthropomorphic Breast Model for Breast Imaging Simulation and Optimization. *Academic radiology*. 2011;18(5):536–546. doi: 10.1016/j.acra.2010.11.009

9. Elangovan P, Mackenzie A, Dance DR, et al. Design and validation of realistic breast models for use in multiple alternative forced choice virtual clinical trials. *Physics in medicine and biology*. 2017;62(7):2778–2794. doi: 10.1088/1361-6560/aa622c
10. Bliznakova K, Suryanarayanan S, Karellas A, Pallikarakis N. Evaluation of an improved algorithm for producing realistic 3D breast software phantoms: Application for mammography. *Medical Physics*. 2010;37(11):5604–5617. doi: 10.1118/1.3491812
11. O'Connor JM, Das M, Dider C, Mahd M, Glick SJ. Generation of voxelized breast phantoms from surgical mastectomy specimens. *Medical Physics*. 2013;40(4). doi: 10.1118/1.4795758
12. Lau BA, Reiser I, Nishikawa RM. A statistically defined anthropomorphic software breast phantom. *Medical Physics*. 2012;39(6):3375–3385. doi: 10.1118/1.4718576
13. Sarno A, Mettievier G, di Franco F, et al. Dataset of patient-derived digital breast phantoms for in silico studies in breast computed tomography, digital breast tomosynthesis, and digital mammography. *Medical Physics*. 2021;48(5):2682–2693. doi: 10.1002/mp.14826
14. Li CM, Segars WP, Tourassi GD, Boone JM, Dobbins JT. Methodology for generating a 3D computerized breast phantom from empirical data. *Medical Physics*. 2009;36(7):3122–3131. doi: 10.1118/1.3140588
15. Bliznakova K, Bliznakov Z, Bravou V, Kolitsi Z, Pallikarakis N. A three-dimensional breast software phantom for mammography simulation. *Physics in medicine and biology*. 2003;48(22):3699–3719. doi: 10.1088/0031-9155/48/22/006
16. Bakic PR, Albert M, Brzakovic D, Maidment AD. Mammogram synthesis using a 3D simulation. I. Breast tissue model and image acquisition simulation. *Medical Physics*. 2002;29(9):2131–2139. doi: 10.1118/1.1501143
17. Bakic PR, Albert M, Brzakovic D, Maidment AD. Mammogram synthesis using a 3D simulation. II. Evaluation of synthetic mammogram texture. *Medical Physics*. 2002;29(9):2140–2151. doi: 10.1118/1.1501144
18. Bakic PR, Albert M, Brzakovic D, Maidment AD. Mammogram synthesis using a three-dimensional simulation. III. Modeling and evaluation of the breast ductal network. *Medical Physics*. 2003;30(7):1914–1925. doi: 10.1118/1.1586453
19. Pokrajac DD, Maidment ADA, Bakic PR. Optimized generation of high resolution breast anthropomorphic software phantoms. *Medical Physics*. 2012;39(4):2290–2302. doi: 10.1118/1.3697523
20. Chen F, Pokrajac D, Shi X, et al. Partial volume simulation in software breast phantoms. *Medical Imaging 2012: Physics of Medical Imaging*. 2012. doi: 10.1117/12.912242
21. Graff CG. A new, open-source, multi-modality digital breast phantom. *Proceedings of the SPIE*. 2016;9783. doi: 10.1117/12.2216312
22. Ikejimba LC, Salad J, Graff CG, et al. A four-alternative forced choice (4AFC) methodology for evaluating microcalcification detection in clinical full-field digital mammography (FFDM) and digital breast tomosynthesis (DBT) systems using an inkjet-printed anthropomorphic phantom. *Medical Physics*. 2019;46(9):3883–3892. doi: 10.1002/mp.13629
23. Imran A-A-Z, Bakic PR, Pokrajac DD. Spatial distribution of adipose compartments size, shape and orientation in a CT breast image of a mastectomy specimen. *2015 IEEE Signal Processing in Medicine and Biology Symposium (SPMB)*. 2015:1–2. doi: 10.1109/SPMB.2015.7405460
24. Imran A-A-Z, Pokrajac DD, Maidment ADA, Bakic PR. Estimation of adipose compartment volumes in CT images of a mastectomy specimen. *Proceedings of the SPIE*. 2016;9783. doi: 10.1117/12.2217175
25. Hoeschen C, Fill U, Zankl M, et al. A high-resolution voxel phantom of the breast for dose calculations in mammography. *Radiation protection dosimetry*. 2005;114(1–3):406–409. doi: 10.1093/rpd/nch558
26. Hsu CM, Palmeri ML, Segars WP, Veress AI, Dobbins JT. An analysis of the mechanical parameters used for finite element compression of a high-resolution 3D breast phantom. *Medical Physics*. 2011;38(10):5756–5770. doi: 10.1118/1.3637500
27. Hsu CML, Palmeri ML, Segars WP, Veress AI, Dobbins JT. Generation of a suite of 3D computer-generated breast phantoms from a limited set of human subject data. *Medical Physics*. 2013;40(4). doi: 10.1118/1.4794924
28. Huang SY, Boone JM, Yang K, et al. The characterization of breast anatomical metrics using dedicated breast CT. *Medical Physics*. 2011;38(4):2180–2191. doi: 10.1118/1.3567147
29. Segars WP, Veress AI, Wells JR, et al. Population of 100 realistic, patient-based computerized breast phantoms for multi-modality imaging research. *Proceedings of the SPIE*. 2014;9033. doi: 10.1117/12.2043868
30. Erickson DW, Wells JR, Sturgeon GM, et al. Population of 224 realistic human subject-based computational breast phantoms. *Medical Physics*. 2015;43(1):23–32. doi: 10.1118/1.4937597
31. Sarno A, Mettievier G, Di Lillo F, et al. Homogeneous vs. patient specific breast models for Monte Carlo evaluation of mean glandular dose in mammography. *Physica Medica*. 2018;51:56–63. doi: 10.1016/j.ejmp.2018.04.392
32. Ivanov D, Bliznakova K, Buliev I, et al. Suitability of low density materials for 3D printing of physical breast phantoms. *Physics in medicine and biology*. 2018;63(17). doi: 10.1088/1361-6560/aad315
33. Santos JC, Almeida CD, Iwahara A, Peixoto JE. Characterization and applicability of low-density materials for making 3D physical anthropomorphic breast phantoms. *Radiation Physics and Chemistry*. 2019;164. doi: 10.1016/j.radphyschem.2019.108361
34. Esposito G, Mettievier G, Bliznakova K, et al. Investigation of the refractive index decrement of 3D printing materials for manufacturing breast phantoms for phase contrast imaging. *Physics in medicine and biology*. 2019;64(7). doi: 10.1088/1361-6560/ab0670
35. Bliznakova K, Buliev I, Bliznakov Z. *Anthropomorphic Phantoms in Image Quality and Patient Dose Optimization*. Philadelphia: IOP Publishing; 2018. doi: 10.1088/2053-2563/aae197
36. Hernandez AM, Seibert JA, Nosratieh A, Boone JM. Generation and analysis of clinically relevant breast imaging x-ray spectra. *Medical Physics*. 2017;44(6):2148–2160. doi: 10.1002/mp.12222
37. Dukov NT, Feradov FN, Gospodinova GD, Bliznakova KS. An Approach for Printing Tissue-mimicking Abnormalities Dedicated to Applications in Breast Imaging. *2019 IEEE XXVIII International Scientific Conference Electronics (ET)*. 2019:1–4. doi: 10.1109/ET.2019.8878587
38. Mäder U, Martin F, Karin B, Stephan S. Concept to extend anthropomorphic breast phantoms for 2D digital mammography with movable lesions at variable reproducible positions. *15th International Workshop on Breast Imaging (IWBI2020)*. 2020. doi: 10.1117/12.2560619
39. Okoh FO, Kabir NA, Mohd FMY, Siti NAA. Measurement of mass attenuation coefficient of polyvinyl alcohol (PVAL) as breast

- tissue equivalent material in the photon energy range of 16.61–25.26 keV. *Journal of Physics: Conference Series*. 2020;1535(1). doi: 10.1088/1742-6596/1535/1/012051
- 40.** Mainprize JG, Mawdsley GE, Carton A-K, et al. Full-size anthropomorphic phantom for 2D and 3D breast x-ray imaging. *Proceedings of the SPIE*. 2020;11513:17. doi: 10.1117/12.2560358
- 41.** Filippou V, Tsoumpas C. Recent advances on the development of phantoms using 3D printing for imaging with CT, MRI, PET, SPECT, and ultrasound. *Medical Physics*. 2018;45(9):e740–e760. doi: 10.1002/mp.13058
- 42.** di Franco F, Mettievier G, Sarno A, Varallo A, Russo P. Manufacturing of physical breast phantoms with 3D printing technology for X-ray breast imaging. *2019 IEEE Nuclear Science Symposium and Medical Imaging Conference (NSS/MIC)*. 2019:1–5. doi: 10.1109/NSS/MIC42101.2019.9059986
- 43.** Sage J, Fezzani KL, Fitton I, et al. Experimental evaluation of seven quality control phantoms for digital breast tomosynthesis. *Physica Medica*. 2019;57:137–144. doi: 10.1016/j.ejmp.2018.12.031
- 44.** Freed M, Badal A, Jennings RJ, et al. X-ray properties of an anthropomorphic breast phantom for MRI and x-ray imaging. *Physics in medicine and biology*. 2011;56(12):3513–3533. doi: 10.1088/0031-9155/56/12/005
- 45.** Ruvio G, Solimene R, Cuccaro A, et al. Multimodal Breast Phantoms for Microwave, Ultrasound, Mammography, Magnetic Resonance and Computed Tomography Imaging. *Sensors*. 2020;20(8):2400. doi: 10.3390/s20082400
- 46.** Baldelli P, Phelan N, Egan G. Investigation of the effect of anode/filter materials on the dose and image quality of a digital mammography system based on an amorphous selenium flat panel detector. *Br J Radiol*. 2010;83(988):290–295. doi: 10.1259/bjr/60404532
- 47.** Park S, Jennings R, Liu H, Badano A, Myers K. A statistical, task-based evaluation method for three-dimensional x-ray breast imaging systems using variable-background phantoms. *Medical Physics*. 2010;37(12):6253–6270. doi: 10.1118/1.3488910
- 48.** Taibi A, Fabbri S, Baldelli P, et al. Dual-energy imaging in full-field digital mammography: a phantom study. *Physics in medicine and biology*. 2003;48(13):1945–1956. doi: 10.1088/0031-9155/48/13/307
- 49.** Cockmartin L, Marshall N, Bosmans H. Design and Evaluation of a Phantom with Structured Background for Digital Mammography and Breast Tomosynthesis. In: Maidment ADA, Bakic PR, Gavenonis S, editors. *Breast Imaging. IWDMM 2012. Lecture Notes in Computer Science, vol 7361*. Berlin: Springer; 2012. doi: 10.1007/978-3-642-31271-7_83
- 50.** Baneva Y, Bliznakova K, Cockmartin L, et al. Evaluation of a breast software model for 2D and 3D X-ray imaging studies of the breast. *Physica Medica*. 2017;41:78–86. doi: 10.1016/j.ejmp.2017.04.024
- 51.** Bliznakova K. Development of breast software phantom dedicated for research and educational purposes. *RAD Association Journal*. 2017;2(1):14–19. doi: 10.21175/RadJ.2017.01.004
- 52.** Marinov S, Carton A-K, Cockmartin L, et al. Evaluation of the visual realism of breast texture phantoms in digital mammography. *Proc. SPIE 11513, 15th International Workshop on Breast Imaging (IWBI2020)*. 2020. doi: 10.1117/12.2564124
- 53.** Feradov F, Marinov S, Bliznakova K. Physical Breast Phantom Dedicated for Mammography Studies. In: Henriques J, Neves N, de Carvalho P, editors. *XV Mediterranean Conference on Medical and Biological Engineering and Computing – MEDICON 2019. IFMBE Proceedings*. 2020;76:344–352. doi: 10.1007/978-3-030-31635-8_41
- 54.** Bliznakova K, Mettievier G, Russo P, Bliznakov Zh. Validation of a software platform for 2D and 3D phase contrast imaging: preliminary subjective evaluation. *15th International Workshop on Breast Imaging (IWBI2020)*. 2020:97. doi: 10.1117/12.2564356
- 55.** Bliznakova K, Mettievier G, Russo P, et al. A software platform for phase contrast x-ray breast imaging research. *Comput Biol Med*. 2015;61:62–74. doi: 10.1016/j.combiomed.2015.03.017
- 56.** Petrov D, Marshall NW, Young KC, Bosmans H. Systematic approach to a channelized Hotelling model observer implementation for a physical phantom containing mass-like lesions: Application to digital breast tomosynthesis. *Physica Medica*. 2019;58:8–20. doi: 10.1016/j.ejmp.2018.12.033
- 57.** Mettievier G, Bliznakova K, Sechopoulos I, et al. Evaluation of the BreastSimulator Software Platform for Breast Tomography: Preliminary Results. *Physics in Medicine and Biology*. 2016;62(16):145–151. doi: 10.1088/1361-6560/aa6ca3
- 58.** Salomon E, Semturs F, Unger E, et al. Equivalent breast thickness and dose sensitivity of a next iteration 3D structured breast phantom with lesion models. *Medical Imaging 2020: Physics of Medical Imaging*. 2020. doi: 10.1117/12.2548956
- 59.** Carton AK, Bakic P, Ullberg C, Derand H, Maidment AD. Development of a physical 3D anthropomorphic breast phantom. *Medical Physics*. 2011;38(2):891–896. doi: 10.1118/1.3533896
- 60.** Mainprize JG, Carton A-K, Klausz R, et al. Development of a physical 3D anthropomorphic breast texture model using selective laser sintering rapid prototype printing. *Medical Imaging 2018: Physics of Medical Imaging*. 2018:9. doi: 10.1117/12.2560358
- 61.** Li Z, Desolneux A, Muller S, Carton A-K. A Novel 3D Stochastic Solid Breast Texture Model for X-Ray Breast Imaging. In: Tingberg A, Lång K, Timberg P, editors. *Breast Imaging. IWDMM 2016. Lecture Notes in Computer Science, vol 9699*. Springer; 2016. P. 660–667. doi: 10.1007/978-3-319-41546-8_822016
- 62.** Prionas ND, Burkett GW, McKenney SE, et al. Development of a patient-specific two-compartment anthropomorphic breast phantom. *Physics in medicine and biology*. 2012;57(13):4293–4307. doi: 10.1088/0031-9155/57/13/4293
- 63.** Badal A, Clark M, Ghammraoui B. Reproducing two-dimensional mammograms with three-dimensional printed phantoms. *Journal of Medical Imaging*. 2018;5(3). doi: 10.1117/1.JMI.5.3.033501
- 64.** Schopphoven S, Cavael P, Bock K, Fiebich M, Mäder U. Breast phantoms for 2D digital mammography with realistic anatomical structures and attenuation characteristics based on clinical images using 3D printing. *Physics in medicine and biology*. 2019;64(21). doi: 10.1088/1361-6560/ab3f6a
- 65.** Clark M, Ghammraoui B, Badal A. Reproducing 2D breast mammography images with 3D printed phantoms. *Medical Imaging 2016: Physics of Medical Imaging*. 2016;9783. doi: 10.1117/12.2217215
- 66.** Okkalidis N. A novel 3D printing method for accurate anatomy replication in patient-specific phantoms. *Medical Physics*. 2018;45(10):4600–4606. doi: 10.1002/mp.13154
- 67.** Daskalov S, Okkalidis N, Boone JM, et al. Anthropomorphic Physical Breast Phantom Based on Patient Breast CT Data: Preliminary Results. In: Henriques J, Neves N, de Carvalho P, editors. *XV Mediterranean Conference on Medical and Biological Engineering and Computing – MEDICON 2019. IFMBE Proceedings, vol 76*. Springer; 2020. P. 367–374. doi: 10.1007/978-3-030-31635-8_442020

68. Kiarashi N, Nolte AC, Sturgeon GM, et al. Development of realistic physical breast phantoms matched to virtual breast phantoms based on human subject data. *Medical Physics*. 2015;42(7):4116–4126. doi: 10.1118/1.4919771
69. Lindfors KK, Boone JM, Nelson TR, et al. Dedicated Breast CT: Initial Clinical Experience. *Radiology*. 2008;246(3):725–733. doi: 10.1148/radiol.2463070410
70. Burgess AE, Judy PF. Signal detection in power-law noise: effect of spectrum exponents. *Journal of the Optical Society of America A*. 2007;24(12):B52–B60. doi: 10.1364/JOSAA.24.000B52
71. Burgess AE, Jacobson FL, Judy PF. Human observer detection experiments with mammograms and power-law noise. *Medical Physics*. 2001;28(4):419–437. doi: 10.1118/1.1355308
72. Rossman AH, Catenacci M, Zhao C, et al. Three-dimensionally-printed anthropomorphic physical phantom for mammography and digital breast tomosynthesis with custom materials, lesions, and uniform quality control region. *Journal of Medical Imaging*. 2019;6(2). doi: 10.1117/1.JMI.6.2.021604
73. Mettievier G, Sarno A, Boone JM, et al. Virtual clinical trials in 3D and 2D breast imaging with digital phantoms derived from clinical breast CT scans. *Medical Imaging 2020: Physics of Medical Imaging*. 2020. doi: 10.1117/12.2548224
74. Mettievier G, Sarno A, di Franco F, et al. The Napoli-Varna-Davis project for virtual clinical trials in X-ray breast imaging. *2019 IEEE Nuclear Science Symposium and Medical Imaging Conference (NSS/MIC)*. 2019:1–5. doi: 10.1109/NSS/MIC42101.2019.9059828
75. Ikejimba LC, Graff CG, Rosenthal S, et al. A novel physical anthropomorphic breast phantom for 2D and 3D x-ray imaging. *Medical Physics*. 2017;44(2):407–416. doi: 10.1002/mp.12062
76. Mei K, Geagan M, Roshkovan L, et al. Three-dimensional printing of patient-specific lung phantoms for CT imaging: Emulating lung tissue with accurate attenuation profiles and textures. *Medical Physics*. 2022;49(2):825–835. doi: 10.1002/mp.15407
77. Ionita CN, Mokin M, Varble N, et al. Challenges and limitations of patient-specific vascular phantom fabrication using 3D Polyjet printing. *Proceedings of SPIE--the International Society for Optical Engineering*. doi: 10.1117/12.2042266
78. Theodorakou C, Horrocks JA, Marshall NW, Speller RD. A novel method for producing x-ray test objects and phantoms. *Physics in medicine and biology*. 2004;49(8):1423–1438. doi: 10.1088/0031-9155/49/8/004
79. Sikaria D, Musinsky S, Sturgeon GM, et al. Second generation anthropomorphic physical phantom for mammography and DBT: Incorporating voxelized 3D printing and inkjet printing of iodinated lesion inserts. *Proc. SPIE 9783, Medical Imaging 2016: Physics of Medical Imaging*. 2016. doi: 10.1117/12.2217667
80. Jahnke P, Limberg FR, Gerbl A, et al. Radiopaque Three-dimensional Printing: A Method to Create Realistic CT Phantoms. *Radiology*. 2017;282(2):569–575. doi: 10.1148/radiol.2016152710
81. de Sisternes L, Brankov JG, Zysk AM, et al. A computational model to generate simulated three-dimensional breast masses. *Medical Physics*. 2015;42(2):1098–1118. doi: 10.1118/1.4905232
82. SUN NUCLEAR. BR3D BREAST IMAGING PHANTOM [Internet] [cited 1 Jan 2023]. Available from: <https://www.cirsinc.com/products/mammography/br3d-breast-imaging-phantom/>
83. Piccolomini EL, Morotti E. A Model-Based Optimization Framework for Iterative Digital Breast Tomosynthesis Image Reconstruction. *Journal of imaging*. 2021;7(2):36. doi: 10.3390/jimaging7020036
84. Cavicchioli R, Hu JC, Loli Piccolomini E, Morotti E, Zanni L. GPU acceleration of a model-based iterative method for Digital Breast Tomosynthesis. *Scientific reports*. 2020;10(1):43. doi: 10.1038/s41598-019-56920-y
85. Gomi T, Kijima Y, Kobayashi T, Koibuchi Y. Evaluation of a Generative Adversarial Network to Improve Image Quality and Reduce Radiation-Dose during Digital Breast Tomosynthesis. *Diagnostics*. 2022;12(2):495. doi: 10.3390/diagnostics12020495
86. Cockmartin L, Bosmans H, Marshall NW. Establishing a quality control protocol for dual-energy based contrast-enhanced digital mammography. *Proceedings of the SPIE*. 2021;11595. doi: 10.1117/12.2581816
87. Marimón E, Marsden PA, Nait-Charif H, Díaz O. A semi-empirical model for scatter field reduction in digital mammography. *Physics in medicine and biology*. 2021;66(4). doi: 10.1088/1361-6560/abd231
88. Silver EH, Shulman SD, Rehani MM. Innovative monochromatic x-ray source for high-quality and low-dose medical imaging. *Medical Physics*. 2021;48(3):1064–1078. doi: 10.1002/mp.14677

СПИСОК ЛИТЕРАТУРЫ

- Leonov D., Venidiktova D., Costa-Júnior J.F.S., et al. Development of an anatomical breast phantom from polyvinyl chloride plastisol with lesions of various shape, elasticity and echogenicity for teaching ultrasound examination // *International Journal of Computer Assisted Radiology and Surgery*. 2023. doi: 10.1007/s11548-023-02911-4
- Nuzov N.B., Bhusal B., Henry K.R., et al. True location of deep brain stimulation electrodes differs from what is seen on postoperative magnetic resonance images: An anthropomorphic phantom study // *Annual International Conference of the IEEE Engineering in Medicine and Biology Society. IEEE Engineering in Medicine and Biology Society*. 2022. P. 1863–1866. doi: 10.1109/EMBC48229.2022.9871619
- Cannella R., Shahait M., Furlan A.A., et al. Efficacy of single-source rapid kV-switching dual-energy CT for characterization of non-uric acid renal stones: a prospective ex vivo study using anthropomorphic phantom // *Abdominal Radiology*. 2020. Vol. 45, N 4. P. 1092–1099. doi: 10.1007/s00261-019-02164-3
- Kramer R., Zankl M., Williams G., Drexler G., et al. The calculation of dose from external photon exposures using reference human phantoms and Monte Carlo methods. 1982.
- Васильев Ю.А., Тыров И.А., Владзимирский А.В., и др. Двойной просмотр результатов маммографии с применением технологий искусственного интеллекта: новая модель организации массовых профилактических исследований // *Digital Diagnostics*. 2023. Т. 4, № 2. С. 93–104. doi: 10.17816/DD3214236.
- Cockmartin L., Bosmans H., Marshall N.W. Comparative power law analysis of structured breast phantom and patient images in digital mammography and breast tomosynthesis // *Med Phys*. 2013. Vol. 40, № 8. P. 81920.
- Ma A.K.W., Gunn S., Darambara D.G. Introducing DeBRa: a detailed breast model for radiological studies // *Physics in medicine and biology*. 2009. Vol. 54, N 14. P. 4533–4545. doi: 10.1088/0031-9155/54/14/010

8. Chen B., Shorey J., Saunders R.S., et al. An Anthropomorphic Breast Model for Breast Imaging Simulation and Optimization // *Academic radiology*. 2011. Vol. 18, N 5. P. 536–546. doi: 10.1016/j.acra.2010.11.009
9. Elangovan P., Mackenzie A., Dance D.R., et al. Design and validation of realistic breast models for use in multiple alternative forced choice virtual clinical trials // *Physics in medicine and biology*. 2017. Vol. 62, N 7. P. 2778–2794. doi: 10.1088/1361-6560/aa622c
10. Bliznakova K., Suryanarayanan S., Karellas A., Pallikarakis N. Evaluation of an improved algorithm for producing realistic 3D breast software phantoms: Application for mammography // *Medical Physics*. 2010. Vol. 37, N 11. P. 5604–5617. doi: 10.1118/1.3491812
11. O'Connor J.M., Das M., Dider C., Mahd M., Glick S.J. Generation of voxelized breast phantoms from surgical mastectomy specimens // *Medical Physics*. 2013. Vol. 40, N 4. doi: 10.1118/1.4795758
12. Lau B.A., Reiser I., Nishikawa R.M. A statistically defined anthropomorphic software breast phantom // *Medical Physics*. 2012. Vol. 39, N 6. P. 3375–3385. doi: 10.1118/1.4718576
13. Sarno A., Mettivier G., di Franco F., et al. Dataset of patient-derived digital breast phantoms for in silico studies in breast computed tomography, digital breast tomosynthesis, and digital mammography // *Medical Physics*. 2021. Vol. 48, N 5. P. 2682–2693. doi: 10.1002/mp.14826
14. Li C.M., Segars W.P., Tourassi G.D., Boone J.M., Dobbins J.T. Methodology for generating a 3D computerized breast phantom from empirical data // *Medical Physics*. 2009. Vol. 36, N 7. P. 3122–3131. doi: 10.1118/1.3140588
15. Bliznakova K., Bliznakov Z., Bravou V., Kolitsi Z., Pallikarakis N. A three-dimensional breast software phantom for mammography simulation // *Physics in medicine and biology*. 2003. Vol. 48, N 22. P. 3699–3719. doi: 10.1088/0031-9155/48/22/006
16. Bakic P.R., Albert M., Brzakovic D., Maidment A.D. Mammogram synthesis using a 3D simulation. I. Breast tissue model and image acquisition simulation // *Medical Physics*. 2002. Vol. 29, N 9. P. 2131–2139. doi: 10.1118/1.1501143
17. Bakic P.R., Albert M., Brzakovic D., Maidment A.D. Mammogram synthesis using a 3D simulation. II. Evaluation of synthetic mammogram texture // *Medical Physics*. 2002. Vol. 29, N 9. P. 2140–2151. doi: 10.1118/1.1501144
18. Bakic P.R., Albert M., Brzakovic D., Maidment A.D. Mammogram synthesis using a three-dimensional simulation. III. Modeling and evaluation of the breast ductal network // *Medical Physics*. 2003. Vol. 30, N 7. P. 1914–1925. doi: 10.1118/1.1586453
19. Pokrajac D.D., Maidment A.D.A., Bakic P.R. Optimized generation of high resolution breast anthropomorphic software phantoms // *Medical Physics*. 2012. Vol. 39, N 4. P. 2290–2302. doi: 10.1118/1.3697523
20. Chen F., Pokrajac D., Shi X., et al. Partial volume simulation in software breast phantoms // *Medical Imaging 2012: Physics of Medical Imaging*. 2012. doi: 10.1117/12.912242
21. Graff C.G. A new, open-source, multi-modality digital breast phantom // *Proceedings of the SPIE*. 2016. Vol. 9783. doi: 10.1117/12.2216312
22. Ikejimba L.C., Salad J., Graff C.G., et al. A four-alternative forced choice (4AFC) methodology for evaluating microcalcification detection in clinical full-field digital mammography (FFDM) and digital breast tomosynthesis (DBT) systems using an inkjet-printed anthropomorphic phantom // *Medical Physics*. 2019. Vol. 46, N 9. P. 3883–3892. doi: 10.1002/mp.13629
23. Imran A.-A.-Z., Bakic P.R., Pokrajac D.D. Spatial distribution of adipose compartments size, shape and orientation in a CT breast image of a mastectomy specimen // *2015 IEEE Signal Processing in Medicine and Biology Symposium (SPMB)*. 2015. P. 1–2. doi: 10.1109/SPMB.2015.7405460
24. Imran A.-A.-Z., Pokrajac D.D., Maidment A.D.A., Bakic P.R. Estimation of adipose compartment volumes in CT images of a mastectomy specimen // *Proceedings of the SPIE*. 2016. Vol. 9783. doi: 10.1117/12.2217175
25. Hoeschen C., Fill U., Zankl M., et al. A high-resolution voxel phantom of the breast for dose calculations in mammography // *Radiation protection dosimetry*. 2005. Vol. 114, N 1–3. P. 406–409. doi: 10.1093/rpd/nch558
26. Hsu C.M., Palmeri M.L., Segars W.P., Veress A.I., Dobbins J.T. An analysis of the mechanical parameters used for finite element compression of a high-resolution 3D breast phantom // *Medical Physics*. 2011. Vol. 38, N 10. P. 5756–5770. doi: 10.1118/1.3637500
27. Hsu C.M.L., Palmeri M.L., Segars W.P., Veress A.I., Dobbins J.T. Generation of a suite of 3D computer-generated breast phantoms from a limited set of human subject data // *Medical Physics*. 2013. Vol. 40, N 4. doi: 10.1118/1.4794924
28. Huang S.Y., Boone J.M., Yang K., et al. The characterization of breast anatomical metrics using dedicated breast CT // *Medical Physics*. 2011. Vol. 38, N 4. P. 2180–2191. doi: 10.1118/1.3567147
29. Segars W.P., Veress A.I., Wells J.R., et al. Population of 100 realistic, patient-based computerized breast phantoms for multi-modality imaging research // *Proceedings of the SPIE*. 2014. Vol. 9033. doi: 10.1117/12.2043868
30. Erickson D.W., Wells J.R., Sturgeon G.M., et al. Population of 224 realistic human subject-based computational breast phantoms // *Medical Physics*. 2015. Vol. 43, N 1. P. 23–32. doi: 10.1118/1.4937597
31. Sarno A., Mettivier G., Di Lillo F., et al. Homogeneous vs. patient specific breast models for Monte Carlo evaluation of mean glandular dose in mammography // *Physica Medica*. 2018. Vol. 51. P. 56–63. doi: 10.1016/j.ejmp.2018.04.392
32. Ivanov D., Bliznakova K., Buliev I., et al. Suitability of low density materials for 3D printing of physical breast phantoms // *Physics in medicine and biology*. 2018. Vol. 63, N 17. doi: 10.1088/1361-6560/aad315
33. Santos J.C., Almeida C.D., Iwahara A., Peixoto J.E. Characterization and applicability of low-density materials for making 3D physical anthropomorphic breast phantoms // *Radiation Physics and Chemistry*. 2019. Vol. 164. doi: 10.1016/j.radphyschem.2019.108361
34. Esposito G., Mettivier G., Bliznakova K., et al. Investigation of the refractive index decrement of 3D printing materials for manufacturing breast phantoms for phase contrast imaging // *Physics in medicine and biology*. 2019. Vol. 64, N 7. doi: 10.1088/1361-6560/ab0670
35. Bliznakova K., Buliev I., Bliznakov Z. *Anthropomorphic Phantoms in Image Quality and Patient Dose Optimization*. Philadelphia : IOP Publishing, 2018. doi: 10.1088/2053-2563/aae197
36. Hernandez A.M., Seibert J.A., Nosratieh A., Boone J.M. Generation and analysis of clinically relevant breast imaging x-ray spectra // *Medical Physics*. 2017. Vol. 44, N 6. P. 2148–2160. doi: 10.1002/mp.12222
37. Dukov N.T., Feradov F.N., Gospodinova G.D., Bliznakova K.S. *An Approach for Printing Tissue-mimicking Abnormalities Dedicated to Applications in Breast Imaging* // *2019 IEEE XXVIII*

- International Scientific Conference Electronics (ET). 2019. P. 1–4. doi: 10.1109/ET.2019.8878587
- 38.** Mäder U., Martin F., Karin B., Stephan S. Concept to extend anthropomorphic breast phantoms for 2D digital mammography with movable lesions at variable reproducible positions // 15th International Workshop on Breast Imaging (IWBI2020). 2020. doi: 10.1117/12.2560619
- 39.** Okoh F.O., Kabir N.A., Mohd F.M.Y., Siti N.A.A. Measurement of mass attenuation coefficient of polyvinyl alcohol (PVAL) as breast tissue equivalent material in the photon energy range of 16.61–25.26 keV // *Journal of Physics: Conference Series*. 2020. Vol. 1535, N 1. doi: 10.1088/1742-6596/1535/1/012051
- 40.** Mainprize J.G., Mawdsley G.E., Carton A.-K., et al. Full-size anthropomorphic phantom for 2D and 3D breast x-ray imaging // *Proceedings of the SPIE*. 2020. Vol. 11513. P. 17. doi: 10.1117/12.2560358
- 41.** Filippou V., Tsoumpas C. Recent advances on the development of phantoms using 3D printing for imaging with CT, MRI, PET, SPECT, and ultrasound // *Medical Physics*. 2018. Vol. 45, N 9. P. e740–e760. doi: 10.1002/mp.13058
- 42.** di Franco F., Mettievier G., Sarno A., Varallo A., Russo P. Manufacturing of physical breast phantoms with 3D printing technology for X-ray breast imaging // 2019 IEEE Nuclear Science Symposium and Medical Imaging Conference (NSS/MIC). 2019. P. 1–5. doi: 10.1109/NSS/MIC42101.2019.9059986
- 43.** Sage J., Fezzani K.L., Fitton I., et al. Experimental evaluation of seven quality control phantoms for digital breast tomosynthesis // *Physica Medica*. 2019. Vol. 57. P. 137–144. doi: 10.1016/j.ejmp.2018.12.031
- 44.** Freed M., Badal A., Jennings R.J., et al. X-ray properties of an anthropomorphic breast phantom for MRI and x-ray imaging // *Physics in medicine and biology*. 2011. Vol. 56, N 12. P. 3513–3533. doi: 10.1088/0031-9155/56/12/005
- 45.** Ruvio G., Solimene R., Cuccaro A., et al. Multimodal Breast Phantoms for Microwave, Ultrasound, Mammography, Magnetic Resonance and Computed Tomography Imaging // *Sensors*. 2020. Vol. 20, N 8. P. 2400. doi: 10.3390/s20082400
- 46.** Baldelli P., Phelan N., Egan G. Investigation of the effect of anode/filter materials on the dose and image quality of a digital mammography system based on an amorphous selenium flat panel detector // *Br J Radiol*. 2010. Vol. 83, N 988. P. 290–295. doi: 10.1259/bjr/60404532
- 47.** Park S., Jennings R., Liu H., Badano A., Myers K. A statistical, task-based evaluation method for three-dimensional x-ray breast imaging systems using variable-background phantoms // *Medical Physics*. 2010. Vol. 37, N 12. P. 6253–6270. doi: 10.1118/1.3488910
- 48.** Taibi A., Fabbri S., Baldelli P., et al. Dual-energy imaging in full-field digital mammography: a phantom study // *Physics in medicine and biology*. 2003. Vol. 48, N 13. P. 1945–1956. doi: 10.1088/0031-9155/48/13/307
- 49.** Cockmartin L., Marshall N., Bosmans H. Design and Evaluation of a Phantom with Structured Background for Digital Mammography and Breast Tomosynthesis. In: Maidment A.D.A., Bakic P.R., Gavenonis S., editors. *Breast Imaging. IWDM 2012. Lecture Notes in Computer Science*, vol 7361. Berlin : Springer, 2012. doi: 10.1007/978-3-642-31271-7_83
- 50.** Baneva Y., Bliznakova K., Cockmartin L., et al. Evaluation of a breast software model for 2D and 3D X-ray imaging studies of the breast // *Physica Medica*. 2017. Vol. 41. P. 78–86. doi: 10.1016/j.ejmp.2017.04.024
- 51.** Bliznakova K. Development of breast software phantom dedicated for research and educational purposes // *RAD Association Journal*. 2017. Vol. 2, N 1. P. 14–19. doi: 10.21175/RadJ.2017.01.004
- 52.** Marinov S., Carton A.-K., Cockmartin L., et al. Evaluation of the visual realism of breast texture phantoms in digital mammography // *Proc. SPIE 11513, 15th International Workshop on Breast Imaging (IWBI2020)*. 2020. doi: 10.1117/12.2564124
- 53.** Feradov F., Marinov S., Bliznakova K. Physical Breast Phantom Dedicated for Mammography Studies. In: Henriques J., Neves N., de Carvalho P., editors. *XV Mediterranean Conference on Medical and Biological Engineering and Computing – MEDICON 2019. MEDICON 2019. IFMBE Proceedings*, vol 76. Springer, 2020. P. 344–352. doi: 10.1007/978-3-030-31635-8_41
- 54.** Bliznakova K., Mettievier G., Russo P., Bliznakov Zh. Validation of a software platform for 2D and 3D phase contrast imaging: preliminary subjective evaluation // 15th International Workshop on Breast Imaging (IWBI2020). 2020. P. 97. doi: 10.1117/12.2564356
- 55.** Bliznakova K., Mettievier G., Russo P., et al. A software platform for phase contrast x-ray breast imaging research // *Comput Biol Med*. 2015. Vol. 61. P. 62–74. doi: 10.1016/j.combiomed.2015.03.017
- 56.** Petrov D., Marshall N.W., Young K.C., Bosmans H. Systematic approach to a channelized Hotelling model observer implementation for a physical phantom containing mass-like lesions: Application to digital breast tomosynthesis // *Physica Medica*. 2019. Vol. 58. P. 8–20. doi: 10.1016/j.ejmp.2018.12.033
- 57.** Mettievier G., Bliznakova K., Sechopoulos I., et al. Evaluation of the BreastSimulator Software Platform for Breast Tomography: Preliminary Results // *Physics in Medicine and Biology*. 2016. Vol. 62, N 16. P. 145–151. doi: 10.1088/1361-6560/aa6ca3
- 58.** Salomon E., Semturs F., Unger E., et al. Equivalent breast thickness and dose sensitivity of a next iteration 3D structured breast phantom with lesion models // *Medical Imaging 2020: Physics of Medical Imaging*. 2020. doi: 10.1117/12.2548956
- 59.** Carton A.-K., Bakic P., Ullberg C., Derand H., Maidment A.D. Development of a physical 3D anthropomorphic breast phantom // *Medical Physics*. 2011. Vol. 38, N 2. P. 891–896. doi: 10.1118/1.3533896
- 60.** Mainprize J.G., Carton A.-K., Klausz R., et al. Development of a physical 3D anthropomorphic breast texture model using selective laser sintering rapid prototype printing // *Medical Imaging 2018: Physics of Medical Imaging*. 2018. P. 9. doi: 10.1117/12.2560358
- 61.** Li Z., Desolneux A., Muller S., Carton A.-K. A Novel 3D Stochastic Solid Breast Texture Model for X-Ray Breast Imaging. In: Tingberg A., Lång K., Timberg P., editors. *Breast Imaging. IWDM 2016. Lecture Notes in Computer Science*, vol 9699. Springer, 2016. P. 660–667. doi: 10.1007/978-3-319-41546-8_822016
- 62.** Prionas N.D., Burkett G.W., McKenney S.E., et al. Development of a patient-specific two-compartment anthropomorphic breast phantom // *Physics in medicine and biology*. 2012. Vol. 57, N 13. P. 4293–4307. doi: 10.1088/0031-9155/57/13/4293
- 63.** Badal A., Clark M., Ghamraoui B. Reproducing two-dimensional mammograms with three-dimensional printed phantoms // *Journal of Medical Imaging*. 2018. Vol. 5, N 3. doi: 10.1117/1.JMI.5.3.033501
- 64.** Schopphoven S., Cavael P., Bock K., Fiebich M., Mäder U. Breast phantoms for 2D digital mammography with realistic anatomical structures and attenuation characteristics based on clinical images

- using 3D printing // *Physics in medicine and biology*. 2019. Vol. 64, N 21. doi: 10.1088/1361-6560/ab3f6a
65. Clark M., Ghamraoui B., Badal A. Reproducing 2D breast mammography images with 3D printed phantoms // *Medical Imaging 2016: Physics of Medical Imaging*. 2016. Vol. 9783. doi: 10.1117/12.2217215
66. Okkalidis N. A novel 3D printing method for accurate anatomy replication in patient-specific phantoms // *Medical Physics*. 2018. Vol. 45, N 10. P. 4600–4606. doi: 10.1002/mp.13154
67. Daskalov S., Okkalidis N., Boone J.M., et al. Anthropomorphic Physical Breast Phantom Based on Patient Breast CT Data: Preliminary Results. In: Henriques J., Neves N., de Carvalho P., editors. *XV Mediterranean Conference on Medical and Biological Engineering and Computing – MEDICON 2019*. MEDICON 2019. IFMBE Proceedings, vol 76. Springer, 2020. P. 367–374. doi: 10.1007/978-3-030-31635-8_442020
68. Kiarashi N., Nolte A.C., Sturgeon G.M., et al. Development of realistic physical breast phantoms matched to virtual breast phantoms based on human subject data // *Medical Physics*. 2015. Vol. 42, N 7. P. 4116–4126. doi: 10.1118/1.4919771
69. Lindfors K.K., Boone J.M., Nelson T.R., et al. Dedicated Breast CT: Initial Clinical Experience // *Radiology*. 2008. Vol. 246, N 3. P. 725–733. doi: 10.1148/radiol.2463070410
70. Burgess A.E., Judy P.F. Signal detection in power-law noise: effect of spectrum exponents // *Journal of the Optical Society of America A*. 2007. Vol. 24, N 12. P. B52–B60. doi: 10.1364/JOSAA.24.000B52
71. Burgess A.E., Jacobson F.L., Judy P.F. Human observer detection experiments with mammograms and power-law noise // *Medical Physics*. 2001. Vol. 28, N 4. P. 419–437. doi: 10.1118/1.1355308
72. Rossman A.H., Catenacci M., Zhao C., et al. Three-dimensionally-printed anthropomorphic physical phantom for mammography and digital breast tomosynthesis with custom materials, lesions, and uniform quality control region // *Journal of Medical Imaging*. 2019. Vol. 6, N 2. doi: 10.1117/1.JMI.6.2.021604
73. Mettievier G., Sarno A., Boone J.M., et al. Virtual clinical trials in 3D and 2D breast imaging with digital phantoms derived from clinical breast CT scans // *Medical Imaging 2020: Physics of Medical Imaging*. 2020. doi: 10.1117/12.2548224
74. Mettievier G., Sarno A., di Franco F., et al. The Napoli-Varna-Davis project for virtual clinical trials in X-ray breast imaging // *2019 IEEE Nuclear Science Symposium and Medical Imaging Conference (NSS/MIC)*. 2019. P. 1–5. doi: 10.1109/NSS/MIC42101.2019.9059828
75. Ikejimba L.C., Graff C.G., Rosenthal S., et al. A novel physical anthropomorphic breast phantom for 2D and 3D x-ray imaging // *Medical Physics*. 2017. Vol. 44, N 2. P. 407–416. doi: 10.1002/mp.12062
76. Mei K., Geagan M., Roshkovan L., et al. Three-dimensional printing of patient-specific lung phantoms for CT imaging: Emulating lung tissue with accurate attenuation profiles and textures // *Medical Physics*. 2022. Vol. 49, N 2. P. 825–835. doi: 10.1002/mp.15407
77. Ionita C.N., Mokin M., Varble N., et al. Challenges and limitations of patient-specific vascular phantom fabrication using 3D Polyjet printing // *Proceedings of SPIE--the International Society for Optical Engineering*. doi: 10.1117/12.2042266
78. Theodorakou C., Horrocks J.A., Marshall N.W., Speller R.D. A novel method for producing x-ray test objects and phantoms // *Physics in medicine and biology*. 2004. Vol. 49, N 8. P. 1423–1438. doi: 10.1088/0031-9155/49/8/004
79. Sikaria D., Musinsky S., Sturgeon G.M., et al. Second generation anthropomorphic physical phantom for mammography and DBT: Incorporating voxelized 3D printing and inkjet printing of iodinated lesion inserts. *Proc. SPIE 9783, Medical Imaging 2016: Physics of Medical Imaging*. 2016. doi: 10.1117/12.2217667
80. Jahnke P., Limberg F.R., Gerbl A., et al. Radiopaque Three-dimensional Printing: A Method to Create Realistic CT Phantoms // *Radiology*. 2017. Vol. 282, N 2. P. 569–575. doi: 10.1148/radiol.2016152710
81. de Sisternes L., Brankov J.G., Zysk A.M., et al. A computational model to generate simulated three-dimensional breast masses // *Medical Physics*. 2015. Vol. 42, N 2. P. 1098–1118. doi: 10.1118/1.4905232
82. SUN NUCLEAR. BR3D BREAST IMAGING PHANTOM [Internet] [дата обращения 01.01.2023]. Доступ по ссылке: <https://www.cirsinc.com/products/mammography/br3d-breast-imaging-phantom/>
83. Piccolomini E.L., Morotti E. A Model-Based Optimization Framework for Iterative Digital Breast Tomosynthesis Image Reconstruction // *Journal of imaging*. 2021. Vol. 7, N 2. P. 36. doi: 10.3390/jimaging7020036
84. Cavicchioli R., Hu J.C., Loli Piccolomini E., Morotti E., Zanni L. GPU acceleration of a model-based iterative method for Digital Breast Tomosynthesis // *Scientific reports*. 2020. Vol. 10, N 1. P. 43. doi: 10.1038/s41598-019-56920-y
85. Gomi T., Kijima Y., Kobayashi T., Koibuchi Y. Evaluation of a Generative Adversarial Network to Improve Image Quality and Reduce Radiation-Dose during Digital Breast Tomosynthesis // *Diagnostics*. 2022. Vol. 12, N 2. P. 495. doi: 10.3390/diagnostics1202049586
86. Cockmartin L., Bosmans H., Marshall N.W. Establishing a quality control protocol for dual-energy based contrast-enhanced digital mammography // *Proceedings of the SPIE*. 2021. Vol. 11595. doi: 10.1117/12.2581816
87. Marimón E., Marsden P.A., Nait-Charif H., Díaz O. A semi-empirical model for scatter field reduction in digital mammography // *Physics in medicine and biology*. 2021. Vol. 66, N 4. doi: 10.1088/1361-6560/abd231
88. Silver E.H., Shulman S.D., Rehani M.M. Innovative monochromatic x-ray source for high-quality and low-dose medical imaging // *Medical Physics*. 2021. Vol. 48, N 3. P. 1064–1078. doi: 10.1002/mp.14677

AUTHORS' INFO

* Anastasia A. Nasibullina;

address: 24/1 Petrovka street, 127051, Moscow, Russia

ORCID: 0000-0003-1695-7731;

eLibrary SPIN: 2482-3372;

e-mail: NasibullinaAA@zdrav.mos.ru

ОБ АВТОРАХ

* Насибуллина Анастасия Александровна;

адрес: Россия, 127051, Москва, ул.Петровка, д.24, стр. 1;

ORCID: 0000-0003-1695-7731;

eLibrary SPIN: 2482-3372;

e-mail: NasibullinaAA@zdrav.mos.ru

* Corresponding author / Автор, ответственный за переписку

Yuriy A. Vasilev, MD, Cand. Sci. (Med.);
ORCID: 0000-0002-5283-5961;
eLibrary SPIN: 4458-5608;
e-mail: VasilevYA1@zdrav.mos.ru

Olga V. Omelyanskaya;
ORCID: 0000-0002-0245-4431;
eLibrary SPIN: 8948-6152;
e-mail: OmelyanskayaOV@zdrav.mos.ru

Denis V. Leonov, Cand. Sci. (Tech.);
ORCID: 0000-0003-0916-6552;
eLibrary SPIN: 5510-4075;
e-mail: LeonovDV2@zdrav.mos.ru

Julia V. Bulgakova;
ORCID: 0000-0002-1627-6568;
eLibrary SPIN: 8945-6205;
e-mail: BulgakovaYV@zdrav.mos.ru

Dina A. Akhmedzyanova, MD;
ORCID: 0000-0001-7705-9754;
eLibrary SPIN: 6983-5991;
e-mail: AkhmedzyanovaDA@zdrav.mos.ru

Yuliya F. Shumskaya, MD;
ORCID: 0000-0002-8521-4045;
eLibrary SPIN: 3164-5518;
e-mail: shumskayayf@zdrav.mos.ru

Roman V. Reshetnikov, Cand. Sci. (Phys. and Math.);
ORCID: 0000-0002-9661-0254;
eLibrary SPIN: 8592-0558;
e-mail: r.reshetnikov@npcmr.ru

Васильев Юрий Александрович, канд. мед. наук;
ORCID: 0000-0002-5283-5961;
eLibrary SPIN: 4458-5608;
e-mail: VasilevYA1@zdrav.mos.ru

Омелянская Ольга Васильевна;
ORCID: 0000-0002-0245-4431;
eLibrary SPIN: 8948-6152;
e-mail: OmelyanskayaOV@zdrav.mos.ru

Леонов Денис Владимирович, канд. техн. наук;
ORCID: 0000-0003-0916-6552;
eLibrary SPIN: 5510-4075;
e-mail: LeonovDV2@zdrav.mos.ru

Булгакова Юлия Владиславовна;
ORCID: 0000-0002-1627-6568;
eLibrary SPIN: 8945-6205;
e-mail: BulgakovaYV@zdrav.mos.ru

Ахмедзянова Дина Альфредовна;
ORCID: 0000-0001-7705-9754;
eLibrary SPIN: 6983-5991;
e-mail: AkhmedzyanovaDA@zdrav.mos.ru

Шумская Юлия Федоровна;
ORCID: 0000-0002-8521-4045;
eLibrary SPIN: 3164-5518;
e-mail: shumskayayf@zdrav.mos.ru

Решетников Роман Владимирович, канд. ф.-м. наук;
ORCID: 0000-0002-9661-0254;
eLibrary SPIN: 8592-0558;
e-mail: r.reshetnikov@npcmr.ru

DOI: <https://doi.org/10.17816/DD501759>

Технологические дефекты программного обеспечения с искусственным интеллектом

В.В. Зинченко, К.М. Арзамасов, Е.И. Кремнева, А.В. Владзимирский, Ю.А. Васильев

Научно-практический клинический центр диагностики и телемедицины, Москва, Российская Федерация

АННОТАЦИЯ

Обоснование. Технологические дефекты в работе программного обеспечения с искусственным интеллектом являются критически важными при принятии решения о практической применимости и клинической ценности программного обеспечения с искусственным интеллектом.

Цель — анализ и систематизация технологических дефектов, возникающих при работе программного обеспечения с искусственным интеллектом для анализа медицинских изображений.

Материалы и методы. В рамках эксперимента по использованию инновационных технологий в области компьютерного зрения для анализа медицинских изображений и дальнейшего применения в системе здравоохранения города Москвы проводится мониторинг технологических параметров для всех участвующих решений как на этапе апробации, так и на этапе опытной эксплуатации. В статье представлена графическая информация о среднем числе технологических дефектов для профилактического направления, модальность «Маммография», за 2021 год. Этот период выбран как наиболее показательный, характеризующийся активным развитием программного обеспечения с искусственным интеллектом с позиции увеличения технической стабильности их работы. С целью оценки применимости подхода по выявлению технологических дефектов аналогичный анализ проводился для направления обнаружения внутричерепных кровоизлияний на компьютерных томограммах головного мозга за 2022–2023 годы.

Результаты. В ходе исследования было проанализировано программное обеспечение с искусственным интеллектом по модальностям «Маммография» (2 алгоритма) и «Компьютерная томография головного мозга» (1). Всего для модальности «Маммография» собрано 14 выборок по 20 исследований; для модальности «Компьютерная томография» — 12 выборок по 80 исследований. Для каждого типа дефекта были построены графики, а для каждой из модальностей были построены линии тренда. Коэффициенты уравнений линий трендов указывают на тенденцию к снижению числа технологических дефектов.

Заключение. Проведённый анализ позволяет проследить тенденцию к снижению числа технологических дефектов, что может свидетельствовать о доработке программного обеспечения с искусственным интеллектом и повышении его качества благодаря периодическому мониторингу. Кроме того, такой результат показывает универсальность использования как для профилактических методов, так и для экстренных.

Ключевые слова: искусственный интеллект; программное обеспечение с искусственным интеллектом; технологический мониторинг; технологические дефекты; Московский эксперимент.

Как цитировать:

Зинченко В.В., Арзамасов К.М., Кремнева Е.И., Владзимирский А.В., Васильев Ю.А. Технологические дефекты программного обеспечения с искусственным интеллектом // Digital Diagnostics. 2023. Т. 4, № 4 С. 593–604. DOI: <https://doi.org/10.17816/DD501759>

DOI: <https://doi.org/10.17816/DD501759>

Technological defects in software based on artificial intelligence

Viktoriya V. Zinchenko, Kirill M. Arzamasov, Elena I. Kremneva, Anton V. Vladzemyrskyy, Yuriy A. Vasilev

Scientific and Practical Clinical Center for Diagnostics and Telemedicine Technologies, Moscow, Russian Federation

ABSTRACT

BACKGROUND: Technological defects in the use of artificial intelligence software are critical when deciding on the practical applicability and clinical value of artificial intelligence software.

AIM: To conduct an analysis and systematization of technological defects occurring when artificial intelligence software analyzes medical images.

MATERIALS AND METHODS: As part of the experiment on the use of innovative computer vision technologies for the analysis of medical images and further application in the Moscow healthcare system, technological parameters of all artificial intelligence software are monitored at the testing and operation stages of the trial. This article presents graphical information on the average number of technological defects in mass mammography screening in 2021. This period was chosen as the most indicative and characterized by the active development of artificial intelligence software and increased technical stability of its performance. To assess the applicability of the analysis for technological defects, a similar analysis was conducted for the direction of detection of intracranial hemorrhage on computed tomography scans of the brain for 2022–2023.

RESULTS: During the study, artificial intelligence software used for mammography (two algorithms) and brain computed tomography (one algorithm) were analyzed. Fourteen mammography samples were collected for technological monitoring during the identified period, each from 20 studies, and 12 brain computed tomography samples were obtained, each from 80 studies. Graphs were constructed for each type of defect, and trend lines were plotted for each modality. The coefficients of the trend line equations indicate a downward tendency in the number of technological defects.

CONCLUSION: This analysis allows tracing a downward trend in the number of technological defects, which may indicate a refinement of artificial intelligence software and an increase in its quality because of periodic monitoring. It also shows the versatility of use for both preventive and emergency methods.

Keywords: artificial intelligence; artificial intelligence software; technological monitoring; technological defects; Moscow experiment.

To cite this article:

Zinchenko VV, Arzamasov KM, Kremneva EI, Vladzemyrskyy AV, Vasilev YuA. Technological defects in software based on artificial intelligence. *Digital Diagnostics*. 2023;4(4):593–604. DOI: <https://doi.org/10.17816/DD501759>

Received: 20.06.2023

Accepted: 21.11.2023

Published online: 06.12.2023

DOI: <https://doi.org/10.17816/DD501759>

人工智能软件的技术缺陷

Viktoria V. Zinchenko, Kirill M. Arzamasov, Elena I. Kremneva, Anton V. Vladzimirskyy, Yuriy A. Vasilev

Scientific and Practical Clinical Center for Diagnostics and Telemedicine Technologies, Moscow, Russian Federation

简评

论证。人工智能软件性能方面的技术缺陷是确定人工智能软件实用性和临床价值的关键。

该研究的目的是对医学影像分析人工智能软件运行中的技术缺陷进行分析并使之系统化。

材料和方法。在莫斯科市进行了一项《使用创新计算机视觉技术进行医学图像分析并进一步应用于莫斯科市医疗系统的实验》。在实验框架内，对所有参与解决方案的技术参数进行监测。监测是在批准阶段和试运行阶段进行的。本文以图表形式介绍2021年“乳房摄影术”预防方向的平均技术缺陷数量。这一时期被选为最有意义的时期。这一时期的特点是从提高操作技术稳定性的角度出发，积极开发人工智能软件。为了评估该方法在发现技术缺陷方面的适用性，我们对2022–2023年脑部CT扫描颅内出血的检测方向进行了类似的分析。

结果。本研究分析了“乳房摄影术”（2种算法）和“脑计算机断层扫描”（1种）模式的人工智能软件。在“乳房X射线照相术”模式中，共收集了14个样本，共有20项研究。在“脑计算机断层扫描”模式中，共收集了12个样本，共有80项研究。我们对每种缺陷类型都绘制了图表，对每种模式绘制了趋势线。趋势线公式的系数表明了，技术缺陷的数量呈下降趋势。

结论。通过分析，我们发现了减少技术缺陷数量的趋势。这可能表明人工智能软件的完善，以及通过定期监测，软件质量的提升。此外，这一结果还显示使用预防和应急方法的通用性。

关键词：人工智能；人工智能软件；技术监测；技术缺陷；莫斯科实验。

引用本文：

Zinchenko VV, Arzamasov KM, Kremneva EI, Vladzimirskyy AV, Vasilev YuA. 人工智能软件的技术缺陷. *Digital Diagnostics*. 2023;4(4):593–604. DOI: <https://doi.org/10.17816/DD501759>

收到: 20.06.2023

接受: 21.11.2023

发布日期: 06.12.2023

BACKGROUND

Artificial intelligence (AI)-based software can assist healthcare professionals (HCPs) with routine and complex tasks and improve the quality, accessibility, and speed of patient care [1–3]. This was largely possible because of the continuity of foreign and domestic experience with AI in healthcare [4–7] and the experiment on the use of innovative computer vision technologies for analysis of medical images and further application in the Moscow healthcare system (hereinafter referred to as “the Experiment”). The Experiment aimed to conduct a scientific study of the possibility of using medical decision support methods in the Moscow healthcare system based on data analysis using advanced innovative technologies. Requirements were developed for AI-based software results in 21 areas of diagnostic radiology. Currently, results obtained using >50 AI-based solutions are available for HCPs. More than 10 million studies have been processed at the end of September 2023.

The use of new technologies in healthcare requires mandatory compliance with safety regulations. Therefore, the development, deployment, and use of AI-based software should be monitored [8]. Furthermore, AI-based software requires special control during operation because it can produce biased results when used on a population other than the one used to train it [9,10].

Some tests are used as part of the Experiment to control the quality of processing AI-based software research. Self-testing is the first step, which is designed to understand the technological AI compatibility of the software and research (input) data submitted for processing. The next step is functional testing. It determines the presence of the declared AI-based software functions, including its performance. The AI-based software is evaluated from both technical and clinical perspectives by technical and medical experts. Calibration testing is the step of determining the performance metrics of AI-based software with the area under the ROC curve as the main indicator.

If all tests are successfully passed, the software is allowed to work with AI, and based on the work results, the technological and clinical monitoring of algorithms is performed. According to international studies, the technological tests (monitoring of technological parameters) are an integral part of product tests and are performed as part of comprehensive tests for the possible use in real clinical practice [11]. Therefore, this study focused on monitoring technological defects.

STUDY AIMS

This study aimed to evaluate the technological defects of AI-based software based on the results of the Experiment, analyze and statistically process them, and assess the impact on the safety and quality of AI-based software in clinical practice.

MATERIALS AND METHODS

Conditions of the study

For all studies analyzed by the AI-based software during the reporting period for the “mammography” modality in 2021, monitoring was performed in accordance with the categories of errors shown in Table 1 (left column, according to order no. 51 of the Moscow Healthcare Department; January 26, 2021) [12]:

- **Group A:** The time to analyze a study exceeds 6.5 min. The time limit was derived as the average time required to describe an AI-based software study to obtain results suitable for use by a radiologist.
- **Group B:** No results from the evaluated studies.
- **Group C:** The images included in the AI-based software results do not match those of the native (source) study (they are damaged). In rare cases, changing the metadata can change the settings when viewing studies, making it more difficult to visualize the original image.
- **Group D:** Incorrect operation of the declared AI-based software functions that complicates the HCP’s work or makes it impossible to perform with adequate quality, including cropping of images, changes in brightness/contrast, missing description of results, and missing markers of abnormalities.
- **Group E:** Other violations of the integrity and content of the study file, limiting its diagnostic interpretation, including off-target markings and AI-based software analysis based on incorrect anatomy.
- **Group F:** A modification of the original series of studies. In 2022, the errors were restructured. This was considered when processing the monitoring data for the CT modality (Table 1, right column).

Study Duration

Monitoring was performed monthly until the end of the use of the AI-based software in the Experiment. The reporting monitoring period is one calendar month. Based on the data from days 10 and 20 of each month, an interim report for monitoring of Group A and B errors was prepared and sent to the AI-based software manufacturer.

For samples of mammograms and brain CTs, the article provides information on defects from March to December 2021 and from May 2022 to May 2023, respectively. For different AI-based software, the frequency of monitoring is different owing to variations in the time of entry into the Experiment and time of improvement after receiving feedback.

Technological monitoring was performed by a group of experts, including technical specialists and radiologists, who received additional training in monitoring and instruction in working with specific AI-based software. Moreover, to report the performed monitoring, a unified internal reporting form

Table 1. Criteria correlation for technological defects in orders from the Moscow Department of Health

Technological defects according to order no. 51 of the Moscow Department of Health dated January 26, 2021 (for mammography data presented in the article)	Technological defects according to Order No. 160 of the Moscow Department of Health dated November 3, 2022 (restructured) (for the brain CT data presented in the article)
Group A: study analysis time >6.5 min	Group A: analysis time of one study >6.5 min
Group B: missing results of the studies evaluated	Group B: missing results of the studies evaluated
–	Group C: incorrect operation of the declared functions of AI-based software, which complicates the work of radiologist or makes it impossible to perform it with proper quality
D2: no additional series	C1: no additional series
D3: no DICOM SR	C2: no DICOM SR
D4: presence of two or more DICOM SRs	C3: presence of two or more DICOM SRs
D5: no name for AI-based software	C4: no name for AI-based software
D6: missing information about the AI-based software version	C5: missing information about the AI-based software version
–	Group D: defects related to the display of the image area
C1: images are cropped	D1: images of additional series are cropped
C2: brightness/contrast changed	D2: brightness/contrast of the additional series does not match the original image
C3: not all necessary images were evaluated	D3: not all necessary images were evaluated
D1: complete absence of AI-based software results	Excluded
D7: no warning label “For research/scientific use only”	D4: no warning label “For research/scientific use only”
D8: missing markings of abnormalities	F: defects related to clinical work
E1: inconsistent DICOM SR information and additional series	Excluded
F: change to the original study series	D5: change to the original study series
–	Group E: other violations of the integrity and content of the study file that limit its diagnostic interpretation, including
E2: off-target markings	E1: off-target markings
E3: incorrect anatomy, projection, or series were analyzed	E2: incorrect anatomy, projection, or series were analyzed

SR: structure report

and technological monitoring instructions were developed and used.

Statistical analysis

A pseudorandomly selected dataset (study sample) was used for testing during technology monitoring, with the following proportions considered: 25% of studies with no abnormalities detected by the AI-based software (no-abnormality group) and 75% of studies with abnormalities detected (abnormality group). Selected studies with AI-based software results were assessed for technological errors. The study was assigned to the abnormality group if it exceeded the optimal threshold set during testing; otherwise, it was classified as a no-abnormality study [13,14].

In 2021, the pseudorandom sample size of the Experiment was 20 studies per month. This was still the pilot phase of the project. The nomogram power level was 42.5%, with a statistical significance level of 0.05. The standard difference between the sample elements was 0.79 [15]. In a full-scale project after 2021, with the use of risk analysis, the sample

size was 80 studies (see the justification in the article by Chetverikov et al. [13]). These 80 exams formed the monthly sample for brain CT scans.

RESULTS

In total, 14 samples from 20 studies were used in technology monitoring for the mammography modality. From March to December 2021, the generated pseudorandom samples were sent monthly for testing to all working (not under development) AI-based software.

To evaluate the applicability of the method for identifying technological defects, a similar analysis of generated pseudorandom samples was performed for the brain CT modality for the detection of intracranial hemorrhage. From May 2022 to May 2023, 80 studies per month were submitted to test the AI-based software (12 samples of 80 studies in total).

To represent changes in technological defects over time, general statistics were used for all technological monitoring

results of the AI-based software from March to December 2021 (for the mammography modality) or from May 2022 to May 2023 (for the CT modality). The number of technological defects was calculated as a percentage of the total number of studies in the dataset.

Figure 1 shows the changes in the average number of technological defects for the mammography modality from March 2021 to December 2021. The y-axis represents the presence of defects (expressed as a percentage of the total number of studies in the sample), and the x-axis represents the reporting period in months. Figure 2 provides similar information for the brain CT modality (from May 2022 to May 2023).

The left column of Table 1 shows the defects of the mammography modality. As shown in Figure 1, at the beginning

of the study period, most errors belonged to groups C, D, and B. At the end of the study period, only Group C errors remained, although their percentage decreased significantly.

Moreover, the right column of Table 1 presents the errors of the CT modality. As shown in Figure 2, the percentage of errors in relation to the sample was lower for all the errors, except for Group B, for the brain CT modality for the detection of intracranial hemorrhage than for the other modalities analyzed. The percentage of Group D and E errors decreased, whereas Group B errors showed a wide range every month.

To quantify this trend, the corresponding trend lines were added. These were linear functions $k \times x + b$, where k indicates the slope of the approximation curve, i.e., it indicates a tendency to increase or decrease the number of defects,

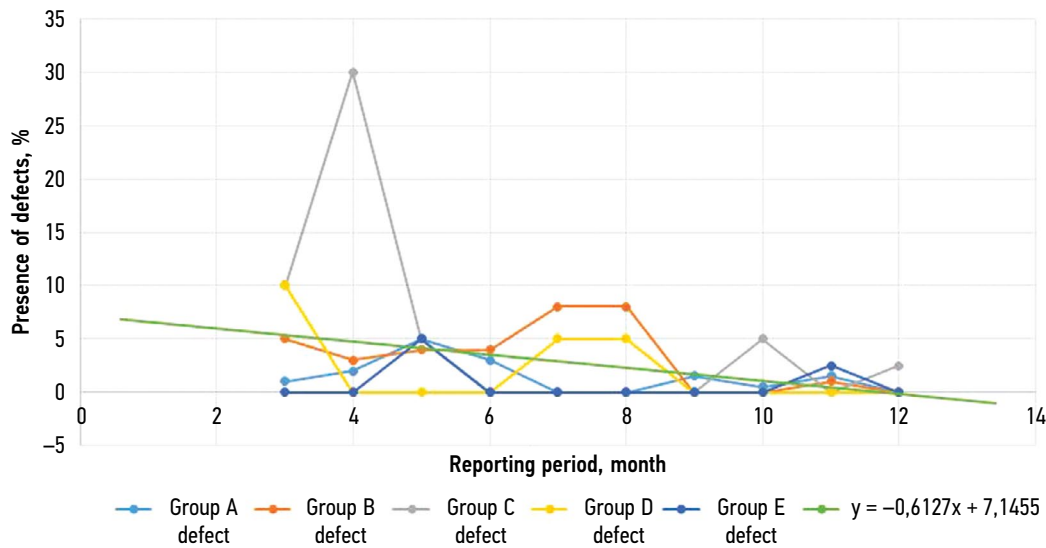


Fig. 1. Changes in detection of the average number of each technological defect for software based on artificial intelligence for mammography. Defects are divided into groups in accordance with order no. 51 of the Moscow Department of Health dated January 26, 2021.

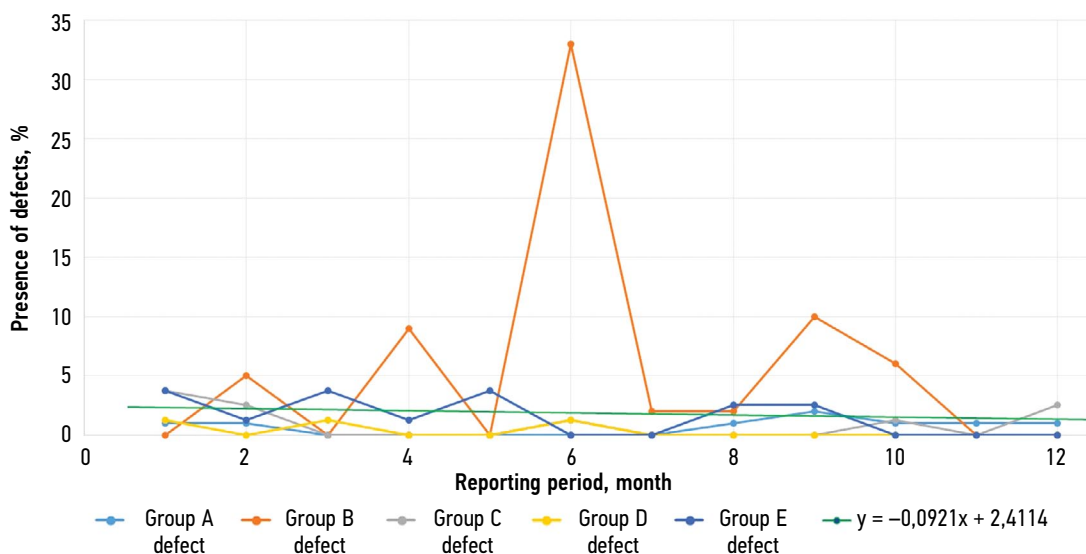


Fig. 2. Changes in the detection of the average number of each technological defect for software based on artificial intelligence for the brain computed tomography modality (presence or absence of intracranial hemorrhage). Defects are divided into groups in accordance with order no. 160 of the Moscow Department of Health dated November 3, 2022.

and b corresponds to the number of defects at the beginning of the monitoring. The approximation was performed for all AI-based software for individual modalities, and the entire data set was approximated at once (Figures 1 and 2). It is possible to predict changes in technological defect removal for each AI-based software product separately or for the entire range if k is known.

Figures 3, 4, 5, and 6 show examples of technological errors in AI-based software.

DISCUSSION

According to the results obtained and evaluated, the mammography modality shows an excellent trend in reducing

the number of technological defects (Figure 1, trend line). The AI-based software with the brain CT modality has a more uniform trend of decreasing the number of technological defects (Figure 2, trend line), despite the values of Group B defects. The reason for this is that the fluctuation of some technological defects is related to the automatic detection, fast feedback, and prompt improvement of the AI-based software by the manufacturer (version change or bug fix).

The AI-based software versions for the mammography modality were changed in September–October 2021, and the average number of Group B and D defects decreased (Figure 1). This may indicate the successful maintenance of AI-based software, which in turn may indicate the effective use of the presented methodology for monitoring technology.

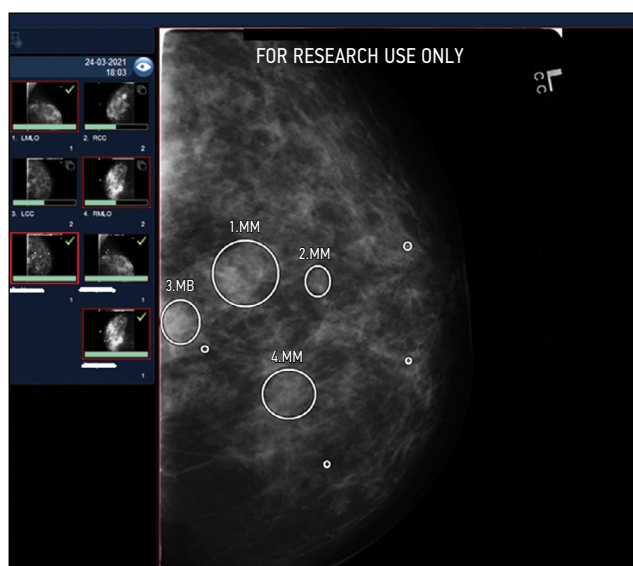


Fig. 3. Defect: not all necessary images have been evaluated. Modality: mammography.

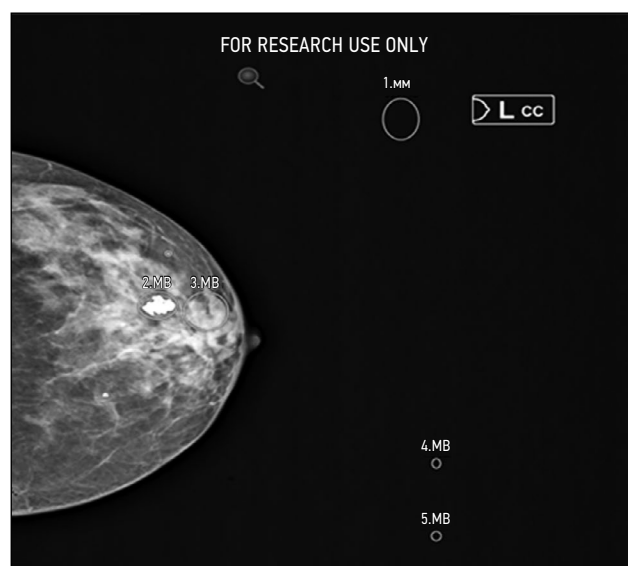


Fig. 4. Defect: off-target markings; Modality: mammography.

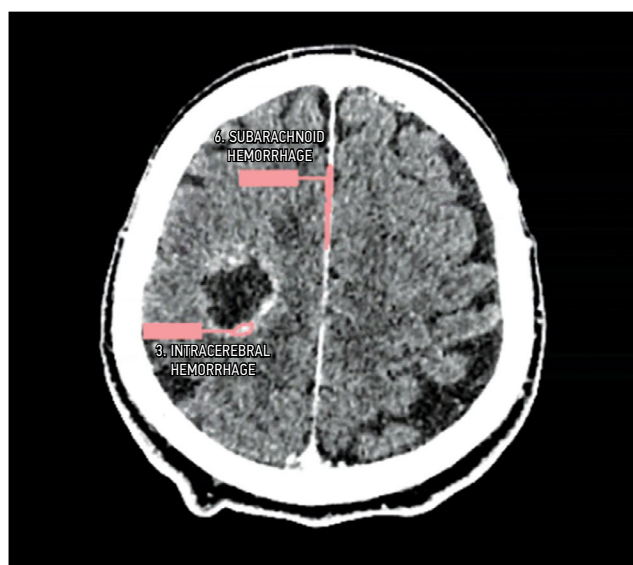


Fig. 5. Defect: an incorrect series was evaluated (contrast-enhanced computed tomography instead of native on). Modality: computed tomography.

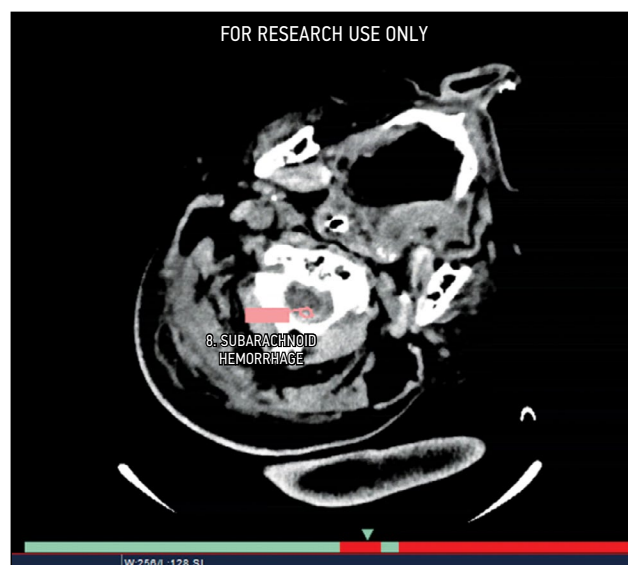


Fig. 6. Defect: off-target markings, contrast-enhanced computed tomography instead of native computed tomography. Modality: computed tomography.

Note that identifying technological defects within technological monitoring may be crucial in comprehensive testing aimed at safer, higher quality, and more efficient software operation using AI not only in diagnostic radiology but also in general healthcare. The analysis showed that the quality of AI-based software increases as the number of defects decreases. Therefore, AI-based software gains more trust from users, minimizes defects, and helps HCPs [16,17].

Restructuring technological defects

In 2022, the groups of technological defects were restructured based on the results of the monitoring of technological defects and their analysis presented in this article. According to the updated group classification (Table 1, right column), AI-based software defects for the brain CT modality were monitored for the presence or absence of intracranial hemorrhage. Group A and B defects were reviewed automatically, whereas Group C, D, and E defects required manual review by experts. The updated list of technological defects is presented in order no. 160 of the Moscow Healthcare Department dated November 3, 2022, which is still valid [18]. The reasons for increasing the number of studies in the sample have been discussed by Chetverikov et al. [13]. Such restructuring of technological defects optimized the work of experts analyzing the AI-based software monitoring results.

In addition, based on the results of technological monitoring of AI-based software under experimental

conditions, technological defects in accordance with the order dated 2021 for the mammography modality can be divided into three groups regarding the safety of AI-based software as a medical product:

- **Defects that affect the safety of patients and work of HCPs:** failure to implement functions declared by the manufacturer; comments that influence a radiologist or complicate their work; and irreversible damage to original research data. This group includes, for example, Group D (D2, D3, D4) and F defects. Separately, a D7 defect (absence of a warning label "For research/scientific use only") should be considered. This defect can only occur in the research setting and can never occur when using AI-based software as a medical device.
- **Defects that do not affect the safety of patients but affect the work of HCPs:** functional defects that do not conform to generally accepted standards for the presentation of research interpretation results. This group includes Group E and C (C1, C2, C3) defects.
- **Defects that do not affect the safety of patients or the work of HCPs:** minor defects that need to be removed to make the work of HCPs more convenient, intuitive, and efficient. This group includes D5, D6, and D8 defects.

For the CT modality, because of the restructuring of the defects (Table 1), three safety subgroups were presented from November 2023 until present, according to the 2021 order:

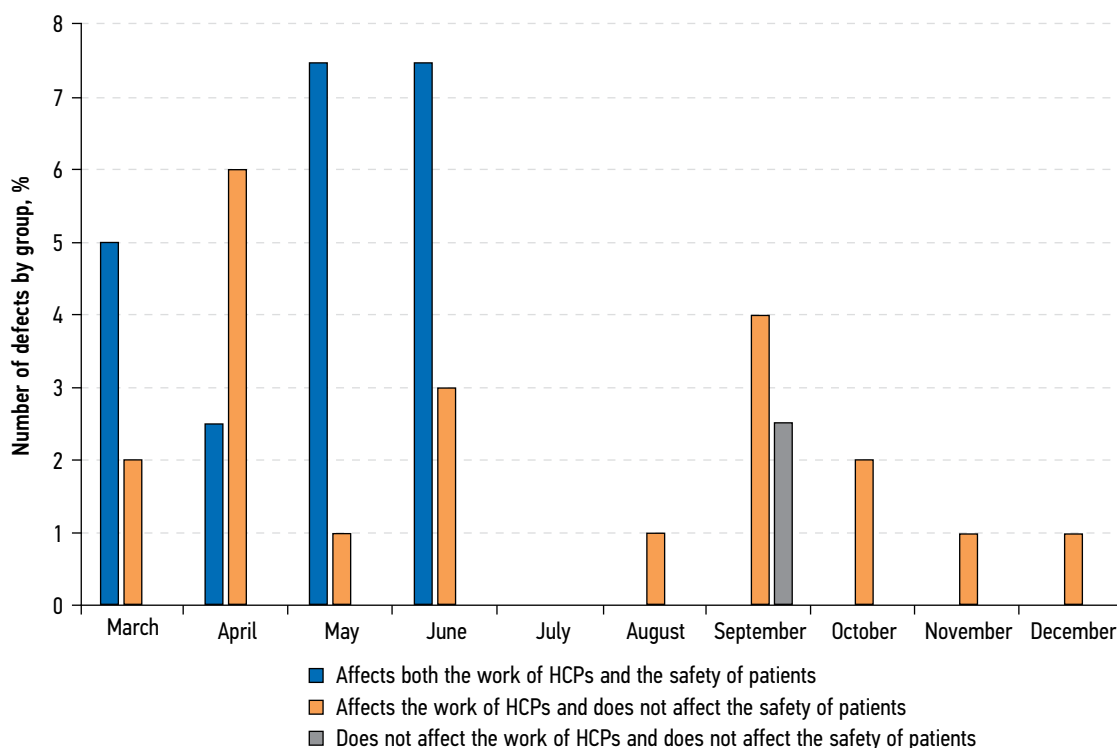


Fig. 7. Number of defects in each group over time; modality: mammography.

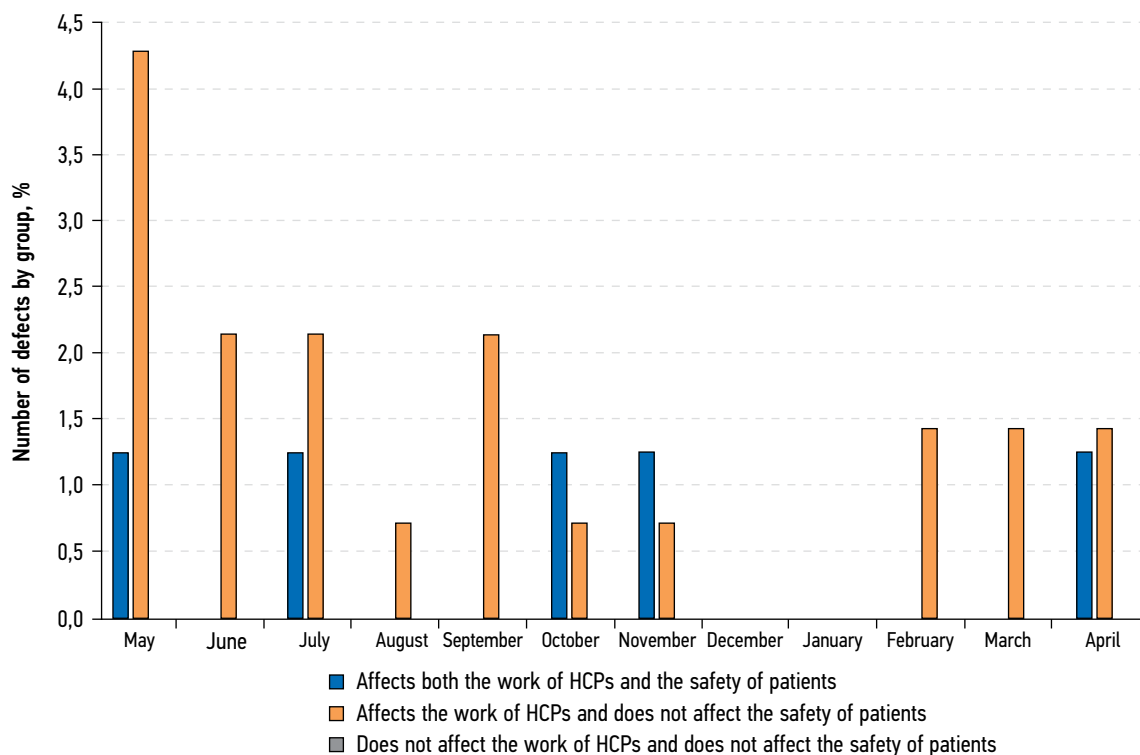


Fig. 8. Number of defects in each group over time; modality: computed tomography.

- **Defects that affect the safety of patients and work of HCPs:** Group C defects (C1, C2, C3) and D4 and D5 defects.
- **Defects that do not affect the safety of patients but affect the work of HCPs:** Group E and D defects (D1, D2, D3).
- **Defects that do not affect the safety of patients and work of HCPs:** C4 and C5 defects.

Figures 7 and 8 show graphical information on the changes in the number of errors by group and month for both modalities.

For the mammography modality (Figure 7), defects that affect patient safety and HCP work were no longer detected after June because of the AI-based software update. Furthermore, defects that affect HCP work but do not affect patient safety tend to decrease by the end of the study period.

For the brain CT modality, the most common defects (those that affect the HCP work but do not affect the patient safety) do not show a clear downward trend.

The methodology presented in the present study allows the monitoring of the technical stability of algorithms. This is of great practical importance when evaluating AI-based software and ensuring its safety. The methodology used to monitor the operation of AI-based software on the stream allowed identifying technological defects and improving solutions, which ultimately led to increasing the technological stability of AI-based software, as shown in the example of brain CT analysis data. Therefore, the

developed methodology proved to be an effective and universal tool for increasing the technical stability of AI-based software.

CONCLUSION

This study presents a list of the main technological defects that occur when implementing AI-based software, as well as a methodology for monitoring technological defects based on regular random control testing, which increases the technical stability of AI-based software. The developed AI-based software testing methodology for identifying technological defects is presented as part of monitoring the safety, quality, and efficiency of AI-based software testing in real world clinical practice.

ADDITIONAL INFORMATION

Funding source. Analysis of technological defects in computed tomography dataset with or without intracranial bleeding was funded by Russian Science Foundation Grant № 22-25-20231, <https://rscf.ru/project/22-25-20231/>.

Competing interests. The authors declare that they have no competing interests.

Authors' contribution. All authors made a substantial contribution to the conception of the work, acquisition, analysis, interpretation of data for the work, drafting and revising the work, final approval of the version to be published and agree to be accountable for all aspects of the work. The contribution is distributed as follows:

V.V. Zinchenko — structuring and analysis of the results obtained (mammography modality), writing the manuscript of the article; K.M. Arzamasov — obtaining technological monitoring data, analyzing the results obtained, correcting the manuscript of the article; E.I. Kremneva — structuring and analysis of the results

obtained (computed tomography modality), writing the manuscript of the article; A.V. Vladzimirskiy — review of the manuscript of the article, formation of the research hypothesis; Yu.A. Vasilev — formation of the research hypothesis, general management of the research.

REFERENCES

1. Vladzimirskii AV, Vasil'ev YuA, Arzamasov KM, et al. *Computer Vision in Radiologic Diagnostics: the First Stage of Moscow experiment*. Vasil'ev YuA, Vladzimirskii AV, editors. Publishing solutions; 2022. (In Russ).
2. Ranschaert ER, Morozov S, Algra PR, editors. *Artificial Intelligence in Medical Imaging*. Berlin: Springer; 2019. doi: 10.1007/978-3-319-94878-2
3. Gusev AV, Dobridnyuk SL. Artificial intelligence in medicine and healthcare. *Information Society Journal*. 2017;(4-5):78–93. (In Russ).
4. Shutov DV, Sharova DE, Abuladze LR, Drozdov DV. Artificial intelligence in clinical physiology: How to improve learning agility. *Digital Diagnostics*. 2023;4(1):81–88. doi: 10.17816/DD123559
5. Meldo AA, Utkin LV, Trofimova TN. Artificial intelligence in medicine: current state and main directions of development of the intellectual diagnostics. *Diagnostic radiology and radiotherapy*. 2020;11(1):9–17. doi: 10.22328/2079-5343-2020-11-1-9-17
6. Recht MP, Dewey M, Dreyer K, et al. Integrating artificial intelligence into the clinical practice of radiology: challenges and recommendations. *European radiology*. 2020;30(6):3576–3584. doi: 10.1007/s00330-020-06672-5
7. Larson DB, Harvey H, Rubin DL, et al. Regulatory Frameworks for Development and Evaluation of Artificial Intelligence-Based Diagnostic Imaging Algorithms: Summary and Recommendations. *Journal of the American College of Radiology*. 2021;18(3 Pt A):413–424. doi: 10.1016/j.jacr.2020.09.060
8. Zinchenko V, Chetverikov S, Ahmad E, et al. Changes in software as a medical device based on artificial intelligence technologies. *International Journal of Computer Assisted Radiology and Surgery*. 2022;17:1969–1977. doi: 10.1007/s11548-022-02669-1
9. Nomura Y, Miki S, Hayashi N, et al. Novel platform for development, training, and validation of computer-assisted detection/diagnosis software. *International Journal of Computer Assisted Radiology and Surgery*. 2020;15(4):661–672. doi: 10.1007/s11548-020-02132-z
10. Methodological recommendations on the procedure for expert examination of quality, efficiency and safety of medical devices (in terms of software) for state registration under the national system FGBU «VNIIMT» Roszdravnadzor. Moscow; 2021. (In Russ).
11. Pemberton HG, Zaki LAM, Goodkin O, et al. Technical and clinical validation of commercial automated volumetric MRI tools for dementia diagnosis — a systematic review. *Neuroradiology*. 2021;63:1773–1789. doi: 10.1007/s00234-021-02746-3
12. Order of the Moscow City Health Department No. 51 dated 26.01.2021 «On approval of the procedure and conditions for conducting an experiment on the use of innovative technologies in the field of computer vision to analyze medical images and further application in the health care system of the city of Moscow in 2021». (In Russ).
13. Chetverikov SF, Arzamasov KM, Andreichenko AE, et al. Approaches to Sampling for Quality Control of Artificial Intelligence in Biomedical Research. *Modern Technologies in Medicine*. 2023;15(2):19. doi: 10.17691/stm2023.15.2.02
14. Zinchenko VV, Arzamasov KM, Chetverikov SF, et al. Methodology for Conducting Post-Marketing Surveillance of Software as a Medical Device Based on Artificial Intelligence Technologies. *Modern Technologies in Medicine*. 2022;14(5):15–25. doi: 10.17691/stm2022.14.5.02
15. Altman DG. Statistics and ethics in medical research: III How large a sample? *British medical journal*. 1980;281(6251):1336. doi: 10.1136/bmj.281.6251.1336
16. Tyrov IA, Vasilyev YuA, Arzamasov KM, et al. Assessment of the maturity of artificial intelligence technologies for healthcare: methodology and its application based on the use of innovative computer vision technologies for medical image analysis and subsequent applicability in the healthcare system of Moscow. *Medical Doctor and IT*. 2022;4(4):76–92. doi: 10.25881/18110193_2022_4_76
17. Vladzimirskiy AV, Gusev AV, Sharova DE, et al. Health Information System Maturity Assessment Methodology. *Medical Doctor and IT*. 2022;3(3):68–84. doi: 10.25881/18110193_2022_3_68
18. Order of the Moscow City Health Department No. 160 dated 03.11.2022 «On Approval of the Procedure and Conditions for Conducting an Experiment on the Use of Innovative Technologies in Computer Vision for Analyzing Medical Images and Further Application in the Moscow City Health Care System in 2022». (In Russ).

СПИСОК ЛИТЕРАТУРЫ

1. Владзими́рский А.В., Васи́льев Ю.А., Арза́масов К.М. и др. Компьютерное зрение в лучевой диагностике: первый этап Московского эксперимента / под ред. Ю.А. Васи́льева, А.В. Влади́мирского. Издательские решения, 2022.
2. Ranschaert E.R., Morozov S., Algra P.R., editors. *Artificial Intelligence in Medical Imaging*. Berlin : Springer, 2019. doi: 10.1007/978-3-319-94878-2
3. Гусев А.В., Добри́днюк С.Л. Искусственный интеллект в медицине и здравоохранении // Информационное общество. 2017. № 4-5. С. 78–93.
4. Шутов Д.В., Шарова Д.Е., Абуладзе Л.П., Дроздов Д.В. Системы искусственного интеллекта в клинической физиологии: как сделать их обучение эффективным? // Digital Diagnostics. 2023. Т. 4, № 1. С. 81–88. doi: 10.17816/DD123559
5. Мелдо А.А., Уткин Л.В., Трофимова Т.Н. Искусственный интеллект в медицине: современное состояние и основные направления развития интеллектуальной диагностики // Лучевая диагностика и терапия. 2020. Т. 11, № 1. С. 9–17. doi: 10.22328/2079-5343-2020-11-1-9-17
6. Recht M.P., Dewey M., Dreyer K., et al. Integrating artificial intelligence into the clinical practice of radiology: challenges and

- recommendations // *European radiology*. 2020. Vol. 30, N 6. P. 3576–3584. doi: 10.1007/s00330-020-06672-5
7. Larson D.B., Harvey H., Rubin D.L., et al. Regulatory Frameworks for Development and Evaluation of Artificial Intelligence-Based Diagnostic Imaging Algorithms: Summary and Recommendations // *Journal of the American College of Radiology*. 2021. Vol. 18, N 3 Pt A. P. 413–424. doi: 10.1016/j.jacr.2020.09.060
8. Zinchenko V., Chetverikov S., Ahmad E., et al. Changes in software as a medical device based on artificial intelligence technologies // *International Journal of Computer Assisted Radiology and Surgery*. 2022. Vol. 17. P. 1969–1977. doi: 10.1007/s11548-022-02669-1
9. Nomura Y., Miki S., Hayashi N., et al. Novel platform for development, training, and validation of computer-assisted detection/diagnosis software // *International Journal of Computer Assisted Radiology and Surgery*. 2020. Vol. 15, N 4. P. 661–672. doi: 10.1007/s11548-020-02132-z
10. Методические рекомендации по порядку проведения экспертизы качества, эффективности и безопасности медицинских изделий (в части программного обеспечения) для государственной регистрации в рамках национальной системы ФГБУ «ВНИИ-ИМТ» Росздравнадзора. Москва, 2021.
11. Pemberton H.G., Zaki L.A.M., Goodkin O., et al. Technical and clinical validation of commercial automated volumetric MRI tools for dementia diagnosis — a systematic review // *Neuroradiology*. 2021. Vol. 63. P. 1773–1789. doi: 10.1007/s00234-021-02746-3
12. Приказ Департамента здравоохранения города Москвы № 51 от 26.01.2021 «Об утверждении порядка и условий проведения эксперимента по использованию инновационных технологий в области компьютерного зрения для анализа медицинских

- изображений и дальнейшего применения в системе здравоохранения города Москвы в 2021 году»
13. Четвериков С.Ф., Арзамасов К.М., Андрейченко А.Е., и др. Подходы к формированию выборки для контроля качества работы систем искусственного интеллекта в медико-биологических исследованиях // *Современные технологии в медицине*. 2023. Т. 15, № 2. С. 19. doi: 10.17691/stm2023.15.2.02
14. Зинченко В.В., Арзамасов К.М., Четвериков С.Ф., и др. Методология проведения пострегистрационного клинического мониторинга для программного обеспечения с применением технологий искусственного интеллекта // *Современные технологии в медицине*. 2022. Т. 14, № 5. С. 15–25. doi: 10.17691/stm2022.14.5.02
15. Altman D.G. Statistics and ethics in medical research: III How large a sample? // *British medical journal*. 1980. Vol. 281, N 6251. P. 1336. doi: 10.1136/bmj.281.6251.1336
16. Тыров И.А., Васильев Ю.А., Арзамасов К.М., и др. Оценка зрелости технологий искусственного интеллекта для здравоохранения: методология и ее применение на материалах Московского Эксперимента по компьютерному зрению в лучевой диагностике // *Врач и информационные технологии*. 2022. № 4. С. 76–92. doi: 10.25881/18110193_2022_4_76
17. Владзимирский А.В., Гусев А.В., Шарова Д.Е., и др. Методика оценки уровня зрелости информационной системы для здравоохранения // *Врач и информационные технологии*. 2022. № 3. С. 68–84. doi: 10.25881/18110193_2022_3_68
18. Приказ Департамента здравоохранения города Москвы от 03.11.2022 № 160 «Об утверждении порядка и условий проведения эксперимента по использованию инновационных технологий в области компьютерного зрения для анализа медицинских изображений и дальнейшего применения в системе здравоохранения города Москвы в 2022 году».

AUTHORS' INFO

* Viktoria V. Zinchenko;

address: 24-1 Petrovka str., 1127051, Moscow, Russian Federation;
ORCID: 0000-0002-2307-725X;
eLibrary SPIN: 4188-0635;
e-mail: ZinchenkoVV1@zdrav.mos.ru

Kirill M. Arzamasov, MD, Cand. Sci. (Med.);

ORCID: 0000-0001-7786-0349;
eLibrary SPIN: 3160-8062;
e-mail: ArzamasovKM@zdrav.mos.ru

Elena I. Kremneva, MD, Cand. Sci. (Med.);

ORCID: 0000-0001-9396-6063;
eLibrary SPIN: 8799-8092;
e-mail: KremnevaEI@zdrav.mos.ru

Anton V. Vladzimirskyy, MD, Dr. Sci. (Med.);

ORCID: 0000-0002-2990-7736;
eLibrary SPIN: 3602-7120;
e-mail: VladzimirskijAV@zdrav.mos.ru

Yuriy A. Vasilev, MD, Cand. Sci. (Med.);

ORCID: 0000-0002-0208-5218;
eLibrary SPIN: 4458-5608;
e-mail: VasilevYA1@zdrav.mos.ru

ОБ АВТОРАХ

* Зинченко Виктория Валерьевна;

адрес: Российская Федерация, 127051, Москва, ул. Петровка, д. 24, стр. 1;
ORCID: 0000-0002-2307-725X;
eLibrary SPIN: 4188-0635;
e-mail: ZinchenkoVV1@zdrav.mos.ru

Арзамасов Кирилл Михайлович, канд. мед. наук;

ORCID: 0000-0001-7786-0349;
eLibrary SPIN: 3160-8062;
e-mail: ArzamasovKM@zdrav.mos.ru

Кремнева Елена Игоревна, канд. мед. наук;

ORCID: 0000-0001-9396-6063;
eLibrary SPIN: 8799-8092;
e-mail: KremnevaEI@zdrav.mos.ru

Владзимирский Антон Вячеславович, д-р мед. наук;

ORCID: 0000-0002-2990-7736;
eLibrary SPIN: 3602-7120;
e-mail: VladzimirskijAV@zdrav.mos.ru

Васильев Юрий Александрович, канд. мед. наук;

ORCID: 0000-0002-0208-5218;
eLibrary SPIN: 4458-5608;
e-mail: VasilevYA1@zdrav.mos.ru

* Corresponding author / Автор, ответственный за переписку

DOI: <https://doi.org/10.17816/DD546163>

Трудности диагностики миокардита: клинический случай

Н.Г. Потешкина^{1,2}, Е.А. Ковалевская^{1,2}, В.Е. Сеницын³, Е.А. Мершина³,
Д.А. Филатова³, Г.Б. Селиванова¹, Я.Р. Шашкина²

¹ Российский национальный исследовательский медицинский университет имени Н.И. Пирогова, Москва, Российская Федерация;

² Городская клиническая больница №52, Москва, Российская Федерация;

³ Медицинский научно-образовательный центр Московского государственного университета имени М.В. Ломоносова, Москва, Российская Федерация

АННОТАЦИЯ

Миокардит нередко является трудным для диагностики заболеванием сердца. Сложности его диагностики объясняются неспецифической симптоматикой или «стёртой» клинической картиной, отсутствием патогномичных признаков при физикальном обследовании, а также тем обстоятельством, что эндомиокардиальная биопсия, являющаяся «золотым стандартом» диагностики, — это инвазивная процедура, которая проводится по строгим показаниям ограниченному количеству пациентов. Тем не менее, по мере развития лучевой диагностики у клиницистов появилась возможность неинвазивной диагностики симптомов воспалительного поражения миокарда, в том числе отёка и миокардиального фиброза, с помощью магнитно-резонансной томографии сердца.

В статье представлен клинический случай пациента молодого возраста с симптомами острого коронарного синдрома, у которого при этом не было выявлено признаков поражения коронарных артерий. С учётом повышения активности кардиоспецифических ферментов и уровней маркёров воспаления, выраженных изменений на электрокардиографии с положительной динамикой, а также факта перенесённой накануне инфекции, был заподозрен миокардит. В результате проведения магнитно-резонансной томографии сердца в динамике диагноз был подтверждён. Таким образом, показана роль визуализирующей методики для дифференциальной диагностики ишемического и воспалительного поражения сердца.

Ключевые слова: миокардит; магнитно-резонансная томография; электрокардиография; тропонин; клинический случай.

Как цитировать:

Потешкина Н.Г., Ковалевская Е.А., Сеницын В.Е., Мершина Е.А., Филатова Д.А., Селиванова Г.Б., Шашкина Я.Р. Трудности диагностики миокардита: клинический случай // Digital Diagnostics. 2023. Т. 4, № 4. С. 605–615. DOI: <https://doi.org/10.17816/DD546163>

DOI: <https://doi.org/10.17816/DD546163>

Difficulties in myocarditis diagnosis: a case report

Natalia G. Poteshkina^{1,2}, Elena A. Kovalevskaya^{1,2}, Valentin E. Sinitsyn³,
Elena A. Mershina³, Daria A. Filatova³, Galina B. Selivanova¹, Yavilika R. Shashkina²

¹The Russian National Research Medical University named after N.I. Pirogov, Moscow, Russian Federation;

²Moscow City Hospital 52, Moscow, Russian Federation;

³Lomonosov Moscow State University Medical Research and Educational Center, Moscow, Russian Federation

ABSTRACT

Myocarditis is often difficult to diagnose. The diagnostic difficulties include nonspecific symptoms or a “vague” clinical picture, absence of pathognomonic signs during physical examination, and endomyocardial biopsy, which is the “gold standard” of diagnosis of myocarditis, being an invasive procedure that is performed under strict indications in certain patients. Nevertheless, as radiology is rapidly developing, clinicians are now able to noninvasively diagnose symptoms of inflammatory myocardial damage, including edema and myocardial fibrosis, using cardiac magnetic resonance imaging. This article presents the clinical case of a young patient with symptoms of acute coronary syndrome, who showed no evidence of coronary artery disease. Myocarditis was suspected because of increased activity of cardiospecific enzymes and high levels of inflammatory markers, pronounced electrocardiography changes with positive dynamics, and recent infection. Magnetic resonance imaging was used to confirm myocarditis diagnosis. Thus, this case study demonstrates the role of imaging techniques in the differential diagnosis of ischemic and inflammatory heart diseases.

Keywords: myocarditis; magnetic resonance imaging; electrocardiography; troponin; case report.

To cite this article

Poteshkina NG, Kovalevskaya EA, Sinitsyn VE, Mershina EA, Filatova DA, Selivanova GB, Shashkina YaR. Difficulties in myocarditis diagnosis: a case report. *Digital Diagnostics*. 2023;4(4):605–615. DOI: <https://doi.org/10.17816/DD546163>

Received: 14.07.2023

Accepted: 31.08.2023

Published online: 14.09.2023

DOI: <https://doi.org/10.17816/DD546163>

心肌炎的诊断难题：临床病例

Natalia G. Poteshkina^{1,2}, Elena A. Kovalevskaya^{1,2}, Valentin E. Sinitsyn³,
Elena A. Merzhina³, Daria A. Filatova³, Galina B. Selivanova¹, Yavilika R. Shashkina²

¹ The Russian National Research Medical University named after N.I. Pirogov, Moscow, Russian Federation;

² Moscow City Hospital 52, Moscow, Russian Federation;

³ Lomonosov Moscow State University Medical Research and Educational Center, Moscow, Russian Federation

简评

心肌炎通常是一种难以诊断的心脏病。非特异性症状或不明显的临床表现、体格检查中缺乏病理征象都是诊断困难的原因。心内膜活检（诊断的“金标准”）是一种侵入性手术，这也是诊断困难的原因。只有在严格的适应症下，才会对少数患者实施这种手术。不过，随着放射诊断技术的发展，医生现在有机会对炎症性心肌损伤症状（包括水肿和心肌纤维化）进行非侵入性诊断。这种诊断是通过心脏磁共振成像（MRI）进行的。

文章介绍一个年轻患者的临床病例，该患者有急性冠状动脉综合症的症状。但是没有发现冠状动脉损伤的迹象。观察到的是，心脏特异性酶活性和炎症标志物的水平升高，心电图检查出现明显变化并呈正方向变动。此外，还注意到患者以前曾感染过病毒。考虑到这些情况，怀疑是心肌炎。心脏动态磁共振成像结果证实了这一诊断。由此可见，本文强调了成像技术在鉴别诊断缺血性和炎症性心脏病变中的作用。

关键词： 心肌炎；磁共振成像；心电图检查；肌钙蛋白；临床病例。

引用本文：

Poteshkina NG, Kovalevskaya EA, Sinitsyn VE, Merzhina EA, Filatova DA, Selivanova GB, Shashkina YaR. 心肌炎的诊断难题：临床病例. *Digital Diagnostics*. 2023;4(4):605–615. DOI: <https://doi.org/10.17816/DD546163>

收到：14.07.2023

接受：31.08.2023

发布日期：14.09.2023

BACKGROUND

Acute myocarditis is defined as a sudden inflammatory injury to the heart muscles. Worldwide, approximately 4–14 cases per 100,000 are reported annually, and 1%–7% die from the disease [1]. Therefore, timely diagnosis is extremely important for clinicians to establish prognosis and treatment strategies.

Poorly defined symptoms at onset, lack of specific clinical signs of myocarditis, minimal changes on physical examination [2], and infrequent use of endomyocardial biopsy as the “gold standard for diagnosis” lead to the underdiagnosis of this disease in real-world practice [3].

However, criteria for diagnosing myocarditis, such as the presence of a previous infection confirmed by clinical and/or laboratory data and the clinical and diagnostic signs of recurrent heart muscle injury remain relevant [4].

Clinical signs:

- Chest pain
- Arrhythmias of unknown origin
- Signs and symptoms of heart failure
- Syncopal episodes and/or sudden death prevented (successfully resuscitated)
- Cardiogenic shock: absence of coronary artery (CA) injury and other cardiovascular diseases that could cause this condition

Diagnostic criteria:

- Laboratory criteria, with grade of recommendation (GoR) C and level of evidence (LoE) 5:
 - Increased:
 - Troponins T and I
 - Lactate dehydrogenase
 - Creatine kinase-MB (CK-MB)
 - N-terminal pro-B-type natriuretic peptide (NT-proBNP)
 - Serum cardiac autoantibodies
- Imaging criteria:
 - Electrocardiography (ECG), GoR C, and LoE 4: blockades, arrhythmias, and ST-T changes

- Electrocardiography (ECG), GoR C, and LoE 4: functional and/or structural changes
- Gadolinium-enhanced magnetic resonance imaging (MRI) of the heart, GoR A, and LoE 2: myocardial edema and/or late contrast enhancement
- Morphological criteria, GoR C, and LoE 4: endomyocardial biopsy results

The prevalence of myocarditis is underestimated because of nonspecific symptoms of its onset and/or asymptomatic course. Therefore, every clinical case is interesting for the possibility of diagnosing this disease.

CASE REPORT

Patient M (33 years old) had no comorbidities or family history of cardiovascular disease. He was a non-smoker with a physically active lifestyle. He was admitted to the cardiac intensive care unit for suspected acute coronary syndrome with ST elevation. On admission, he complained of severe retrosternal pain that was “searing and burning.”

Case History

Two days before his hospitalization, the described pain appeared for the first time while resting at night. It lasted for more than an hour and then disappeared spontaneously.

A similar pain attack recurred the next night. However, the pain syndrome lasted longer. ECG recorded by the emergency team showed an inferior atrial rhythm. The heart rate (HR) was 55 beats per minute. II, III, aVF, and V5–6 leads showed ST elevation up to 2 mm. aVR and aVL leads showed ST depression (Figure 1).

The patient presented with severe retrosternal pain and ECG changes that were detected before hospitalization. The patient was treated with 10 mg of intravenous morphine, 600 mg of clopidogrel, and 250 mg of acetylsalicylic acid.

Examination

During admission, the patient’s consciousness was clear; the patient was cooperative, adequate, and oriented. The

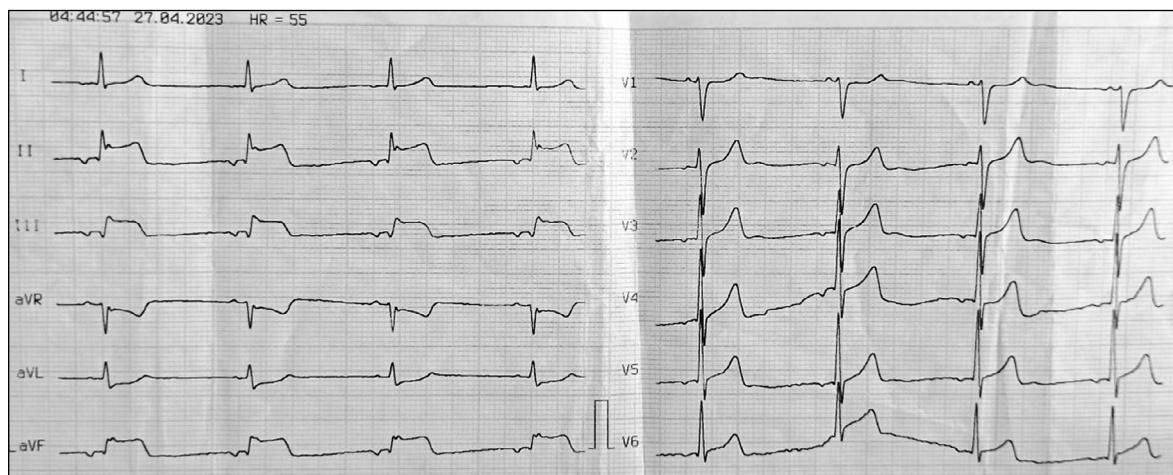


Fig. 1. Pre-hospital ECG of patient M.

skin had normal color and moisture. His vital signs were as follows:

- Body temperature of 36.8°C
- Subcutaneous fat was moderately developed. The body mass index was 27.6 kg/m². No peripheral edema
- Resting respiratory rate: 16 breaths/min
- Saturation: 98% in ambient air
- Blood pressure: 130/80 mmHg
- HR: 100 beats /min, the rhythm was normal

The left border of relative cardiac dullness in the fifth intercostal space was 1.5 cm medial to the left midclavicular line. The right border was along the right edge of the sternum. The upper border was in the third intercostal space.

Physiological accentuation of heart sounds was preserved. No heart murmurs were heard. Lung breathing was vesicular. No wheezing was heard. The abdomen was soft and painless. The liver was not enlarged (Kurlov ordinates were 10 × 8 × 7 cm). The spleen was not palpable. Stool and diuresis were normal.

C-reactive protein, antistreptolysin O, troponin I, and aspartate aminotransferase levels were elevated (Table 1).

Based on the clinical picture, ECG changes, and elevated cardiac enzymes on admission, the diagnosis was ST-elevation myocardial infarction. Emergency coronary angiography (CAG) was performed, which showed no stenotic lesions of the coronary bed in the left (Figure 2, *a*) and right (Fig. 2, *b*) coronary arteries. Signs of moderate peripheral vasospasm were observed (Figure 2).

Based on ECHO-CG data, the left ventricular (LV) ejection fraction was 60%. No abnormalities in local contractility were reported. The diastolic function of the left ventricle was not affected. No signs of myocardial hypertrophy of the left ventricle were observed. The cardiac cavities were not dilated. The contractile function of the right ventricular (RV) myocardium was preserved. The systolic pressure of the pulmonary artery was 23 mmHg with grade 0–1 tricuspid regurgitation. Some pericardial thickening was detected.

Table 1. Laboratory data of patient M.

Parameter	Results	Reference
Hemoglobin, g/L	140	130–160
RBC, 10 ¹² /L	5.04	4.00–5.00
WBC, 10 ⁹ /L	6.5	4.00–9.00
Lymphocytes, 10 ⁹ /L	2.5	2.0–6.5
C-reactive protein, mg/L	10.45*	up to 6
Aspartate aminotransferase, U/L	65*	up to 50
CK-MB, U/L	1.0	up to 25
Antistreptolysin O, GE/mL	738.9*	up to 200
Total anticardiolipin antibodies, IU/L	1.7	up to 12
dsDNA IgG antibodies, IU/mL	2.6	up to 20.0
Antinuclear antibodies (semiquantitative)	0.2	up to 1.0
Troponin I (quantitative), ng/mL	2.6*	up to 0.2
NT-proBNP	54	0–125

Daily ECG monitoring showed the following:

- The main rhythm was sinus one with episodic sinus tachycardia, moderate sinus bradycardia, and sinus arrhythmia.
- The mean HR was 73 beats per minute.
- The maximum mean HR was 111 beats per minute.
- The minimum mean HR was 53 beats per minute.
- Three individual supraventricular extrasystoles occurred; no rhythm pauses lasting >2 s were reported.
- ST elevation was recorded up to 0.2–1.0 mm (in one lead).

Treatment

The patient was treated with angiotensin-converting enzyme inhibitors, mineralocorticoid receptor antagonists,

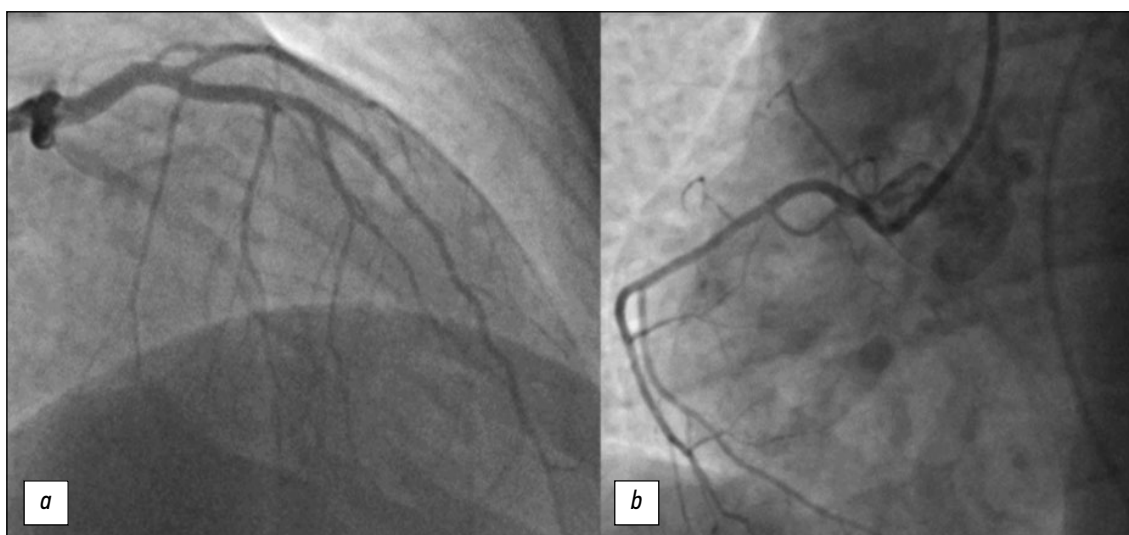


Fig. 2. Coronary angiography of patient M. (*a*) left coronary artery, (*b*) right coronary artery.

and beta-blockers. During therapy, his condition improved, and the chest pain did not recur. Troponin I and inflammatory marker levels normalized within 10 days.

ECG showed positive changes (Figure 3):

- Focal myocardial changes in posterior phrenic and lateral LV walls in qR II, Qr III, and qr aVF leads.
- SR elevation in II, III, aVF, and V4–6 leads to 0.8 mm (over time, regression was >50% of the baseline one) with negative T waves in II, III, aVF, and V5–6 leads.

Clinical diagnosis

Therefore, according to ECHO-CG data, a young patient with severe chest pain had intact coronary arteries and preserved LVEF with no abnormalities in local/diffuse contractility. Moreover, the initial increase in troponin, antistreptolysin O, aspartate aminotransferase, and C-reactive protein levels was noted with significant positive ECG changes, so the diagnosis of myocarditis was discussed.

A detailed interview revealed that 10–12 days before admission, the patient had a sore throat and a fever exceeding 38°C for 3 days. A nasopharyngeal swab was negative for coronavirus infection by polymerase chain reaction. The outpatient antibacterial therapy was reported to reduce fever and sore throat.

Since the infection was chronologically associated with clinical signs of the disease and pseudo-infarction ECG changes in the absence of coronary artery disease and with elevated cardiac enzymes, the possibility of acute myocarditis was high. To confirm the diagnosis, a cardiac MRI was performed using a gadolinium contrast agent.

The contrast-enhanced cardiac MRI did not show any enlargement of the heart chambers.

- An end-diastolic size (EDD) of the left ventricle was 52 mm.
- An indexed end-diastolic volume (EDV) of the left ventricle was 59 (reference, 59) mL/m².
- The EDD of the right ventricle was 43 mm.
- The indexed EDV of the right ventricle was 72 (reference, 57–109) mL/m².

- The sizes of the left and right atria were 41 and 48 mm, respectively.

The RV myocardium was 3–4 mm thick. No areas of local bulging or dyskinesia of the free RV wall were identified.

The LV myocardium was not hypertrophied: the thickness of the basal and middle segments did not exceed 10 mm, the thickness of the apical segments was 4–5 mm, and the indexed LV myocardial mass was 56 (reference, 41–86) g/m². Uniform thickening of the LV myocardium was reported during systole. No abnormalities in segmental contractility of the LV myocardium were detected. No decrease in overall LV contractility was reported with an LVEF of 64%.

No blood clots were found in the heart chambers. First-degree mitral regurgitation and first-degree tricuspid regurgitation were reported. The thoracic aorta had smooth contours and was not dilated, and the blood flow signal in its lumen was uniform. The pulmonary artery and its branches were not dilated. The superior and inferior vena cava were not dilated. In the pericardial cavity, trace amounts of free fluid were found at the level of the basal lateral LV and middle RV segments. The pericardial layers were not thickened, and the contrast agent did not accumulate. No hydrothorax was reported.

Signs of myocardial inflammation were noted including areas of early and delayed contrast enhancement in the basal and middle lateral and lower segments with the transition to the apical lower segment of the left ventricle (Figure 4a–c), as well as signs of myocardial edema in these segments (Figure 5a).

Conclusion on the cardiac MRI: MR signs of early subacute myocarditis (myocardial areas of early and delayed contrast enhancements in the lower and lateral LV walls with signs of edema).

Based on clinical, historical, laboratory, and instrumental data, the following diagnosis was made: acute infectious and allergic myocarditis, pseudocoronary clinical variant, subacute course; CAG: without stenotic lesions of the coronary arteries.

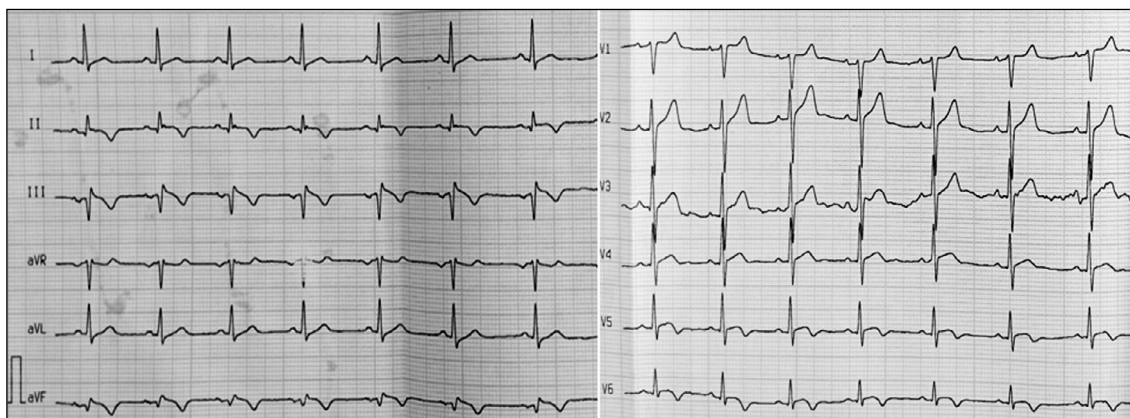


Fig. 3. ECG of patient M. over time.

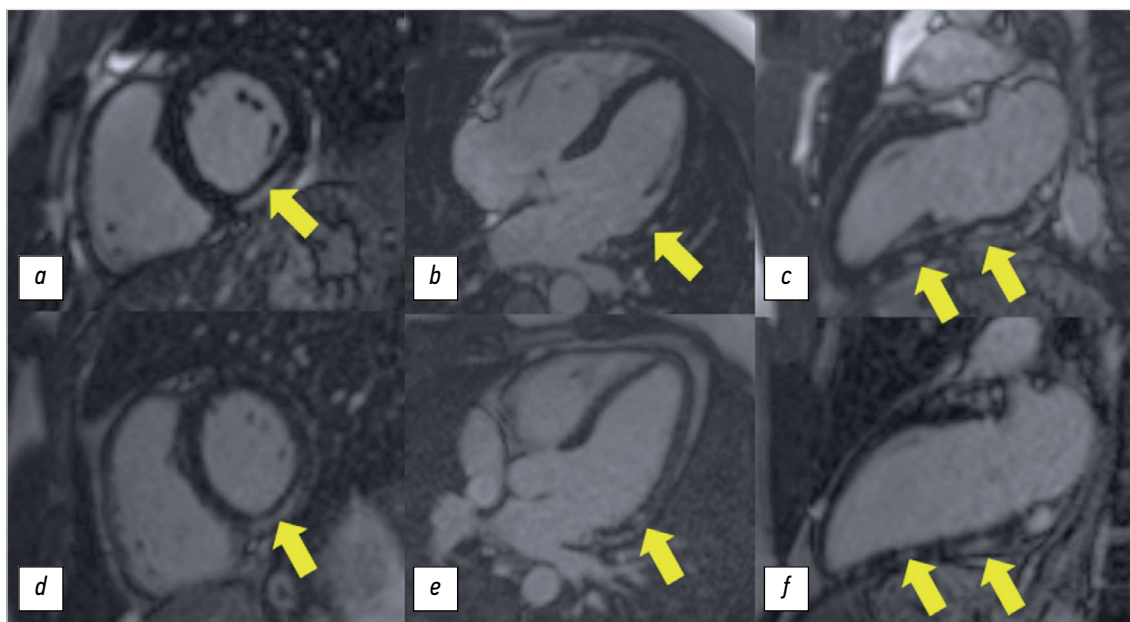


Fig. 4. Cardiac MRI in the delayed gadolinium enhancement mode (7–15 min after the administration of the contrast agent): *a, d*, short axis of the left ventricle in the basal segments; *b, e*, long axis of the left ventricle, four-chamber projection; *c, f*, long axis of the left ventricle, two-chamber projection. Top row, *a–c*, cardiac MRI initially: subepicardial areas of contrast enhancement (yellow arrows) are located in the basal and medial lateral and inferior segments with the transition to the apical inferior segment of the left ventricle; *d–f*, cardiac MRI in dynamics after 1.5 months: areas of delayed enhancement of the same localization and intensity remain.

According to the Mayo Clinic, myocarditis classification [5] using baseline characteristics, the patient had a low risk of cardiovascular complications and a favorable prognosis (Table 2). However, an intermediate-risk group could be considered based on cardiac MRI data.

The patient was discharged with improvement. He was recommended to continue the prescribed therapy and subject to cardiac MRI over time.

After 1.5 months, the contrast-enhanced MRI of the heart showed that the area of subepicardial delayed enhancement

of the previous extent remained in the basal and middle inferior segments (Figure 4*d–f*), and no evidence of myocardial edema was found in these segments (Figure 5*b*).

DISCUSSION

The guidelines of the European Society of Cardiology [6] and the Russian clinical guidelines for the diagnosis of myocarditis [4] emphasize the effectiveness of cardiac MRI. For this purpose, the Lake Louise criteria were developed

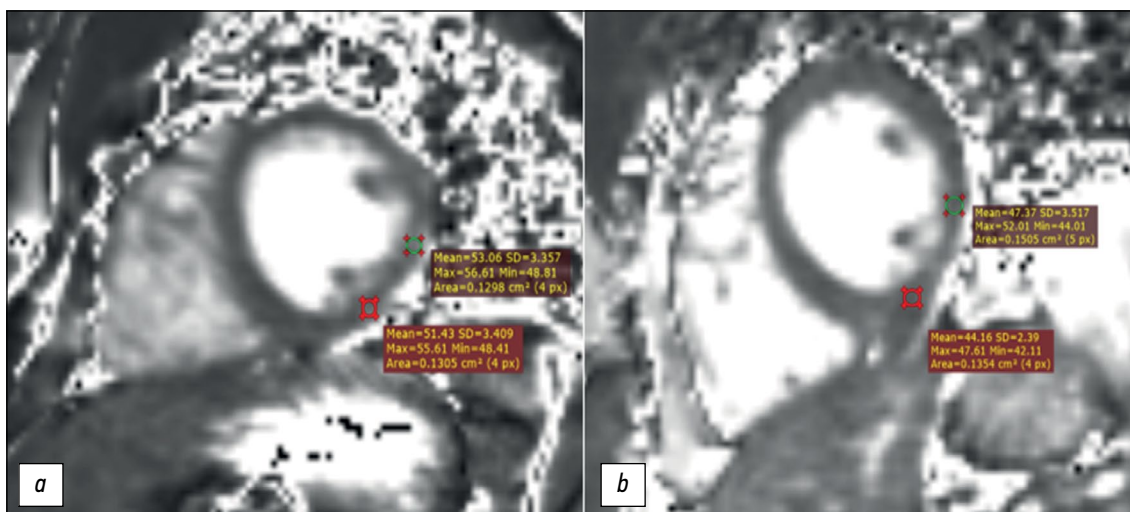


Fig. 5. Cardiac MRI T2 mapping along the short axis of the left ventricle in the basal segments: *a*, cardiac MRI at baseline: there is an increase in T2 parameter (>50 ms) in the inferior and inferolateral segments, indicating the presence of edema; *b*, cardiac MRI after 1.5 months: native T2 parameter within normal values (<50 ms). The numbers indicate the T2 parameter values in msec.

Table 2. Clinical variants of myocarditis onset (Mayo Clinic)

Low risk	Intermediate risk ("gray area")	High risk
Chest pain	Moderate persistent structural and functional changes in the myocardium	Severe persistent LV dysfunction and circulatory decompensation
Supraventricular rhythm disorders	Nonsustained ventricular arrhythmias	Life-threatening arrhythmias
AV block	No life-threatening rhythm and conduction disorders	Persistent AV block
Preserved LVEF	Late gadolinium accumulation in the myocardium without cardiac chamber remodeling	Recurrent syncope
Rapid response to therapy (1–4 weeks)		
Favorable prognosis	Uncertain prognosis	Unfavorable prognosis

and first published in 2009. They included the assessment of signal hyperintensity on T2-weighted images (T2WI), short T1 inversion recovery sequences, and delayed non-coronary enhancement [7].

As the effectiveness of the original Lake Louise criteria was limited by the subjective nature of the qualitative assessment of the above signs, the criteria were revised in 2018. They have been supplemented with parametric mapping, which allows the quantitative assessment of regional and global myocardial relaxation times T1 and T2 and extracellular volume (ECV). As a result, the new Lake Louise criteria have higher rates of sensitivity and specificity (88% and 96%, respectively) than the old Lake Louise criteria [8].

If at least one criterion in each category is met, cardiac inflammation is confirmed:

- T2WI signs of myocardial edema (myocardial T2WI hyperintensity or high T2 relaxation index) [9]
- T1WI signs of myocardial injury (non-ischemic pattern of delayed contrast enhancement or high T1 relaxation index and/or ECV) [10]

If only one marker is present, myocardial inflammation may be considered in the presence of clinical and/or laboratory manifestations; however, the specificity of MRI in this case is lower. Other signs of heart inflammation include systolic dysfunction (areas of hypokinesia or akinesia) and signs of pericarditis (contrast enhancement of the pericardial layers). The use of these criteria is warranted only when symptoms and signs of inflammatory heart diseases are present and not as a screening technique for asymptomatic patients [11, 12].

In this case report, contrast-enhanced cardiac MRI confirmed the clinical diagnosis. According to cardiac MRI, the patient initially had one of the above criteria for diagnosing

myocarditis (myocardial edema on T2 mapping and evidence of non-ischemic myocardial injury on delayed gadolinium enhancement). MRI performed after 1.5 months showed no signs of myocardial edema, indicating a decrease in acute myocardial inflammation.

CONCLUSION

Therefore, contrast-enhanced cardiac MRI is a highly informative imaging modality for myocardial inflammation, for primary diagnosis and long-term assessment, allowing for definitive confirmation of the diagnosis.

ADDITIONAL INFORMATION

Funding source. This article was not supported by any external sources of funding.

Competing interests. The authors declare that they have no competing interests.

Authors' contribution. All authors made a substantial contribution to the conception of the work, acquisition, analysis, interpretation of data for the work, drafting and revising the work, final approval of the version to be published and agree to be accountable for all aspects of the work. Poteshkina N.G. — development of the article concept, text writing; Kovalevskaya E.A. — text writing and reviewing, Sinitsyn V.E. — development of the article concept, approval of the final version of the text, Mershina E.A. — approval of the final version of the text, Filatova D.A. — text writing and reviewing, Selivanova G.B. — text writing and reviewing, Shashkina Y.R. — text writing and reviewing.

Consent for publication. Written consent was obtained from the patient for publication of relevant medical information and all of accompanying images within the manuscript in Digital Diagnostics Journal.

REFERENCES

1. Ammirati E, Moslehi JJ. Diagnosis and Treatment of Acute Myocarditis: A Review. *JAMA*. 2023;329(13):1098–1113. doi: 10.1001/jama.2023.3371
2. Caforio ALP, Calabrese F, Angelini A, et al. A prospective study of biopsy-proven myocarditis: prognostic relevance of clinical and aetiopathogenetic features at diagnosis. *European Heart Journal*. 2007;28(11):1326–1333. doi: 10.1093/eurheartj/ehm076
3. Leone O, Veinot JP, Angelini A, et al. 2011 Consensus statement on endomyocardial biopsy from the Association for European

Cardiovascular Pathology and the Society for Cardiovascular Pathology. *Cardiovascular Pathology*. 2012;21(4):245–274. doi: 10.1016/j.carpath.2011.10.001

4. Arutyunov GB, Paleev FN, Moiseeva OM, et al. 2020 Clinical practice guidelines for Myocarditis in adults. *Russian Journal of Cardiology*. 2021;26(11):4790. (In Russ) doi: 10.15829/1560-4071-2021-4790

5. Schultz JC, Hilliard AA, Cooper LT, et al. Diagnosis and Treatment of Viral Myocarditis. *Mayo Clinic Proceedings*. 2009;84(11):1001–1009. doi: 10.1016/s0025-6196(11)60670-8

6. Caforio ALP, Pankuweit S, Arbustini E, et al. Current state of knowledge on aetiology, diagnosis, management, and therapy of myocarditis: a position statement of the European Society of Cardiology Working Group on Myocardial and Pericardial Diseases. *European Heart Journal*. 2013;34(33):2636–2648. doi: 10.1093/eurheartj/ehz210

7. Friedrich MG, Sechtem U, Schulz-Menger J, et al. Cardiovascular Magnetic Resonance in Myocarditis: A JACC White Paper. *Journal of the American College of Cardiology*. 2009;53(17):1475–1487. doi: 10.1016/j.jacc.2009.02.007

8. Tijmes FS, Thavendiranathan P, Udell JA, et al. Cardiac MRI Assessment of Nonischemic Myocardial Inflammation: State of the

Art Review and Update on Myocarditis Associated with COVID-19 Vaccination. *Radiology: Cardiothoracic Imaging*. 2021;3(6):e210252. doi: 10.1148/ryct.210252

9. Srichai MB, Lim RP, Lath N, et al. Diagnostic performance of dark-blood T2-weighted CMR for evaluation of acute myocardial injury. *Investigative Radiology*. 2013;48(1):24–31. doi: 10.1097/rli.0b013e3182718672

10. Galán-Arriola C, Lobo M, Vilchez-Tschischke JP, et al. Serial Magnetic Resonance Imaging to Identify Early Stages of Anthracycline-Induced Cardiotoxicity. *Journal of the American College of Cardiology*. 2019;73(7):779–791. doi: 10.1016/j.jacc.2018.11.046

11. Blagova OV, Pavlenko EV, Varionchik NV, et al. Myocarditis as a legitimate phenomenon in patients with primary noncompaction myocardium: diagnosis, treatment and impact on outcomes. *Russian Journal of Cardiology*. 2018;23(2):44–52. (In Russ) doi: 10.15829/1560-4071-2018-2-44-52

12. Filatova DA, Mershina EA, Sinitsyn VE. COVID-19-related cardiac lesion: The questions of pathogenesis and diagnostics. *Digital Diagnostics*. 2023;4(2):156–169. (In Russ) doi: 10.17816/DD284706

СПИСОК ЛИТЕРАТУРЫ

1. Ammirati E, Moslehi J.J. Diagnosis and Treatment of Acute Myocarditis: A Review // *JAMA*. 2023. Vol. 329, N 13. P. 1098–1113. doi: 10.1001/jama.2023.3371

2. Caforio A.L.P., Calabrese F., Angelini A., et al. A prospective study of biopsy-proven myocarditis: prognostic relevance of clinical and aetiopathogenetic features at diagnosis // *European Heart Journal*. 2007. Vol. 28, N 11. P. 1326–1333. doi: 10.1093/eurheartj/ehm076

3. Leone O., Veinot J.P., Angelini A., et al. 2011 Consensus statement on endomyocardial biopsy from the Association for European Cardiovascular Pathology and the Society for Cardiovascular Pathology // *Cardiovascular Pathology*. 2012. Vol. 21, N 4. P. 245–274. doi: 10.1016/j.carpath.2011.10.001

4. Арутюнов Г.Б., Палеев Ф.Н., Моисеева О.М., и др. Миокардиты у взрослых. Клинические рекомендации 2020 // *Российский кардиологический журнал*. 2021. Т. 26, №11. С. 4790. doi: 10.15829/1560-4071-2021-4790

5. Schultz J.C., Hilliard A.A., Cooper L.T., et al. Diagnosis and Treatment of Viral Myocarditis // *Mayo Clinic Proceedings*. 2009. Vol. 84, N 11. P. 1001–1009. doi: 10.1016/s0025-6196(11)60670-8

6. Caforio A.L.P., Pankuweit S., Arbustini E., et al. Current state of knowledge on aetiology, diagnosis, management, and therapy of myocarditis: a position statement of the European Society of Cardiology Working Group on Myocardial and Pericardial Diseases // *European Heart Journal*. 2013. Vol. 34, N 33. P. 2636–2648. doi: 10.1093/eurheartj/ehz210

7. Friedrich M.G., Sechtem U., Schulz-Menger J., et al. Cardiovascular Magnetic Resonance in Myocarditis: A JACC White Paper // *Journal of the American College of Cardiology*. 2009. Vol. 53, N 17. P. 1475–1487. doi: 10.1016/j.jacc.2009.02.007

8. Tijmes F.S., Thavendiranathan P., Udell J.A., et al. Cardiac MRI Assessment of Nonischemic Myocardial Inflammation: State of the Art Review and Update on Myocarditis Associated with COVID-19 Vaccination // *Radiology: Cardiothoracic Imaging*. 2021. Vol. 3, N 6. P. e210252. doi: 10.1148/ryct.210252

9. Srichai M.B., Lim R.P., Lath N., et al. Diagnostic performance of dark-blood T2-weighted CMR for evaluation of acute myocardial injury // *Investigative Radiology*. 2013. Vol. 48, N 1. P. 24–31. doi: 10.1097/rli.0b013e3182718672

10. Galán-Arriola C., Lobo M., Vilchez-Tschischke J.P., et al. Serial Magnetic Resonance Imaging to Identify Early Stages of Anthracycline-Induced Cardiotoxicity // *Journal of the American College of Cardiology*. 2019. Vol. 73, N 7. P. 779–791. doi: 10.1016/j.jacc.2018.11.046

11. Благова О.В., Павленко Е.В., Вариончик Н.В., и др. Миокардит как закономерный феномен у больных с первичным некомпактным миокардом: диагностика, лечение и влияние на исходы // *Российский кардиологический журнал*. 2018. Т. 23, № 2. С. 44–52. doi: 10.15829/1560-4071-2018-2-44-52

12. Филатова Д.А., Мершина Е.А., Синицын В.Е. Поражение сердца при COVID-19: вопросы патогенеза и диагностики // *Digital Diagnostics*. 2023. Т. 4, № 2. С. 156–169. doi: 10.17816/DD284706

AUTHORS' INFO

* **Natalia G. Poteshkina**, MD, Dr. Sci. (Med.), Professor; address: Moscow, Barrikadnaya str, 2/1, 123242 Russian Federation; ORCID: 0000-0001-9803-2139; eLibrary SPIN: 2863-4840; e-mail: nat-pa@yandex.ru

ОБ АВТОРАХ

* **Потешкина Наталия Георгиевна**, д-р мед. наук, профессор; адрес: 123242 г. Москва, ул. Баррикадная, д. 2/1; ORCID: 0000-0001-9803-2139; eLibrary SPIN: 2863-4840; e-mail: nat-pa@yandex.ru

* Corresponding author / Автор, ответственный за переписку

Elena A. Kovalevskaya, MD, Cand. Sci. (Med.), Assistant professor;
ORCID: 0000-0002-0787-4347;
eLibrary SPIN: 8853-2700;
e-mail: tolyaaa@mail.ru

Valentin E. Sinitsyn, MD, Dr. Sci. (Med.), Professor;
ORCID: 0000-0002-5649-2193;
eLibrary SPIN: 8449-6590;
e-mail: vsini@mail.ru

Elena A. Mershina, MD, Cand. Sci. (Med.), Assistant professor;
ORCID: 0000-0002-1266-4926;
eLibrary SPIN: 6897-9641;
e-mail: vsini@mail.ru

Daria A. Filatova, MD;
ORCID: 0000-0002-0894-1994;
eLibrary SPIN: 2665-5973;
e-mail: dariafilatova.msu@mail.ru

Galina B. Selivanova, MD, Dr. Sci. (Med.), Professor;
ORCID: 0000-0003-2980-9754;
eLibrary SPIN: 9711-5041;
e-mail: galina.selivanova@rambler.ru

Yavilika R. Shashkina, MD;
ORCID: 0000-0002-2194-0785;
eLibrary SPIN: 6091-0911;
e-mail: yavilika-medik@mail.ru

Ковалевская Елена Анатольевна, канд. мед. наук, доцент;
ORCID: 0000-0002-0787-4347;
eLibrary SPIN: 8853-2700;
e-mail: tolyaaa@mail.ru

Синицын Валентин Евгеньевич, д-р мед. наук, профессор;
ORCID: 0000-0002-5649-2193;
eLibrary SPIN: 8449-6590;
e-mail: vsini@mail.ru

Мершина Елена Александровна, канд. мед. наук, доцент;
ORCID: 0000-0002-1266-4926;
eLibrary SPIN: 6897-9641;
e-mail: vsini@mail.ru

Филатова Дарья Андреевна;
ORCID: 0000-0002-0894-1994;
eLibrary SPIN: 2665-5973;
e-mail: dariafilatova.msu@mail.ru

Селиванова Галина Борисовна, д-р мед. наук, профессор;
ORCID: 0000-0003-2980-9754;
eLibrary SPIN: 9711-5041;
e-mail: galina.selivanova@rambler.ru

Шашкина Явилка Романовна;
ORCID: 0000-0002-2194-0785;
eLibrary SPIN: 6091-0911;
e-mail: yavilika-medik@mail.ru;

DOI: <https://doi.org/10.17816/DD508786>

Симптом «рисовых телец» при магнитно-резонансной томографии плечевого сустава у пациентки с ревматоидным артритом

С.Ф. Агеева, Д.А. Филатова, Е.А. Мершина, В.Е. Сеницын

Московский государственный университет имени М.В. Ломоносова, Москва, Российская Федерация

АННОТАЦИЯ

Симптом «рисовых телец» при магнитно-резонансной томографии плечевого сустава у пациентов с ревматоидным артритом — редкая, но специфическая находка, характеризующаяся наличием в синовиальной жидкости сустава, синовиальных сумках или влагаллицах множественных мелких округлых структур, схожих друг с другом, похожих на зёрнышки риса. Этиология «рисовых телец» до сих пор окончательно не ясна. Предполагается, что они образуются в результате микроинфарктов синовиальной оболочки у пациентов с ревматоидным артритом или некоторыми другими воспалительными заболеваниями суставов. Клинически наличие «рисовых телец» может вызывать у пациента болевой синдром, однако так происходит не всегда. Среди методов лучевой диагностики ведущей ролью для выявления «рисовых телец» обладает магнитно-резонансная томография.

В данной статье представлено описание клинического случая выявления этого симптома при магнитно-резонансной томографии плечевого сустава у пациентки с длительным анамнезом ревматоидного артрита, обратившейся в связи с безболезненным увеличением в объёме левого плеча. Выполненные исследования (компьютерная томография и магнитно-резонансная томография левого плечевого сустава) позволили обнаружить симптом «рисовых телец» как проявление основного заболевания и определить дальнейшую тактику лечения.

Ключевые слова: ревматоидный артрит; плечевой сустав; рисовые тельца; магнитно-резонансная томография; компьютерная томография; клинический случай.

Как цитировать:

Агеева С.Ф., Филатова Д.А., Мершина Е.А., Сеницын В.Е. Симптом «рисовых телец» при магнитно-резонансной томографии плечевого сустава у пациентки с ревматоидным артритом // Digital Diagnostics. 2023. Т. 4, №4. С. 616–624. DOI: <https://doi.org/10.17816/DD508786>

DOI: <https://doi.org/10.17816/DD508786>

“Rice bodies” symptoms on magnetic resonance imaging of the shoulder in a patient with rheumatoid arthritis

Sofia F. Ageeva, Daria A. Filatova, Elena A. Mershina, Valentin E. Sinitsyn

Lomonosov Moscow State University, Moscow, Russian Federation

ABSTRACT

The “rice bodies” symptom on magnetic resonance imaging of the shoulder joint in patients with rheumatoid arthritis is a rare but specific finding characterized by the presence of multiple small, round, rice-grain-like structures in the synovial fluid of the joint, synovial pouches, or sheaths. The etiology of the “rice bodies” is still not fully understood. They are suggested as the result of microinfarcts of the synovial membrane in patients with rheumatoid arthritis or other inflammatory joint diseases. Clinically, the “rice bodies” symptom may cause pain, but not in every case. Among radiological diagnostic methods, magnetic resonance imaging is the leading method for the detection of rice bodies. This article presents a clinical case of “rice bodies” symptoms diagnosed by magnetic resonance imaging in a patient with a long history of rheumatoid arthritis who presented with a painless enlargement in the left shoulder. Computed tomography and magnetic resonance imaging of the left shoulder could detect “rice bodies” as a manifestation of an underlying disease and determine further treatment techniques.

Keywords: rheumatoid arthritis; shoulder joint; rice bodies; magnetic resonance imaging; computed tomography; case report.

To cite this article

Ageeva SF, Filatova DA, Mershina EA, Sinitsyn VE. “Rice bodies” symptoms on magnetic resonance imaging of the shoulder in a patient with rheumatoid arthritis. *Digital Diagnostics*. 2023;4(4):616–624. DOI: <https://doi.org/10.17816/DD508786>

Received: 26.06.2023

Accepted: 05.09.2023

Published online: 14.09.2023

DOI: <https://doi.org/10.17816/DD508786>

类风湿性关节炎患者肩关节磁共振成像上的米粒体症状

Sofia F. Ageeva, Daria A. Filatova, Elena A. Mershina, Valentin E. Sinitsyn

Lomonosov Moscow State University, Moscow, Russian Federation

简评

类风湿性关节炎患者肩关节磁共振成像（MRI）上的米粒体症状是一种罕见但特殊的发现。其特征是关节滑液、滑膜囊或滑膜鞘中出现多个圆形小结构。这些结构彼此相似，就像米粒一样。米粒体的成因至今不明。据推测，米粒体是因类风湿性关节炎或其他炎症性关节病患者滑膜微梗塞而形成的。在临床上，米粒体的存在可能会使患者感到疼痛。然而，情况并非总是如此。在放射诊断方法中，磁共振成像在检测米粒体方面发挥着主导作用。

本文介绍一例在肩关节磁共振成像中发现该症状的临床病例。该症状是在一名有长期类风湿性关节炎病史的患者身上发现的。患者因左肩部无痛性增大而就医。对左肩关节进行了电子计算机断层扫描（CT）和磁共振成像检查。医生通过这些检查发现了，米粒体症状是基础疾病的一种表现形式。这些检查有助于确定进一步的治疗策略。

关键词： 类风湿性关节炎； 肩关节； 米粒体； 磁共振成像； 电子计算机断层扫描； 临床病例。

引用本文：

Ageeva SF, Filatova DA, Mershina EA, Sinitsyn VE. 类风湿性关节炎患者肩关节磁共振成像上的米粒体症状. *Digital Diagnostics*. 2023;4(4):616–624. DOI: <https://doi.org/10.17816/DD508786>

收到: 26.06.2023

接受: 05.09.2023

发布日期: 14.09.2023

BACKGROUND

Rheumatoid arthritis (RA) is a chronic systemic autoimmune disorder characterized by articular and extraarticular involvement. RA is more common in women. Generally, RA onset occurs at the age of 35–60 years, except for juvenile RA [1–3].

In the adult general population, the incidence of RA ranges from 0.5% to 2%, which is quite high. The World Health Organization reported that 18 million people had RA in 2019 [4]. In Russia, the official number of registered patients with RA was 301,200 as of 2017; however, the results of a Russian epidemiology study suggested that RA affected approximately 0.6% of the general population [2].

RA is diagnosed based on clinical and laboratory results, including radiological examinations. According to the criteria issued by the American College of Rheumatology and the European League against Rheumatism in 2010 (2010 ACR-EULAR), a patient's score ≥ 6 (out of 10 possible) is indicative of RA (Table 1) [2, 5].

The following clinical signs are the most common for RA:

- Arthralgia
- Morning stiffness of the affected joints (>30 min)
- Fever
- Rheumatoid nodules under the skin

Table 1. 2010 American College of Rheumatology and European League against Rheumatism criteria for the diagnosis of rheumatoid arthritis [2, 5].

Clinical signs of joint involvement (swelling and/or tenderness in physical examination) (a score of 0–5)	
1 large joint involved	0
2–10 large joints involved	1
1–3 small joints involved	2
4–10 small joints involved	3
>10 joints involved, including at least one small joint	5
Laboratory results for RF and ACPA (a score of 0–3; positive by at least one method)	
RF neg.; ACPA neg.	0
RF weak + / ACPA weak + (>ULN to $\leq 3 \times$ ULN)	2
RF high + / ACPA high + (>3 \times ULN)	3
Laboratory results for acute-phase reactants (a score of 0–1; positive by at least one method)	
Normal ESR and CRP levels	0
Increased ESR/increased CRP	1
Duration of arthritis (a score of 0–1)	
<6 months	0
≥ 6 months	1

Notes: +, positive; ACPA, anticyclic citrullinated peptide antibodies; CRP, C-reactive protein; ESR, erythrocyte sedimentation rate; neg., negative; RF, rheumatoid factor; ULN, upper limit of normal.

- Fatigue
- Weight loss

Usually, small joints are involved first (proximal interphalangeal and metacarpophalangeal) symmetrically. Later, as the disease progresses, larger joints are involved. RA may have pulmonary, renal, cardiovascular, and cutaneous manifestations [1–3].

X-ray methods are widely used for RA diagnosis and follow-up. They allow the identification and evaluation of articular and extraarticular RA signs (e.g., respiratory involvement, heart damage, splenomegaly in the Felty syndrome).

Currently, magnetic resonance imaging (MRI) is often used to evaluate articular involvement in RA. This method offers high-resolution imaging of soft tissues, allowing the detection of early signs of RA (e.g., synovitis, bone erosion, and cartilage lesions) [6].

In some RA cases, small rice-shaped structures, so-called “rice bodies,” may be visualized in the synovial fluid and synovial bursae. Rice bodies are multiple small rounded inclusions of similar shape resembling rice (hence, their name). When examined histologically, they have an amorphous core surrounded by fibrin or collagen. The exact etiology of rice bodies remains unknown. It was suggested to be caused by the detachment of small particles of synovium because of local microinfarctions, and their surface is later covered by fibrin. Rice bodies are possibly associated with inflammatory joint diseases. They are common in RA but may also appear in tuberculous arthritis, chronic bursitis and synovitis, and other diseases. Rice body formation may be asymptomatic or manifest clinically with pain [3, 9]. The most efficient method of rice body visualization is MRI [9, 10].

CASE REPORT

The patient was a 59-year-old woman who had a chronic RA. In September 2022, she presented to a clinic with nontender swelling of the left shoulder joint and underwent MRI.

History of the disease

2015: The patient was diagnosed with RA, with involvement of the left knee and foot joint arthritis. The patient scored 7 ACR-EULAR points out of 10 (scores >6 are required for a definite diagnosis).

2017: The patient was diagnosed with Hashimoto thyroiditis.

2021: The patient presented to a rheumatologist with significant handwriting difficulties. MRI interpretations of both shoulder joints dated February 2021 (scans were performed in another clinic) were as follows:

- A significant amount of effusion was visualized in the subdeltoid and subacromial bursa, which was more pronounced on the right side.

- Joint synovia were thickened, and a small amount of effusion was observed in the joint cavity.
- The signal intensity of the cartilage surfaces decreased.

Laboratory results

On September 16, 2022, blood tests were performed to evaluate the ongoing therapy (methotrexate 17.5 mg; folic acid):

- Thyroid-stimulating hormone, normal (4.08 μ U/mL; N: 0.27–4.2 μ U/mL)
- Rheumatoid factor, increased (107.9 IU/mL; N: 0–14 IU/mL)
- C-reactive protein, increased (11.84 mg/L; N: 0–5 mg/L)
- Erythrocyte sedimentation rate, increased (36 mm/h; N: <30 mm/h)

Investigations

On September 17, 2022, CT of both shoulder joints was performed because of further swelling of the left shoulder joint, based on the patient's complaints. MAGNETOM Vida (Siemens Healthineers, Germany) was used at a field

magnitude of 3 Tesla for a standard-protocol MRI scan (T1- and T2-weighted images with/without fat suppression; transverse, frontal, sagittal, and oblique slices) with a surface radiofrequency coil for the shoulder joint.

Under the deltoid, inside the subacromial bursa and subdeltoid bursa enlarged to the size of 7.7 \times 2.5 \times 5 cm, T2-weighted imaging (WI) showed multiple similarly shaped oval structures measuring 2–3 mm to 8–10 mm in diameter with an intermediate signal intensity, separated by areas of increased signal intensity (in T2-WI). In T1-WI, these structures demonstrated homogeneous intermediate signal intensity (Figs. 1 and 2). Agglomerations of small inclusions resembled space-occupying masses in the joint cavity.

Noncontrasted CT images of the shoulder joints obtained with Somatom Drive (Siemens Healthineers, Germany) with a 0.625-mm slice thickness showed large lens-shaped hypodense structures on both sides in the subacromial and subdeltoid bursae (Fig. 3):

- On the left side: 7.5 \times 4 \times 9 cm; the mass is bigger than the MR evaluation (7.7 \times 2.5 \times 5 mm)
- On the right side: 4 \times 1.4 \times 4 cm

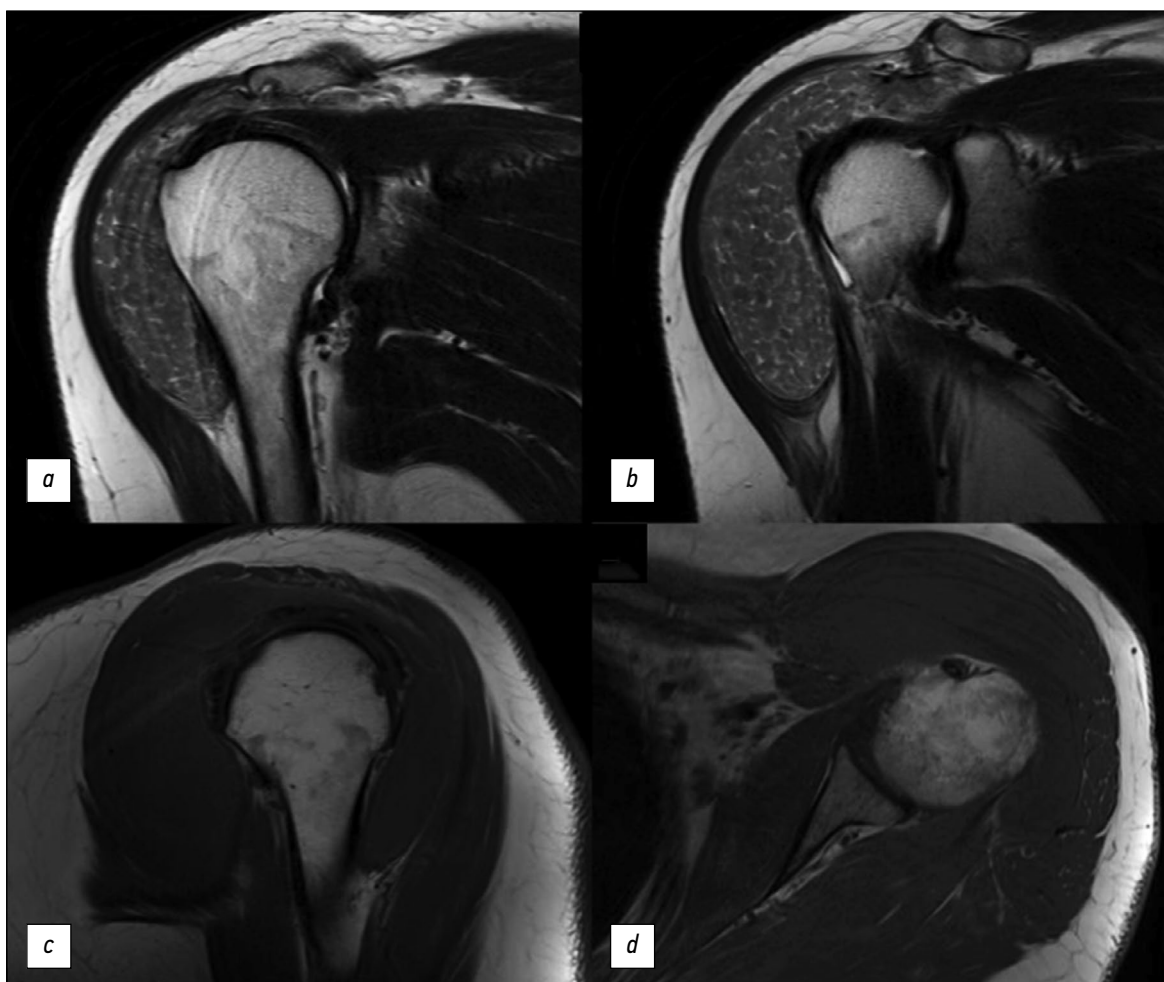


Fig. 1. Magnetic resonance imaging (MRI) of the left shoulder joint. (a), (b): T2-weighted images, coronal projections; (c): T1-weighted image, sagittal projection; (d): T1-weighted image, transverse projection.

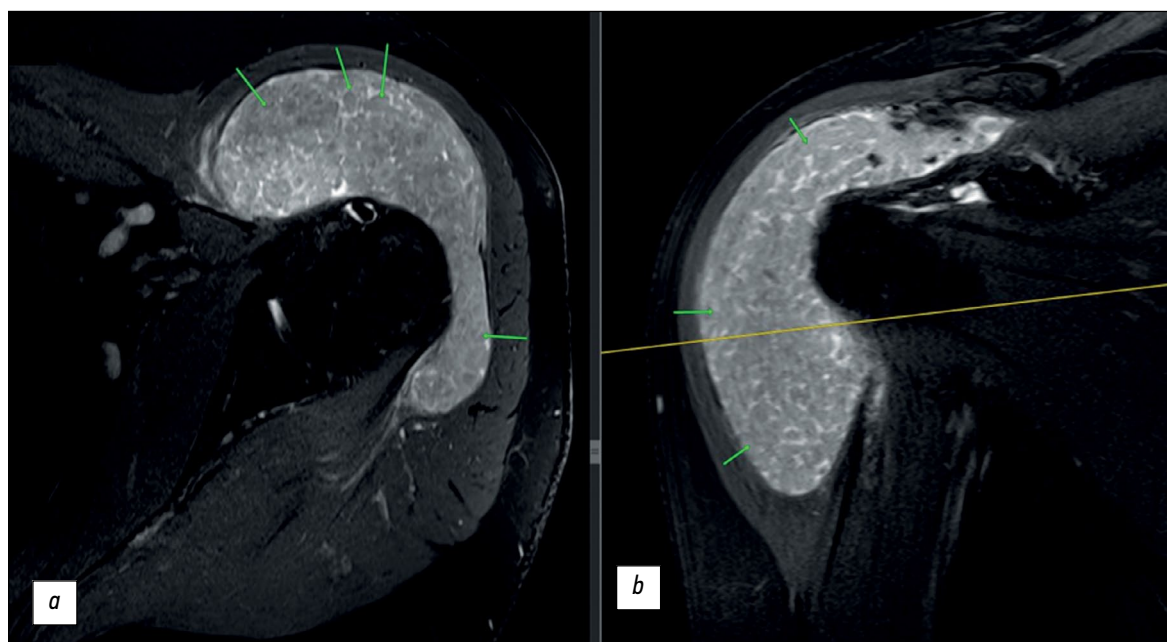


Fig. 2. Magnetic resonance imaging of the left shoulder joint, T2-weighted images with fat suppression: *a*, transverse view; *b*, coronal view. Small structures within the synovial sacs are indicated by arrows.

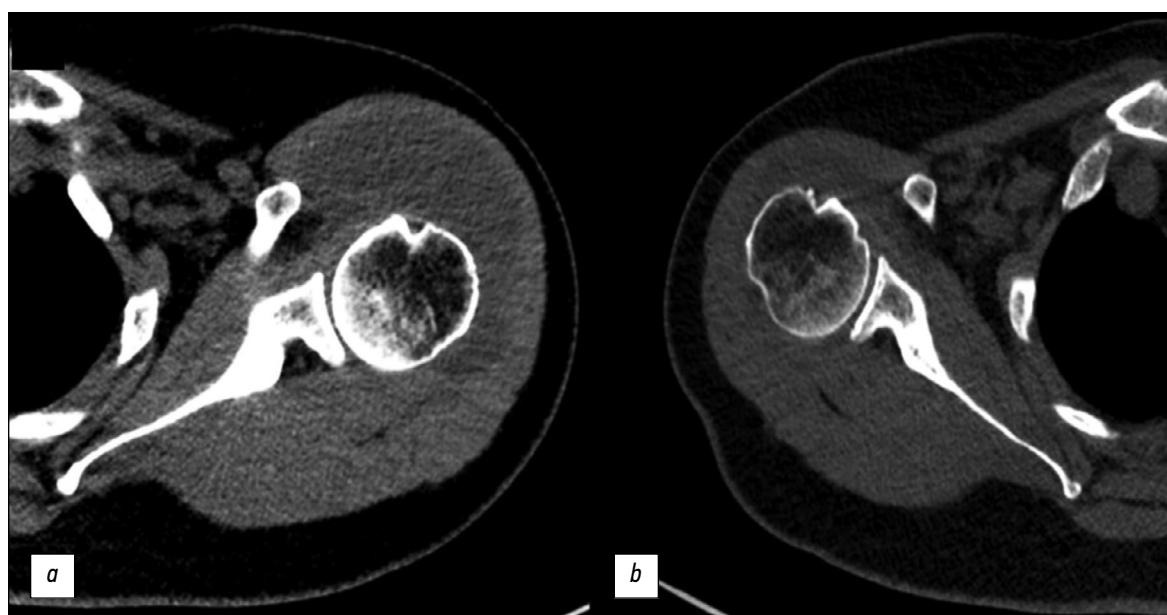


Fig. 3. Computed tomography of the shoulder joints, axial view: *a*, left shoulder joint; *b*, right shoulder joint.

Their structure appeared homogeneous in the CT images, without calcification or solid inclusions; the structure density was ~35 HU. Reactive lymphadenopathy associated with the underlying disease was observed in the axillary areas.

DISCUSSION

Rice body formation in the joints is a rare phenomenon associated with inflammatory joint diseases. It is most frequently observed in patients with RA. Rice bodies may be a sign of RA or precede disease onset in rare cases [11]. Rice

bodies may be asymptomatic or manifest as joint swelling (as in the case described) and pain.

In MRI, rice bodies are visualized as multiple small, similarly shaped, rounded structures. In T1-WI, they are isointense or hypointense; in T2-WI, they are hypointense. The T2-WI pattern in the described case consisted of densely agglomerated inclusions, which were hyperintense compared with the muscle tissue, which is typical in RA. As demonstrated in the case presented, MRI is superior to CT in identifying rice bodies.

Rice bodies are not only seen in RA but also in other diseases, such as synovial chondromatosis and pigmented

villonodular synovitis (PVNS), and chronic bursitis, including tuberculous etiology. MRI significantly facilitates the differential diagnosis of the listed disorders. In synovial chondromatosis, the cartilage is isointense or hyperintense in T1-WI, whereas rice bodies are hypointense in T2-WI compared with hyperintense fluid. Moreover, synovial chondromatosis is more commonly seen in men and affects a single joint. In patients with PVNS, the signal of the thickened synovia is inhomogeneously reduced in T1-WI and T2-WI because of hemosiderin accumulation [8].

Since fibrin causes irritation, rice bodies, once formed, may also cause synovial inflammation. Surgery is considered to improve a patient's clinical condition [12, 13], particularly in severe pain syndrome. In the case presented herein, further management techniques involved surgical treatment.

CONCLUSION

We report a rare case of intraarticular rice bodies in a patient with chronic RA. A brief literature review on the subject was provided, and the MR and CT signals of this phenomenon were described. Although rice bodies are rare,

knowledge of their potential presence in joint capsules of patients with RA and differentiation from similar signs of other disorders is necessary.

ADDITIONAL INFORMATION

Funding source. This article was not supported by any external sources of funding.

Competing interests. The authors declare that they have no competing interests.

Authors' contribution. All authors made a substantial contribution to the conception of the work, acquisition, analysis, interpretation of data for the work, drafting and revising the work, final approval of the version to be published and agree to be accountable for all aspects of the work. S.F. Ageeva — writing the text; D.A. Filatova — writing and reviewing the text; E.A. Mershina — concept development, approval of the final text; V.E. Sinitsyn — concept development, approval of the final text.

Consent for publication. Written consent was obtained from the patient for publication of relevant medical information and all of accompanying images within the manuscript in Digital Diagnostics Journal.

REFERENCES

1. Nasonov EL, Karateev DE, Balabanova RM. Rheumatoid arthritis. In: Nasonov EL, Nasonova VA, editors. *Rheumatology. National manual*. Moscow : GEOTAR-Media. 2008. P. 290–331 (In Russ)
2. *Rheumatoid arthritis. Clinical Guidelines*. ID 250. Approved by the Scientific and Practical Council of the Ministry of Health of the Russian Federation. 2021. Available from: <https://cr.minzdrav.gov.ru/schema/250> (In Russ)
3. Bullock J, Rizvi SA, Saleh AM, et al. Rheumatoid Arthritis: A Brief Overview of the Treatment. *Medical Principles and Practice*. 2018;27(6):501–507. doi: 10.1159/000493390
4. who.int [Internet]. World Health Organization [cited 6 September 2023]. Available from: <https://www.who.int>
5. Kay J, Upchurch KS. ACR/EULAR 2010 rheumatoid arthritis classification criteria. *Rheumatology*. 2012;51 Suppl. 6:vi5–vi9. doi: 10.1093/rheumatology/kes279
6. Narvaez JA, Narváez J, De Lama E, et al. MR Imaging of Early Rheumatoid Arthritis. *RadioGraphics*. 2010;30(1):143–163. doi: 10.1148/rg.301095089
7. Edison MN, Caram A, Flores M, et al. Rice Body Formation Within a Peri-Articular Shoulder Mass. *Cureus*. 2016;8(8):e718. doi: 10.7759/cureus.718
8. Forse CL, Mucha BL, Santos MLZ., et al. Rice body formation without rheumatic disease or tuberculosis infection: a case report and literature review. *Clinical Rheumatology*. 2012;31(12):1753–1756. doi: 10.1007/s10067-012-2063-8
9. Narváez JA, Narváez J, Roca Y, et al. MR imaging assessment of clinical problems in rheumatoid arthritis. *European Radiology*. 2002;12(7):1819–1828. doi: 10.1007/s00330-001-1207-z
10. Griffith JF, Peh WCG, Evans NS, et al. Multiple rice body formation in chronic subacromial/subdeltoid bursitis: MR appearances. *Clinical Radiology*. 1996;51(7):511–514. doi: 10.1016/s0009-9260(96)80193-0
11. Kataria RK, Chaiamnuay S, Jacobson LD, et al. Subacromial bursitis with rice bodies as the presenting manifestation of rheumatoid arthritis. *The Journal of rheumatology*. 2003;30(6):1354–1355.
12. Popert AJ, Scott DL, Wainwright AC, et al. Frequency of occurrence, mode of development, and significance of rice bodies in rheumatoid joints. *Annals of the Rheumatic Diseases*. 1982;41(2):109–117. doi: 10.1136/ard.41.2.109
13. Reid HS, McNally E, Carr A. Soft tissue mass around the shoulder. *Annals of the Rheumatic Diseases*. 1998;57(1):6–8. doi: 10.1136/ard.57.1.6

СПИСОК ЛИТЕРАТУРЫ

1. Насонов Е.Л., Каратеев Д.Е., Балабанова Р.М. Ревматоидный артрит. В кн.: Ревматология. Национальное руководство / под ред. Е.Л. Насонова, В.А. Насоновой. Москва : ГЭОТАР-Медиа, 2008. С. 290–331
2. Клинические рекомендации — Ревматоидный артрит. ID 250. Одобрено Научно-практическим Советом Минздрава РФ. 2021. Режим доступа: <https://cr.minzdrav.gov.ru/schema/250> Дата обращения: 06.09.2023
3. Bullock J., Rizvi S.A., Saleh A.M., et al. Rheumatoid Arthritis: A Brief Overview of the Treatment // *Medical Principles and Practice*. 2018. Vol. 27, N 6. P. 501–507. doi: 10.1159/000493390

4. who.int [интернет]. Всемирная организация здравоохранения [дата обращения: 06.09.2023]. Доступ по ссылке: <https://www.who.int>
5. Kay J., Upchurch K.S. ACR/EULAR 2010 rheumatoid arthritis classification criteria // *Rheumatology*. 2012. Vol. 51, Suppl. 6. P. vi5–vi9. doi: 10.1093/rheumatology/kes279
6. Narvaez J.A., Narváez J., De Lama E., et al. MR Imaging of Early Rheumatoid Arthritis // *RadioGraphics*. 2010. Vol. 30, N 1. P. 143–163. doi: 10.1148/rq.301095089
7. Edison M.N., Caram A., Flores M., et al. Rice Body Formation Within a Peri-Articular Shoulder Mass // *Cureus*. 2016. Vol. 8, N. 8. P. e718. doi: 10.7759/cureus.718
8. Forse C.L., Mucha B.L., Santos M.L.Z., et al. Rice body formation without rheumatic disease or tuberculosis infection: a case report and literature review // *Clinical Rheumatology*. 2012. Vol. 31, N 12. P. 1753–1756. doi: 10.1007/s10067-012-2063-8
9. Narváez J.A., Narváez J., Roca Y., et al. MR imaging assessment of clinical problems in rheumatoid arthritis // *European Radiology*. 2002. Vol. 12, N 7. P. 1819–1828. doi: 10.1007/s00330-001-1207-z
10. Griffith J.F., Peh W.C.G., Evans N.S., et al. Multiple rice body formation in chronic subacromial/subdeltoid bursitis: MR appearances // *Clinical Radiology*. 1996. Vol. 51, N 7. P. 511–514. doi: 10.1016/s0009-9260(96)80193-0
11. Kataria R.K., Chaiamnuy S., Jacobson L.D., et al. Subacromial bursitis with rice bodies as the presenting manifestation of rheumatoid arthritis // *The Journal of rheumatology*. 2003. Vol. 30, N 6. P. 1354–1355.
12. Popert A.J., Scott D.L., Wainwright A.C., et al. Frequency of occurrence, mode of development, and significance of rice bodies in rheumatoid joints // *Annals of the Rheumatic Diseases*. 1982. Vol. 41, N 2 P. 109–117. doi: 10.1136/ard.41.2.109
13. Reid H.S., McNally E., Carr A. Soft tissue mass around the shoulder // *Annals of the Rheumatic Diseases*. 1998. Vol. 57, N 1. P. 6–8. doi: 10.1136/ard.57.1.6

AUTHORS' INFO

* Sofia F. Ageeva;

address: Lomonosovsky av., 27/10, Moscow, 119991 Russian Federation;

ORCID: 0000-0003-4726-0806;

eLibrary SPIN: 9695-3717;

e-mail: son.ageeva13@gmail.com

Daria A. Filatova;

ORCID: 0000-0002-0894-1994;

eLibrary SPIN: 2665-5973;

e-mail: dariafilatova.msu@mail.ru

Elena A. Mershina, MD, Cand. Sci. (Med.), Assistant professor;

ORCID: 0000-0002-1266-4926;

eLibrary SPIN: 6897-9641;

e-mail: elena_mershina@mail.ru

Valentin E. Sinitsyn, MD, Dr. Sci. (Med.), Professor;

ORCID: 0000-0002-5649-2193;

eLibrary SPIN: 8449-6590;

e-mail: vsini@mail.ru

ОБ АВТОРАХ

* Агеева София Фаильевна,

адрес: 119991 Москва, Ломоносовский пр-т, 27к10;

ORCID: 0000-0003-4726-0806;

eLibrary SPIN: 9695-3717;

e-mail: son.ageeva13@gmail.com

Филатова Дарья Андреевна;

ORCID: 0000-0002-0894-1994;

eLibrary SPIN: 2665-5973;

e-mail: dariafilatova.msu@mail.ru

Мершина Елена Александровна, канд. мед. наук, доцент;

ORCID: 0000-0002-1266-4926;

eLibrary SPIN: 6897-9641;

e-mail: elena_mershina@mail.ru

Синицын Валентин Евгеньевич, д-р мед. наук, профессор;

ORCID: 0000-0002-5649-2193;

eLibrary SPIN: 8449-6590;

e-mail: vsini@mail.ru

* Corresponding author / Автор, ответственный за переписку

DOI: <https://doi.org/10.17816/DD551837>

Некомпактный миокард и аневризма левого желудочка у 6-летнего ребёнка

Т.Б. Даутов¹, Б.Б. Калиев¹, Б.Т. Ерекеш²

¹ Корпоративный фонд «University Medical Center», Астана, Казахстан;

² Национальный научный кардиохирургический центр, Астана, Казахстан

АННОТАЦИЯ

Некомпактный миокард — редкий тип кардиомиопатии, часто сопровождающийся аневризмой желудочка. В статье описан клинический случай 6-летней девочки, поступившей в нашу клинику с жалобами на плохое самочувствие при физической нагрузке. Эхокардиография выявила выраженную трабекулярность стенки левого желудочка и выбухание в области базально-боковой стенки, что соответствует аневризме и некомпактности миокарда левого желудочка. На магнитно-резонансной томографии сердца наличие некомпактности миокарда было подтверждено соотношением некомпактного слоя к компактному 2,6:1. Кроме того, была выявлена систолическая дисфункция и аневризма левого желудочка с рубцеванием миокарда. Коронарная ангиография исключила поражение коронарных артерий, что позволило предположить природу рубцевания эндомиокарда как результат нарушения микроциркуляции в некомпактном слое миокарда.

Ключевые слова: кардиомиопатия; клинический случай; некомпактность миокарда левого желудочка; аневризма левого желудочка; рубцевание.

Как цитировать:

Даутов Т.Б., Калиев Б.Б., Ерекеш Б.Т. Некомпактный миокард и аневризма левого желудочка у 6-летнего ребёнка // Digital Diagnostics. 2023. Т. 4, № 4. С. 625–632. DOI: <https://doi.org/10.17816/DD551837>

DOI: <https://doi.org/10.17816/DD551837>

Left ventricular noncompaction with ventricular aneurysm in a 6-year-old patient

Tairkhan B. Dautov¹, Bauyrzhan B. Kaliyev¹, Bibissara T. Yerekesh²

¹ «University Medical Center» Corporate Fund, Astana, Kazakhstan;

² National Research Cardiac Surgery Center, Astana, Kazakhstan

ABSTRACT

Ventricular noncompaction is a rare type of cardiomyopathy often associated with a ventricular aneurysm. We present a clinical case of a 6-year-old female who arrived at our clinic complaining of physical exertion. Echocardiography revealed prominent trabeculations in the left ventricular wall and a lateral-basal part bulging out, indicating noncompaction of the left ventricular myocardium with an aneurysm. With a noncompacted-to-compacted myocardium ratio of 2.6, magnetic resonance imaging revealed the presence of noncompacted myocardium. It also revealed impaired left ventricular systolic function and a left ventricular aneurysm with myocardial scarring. Coronary angiography ruled out coronary artery disease. Therefore, myocardial scarring was caused by noncompacted myocardium microcirculatory disorder.

Keywords: cardiomyopathy; case report; left ventricle noncompaction; left ventricular aneurysm; scarring.

To cite this article:

Dautov TB, Kaliyev BB, Yerekesh BT. Left ventricular noncompaction with ventricular aneurysm in a 6-year-old patient. *Digital Diagnostics*. 2023;4(4):625–632. DOI: <https://doi.org/10.17816/DD551837>

Received: 17.07.2023

Accepted: 06.09.2023

Published: 17.10.2023

DOI: <https://doi.org/10.17816/DD551837>

一名6岁儿童的左室心肌致密化不全和左心室动脉瘤

Tairkhan B. Dautov¹, Bauyrzhan B. Kaliyev¹, Bibissara T. Yerekesh²

¹ «University Medical Center» Corporate Fund, Astana, Kazakhstan;

² National Research Cardiac Surgery Center, Astana, Kazakhstan

简评

左室心肌致密化不全是一种罕见的心肌病。它通常伴有心室动脉瘤。本文描述了一个6岁女孩的临床病例。这名女孩因主诉在体育活动时身体不适而被送进本诊所。超声心动图检查显示了左心室壁有明显的小梁，侧壁基底部有隆起。这些症状与左心室动脉瘤和左室心肌致密化不全相符。心脏磁共振成像显示了，非致密层与致密层的比例为2.6:1，证实了存在左室心肌致密化不全。此外，还发现了收缩功能障碍和伴有心肌瘢痕形成的左心室动脉瘤。冠状动脉造影排除了冠状动脉病变。在这种情况下，我们可以认为心内膜瘢痕形成的性质是非致密心肌层微循环障碍的结果。

关键词： 心肌病； 临床病例； 左室心肌致密化不全； 左心室动脉瘤； 瘢痕形成。

引用本文：

Dautov TB, Kaliyev BB, Yerekesh BT. 一名6岁儿童的左室心肌致密化不全和左心室动脉瘤. *Digital Diagnostics*. 2023;4(4):625–632.

DOI: <https://doi.org/10.17816/DD551837>

收到: 17.07.2023

接受: 06.09.2023

发布日期: 17.10.2023

ABBREVIATIONS

Ao: aorta
 CMR: cardiac magnetic resonance imaging
 EF: ejection fraction
 HF: heart failure
 LA: left atrium
 LGE: late gadolinium enhancement

LV: left ventricle
 LVNC: left ventricular noncompaction
 NC: noncompact myocardium
 NC-to-C ratio: noncompact-to-compact ratio
 RA: right atrium
 RV: right ventricle

INTRODUCTION

Left ventricular noncompaction (LVNC) is a rare type of cardiomyopathy caused by myocardial compaction failure during embryogenesis. It has multiple prominent trabeculations with deep intertrabecular recesses [1]. Its clinical manifestations vary from no symptoms to cardiac dysfunction, heart failure (HF), arrhythmias, and systemic thromboembolism [2]. However, there are only a few reports of LVNC being aggravated by LV aneurysm [3], particularly in children, which is uncommon. Clinically, most LV aneurysms are asymptomatic, although they may cause arrhythmias (18.4%), embolic events (5.4%), rupture (4%), congestive HF (21.5%), and angina pectoris in rare cases [4]. In recent years, two major ideas on the development of LVNC have emerged: the embryogenesis hypothesis and the molecular genetic mechanism. Initially, it was believed that the inadequate consolidation of cardiomyocytes during abnormal embryonic morphogenesis led to the formation of prominent myocardial trabeculae and spaces between them. However, recent improvements in molecular genetic research techniques have revealed a growing number of genes associated with LVNC. Most identified

genes are sarcomere protein genes, ion channel genes, and mitochondrial genes, with sarcomere protein genes most often implicated in pathogenesis [5]. In adults, the prevalence of isolated LVNC varies from 0.01% to 0.3% [6]. LVNC is classified as primary genetic cardiomyopathy by the American Heart Association. Conversely, the European Society of Cardiology classifies it under “unclassified cardiomyopathies” [7].

CASE REPORT

A 6-year-old female was admitted to our clinic with complaints of physical exertion. At 26 weeks of gestation, she had exudative pericarditis due to anamnesis. Echocardiography at 15 months revealed pericardial fluid up to 600 mL, prompting pericardiocentesis when the patient was diagnosed with hemopericarditis. Before admission, the patient was diagnosed with HF with a slightly decreased ejection fraction of LV (53). Body temperature was 36.6 C at the time of admission. SpO₂ is 98%. The breath rate is 23 per minute. There is no organic noise in the heart tones, which are rhythmic and muffled. Blood pressure is 115/83 mmHg. The heart rate is 110 per minute.

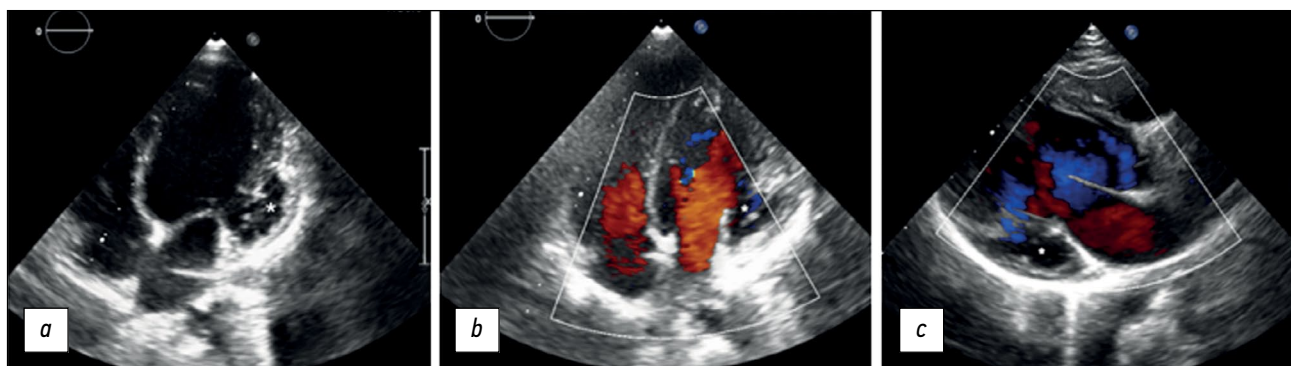


Fig. 1. (a) A 6-year-old female patient was diagnosed with left ventricular noncompaction with an aneurysm. An apical four-chamber view demonstrates outpouching of the left ventricular wall with noncompact myocardium. The ventricle is connected to the aneurysm (asterisk). Transthoracic echocardiography (cardiac transducer, two-dimensional scanning), greyscale. (b) A 6-year-old female patient with left ventricular noncompaction and an aneurysm. An apical four-chamber view shows a large anechoic lesion (aneurysm denoted by an asterisk) with prominent trabeculation of the apical and lateral walls of LV. Transthoracic echocardiography (cardiac transducer, two-dimensional scanning), color Doppler images. (c) A 6-year-old female patient was diagnosed with left ventricular noncompaction with an aneurysm. A three-chamber view shows an aneurysm (asterisk), inlet and outlet of LV. Transthoracic echocardiography (cardiac transducer, two-dimensional scanning), color Doppler images.

During hospitalization, echocardiography revealed LV dilatation, increased trabecularity of the apex and lateral wall of the LV, sac-like bulging of the lateral-basal part as aneurysm, and possibly deep trabeculae (Figure 1a–c). The echocardiography revealed a decline in LV systolic function and a 48% LV ejection fraction. There was minimal regurgitation on the tricuspid, mitral, and pulmonary valves.

The main rhythm, according to the echocardiography, was sinus rhythm. The 24-h ECG Holter monitoring showed sinus rhythm, a mean heart ratio of -109 bpm, a minimum heart ratio of -64 bpm, a maximum heart ratio of -173 bpm, no pauses longer than 2 s, and no tachy-bradyarrhythmia.

A cardiac magnetic resonance imaging (CMR) with contrast enhancement (Gadobutrol 2.0 mL) was performed to exclude congenital heart diseases. The systolic function of both ventricles was reduced (LV EF [41%] and RV EF [45%]). The total LV mass of the myocardium was 54.6 g, with noncompacted myocardium accounting for 14.4 g or 26.3% of the total. CMR revealed signs of myocardial scarring and aneurysmatic ballooning of the basal anterior and lateral-basal walls of the left ventricle, noncompact myocardium (with an NC-to-C ratio = 2.6:1), and left ventricular dilatation. Accumulation of contrast media (one, five, and six segments) in delayed scans was observed (Figure 2a–e).

According to EchoCG and CMR, the patient has a noncompact left ventricular myocardium and aneurysm. Given

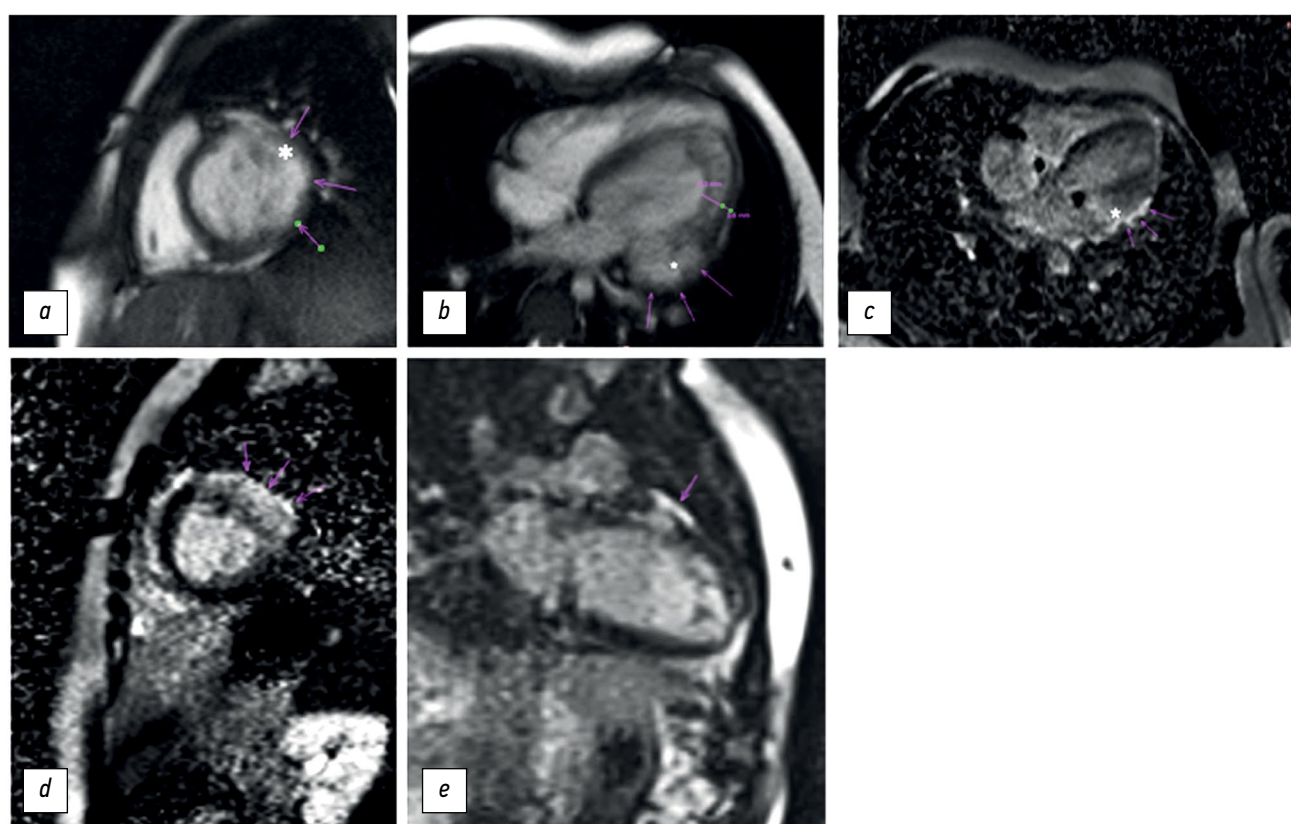


Fig. 2. (a) A 6-year-old female patient with left ventricular noncompaction and an aneurysm. Cardiac magnetic resonance imaging (MRI) showed a well-defined outpouching (asterisk) of the left ventricle's lateral wall, as well as local thinning of the myocardium (arrows). Cardiac magnetic resonance, 1.5-T MR System (MAGNETOM Avanto, Siemens Healthcare, Germany) with breath-holding, short-axis view, before the administration of contrast agent, Cine-two-chamber short-axis images, time to echo (TE) of 1.5 ms, repetition time (TR) of 42 ms. (b) A 6-year-old female patient with left ventricular noncompaction and an aneurysm. Cardiac magnetic resonance imaging in the four-chamber view demonstrates ventricular aneurysms (asterisk) in the lateral-basal segments of the left ventricle (LV) with noncompaction of the myocardium with a ratio 2.6:1. Cardiac magnetic resonance, 1.5-T MR System (MAGNETOM Avanto, Siemens Healthcare, Germany) with breath-holding, four-chamber long-axis view, before the administration of contrast agent, Cine-four-chamber long-axis images, TE of 1.5 ms, and repetition time (TR) of 42 ms. (c) A 6-year-old female patient with left ventricular noncompaction and an aneurysm. LGE, four-chamber view shows late gadolinium enhancement (arrows) on the basal anterolateral wall of the LV, where the aneurysm (asterisk) is located. CMR, 1.5-T MR System (MAGNETOM Avanto, Siemens Healthcare, Germany) with breath-holding, LGE, four-chamber long-axis view, TE of 1.5 ms, and repetition time (TR) of 700 ms. (d) A 6-year-old female patient with left ventricular noncompaction and an aneurysm. Cardiac magnetic resonance in the two-chamber short-axis view with LGE demonstrates contrast agent accumulation in the one, five and six segments. CMR, 1.5-T MR System (MAGNETOM Avanto, Siemens Healthcare, Germany) with breath-holding, LGE, two-chamber short-axis view, TE of 1.5 ms, and repetition time (TR) of 2,000 ms. (e) LGE, two-chamber long-axis view shows late gadolinium enhancement on the anterior basal wall of the LV. CMR, 1.5-T MR System (MAGNETOM Avanto, Siemens Healthcare, Germany) with breath-holding, LGE, two-chamber long-axis view, TE of 1.4 ms, and repetition time (TR) of 700 ms.

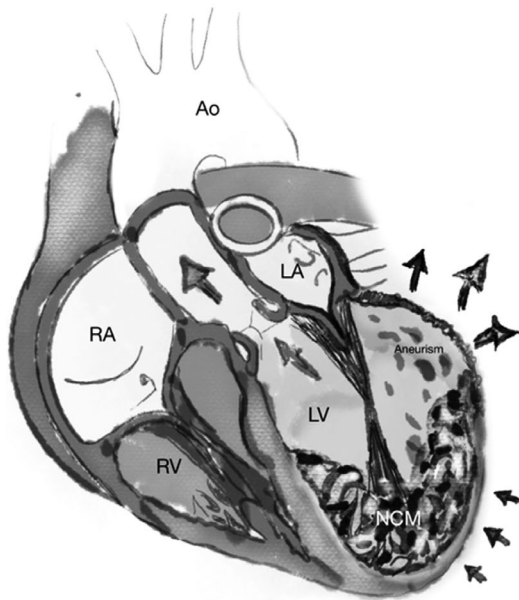


Fig. 3. Noncompaction of the left ventricle with the thin-walled aneurysm with a wide connection to the LV. Aneurysm bulges out from the anterior basal wall during systole. Arrows show the direction of the blood flow. Ao, aorta; LA, left atrium; LV, left ventricle; NCM, noncompact myocardium; RA, right atrium; RV, right ventricle.

the findings, it was decided to have a coronary angiography to assess the coronary vessels and exclude coronary artery anomalies. Coronary angiography showed no evidence of coronary artery abnormalities (Figure 4a and b).

Based on these findings, he was diagnosed with LVNC complicated by an aneurysm.

Given the examination results, weight gain, preserved tolerance to physical activity, and NT-proBNP level of 43.60 pg/mL, the patient was referred to a local hospital for continued monitoring with prescribed medication.

Treatment

Due to limited data on the treatment of this condition, it is recommended that clinical complications be managed in accordance with current guidelines for each specific complication. Anticoagulation therapy is recommended in LVNC patients with a history of thromboembolism, atrial fibrillation, and/or impaired systolic function (LV ejection fraction of <40%) due to an increased risk of thrombus formation resulting from deep intertrabecular recesses and slow blood flow [6]. Therefore, it is suggested that anticoagulation therapy may be necessary in patients with LVNC and accompanying LV aneurysms, even in the absence of systolic dysfunction or atrial fibrillation. However, there have been reports of patients undergoing more radical therapy, including surgical removal, to prevent stress and rupture of the aneurysm wall and the risk of thrombus formation. Furthermore, excising the fibrotic tissue of the LV aneurysm could help prevent arrhythmias, and reshaping the ventricle could improve the patient's HF symptoms. Surgery is considered a definitive treatment that can be used in conjunction with optimal medical therapy [8].

DISCUSSION

The diagnosis of LVNC is mainly based on imaging anatomical characteristics. Although there is no universally established definition of LVNC, the following echocardiographic criteria are widely accepted: (a) two-layered myocardium with multiple, prominent trabeculations in end-systole; (b) NC-to-C ratio of >2; (c) Doppler color flow within the recesses and communication between the intertrabecular space and LV; and (d) absence of coexisting cardiac abnormalities. The classic triad of complications comprises HF, ventricular arrhythmia, and systemic embolic events [9].

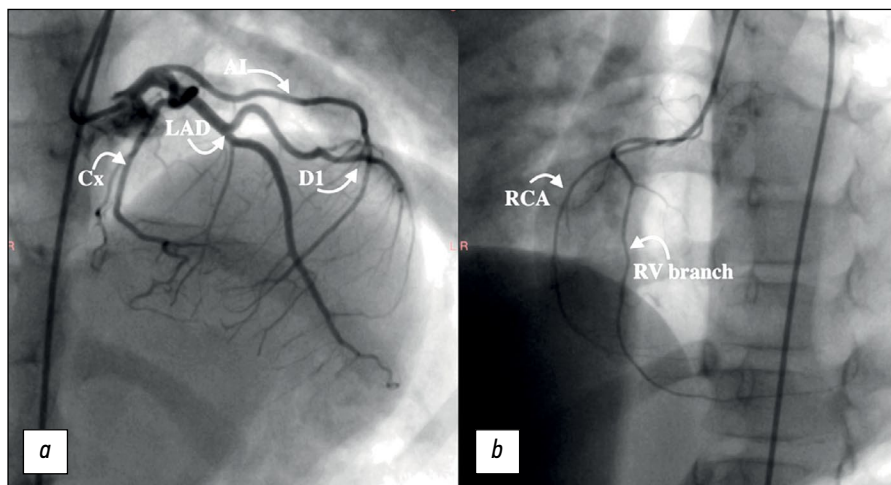


Fig. 4. (a and b) Coronary angiography of a 6-year-old female patient diagnosed with left ventricular noncompaction and an aneurysm. Coronary arteriography using two catheters revealed no evidence of changes in the coronary arteries. Cx was found in a left dominant pattern of coronary circulation. Coronary angiography using introducer 4Fr and two catheters with 5Fr size. AI, intermediate artery; Cx, circumflex artery; D1, diagonal artery; LAD, left anterior descending; RCA, right coronary artery; RV branch, right ventricular branch.

We encountered a rare case of LVNC with an LV aneurysm formation due to microcirculatory disorder. As demonstrated in our patient, the CMR criterion for diagnosing LVNC is a ratio of maximum thickness between the noncompaction and compaction layer of more than 2.3 in end-diastole, and the mass of trabeculated lv myocardium represents >25% of the total LV mass [10]. Myocardial delayed enhancement revealed scars along the aneurysm wall. Aneurysms have a large connection to the ventricular cavity (Figure 3), whereas diverticula are typically elongated and have a narrowed neck. Aneurysms are most commonly observed in the LV apex (28%) and the perivalvular area close to the mitral valve (49%). LV aneurysms are typically acquired following an acute myocardial infarction with systolic bulging and scar formation in the myocardium. Without knowledge of the patient's medical history and coronary angiogram, acquired aneurysms are difficult to distinguish from congenital left ventricular aneurysms [11]. However, poor microcirculation is believed to be the etiology of aneurysm and scar formation in LVNC [12]. The aneurysm was unrelated to coronary artery territory because our patient's coronary angiography was normal. In our case, an aneurysm appears to be acquired because her previous echocardiography analysis showed EF above 50%; subsequently, when symptoms of cardiac failure began to manifest, it began to diminish. Complications from ventricular aneurysms include intramural thrombus, cardiac output impairment, and aneurysm rupture.

REFERENCES

1. Srivastava S, Yavari M, Al-Abcha A, Banga S, Abela G. Ventricular non-compaction review. *Heart Failure Reviews*. 2022;27(4):1063–1076. doi:10.1007/s10741-021-10128-3
2. Petersen SE, Jensen B, Aung N, et al. Excessive Trabeculation of the Left Ventricle. *JACC: Cardiovascular Imaging Expert Panel Paper*. 2023;16(3):408–425. doi: 10.1016/j.jcmg.2022.12.026
3. Catalano MA, Hemli JM, Lasic Z, Patel NC. Repair of left ventricular aneurysm in the setting of noncompaction. *Journal of Cardiology Cases*. 2022;25(6):416–419. doi: 10.1016/j.jccase.2022.01.008
4. Tilahun T, Kedir E, Eshetu B. Fatal Left Ventricular Aneurysm in a 13 Years Old Male Child: A Case Report. *Ethiopian journal of health sciences*. 2021;31(4):903–906. doi: 10.4314/ejhs.v31i4.26
5. Tian S, Liang H, Li X, et al. A novel mutation in the TTN gene resulted in left ventricular noncompaction: a case report and literature review. *BMC Cardiovascular Disorders*. 2023;23(1):352. doi: 10.1186/s12872-023-03382-w
6. Yakabe D, Matsushima S, Uchino S, et al. Left Ventricular Noncompaction with Multiple Thrombi in Apical Aneurysm. *Internal Medicine*. 2020;59(3):377–381. doi: 10.2169/internalmedicine.3489-19
7. Gerecke BJ, Engberding R. Noncompaction Cardiomyopathy—History and Current Knowledge for Clinical Practice. *Journal of Clinical Medicine*. 2021;10(11):2457. doi: 10.3390/jcm10112457
8. Daprati A, Sassi CG, Garatti A, Saitto G, Menicanti L. Congenital left ventricular aneurysm with myocardial noncompaction pattern. *Asian Cardiovascular and Thoracic Annals*. 2020;28(8):504–506. doi: 10.1177/0218492320949833
9. Ogah OS, Iyawe EP, Orimolade OA, et al. Left ventricular noncompaction in Ibadan, Nigeria. *The Egyptian Heart Journal*. 2023;75(1):69. doi: 10.1186/s43044-023-00396-9
10. Gaižauskienė K, Glembockytė G, Glaveckaitė S, Valevičienė N. Magnetic resonance diagnostic criteria of non-compaction cardiomyopathy: new diagnostic criteria still needed? *Seminars in Cardiovascular Medicine*. 2023;29(1):1–13. doi: 10.2478/semcard-2022-0003
11. Ohlow MA. Congenital left ventricular aneurysms and diverticula: an entity in search of an identity. *Journal of Geriatric Cardiology*. 2017;14(12):750–762. doi: 10.11909/j.issn.1671-5411.2017.12.005
12. Siripornpitak S, Khositseth A, Sriprachyakul A. Left Ventricular Non-compaction with Ventricular Aneurysms. *Journal of Cardiovascular Imaging*. 2020;28(3):222–225. doi: 10.4250/jcvi.2019.0091

TEACHING POINT

A highly uncommon variant of cardiomyopathy is the combination of ventricular noncompaction and ventricular aneurysm. Echocardiography, CMR, and coronary angiography are valuable techniques for identifying the components of LVNC. Surgery can be combined with medical treatment, regardless of the prevalence of symptoms.

ADDITIONAL INFORMATION

Funding source. This article was not supported by any external sources of funding.

Competing interests. The authors declare that they have no competing interests.

Authors' contribution. All authors made a substantial contribution to the conception of the work, acquisition, analysis, interpretation of data for the work, drafting and revising the work, final approval of the version to be published and agree to be accountable for all aspects of the work. Dautov TB — contribution to the study concept, approved the final version of the work; Kaliyev BB — revising and editing the manuscript; Yerekesh BT — data sources collection and analysis, preparation of the manuscript.

Consent for publication. Written consent was obtained from the patient's legal representatives for publication of relevant medical information and all of accompanying images within the manuscript.

СПИСОК ЛИТЕРАТУРЫ

1. Srivastava S., Yavari M., Al-Abcha A., Banga S., Abela G. Ventricular non-compaction review // *Heart Failure Reviews*. 2022. Vol. 27, N 4. P. 1063–1076. doi:10.1007/s10741-021-10128-3
2. Petersen S.E., Jensen B., Aung N., et al. Excessive Trabeculation of the Left Ventricle // *JACC: Cardiovascular Imaging Expert Panel Paper*. 2023. Vol. 16, N 3. P. 408–425. doi: 10.1016/j.jcmg.2022.12.026
3. Catalano M.A., Hemli J.M., Lasic Z., Patel N.C. Repair of left ventricular aneurysm in the setting of noncompaction // *Journal of Cardiology Cases*. 2022. Vol. 25, N 6. P. 416–419. doi: 10.1016/j.jccase.2022.01.008
4. Tilahun T., Kedir E., Eshetu B. Fatal Left Ventricular Aneurysm in a 13 Years Old Male Child: A Case Report // *Ethiopian journal of health sciences*. 2021. Vol. 31, N 4. P. 903–906. doi: 10.4314/ejhs.v31i4.26
5. Tian S., Liang H., Li X., et al. A novel mutation in the TTN gene resulted in left ventricular noncompaction: a case report and literature review // *BMC Cardiovascular Disorders*. 2023. Vol. 23, N 1. P. 352. doi: 10.1186/s12872-023-03382-w
6. Yakabe D., Matsushima S., Uchino S., et al. Left Ventricular Noncompaction with Multiple Thrombi in Apical Aneurysm // *Internal Medicine*. 2020. Vol. 59, N 3. P. 377–381. doi: 10.2169/internalmedicine.3489-19
7. Gerecke B.J., Engberding R. Noncompaction Cardiomyopathy- History and Current Knowledge for Clinical Practice // *Journal of Clinical Medicine*. 2021. Vol. 10, N 11. P. 2457. doi: 10.3390/jcm10112457
8. Daprati A., Sassi C.G., Garatti A., Saitto G., Menicanti L. Congenital left ventricular aneurysm with myocardial noncompaction pattern // *Asian Cardiovascular and Thoracic Annals*. 2020. Vol. 28, N 8. P. 504–506. doi: 10.1177/0218492320949833
9. Ogah O.S., Iyawe E.P., Orimolade O.A., et al. Left ventricular noncompaction in Ibadan, Nigeria // *The Egyptian Heart Journal*. 2023. Vol. 75, N 1. P. 69. doi: 10.1186/s43044-023-00396-9
10. Gaižauskienė K., Glembockytė G., Glaveckaitė S., Valevičienė N. Magnetic resonance diagnostic criteria of non-compaction cardiomyopathy: new diagnostic criteria still needed? // *Seminars in Cardiovascular Medicine*. 2023. Vol. 29, N 1. P. 1–13. doi: 10.2478/semcard-2022-0003
11. Ohlow M.A. Congenital left ventricular aneurysms and diverticula: an entity in search of an identity // *Journal of Geriatric Cardiology*. 2017. Vol. 14, N 12. P. 750–762. doi: 10.11909/j.issn.1671-5411.2017.12.005
12. Siripornpitak S., Khositseth A., Sriprachyakul A. Left Ventricular Non-compaction with Ventricular Aneurysms // *Journal of Cardiovascular Imaging*. 2020. Vol. 28, N 3. P. 222–225. doi: 10.4250/jcvi.2019.0091

AUTHORS' INFO

* **Bauyrzhan B. Kaliyev**, MD;
address: 36 Turan Avenue, 010000, Astana, Kazakhstan;
ORCID: 0000-0003-4825-749X;
eLibrary SPIN: 7315-9129;
e-mail: baur233113@mail.ru

Tairkhan B. Dautov, MD, Dr. Sci. (Med.), Assistant Professor;
ORCID: 0000-0002-5267-0108;
eLibrary SPIN: 8632-6605;
e-mail: tairkhan.dautov@mail.ru

Bibissara T. Yerekesh, MD;
ORCID: 0009-0002-0185-3278;
e-mail: Bibisara_97@mail.ru

ОБ АВТОРАХ

* **Калиев Бауыржан Бахытович**;
адрес: проспект Туран, 36, 010000, Астана, Казахстан;
ORCID: 0000-0003-4825-749X;
eLibrary SPIN: 7315-9129;
e-mail: baur233113@mail.ru

Даутов Таирхан Бекполатович, д-р мед. наук, доцент;
ORCID: 0000-0002-5267-0108;
eLibrary SPIN: 8632-6605;
e-mail: tairkhan.dautov@mail.ru

Ерекеш Бибисара Туреханкызы;
ORCID: 0009-0002-0185-3278;
e-mail: Bibisara_97@mail.ru

* Corresponding author / Автор, ответственный за переписку

DOI: <https://doi.org/10.17816/DD561354>

Ограничения использования гистологического исследования биоптатов как «золотого стандарта» диагностики на примере аденокарциномы пищевода: описание случая

Д.А. Ахмедзянова¹, О.К. Юцевич², Р.В. Решетников¹, О.В. Тащян³, С.С. Пирогов², М.П. Мазурова², Н.Н. Волченко², А.К. Камалов², Ю.Ф. Шумская¹, М.Г. Мнацаканян³

¹ Научно-практический клинический центр диагностики и телемедицинских технологий, Москва, Российская Федерация;

² Московский научно-исследовательский онкологический институт имени П.А. Герцена — филиал Национального медицинского исследовательского центра Радиологии, Москва, Российская Федерация;

³ Первый Московский государственный медицинский университет имени И.М. Сеченова, Москва, Российская Федерация

АННОТАЦИЯ

Аденокарцинома пищевода — одно из самых распространённых злокачественных новообразований желудочно-кишечного тракта. Для выявления заболевания на ранних стадиях используют эндоскопические, морфологические, иммуногистохимические методы обследования, однако они требуют не только применения высокоспециализированного оборудования, но и зависят от профессионализма врача-эндоскописта и врача-патоморфолога.

В статье описано клиническое наблюдение пациента с прогрессирующей дисфагией, вызванной опухолью пищевода, распространяющейся на субкардиальный отдел желудка, которую не удавалось патоморфологически верифицировать в течение одного года. Данные эзофагогастродуоденоскопии, выполненной в медицинской организации по месту жительства, компьютерной томографии и рентгеноскопии пищевода с двойным контрастированием не оставляли сомнений в злокачественности новообразования, однако результаты многочисленных гистологических исследований свидетельствовали в пользу аденомы пилорических желёз, аденомы из париетальных, либо онкоцитарных клеток с фокусами дисплазии эпителия высокой степени. Эндоскопическое исследование с таргетированной биопсией в условиях специализированного учреждения позволило доказать злокачественность опухолевого процесса.

Результаты исследования демонстрируют важность клинической картины и инструментальных методов для постановки заключительного диагноза при противоречивых данных патоморфологических исследований и в очередной раз поднимают проблему ограничений гистологического исследования биоптатов как «золотого стандарта» диагностики злокачественных новообразований.

Ключевые слова: аденокарцинома пищевода; пищевод Барретта; кардиоэзофагеальный переход; эзофагогастродуоденоскопия; компьютерная томография; биопсия.

Как цитировать:

Ахмедзянова Д.А., Юцевич О.К., Решетников Р.В., Тащян О.В., Пирогов С.С., Мазурова М.П., Волченко Н.Н., Камалов А.К., Шумская Ю.Ф., Мнацаканян М.Г. Ограничения использования гистологического исследования биоптатов как «золотого стандарта» диагностики на примере аденокарциномы пищевода: описание случая // Digital Diagnostics. 2023. Т. 4, № 4. С. 633–642. DOI: <https://doi.org/10.17816/DD561354>

DOI: <https://doi.org/10.17816/DD561354>

Tissue sampling and histopathological limitations in esophageal cancer

Dina A. Akhmedzyanova¹, Olga K. Yutsevich², Roman V. Reshetnikov¹, Olga V. Tashchyan³, Sergey S. Pirogov², Maria P. Mazurova², Nadezhda N. Volchenko², Aziz K. Kamalov², Yuliya F. Shumskaya¹, Marina G. Mnatsakanyan³

¹ Research and Practical Clinical Center for Diagnostics and Telemedicine Technologies, Moscow, Russian Federation;

² P.A. Herzen Moscow Oncology Research Institute, Branch, National Medical Research Radiological Center, Moscow, Russian Federation;

³ The First Sechenov Moscow State Medical University, Moscow, Russian Federation

ABSTRACT

Esophageal adenocarcinoma is a common gastrointestinal cancer. Esophagogastroduodenoscopy with biopsy and immunohistochemistry are used to detect the neoplasm at an early stage. Definitive diagnosis requires not only highly specialized equipment but also the skills of the endoscopist and pathologist. We report the case of a 35-year-old man with progressive dysphagia caused by gastroesophageal cancer. Numerous esophagogastroduodenoscopy studies, computed tomography, and barium X-ray swallow revealed an extensive esophageal lesion; however, pathomorphologic examinations did not confirm malignancy within a year. Histological studies showed pyloric gland adenoma and adenoma from parietal or oncocytic cells with high-grade dysplasia. Esophagogastroduodenoscopy with targeted biopsy at a specialized center confirmed the tumor malignancy. This clinical case demonstrates the importance of summing clinical symptoms and using additional instrumental methods to make a definitive diagnosis if biopsy results are ambiguous.

Keywords: esophageal adenocarcinoma; Barrett's esophagus; gastroesophageal junction; esophagogastroduodenoscopy; computed tomography; biopsy.

To cite this article:

Akhmedzyanova DA, Yutsevich OK, Reshetnikov RV, Tashchyan OV, Pirogov SS, Mazurova MP, Volchenko NN, Kamalov AK, Shumskaya YuF, Mnatsakanyan MG. Tissue sampling and histopathological limitations in esophageal cancer. *Digital Diagnostics*. 2023;4(4):633–642. DOI: <https://doi.org/10.17816/DD561354>

Received: 18.07.2023

Accepted: 16.11.2023

Published online: 21.11. 2023

DOI: <https://doi.org/10.17816/DD561354>

将活检标本的组织学检查作为诊断“金标准”的局限性：一个例子

Dina A. Akhmedzyanova¹, Olga K. Yutsevich², Roman V. Reshetnikov¹, Olga V. Tashchyan³, Sergey S. Pirogov², Maria P. Mazurova², Nadezhda N. Volchenko², Aziz K. Kamalov², Yuliya F. Shumskaya¹, Marina G. Mnatsakanyan³

¹ Research and Practical Clinical Center for Diagnostics and Telemedicine Technologies, Moscow, Russian Federation;

² P.A. Herzen Moscow Oncology Research Institute, Branch, National Medical Research Radiological Center, Moscow, Russian Federation;

³ The First Sechenov Moscow State Medical University, Moscow, Russian Federation

简评

食管腺癌是胃肠道最常见的恶性肿瘤之一。为了在早期阶段发现这种疾病，医生采用内窥镜、形态学、免疫组化等检查方法。但是，这些方法不仅需要使用高度专业化的设备，还取决于内镜医师和病理形态学医师的专业水平。

本文描述了对一名进行性吞咽困难患者的临床观察。吞咽困难是由食道肿瘤引起的。肿瘤已扩散到胃的贲门下段。肿瘤在一年内无法进行病理形态学验证。在居住地医疗机构进行的食管胃十二指肠镜检查、电子计算机断层扫描和食管双对比透视检查的数据证实了肿瘤的恶性程度。然而，大量组织学检查的结果都支持幽门腺腺瘤、顶体腺瘤或带有高度上皮发育不良病灶的肿瘤细胞腺瘤。在专业机构的条件下，通过内窥镜检查 and 靶向活检，才有可能证实肿瘤的恶性程度。

研究表明，在病理形态学检查数据相互矛盾的情况下，临床表现和仪器方法对最终诊断的重要。这再次提出活检标本的组织学检查作为诊断恶性肿瘤“金标准”的局限性问题。

关键词：食管腺癌；巴雷特食管；食管贲门交界处；食管胃十二指肠镜检查；电子计算机断层扫描；活检。

引用本文：

Akhmedzyanova DA, Yutsevich OK, Reshetnikov RV, Tashchyan OV, Pirogov SS, Mazurova MP, Volchenko NN, Kamalov AK, Shumskaya YuF, Mnatsakanyan MG. 将活检标本的组织学检查作为诊断“金标准”的局限性：一个例子. *Digital Diagnostics*. 2023;4(4):633–642.

DOI: <https://doi.org/10.17816/DD561354>

收到: 18.07.2023

接受: 16.11.2023

发布日期: 21.11.2023

BACKGROUND

Esophageal cancer is the sixth most common cause of cancer deaths worldwide [1], and the incidence of esophageal adenocarcinoma is rapidly increasing in developed countries [2]. This type of esophageal cancer is extremely aggressive, with a 5-year survival rate <20% [3]. Risk factors for esophageal adenocarcinoma and gastroesophageal junction adenocarcinoma include mechanical, chemical, and thermal injury to the esophageal mucosa, male sex, obesity, and smoking [4], with the most significant risk factor being Barrett's esophagus caused by gastroesophageal reflux disease [5]. Prognosis is determined by both the tumor stage and its macroscopic morphology [6–8]. W.R.C. Knight et al. showed that ulcerating tumors were associated with a more favorable prognosis than exophytic or stenotic lesions [9].

Esophageal cancer is commonly diagnosed using radiological methods, specifically with double-contrast upper gastrointestinal radiography and computed tomography (CT) of the chest [10]. These methods allow evaluation of the lesion size, invasion depth, and tumor type. However, these findings must be verified by histopathology [3]. Esophagogastroduodenoscopy (EGD) and transnasal endoscopy are used to diagnose esophageal tumors. They allow visual examination of the organs for abnormalities and obtain biopsy specimens for morphological examination, which is considered the “gold standard” for tumor verification [11]. However, histological findings are dependent on various factors, including the qualifications and experience of the pathologist and endoscopist, quality of reagents used in specimen preservation, and quality of biopsy specimens obtained by endoscopic forceps biopsy. Therefore, biopsy results may not always match the clinical, endoscopic, or radiological findings [12]. Furthermore, diagnosing adenocarcinoma in the setting of Barrett's esophagus is challenging because of its typically endophytic growth pattern, which necessitates a specific biopsy technique [13].

Herein, a case of a patient with progressive dysphagia who was diagnosed with esophageal adenocarcinoma that had spread to the middle third of the esophagus and subcardial stomach is presented. Clinical and instrumental findings were unambiguously indicative of malignancy. However, repeated morphological examinations did not confirm the diagnosis. A definitive diagnosis was made after an EGD-guided targeted biopsy at a tertiary cancer center.

This case report was prepared in accordance with the CARE Case Report Guidelines [14].

CASE REPORT

Medical History

Patient N was a 35-year-old man.

In **March 2021**, he experienced a gradual loss of appetite. He did not seek medical advice because he believed that the symptoms were caused by work-related stress.

In **March 2022**, he presented to his primary care physician with symptoms of difficulty swallowing, nausea and vomiting, and a throat lump sensation. At presentation, he was 192 cm tall and weighed 185 kg (body mass index, 50.18 kg/m², class III obesity).

EGD revealed a tumor mass with multiple ulcerations in the esophagus, beginning 30 cm from the incisors and nearly extending to the cardia. No reliable pathological evidence of tumor cells, dysplastic cells, or atypical cells was found in the biopsy specimens.

In **April 2022**, the patient visited a gastroenterologist and underwent EGD at follow-up. The examination revealed a significantly narrowed lumen in the middle and lower thirds of the esophagus, which was caused by a circumferential tumor with focal destruction. The tumor's proximal and distal edges were visualized at 25 and 45 cm from the incisors, respectively. Submucosal tumor infiltration was observed in the subcardial stomach. Repeated biopsy of the ulcerations demonstrated fragments of a villous tumor lined with columnar epithelium with low-grade dysplasia. Another EGD-guided biopsy revealed no signs of atypical cells.

Preliminary diagnosis. The observed pathological changes were consistent with the presentation of a pyloric gland adenoma with focal high-grade dysplasia arising from parietal or oncocytic cells that were highly suspicious of malignancy. Histological findings were inconsistent with clinical presentation and endoscopy. To address the inconsistencies between the endoscopic and histological findings, the tumor immunophenotype was examined by immunohistochemistry, which correlated with the pyloric tumor expressing gastric superficial-foveolar epithelial mucins and pyloric gland mucins. No *p53* mutation was detected in the tumor cells, which did not exhibit high proliferative activity. Because the malignant nature of the tumor could not be conclusively established through immunohistochemistry, the mass was considered a pyloric gland adenoma. A local gastroenterologist suggested a dynamic follow-up.

In **May 2022**, the patient presented to a gastroenterologist with worsening symptoms of impaired food passage from the mouth to the stomach and a weight loss of 15 kg over the past 3 months (body mass index, 46.12 kg/m²). The patient was admitted to the gastroenterology department for examination and diagnosis verification.

Laboratory Data

Blood chemistry revealed hyperuricemia (uric acid, 634.8 mmol/L; normal range, 154–357 mmol/L) and high levels of nonspecific inflammatory markers:

- Erythrocyte sedimentation rate: elevation to 50 (normal range, 2–20) mm/h
- Fibrinogen: elevation to 4.81 (normal range, 1.8–4) g/L
- C-reactive protein: elevation to 11.4 (normal range, 0–5) mg/L.

Latent iron deficiency was also found:

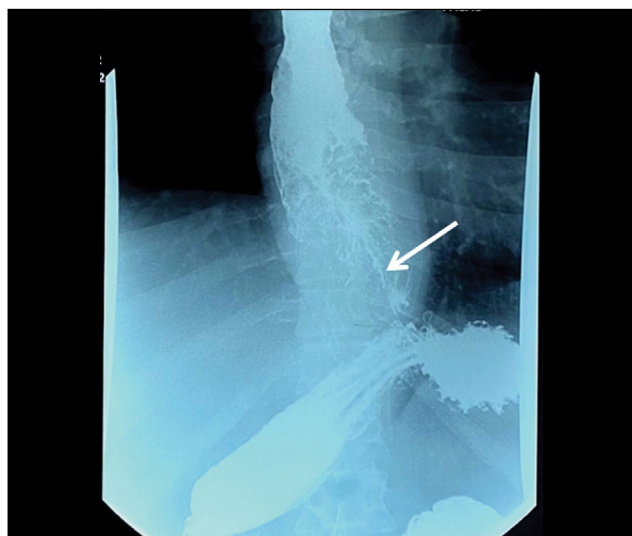


Fig. 1. Upper GI X-ray. Circumferential narrowing of the esophagus; a thin passage of barium leakage (arrow).

- Hemoglobin: 147 (normal range, 132–180) g/L
- Color index: 0.9
- Iron: 5.9 (normal range, 10.7–32.2) mmol/L

Imaging Studies

Barium-contrast upper gastrointestinal X-ray findings were suggestive of an extended mass lesion in the middle and lower thirds of the esophagus with luminal stenosis (Fig. 1).

Chest CT showed a 186-mm esophageal tumor that had extended to the cardia. The esophageal walls had a polypoid

thickening of up to 41 mm, and a significant narrowing of the esophageal lumen to 2 mm was observed. Signs of regional lymph node involvement were also visible (Fig. 2).

Abdominal CT did not reveal any distant metastases. The results demonstrated a locally advanced malignant esophageal tumor involving the cardia.

The patient was referred to a tertiary cancer center. Endoscopy at the cancer center showed the proximal edge of esophageal tumor infiltration at a site 24 cm from the incisors. The tumor appeared as multiple whitish-red merging lesions that spread circumferentially to the subcardial stomach. Deep ulcers covered with fibrin and necrotic plaque were observed. A fistula opening was found in the tumor tissue at a site 36 cm from the incisors, with the creamy opalescent contents flowing into the lumen. The esophageal lumen was significantly narrowed by the exophytic component of the tumor (Fig. 3). The tumor tissue was dough-like in texture and bled easily upon contact. The circumferentially infiltrated cardioesophageal junction was visualized at a site 44 cm from the incisors. The tumor infiltrated along the posterior wall to the subcardia (Fig. 4).

Targeted stepwise biopsy of the non-necrotic regions was performed. The pathology results indicated low-grade esophageal adenocarcinoma progressing from Barrett's esophagus.

Diagnosis and Treatment

The patient was diagnosed with low-grade cT3N1M0 adenocarcinoma progressing from Barrett's esophagus. The



Fig. 2. Computed tomography of the chest. The white arrows show pathological changes: *a*, a 186-mm esophageal tumor extending to the cardia; *b*, massive invasion of the tumor tissue with narrowed lumen in the middle third of the esophagus; *c*, tumor involvement of the regional para-aortic lymph node; *d*, luminal narrowing to 2 mm in the lower third.

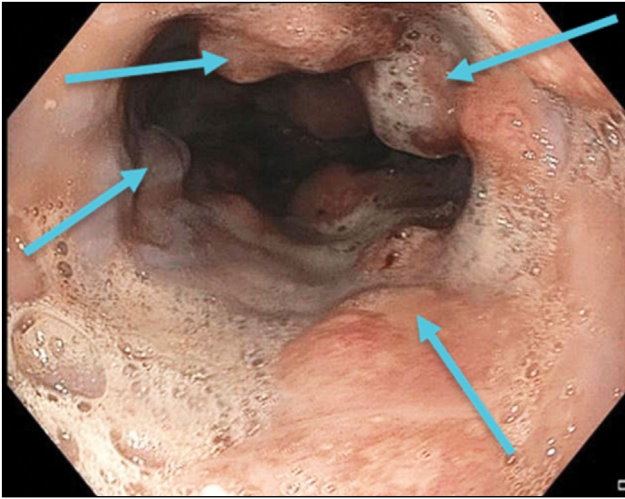


Fig. 3. Endoscopic image. Stenosing adenocarcinoma progressing from Barrett's esophagus. The circumferential tumor is indicated by the blue arrows.

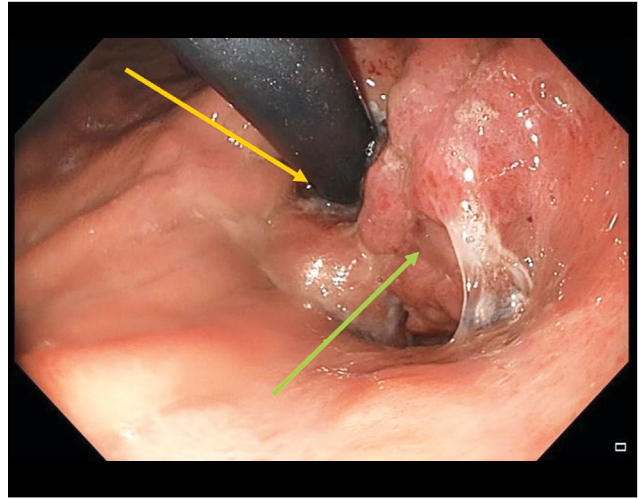


Fig. 4. Endoscopic image. Stenosing adenocarcinoma progressing from Barrett's esophagus. The yellow arrow shows the endoscope located at the stomach entrance, and the green arrow shows the tumor tissue.

tumor had spread to the cardia and was complicated by an esophageal–mediastinal fistula.

Given the patient's young age and absence of long-term tumor metastasis, radical surgical treatment was deemed appropriate. In July 2022, the patient underwent single-step surgery including thoracoscopic esophageal resection, esophageal repair with a pedicle flap composed of a segment of the greater curvature of the stomach, cervical anastomosis formation, and 2S lymphadenectomy. During the surgical intervention, an esophageal–mediastinal fistula was also removed.

Pathological examination of the surgical specimen confirmed a low-grade esophageal adenocarcinoma progressing from Barrett's esophagus with necrotic sites and surface ulceration. The tumor had infiltrated the mucous membrane and the submucosal muscle layer of the esophageal wall and had spread to the cardia. Tumor metastases were detected in 4 of 11 esophageal lymph nodes and 4 of 6 lymph nodes along the lesser curvature of the stomach.

The final diagnosis was stage III pT4N1M0 esophageal adenocarcinoma progressing from Barrett's esophagus.

The postoperative period was complicated by a tracheoesophageal fistula, which was epithelialized after 3 weeks of endoscopic vacuum therapy. Given the advanced stage of the primary tumor, the high risk of disease recurrence, and young patient age, he received nine cycles of adjuvant FOLFOX (calcium folinate, fluorouracil, and oxaliplatin).

Follow-up examinations in December 2022 and April 2023 showed no signs of local tumor recurrence or progression.

DISCUSSION

This clinical case report discloses several problems associated with the endoscopic and pathological diagnosis of a malignant tumor progressing from Barrett's esophagus.

Histological confirmation of the tumor process and its type is vital before surgery, or other treatments can be performed. The decision to use chemotherapy or combined chemoradiotherapy, either as an adjuvant or neoadjuvant treatment, depends on both the tumor stage and its histological pattern. In this case, the main issue was the inconsistency between the endoscopy and radiology results and the histological findings.

Advanced endoscopic equipment provides high-resolution imaging of the mucous membrane of hollow organs. The primary principle should be to perform a comprehensive examination of the entire organ and identify the most suspicious regions of the mucous membrane. This is a more labor-intensive and time-consuming manipulation. The decision to perform a targeted biopsy should only be made after a detailed endoscopy. Targeted biopsy differs from blind biopsy and classic forceps biopsy by taking specimens from the most suspicious regions using more specific techniques such as narrowed-spectrum endoscopy combined with near-focus mode [15].

Early-stage adenocarcinoma progressing from Barrett's esophagus is most commonly characterized by a flat growth pattern within the metaplasia segment [16]. In our case, the esophageal carcinoma was accompanied by massive adenomatous tissue growth, which delayed the malignancy verification because adenomatous tissue samples were taken in multiple nontargeted biopsies. The diagnosis was established accurately through a targeted, stepwise biopsy of the non-necrotic regions.

A study reported that only 35% of patients experience correct detection and preoperative staging of esophageal adenocarcinomas [17], a finding supported by this case. One reason for this is the insufficient accuracy of forceps biopsy as a means of obtaining pathology specimens. If esophageal malignancy is suspected, endoscopic mucosal resection is warranted [18]. The value of a biopsy is increased when at

least five tissue fragments are obtained. This increases the likelihood of detecting atypical tumor cells, even incidentally, in one of the fragments [19, 20].

Pathologists may disagree on whether the changes detected in the biopsy specimens are caused by dysplasia or signs of a malignant tumor. According to A.H. Ormsby et al., pathologists specializing in gastrointestinal tissues frequently disagree on the diagnosis of high-grade dysplasia versus adenocarcinoma, even when evaluating total resection specimens [21]. The authors suggested revising treatment strategies that differentiate between severe dysplasia and intramucosal adenocarcinoma based on histological differences using a limited number of biopsies.

CONCLUSION

This case report demonstrates the significance of a clinician's critical approach to pathology results. The diagnosis should also be based on the clinical presentation and instrumental findings. However, in cases of unclear histological findings, biopsy samples from the tumor sites with the highest quality or volume are recommended, even if multiple biopsies are required.

ADDITIONAL INFORMATION

Funding source. This article was prepared by a group of authors as a part of the research and development effort titled "Opportunistic

screening of high-profile and other common diseases", No. 123031400009-1", (USIS No. 123031400009-1) in accordance with the Order No. 1196 dated December 21, 2022 "On approval of state assignments funded by means of allocations from the budget of the city of Moscow to the state budgetary (autonomous) institutions subordinate to the Moscow Health Care Department, for 2023 and the planned period of 2024 and 2025" issued by the Moscow Health Care Department.

Competing interests. The authors declare that they have no competing interests.

Authors' contribution. All authors made a substantial contribution to the conception of the work, acquisition, analysis, interpretation of data for the work, drafting and revising the work, final approval of the version to be published and agree to be accountable for all aspects of the work. D.A. Akhmedzyanova — concept, collection and processing of data, data analysis, manuscript writing; O.K. Yutsevich — collection and processing of data, manuscript writing; R.V. Reshetnikov — concept, manuscript editing; O.V. Tashchyan, S.S. Pirogov, M.P. Mazurova, N.N. Volchenko, A.K. Kamalov, Y.F. Shumskaya — manuscript editing, preparation of illustrative material; M.G. Mnatsakanyan — final editing, manuscript approval.

Consent for publication. Written consent was obtained from the patient for publication of relevant medical information and all of accompanying images within the manuscript in Digital Diagnostics Journal.

Acknowledgments. The authors express their gratitude to Ivan A. Blokhin for his support in the text editing.

REFERENCES

1. Bray F, Ferlay J, Soerjomataram I, et al. Global cancer statistics 2018: GLOBOCAN estimates of incidence and mortality worldwide for 36 cancers in 185 countries. *CA Cancer J Clin.* 2018;68(6):394–424. doi: 10.3322/caac.21492
2. McColl KEL. What is causing the rising incidence of esophageal adenocarcinoma in the West and will it also happen in the East? *J Gastroenterol.* 2019;54(8):669–673. doi: 10.1007/s00535-019-01593-7
3. Joseph A, Raja S, Kamath S, et al. Esophageal adenocarcinoma: A dire need for early detection and treatment. *Cleve Clin J Med.* 2022;89(5):269–279. doi: 10.3949/ccjm.89a.21053
4. Uhlenhopp DJ, Then EO, Sunkara T, Gaduputi V. Epidemiology of esophageal cancer: update in global trends, etiology and risk factors. *Clin J Gastroenterol.* 2020;13(6):1010–1021. doi: 10.1007/s12328-020-01237-x
5. Zhang HY, Spechler SJ, Souza RF. Esophageal adenocarcinoma arising in Barrett esophagus. *Cancer Lett.* 2009;275(2):170–177. doi: 10.1016/j.canlet.2008.07.006
6. Deng HY, Alai G, Luo J, et al. Cancerous esophageal stenosis before treatment was significantly correlated to poor prognosis of patients with esophageal cancer: a meta-analysis. *J Thorac Dis.* 2018;10(7):4212–4219. doi: 10.21037/jtd.2018.06.89
7. Sillah K, Pritchard SA, Watkins GR, et al. The degree of circumferential tumour involvement as a prognostic factor in oesophageal cancer. *Eur J Cardiothorac Surg.* 2009;36(2):368–373. doi: 10.1016/j.ejcts.2008.12.052
8. Deng HY, Li G, Luo J. Does oesophageal stenosis have any impact on survival of oesophageal cancer patients? *Interact Cardiovasc Thorac Surg.* 2018;27(3):384–386. doi: 10.1093/icvts/ivy095
9. Knight WRC, McEwen R, Byrne BE, et al. Endoscopic tumour morphology impacts survival in adenocarcinoma of the oesophagus. *Eur J Surg Oncol.* 2020;46(12):2257–2261. doi: 10.1016/j.ejso.2020.07.003
10. Morozov SP, editor. *I-74 Informativeness of radial diagnostics methods in various pathological conditions of the organism. Section 2: Diagnostics of pathological conditions and diseases of the gastrointestinal tract.* Moscow; 2018. (In Russ).
11. Ishihara R, Goda K, Oyama T. Endoscopic diagnosis and treatment of esophageal adenocarcinoma: introduction of Japan Esophageal Society classification of Barrett's esophagus. *J Gastroenterol.* 2019;54(1):1–9. doi: 10.1007/s00535-018-1491-x
12. Zagajnova EV, Zagajnov VE, Gladkova ND, et al. Optical coherence tomography in surgical treatment of esophageal cancer. *Grekov's Bulletin of Surgery.* 2007;166(2):22–26.
13. Davydov MI, Ter-Ovanesov MD, Stilidi IS, et al. Barrett's esophagus: from theoretical foundations to practical recommendations. *Practical oncology.* 2003;4(2):109–119. (In Russ).
14. Barber MS, Aronson JK, von Schoen-Angerer T, et al. CARE guidelines for case reports: explanation and elaboration document.

Translation into Russian. *Digital Diagnostics*. 2022;3(1):16–42. doi: 10.17816/DD105291

15. Wani S, Rubenstein JH, Vieth M, Bergman J. Diagnosis and Management of Low-Grade Dysplasia in Barrett's Esophagus: Expert Review From the Clinical Practice Updates Committee of the American Gastroenterological Association. *Gastroenterology*. 2016;151(5):822–835. doi: 10.1053/j.gastro.2016.09.040

16. di Pietro M, Canto MI, Fitzgerald RC. Endoscopic Management of Early Adenocarcinoma and Squamous Cell Carcinoma of the Esophagus: Screening, Diagnosis, and Therapy. *Gastroenterology*. 2018;154(2):421–436. doi: 10.1053/j.gastro.2017.07.041

17. Winiker M, Mantziari S, Figueiredo SG, et al. Accuracy of preoperative staging for a priori resectable esophageal cancer. *Dis Esophagus*. 2018;31(1):1–6. doi: 10.1093/dote/dox113

18. Elsadek HM, Radwan MM. Diagnostic Accuracy of Mucosal Biopsy versus Endoscopic Mucosal Resection in Barrett's Esophagus and Related Superficial Lesions. *Int Sch Res Notices*. 2015;2015. doi: 10.1155/2015/735807

19. Tryakin AA, Besova NS, Volkov NM, et al. Practice guidelines for drug treatment of esophageal and gastroesophageal junction cancers. *Malignant tumours (Zlokačestvennye opuholi)*. 2021;11(3S2-1):299–313. (In Russ). doi: 10.18027/2224-5057-2021-11-3s2-20

20. Ajani JA, D'Amico TA, Bentrem DJ, et al. Esophageal and Esophagogastric Junction Cancers, Version 2.2023, NCCN Clinical Practice Guidelines in Oncology. *J Natl Compr Canc Netw*. 2023;21(4):393–422. doi: 10.6004/jnccn.2023.0019

21. Ormsby AH, Petras RE, Henricks WH, et al. Observer variation in the diagnosis of superficial oesophageal adenocarcinoma. *Gut*. 2002;51(5):671–676. doi: 10.1136/gut.51.5.671

СПИСОК ЛИТЕРАТУРЫ

1. Bray F., Ferlay J., Soerjomataram I., et al. Global cancer statistics 2018: GLOBOCAN estimates of incidence and mortality worldwide for 36 cancers in 185 countries // *CA Cancer J Clin*. 2018. Vol. 68, N 6. P. 394–424. doi: 10.3322/caac.21492

2. McColl K.E.L. What is causing the rising incidence of esophageal adenocarcinoma in the West and will it also happen in the East? // *J Gastroenterol*. 2019. Vol. 54, N 8. P. 669–673. doi: 10.1007/s00535-019-01593-7

3. Joseph A., Raja S., Kamath S., et al. Esophageal adenocarcinoma: A dire need for early detection and treatment // *Cleve Clin J Med*. 2022. Vol. 89, N 5. P. 269–279. doi: 10.3949/ccjm.89a.21053

4. Uhlenhopp D.J., Then E.O., Sunkara T., Gaduputi V. Epidemiology of esophageal cancer: update in global trends, etiology and risk factors // *Clin J Gastroenterol*. 2020. Vol. 13, N 6. P. 1010–1021. doi: 10.1007/s12328-020-01237-x

5. Zhang H.Y., Spechler S.J., Souza R.F. Esophageal adenocarcinoma arising in Barrett esophagus // *Cancer Lett*. 2009. Vol. 275, N 2. P. 170–177. doi: 10.1016/j.canlet.2008.07.006

6. Deng H.Y., Alai G., Luo J., et al. Cancerous esophageal stenosis before treatment was significantly correlated to poor prognosis of patients with esophageal cancer: a meta-analysis // *J Thorac Dis*. 2018. Vol. 10, N 7. P. 4212–4219. doi: 10.21037/jtd.2018.06.89

7. Sillah K., Pritchard S.A., Watkins G.R., et al. The degree of circumferential tumour involvement as a prognostic factor in oesophageal cancer // *Eur J Cardiothorac Surg*. 2009. Vol. 36, N 2. P. 368–373. doi: 10.1016/j.ejcts.2008.12.052

8. Deng H.Y., Li G., Luo J. Does oesophageal stenosis have any impact on survival of oesophageal cancer patients? // *Interact Cardiovasc Thorac Surg*. 2018. Vol. 27, N 3. P. 384–386. doi: 10.1093/icvts/ivy095

9. Knight W.R.C., McEwen R., Byrne B.E., et al. Endoscopic tumour morphology impacts survival in adenocarcinoma of the oesophagus // *Eur J Surg Oncol*. 2020. Vol. 46, N 12. P. 2257–2261. doi: 10.1016/j.ejso.2020.07.003

10. И–74 Информативность методов лучевой диагностики при различных патологических состояниях организма. Раздел 2. Диагностика патологических состояний и заболеваний желудочно-кишечного тракта / под ред. С.П. Морозова. Москва, 2018.

11. Ishihara R., Goda K., Oyama T. Endoscopic diagnosis and treatment of esophageal adenocarcinoma: introduction of Japan Esophageal

Society classification of Barrett's esophagus // *J Gastroenterol*. 2019. Vol. 54, N 1. P. 1–9. doi: 10.1007/s00535-018-1491-x

12. Загайнова Е.В., Загайнов В.Е., Гладкова Н.Д., и др. Оптическая когерентная томография при хирургическом лечении рака пищевода // *Вестник хирургии имени И.И. Грекова*. 2007. Т. 166(2). С. 22–26.

13. Давыдов М.И., Тер-Ованесов М.Д., Стилиди И.С., и др. Пищевод Барретта: от теоретических основ к практическим рекомендациям // *Практическая онкология*. 2003. Т. 4, № 2. С. 109–119.

14. Barber M.S., Aronson J.K., von Schoen-Angerer T., et al. Рекомендации CARE для описания случаев: разъяснения и уточнения // *Digital Diagnostics*. Vol. 3, N 1. С. 16–42. doi: 10.17816/DD105291

15. Wani S., Rubenstein J.H., Vieth M., Bergman J. Diagnosis and Management of Low-Grade Dysplasia in Barrett's Esophagus: Expert Review From the Clinical Practice Updates Committee of the American Gastroenterological Association // *Gastroenterology*. 2016. Vol. 151, N 5. P. 822–835. doi: 10.1053/j.gastro.2016.09.040

16. di Pietro M., Canto M.I., Fitzgerald R.C. Endoscopic Management of Early Adenocarcinoma and Squamous Cell Carcinoma of the Esophagus: Screening, Diagnosis, and Therapy // *Gastroenterology*. 2018. Vol. 154, N 2. P. 421–436. doi: 10.1053/j.gastro.2017.07.041

17. Winiker M., Mantziari S., Figueiredo S.G., et al. Accuracy of preoperative staging for a priori resectable esophageal cancer // *Dis Esophagus*. 2018. Vol. 31, N 1. P. 1–6. doi: 10.1093/dote/dox113

18. Elsadek H.M., Radwan M.M. Diagnostic Accuracy of Mucosal Biopsy versus Endoscopic Mucosal Resection in Barrett's Esophagus and Related Superficial Lesions // *Int Sch Res Notices*. 2015. Vol. 2015. doi: 10.1155/2015/735807

19. Трякин А.А., Бесова Н.С., Волков Н.М., и др. Практические рекомендации по лекарственному лечению рака пищевода и пищеводно-желудочного перехода // *Злокачественные опухоли*. 2021. Т. 11, № 3S2-1. С. 299–313. doi: 10.18027/2224-5057-2021-11-3s2-20

20. Ajani J.A., D'Amico T.A., Bentrem D.J., et al. Esophageal and Esophagogastric Junction Cancers, Version 2.2023, NCCN Clinical Practice Guidelines in Oncology // *J Natl Compr Canc Netw*. 2023. Vol. 21, N 4. P. 393–422. doi: 10.6004/jnccn.2023.0019

21. Ormsby A.H., Petras R.E., Henricks W.H., et al. Observer variation in the diagnosis of superficial oesophageal adenocarcinoma // *Gut*. 2002. Vol. 51, N 5. P. 671–676. doi: 10.1136/gut.51.5.671

AUTHORS' INFO

*** Dina A. Akhmedzyanova;**

address: 24 Petrovka st. bld. 1, Russia, Moscow;
ORCID: 0000-0001-7705-9754;
eLibrary SPIN: 6983-5991;
e-mail: AkhmedzyanovaDA@zdrav.mos.ru

Olga K. Yutsevich;

ORCID: 0000-0002-3860-9853;
e-mail: o.yutsevitch@yandex.ru

Roman V. Reshetnikov, Cand. Sci. (Phys.-Math.);

ORCID: 0000-0002-9661-0254;
eLibrary SPIN: 8592-0558;
e-mail: r.reshetnikov@npcmr.ru

Olga V. Tashchyan, MD, Cand. Sci. (Med.);

ORCID: 0000-0001-6759-6820;
eLibrary SPIN: 3658-1120;
e-mail: olgatash1@rambler.ru

Sergey S. Pirogov, MD, Dr. Sci. (Med.);

ORCID: 0000-0002-8101-2155;
eLibrary SPIN: 7812-5502;
e-mail: pirogov@mail.ru

Maria P. Mazurova, MD, Cand. Sci. (Med.);

ORCID: 0000-0002-4873-4455;
eLibrary SPIN: 4455-3055;
e-mail: mnioi_morphology@mail.ru

Nadezhda N. Volchenko, MD, Dr. Sci. (Med.), Professor;

ORCID: 0000-0003-0421-4172;
e-mail: mnioi_morphology@mail.ru

Aziz K. Kamalov;

ORCID: 0000-0001-7376-6056;
eLibrary SPIN: 1671-1600;
e-mail: kak6768@mail.ru

Yuliya F. Shumskaya;

ORCID: 0000-0002-8521-4045;
eLibrary SPIN: 3164-5518;
e-mail: shumskayayf@zdrav.mos.ru

Marina G. Mnatsakanyan, MD, Dr. Sci. (Med.), Professor;

ORCID: 0000-0001-9337-7453;
eLibrary SPIN: 2015-1822;
e-mail: mnatsakanyan08@mail.ru

ОБ АВТОРАХ

*** Ахмедзянова Дина Альфредовна;**

адрес: г. Москва, ул. Петровка, д. 24, стр. 1;
ORCID: 0000-0001-7705-9754;
eLibrary SPIN: 6983-5991;
e-mail: AkhmedzyanovaDA@zdrav.mos.ru

Юцевич Ольга Константиновна;

ORCID: 0000-0002-3860-9853;
e-mail: o.yutsevitch@yandex.ru

Решетников Роман Владимирович, канд. ф.-м. наук;

ORCID: 0000-0002-9661-0254;
eLibrary SPIN: 8592-0558;
e-mail: r.reshetnikov@npcmr.ru

Тащян Ольга Валерьевна, канд. мед. наук;

ORCID: 0000-0001-6759-6820;
eLibrary SPIN: 3658-1120;
e-mail: olgatash1@rambler.ru

Пирогов Сергей Сергеевич, д-р мед. наук;

ORCID: 0000-0002-8101-2155;
eLibrary SPIN: 7812-5502;
e-mail: pirogov@mail.ru

Мазурова Мария Павловна, канд. мед. наук;

ORCID: 0000-0002-4873-4455;
eLibrary SPIN: 4455-3055;
e-mail: mnioi_morphology@mail.ru

Волченко Надежда Николаевна, д-р мед. наук, профессор;

ORCID: 0000-0003-0421-4172;
e-mail: mnioi_morphology@mail.ru

Камалов Азиз Кураглиевич;

ORCID: 0000-0001-7376-6056;
eLibrary SPIN: 1671-1600;
e-mail: kak6768@mail.ru

Шумская Юлия Федоровна;

ORCID: 0000-0002-8521-4045;
eLibrary SPIN: 3164-5518;
e-mail: shumskayayf@zdrav.mos.ru

Мнацакян Марина Генриковна, д-р мед. наук, профессор;

ORCID: 0000-0001-9337-7453;
eLibrary SPIN: 2015-1822;
e-mail: mnatsakanyan08@mail.ru

* Corresponding author / Автор, ответственный за переписку

DOI: <https://doi.org/10.17816/DD568134>

Сложность дифференциальной диагностики карциноматоза и туберкулёза брюшины у молодой пациентки с асцитом: описание случая

Т.С. Нефедова¹, Ю.Ф. Шумская², М.В. Юраж¹, А.С. Панферов¹, П.В. Сенчихин^{1,3}, А.Е. Грабарник⁴, И.О. Щекотуров¹, М.Г. Мнацаканян¹

¹ Первый Московский государственный медицинский университет имени И.М. Сеченова, Москва, Российская Федерация;

² Научно-практический клинический центр диагностики и телемедицинских технологий, Москва, Российская Федерация;

³ Национальный медицинский исследовательский центр фтизиопульмонологии и инфекционных заболеваний, Москва, Российская Федерация;

⁴ Московский городской научно-практический центр борьбы с туберкулёзом, Москва, Российская Федерация;

АННОТАЦИЯ

Сложность дифференциальной диагностики между туберкулёзом брюшины и карциноматозом брюшины заключается в схожести клинической картины, а также данных лабораторных и инструментальных методов обследования. Туберкулёз брюшины, так же, как и карциноматоз брюшины, может сопровождаться развитием асцита, конгломератов лимфоузлов и петель кишечника.

В статье описано клиническое наблюдение молодой пациентки, которая после вторых родов отметила появление интенсивных болей в шее, между лопатками. В дальнейшем, через два месяца с начала симптомов, пациентка перенесла пневмонию с положительным ответом на антибактериальную терапию. Ещё через два месяца она впервые отметила появление рецидивирующего асцита и гастроинтестинальной симптоматики. При обследовании были выявлены изменения яичников и признаки карциноматоза брюшины, а также очаги в лёгких. Однако нетипичная для карциноматоза брюшины клиническая картина и специфическое поражение лёгких позволили заподозрить туберкулёз множественных локализаций. Диагноз был подтверждён по данным лапароскопии с биопсией поражённых тканей и последующим гистологическим и лабораторным подтверждением этиологической роли *Mycobacterium tuberculosis*. Описанный случай показывает важность использования всех доступных методов диагностики в установлении причин асцита у молодых пациенток для дифференциальной диагностики между специфической и неопластической этиологией.

Ключевые слова: туберкулёз множественных локализаций; абдоминальный туберкулёз; туберкулёз органов брюшной полости; карциноматоз брюшины; асцит; описание случая.

Как цитировать:

Нефедова Т.С., Шумская Ю.Ф., Юраж М.В., Панферов А.С., Сенчихин П.В., Грабарник А.Е., Щекотуров И.О., Мнацаканян М.Г. Сложность дифференциальной диагностики карциноматоза и туберкулёза брюшины у молодой пациентки с асцитом: описание случая // Digital Diagnostics. 2023. Т. 4, № 4. С. 643–652. DOI: <https://doi.org/10.17816/DD568134>

DOI: <https://doi.org/10.17816/DD568134>

Difficulty in the differential diagnosis of peritoneal carcinomatosis and tuberculosis in a young female patient with ascites: a case report

Tamara S. Nefedova¹, Yuliya F. Shumskaya², Marta V. Yurazh¹, Alexandr S. Panferov¹, Pavel V. Senchikhin^{1,3}, Alexei E. Grabarnik⁴, Igor O. Shchekoturov¹, Marina G. Mnatsakanyan¹

¹ The First Sechenov Moscow State Medical University, Moscow, Russian Federation;

² Research and Practical Clinical Center for Diagnostics and Telemedicine Technologies, Moscow, Russian Federation;

³ National Medical Research Center for Phthisiopulmonology and Infectious Diseases, Moscow, Russian Federation;

⁴ Moscow Scientific and Clinical Center for Tuberculosis Control, Moscow, Russian Federation;

ABSTRACT

The differential diagnosis between peritoneal tuberculosis and peritoneal carcinomatosis is quite challenging because of the similarity of the clinical picture and laboratory and instrumental examination data. Peritoneal tuberculosis and peritoneal carcinomatosis may present with the development of ascites, lymph nodes, and intestinal loop conglomerates. This article presents the clinical case of a young patient who, after her second childbirth, noted the appearance of intense pain in the neck and between the scapulae. Two months later, she experienced pneumonia with a positive reaction to antibiotic therapy. After another 2 months, she experienced recurrent ascites and gastrointestinal symptoms for the first time. The examination revealed ovarian masses and signs of peritoneal carcinomatosis and lung nodules. However, the clinical presentation was atypical for peritoneal carcinomatosis, and lung lesions were suspicious for tuberculosis, which allowed us to hypothesize the presence of tuberculosis of multiple localizations. The diagnosis was confirmed by laparoscopy with a biopsy of the involved tissues and subsequent histological and laboratory confirmation of the etiological role of *Mycobacterium tuberculosis*. The described case demonstrates the importance of using all available diagnostic methods to establish the causes of ascites in young female patients for differential diagnosis between specific and neoplastic etiologies.

Keywords: tuberculosis of multiple localizations; peritoneal tuberculosis; tuberculosis of abdominal organs; peritoneal carcinomatosis; ascites; case report.

To cite this article:

Nefedova TS, Shumskaya YuF, Yurazh MV, Panferov AS, Senchikhin PV, Grabarnik AE, Shchekoturov IO, Mnatsakanyan MG. Difficulty in the differential diagnosis of peritoneal carcinomatosis and tuberculosis in a young female patient with ascites: a case report. *Digital Diagnostics*. 2023;4(4):643–652. DOI: <https://doi.org/10.17816/DD568134>

Received: 08.08.2023

Accepted: 07.11.2023

Published online: 16.11.2023

DOI: <https://doi.org/10.17816/DD568134>

一名年轻腹水患者腹膜转移癌和腹部结核的鉴别诊断难题：病例介绍

Tamara S. Nefedova¹, Yuliya F. Shumskaya², Marta V. Yurazh¹, Alexandr S. Panferov¹, Pavel V. Senchikhin^{1,3}, Alexei E. Grabarnik⁴, Igor O. Shchekoturov¹, Marina G. Mnatsakanyan¹

¹ The First Sechenov Moscow State Medical University, Moscow, Russian Federation;

² Research and Practical Clinical Center for Diagnostics and Telemedicine Technologies, Moscow, Russian Federation;

³ National Medical Research Center for Phthisiopulmonology and Infectious Diseases, Moscow, Russian Federation;

⁴ Moscow Scientific and Clinical Center for Tuberculosis Control, Moscow, Russian Federation;

简评

腹部结核和腹膜转移癌的鉴别诊断难点在于临床表现、实验室和仪器检查方法的数据的相似性。腹腔结核和腹膜转移癌都可能伴有腹水、淋巴聚集体和肠襻的形成。

文章描述了对一名年轻患者的临床观察。第二次分娩后，患者发现了肩胛骨之间的颈部出现剧烈疼痛。随后，在出现症状两个月后，患者患上了肺炎，并对抗生素治疗产生了积极反应。两个月后，她首次发现了反复腹水和胃肠道症状。检查发现了卵巢病变、腹膜转移癌征候以及肺部病灶。然而，腹膜转移癌的临床表现并不典型，而且肺部有特殊病变，因此怀疑是多部位结核。通过腹腔镜检查和受影响组织的活检，以及随后的组织学和实验室检查，确诊为 *Mycobacterium tuberculosis*。

该病例表明，在确定年轻女性患者腹水的病因时，必须使用所有可用的诊断方法，以便对特异性病因和肿瘤性病因进行鉴别诊断。

关键词：多部位结核；腹部结核；腹腔结核；腹膜转移癌；腹水；病例介绍。

引用本文：

Nefedova TS, Shumskaya YuF, Yurazh MV, Panferov AS, Senchikhin PV, Grabarnik AE, Shchekoturov IO, Mnatsakanyan MG. 一名年轻腹水患者腹膜转移癌和腹部结核的鉴别诊断难题：病例介绍. *Digital Diagnostics*. 2023;4(4):643–652. DOI: <https://doi.org/10.17816/DD568134>

收到: 08.08.2023

接受: 07.11.2023

发布日期: 16.11.2023

BACKGROUND

Abdominal tuberculosis (TB) affects the liver, spleen, large and small intestines, intra-abdominal lymph nodes, pelvic organs, and peritoneum [1]. Peritoneal TB may manifest as ascites, conglomeration of lymph nodes and intestinal loops, and high levels of cancer antigen (CA)-125, which requires differential diagnosis with peritoneal carcinomatosis because of the progression of ovarian cancer, particularly in routine clinical practice [2, 3]. The situation is further complicated by the lack of a noninvasive “gold standard” for diagnosing tuberculous peritonitis [4].

Herein, the case of a 21-year-old woman with multifocal TB, with recurrent ascites as a leading clinical manifestation, was presented. The case description was prepared in accordance with the CAse REports guidelines [5].

CASE REPORT

In January 2021, a 21-year-old female patient (born and living in Dagestan) presented to a gastroenterologist with the following complaints:

- Abdominal enlargement
- Hypogastric pain predominantly on the right side radiating to the right lower extremity
- Diarrhea occurring up to 3 times per day without abnormal admixtures
- Decreased appetite
- Exertional dyspnea
- General weakness

Case History

In February 2020, 2 days after the second delivery, the patient experienced pain in her left neck, shoulder, and scapula, including at night. However, she did not seek medical attention.

In April 2020, the patient experienced pain in the right chest and right hypochondrium with a fever up to 39°C. A local outpatient chest X-ray imaging revealed right-sided multifocal pneumonia complicated by pleurisy. Antibacterial therapy (meropenem and azithromycin) was initiated with a positive clinical effect. Because of the positive clinical response, lung changes were interpreted by the local healthcare professionals as community-acquired nonspecific bacterial pneumonia.

Since June 2020, the patient noticed an increase in abdominal volume with decreased appetite. Abdominal ultrasonography showed a moderate amount of free fluid. Spironolactone 50 mg/day was ineffective, and the abdominal volume continued to increase.

In September 2020, an abdominal tap was performed at a local inpatient hospital. Approximately 500 mL of light fluid was obtained; however, it was not tested.

In December 2020, ascites had increased again. Blood tests showed a high C-reactive protein (CRP) level of 28.4

(reference, <5) mg/L and a high erythrocyte sedimentation rate (ESR) of 48 (reference, <20) mm/h, with leukopenia of up to 3 (reference, 4–9) mln/ μ L. Computed tomography (CT) of the chest and abdomen revealed bilateral multifocal pulmonary inflammation, hepatosplenomegaly, ascites, a conglomerate of large- and small-bowel loops in the left abdomen, and retroperitoneal lymphadenopathy. Pelvic ultrasonography showed an enlarged left ovary with cystic transformation and a large amount of pelvic fluid. A puncture of the rectouterine pouch yielded 1100 mL of straw-colored fluid. Cytology revealed focal accumulations of neutrophils, rare lymphocytes, and mesotheliocytes on a structureless substance background. No microflora growth was observed in the culture. Treatment included amoxicillin + clavulanic acid 875/125 mg twice daily and spironolactone 100 mg/day. After the initiation of therapy, the patient had diarrhea up to 5–7 times per day. A stool test for *Clostridium difficile* toxins A and B was negative.

In January 2021, the patient consulted a gastroenterologist with the abovementioned complaints and was admitted to the Gastroenterology Department of the Sechenov University Clinical Hospital.

Physical, Laboratory, and Instrumental Data

CRP and ESR remained unchanged in the presence of leukopenia. Esophagogastroduodenoscopy revealed no abnormalities. Colonoscopy revealed intact mucosa. Biopsies showed no microscopic changes in the colon or ileum.

CT of the lungs showed the following:

- In segments I, II, and VI: “tree-and-bud” structures and peribronchial lesions up to 8 mm in size with a tendency to merge.
- In the apex of the left lung: an irregularly shaped subpleural consolidation zone of 15 × 11 mm,
- Mediastinal lymphadenopathy of up to 12 mm (Figure 1).

Pelvic ultrasonography findings were as follows:

- The contours of both ovaries were uneven because of small echogenic round masses with relatively clear and uniform contours (up to 3 mm diameter, no blood flow reported).
- Free pelvic fluid
- In the presence of free fluid bilaterally adjacent to the ovaries: echogenic elongated structures with a clear and relatively uniform contour, approximately 56 mm long and 15 mm thick, with visible changes in blood flow.

An abdominal CT with intravenous contrast was performed because of changes seen on previous examinations:

- A large amount of free liquid
- The mesentery and greater omentum were compressed and edematous, and lymph nodes up to 8 mm were visualized.
- The ovaries were not enlarged. They had an uneven contour and a heterogeneous structure (Figure 2).

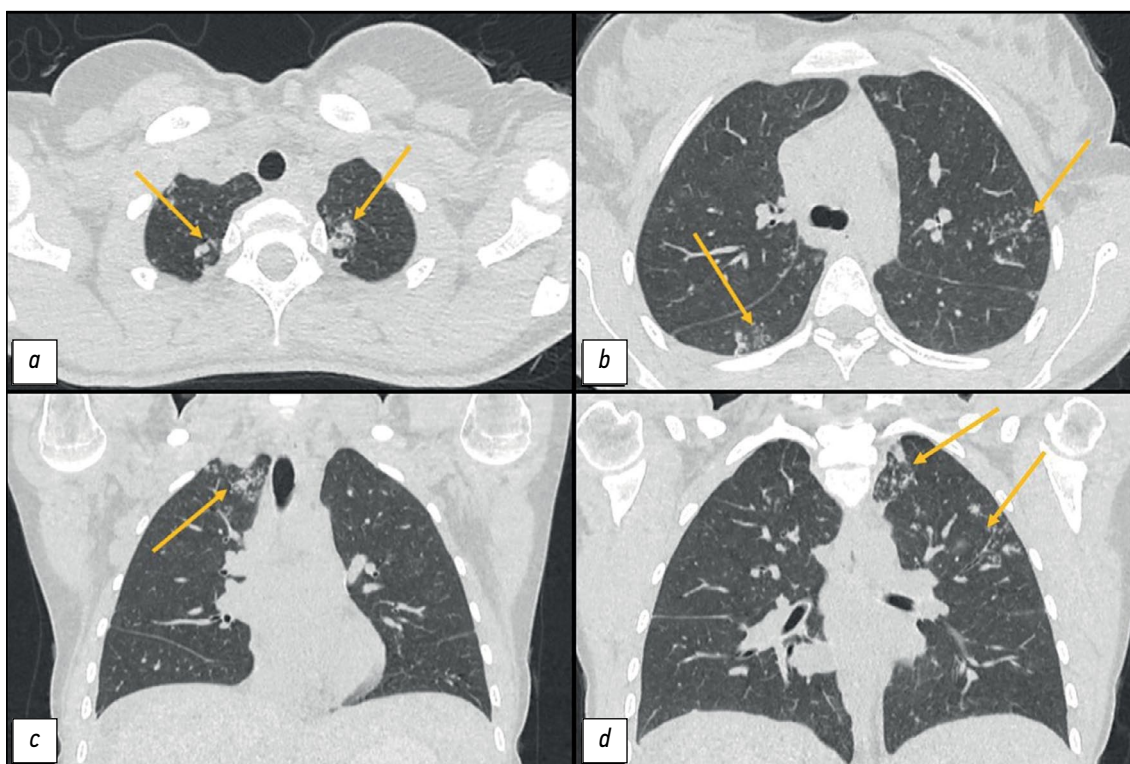


Fig. 1. Computed tomography of the chest: *a, d*, axial plane; *b, c*, coronal plane. The arrows indicate the peribronchial lesions and areas of consolidation in the lung apices.

The patient also had a consultation with a gynecologist. The serum CA-125 level was 268 (reference, <35) IU/mL. However, the angiotensin-converting enzyme activity and levels of carcinoembryonic antigen, β -subunit of human chorionic gonadotropin, and tumor marker HE4 were within the reference ranges.

Given the history of conglomerate small and large bowel loops and intestinal symptoms, magnetic resonance (MR) enterography was performed, which showed circular homogeneous thickening of the wall and narrowing of the lumen of the first parts of the small intestine to 12 mm over approximately 50 cm with increased contrast enhancement. A “pie-shaped” infiltration of the greater omentum and a large amount of free fluid in the abdominal cavity was observed (Figure 3).

A TB specialist suggested that the patient had peritonitis and a pulmonary inflammatory process. Repeat abdominal puncture revealed a clear fluid with a predominance of lymphocytes, 58

g/L of protein, 200 mmol/L of glucose, and a serum ascitic albumin gradient of 9.6 g/L. Acid-fast mycobacteria were not detected. However, polymerase chain reaction revealed the DNA of *Mycobacterium tuberculosis* (MBT).

The patient was further evaluated at a specialized clinic. Positive T-SPOT.TB and ascitic fluid test results were obtained. Diagnostic laparoscopy revealed disseminated lesions of the parietal and visceral peritoneum and infiltrative lesions of the fallopian tubes. Ziehl–Neelsen staining of biopsy specimens from the peritoneum and fallopian tubes did not reveal acid-fast mycobacteria or MBT complex DNA. On histological examination, all the materials consisted of fragments of granulation tissue with many macrophage–epithelioid giant–cell granulomas, some with areas of caseous necrosis.

Diagnosis

Based on the examination data, the patient was diagnosed with “multifocal tuberculosis: disseminated pulmonary

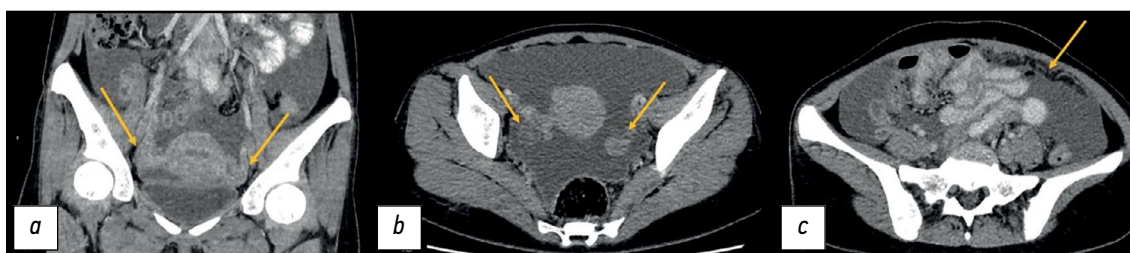


Fig. 2. Contrast-enhanced computed tomography of the abdomen and pelvis: *a*, coronal plane; *b, c*, axial plane. The arrows indicate (*a, b*) the ovaries with a heterogeneous structure and uneven contours and (*c*) infiltration and swelling of the greater omentum.

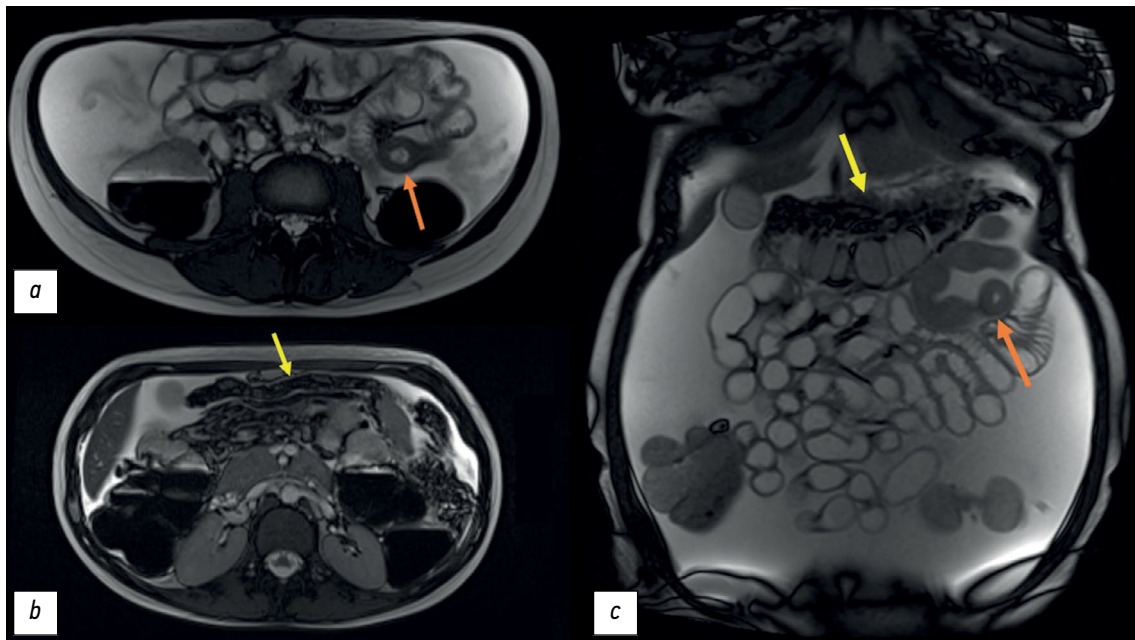


Fig. 3. Magnetic resonance imaging, T2-weighted images: *a, b*, axial plane; *c*, coronal plane. The orange arrow indicates the thickened wall of the jejunum. The yellow arrow indicates the compressed and thickened greater omentum.

tuberculosis in the infiltration phase, MBT (-); tuberculosis of the intrathoracic lymph nodes in the infiltration phase; peritoneal tuberculosis, active phase, MBT(-), MBT DNA(+); tuberculous salpingo-oophoritis, active phase, MBT (-); tuberculosis of the intra-abdominal lymph nodes in the infiltration phase. Ascites.”

Treatment

Based on clinical guidelines, the treatment was as follows:

- Meropenem 1.0 g three times daily IV
- Isoniazid 10% 5.0 mL IV
- Moxifloxacin 0.4 g IV
- Rifampicin 0.45 g PO
- Pyrazinamide 1.5 g

The above treatment was supplemented with hepatoprotective and detoxifying therapy.

Follow-up and Outcomes

During treatment, positive changes were noted: the pain syndrome was relieved, and the ascites was completely resolved. The patient was discharged for follow-up by a local TB specialist. Six months later, with specific therapy, the patient's condition was satisfactory, stable normothermia was reported, she had no pain, and ascites did not recur.

DISCUSSION

Diagnosis of peritoneal TB is difficult because of the nonspecific presentation and lack of relevant diagnostic markers. A primary peritoneal TB is extremely rare. Therefore, signs of specific lesions in the most common sites, particularly the lungs, should be excluded. Peritoneal

contamination is possible from primary lesions in the intestine or fallopian tubes, and in this case, the lung tissue would be intact [6].

In this case, whether the primary lesion was the lung or the small intestine, which was involved according to MR enterography, was unclear.

The present TB course is characterized by a tendency to generalize and an increased incidence of exudative forms. As in our case, high CA-125 levels make the differential diagnosis of cancer difficult. I.H. Chen et al. reported that the CA-125 level increase in TB is 3–5 times lower than that in malignant ovarian tumors [7]. However, other authors reported an increase in CA-125 of up to 18,554 U/mL [8].

Peritoneal TB is characterized by recurrent ascites, although adhesive and caseous necrosis is possible. The examination of the ascitic fluid revealed pleocytosis caused by lymphocytosis and a high protein concentration with a serum ascitic albumin gradient of <11 g/L, which was also reported in our case. Many foreign studies have confirmed the high diagnostic value of determining adenosine deaminase in ascitic fluid [9]; however, this technique is not widely used at present. Among laboratory methods, interferon-gamma release assays (IGRAs) have the greatest diagnostic value for peritoneal TB, with a sensitivity of 91.18%, specificity of 83.33%, and accuracy of 90% [10]. Initially, IGRAs were specifically designed to replace tuberculin tests in the diagnosis of latent TB and were not intended for diagnosing active TB, which can only be determined by microbiological tests. However, EL-Deeb et al. showed a high specificity of this method in diagnosing the active form of TB and advantages in diagnosing the latent form in high-risk groups; however, this issue requires further research [10]. In our case, the results of the T-SPOT.

TB tests of both blood and ascitic fluid were positive while the TB process was active.

Radiological methods play an important role in the differential diagnosis of TB and peritoneal carcinomatosis. RV Ramanan and V. Venu described the CT sign of “omental cake” (radiologically detected diffuse infiltration of the omentum). According to the authors, it helps in differentiating between these conditions [11]. However, other authors have pointed out the insufficient diagnostic value of radiological methods in such a clinical setting. For example, J. Kattan et al. reported that when CT and MRI suggested peritoneal carcinomatosis, laparoscopy and biopsy confirmed the TB origin of the lesion [12]. In abdominal TB, wall thickening predominated in the terminal ileum and cecum [13]. In our case, MR enterography of the abdomen showed a homogeneous, actively contrast-enhancing, stenotic thickening of the proximal small intestine, infiltration of the omentum, and small peritoneal lesions, suggesting miliary dissemination (see Figure 1).

The “gold standard” for diagnosing peritoneal TB is laparoscopy, followed by the histological examination of intraoperative biopsy specimens. The diagnosis was confirmed by the visualization of the miliary lesion and detection of specific granulomas with caseous necrosis [14]. Note that B. Huang et al. reported the lack of advantages of laparoscopy as an independent diagnostic method over a combination of laboratory tests (CA-125, T-SPOT.TB, and ESR) [15].

CONCLUSION

The differential diagnosis between TB and peritoneal carcinomatosis requires the use of all available techniques because of the similarity of the clinical manifestations of the diseases. Peritoneal TB should be considered one of the

possible etiologic causes of ascites, including in women with peritoneal abnormalities and high CA-125 levels, even when the clinical picture suggests a malignant ovarian tumor with carcinomatosis.

ADDITIONAL INFORMATION

Funding source. This article was prepared by a group of authors as a part of the research and development effort titled “Opportunistic screening of high-profile and other common diseases,” No. 123031400009-1, (USIS No. 123031400009-1) in accordance with the Order No. 1196 dated December 21, 2022 “On approval of state assignments funded by means of allocations from the budget of the city of Moscow to the state budgetary (autonomous) institutions subordinate to the Moscow Health Care Department, for 2023 and the planned period of 2024 and 2025” issued by the Moscow Health Care Department.

Competing interests. The authors declare that they have no competing interests.

Authors’ contribution. All authors made a substantial contribution to the conception of the work, acquisition, analysis, interpretation of data for the work, drafting and revising the work, final approval of the version to be published and agree to be accountable for all aspects of the work. The major contributions are distributed as follows: T.S. Nefedova, Yu.F. Shumskaya — concept, collection and processing of data, data analysis, manuscript writing; P.V. Senchikhin, M.V. Yurazh — collection and processing of data, manuscript writing; A.S. Panferov — concept, manuscript editing; I.O. Shchekoturov — manuscript editing, preparation of illustrative material; A.E. Grabarnik, M.G. Mnatsakanyan — final editing, manuscript approval.

Consent for publication. Written consent was obtained from the patient for publication of relevant medical information and all of accompanying images within the manuscript in Digital Diagnostics Journal.

REFERENCES

1. Hopewell PC, Jasmer RM. Overview of clinical tuberculosis. In: *Tuberculosis and the tubercle bacillus*. 2004:13–31. doi: 10.1128/9781555817657.ch2
2. Oge T, Ozalp SS, Yalcin OT, et al. Peritoneal tuberculosis mimicking ovarian cancer. *European Journal of Obstetrics & Gynecology and Reproductive Biology*. 2012;162(1):105–108. doi: 10.1016/j.ejogrb.2012.02.010
3. Nissim O, Ervin FR, Dorman SE, Jandhyala D. A Case of Peritoneal Tuberculosis Mimicking Ovarian Cancer in a Young Female. *Case Reports in Obstetrics and Gynecology*. 2022;2022. doi: 10.1155/2022/4687139
4. Zhou XX, Liu Y-L, Zhai K, Shi H-Z, Tonga Z-H. Body fluid interferon- γ release assay for diagnosis of extrapulmonary tuberculosis in adults: a systematic review and meta-analysis. *Scientific Reports*. 2015;5(1):15284. doi: 10.1038/srep15284
5. Barber MS, Aronson JK, von Schoen-Angerer T, et al. CARE guidelines for case reports: explanation and elaboration document. Translation into Russian. *Digital Diagnostics*. 2022;3(1):16–42. doi: 10.17816/DD105291
6. Gudu W. Isolated ovarian tuberculosis in an Immuno-competent woman in the post partum period: case report. *Journal of Ovarian Research*. 2018;11:1–4. doi: 10.1186/s13048-018-0472-2
7. Chen IH, Torng P-L, Lee C-Y, et al. Diagnosis of peritoneal tuberculosis from primary peritoneal cancer. *International Journal of Environmental Research and Public Health*. 2021;18(19):10407. doi: 10.3390/ijerph181910407
8. Maheshwari A, Gupta S, Rai S, et al. Clinical and laboratory characteristics of patients with peritoneal tuberculosis mimicking advanced ovarian cancer. *South Asian Journal of Cancer*. 2021;10(2):102–106. doi: 10.1055/s-0041-1736030
9. Zhou R, Qiu X, Ying J, et al. Diagnostic performance of adenosine deaminase for abdominal tuberculosis: A systematic review and meta-analysis. *Frontiers in Public Health*. 2022;10:938544. doi: 10.3389/fpubh.2022.938544
10. EL-Deeb M, Malwany HEL, Khalil Y, Mourad S, et al. Interferon Gamma Release Assays (IGRA) in the Diagnosis of Active Pulmonary Tuberculosis. *Journal of High Institute of Public Health*. 2014;44(1):33–40. doi: 10.21608/JHIPH.2014.20355

11. Ramanan RV, Venu V. Differentiation of peritoneal tuberculosis from peritoneal carcinomatosis by the Omental Rim sign. A new sign on contrast enhanced multidetector computed tomography. *European Journal of Radiology*. 2019;113:124–134. doi: 10.1016/j.ejrad.2019.02.019
12. Kattan J, Haddad FGh, Menassa-Moussa L, et al. Peritoneal tuberculosis: A forsaken yet misleading diagnosis. *Case Reports in Oncological Medicine*. 2019;2019. doi: 10.1155/2019/5357049
13. Debi U, Ravisankar V, Prasad KK, et al. Abdominal tuberculosis of the gastrointestinal tract: revisited.

- World Journal of Gastroenterology*. 2014;20(40):14831. doi: 10.3748/wjg.v20.i40.14831
14. Purbadi S, Indarti J, Winarto H, et al. Peritoneal tuberculosis mimicking advanced ovarian cancer case report: Laparoscopy as diagnostic modality. *International Journal of Surgery Case Reports*. 2021;88:106495. doi: 10.1016/j.ijscr.2021.106495
15. Huang B, Cui DJ, Ren Y, et al. Comparison between laparoscopy and laboratory tests for the diagnosis of tuberculous peritonitis. *Turkish journal of medical sciences*. 2018;48(4):711–715. doi: 10.3906/sag-1512-147

СПИСОК ЛИТЕРАТУРЫ

1. Hopewell P.C., Jasmer R.M. Overview of clinical tuberculosis. In: *Tuberculosis and the tubercle bacillus*. 2004. P. 13–31. doi: 10.1128/9781555817657.ch2
2. Oge T., Ozaalp S.S., Yalcin O.T., et al. Peritoneal tuberculosis mimicking ovarian cancer // *European Journal of Obstetrics & Gynecology and Reproductive Biology*. 2012. Vol. 162, N 1. C. 105–108. doi: 10.1016/j.ejogrb.2012.02.010
3. Nissim O., Ervin F.R., Dorman S.E., Jandhyala D. A Case of Peritoneal Tuberculosis Mimicking Ovarian Cancer in a Young Female // *Case Reports in Obstetrics and Gynecology*. 2022. Vol. 2022. doi: 10.1155/2022/4687139
4. Zhou X.X., Liu Y.-L., Zhai K., Shi H.-Z., Tonga Z.-H. Body fluid interferon- γ release assay for diagnosis of extrapulmonary tuberculosis in adults: a systematic review and meta-analysis // *Scientific Reports*. 2015. Vol. 5, N 1. P. 15284. doi: 10.1038/srep15284
5. Barber M.S., Aronson J.K., von Schoen-Angerer T., и др. Рекомендации CARE для описания случаев: разъяснения и уточнения // *Digital Diagnostics*. 2022. Т. 3, № 1. С. 16–42. doi: 10.17816/DD105291
6. Gudu W. Isolated ovarian tuberculosis in an Immuno-competent woman in the post partum period: case report // *Journal of Ovarian Research*. 2018. Vol. 11. P. 1–4. doi: 10.1186/s13048-018-0472-2
7. Chen I.H., Torng P.-L., Lee C.-Y., et al. Diagnosis of peritoneal tuberculosis from primary peritoneal cancer // *International Journal of Environmental Research and Public Health*. 2021. Vol. 18, N 19. P. 10407. doi: 10.3390/ijerph181910407
8. Maheshwari A., Gupta S., Rai S., et al. Clinical and laboratory characteristics of patients with peritoneal tuberculosis mimicking advanced ovarian cancer // *South*

- Asian Journal of Cancer*. 2021. Vol. 10, N 2. P. 102–106. doi: 10.1055/s-0041-1736030
9. Zhou R., Qiu X., Ying J., et al. Diagnostic performance of adenosine deaminase for abdominal tuberculosis: A systematic review and meta-analysis // *Frontiers in Public Health*. 2022. Vol. 10. P. 938544. doi: 10.3389/fpubh.2022.938544
10. EL-Deeb M., Malwany H.E.L., Khalil Y., Mourad S., et al. Interferon Gamma Release Assays (IGRA) in the Diagnosis of Active Pulmonary Tuberculosis // *Journal of High Institute of Public Health*. 2014. Vol. 44, N 1. P. 33–40. doi: 10.21608/JHIPH.2014.20355
11. Ramanan R.V., Venu V. Differentiation of peritoneal tuberculosis from peritoneal carcinomatosis by the Omental Rim sign. A new sign on contrast enhanced multidetector computed tomography // *European Journal of Radiology*. 2019. Vol. 113. P. 124–134. doi: 10.1016/j.ejrad.2019.02.019
12. Kattan J., Haddad F.Gh., Menassa-Moussa L., et al. Peritoneal tuberculosis: A forsaken yet misleading diagnosis // *Case Reports in Oncological Medicine*. 2019. Vol. 2019. doi: 10.1155/2019/5357049
13. Debi U., Ravisankar V., Prasad K.K., et al. Abdominal tuberculosis of the gastrointestinal tract: revisited // *World Journal of Gastroenterology*. 2014. Vol. 20, N 40. P. 14831. doi: 10.3748/wjg.v20.i40.14831
14. Purbadi S., Indarti J., Winarto H., et al. Peritoneal tuberculosis mimicking advanced ovarian cancer case report: Laparoscopy as diagnostic modality // *International Journal of Surgery Case Reports*. 2021. Vol. 88. P. 106495. doi: 10.1016/j.ijscr.2021.106495
15. Huang B., Cui D.J., Ren Y., et al. Comparison between laparoscopy and laboratory tests for the diagnosis of tuberculous peritonitis // *Turkish journal of medical sciences*. 2018. Vol. 48, N 4. P. 711–715. doi: 10.3906/sag-1512-147

AUTHORS' INFO

* Yuliya F. Shumskaya;
address: 24/1 Petrovka street, 127051, Moscow, Russia;
ORCID: 0000-0002-8521-4045;
eLibrary SPIN: 3164-5518;
e-mail: shumskayayf@zdrav.mos.ru

ОБ АВТОРАХ

* Шумская Юлия Фёдоровна;
адрес: Россия, 127051, Москва, ул.Петровка, д.24, стр. 1;
ORCID: 0000-0002-8521-4045;
eLibrary SPIN: 3164-5518;
e-mail: shumskayayf@zdrav.mos.ru

* Corresponding author / Автор, ответственный за переписку

Tamara S. Nefedova, MD;
ORCID: 0000-0002-6718-8701;
eLibrary SPIN: 3097-4977;
e-mail: prosto.toma.22@gmail.com

Marta V. Yurazh, MD;
ORCID: 0000-0001-6759-6820;
eLibrary SPIN: 4872-7130;
e-mail: yurazh_m_v@staff.sechenov.ru

Alexandr S. Panferov, MD, Cand. Sci. (Med.), Assistant Professor;
ORCID: 0000-0002-4324-7615;
eLibrary SPIN: 5747-9842;
e-mail: panferov_a_s@staff.sechenov.ru

Pavel V. Senchikhin, MD, Cand. Sci. (Med.);
ORCID: 0000-0003-0496-4504;
eLibrary SPIN: 8293-6144;
e-mail: paulus200271@mail.ru

Alexei E. Grabarnik, MD, Cand. Sci. (Med.);
ORCID: 0009-0009-4885-3321;
eLibrary SPIN: 5923-8630;
e-mail: a.grabarnik@mail.ru

Igor O. Shchekoturov, MD, Cand. Sci. (Med.);
ORCID: 0000-0002-2167-8908;
eLibrary SPIN: 6885-6834;
e-mail: samaramail@bk.ru

Marina G. Mnatsakanyan, MD, Dr. Sci. (Med.), Professor;
ORCID: 0000-0001-9337-7453;
eLibrary SPIN: 2015-1822;
e-mail: mnatsakanyan08@mail.ru

Нефедова Тамара Сергеевна;
ORCID: 0000-0002-6718-8701;
eLibrary SPIN: 3097-4977;
e-mail: prosto.toma.22@gmail.com

Юразь Марта Валериевна;
ORCID: 0000-0001-6759-6820;
eLibrary SPIN: 4872-7130;
e-mail: yurazh_m_v@staff.sechenov.ru

Панферов Александр Сергеевич, канд. мед. наук, доцент;
ORCID: 0000-0002-4324-7615;
eLibrary SPIN: 5747-9842;
e-mail: panferov_a_s@staff.sechenov.ru

Сенчихин Павел Владимирович, канд. мед. наук,
ORCID: 0000-0003-0496-4504;
eLibrary SPIN: 8293-6144;
e-mail: paulus200271@mail.ru

Грaбарник Алексей Ефимович, канд. мед. наук;
ORCID: 0009-0009-4885-3321;
eLibrary SPIN: 5923-8630;
e-mail: a.grabarnik@mail.ru

Щекотуров Игорь Олегович, канд. мед. наук;
ORCID: 0000-0002-2167-8908;
eLibrary SPIN: 6885-6834;
e-mail: samaramail@bk.ru

Мнацакaнян Марина Генриковна, д-р мед. наук, профессор;
ORCID: 0000-0001-9337-7453;
eLibrary SPIN: 2015-1822;
e-mail: mnatsakanyan08@mail.ru